5-2017

Development of a Multiband Remote Sensing System for Determination of Unsaturated Soil Properties

Cyrus D. Garner
University of Arkansas, Fayetteville

Development of a Multiband Remote Sensing System for Determination of Unsaturated Soil Properties

A dissertation submitted in partial fulfillment
of the requirements for the degree of
Doctor of Philosophy in Civil Engineering

by

Cyrus Garner
Northwestern University
Bachelor in Science in Civil Engineering, 2006
University of Arkansas
Master of Science in Civil Engineering, 2011

May 2017
University of Arkansas

This dissertation is approved for recommendation to the Graduate Council.

_____
Richard A. Coffman, Ph.D., P.E., P.L.S.
Thesis Director

_____
Michelle Bernhardt, Ph.D.
Committee Member

_____
Kristofor Brye, Ph.D.
Committee Member

_____
Norman Dennis, Jr., Ph.D., P.E.
Committee Member

_____
Jason Tullis, Ph.D.
Committee Member

ABSTRACT

A multiband system including active microwave sensing and visible-near infrared reflectance spectroscopy was developed to measure unsaturated soil properties in both field and laboratory environments. Remote measurements of soil volumetric water content (θ_v), soil water matric potential (ψ), and soil index properties (liquid limit [LL], plastic limit [PL], and clay fraction [CF]) were conducted. Field-based measurement of θ_v was conducted using a ground-based radar system and field measurements within 10 percentage points of measurements acquired with traditional sampling techniques were obtained. Laboratory-based, visible and near infrared spectroscopy was found to be capable of obtaining empirical, soil specific regression functions (partial least squares [PLS]) with coefficient of determination (R^2) values greater than 0.9 for the LL, PL, and CF. A silt sized granite material, a silt sized illite clay, and a silt sized kaolinite clay were optically characterized within the visible to near-infrared wavelength range and were found to have absorption coefficient values of 0.81 to 78.8cm^{-1}, 0.93 to 150.0cm^{-1}, and 0.12 to 4.02cm^{-1}, respectively.

Measurements of θ_v and ψ using an analytical solution based on the Kubelka-Munk color theory were found not to provide viable results. Soil water characteristic curves (SWCC) were fitted to both laboratory-obtained and remotely-sensed data between -10 and -1500kPa. θ_v for the laboratory-obtained SWCC (SWCC-L) and remotely-obtained SWCC (SWCC-R) for the granite silt were within 1 percentage points for ψ values less than -100kPa. The SWCC-L and SWCC-R values for the silt sized illite clay were within 2 percentage points for values of ψ greater than 400kPa. The SWCC-L and SWCC-R for the silt sized kaolinite clay were within 8 percentage points for all ψ values. For the Donna Fill and illite soil types ψ values within 150kPa of the applied pressure were obtained.

Specific contributions of this research project were the evaluation of remote and proximal (active microwave and diffuse reflectance spectroscopy) sensing techniques as a means of acquiring measurements of soil properties. Microwave measurements of field θ_v were demonstrated for ground based systems. Additional areas of research in both laboratory- and field-scale measurements of soil hydraulic and index properties are identified and discussed.

ACKNOWLEDGEMENTS

The author would like to offer his most heartfelt thanks to everyone who helped support him throughout his graduate studies. First and foremost, I would like to thank my wife, Diane, for her support and infinite patience for helping during the revision process and for putting up with the stress, late nights, and general panic. In many ways she has contributed as much to this process as I have and I doubt that I would have been able to complete this without her. I would like to thank the research committee for their time, support, and guidance from the beginning to the end of this research project. Finally, I would like my fellow graduate students for providing technical, academic, and emotional support. Specifically, I would like to thank, in no particular order, Sarah Bey, Johnathon Blanchard, Ali Boga, Deshinka Bostwick, Omar Conte, Eric Fernstrom, Elvis Ishimwe, Nabil Mahmood, Matt Nanak, Morgan Race, Sean Salazar, Matt Strasser, Tim Wank, and Yi Zhao.

TABLE OF CONTENTS

LIST OF FIGURES

LIST OF TABLES

LIST OF SYMBOLS AND ACRONYMS

A list of symbols and acronyms presented in this manuscript has been provided. Some of the included mathematical equations included in this manuscript use identical symbols to represent different quantities and variables. Where possible, equations obtained from the literature have been left in their original formulations for clarity. To determine which specific definition is applicable in a specific case, the definition of terms included with each equation should take precedence.

Symbol	Definition
A	Absorption
A	Antenna Area
a	Area of the Upstream Collection Basin
A	Empirical Coefficient in Stephen et al. (2010)
A	Empirical Coefficient in Topp et al. (1980) Equation
a	Fitting Parameter for Fredlund and Xing (1994)
a	Number of Acquired Spectra
A	Relative Absorption
A_∞	Infinite Depth Absorption
AASHTO	**A**merican **A**ssociation of **S**tate **H**ighway **T**ransportation **O**rganizations
A_{eff}	Effective Transmitter Area
ANSI	**A**merican **N**ational **S**tandards **I**nstitute
ASCII	**A**merican **S**tandard **C**ode for **I**nformation **I**nterchange
ASD	**A**nalytical **S**pectral **D**evices
ASTM	**A**merican **S**ociety for **T**esting **M**aterials
ATR	**A**ttenuated **T**otal **R**eflectance
B	Empirical Coefficient in Stephen et al. (2010)
B	Empirical Coefficient in Topp et al. (1980) Equation
b	Number of Wavelength Values in Each Spectra
BSI	**B**ritish **S**tandard **I**nstitute
c	Concentration of the Chemical Species
C	Empirical Coefficient in Stephen et al. (2010)
C	Empirical Coefficient in Topp et al. (1980) Equation
C	Gas Concentration
C	Solute Concentration
c_0	Speed of Light in A Vacuum

C-Band	Microwave Band (3.75-7.5cm)
CCD	**C**harged **C**oupled **D**evice
CF	**C**lay **F**raction
CGA	**C**ompressed **G**as **A**ssociation
CMH	**C**hilled **M**irror **H**ygrometer
CMU	**C**oncrete **M**asonry **U**nit
CSRC	**C**ato **S**prings **R**esearch **C**enter
d	Cone Penetration Depth
D	Empirical Coefficient in Stephen et al. (2010)
D	Empirical Coefficient in Topp et al. (1980) Equation
DEM	**D**igital **E**levation **M**odels
DIAL	**DI**fferential **A**bsorption **L**IDAR
DI-DA	**D**e-**A**ired, **D**e-**I**onized
DRIFT	**D**iffuse **R**eflectance **I**nfrared **F**ourier **T**ransform
DTM	**D**igital **T**errain **M**odel
e	Euler's Number
EM	**E**lectro**M**agnetic
EMSPE	**E**stimated **M**ean **S**quared **P**redictive **E**rror
ERS	**E**uropean **R**adar **S**atellite
F	Magnitude of the Electric Field at the Point Where τ is Evaluated
F	Vector Containing the Y-residual Values
$f(R_\infty)$	Kubelka-Munk Function
F_c	Sensor Calibration Factor
FCD	**F**all **C**one **D**evice
FFT	**F**ast **F**ourier **T**ransform
FTIR	**F**ourier **T**ransform **I**nfra**R**ed
G	Antenna Gain
GPRI-2	**G**amma **P**ortable **R**ADAR **I**nterferometer - **2**nd Generation
GRS	**G**amma **R**emote **S**ensing
G_s	Specific Gravity of Soil Solids
h	Absolute Surface Roughness
H	**H**orizontal
H_c	Capillary Term of Matrix Potential
HH	**H**orizontally Transmitted, **H**orizontally Received
HV	**H**orizontally Transmitted, **V**ertically Received
I	Empirical Function of Incidence Angle and Fresnel Reflection Coefficient
I	Received Intensity
i	Wegmuller (1997) Term
i subscript	Component Value

I_0	Incident Intensity
IEEE	**I**nstitute of **E**lectrical and **E**lectronic **E**ngineers
IEM	**I**ntegral **E**quations **M**ethod
IFOV	**I**nstantaneous **F**ield **O**f **V**iew
I_p	Plasticity Index
IR	**I**nfra**R**ed
JEC	**J**effery **E**nergy **C**enter
k	Absorption Coefficient
k	Wavelength
k	Wavenumber
k	Mass Absorption Coefficient
K_a	Apparent Dielectric Permittivity
k_a	Cone Factor (0.29)
KBr	Potassium-Bromide
KCl	Potassium-Chloride
k_{KBr}	Absorption Coefficient of the KBr Substrate
KM	Kubelka Munk
ks	Normalized Surface Roughness
k_{soil}	Soil Absorption Coefficient Values
k_t	Measured Absorption of the Mixed Sample
K_u-Band	Microwave Band (1.67-2.5cm)
k_x	$k\sin(\theta)$
KXNA	Drake Airfield
k_z	$k\cos(\theta)$
l	Empirical Path Length
L	Length of Unshielded Probe Head
L_a	Apparent Length of Unshielded Probe Head
L_a	Atmospheric Loss Factor
LAST	**L**aser **A**nalysis of **S**oil **T**ension
L-Band	Microwave Band (5-7.5mm)
LIDAR	**LI**ght **D**etection **A**nd **R**anging
LL	**L**iquid **L**imit
L_s	System Loss Factor
LWC	**L**ight **W**eight **C**oated
m	Mass Fraction
m	van Genuchten (1980) SWCC Fitting Parameter
MATLAB	**MA**trix **LAB**oratory Software and Programming Environment
MBTC	**M**ack-**B**lackwell **T**ransportation **C**enter

m_c	Mass of Cone
M_{can}	Mass of Can
M_{dry}	Mass of Dry Soil and Can
MIR	**M**iddle **I**nfra**R**ed
m_{KBr}	Mass Fraction of KBr Substrate
ML	Low Plasticity Silt
MLI	**M**ulti-**L**ook **I**ntensity
MNPT	**M**ale **N**ipple **P**ipe **T**hread
m_s	Backscatter Amplitude Containing Roughness Information
m_s	Soil Moisture Content
m_{soil}	Mass Fraction of Soil
m_v	Pixel Moisture Content
M_{water}	Mass of Water
M_{wet}	Mass of Wet Soil and Can
N	Empirical Coefficient in Stephen et al. (2010)
N_w	Number Density of Water
n	van Genuchten (1980) SWCC Fitting Parameter
N_0	Avogadro's Number ($6.0221409 \cdot 10^{23}$)
N_A	Gas Concentration
NDG	**N**uclear **D**ensity **G**auge
NDVI	**N**ormalized **D**ifference **V**egetation **I**ndex
NIR	**N**ear **I**nfra**R**ed
NOAA	**N**ational **O**ceanic and **A**tmospheric **A**dministration
OS-BAR	**O**ne **S**tationary **B**istatic **S**ynthetic **A**perture **R**adar
OST-R	**O**ffice of the Assistant **S**ecretary for **R**esearch and **T**echnology
p and q	Cross Polarization Ratios
P_0	Dipole Moment of Water (1.85 Debye)
PCR	**P**rinciple **C**omponents **R**egression
PGA	**P**istol **G**rip **A**ssembly
PI	**P**lasticity **I**ndex
PL	**P**lastic **L**imit
PLS	**P**artial **L**east **S**quares
PPE	**P**ressure **P**late **E**xtractor
P_r	**P**ower **R**eceived
primes	In Equation 2.43 Indicates Off-Peak Values
P_s	Soil Water Potential

P_t	Power Transmitted
PTFE	**P**oly**T**etra**F**luoro**E**thylene
PVC	**P**oly**V**inyl **C**hloride
QA/QC	**Q**uality **A**ssurance and **Q**uality **C**ontrol
R	Distance to Target
r	Equivalent Radius of the Tube
R	Ideal Gas Constant (8.3144598 $J \cdot K^{-1} \cdot mol^{-1}$)
R	Relative Reflection
R_0	Range
$R^0_{h/v}$	Fresnel Reflection Coefficient
R^2	Coefficient of Determination
R_∞	Infinite Depth Reflection
Radar	**RA**dio **D**etection and **R**anging
r_aMLI	Averaged rMLI
RFA	**R**adio **F**requency **A**ssembly
R_h	Fresnel Reflection Coefficient
RH	**R**elative **H**umidity
R^h_0	Fresnel Reflection Coefficient
rMLI	**r**esampled **MLI**
RMS	**R**oot-**M**ean **S**quared
RPM	**R**evolutions **P**er **M**inute
RSLC	**R**egistered (Resampled) **S**ingle **L**ook **C**omplex
rSLC	**R**esampled **SLC**
R_v	Fresnel Reflection Coefficient
R^v_0	Fresnel Reflection Coefficient
RX-1 V	**R**eceive Channel **1** - **V**ertically Polarized
RX-2 V	**R**eceive Channel **2** - **V**ertically Polarized
S	Bragg Scattering Matrix
S	Saturation
s	Scattering Coefficient
s	Surface Roughness
s subscript	Soil Phase of the System
SAR	**S**ynthetic **A**perture **R**adar
SEM	**S**canning **E**lectron **M**icroscope
S_{hh}	Bragg Scattering Coefficient - HH
S_{hv}	Bragg Scattering Coefficient - HV
SIMPLS	**S**tatistically **I**nspired **M**odification of the **P**artial **L**east **S**quares

s_{KBr}	Scattering Coefficient of the KBr Substrate
SL	**S**hrinkage **L**imit
SLC	**S**ingle **L**ook **C**omplex
SNR	**S**ignal-to-**N**oise **R**atio
SPM	**S**mall **P**erturbation **M**ethod
s_{soil}	Scattering Coefficient of Soil
S_u	Undrained Shear Strength
S_{vh}	Bragg Scattering Coefficient - VH
S_{vv}	Bragg Scattering Coefficient - VV
SWCC	**S**oil **W**ater **C**haracteristic **C**urve
SWCC-L	**S**oil **W**ater **C**haracteristic **C**urve - **L**aboratory Obtained
SWCC-R	**S**oil **W**ater **C**haracteristic **C**urve - **R**emotely Obtained
SWIR	**S**hort**W**ave **I**nfra**R**ed
T	Relative Transmission
T	Temperature
T	Transmittance
T_1	Temperature of Probe Head after 1 Second of Heating
T_{30}	Temperature of Probe Head after 30 Second of Heating
TAMU	**T**exas **A**gricultural and **M**echanical **U**niversity
tan(b)	Local Slope in Radians
TDR	**T**ime **D**omain **R**eflectometry
the i subscript	Individual Species
t_t	Travel Time
TWI	**T**opographic **W**etness **I**ndex
TX	**T**ransmit **C**hannel
TX-V	**T**ransmit **C**hannel - **V**ertically Polarized
UA	**U**niversity of **A**rkansas
UACNBMC	**U**niversity of **A**rkansas **C**enter for **N**ano-**B**io **M**aterial Characterization
UACSRC	**U**niversity of **A**rkansas **C**ato **S**prings **R**esearch **C**enter
UM	**U**niversity of **M**issouri
UMC	**U**niversity of **M**issouri at **C**olumbia
USB	**U**niversal **S**erial **B**us
USCS	**U**nified **S**oil **C**lassification **S**ystem
USDA	**U**nited **S**tates **D**epartment of **A**griculture
USDOT	**U**nited **S**tates **D**epartment of **T**ransportation
UV-Vis	**U**ltra-**V**iolet to **Vis**ible

V	Vertical
v subscript	Vapor Phase
VDC	**V**olts **D**irect **C**urrent
V_E	Excitation Voltage
Vis-NIR	**Vis**ible to **N**ear-**I**nfra**R**ed
Vis-NIR-DRY	**Vis**ible to **N**ear-**I**nfra**R**ed from Oven **Dry** Samples
Vis-NIR-Wet	**Vis**ible to **N**ear-**I**nfra**R**ed Spectra from **Wet** Samples
V_m	Measured (Signal) Voltage
V_T	Total Volume of the Soil Sample
V_{total}	Total Volume of Soil Sample
VV	**V**ertically Transmitted, **V**ertically Received
V_w	Molar Volume of Water (18.03 $mL \cdot mol^{-1}$)
w	Gravimetric Water Content ($g \cdot g^{-1}$)
W	Surface Roughness Spectrum
w subscript	Water Phase of the System
W_1	Weight of Cone Configuration 1
$W_{1,2}$	Weight of the Cone (80g or 30g)
W_2	Weight of Cone Configuration 2
w_{dry}	Weight of the Oven Dry Sample and the Tin
WJEC	**W**ESTAR **J**effery **E**nergy **C**enter
W_n	Frequency Domain of the nth Power of the Surface Correlation Function
w_{tin}	Empty Weight of the Sample Tin
w_{wet}	Weight of the Wet Sample and the Tin
X	Sum of Squared Error
XRD	**X**-**R**ay **D**iffraction
$X_{validation}$	Matrix Containing the Observed Reflectance Spectrum
Y_{pred}	Vector
α	Absorption Coefficient
α	Atmospheric Absorption Coefficient
α	van Genuchten (1980) SWCC Fitting Parameter
α	Molar Absorption Coefficient
β	Extinction Coefficient
β	van Genuchten (1980) SWCC Fitting Parameter
γ	Contact Angle Between Water and Soil
Γ^0	Fresnel Reflection Ratio at Nadir
γ_d	Dry Unit Weight
γ_w	Unit Weight of Water
Δ	Difference in Penetration Between W_1 and W_2
δ	Grazing Angle

Δ	Vertical Separation
$\Delta m_{v,0}$	Reference Pixel Moisture Content
ΔR	Range Resolution
$\Delta\sigma^0$	Change in Pixel Backscatter Coefficient
ε	Complex Dielectric Permittivity
ε	Dielectric Constant of Cable Shielding
ε'	Real Component of Dielectric Permittivity
ε''	Imaginary Component of Dielectric Permittivity
ε_a	Apparent Dielectric Constant of Soil
η	Porosity
η	System Optical Efficiency
θ	Angle of Incidence
θ	Incidence Angle
θ	Volumetric Water Content
θ_0	Reference Incident Angle
θ_r	Residual Volumetric Water Content
θ_s	Saturated Volumetric Water Content
θ_v	Volumetric Water Content
λ	Wavelength
μ	Magnetic Permeability of the Dielectric Material
μ_{NDVI}	Annual Mean in NDVI
μ_s	Annual Soil Moisture
ν	Velocity of Propagation Through the Shielded Cable
ν_p	Velocity Factor
ξ_3	3dB Azimuth Beamwidth
π	Mathematical Constant
Π	Osmotic Soil Water Potential
ρ	Surface Reflectance
ρ_b	Soil Bulk Density
ρ_{sat}	Saturation Water Vapor Density
ρ_w	Density of Water (998 kg·m3 at 293.15K)
σ	Atmospheric Absorption Coefficient
σ	Normalized Backscatter Coefficient
σ	Surface Tension of Fluid Relative to Air for Water
σ^0	Backscatter Coefficient
σ^0_0	Reference Pixel Backscatter Coefficient
σ^0_1	Backscatter Coefficient at Time 1
σ^0_2	Backscatter Coefficient at Time 2

σ^0_{Dry}	Pixel Backscatter Coefficient (at Reference Angle) when Soil is Dry
σ^0_{HH}	Backscatter Coefficient HH
σ^0_{HV}	Backscatter Coefficient - HV
σ^0_{qq}	Polarized (HH or VV) backscatter coefficient
σ^0_{VV}	Backscatter Coefficient - VV
σ^0_{VV}	Backscatter Coefficient VV
σ^0_{wet}	Pixel Backscatter Coefficient (at Reference Angle) at Saturation
$\sigma_{kh,\varepsilon}{}^{HH}$	Predicted HH Backscatter Coefficient
$\sigma_{kh,\varepsilon}{}^{VV}$	Predicted VV Backscatter Coefficient
$\sigma_M{}^{HH}$	Measured HH Backscatter Coefficient
$\sigma_M{}^{VV}$	Measured VV Backscatter Coefficient
τ	Electro-Kinetic Potential of Water in an Electric Field Near Soil Particle
ψ	Matric Potential
Ψ	Soil Water Potential
Ψ_0	Elevation Datum or Reference Correction for Soil Water Potential
ψ_b	Air Entry Pressure
ψ_m	Matric or Matrix Potential
Ψ_m	Matric or Matrix Soil Water Potential
Ψ_o	Osmotic Soil Water Potential
Ψ_p	Hydrostatic Soil Water Potential
Ψ_s	Gravitational Soil Water Potential
Ψ_T	Total Soil Water Potential
Ψ_π	Osmotic Soil Water Potential

LIST OF PUBLISHED OR SUBMITTED PAPERS

Chapter 5: Volumetric Water Content Obtained via Single Poliarization Change Detection Methodology at UACSRC. Previously submitted as: *Garner, C., Coffman, R., (2016). "Volumetric Water Content Measurements as Obtained from Remote Sensing and In-Situ Instrumentation." Journal of Environmental and Engineering Geophysics, Accepted for Publication, Manuscript Number 15-022R.*

Chapter 6: Field Volumetric Water Content and Dry Density as Obtained with Palarimetric Methods. Previously submitted as: *Garner, C., Coffman, R., (2017a). "Remotely Sensed Soil Volumetric Water Content and Dry Density as Obtained Utilizing Change Detection and Polarimetric Methods." Journal of Environmental and Engineering Geophysics, Submitted for Review.*

Chapter 7: Optical Absorption and Scattering Properties of Investigated Soils. Previously submitted as: *Garner, C., Coffman, R., (2017b). "Visible and Near-Infrared Diffuse Reflectance Properties of Geotechnical Reference Soils" Applied Clay Science. Submitted for Review.*

Chapter 8: Evaluation of Visible-Near Infrared Reflectance Spectrocopy as a Rapid Non-Destructive Measurment of Soil Hydraulic Properties and Soil Index Properties. Previously submitted as: *Garner, C., Salazar, S., Coffman, R., (2017). "Index and Hydraulic Properties of Soil Using Visible-Through Near-Infrared Spectroscopy." Soil Science. Submitted for Review*

CHAPTER 1: INTRODUCTION

1.1. Chapter Overview

The development of a multiband remote sensing technique for the measurement of unsaturated soil properties, soil index properties, and soil characteristics is described in this document. Two active and passive techniques: 1) radio detection and ranging (radar) imaging and 2) ultraviolet-near infrared diffuse reflection spectroscopy (UV-NIR DRIFT) were incorporated into the system. The combined technique leverages unique advantages of the aforementioned remote sensing systems to detect and quantity the soil volumetric water content (radar and UV-NIR DRIFT), soil water potential (UV NIR DRIFT), soil index properties (UV-NIR DRIFT), and soil texture (UV-NIR DRIFT). Both of the aforementioned techniques rely upon the interaction of electromagnetic radiation with the soil-water-air composite material to infer measurements of soil properties that are of interest to individuals within the geotechnical, agricultural, and geoscience fields. The particular interest for this project was to obtain measurements of the coupled soil volumetric water content and soil water potential values without touching the soil surface. The proposed technique that is described within this document may provide a previously unrealized capability to acquire these coupled measurements. This chapter is divided into the following sections: 1) an overview of the research project (Section 1.2), 2) the motivation for this research project (Section 1.3), and 3) an overview of the entire manuscript (Section 1.4).

1.2. Project Description

A brief description of the development of a remote sensing system for unsaturated soil properties is described in this section. The described research project consisted of two primary areas of research. These areas included: 1) the evaluation and development of a field-based, active, microwave, system for the measurement of soil volumetric water content and 2) the evaluation and development of a laboratory-based proof-of-concept visible through near infrared

(Vis-NIR) device for the measurement of soil water potential and soil volumetric water content. Specifically, for the laboratory-based component it was proposed that the "*Soil matric potential (+/- 20kPa for matric potentials between 0 and -1500kPa) can be detected and quantified using a remote sensing technique.*"

1.2.1. *Active Microwave, Radio Detection and Ranging (Radar), Remote Sensing System*

The active, microwave, remote sensing system included the use of two different ground-based radio detection and ranging (radar) imaging systems. While radar systems have been employed by previous researchers to measure soil water content due to the influence of the water within the soil on the complex dielectric permissivity (sometimes referred to using the depreciated term dielectric constant) of the soil-water system, this research has primarily involved aerial- or orbital- based sensor platforms. The utilization of a ground-based system may offer an increase in the 1) spatial resolution and 2) temporal resolution of the acquired measurements in comparison to traditional measurement techniques (e.g. sample recovery, *in situ* instrumentation or proximal nuclear or electrical techniques) or aerial- or orbital-based remotely sensed measurements. The two different measurement techniques and instruments that were employed for this research project included a K_u-Band single polarization change detection methods and C-Band full-polarization change detection methods.

Data and traditional measurements of soil volumetric water content were collected from two project sites. The two project sites were located at the University of Arkansas Cato Springs Research Center (UACSRC) in Fayetteville, Arkansas and the WESTAR Jeffery Energy Center (WJEC) in St. Marys, Kansas. At both project sites, temporally separated, spatially registered radar imagery was collected from a fixed location. Traditional data from nuclear density gauge (NDG), time domain reflectometry (TDR), and manual sample recovery were also collected.

1.2.2. *Visible through Near Infrared (Vis-NIR) Remote Sensing*

The laboratory-component of the research plan was intended to demonstrate the feasibility of obtaining matric potential values, for various soil types, without directly contacting the soil. To accomplish this plan, three different soil types were tested (Donna Fill, illite, and kaolinite) using 1) the proposed Laser Analysis of Soil Tension (LAST) proof-of-concept device, 2) a Diffuse Reflectance Infrared Fourier Transform (DRIFT) spectroscopy technique, 3) a Pressure Plate Extractor (PPE) apparatus, and 4) traditional laboratory techniques (gravimetric water content, Atterberg limits, and phase relationships). To validate the aforementioned hypothesis, results obtained using the experimental LAST technique were compared with results obtained using the PPE apparatus (volumetric water content and matric potential). The obtained LAST data were also compared with the results from traditional Atterberg limits testing (ASTM D4318 2014), and DRIFT testing (Atterberg limits using an empirical relationship proposed by Waruru et al. 2014). A matrix of the properties that were acquired within the laboratory, and the related testing techniques is presented in Table 1.1. The project work flow is presented in Figure 1.1.

Table 1.1. Proposed laboratory testing methods to obtain matric potential, volumetric water content, and Atterberg limits.

Parameter	Sym.	FT-IR Spectroscopy (DRIFTS)	Proof-of-Concept Device (LAST)	Pressure Plate Extractor (PPE)	Gravimetric Water Content (ASTM D2216)	Atterberg Limits (ASTM D4318)
Volumetric Water Content	[θ]	N	Y	Y	Y	N
Matric Potential	[ψ]	N	Y	Y	N	N
Atterberg Limits	[LL,PL,PI]	Y	Y	N	N	Y
Absorption Coeffecient	[k]	Y	Y	N	N	N
Scattering Coefficient	[s]	Y	Y	N	N	N

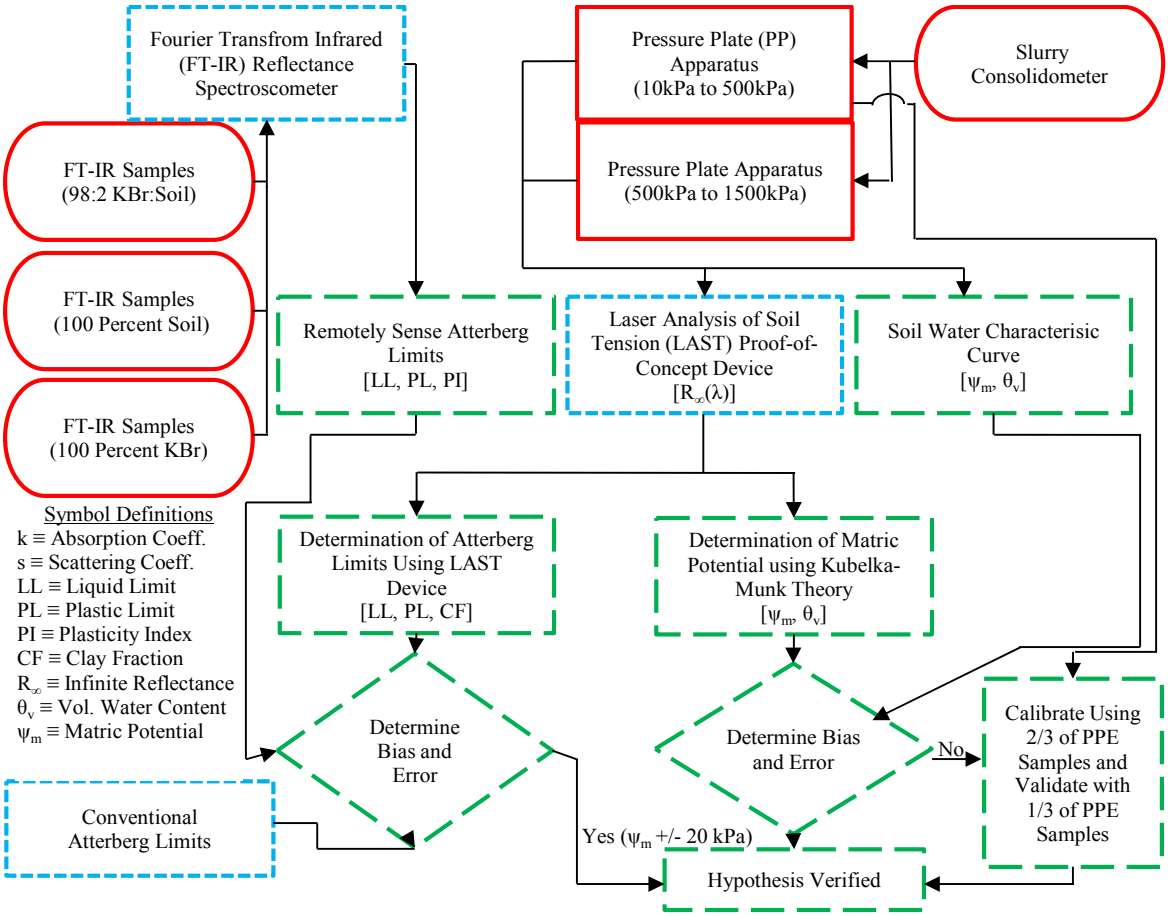

Figure 1.1. Proposed work flow indicating sample preparation (red solid outlines), data collection (blue dotted outlines), and data processing (green long dashed outlines), [in color].

1.3. Motivation

The motivation behind the research that was conducted for this project is described in this section. Specifically, the limitations of currently employed instrumentation for the measurement of unsaturated soil properties are presented and discussed in Section 1.3.1. Likewise, the potential benefits that may be realized by the technology that was developed as part of this research project, specifically for geotechnical engineering researchers and practitioners, are presented in Section 1.3.2. Similarly, the broader, multidisciplinary benefits associated with the developed remote measurement technique for soil water potential and soil volumetric water content are presented in Section 1.3.3.

1.3.1. *Limitations to the Currently Employed Instrumentation*

Limitations associated with existing instrumentation include poor temporal resolution and/or poor spatial resolution. Laboratory and *in situ* tests are limited by the studied area and the number of 1) samples acquired and 2) instruments installed, respectively. Furthermore, laboratory tests are limited by sample disturbance and difficulties in simulating the *in situ* conditions in the laboratory environment. Results from laboratory testing also suffer from temporal delays associated with sampling, testing, and reporting results (i.e. an extended amount of time required to mobilize the sampling equipment to the field, sample, transport specimen to the laboratory, perform the required tests, and analyze the data). While *in situ* instrumentation is capable of monitoring real-time changes within the soil in response to changes in environmental conditions, limitations still exist with respect to obtaining results in a timely fashion. *In situ* instrumentation is also limited by data storage device capabilities and the required access to the project site for retrieval of the data. To provide accurate results, the instrumentation must be carefully installed within the area of interest. Furthermore, existing laboratory and field instrumentation techniques are intrusive and require alteration or destruction of the *in situ* soil conditions and soil structure.

For hazard monitoring applications it may not be practical or safe to deploy personnel and equipment to the area of interest (e.g. post-wildfire monitoring or monitoring of levees or dams during a flood event). In addition, for all applications, *in situ* instrumentation and the associated support elements (data acquisition system, power supply, and exposed wiring) are vulnerable to theft and/or damage during extreme or unanticipated events. Conversely, existing remote sensing systems are capable of monitoring sites during hazardous conditions with minimum risk to equipment and personnel. To date, no remote sensing method of matric potential has been

documented within archival literature. As such, existing remote sensing methods have not provided a complete measurement of soil hydraulic parameters.

1.3.2. *Benefits to Geotechnical Engineers*

Damage resulting from unsaturated soil behavior (a coupled hydro-mechanical process) is dependent on the *in situ* hydraulic and mechanical properties of a given soil deposit and the local site conditions (e.g. precipitation, evapo-transpiration, land use, and land cover). Expansive clay behavior is responsible for more economic damage in the United States than all other natural disasters combined (Jones and Holtz 1973, Chen 1988, Karrane 2011). By providing a method for engineers to remotely detect both the surface volume change (shrink-swell) of expansive soils and to monitor the soil water characteristic curve (SWCC), the proposed remote sensing techniques may allow for rapid determination and real-time monitoring of expansive clay conditions. The improved temporal resolution, as obtained from remote sensing may allow engineers to intervene with a faster response time than the response time possible using traditional sampling and laboratory-based testing methods. Thereby, a reduction in the amount of damage to affected infrastructure is anticipated by utilizing the proposed remote sensing methodology (specifically, in regards to monitoring soil volumetric water content).

Additionally, the use of remote sensing measurements may allow for the quantification and characterization of the behavior of specific soil groups. For instance, for the majority of cases encountered in geotechnical engineering and other soil related disciplines, ground conditions may be considered as unsaturated. However, the current standard of practice is to assume that a soil deposit is either completely dry or completely saturated. The use of the assumed saturated behavior within geotechnical engineering has been historically justified by the difficulty in obtaining unsaturated soil parameters (θ and ψ_m) and the assumption that saturated soil behavior

always represents the worst case, most conservative conditions (Shackleford 2004). Subsequently, cases have been identified where the assumption of saturated conditions may be dangerously under-conservative (e.g. clay shrink-swell behavior).

The use of over-conservative design paradigms in geotechnical engineering is often counterproductive, inducing negative economic, scheduling, and performance impacts. The development of a proof-of-concept device for the remote measurement of soil matric potential may provide a new method for obtaining unsaturated soil parameters in both the field- and the laboratory-environments. By using the remotely sensed matric potential and volumetric water content values the method proposed by Bishop (1959), the ability to compute the values of unsaturated effective stress will aid in the solution of many geotechnical related problems.

1.3.3. *Benefits to Multidisciplinary Fields*

In addition to geotechnical engineering, the validation of the proposed hypothesis has potential applications across multiple academic and industrial disciplines. Two such disciplines are the agricultural sciences and the geological sciences. A potential agricultural use for the techniques and technology that will be developed as part of this research program is to monitor the response (changes in θ_v and ψ_m) of agricultural soils to irrigation and natural precipitation. The use of coupled remote sensing (microwave and visible-near infrared) may allow for rapid (near real time) measurements of soil matric potential and volumetric water content. It is anticipated that these rapid measurements will allow researchers and practitioners to develop a field/soil specific SWCC. The use of field/soil specific SWCC may allow agricultural producers to tailor irrigation strategies to minimize input costs (fuel, fertilizer, and chemicals), conserve water and prevent soil erosion while maintaining crop yield. Furthermore, the effects of land management practices (e.g. tillage, irrigation, cover crops, crop rotation, and precision leveling)

may be characterized and quantified through the use of remote sensing technologies that were developed as part of this research project. The technologies and techniques developed as part of the proposed research may also be applied to research in the geoscience disciplines for use in monitoring the effects of land use, topography, and soil type on the hydraulic cycle.

1.4. Document Overview

This manuscript consists of ten chapters. A brief overview of the project and the manuscript was provided within this chapter (Chapter 1). A review of the relevant literature describing the laboratory, remote, and proximal sensing techniques as well as the constitutive models (soil water characteristic curve and mathematical models) is presented in Chapter 2. A description of the second generation Gamma portable radar interferometer (GPRI-2), the project sites, the procedures employed to capture radar imagery, and the data processing techniques that were used to execute the soil moisture inversions from microwave imagery are described in Chapter 3. A description of the laboratory-based techniques that were employed to prepare soil samples, determine the index properties of the soil (liquid limit, plastic limit, and plasticity index), determine the texture of the soil (soil silt fraction and soil clay fraction), and to quantify the clay mineralogy of the soil using both traditional techniques (e.g. Skempton 1953) and advanced testing techniques (scanning electron microscopy and x-ray diffraction) are contained within Chapter 4.

The instruments, data collection methodology, and data processing techniques that were used to obtain measurements of the soil absorption and scattering coefficients as well as to acquire LAST and process spectral data to obtain measurements of soil volumetric water content and soil water potential (using both analytical and empirical techniques) are also documented in Chapter 4. The results obtained for soil volumetric water content measurements, as obtained using

the UA K_u-Band GPRI-2 instrument and single-pol change detection methods, as described in Garner and Coffman (2016), is presented as Chapter 5. The results obtained for measurements of soil volumetric water content at the Jeffery Energy Center, as documented in Garner and Coffman (2017a), are presented in Chapter 6. The results obtained for an optical characterization of the soil absorption and scattering spectra for the Donna Fill, illite, and kaolinite soils that were utilized for this project, as documented in Garner and Coffman (2017b), is contained in Chapter 7. The results obtained by the analytical and empirical inversions that were used to extract coupled measurements of soil volumetric water content and soil water potential from UV-NIR spectral data in the LAST device (Garner et al. 2017) are presented in Chapter 8. Finally, 1) conclusions drawn from the previously presented results (Chapters 5, 6, 7, and 8) as well as recommendations for future research and development of remote sensing for unsaturated soil properties and 2) a complete list of the works cited for the document are presented in Chapters 9 and 10, respectively.

1.5. Works Cited

3M Corporation (2015). "Product Information and Material Safety Data Sheet for Classic Roofing Granules." http://solutions.3m.com/wps/portal/3M/en_US/IMPD/Roofing-Granules/Products/Classic-Roofing-Granules/. Retrieved December 2015.

American Society for Testing and Materials D5298, (2014). "Standard Test Method for Measurement of Soil Potential (Suction) Using Filter Paper." Annual Book of ASTM Standards, Designation D5298, Vol. 4.08, ASTM, West Conshohocken, PA.

Blumberg, D., Freilikher, V., Lyalko, I., Vulfson, L., Kotlyar, A., Shevchenko, V., Ryabokenko, A., (2000). "Soil Moisture (Water Content) Assessment by an Airborne Scatterometer; The Chernobyl Disaster Area and the Negev Desert." Remote Sensing of the Environment. Vol. 71, pp. 309-319.

Chen, K., Wu, T., Tsang, L., Li, Q., Shi, J., Fung, A., (2003). "Emission of rough surfaces calculated by the integral method with comparison to three dimensional moment method simulations." IEEE Transaction on Geoscience and Remote Sensing. Vol. 41, p 90-101.

Garner, C., Coffman, R., (2017a). "Remotely Sensed Soil Volumetric Water Content and Dry Density as Obtained Utilizing Change Detection and Polarimetric Methods." Journal of Environmental and Engineering Geology. (Submitted for Review).

Garner, C., Coffman, R., (2017b). "Visible and Near-Infrared Diffuse Reflectance Properties of Geotechnical Reference Soils" Applied Clay Science (Submitted for Review).

Garner, C., Salazar, S., Coffman, R., (2017c). "Volumetric Water Content Measurements as Obtained from Remote Sensing and In-Situ Instrumentation." Soil Science (Submitted for Review).

van Genuchten, M., (1980). "A Closed-Form Equation for Predicting the Hydraulic Conductivity of Unsaturated Soils." Soil Science Society of America Journal, Vol. 44, No. 5, pp. 892-898.

Judd, D., Wyszecki, G., (1975). "Color in Business, Science, and Industry." John Wiley and Sons, New York.

Kedenburg, S., Vieweg, M., Gissibl, T., Giessen, H., (2012). "Linear Refractive Index and Absorption Measurements in Non-Linear Optical Liquids in the Visible and Near-Infrared Spectral Region." Optical Materials Express, Vol. 2, pp. 1588-1611.

Shepherd, K., Walsh, M., (2002). "Development of Reflectance Spectral Libraries for Characterization of Soil Properties." Soil Science Society for American Journal, Vol. 66, pp. 988-998.

Skempton, A., (1953). “The Colloidal Activities of Clays.” Proceedings of the 3rd International Conference on Soil Mechanics and Foundation Engineering. Zurich, Switzerland.

Wasti, Y., (1987). “Liquid and Plastic Limits as Determined from the Fall Cone and the Casagrande Methods.” Geotechnical Testing Journal, GTJODJ, Vol. 10, No. 1, pp. 26-30.

CHAPTER 2: LITERATURE REVIEW

2.1. Chapter Overview

A review of the existing literature regarding 1) unsaturated soil properties (soil volumetric water content and soil water potential), 2) soil characteristics (soil texture, soil index properties, clay mineralogy), and 3) laboratory and field measurement techniques is contained in this chapter. The unsaturated soil properties (soil volumetric water content and soil water potential) and the graphical representation of their relationship, as the soil water characteristic curve, are presented in Section 2.2. Traditional laboratory and *in situ* methods of obtaining the aforementioned soil properties are discussed in Section 2.3 and Section 2.4, respectively. Remote sensing measurements of parameters of interest for unsaturated soil mechanics are described in Section 2.5.

2.2. Soil Water Potential, Volumetric Water Content, and the Soil Water Characteristic Curve

Unsaturated or partially saturated soil behavior is significantly more complex than the behavior of completely dry or completely saturated soils. Partially saturated soil properties have been estimated using a mathematical formula that includes the amount of surface tension and ionic bonding between soil particles (Fredlund and Rahardjo 1993). At the most basic level, soil water potential (ψ or Ψ) has been described by previous researchers as a function of soil type (mineralogy, particle size distribution, and depositional history) and volumetric water content (Richards 1941, Brooks and Corey 1964, van Genuchten 1980, Fredlund and Xing 1994, and Lu and Likos 2002). As proposed by Aslyng et al. (1963) and reported by Hillel (2012), the formal definition of soil water potential is:

> *"Total soil water potential is defined as the amount of work per unit quantity of water that must be done by external forces to transfer reversible and isothermally an infinitesimal amount of water from the standard state to the soil at the point under consideration." – (Hillel 2012 pp. 51).*

Mathematically, the soil water potential has been described with a variable number of constitutive terms. The exact number of terms has varied depending on the literature source and the dominant physical properties (Hillel 2012). As indicated in the previously presented definition, the value soil water potential has always been referenced to a specific point or elevation datum (Ψ_0) within the soil column. Typically, the most significant terms are the gravitational potential (Ψ_s), the hydrostatic pressure potential (Ψ_p), the matrix or matric potential (Ψ_m), and the osmotic potential (Ψ_o or Ψ_π), as represented in Equation 2.1. The osmotic potential term has been mathematically described as Equation 2.2. Furthermore, the matrix potential has been described (Equation 2.3) as being a function of water surface tension and adhesive electro-kinetic forces (Tyree 2003, Hillel 2012). The water surface tension and adhesive electro-kinetic forces have been mathematically described as Equation 2.4 and Equation 2.5, respectively.

$$\Psi_T = \Psi_0 + \Psi_\pi + \Psi_p + \Psi_s + \Psi_v + \Psi_m \quad \text{(Taiz 2002)} \quad \text{Equation 2.1}$$

$$\Pi = CRT \quad \text{(Hillel 2012)} \quad \text{Equation 2.2}$$

$$\Psi_m \cong H_c + \tau \quad \text{Equation 2.3}$$

$$H_c = \frac{2\sigma\cos(\gamma)}{\rho_w g R} \quad \text{(Hillel 2012)} \quad \text{Equation 2.4}$$

$$\tau = \left(\frac{N_0^2 P_0^2}{3V_w RT}\right) F^2 \quad \text{(Tyree 2003)} \quad \text{Equation 2.5}$$

In Equation 2.1 through Equation 2.5, Ψ_T is the total soil water potential, $\Psi 0$ is the reference correction, Ψ_π is the osmotic potential, Ψ_s is the gravimetric or gravitational potential, Ψ_p is the hydrostatic potential, Ψ_v is the potential due to atmospheric humidity, Ψ_m is the matric or matrix potential, Π is the osmotic potential (in pressure units), C is the solute concentration, R is the ideal gas constant ($8.3144598 J \cdot K^{-1} \cdot mol^{-1}$), T is the temperature in degrees Kelvin, H_c is the capillary term of matrix potential, σ is the surface tension of fluid in relative to air for water ($0.073 kg \cdot s^{-2}$ at 293.15K), γ is the contact angle between the water and the soil (radians), ρ_w is the density of water ($998 kg \cdot m^3$ at 293.15K), g is the acceleration due to gravity ($9.81 m \cdot s^{-2}$), r is the equivalent radius of the tube, τ is the electro-kinetic potential of water in the electrical field near a soil particle, N_0 is Avogadro's number ($6.0221409 \cdot 10^{23}$), P_0 is the magnitude of the dipole moment of water (1.85 Debye), V_w is molar volume of water ($18.03 mL \cdot mol^{-1}$), and F is the magnitude of the electric field at the point where τ is evaluated.

The relationship between the two components (volumetric water content [θ_v] and soil water potential [ψ]) is typically presented using a soil water characteristic curve (Figure 2.1) or a

mathematical model such as the model proposed by van Genuchten (1980). The soil water characteristic curve (SWCC) or soil water moisture curve was originally proposed by Buckingham (1907) and has been described as a constitutive model between the soil water potential energy and the volumetric water content in a soil body (Lu and Likos 2002). Specifically, the SWCC describes the thermodynamic state (soil water potential energy) in relationship with the amount of water adsorbed in a soil-water-air system (Lu and Likos 2002). This relationship has been extensively investigated and experimentally validated by previous researchers (Brooks and Corey 1964, van Genuchten 1980, Fredlund and Xing 1994).

Historically after the SWCC has been experimentally or theoretically derived, for a particular soil, the SWCC has been used to calculate the soil water potential from a laboratory or *in situ* measurement of the soil volumetric water content. The volumetric water content has typically been the measured quantity because it has been shown to be more easily obtained than the soil water potential. Furthermore, the SWCC was developed as a convenient way to graphically represent and numerically evaluate changes in soil-water interaction during both drying and wetting phenomenon. An example SWCC for a soil is presented as Figure 2.1.

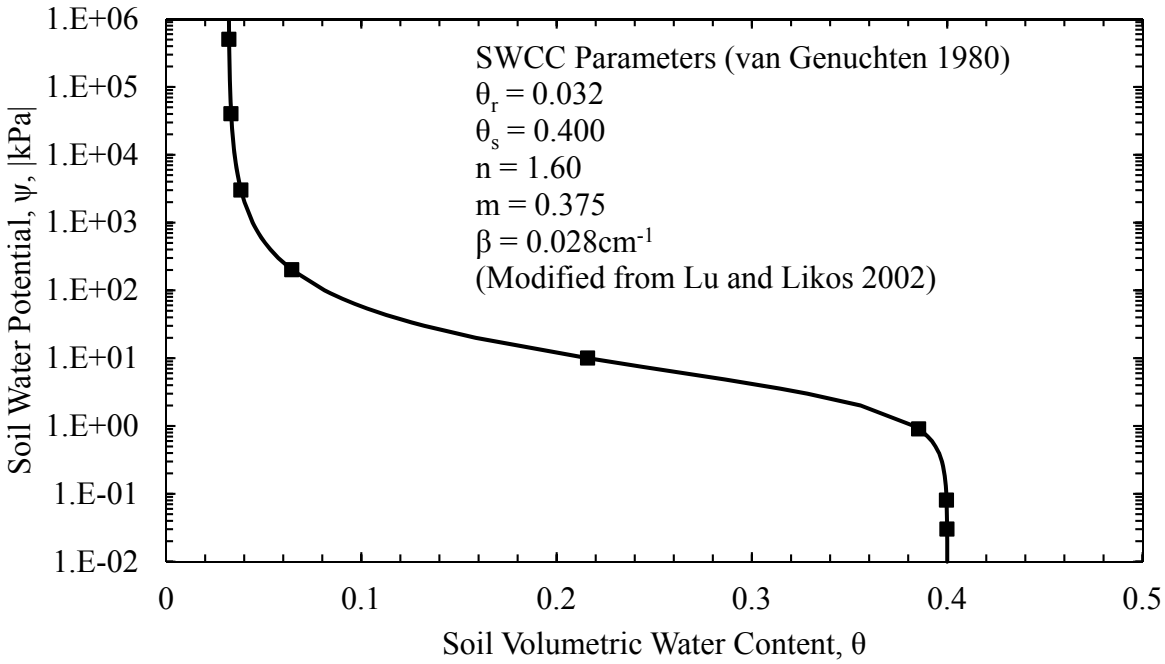

Figure 2.1. An example of a soil water characteristic curve as modeled using the van Genuchten (1980) equation.

Previous researchers within the engineering, agricultural, and geo-science fields have employed a SWCC to obtain estimates of physical parameters which are of interest to practitioners in the respective fields (van Genuchten 1980). Examples of such parameters have included: hydraulic conductivity (van Genuchten 1980, Fredlund and Xing 1994), plant available water (Veihmeyer and Hendrickson 1927, Richards 1928, Richards and Waldleigh 1952) and specific storage (Israelsen and West 1922). The shape of the curve has been described as consisting of three distinct regions of soil behavior (Wilson et al. 1999). These three regions have included, from dry to wet, 1) the residual saturation zone, 2) the desaturation zone, and 3) the capillary saturation zone (Wilson et al. 1999). As described in Wilson et al. (1999), within the residual saturation zone (sometimes referred to as the hygroscopic zone) all remaining water was chemically adsorbed onto the soil particles. All liquid flow in this region occurred in the vapor phase. In the desaturation zone (the flat middle portion of the SWCC) with a volumetric water

content between the air entry pressure and the residual water content, the water within the soil was either replaced by air (drying) or displaced air within the void space of the soil (wetting). Water within the soil, in this phase, was shown to be potentially discontinuous and water flow was greatly reduced from the saturated condition. In the capillary saturation zone the soil remained saturated with continuous connectivity between the water within the pores.

2.2.1. *Parameters of Interest for Soil Water Characterization*

Previous research has demonstrated that the SWCC, for any specific soil, is a function of the physical, chemical, hydraulic, and biological processes that have acted on the soil. Examples of these parameters include the following five items that will be discussed in more detail.

1) Soil texture.
2) Soil structure.
3) Soil density.
4) Soil mineralogy.
5) Groundwater chemistry.

The soil structure, and specifically the development of soil macro-structures (peds), has been shown to influence the influence the ability of a soil body to imbibe and store moisture at the wet end of the SWCC (the previously mentioned capillary saturation zone and the desaturation zone). Conversely at higher (more negative) soil water potential values (the desaturation zone and the residual saturation zone), the effects of soil chemistry and soil mineralogy have been described as controlling the relationship between soil water potential and volumetric water content. Of several particular points of interest in the SWCC have been identified by previous researchers in the geotechnical and agricultural fields. These points of interest include the air-entry pressure (Brooks and Corey 1964, Fredlund and Xing 1994), the saturated volumetric water

content (Brooks and Corey 1964, van Genuchten 1980, Fredlund and Xing 1994), the residual water content (Brooks and Corey 1964, van Genuchten 1980), the field capacity (Veihmeyer and Hendrickson 1927, Richards 1928, Richards and Waldleigh 1952), and the plant wilting point (Veihmeyer and Hendrickson 1927, Richards 1928).

As described in Norman et al. (2015), the saturated volumetric water content and air entry pressure have been described as a function of the soil structure and density (from the phase relationships in the water-soil-air system). The residual water content was a function of the soil mineralogy and texture (percentage of sand, silt, and clay particles). The field capacity and the plant wilting point have been primarily described in the agricultural literature (Israelson and West 1922, Veihmeyer and Hendrickson 1927, Richards and Waldleigh 1952). The field capacity and the plant wilting point have been traditionally described as the volumetric water content at a matric potential value of 33kPa and 1500kPa, respectively. The difference in volumetric water content between these two values of soil water potential has been described as the plant available water for a particular soil.

As reported by Veihmeyer and Hendrickson (1927, 1949) and ICID (1996), it has been estimated that for most plant species, the root system was not able to access free water at absolute soil potential values less than 33kPa (the water would have drained under gravity before the plant can remove the water through osmosis). For absolute soil matric potential values greater than 1500kPa, it has been reported that most plant species cannot exert enough osmotic potential to draw water into the root system (ICID 1996). Therefore, water that was entrained within the soil body, at absolute soil water potential values in excess of 1500kPa, were not able to be used by most plant species. However, significant variation has been observed for the soil water potential value at which wilting was observed for individual plant species and soils (Richards and

Waldleigh 1952, Novak and Havrila 2006). These points of interest on the SWCC are presented graphically in Figure 2.2.

As described by Hillel (2012), soil bulk density (mass of dry soil divided by total volume of a given soil sample) is a primary influence on the amount of water that a soil is capable of storing. Specifically, the total volume of stored water may not exceed the available void space in the soil matrix. Therefore, as the bulk density of a given soil increased, for a fixed specific gravity of soil solids, the porosity of a soil decreases, resulting in a reduction in the amount of water content that is capable of being stored. This influence of bulk density has been shown in in the SWCC as a shift to the left (along the x-axis) and a steeper slope if the SWCC within the transition zone (previously described as the desaturation region).

Soil texture has been shown to affect the SWCC through the influence of macro pores within the soil matrix (Hillel 2012). Specifically, the space between individual peds provided a large void with low capillarity (due to a large radius) allowing the soil to rapidly imbibe, transport, and store water. Typically, as soil structure developed, the capacity of the soil to store water (specific storage) was found to increase as well (Norman et al. 2015). However, at increasing absolute values of soil water potential, the larger macropores have been drained and the SWCC was controlled by the effects of soil texture and soil mineralogy.

At high absolute values of ψ, the soil particle size distribution has been shown to affect the size of the pores between individual soil particles due to geometric packing (Lu and Likos 2002). The pore size effects were quantified using the capillarity term of the soil matric potential term (Equation 2.4). Similarly, the soil mineralogy controlled the adhesive term of the soil matric potential (Equation 2.5) by influencing the magnitude of the electrical field (F) near the surface of the soil particles. Previous researchers have reported that the residual water content has

corresponded to a soil water potential of approximately 10^6kPa (~1000 atmospheres) by both experimental and thermodynamic evaluations (Croney and Coleman 1961, Richards 1965, Fredlund and Xing 1994).

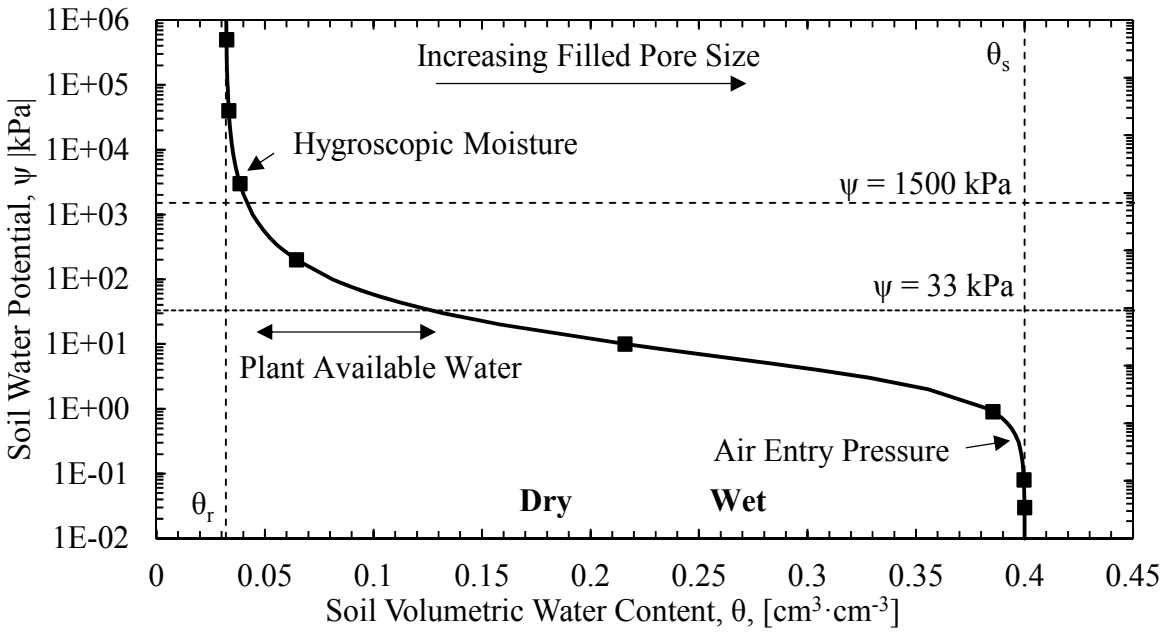

Figure 2.2. SWCC with points of interest labeled.

2.2.2. *Existing Models for Soil Water Characteristics*

Proposed mathematical SWCC models include Brooks and Corey (1964), van Genuchten (1980), and Fredlund and Xing (1994). Furthermore, empirical or semi-empirical relations have been presented in the literature to provide an estimated SWCC using soil properties that are more easily obtained. Example of these models have been based upon: grain size distribution (Ahuja et al. 1985), dry bulk density (Rawls and Brakensiek 1985), and porosity (Bouma and Van Lanen 1987). For completeness, the Brooks and Corey (1964), van Genuchten (1980), and Fredlund and Xing (1994) models are presented Equation 2.6, Equation 2.7 and Equation 2.8, and Equation 2.9, respectively. Examples of the Brooks and Corey (1964) and the van Genuchten (1980) equations are presented graphically in Figure 2.3.

$$\begin{bmatrix} for \quad |\psi| \geq |\psi_b|, & \left(\frac{\theta - \theta_r}{\theta_s - \theta_r}\right) = \left(\frac{\psi_b}{\psi}\right)^{\lambda} \\ for \quad |\psi| < |\psi_b|, & \theta = \theta_s \end{bmatrix}$$ Brooks and Corey (1964) Equation 2.6

$$\theta(\psi) = \theta_r + \left[\frac{\theta_s - \theta_r}{\left[1 + \left(\beta|\psi|\right)^n\right]^m}\right]$$ Van Genuchten (1980) Equation 2.7

$$m = 1 - \frac{1}{n}$$ Van Genuchten (1980) Equation 2.8

$$\theta(\psi) = \theta_s \left[\frac{1}{\ln\left(e + \left(\frac{\psi}{a}\right)^n\right)}\right]$$ Fredlund and Xing (1994) Equation 2.9

In Equation 2.6 through Equation 2.9, θ is the volumetric water content, θ_r is the residual volumetric water content, θ_s is the saturated volumetric water content, ψ_b is the air entry value, ψ is the soil potential, β is a fitting parameter, m is a fitting parameter (solved for in Equation 2.8), n is a fitting parameter, a is a fitting parameter, and e is Euler's number.

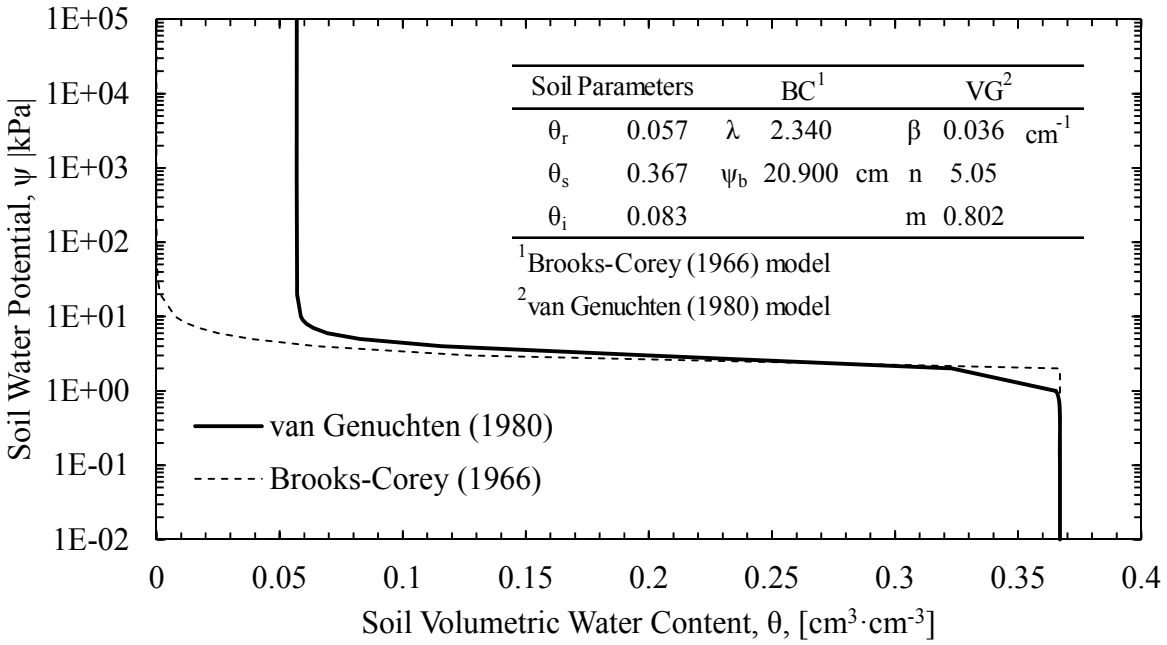

Figure 2.3. Comparison of the Brooks and Corey (1966) and the van Genuchten (1980) SWCC mathematical models for a single soil (data obtained from Lu and Likos 2002).

2.3. Traditional Laboratory-Based Methods to Determined Unsaturated Soil Properties

Laboratory-based methods to obtain unsaturated soil properties have been widely investigated and employed in both research and geotechnical practice. The most commonly employed method to obtain soil water content has been the gravimetric method described in Section 2.3.1. Also discussed is the pressure plate extractor method that has been widely employed in both research and practice to obtain a laboratory-based measurement of the SWCC (Section 2.3.2). Similarly, a description of the laboratory techniques used to obtain measurements of soil index properties and soil texture and mineralogy are contained in Section 2.3.3 and Section 2.3.4, respectively.

2.3.1. *Traditional Laboratory-Based Methods to Determine Soil Water Content*

Laboratory determination of soil water content has been traditionally obtained using gravimetric methods such as the procedure described in ASTM D2216 (2014). Volumetric measurements of soil water content are typically then calculated by using the gravimetric water content and phase relationships of the soil-water-air system. In such gravimetric methods a known quantity (mass) of soil sample has been placed into a drying oven to expel water from the soil sample by evaporation. The mass lost by the soil sample, as a function of time, was assumed to be dependent on the loss of water from the soil sample. The expulsion of all free (not chemically bound water) was typically verified by observing the change in sample mass over time. By comparing the initial (wet) mass of a soil sample to the final (dry) mass of a soil sample the mass of soil water and the mass of dry soil in the sample was then obtained. Based on the ASTM D2216 (2014) standard procedure, the gravimetric water content of the soil sample was then calculated using Equation 2.10. If the total volume of the wet sample was known or measured

prior to drying, then the soil volumetric water content could have been determined using Equation 2.11.

$$w = \frac{\left(M_{wet} - M_{can}\right) - \left(M_{dry} - M_{can}\right)}{\left(M_{dry} - M_{can}\right)} \quad \text{(ASTM D2216 2014)} \quad \text{Equation 2.10}$$

$$\theta = \frac{M_{water}}{\rho_{water} V_{total}} \quad \text{Equation 2.11}$$

In Equation 2.10 and Equation 2.11, w is the gravimetric water content, M_{wet} is the mass of the wet sample and container, M_{can} is the mass of the sample container, M_{dry} is the mass of the oven-dried sample and container, θ is the volumetric water content, M_{water} is the mass of water in the sample (the numerator of Equation 2.10), ρ_{water} is the density of water (usually assumed to be $1 g \cdot cm^{-1}$), and Vtotal is the total volume of the sample.

2.3.2. *Traditional Laboratory-based Methods to Determine Soil Water Potential*

The laboratory techniques which have been previously developed to measure unsaturated soil properties including soil water potential and volumetric water content are discussed in this section. The development and theory of operation of the chilled mirror hygrometer are presented and discussed in Section 2.3.3.1. Similarly, the pressure plate extractor method, originally described by Richards (1941), is presented in Section 2.3.3.2.

2.3.2.1. Chilled Mirror Hygrometer

In the 1940's, Chilled mirror hygrometer (CMH) testing was first developed to measure the water vapor distribution in the Earth's atmosphere (Dobson et al. 1946, Mastenbrook and Dinger 1961). The original instruments were frost-point hygrometers (measuring the relative humidity by determining the temperature at which air condenses over a surface of water ice). The first use of a dew-point chilled mirror hygrometer for measurement of soil water potential was initially described in Neumann and Thurtell (1972), and an improved device was presented in Campbell et al. (1973).

Historically, for chilled mirror hygrometer (CMH) tests, a cooled mirror (cooled using a Peltier solid state cooling element) was placed inside a sealed chamber containing a soil sample at

an unknown soil matric potential. The atmosphere within the test chamber was then allowed to come to thermodynamic equilibrium with the potential in the soil. Specifically, the relative humidity in the void space of the soil equilibrated with the relative humidity within the test chamber. A laser or other collimated light source was propagated through the test chamber impinging on the mirror surface before being reflected onto a photo receiver (Watanabe et al. 2012). Using the cooling element, the mirror surface was cooled until the temperature of the reflective surface reached the vapor saturation temperature and condensation formed on the mirror surface. The temperature of the mirror was recorded using a thermocouple. The volumetric water content, if required, was then determined by using the phase relationships at the time of measurements.

Instrument calibration for CMH devices has typically been accomplished by using samples with a known osmotic potential by preparing a salt solution (KCl, NaCl) at a specific molar concentration. Advantages of the CMH are the rapid testing time (minutes) and the highly automated test procedure. Disadvantages associated with this test have been the small sample size and the high equipment cost. In addition, the sample has been completely disturbed during preparation which may induce measurement error at low absolute values of soil water potential. A final consideration is that the instrument is sensitive to contamination of the sample chamber, the optical sensor, or the mirror surface. An example of a commercially available CMH (a Decagon model WP-4) and a schematic of the principle of operation is presented in Figure 2.4.

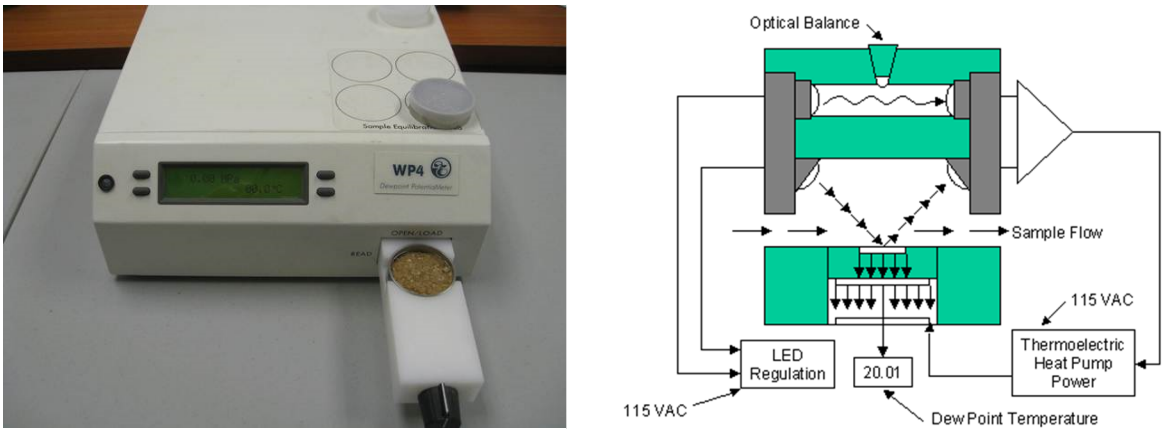

(a) (b)

Figure 2.4. a) Exterior view of WP-4 CMH showing sample in instrument tray prior to testing (image from Applied Soil Water 2015), and b) a schematic of the CMH principle of operation (image from Thunder Scientific 2015).

2.3.2.2. Pressure Plate Extractor

The pressure plate apparatus, which has been commonly employed in geotechnical engineering and soil science, was first proposed in Richards (1941). The device consisted of a pressure vessel with a removable, pressure tight lid. A high air entry porous plate was placed on the bottom of the pressure vessel. A drainage port and water collection system (volumetric flask and bubble trap) were connected to the porous plate via a high pressure fitting penetrating through the pressure vessel. Soil samples were radially constrained using open bottomed metal cylinders, and the samples were placed in hydraulic contact with the porous stone. If required, hydraulic contact (between the sample and the device) was achieved by placing the soil on a layer of fine grained material (silica powder). The pressure vessel lid was then placed on the apparatus and sealed. Pressure was applied to the apparatus pneumatically and water was forced out of the soil pores into the porous plate. Expelled water was captured and recorded using a collection system.

The system was maintained at the desired pressure until no further water was expelled from the device, indicating the water matric potential was in equilibrium with the applied pressure increment. The water content of the soil at that matric potential was then determined by opening

the pressure vessel and removing one or more samples for gravimetric water content testing. Further pressure increments were applied (and each corresponding water content recorded) to determine multiple points of the SWCC.

Advantages of the Richards (1941) pressure plate include the low equipment cost and simple data analysis. Disadvantages of the pressure plate include the extended time required to achieve equilibrium (days or weeks per pressure increment), and the potential for erroneous readings when using a large pressure cell with multiple samples due to differential evaporation (Smith and Mullins 2001). Additionally, the design of the pressure plate cell has made it difficult to accurately resolve the SWCC at low matric potential values due to the disturbed nature of pressure plate samples (Smith and Mullins 2001). An example of a commercially available PPE device is presented as Figure 2.5.

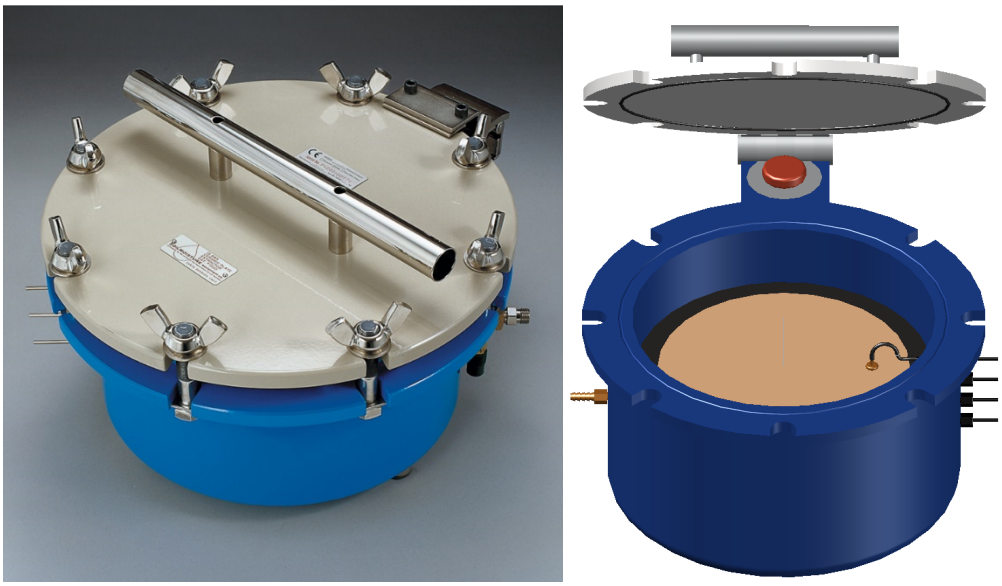

(a) *(b)*

Figure 2.5. a) Soil Moisture Inc. model 1500 PPE (image from Soil Moisture 2015), and b) schematic of PPE illustrating the interior of the apparatus.

2.3.3. *Laboratory Determination of Atterberg Index Properties*

Soil index properties ("Atterberg limits") have been widely utilized to provide a qualitative analysis of soil properties by using easily obtained measurements. As originally proposed by Atterberg (1912), agricultural soil has been characterized as sticky, plastic, soft, and harsh. The proposed "Atterberg limits" were extended to engineering practice and the testing methodology was formalized by Casagrande (1932). Casagrande (1932) proposed that soil consistency could be divided into four categories with delimited boundaries, as a function of gravimetric water content. The four material categories proposed by Casagrande (1932) were liquid, plastic, semi-solid, and solid. Therefore, the liquid limit (LL) was the water content that delineated between liquid and plastic material, the plastic limit (PL) was the water content that delineated between plastic and semi-solid material, and the shrinkage limit (SL) was the water content that delineated between semi-solid and solid material.

The fundamental soil behaviors behind the Atterberg limits were described in Seed et al. (1964). In common geotechnical practice, the LL and PL values have been used to characterize soil samples by using the derived quantity of the plasticity index (PI). The commonly employed Unified Soil Classification System (USCS) and the American Association of State Highway Transportation Organizations (AASHTO) soil classification systems have both employed Atterberg limits, in addition to soil particle size information, to assign soil classification. Subsequent researchers have empirically related the easily obtained index properties to estimate engineering values including: coefficient of consolidation (Skempton 1944), permeability (Carrier and Beckman 1984), normalized void ratio (Morris et al. 2000), and shear strength (Skempton and Northey 1953, Casagrande 1958, Youssef et al. 1965, Wroth and Houlsby 1985, Jamiokowski et al. 1985, Dolinar 2009).

In the United States, the traditional methods of obtaining the Atterberg limits (LL and PL) have been described in ASTM D4318 (2014). In the ASTM D4318 (2014) test methodology, samples are commonly prepared by remolding disturbed soil samples. The soil sample was then subjected to a mechanical testing criteria to determine if a soil was behaving as a liquid, plastic or solid material. When the soil sample was observed to achieve the specified material behavior, the soil gravimetric water content was obtained using the procedures described in ASTM D2216 (2014). For the plastic limit test the material behavior criteria was described as a soil sample, that begins cracking when rolled to a diameter of 0.32cm (Terzaghi 1926a, Terzaghi 1926b, Casagrande 1932, ASTM D4318 2014). Casagrande (1932, 1958) defined the liquid limit as the water content at which the soil had an undrained shear strength of $1.7 kN \cdot m^{-3}$. An image of a typically employed Casagrande drop cup is presented in Figure 2.6 and an example of typically obtained data illustrating the computation of liquid limit is presented in Figure 2.7. Despite the wide spread use of the ASTM D4318 (2014) procedure, previous researchers have reported that the test is poorly repeatable (Wroth and Wood 1978, Shepard and Walsh 2002, Waruru et al. 2014).

Another method of obtaining the soil LL and PL that has been commonly employed in geotechnical practice in Europe is the fall cone apparatus (BSI 1990, Spagnoli 2012, Tefera 2013). As described in BSI (1990) and Tefera (2013), the fall cone test consists of a weighted cone with a known geometry and weight that is allowed to fall a set distance onto a soil surface recording the resulting penetration of the cone into the soil sample (Figure 2.6). The depth of penetration has been reported by previous researchers to be a function of the undrained shear strength of the soil. For the commonly employed Swedish (150g, 20 degree) cone the penetration, at the liquid limit, is defined to be 20mm (Wood 1990). Alternatively, an equation to directly

calculate the undrained shear strength of a soil (and therefore assign a liquid limit value) from the measured has been proposed (Wood 1990) and is presented as Equation 2.12. A graphical representation of the fall cone method to obtain liquid limit is presented in Figure 2.7. The plastic limit may be determined by altering the cone drop height (Tefera 2013). Similarly, the plastic limit can be obtained using a different weight to the cone and then computing the plastic index using Equation 2.13.

$$S_u = k_a\left(\frac{m_c g}{d^2}\right) \qquad \text{(Wood 1990)} \qquad \text{Equation 2.12}$$

$$I_p = \Delta\frac{Log_{100}(100)}{\log_{100}\left(\frac{W_1}{W_2}\right)} \qquad \text{(Wasti 1987)} \qquad \text{Equation 2.13}$$

In Equation 2.12 and Equation 2.13, S_u is the soil undrained shear strength, k_a is the cone factor (0.29 for 60 degree cones), g is the acceleration of gravity (9.81m·s^2), d is the penetration depth of the cone, Δ is the differential penetration between liquid limit test penetration (W_1) and plastic limit penetration (W_2), Ip is the plasticity index, and $W_{1,2}$ is the weight of the cone.

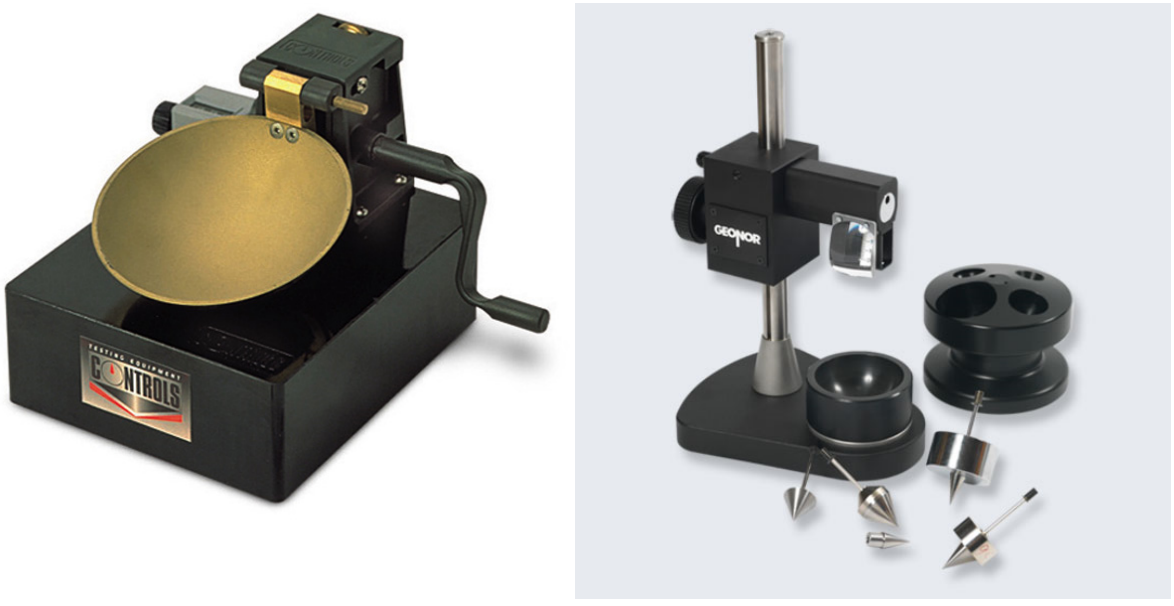

(a) (b)

Figure 2.6. a) Casagrande drop cup as specified in ASTM D4318 2014, and b) a GeoNor fall cone apparatus (image from Controls Group 2015 and GeoNor 2015, respectively, in color).

While the literature supports the contention that the liquid limit transition can be described as an undrained shear strength criteria (Haigh 2012), there is some debate as to the fundamental underlying mechanism which occurs at the semi-solid to plastic transition. Some researchers (Wroth and Wood 1978, Whyte 1982) described the transition between plastic and semi-solid behavior as an undrained shear strength phenomena. The value of soil undrained shear strength at the plastic limit has been assigned by some researchers as 100 times the value of the shear strength at the liquid limit (Campbell 1976, Wroth and Wood 1978, Whyte 1982). However, recent research published by Haigh et al. (2013) proposed that the plastic limit was an unsaturated soil behavior causing a brittle transition to be observed. Specifically, as the water content value decreased, the entrained soil water became discontinuous due to air entry or cavitation in the soil water (Bolton and Cheng 2002, Or and Tuller 2002). The development of soil potential then caused a tensile loading of the soil, allowing for plastic behavior. The plastic limit would, therefore, be a function of soil classification. Haigh et al. (2013) further proposed that this behavior could be explained by the critical state theory presented by Schofield and Wroth (1968).

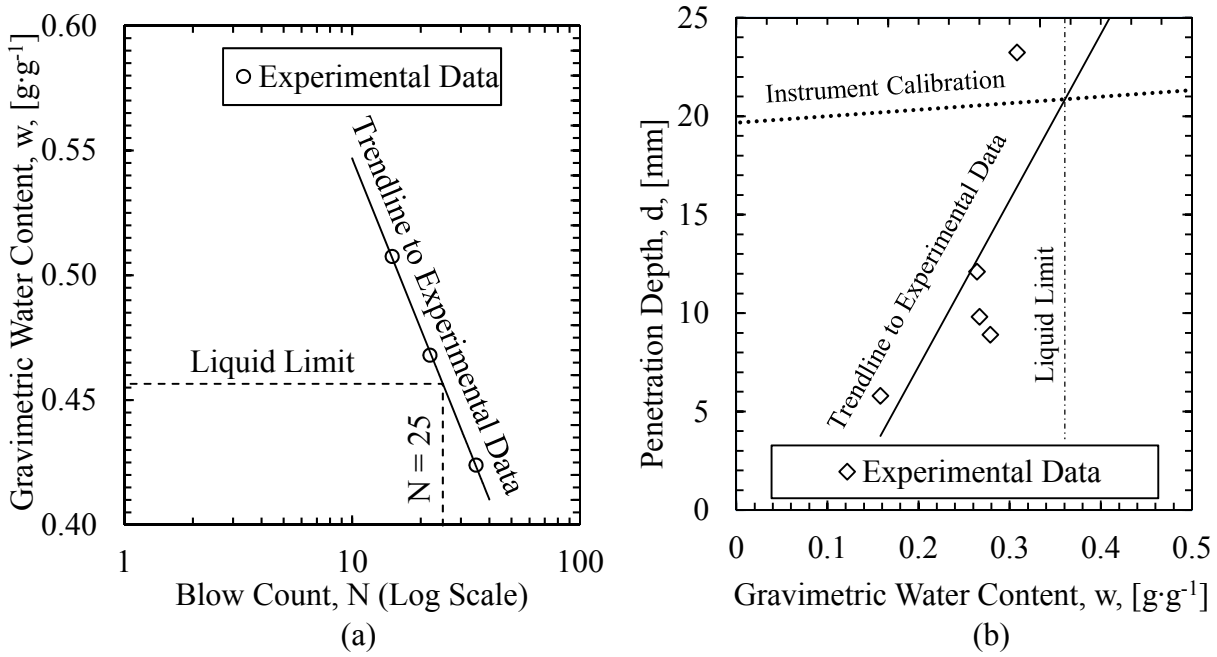

Figure 2.7. Example plots for the determination of liquid limit using a) the method documented in ASTM D4318 (2014), and b) the fall cone method.

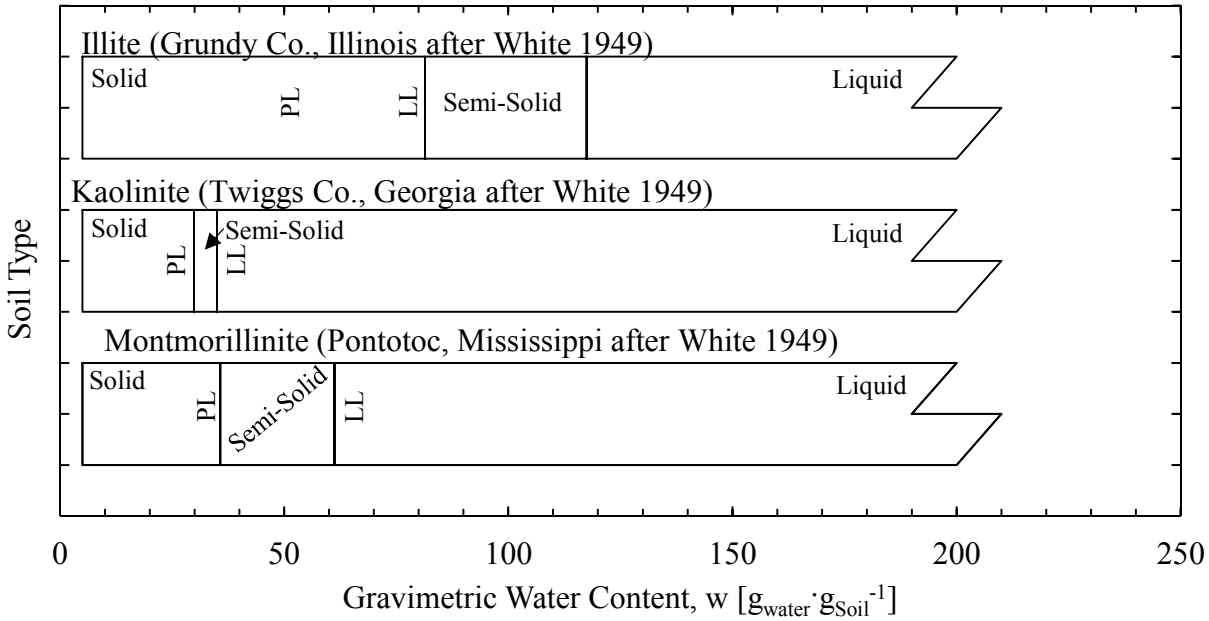

Figure 2.8. Atterberg limits as a function of water content for an illite, kaolinite, and montmorillonite soils (after White 1949).

2.3.4. *Laboratory Determination of Soil Texture and Mineralogy*

Soil texture (percent sand, silt, and clay) and mineralogy have been traditionally obtained using laboratory techniques. Specifically, the percent sand, silt, and clay (soil texture) by weight

has been determined through a combination of mechanical separation (sieving) and hydrometer testing. The transition between the sand, silt, and clay have been traditionally described using either a size criteria or a size and mechanical behavior criteria. In the United States, the USCS, AASHTO soil classification system, and the United States Department of Agriculture (USDA) soil classification systems have been commonly utilized.

The USCS has included a size criteria to separate gravel, sand, and fine particles for particle diameters greater than 4.75 mm, between 4.75 mm and 0.075 mm, and smaller than 0.075 mm as determined by mechanical sieving, respectively. Classification of silt and clay particles under the USCS criteria is typically completed by mechanical behavior, as determined by the plastic index (as previously described in Section 2.3.3 and as determined by ASTM D4318 2014). Conversely, the USDA classification system commonly uses a hydrometer test to separate clay from silt sized particles based on settling time.

For the hydrometer test a dispersed soil sample is typically prepared by treating a soil slurry with a dispersant compound (40 $mg \cdot L^{-1}$ Sodium Hexametaphosphate per ASTM D422 2014). The suspended soil particles are then allowed to settle through a column of water with a known height. The change in density (a function of the mass of suspended solids) in the solution is then measured using a calibrated hydrometer. Since settling time is a function of terminal velocity of particles through a fluid, the particle size of the suspended solids decreases as a function of time. Any particles larger than 0.002 mm were considered to be silt particles. Accordingly, particles with a diameter beneath 0.002 mm are considered to be clay particles. The clay fraction is the mass fraction of soil particles that are smaller than 0.002 mm.

Clay mineralogy has been traditionally obtained using the clay fraction, as obtained through hydrometer testing (ASTM D422 2014), and the clay activity, as obtained through

Atterberg index testing (ASTM D4318 2014). As shown in Figure 2.9, the relationship between clay mineralogy, clay content, and clay activity was originally presented by Skempton (1953). Additional relationships between clay mineralogy and the measured soil Atterberg limits have been proposed by Casagrande (1948) and Holtz and Kovacs (1981).

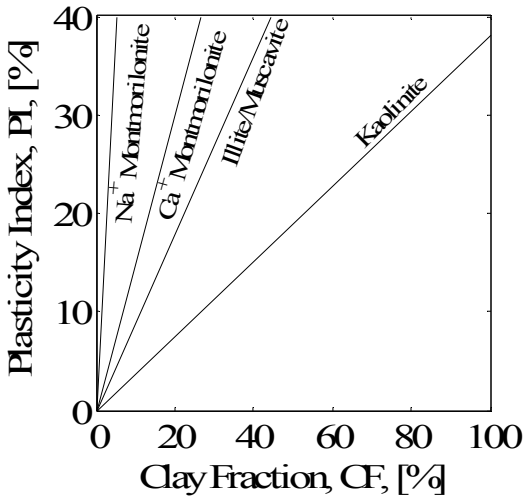

Figure 2.9. Relationship between plasticity and clay fraction for kaolinite, illite, and montmorillonite clays (after Skempton 1953).

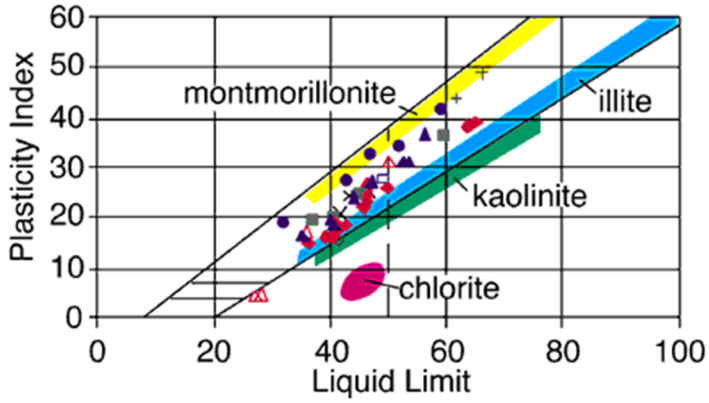

Figure 2.10. Plasticity chart with typical values for various clay mineralogies (from Kansas Geological Survey 2015 after Casagrande 1948, Holtz and Kovacs 1981).

2.4. Traditional In Situ Instrumentation and Proximal Sensing Techniques to Determine Unsaturated Soil Properties.

In situ, or field-based, measurement of soil properties have been obtained using both *in situ* instrumentation and proximal (touching the soil surface) sensors. *In situ* instrumentation has

been developed to measure both soil water content (time domain reflectometry, frequency domain reflectometry, electrical conductivity sensors) and soil water potential (tensiometers, psychrometers, gypsum block sensors). *In situ* instrumentation for measurement of soil water content is discussed in Section 2.4.1. *In situ* instrumentation for measurement of soil water potential is discussed in Section 2.4.2.

2.4.1. *In Situ and Proximal Measurement Techniques to Determined Soil Water Content*

The volumetric water content of soil in the field has been determined via sample recovery and laboratory testing techniques as previously presented in Section 2.2. Discussed in this section are two proximal and *in situ* methods developed to measure soil water content in the field. The proximal measurement technique discussed in this section is the nuclear backscatter technique commonly employed as a construction quality assurance / quality control (QA/QC) technique (Padlo et al. 2005). Another method that has also been used was time domain reflectometry (TDR) techniques (Nemmers 1998, Evett 2003).

2.4.1.1. Proximal Nuclear Sensing Techniques (Neutron Backscatter, neutron logging, etc.)

Proximal nuclear sensing techniques have been widely employed in engineering practice since its initial development and use in California in 1954 (Padlo et al. 2005). Specifically, the nuclear density gauge (NDG) has been commonly employed as part of a QA/QC testing regime to ensure the proper placement of soil and asphalt pavement. Because many earthwork specifications include both a density parameter (e.g. 95 percent of standard proctor density as determined using ASTM D698 2014) and a moisture condition (e.g. +/- 2 percent of optimum moisture content), the NDG provides a method to obtain measurements of both properties of interest simultaneously with a single instrument. Similarly, the neutron logging probe has been employed since the 1920s in deep geological investigations using the same principle (Kerr and Worthington 1988). With

respect to obtaining measurements of soil water content, the principle of neutron moderation was employed to provide an estimate of soil water content adjacent to the instrument (Kerr and Worthington 1988, International Atomic Energy Agency 2005). As reported by International Atomic Energy Agency (2005), typical neutron backscatter instruments have consisted of an Americium-241 (^{241}Am) or Californium-242 (^{242}Ca) source material, a beryllium matrix, and either a slow (thermal) neutron counter or a Geiger-Muller tube (for gauges which recorded secondary gamma radiation). For these instruments, alpha (${}^{4}_{2}He$) particles emitted by the decay of the ^{241}Am were captured by the beryllium matrix material, resulting in the release a neutron, a gamma photon, and an average of 5.71 MeV (Equation 2.14 and Equation 2.15).

$$ {}^{241}_{95}Am \Rightarrow (5.46\ MeV\ ) {}^{4}_{2}He + {}^{237}_{93}Np \qquad \text{Equation 2.14} $$

$$ {}^{9}_{4}Be + {}^{4}_{2}He \rightarrow {}^{12}_{6}C + n + (5.71\ Mev\ )\gamma \qquad \text{Equation 2.15} $$

In Equation 2.14 and Equation 2.15, the upper subscript indicates the number of neutrons in the nucleus, the lower number indicates the number of protons in the nucleus.

These fast (> 1 MeV) neutrons escaped the instrument and were propagated into the environment. The emitted fast neutrons are moderated by random interactions with matter in the environment (Figure 2.11). In the soil-water-air system, hydrogen nuclei provide the most efficient moderation (due to its low capture cross section) by absorbing the kinetic energy of the neutron through elastic collisions or, less likely, by capturing the neutron to convert the hydrogen into deuterium (^{2}H). After sufficient elastic collisions ("moderation") have occurred the neutron's kinetic energy is reduced to what would be expected at the temperature of the surrounding space (~0.0025 eV). The thermalized neutrons, which were backscattered to the sensors, are preferentially captured by a detector material (typically helium gas, cadmium, or lithium) and counted using a scintillion counter. Therefore, the ratio of backscattered thermal neutrons to emitted fast neutrons has been found to be proportional to the amount of hydrogen in the

environment around the instrument. In soil-water-air systems the majority of hydrogen nuclei are contained in water molecules and therefore the magnitude of the thermal neutron flux were found to be proportional to the soil water content.

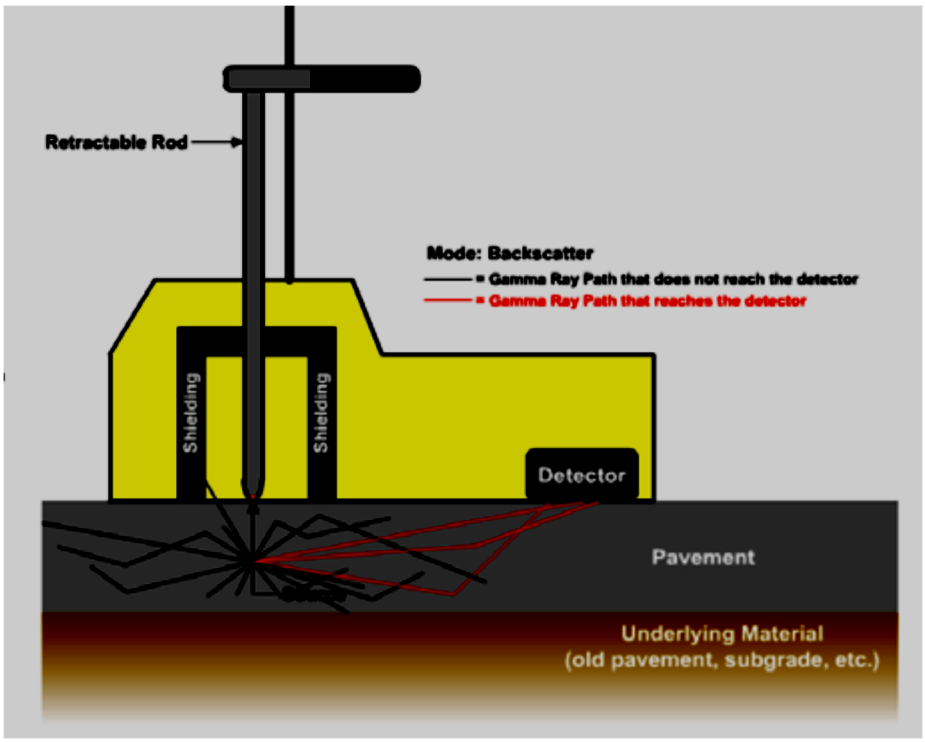

Figure 2.11. The principle of operation for the neutron backscatter moisture sensor (Padlo et al. 2005).

2.4.1.2. Time Domain Reflectometry (TDR)

TDR systems operate by sending individual stepped voltage increases with a fast rise time (<300 ps [Evett 2003]), through the center conductor of a coaxial cable into probes installed within the soil body. Because the physical dimensions and material properties of the cabling and probes were known (e.g. the speed of propagation through the shielded cable, the length of the cable [including system latency], the length of the epoxy coated probe head, and the length of the three unshielded probe leads), the variance in travel time has been shown to only be a function of the wave propagation speed in the unshielded portion of the probe. While the dielectric constant (or more properly dielectric permissivity) for soil is a complex frequency dependent number, only

the imaginary component has been reported to provide a significant contribution to the electric loss term over the range of frequencies employed in TDR systems (Nemmers 1998) and is computed using Equation 2.16 through Equation 2.18.

$$v_p = \frac{v}{c_0} = (\varepsilon\mu)^{-\frac{1}{2}} \quad \text{(Evett 2003)} \quad \text{Equation 2.16}$$

$$v = \frac{2L}{t_t} \quad \text{(Evett 2003)} \quad \text{Equation 2.17}$$

$$\varepsilon_a = \left[\frac{c_0 t_t}{2L}\right]^2 \quad \text{(Evett 2003)} \quad \text{Equation 2.18}$$

In Equation 2.16 to Equation 2.18, v_p is the velocity factor setting, v is the velocity of propagation through the shielded cable, c_0 is the speed of light in a vacuum, ε is the dielectric constant of the cable shielding, μ is the magnetic permeability of the dielectric material, L is the length of the unshielded probe lead, t_t is the travel time, and ε_a is the apparent dielectric constant of the soil.

The travel time in the unshielded probes is determined by an examination of the reflected waveform. This term may also be represented as an apparent length (L_a) which was equivalent to the square root of the apparent dielectric constant ($K_a^{0.5}$ or $\varepsilon_a^{0.5}$). An example of a returned TDR waveform for a compacted sample, showing the implementation of the tangent method, is presented in Figure 2.12. Moreover, a conceptual diagram of the propagation of the electrical signal, the multiple internal reflections, and the returned signal is presented as Figure 2.13.

The volumetric moisture content of the soil body is calculated from the apparent probe length (L_a) using an empirically derived correlation between the volumetric water content (θ) and the measured apparent dielectric constant (K_a). Multiple relationships have been proposed but the most commonly employed relationship was proposed by Topp et al. (1980) and is presented as Equation 2.19. The Topp et al. (1980) equation has been generally considered to provide acceptable results for most soil types. However, the best practice has been to generate a soil/site specific relationship using laboratory compacted samples of the site specific soil (Take et al.

2007). Specifically, the development of a soil/site specific volumetric water content and dielectric constant relationship was presented in Take et al. (2007).

Advantages of TDR measurement have included the ability to rapidly obtain results, the ease of data processing, and the automation of data collection (if required). The primary disadvantage of TDR measurements has been the empirical nature of the volumetric water content and apparent dielectric constant. Specifically, measurement error has been influenced by the presence of organic material, salinity, clay content, and soil constituents (Nemmers 1998).

$$\theta = AK_a^3 - BK_a^2 + CK_a - D$$ (Topp et al. 1980) Equation 2.19

In Equation 2.19, θ is the volumetric water content, and K_a is the apparent dielectric constant. The constants A, B, C, and D are empirically determined coefficients with values of $4.3 \cdot 10^{-6}$, $5.5 \cdot 10^{-4}$, $2.92 \cdot 10^{-2}$, and $5.3 \cdot 10^{-2}$, respectively.

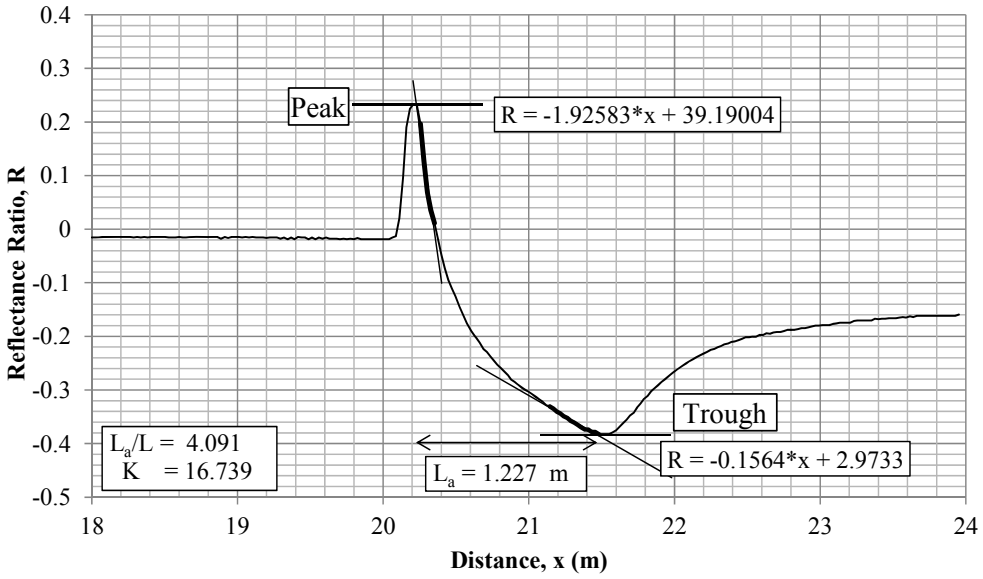

Figure 2.12. An example of returned TDR waveform with an illustration of the tangent method (Nemmers 1998) to determine the probe apparent length.

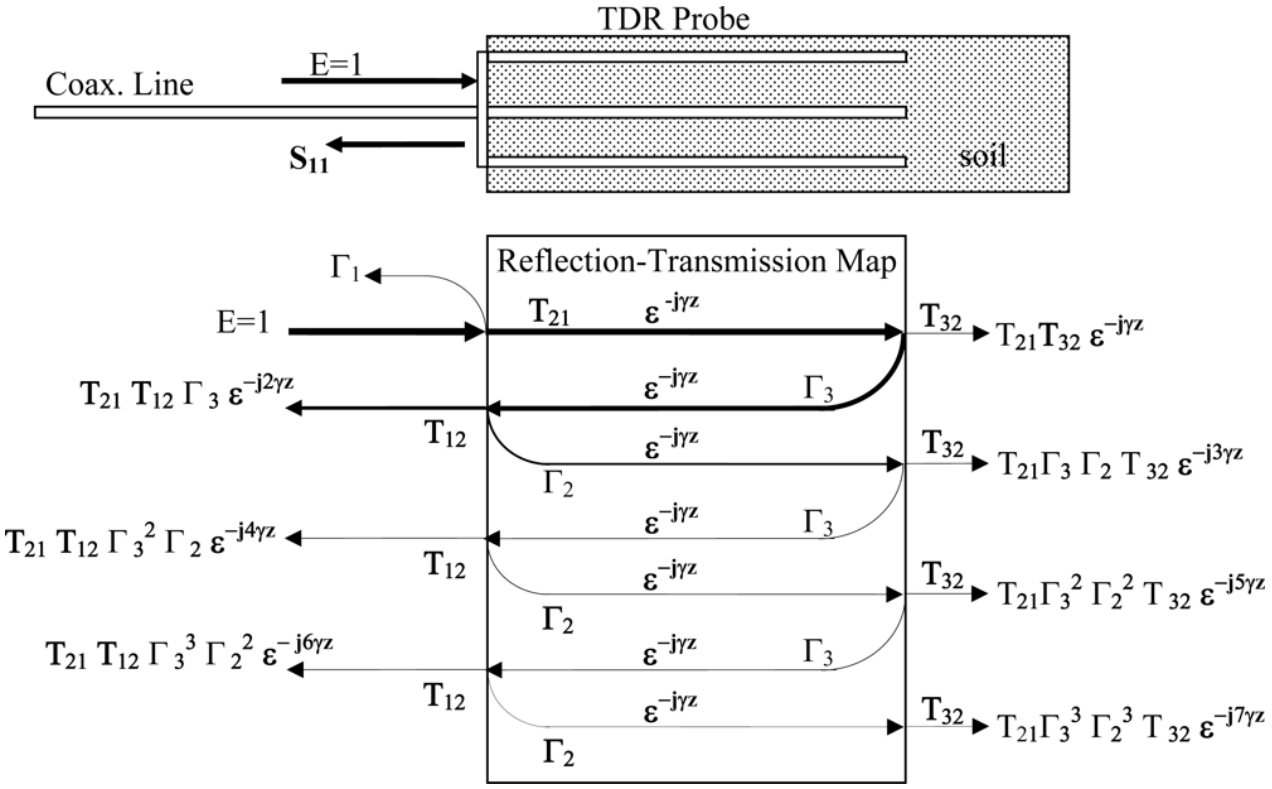

Figure 2.13. A schematic of the reflected TDR waveform illustrating the electric field propagation (E), multiple reflections (Γ), and re-transmission (T) for a TDR probe embedded in the soil (Pelletier et al. 2011).

2.4.2. *Traditional In Situ Methods to Determine Soil Water Potential*

Two *in situ* instruments which have been employed to measure the soil water potential in the field are tensiometers and the heat dissipation sensors. While both tensiometers and heat dissipation sensors operate by placing the sensor in intimate, hydraulic, contact with the soil, the theory of operation and the applicable ranges of soil water content that the instruments can measure are different (Lu and Likos 2002). The theory of operation and the advantages and disadvantages which have been associated with the tensiometer are presented in discussed in Section 2.4.2.1. Similarly, the theory of operation and limitations of the heat dissipation sensors are discussed in Section 2.4.2.2.

2.4.2.1. Tensiometers

As described by Stannard (1986), tensiometers consist of a porous tip hydraulic connected through a water column to a pressure transducer or a suction gauge. The tensiometer was initially developed by Richards and Gardner (1936). The Irrometer Model-E tensiometer (an example of a commercially available tensiometer) is comprised of a ceramic tip, acrylic standpipe, and acrylic reservoir, and an electric vacuum gauge. The probe body is fabricated out of a butyrate plastic body and a porous, high air entry, ceramic filter stone. An image of the probe is presented in Figure 2.14.

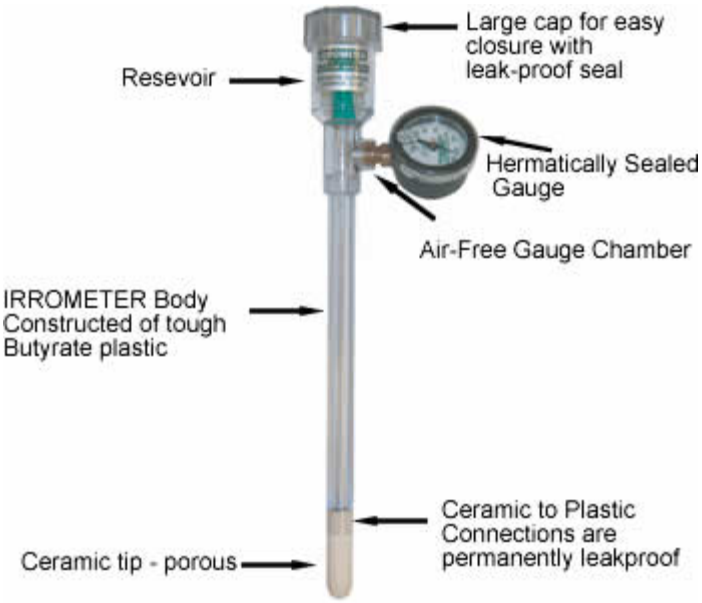

Figure 2.14. Irrometer tensiometer (image from Calafrica, 2015).

Each probe is commonly filled with a de-aired fluid mixture as specified by the manufacturer (Irrometer, 2012). To provide a method to automatically collect data, some probes (e.g. the Irrometer Model-E) have a variable resistor coupled to the analog suction gauge that causes a suction (potential) dependent voltage drop relative to the input voltage. As the gauge reading increases (more suction), the resistance of the gauge linearly increases. The resulting

voltage drop is then read by using a data logging system to measure the potential of the water in the soil. The soil water potential is then determined using Equation 2.20.

$$P_s = \frac{(V_E - V_m)}{265^{\circ} * F_c} \qquad \text{(Irrometer, 2012)} \qquad \text{Equation 2.20}$$

In Equation 2.20, P_s is the soil water potential; V_E is the excitation voltage; Vm is the measured (signal) voltage; and Fc is the sensor calibration factor (0.00111 Volts / Degree / Centibar).

2.4.2.2. Heat Dissipation Sensors

In situ measurements of soil matric potential have been commonly obtained by using a heat dissipation sensor (Phene et al. 1971, Reece 1996, Campbell Scientific 2013). Heat dissipation sensors consist of two thermocouples placed inside of a ceramic matrix that are then surrounded with soil. The soil potential between the soil and the ceramic matrix is allowed to equilibrate over time. In the heat dissipation sensor test procedure the probe temperature (relative to the end of thermocouple circuit) has been determined *in situ* by measuring the voltage differential across the electrical coupling of one of the thermocouples. If the temperature at the end of the thermocouple circuit is known (e.g. by using the datalogger internal temperature or more accurately using a thermistor) then the *in situ* soil temperature can be calculated. By applying a voltage to the other thermocouple, heating of the ceramic is initiated. Specifically, in previous applications, the temperature of the ceramic was measured initially (before excitation), at one second after excitation (T_1), and 30 seconds after excitation (T_{30}). The difference in the probe temperature between T_1 and T_{30} was logarithmically proportional to the soil potential.

As previously described, advantages inherent to the heat dissipation method have included a non-soluble, chemically stable matrix material, low cost, and the ability to obtain measurements over a large range of water potential values. The primary disadvantage of the heat dissipation sensor has been that each sensor requires individual calibration prior to use (because of

manufacturing variations in the ceramic probe tip). Additionally, heat dissipation sensors, while capable of measuring a large range of soil water potential values (0 to 5000kPa), have reduced resolution (compared to tensiometers) at low absolute values of soil water potential.

2.5. Remote Sensing Methods to Determine Unsaturated Soil Properties

Remote sensing techniques have been broadly divided into two categories (active and passive). In historic applications, active remote sensing techniques have "illuminated" the target region with some form of electromagnetic (EM) energy and then extracted the data from the backscattered emission. Conversely, passive systems have relied on the reflection or emission of ambient EM energy to provide information about the scattering material. Remote sensing systems operate over a wide range of the EM spectrum from gamma rays (<0.3nm) to radio waves (~30m). As per Coffman (2013a), the EM bandwidths of interest for unsaturated soils are presented in Figure 2.15.

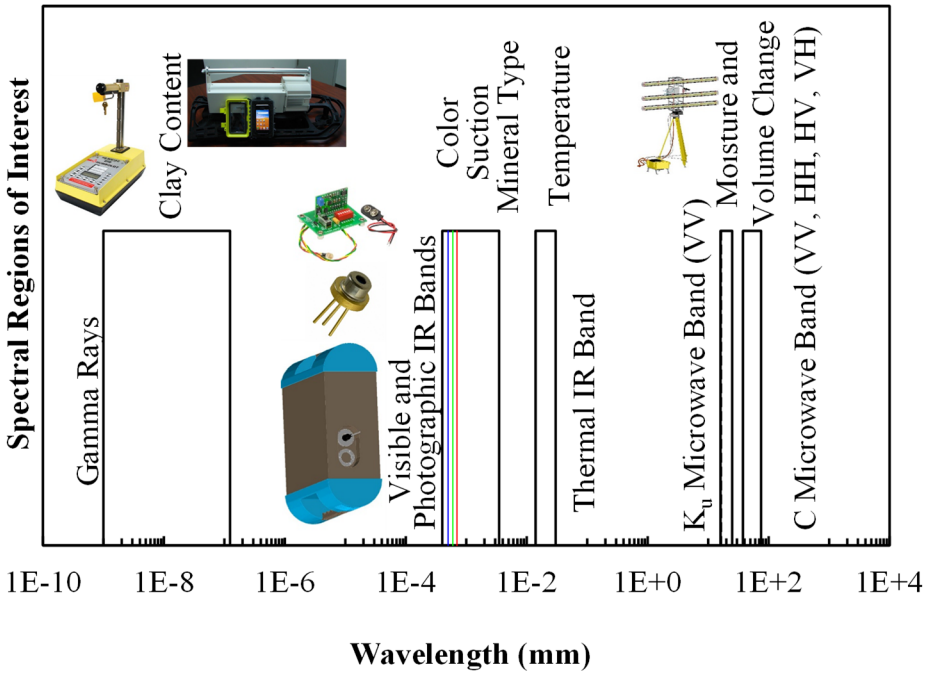

Figure 2.15. Electromagnetic spectrum with bands of interest for remote and proximal sensing in soils (modified from Coffman 2013a).

2.5.1. *Active and Passive Microwave Techniques to Determine Soil Water Content*

Measurements of water content have been obtained by observing the effects of water on the complex dielectric permittivity of the soil (previously referred to as the dielectric constant) through the intensity of reflected energy (Ulaby 1974, Fung et al. 1992, Oh et al. 1992, Sarabandi et al. 1994, Dubois et al. 1995, Chen et al. 2003, Dash and Prusty 2007, Stephen et al. 2010). A discussion of two methodologies for water content determination by employing active microwave data (change detection and EM scattering theory) is presented in Section 2.5.1.1 and Section 2.5.1.2. Previous researchers have used radio detection and ranging (radar) technology to analyze soil moisture content using ground-based systems (Ulaby 1974, Sarabandi et al. 1994). However, the most commonly employed systems for geoscience research have been orbital synthetic aperture radar (SAR) systems as described in Dubois et al. (1995), Wegmuller (1997), and Wagner (1998). Specifically, extraction of soil moisture data has been conducted by observing the influence of soil moisture (via dielectric permittivity) on the radar backscatter coefficient, σ^0. Furthermore, soil moisture inversion techniques have been conducted using both polarimetric and non-polarimetric instruments.

For both polarimetric and non-polarimetric studies, previous research into determining volumetric water content in soils using radar has focused on the use of aerial or orbital SAR platforms (Fung et al. 1992, Wegmuller 1997, Blumberg et al. 2000, Blumberg and Freilikher 2001). The intensity of the radar return has been shown to be a function of transmitted power, effective antenna area, angle of incidence, surface roughness, and material dielectric constant as described in Richards (2005, Equation 2.21). The transmitted power, effective antenna area, and angle of incidence were properties of the sensor and geometry of the imaging relative to the target area. The surface roughness and dielectric constant were dependent upon the surface material, the

water content, and the surface geometry (tilled, compacted, bare earth, etc.). Using multiple viewing geometries (or sensors) it was possible to directly solve for both the surface roughness and the material dielectric constant by using surface scattering models. Typical surface scattering models have included normalized difference vegetation index (NDVI) correlated models (Equation 2.22), the Integral Equation Model (IEM), as presented in Equation 2.23, and the geometric optics model (Fung et al. 1992). Like with TDR, after the dielectric constant was determined, the dielectric constant was related to volumetric water content by using empirical relationships. Unlike TDR measurements (where the real component of the complex dielectric permittivity was negligible), the frequency dependence of the complex electrical loss term had to be corrected (Njoku and Entekhabi 1994) or modeled through the use of a dielectric mix model (Wang 1980, Wang and Schmugge 1980, Dobson et al. 1985).

$$P_r = \frac{P_t G^2 \lambda^2 \sigma^0 \Delta R \xi_3}{(4\pi)^3 R_0^3 L_s L_a (R_0) \cos(\delta)} \quad \text{(Richards 2005)} \quad \text{Equation 2.21}$$

$$m_s = \mu_s + \frac{\sigma^\circ - A - B(\theta - \theta_{ref}) - N(NDVI) - \mu_{NDVI}}{C(\theta - \theta_{ref}) + D} \quad \text{(Stephen et al. 2010)} \quad \text{Equation 2.22}$$

$$\sigma_{hh}^0 = -\frac{k^2}{2} \exp(-2k_z^2 \sigma^2) \sum_{n=1}^{\infty} \sigma^{2n} \left| I_{hh}^n \right|^2 \frac{W^n(-2k_x, 0)}{n!} \quad \text{(Dash and Prusty 2007)} \quad \text{Equation 2.23}$$

In Equation 2.21 to Equation 2.23, P_r is the power received, P_t is power transmitted, G is the antenna gain, λ is the wavelength, σ^o is the backscatter coefficient; θ is the angle of incidence (reference is typically 10 degrees); m_s is the soil moisture content; μ_s is the annual soil moisture; NDVI is the Normalized Difference Vegetation Index; μ_{NDVI} is the annual mean of NDVI; A, B, C, D, and N are empirical coefficients; ΔR is the range resolution; ξ_3 is the 3-dB azimuth beamwidth; R_0 is range; L_s is the system loss factor; L_a is the atmospheric loss factor; δ is the grazing angle; σ^0_{hh} is the horizontal transmitted horizontally received backscatter coefficient; k is the wavenumber, k_z is $k\cos(\theta)$; I is a function of the incidence angle and Fresnel reflection coefficient; σ is the normalized (roughness, wavelength, and incident angle) backscatter coefficient, W_n is the frequency domain of the nth power of the surface correlation function; and k_x is $k\sin(\theta)$.

2.5.1.1. Change Detection Methods (Single Polarization)

Wegmuller (1997) and Wagner (1998) presented non-polarimetric change detection algorithms where the change in reflectivity of a target was correlated to temporal changes in water content (m_s). The primary advantage of these methods was the assumption that the physical site geometry was not significantly altered and that the observed changes in backscatter intensity ($\sigma^{\circ}_{0,t}$ corrected for vegetation and incident angle) were solely attributed to changes in the soil dielectric constant. An example of a non-polarimetric method, as used to determine water content (as proposed in Wagner 1998), is presented using Equation 2.24 and Equation 2.25.

$$\sigma^0(dB) = 10 * \log(\sigma^0)(m^2 m^{-2}) \quad \text{(Wagner 1998)} \quad \text{Equation 2.24}$$

$$m_s(t) = \frac{\sigma^0(\theta_{0'}, t) - \sigma^0_{dry}(\theta_{0'}, t)}{\sigma^0_{wet}(\theta_{0'}, t) - \sigma^0_{dry}(\theta_{0'}, t)} \quad \text{(Wagner 1998)} \quad \text{Equation 2.25}$$

The Wegmuller (1997) method was originally proposed for use with the European Space Agencies (ESA) European Remote Sensing satellite (ERS-1). The Wegmuller (1997) method, like the method proposed by Wagner (1998), correlates signal intensity with soil moisture content. An empirical correlation between logarithmic changes in backscatter intensity and changes in volumetric water content (Equation 2.26 and Equation 2.27) was developed by Wegmuller (1997), enabling the calculation of the absolute volumetric water content of the soil (Equation 2.28) when coupled with a reference image with a known water content. Wegmuller (1997) further extended the empirical relationship by using data collected from satellite observations on test sites in the United States and Europe (Equation 2.29 and Equation 2.30).

$$\Delta m_v = 0.042\ \Delta\sigma^0|dB| \quad \text{(Wegmuller 1997)} \quad \text{Equation 2.26}$$

$$\Delta\sigma^0 = \sigma^0_2|dB| - \sigma^0_1|dB| \quad \text{(Wegmuller 1997)} \quad \text{Equation 2.27}$$

$$m_v = m_{v.o} + 0.042\ (\Delta\sigma^0|dB| - \Delta\sigma^0_0|dB|) \quad \text{(Wegmuller 1997)} \quad \text{Equation 2.28}$$

$$i = \frac{\sigma^0_0 - 8.56\, m_{v.0}}{8.56 - 1.56\, i} \quad \text{(Wegmuller 1997)} \quad \text{Equation 2.29}$$

$$m_v = \frac{\sigma^0 - i}{8.56 - 1.56\, i} \quad \text{(Wegmuller 1997)} \quad \text{Equation 2.30}$$

In Equation 2.26 to Equation 2.30, Δm_v is the change in volumetric water content, $\Delta\sigma^0$ is the difference in corrected backscatter coefficient, σ^0_1 and σ^0_2 are the backscatter coefficient of temporally separated returns, $m_{v.0}$ is the known moisture content at the reference image, σ^0_0 is the reference backscatter coefficient, and i is the intercept value.

2.5.1.2. Methods for Data with Multiple Polarization

Polarimetric methods have been underpinned by a theoretical analysis of electromagnetic scattering theory. Using EM theory and the assumption of a smooth (small perturbation method) or rough (integral equations method) soil surface, previous researchers (Rice 1951, Oh et al. 1992, Dubois et al. 1995, Fung et al. 1992, and Chen 2003) have proposed solutions to the Bragg scattering matrix (Equation 2.31) and the associated Fresnel reflection equations (Equation 2.32 and Equation 2.33). Polarimetric soil moisture inversions have allowed for the absolute soil moisture content to be computed from a single pass (as opposed to the change detection algorithms that require multiple passes) by comparing the reflection from two different polarizations.

Methods for polarimetric moisture inversion have included the Small Perturbation Method (SPM) as introduced by Ulaby et al. (1986), the Integral Equations Method (IEM) as introduced by Fung et al. (1992), and the Advanced Integral Equations Method (AIEM) as introduced by Chen et al. (2003). The incoherent backscatter intensity has been dependent on polarization, incident angle, soil properties, vegetation, and surface roughness. Therefore, to extract the apparent dielectric constant of the soil it was necessary to know some of the site parameters, a priori. Specifically, these methods were computationally intensive and required an estimation (and/or measurement) of the ground surface roughness magnitude and distribution.

Typically, the surface roughness was obtained by field measurements in both the range and azimuth directions. The actual method employed was dictated by the assumptions used in the derivation of each method. In practice, due to the computational demands of the SPM and IEM methods, semi-empirical formulations based on *in situ* data and specific equipment (λ) and viewing geometry (θ) were adopted. Examples of the semi-empirical formulations of the SPM

method as proposed by Oh et al. (1992) and Dubois et al. (1995) are presented in Equation 2.34 through Equation 2.36, and Equation 2.37 through Equation 2.41, respectively.

$$[S]=\begin{bmatrix} S_{hh} & S_{hv} \\ S_{vh} & S_{vv} \end{bmatrix} = m_s \begin{bmatrix} R_h(\theta,\varepsilon) & 0 \\ 0 & R_v(\theta,\varepsilon) \end{bmatrix}$$ (modified from ESA 2013) Equation 2.31

$$R_0^h = \frac{\cos(\theta) - \left(\varepsilon - \sin^2(\theta)\right)^{\frac{1}{2}}}{\cos(\theta) + \left(\varepsilon - \sin^2(\theta)\right)^{\frac{1}{2}}}$$ (modified from ESA 2013) Equation 2.32

$$R_0^v = \frac{(\varepsilon - 1)\left(\sin^2(\theta) - \varepsilon\left(1 - \sin^2(\theta)\right)\right)}{\varepsilon\cos(\theta) + \left(\varepsilon - \sin^2(\theta)\right)^{\frac{1}{2}}}$$ (modified from ESA 2013) Equation 2.33

$$p = \frac{\sigma_{hh}^0}{\sigma_{vv}^0} = \left(1 - \left(\frac{2\theta}{\pi}\right)^{\frac{1}{3\Gamma^0}} e^{-ks}\right)^2$$ (Oh et al. 1992) Equation 2.34

$$q = \frac{\sigma_{hv}^0}{\sigma_{vv}^0} = 0.23\sqrt{\Gamma^0}\left(1 - e^{-ks}\right)$$ (Oh et al. 1992) Equation 2.35

$$\Gamma^0 = \left|\frac{1-\sqrt{\varepsilon'}}{1+\sqrt{\varepsilon'}}\right|$$ (Oh et al. 1992) Equation 2.36

$$\sigma_{hh}^0 = 10^{-2.75}\frac{\cos^{1.5}(\theta)}{\sin^5(\theta)} 10^{0.028\varepsilon'\tan(\theta)}\left(ks\cdot\sin(\theta)\right)^{1.4}\lambda^{0.7}$$ (Dubois et al. 1995) Equation 2.37

$$\sigma_{vv}^0 = 10^{-2.37}\frac{\cos^3(\theta)}{\sin^3(\theta)} 10^{0.046\varepsilon'\tan(\theta)}\left(ks\cdot\sin(\theta)\right)^{1.1}\lambda^{0.7}$$ (Dubois et al. 1995) Equation 2.38

$$\sigma_{qq}^0 = 8k^4h^2\cos^4(\theta)W\left(2k\sin(\theta)\right)\left|\alpha_{qq}(\theta)\right|^2$$ (Dubois et al. 1995) Equation 2.39

$$\alpha_{HH}^0 = \frac{\left(1-\varepsilon'\right)}{\left(\cos(\theta) + \sqrt{\varepsilon' - \sin^2(\theta)}\right)^2}$$ (Dubois et al. 1995) Equation 2.40

$$\alpha_{HH}^0 = \frac{\left(\varepsilon'-1\right)\left(\sin^2(\theta) - \varepsilon'\left(1+\sin^2(\theta)\right)\right)}{\left(\varepsilon'\cos(\theta) + \sqrt{\varepsilon' - \sin^2(\theta)}\right)^2}$$ (Dubois et al. 1995) Equation 2.41

In Equation 2.31 to Equation 2.41, S is the Bragg scattering matrix; m_s is the backscatter amplitude containing roughness information; $R^0_{h/v}$ are the Bragg scattering coefficients for vertically and horizontally polarized incident waves; ε is the complex dielectric permittivity constant; p and q are cross polarization ratios; θ is the incident angle, Γ^0 is the Fresnel reflection ratio at nadir; ε' is the real component of dielectric permittivity; ks is the normalized surface roughness; σ^0_{qq} is the polarized (HH or VV) backscatter coefficient; k is the wavelength; h is the absolute surface roughness; and W is the surface roughness spectrum.

2.5.2. *Ultraviolet – Visible and Infrared Reflectance to Determine Soil Water Content*

LIDAR systems have also been used by other researchers to generate high resolution digital elevation models (DEM), as presented in Haile and Rientjes (2005), Filin et al. (2007), and Liu (2008). Commercially available LIDAR systems (e.g. the Leica C-10 Laser Scanner) traditionally operate in the visible portion of the EM spectrum. LIDAR derived DEM have been used to monitor ground movements associated with slope stability, ground subsidence, and construction activities (Morris et al. 2007, Froese and Mei 2008, Stewart et al. 2009, Conte 2012, Garner and Coffman 2014).

While LIDAR systems have not been previously described to actively measure surface soil parameters, the acquired DEM data have been utilized to obtain an inference of soil parameters including topographic wetness index (TWI), horizon depth, soil organic content, soil potassium content, soil pH, and soil silt content. TWI, which is often referred to in the archival literature in the shortened form "wetness index", is an index property that was derived by modeling the effects of topography on the flow of water (Bevin and Kirkby 1979). In the computation of TWI, a surface flow model is employed to determine the drainage area and curvature of slope throughout a DEM model (Equation 2.42). The TWI is not a direct measurement but can be used with meteorological simulations to predict the concentration of water based on changes in solar irradiation, wind speed, and precipitation.

$$TWI = \ln\left(\frac{a}{\tan(b)}\right) \qquad \text{(Bevin and Kirkby 1979)} \qquad \text{Equation 2.42}$$

In Equation 2.42, TWI is the topographic wetness index, a is the area of the upstream collection basin (as determined using a terrain model), and tan(b) is the local slope in radians.

LIDAR based systems have also been used to monitor atmospheric profiles using differential absorption LIDAR (DIAL). As presented in Grant (1982), Machol et al. (2004), Sira

Ltd (2004), and NOAA (2012a), measurements of atmospheric gas species utilizing DIAL techniques were conducted by employing the differing absorption rates of specific gas species for EM energy at various wavelengths. Specifically, the wavelength dependency of EM absorption by atmospheric gas species was utilized to determine the concentration of gas species by analyzing the diffuse backscatter at two or more wavelengths. The sensor platform typically consists of an active source (laser) that emitted a pulse of light that interacted with the atmosphere. A portion of the emitted energy was scattered by atmospheric aerosols back towards the sensor where the intensity of the returned energy was recorded.

Traditional surveying LIDAR systems function by measuring the travel time of a light pulse between the target and the sensor either through direct timing or interferometric techniques. Historically, the distance between the sensor and the target was determined from the travel time and the speed with which the light propagated through the atmosphere. For DIAL systems, the system also records the signal intensity for multiple wavelengths. It was possible to use the difference between the energy received on each wavelength to calculate the concentration of the target gas as a function of range. Equations derived by Grant (1982) and NASA (2013) have been used to calculate the concentration of the target gas as a function of the relative return intensity (Equation 2.43 through Equation 2.46).

$$P_r = \frac{P_t \rho A \eta \cos(\theta)}{\pi R^2} e^{[-2(\alpha C + \beta)R]} \qquad \text{(Grant 1982)} \qquad \text{Equation 2.43}$$

$$CR = \frac{\ln\left(\frac{P}{P'}\right) + \ln\left(\frac{\rho'}{\rho}\right) + 2(\beta - \beta')R + \ln\left(\frac{\eta'}{\eta}\right)}{2\alpha' - 2\alpha} \qquad \text{(Grant 1982)} \qquad \text{Equation 2.44}$$

$$P = \frac{P_r}{P_t} \qquad \text{(Grant 1982)} \qquad \text{Equation 2.45}$$

$$N_A = \frac{1}{2(R_2 - R_1)(\sigma_A - \sigma'_A)} \ln\left[\frac{P_r(R_1) * P_r(R_2)}{P'_r(R_1) * P_r(R_2)}\right] \qquad \text{(NASA 2013)} \qquad \text{Equation 2.46}$$

In Equation 2.43 to Equation 2.46, P_r is the LIDAR power received; P_t is the transmission power; ρ is the surface reflectance; A is the antenna area; η is the system optical efficiency; θ is the incidence angle; R is the distance to target; α and σ are the atmospheric absorption coefficient; C and N_A are the gas concentration; β is the extinction coefficient; and primes denote the off-peak (non-absorbed) properties.

2.5.3. *Remote Sensing Techniques to Determine Soil Characterization*

Microwave techniques have been used to determine the soil texture and mineralogy. Specifically, the dielectric constant at certain wavelengths have been used to infer soil mineralogy and clay content. Clay content and mineralogy have been inferred by measuring the effects of adsorbed water on the complex permittivity of soils for microwave (25 MHz – 4 GHz) frequencies by using ground penetrating radar (Arcone et al. 2008, Aqil and Schmitt 2010).

Passive infrared remote sensing has also been used to determine clay mineralogy by previous researchers (Chabrillat et al. 2002, Goetz et al. 2006). Different clay mineralogies have been found to exhibit specific reflection spectra (Figure 2.16).

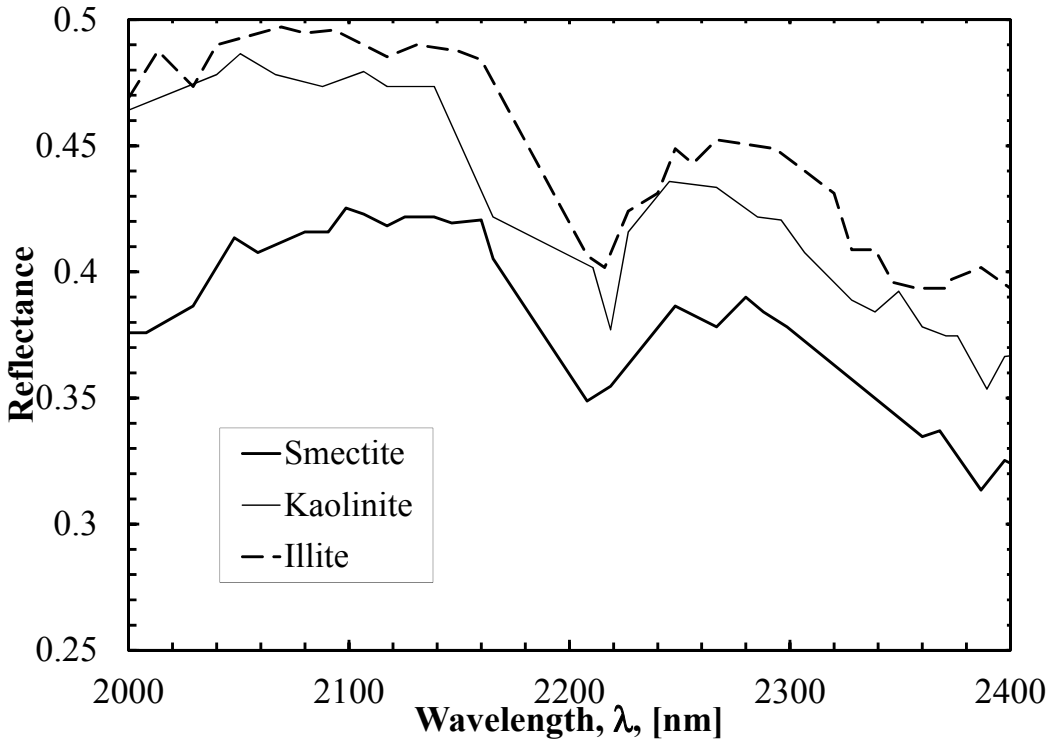

Figure 2.16. Reflectance spectra for three clay mineralogies (after Chabrillat et al. 2002).

Specifically, passive infrared spectroradiometry utilizes the frequency dependence of EM reflection and absorption of differing crystalline materials. At the most basic level, research has shown that EM energy was preferentially absorbed when the energy of constituent photons approach the energy of the covalent bonds within a material. Passive infrared remote sensing (spectroradiometry) has utilized the same theory employed in laboratory reflectance techniques such as attenuated total reflectance (ATR) spectroscopy, Fourier transform (FT), and diffuse reflectance infrared Fourier transform (DRIFT) spectroscopy (Schoeder 2002). Specifically, the hydroxyl groups, tetrahedral groups, silicate/aluminate anions, octahedral metal cations, and interlayer cations encountered in clay mineralogy have specific EM reflectance signatures (Farmer 1974, Busca and Resini 2000, Schroeder 2002, Stuart 2004). For example, hydroxyl (Oxygen-Hydrogen) stretching modes were excited by EM energy at 600 to 950cm^{-1} (Schroeder 2002, Stuart 2004). While crystalline vibrations have been difficult to predict using theoretical models, experimentally derived IR reflectance and absorption spectra for materials of interest in clay and soil chemistry have been commonly available.

Traditional Fourier transform infrared (FTIR) spectroscopy has utilized a transmission scheme to quantitatively identify material components. This transmission scheme has been previously employed due to the simplified computational and theoretical analysis associated with the reduced number of unknowns that were required to be evaluated. Specifically, the Beer-Lambert law has been commonly employed to identify and quantify chemical species in optically translucent samples. Utilizing the transmission scheme, the transmission length (l) was a known parameter of the length of the sample chamber and the quantity of a chemical species in a sample could be determined by using an empirically obtained absorption coefficient (α or k), the sample

length (l), and the optical transmission ratio (I/I_0), as presented in Equation 2.47 and Equation 2.48.

$$\frac{I}{I_0} = 10^{-\alpha c l} \quad \text{(Hapke 2012)} \quad \text{Equation 2.47}$$

$$\alpha c l = \sum_{i=1}^{n} a_i c_i l_i \quad \text{(Hapke 2012)} \quad \text{Equation 2.48}$$

In Equation 2.47 and Equation 2.48, I is the received intensity, I_0 is the output intensity, α is the absorption coefficient, c is the concentration of the chemical species, l is the path length, and the i subscript indicates the individual species.

However, the use of transmission spectroscopy has been historically limited by the requirement of an optically translucent sample. Therefore the DRIFT spectroscopy technique was developed to analyze optically opaque samples. While the majority of DRIFT spectroscopy has been employed to qualitatively detect the presence of chemical species in a sample (e.g. to detect impurities in pharmaceutical products), theoretical methods have also been developed to quantify the chemical species using a reflectance technique.

For example, the Kubelka-Munk color theory (Kubelka and Munk 1931, Kubelka 1947) was developed to allow for the analysis of industrial pigment samples (Judd and Wyszeki 1975). Specifically, the Kubelka-Munk theory enabled quantitative analysis by using empirically determined optical parameters (absorption [k] and scattering [s] coefficients). The Kubelka-Munk theory was developed using theoretical transfer equations to model a one-dimensional optical flux through a heterogeneous opaque medium (containing both scattering and absorbing particles) under perfectly diffuse and isotropic illumination. A two-flux condition was modeled (containing incident and reflected optical energy) for a thin layer of material underlain by either a perfectly black (absorbing) or perfectly white (reflecting) substrate. However, in experimental applications the sample is assumed to be sufficiently thick such that no energy penetrates to the substrate layer (as indicated by the subscript ∞ to denote a sample of infinite thickness).

The majority of quantitative DRIFT testing has been conducted using samples diluted with a reference material. The Kubelka-Munk function (Equation 2.49) has been used to relate the absorption and scattering behavior of a sample to the properties of the individual components (Equation 2.50). Specifically, the use of strongly scattering, weakly absorbing materials (over the ultra-violet, visible, and infrared spectrum) such as Potassium-Bromide (KBr) or Potassium Chloride (KCl) have been employed due to the uniform behavior of the dilutent material within the visible- to near-infrared (Vis-NIR) range of optical energy.

In a dilute sample, the sample scattering coefficient has been assumed to be solely dependent on the diluent material (e.g. S_{KBr} is equivalent to the S_{sample}). The mass fraction of the sample material has then been computed using the sample absorption coefficient and the Kubelka-Munk function (Equation 2.49 and Equation 2.50). Furthermore, the Kubelka-Munk theory has allowed for the numerical transformation of a reflectance spectrum to a pseudo-absorption spectrum (for use with the Beer-Lambert equation) using the relationship between reflectance, transmission, and absorption (Equation 2.51 and Equation 2.52).

$$f(R_\infty) = \frac{k}{s} = \frac{(1-R_\infty)^2}{2R_\infty} \quad \text{(Hapke 2012)} \quad \text{Equation 2.49}$$

$$\frac{k}{s} = \sum_{i=1}^{n} \frac{k_i m_i}{s_i m_i} \quad \text{(Hapke 2012)} \quad \text{Equation 2.50}$$

$$1 = R + A + T \quad \text{(Rossel et al. 2010a)} \quad \text{Equation 2.51}$$

$$A_\infty = Log_{10}\left(\frac{1}{R_\infty}\right) \quad \text{(Rossel et al. 2010a)} \quad \text{Equation 2.52}$$

In Equation 2.49 to Equation 2.52, $f(R_\infty)$ is the Kubelka-Munk function, k is the absorption coefficient, s is the scattering coefficient, R_∞ is the infinite depth reflectance, m is the mass fraction, the i subscript indicates a component value, R is relative reflection, A is the relative absorption, and T is the relative transmission, and A_∞ is the simulated absorption.

DRIFT spectroscopy has been previously employed to determine soil properties include the following. Soil textural qualities that have been measured using DRIFT spectroscopy include

Biomass content (Reeves et al. 1999, Reeves and McCarty 2001), Sand content (Janik et al. 1995, Chang et al. 2001, Islam et al. 2003), Silt content (Janik et al. 1995, Chang et al. 2001, Cozzolino and Moron 2003, Shepherd and Walsh 2002, Islam et al. 2003), and Soil specific surface area (Ben-Dor and Banin 1995). Soil chemical properties which have been measured using DRIFT spectroscopy include pH (Chang et al. 2001, Janik et al. 1995, Islam et al. 2003, Shibusawa et al. 2001, Kodaira and Shibusawa 2013), Carbon:nitrogen ratio (Chang and Laird 2002), Calcium content (Janik et al. 1995, Islam et al. 2003, Cozzolino and Moron 2003, Shepherd and Walsh 2002), Copper content (Chang et al. 2001, Cozzolino and Moron 2003), Carbonate content (Janik and Skjemsted 1995, Ben-Dor and Banin 1995), Iron content (Barron and Torrent 1986, Janik et al 1995, Islam et al. 2003, Cozzolino and Moron 2003, Chang et al. 2001), Potassium content (Janik et al. 1995, Islam et al. 2003, Daniel et al. 2003), Magnesium content (Janik et al. 1995), Nitrogen content (Janik and Skjemsted 1995, Reeves et al. 1999, Chang et al. 2001, Reeves and McCarty 2001, Walvoort and McBratney 2001, Chang and Laird 2002), and Zinc content (Chang et al. 2001).

Soil biological processes and properties which have been measured using DRIFT spectroscopy include inorganic and organic carbon content (McCarty et al. 2002, Chang and Laird 2002, Reeves et al. 1999, Chang et al. 2001, Nocita et al. 2013), available phosphorous (Janik et al. 1995, Daniel et al. 2003), clay content (Janik and Skjemstad 1995, Ben-Dor and Banin 1995, Janik et al. 1995, Chang et al. 2001, Shepherd and Walsh 2002, Walvoort and McBratney 2001, Cozzolino and Moron 2003), and soil respiration rate (Chang et al. 2001). Soil water content has also been measured using DRIFT spectroscopy (Park 1980, Dalal and Henry 1986, Ben-Dor and Banin 1995, Janik et al. 1995, Islam et al. 2003). While the majority of previously performed research using DRIFT spectroscopy to measure soil parameters has been conducted on dilute

ground samples, examples of testing intact soil samples (e.g. not diluted) for a quantitative analysis of soil mineralogy can also be found in the literature (Nguyen et al. 1991).

2.6. Works Cited

Ahuja, L., Naney, J., Williams, R., (1985). "Estimating Soil Water Characteristics from Simpler Properties or Limited Data." Soil Science Society of America Journal, Vol. 49, No. 5, pp. 1100-1105.

American Society for Testing and Materials (ASTM) D422, (2014). "Standard Test Method for Particle-Size Analysis of Soils." American Society for Testing and Materials, Vol. 4.08, Soil and Rock (I). West Conshohocken, PA.

American Society for Testing and Materials (ASTM) D698, (2012). "Standard test methods for laboratory compaction characteristics of soil using standard effort (12400 ft-lbf/ft3 (600 kN-m/m3))." Annual Book of ASTM Standards, 04.08, ASTM, West Conshohocken, PA, USA: 80-90.

American Society for Testing and Materials D2216, (2014). "Standard Test Methods for Laboratory Determination of Water (Moisture) Content of Soil and Rock by Mass." Annual Book of ASTM Standards, Designation D2216, Vol. 4.08, ASTM, West Conshohocken, PA.

American Society for Testing and Materials D4318, (2014). "Standard Test Methods for Liquid Limit, Plastic Limit, and Plasticity of Soils." Annual Book of ASTM Standards, Designation D4318, Vol. 4.08, ASTM, West Conshohocken, PA.

Applied Soil Water, (2015). "Applied Soil Water Technologies, LLC. Website." http://www.appliedsoilwater.com/. Accessed October 2015.

Aqil, S., Schmitt, D., (2010). "Dielectric Permittivity of Clay Adsorbed Water: Effect of Salinity." Proceedings of GeoConvention 2010, Calgary, Canada. No pages listed.

Arcone, S., Grant, S., Boitnott, G., Bostick, B., (2008). "Complex Permittivity and Mineralogy of Grain Size Fractions in a Wet Silt Soil." Geophysics, Vol. 73, No. 4, DOI:10.1190/1.2890776.

Aslyng, H. (Chairman), (1963). "Soil Physics Terminology." International Society of Soil Science Bulletin No. 23, pp. 7-10.

Atterberg, A., (1912). "Die Plastizitat der Tone." Internationale Mitteilungen fur Bodenkunde, Vol. 2, pp. 149-188 (in German).

Barron, V., Torrent, J., (1986). "Use of the Kubelka-Munk Theory to Study the Influence of Iron Oxides on Soil Colour." Journal of Soil Science, Vol. 37, pp. 499-510.

Ben-Dor, E., Banin, A., (1995). "Near-Infrared Analysis as a Rapid Method to Simultaneously Evaluate Several Soil Properties." Soil Science Society of America Journal, Vol. 59, pp. 364-372.

Bevin, K., Kirkby, M., (1979). “A physical based, variable contributing area model of basin hydrology.” Hydrological Science Bulletin, Vol. 24, pp. 43-69.

Blumberg, D., Freilikher, V., (2001). “Soil Water-Content and Surface Roughness Retrieval Using ERS-2 SAR Data.” Journal of Arid Environments, Vol. 49, pp. 449-464.

Blumberg, D., Freilikher, V., Lyalko, I., Vulfson, L., Kotlyar, A., Shevchenko, V., Ryabokenko, A., (2000). “Soil Moisture (Water Content) Assessment by an Airborne Scatterometer; The Chernobyl Disaster Area and the Negev Desert.” Remote Sensing of the Environment. Vol. 71, pp. 309-319.

Bolton, M., Cheng, Y., (2002). "Micro-Geomechanics." Proceedings of a Workshop on “Constitutive and Centrifuge Modelling: A Contrast.” Ascona, Switzerland, July.

Bouma, J., van Lanen, J., (1987). “Transfer Functions and Threshold Values: From Soil Characteristics to Land Qualities.” In Beek, K., Burrough, P., McCormack, D., “Proceedings of the International Workshop on Quantified Land Evaluation. Washington, DC, International Institute of Aerospace Surveying and Earth Science, Publication No. 6.

British Standard Institute (BSI), (1990) “Methods of Test for Soils for Civil Engineering Purposes.” British Standard Institute, London, UK.

Brooks, R., Corey, A., (1964). “Hydraulic Properties of Porous Media.” Colorado State University. Fort Collins, Colorado.

Brooks, R., Corey, A., (1966). “Properties of Porous Media Affecting Fluid Flow.” Journal of Irrigation Drainage Division of the American Society of Civil Engineers, Vol. 91, pp. 61-87.

Buckingham, E., (1907). “Studies on the movement of soil moisture.” Soil Bulletin No. 38, United States Department of Agriculture, Washington D.C.

Busca, G., Resini, C., (2000). “Vibrational Spectroscopy for the Analysis of Geological and Inorganic Materials.” Encyclopedia of Analytical Chemistry, Vol. 12, pp. 10984-11020.

Calafrica, (2015). “Cal Africa: Efficient Irrigation Scheduling Systems Website.” http://www.calafrica-sa.co.za/. Accessed October 2015.

Campbell Scientific, (2013). “CS-229 Heat Dissipation Sensors. Use and Calibration.” Campbell Scientific Website. Retrieved July 2013.

Campbell, D., (1976). “Plastic Limit Determination Using a Drop Cone Penetrometer.” Journal of Soil Science, Vol. 27, No. 3, pp. 295-300.

Campbell, E., Campbell, G., Barlow, W., (1973). "A Dew Point Hygrometer for Water Potential Measurement." Agricultural Meteorology, Vol. 12, pp. 113-121.

Carrier, W., Beckman, J., (1984). "Correlations between Index Properties of Remolded Clays." Geotechnique, Vol. 34, pp. 211-228.

Casagrande, A., (1932). "Research on the Atterberg Limits of Soils." Public Roads, Vol. 12, No. 8.

Casagrande, A., (1948), "Classification and Identification of soils: Transactions of the American Society of Civil Engineers." Vol. 113, pp. 901-930.

Casagrande, A., (1958). "Notes on the Design of the Liquid Limit Device." Geotechnique, Vol. 8, No. 2, pp. 84-91.

Chabrillat, S., Goetz, A., Krosley, L., Olsen, H., (2002). "Use of Hyperspectral Images in the Identification and Mapping of Expansive Clay Soils and the Role of Spatial Resolution." Remote Sensing of Environment, Vol. 82, pp. 431-445.

Chang, C., Laird, D., (2002). "Near-Infrared Reflectance Spectroscopic Analysis of Soil C and N." Journal of Soil Science, Vol. 17, pp. 110-116.

Chang, C., Laird, D., Mausbach, M., Hurburg, C., (2001). "Near-Infrared Reflectance Spectroscopy-Principle Components Regression Analysis of Soil Properties." Soil Science Society of America Journal, Vol. 65, pp. 480-490.

Chen, K., Wu, T., Tsang, L., Li, Q., Shi, J., Fung, A., (2003). "Emission of rough surfaces calculated by the integral method with comparison to three dimensional moment method simulations." IEEE Transaction on Geoscience and Remote Sensing. Vol. 41, p 90-101.

Coffman, R., (2013a). "CAREER: Incorporation of Statistics and Remote Sensing into Thermal-Hydraulic-Mechanical Modeling of Soils." A Proposal to the National Science Foundation.

Conte, O., Coffman, R., (2012). "Slope Stability Monitoring Using Remote Sensing Techniques." ASCE Geotechnical Special Publication No. 225, Proc. GeoCongress 2012: State of the Art and Practice in Geotechnical Engineering, Oakland, California, March, pp. 3060-3068.

Controls Group (2015). "Liquid Limit Devices – Casagrande." http://www.controls-group.com/eng/soil-testing-equipment/liquid-limit-devices-casagrande.php. Retrieved November 2015.

Cozzolino, D., Moron, A., (2003). "The Potential of Near-Infrared Reflectance Spectroscopy to Analyze Soil Chemical and Physical Characteristics." Journal of Agricultural Sciences, Vol. 140, pp. 65-71.

Croney, D., Coleman, J., (1961). “Pore Pressure and Suction in Soils.” Proceedings of the Conference on Pore Pressure and Suction in Soils, London. pp. 31-37.

Dalal, R., Henry, R., (1986). “Simultaneous Determination of Moisture, Organic Carbon, and Total Nitrogen by Near Infrared Reflectance Spectrophotometry.” Soil Science Society of America Journal, Vol. 50, pp. 120-123.

Daniel, K., Tripathi, N., Honda, K., (2003). “Artificial Neural Network Analysis of Laboratory and In Situ Spectra for the Estimation of Macronutrients in Soils of Lop Buri (Thailand).” Australian Journal of Soil Research, Vol. 41, pp. 47-595.

Dash, S., Prusty, G., (2007). “Simulation of Radar Backscattering Coefficients Using IEM Soil Moisture Retrieval.” Proceedings of the Third International Conference on Recent Advances in Space Technologies (RAST ’07). Istanbul, Turkey. pp. 383-388.

Dobson, G., Brewere, A., Cwilong, B., (1946). “Meteorology of the Lower Stratosphere.” Proceedings of the Royal Society (London), Vol. A185, pp. 144-175.

Dobson, M., Ulaby, F., Hallikainen, M., El-Rayes, M., (1985). “Microwave Dielectric Behavior of Wet Soil – Part II: Dielectric Mixing Models.” IEEE Transactions on Geoscience and Remote Sensing, Vol. GE-23, No. 1.

Dolinar, B., (2009). “Predicting the Normalized Undrained Shear Strength of Saturated Fine-Grained Soils Using Plasticity-Value Correlations.” Applied Clay Science, pp. 428-432.

Dubois, P., van Zyl, J., Engman, E., (1995) “Measuring Soil Moisture with Imaging Radar.” IEEE Transactions of Geoscience Remote Sensing, Vol. 33, pp. 916–926.

European Space Agency (ESA), (2013). “Rough Surface Scattering Models.” European Space Agency Online Manual. http://earth.eo.esa.int/polsarpro/Manuals/2_Rough_Surface_ Scattering_ Models.pdf. Retrieved December 2013.

Evett, S., (2003). “Soil Water Measurement by Time Domain Reflectrometry.” Encyclopedia of Water Science, Marcel Dekker, Inc. New York p 894-898.

Farmer, V., (ed.), (1974). “Infrared Spectra of Minerals.” Mineralogical Society. London.

Filin, S., Abo Akel, N., Kremeike, K., Sester, M., Doytsher, Y., (2007). “Interpretation and Generalization of 3D Landscapes from LIDAR Data.” Cartography and GeoInformation Science, Vol. 34, pp. 231-243.

Fredlund, D., Xing, A., (1994). “Equations of the Soil-Water Characteristic Curve.” Canadian Geotechnical Journal, Vol. 31, pp. 521-532.

Fredlund, D., Rahardjo, H., (1993). “Soil Mechanics for Unsaturated Soils.” Wiley, New York.

Froese, C., Mei, S., (2008). “Mapping and Monitoring Coal Mine Subsidence using LiDAR and InSAR.” GeoEdmonton 2008. Proceedings of the 61st Canadian Geotechnical Conference and Ninth Joint CGS/IAH-CNC Groundwater Conference. September 21-24, Edmonton Canada. pp. 1127-1132.

Fung, A., Li, Z., Chen, K., (1992). “Backscattering from a Randomly Rough Dielectric Surface.” IEEE Transaction on Geoscience and Remote Sensing, Vol. 30, pp. 356-369.

Garner, C., Coffman, R., (2014). “Remote Sensing Methods for Monitoring Ground Surface Deformation of Compacted Clay Test Sections.” ASCE Geotechnical Special Publication No. 234, Proceedings of the GeoCongress 2014: Geo-Characterization and Modeling for Sustainability, Atlanta, Georgia, February, pp. 963-978.

van Genuchten, M., (1980). “A Closed-Form Equation for Predicting the Hydraulic Conductivity of Unsaturated Soils.” Soil Science Society of America Journal, Vol. 44, No. 5, pp. 892-898.

GeoNor, (2015). “GeoNor Website.” http://geonor.com/live/. Accessed October 2015.

Goetz, A., Olsen, H., Noe, D., Koehler, J., Humble, J., Fuschino, J., Johnson, E., Johnson, B., (2006). “Spectral Reflectance as a Rapid Technique for Field Determination of Soil Engineering Properties.” Proceedings Geo-volution 2006, pp. 33-61.

Grant, W., (1982). "Effect of Differential Spectral Reflectance on DIAL Measurements using Topographic Targets." Applied Optics, Vol. 21, Issue 13, P 2390-2394.

Haigh, S., (2012). “Mechanics of the Casagrande Liquid Limit Test.” Canadian Geotechnical Journal, Vol. 49, No. 9, pp. 1015-1023.

Haile, A., Rientjes, T., (2005). “Effects of LIDAR DEM Resolution in Flood Modeling: a Model Sensitivity Study for the City of Tegucigalpa, Honduras.” ISPRS WG III/3 III/4 V/3 Workshop – Laser scanning. Enschede, the Netherlands. September 2005.

Hapke, B., (2012). “Theory of Reflectance and Remittance Spectroscopy.” 2 ed., Cambridge University Press.

Hillel, D., (2012). “Introduction to Environmental Soil Physics.” Elsevier Academic Press.

Holtz, R., and Kovacs, W., (1981). “An Introduction to Geotechnical Engineering: Englewood Cliff.” New Jersey, Prentice-Hall.

International Atomic Energy Agency (IAEA), (2005). “Technical Data on Nucleonic Gauges.” IAEA Technical Doc No. IAEA-TECDOC-1459. July 2005.

International Commission on Irrigation and Drainage (ICID), (1996). “Multilingual Technical Dictionary on Irrigation and Drainage.” 2nd ed. ICID-CIID, New Delhi, India.

Irrometer, (2012). “Irrometer-E Gauge and Probe Documentation.” Irrometer website. http://www.irrometer.com/pdf/instruction%20manuals/IRROMETERs/755%20E%20GaugeVACUUM%20hi%20Web4.pdf. Retrieved June, 2012.

Islam, K., Singh, B., McBratney, A., (2003). “Simultaneous Estimation of Various Soil Properties by Ultra-Violet, Visible, and Near-Infrared Reflectance Spectroscopy.” Australian Journal of Soil Research, Vol. 41, pp. 1101-1114.

Israelsen, O., West, F., (1922). “Water Holding Capacity of Irrigated Soils.” Bulleting No. 183, Utah Agricultural Experiment Station Bulletins, Paper 149.

Jamiolkowski, M., Ladd, C., Germaine, J., Lancellotta, R., (1985). “New Development in Field and Laboratory Testing of Soils.” Proceedings of the 11th International Conference on Soil Mechanics and Foundation Engineering, Vol. 1, pp. 57-153.

Janik, L., Skjemstad, J., (1995). “Characterization and Analysis of Soils using Mid-Infrared Partial Least Squares: II. Correlations with Some Laboratory Data.” Australian Journal of Soil Research, Vol. 33, pp. 637-650.

Janik, L., Skjemstad, J., Raven, M., (1995). “Characterization and Analysis of Soils Using Mid Infrared Partial Least-Squares. I. Correlations with XRF-Determined Major-Element Compositions.” Australian Journal of Soil Research, Vol. 33, pp. 621-636.

Judd, D., Wyszecki, G., (1975). “Color in Business, Science, and Industry.” John Wiley and Sons, New York.

Kansas Geological Society (KGS), (2015). “Kansas Geological Society Website.” http://www.kgs.ku.edu/. Accessed October 2015.

Kerr, S., Worthington, P., (1988). “Nuclear Logging Techniques for Hydrocarbon, Mineral, and Geological Applications." IEEE Transaction on Nuclear Science, Vol. 35, pp. 794-799.

Kodaira, M., Shibusawa, S., (2013). “Using a Mobile Real-Time Soil Visible Infrared Sensor for High Resolution Soil Properties Mapping.” Geoderma, Vol. 199, pp. 64-79.

Kubelka, P., (1947). “New Contributions to the Optics of Intensely Light-Scattering Materials, Part I.” Journal of the Optical Society of America, Vol. 38, Number 5, pp. 448-457.

Kubelka, P., Munk, F., (1931). “Ein Beitragzur Optik der Farbanstriche.” (in German), Z. Technol. Physics., Vol. 12, pp. 593-620.

Liu, X., (2008). “Airborne LIDAR for DEM Generation: Some Critical Issues.” Progress in Physical Geology. Vol. 32, No. 1, pp. 31-49.

Lu, N., Likos, W., (2002). “Unsaturated Soil Mechanics.” John Wiley and Sons, Hoboken, NJ.

Machol, J., Ayers, T., Schwenz, K., Koenig, K., Hardesty, R., Senff, C., Krainak, M., Abshire, J., Bravo, H., Sandberg, S., (2004). "Preliminary Measurements with an Automated Compact Differential Absorption LIDAR for Profiling Water Vapor." Applied Optics 43, pp. 3110-3121.

Mastenbrooke, H., Dinger, J., (1961). "The Measurement of Water-Vapor Distribution in the Stratosphere." Naval Research Laboratory. Report No. 5551.

McCarty, G., Reeves, J., Reeves, V., Follet, R., Kimble, J., (2002). "Mid-Infrared and Near-Infrared Diffuse Reflectance Spectroscopy for Soil Carbon Measurement." Soil Science Society of America Journal, Vol. 66, pp. 640-646.

Morris, J., Porter, D., Neet, M., Noble, P., Schmidt, L., Lapine, L., Jensen, J., (2007). "Integrating LIDAR Elevation Data, Multi-Spectral Imagery and Neural Network Modelling for Marsh Characterization." International Journal of Remote Sensing, Vol. 23, Issue 23, pp. 5221-5234.

Morris, P., Lockington, D., Apelt, C., (2000). "Correlations for Mine Tailings Consolidation Parameters." International Journal of Surface Mining, Reclamation and Environment, Vol. 14, pp. 171-443.

National Aeronautics and Space Administration (NASA), (2013). "DIAL Concept Description." http://asd-www.larc.nasa.gov/lidar/concept.html. Retrieved October, 2013.

National Oceanic and Atmospheric Agency (NOAA), (2012a). "Compact Water Differential Absorption LIDAR (CODI)." NOAA CODI project website. http://www.esrl.noaa.gov/csd/groups/ csd3 /instruments /wv_dial/. Retrieved December 2012.

Nemmers, C., (1998). "Volumetric Moisture Content Using Time Domain Reflectometry." FHWA publication number: FHWA-RD-97-139.

Neumann, H., and Thurtell, G., (1972). "A Peltier Cooled Thermocouple Dew Point Hygrometer for In Situ Measurement of Water Potentials." In Brown, R., Haveren, B., (eds.). "Psychometry in Water Relations Research." Utah Agricultural Experiment Station.

Nguyen, T., Janik, L., Raupach, M., (1991). "Diffuse Reflectance Infrared Fourier Transform (DRIFT) Spectroscopy in Soil Studies." Australian Journal of Soil Research Vol. 29, pp. 49-67.

Njoku, E., Entekahbi, D., (1994). "Passive Microwave Remote Sensing of Soil Moisture." Journal of Hydrology, Vol. 184, Issue 1-2, pp. 101-129.

Nocita, M., Stevens, A., Noon, C., van Wesemael, B., (2013). “Prediction of Soil Organic Carbon for Different Levels of Soil Moisture Using Vis-NIR Spectroscopy.” Geoderma, Vol. 199, pp. 37-42.

Norman, R., Brye, K., Gbur, E., Chen, P., Rupe, J., (2015). “Long-Term Effects of Alternative Residue Management Practices on Soil Water Retention in a Wheat-Soybean, Double-Crop System in Eastern Arkansas.” Open Journal of Soil Science, Vol. 5, pp. 199-209.

Novak, V., Havrila, J., (2006). “Method to Estimate the Critical Soil Water Content of Limited Availability for Plants.” Biologia, Bratislava, Vol. 61, Supplemental 19, pp. S289-293.

Oh, Y., Sarabandi, K., Ulaby, F., (1992). “An Empirical Model and an Inversion Technique for Radar Scattering from Bare Soil Surfaces.” IEEE Transactions on Geoscience and Remote Sensing, Vol. 30, No. 2, pp. 370-381.

Or, D., Tuller, M., (2002). “Cavitation During Desaturation of Porous Media Under Tension.” Water Resources Research, Vol. 38, No. 5, pp. 1-4.

Padlo, P., Mahoney, J., Aultman-Hall, L., Zinke, S., (2005). “Correlation of Nuclear Density Readings with Cores Cut from Compacted Roadways.” Report No. CT-2242-F-05-5. Report to the Connecticut Department of Transportation. Connecticut Advanced Pavement Laboratory, Connecticut Transportation Institute, School of Engineering, University of Connecticut.

Park, John K., (1980). “A Soil Moisture Reflectance Model in Visible and Near IR Bands.” Symposium on Machine Processing of Remotely Sensed Data and Soil Information Systems and Remote Sensing and Soil Survey. The Laboratory for Applications of Remote Sensing, West Lafayette, Indiana.

Pelletier, M., Viera, J., Schwartz, R., Evett, S., Lascano, R., McMichael, R., (2011). "Analysis of Coaxial Soil Cell in Reflection and Transmission." Sensors, Vol. 11, No. 3, pp. 2592-2610.

Phene, C., Rawlins, S., Hoffman, G., (1971). “Measuring Soil Matric Potential In Situ by Sensing Heat Dissipation within a Porous Body: I. Theory and Sensor Construction.” Soil Science Society of America Journal. Vol. 35, pp. 27-33.

Rawls, W., Brakensiek, D., (1985). “Prediction of Soil Water Properties for Hydrologic Modeling.” In Jones, E., and Ward, T., (eds.). “Proceedings of the Symposium on Watershed Management in the Eighties.” Denver, Colorado. pp. 293-299.

Reece, C., (1996). “Evaluation of a Line Heat Dissipation Sensor for Measuring Soil Matric Potential.” Soil Science Society of America Journal. Vol, 60, pp. 1022-1028.

Reeves, J., McCarty G., (2001). "Quantitative Analysis of Agricultural Soils Using Near Infrared Reflectance Spectroscopy and Fibre-Optic Probe." Journal of Near Infrared Spectroscopy, Vol. 7, pp. 179-193.

Reeves, J., McCarty G., Meisinger, J., (1999). "Near Infrared Reflectance Spectroscopy for the Analysis of Agricultural Soils." Journal of Near Infrared Spectroscopy, Vol. 7, pp. 179-193.

Rice, S., (1951). "Reflection of Electromagnetic Waves by Slightly Rough Surfaces." Community of Pure Applied Math. Vol. 4, p. 351-378.

Richards, B., (1965). "Measurement of the Free Energy of Soil Moisture by the Psychrometric Technique using Thermistors." In Aitchison, G., (ed.) "Moisture Equilibria and Moisture Changes in Soils Beneath Covered Areas." Butterworth and Co., Sydney, Australia, pp. 39-46.

Richards, L., (1928). The Usefulness of Capillary Potential to Soil Moisture and Plant Investigators." Journal of Agricultural Research, Vol. 37, 719-742.

Richards, L., (1941). "A Pressure Membrane Apparatus for Soil Solution Extraction." Soil Science, Vol. 51, pp. 377-385.

Richards, L., Gardner, W., (1936). "Tensiometers for Measuring the Capillary Tension of Soil Water." Journal of American Society of Agronomy, Vol. 28, pp. 352-358.

Richards, L., Waldleigh, C., (1952). "Soil Water and Plant Growth." In Shaw, B., (ed.) Soil Physical Conditions and Plant Growth. American Society of Agronomy Series Monographs, Vol. 2, pp. 74-251.

Richards, M., (2005). "Fundamentals of Radar Signal Processing." Mc-Graw Hill. New York.

Rossel, R., McBratney, A., Minasny, B., (eds.), (2010a). "Proximal Soil Sensing. Volume 1 of Progress in Soil Science." Springer Science and Business Media. Springer, New York.

Sarabandi, K., Pierce, L., Oh, Y., Dobson, M., Ulaby, F., Freeman, A., (1994). "Cross-Calibration Experiment of JPL AIRSAR and Truck-Mounted Polarimetric Scatterometer." IEEE Transactions on Geoscience and Remote Sensing. Vol. 32, No.5, pp. 975-985.

Schofield, A., Wroth, C., (1968). "Critical State Soil Mechanics." McGraw-Hill, London, UK.

Schroeder, P., (2002). "Infrared Spectroscopy in Clay Science." In Teaching Clay Science, Guggenheim, S., Rule, A., (eds.). Clay Minerals Society Workshop Series. The Clay Mineral Society, Aurora, Colorado Vol. 13, pp. 181-202.

Seed, H., Woodward, R., Lundgren, R., (1964). "Fundamental Aspects of the Atterberg Limits." Proceedings of the Soil Mechanics and Foundation Division, ASCE, SM6, pp. 75-104.

Shepherd, K., Walsh, M., (2002). “Development of Reflectance Spectral Libraries for Characterization of Soil Properties.” Soil Science Society for American Journal, Vol. 66, pp. 988-998.

Shibusawa, S., Imade-Amon, S., Sato, S., Sasao, A., Harako, S., (2001). “Soil Mapping Using the Real-Time Soil Spectrophotometer.” Proceedings of the Third European Conference on Precision Agriculture, Vol. 1, Agro Montpellier, pp. 497-508.

Sira Ltd., (2004). "Recommendations for Best Practice in the Use of Open-Path Instrumentation." A Review of Best Practice Based on the Project 'Remote Optical Sensing Evaluation' (ROSE) August 2001-2004.

Skempton, A., (1944). “Notes on the Compressibility of Clays.” Quarterly Journal of the Geological Society of London, Vol. 100, C: Parts 1 and 2. Pp. 119-135.

Skempton, A., (1953). “The Colloidal Activities of Clays.” Proceedings of the 3rd International Conference on Soil Mechanics and Foundation Engineering. Zurich, Switzerland.

Skempton, A., Northey, R., (1953). “The Sensitivity of Clays.” Geotechnique, Vol. 3, No. 1, pp. 30-53.

Smith, K., Mullins, C., (eds.), (2001). “Soil and Environmental Analysis: Practical Methods.” Marcel Dekker, New York.

Soil Moisture, (2015). “Soil Moisture Inc. Website.” http://www.soilmoisture.com/landing.php. Accessed 2015.

Spagnoli, G., (2012). “Comparison between Casagrande and Drop-Cone Methods to Calculate Liquid Limit for Pure Clay.” Canadian Journal of Soil Science, Vol. 92, No. 6, pp. 859-864.

Stannard, D., (1986). "Theory, Construction and Operation of Simple Tensiometers." Groundwater Monitoring and Remediation, Vol. 6, Issue 3. pp. 70-78.

Stephen, H., Ahmad, S., Piechota, T., (2010). “Relating Surface Backscatter Response from TRMM Precipitation RADAR to Soil Moisture: Results over a Semi-Arid Region.” Hydrology and Earth System Sciences, Vol. 14, Issue, 2, pp. 193-204.

Stewart, J., Hu, J., Kayen, R., Lembo, A., Collins, B., Davis, C., O’Rourke, T., (2009). “Use of Airborne and Terrestrial LIDAR to Detect Ground Displacement Hazards to Water Systems.” Journal of Surveying Engineering, Vol. 135, pp. 113-124.

Stuart, B., (2004). “Infrared Spectroscopy: Fundamentals and Applications.” John Wiley and Sons. ISBN 0-470-85427-8.

Taiz, Z., (2002). “Plant Physiology.” 4 ed. Sinauer Associates.

Take, W., Arnepalli, D., Brachman, R., and Rowe. R., (2007). “Laboratory and Field Calibration of TDR Probes for Water Content Measurement.” Ottawa Geo 2007. Ottawa, Canada

Tefera, T., (2013). “Measurement of Plastic Limit of Cohesive Soils.” Report No. 208 for Norwegian Public Roads Administration. Project 603152.

Terzaghi, K., (1926b). “Principle of Final Soil Classification.” Public Roads, Vol. 8, No. 3, pp. 41-53.

Terzaghi, K., (1926a). “Simplified Soil Tests for Subgrades and Their Physical Significance.” Public Roads, No. 8, pp. 153-170.

Thunder Scientific, (2015). “Thunder Scientific Corporation Website.” http://www.thunderscientific.com/. Accessed October 2015.

Topp, G., Davis, J., Annan, A., (1980). “Electromagnetic Determination of Soil Water Content: Measurements in Coaxial Transmission Lines.” Water Resources Research, Vol. 16, Issue 3, pp. 574-582.

Tyree, M., (2003). “Matric Potential.” Encyclopedia of Water Science. doi: 101.108/E-EWS. pp. 615-617.

Ulaby, F., (1974). “Radar Measurement of Soil Moisture Content.” IEEE Transactions on Antennas Propagation. Vol. AP-22, pp. 257–265.

Ulaby, F., Moore, R., Fung, A., (1986). “Microwave Remote Sensing, Active and Passive. Volume III, from Theory to Application.” Artech House, Massachusetts.

Veihmayer, F., Hendrickson, A., (1949). “Methods of Measuring Field Capacity and Permanent Wilting Percentage of Soils.” Soil Science, Vol. 68, No. 75-94.

Veihmeyer, F., Hendrickson, A., (1927). “+B375+B9” Proceedings of the 1st International Congress on Soil Science, Vol. 3, pp. 498-513.

Wagner, W., (1998). “Soil Moisture Retrieval from ERS Scatterometer Data.” PhD Dissertation, Vienna University of Technology. November.

Walvoort, D., McBratney, A., (2001). “Diffuse Reflectance Spectrometry as a Proximal Sensing Tool for Precision Agriculture.” Proceedings of the Third European Conference on Precision Agriculture, Agro Montpellier, Vol. 1, pp. 503-507.

Wang, J., (1980). “The Dielectric Properties of Soil-Water Mixtures at Microwave Frequencies.” Radio Science, Vol. 15, pp. 977-985.

Wang, J., Schmugge, T., (1980). “An Empirical Model for the Complex Dielectric Permittivity of Soils as a Function of Water Content”. IEEE Transactions on Geoscience and Remote Sensing, pp. 288-295.

Waruru, B., Shepherd, K., Ndegwa, G., Kamoni, P., Sila, A., (2014). “Rapid Estimation of Soil Engineering Properties Using Diffuse Reflectance Near Infrared Spectroscopy.” Journal of Biosystems Engineering, Vol. 121, pp. 177-185.

Wasti, Y., (1987). “Liquid and Plastic Limits as Determined from the Fall Cone and the Casagrande Methods.” Geotechnical Testing Journal, GTJODJ, Vol. 10, No. 1, pp. 26-30.

Watanabe, K., Takeuchi, M., Osada, Y., Ibata, K., (2012). “Micro-Chilled-Mirror Hygrometer for Measuring Water Potential in Relatively Dry and Partially Frozen Soils.” Soil Science Society of America Journal, Vol. 76, pp. 1935-1945.

Wegmuller, U., (1997). “Soil Moisture Monitoring with ERS SAR Interferometry.” European Space Agency Special Publication ESA SP-414. Proceedings of the 3rd ERS Symposium. pp. 47-51.

White, W., (1949). “Atterberg Plastic Limits of Clay Minerals.” Clay Minerals, Vol. 34, No. 7, No pages listed.

Whyte, I., (1982). “Soil Plasticity and Strength: A New Approach Using Extrusion.” Ground Engineering, Vol. 15, No. 1, pp. 16-24.

Wilson, G., Clifton, A., Barbour, S., (1999). “The Emergence of Unsaturated Soil Mechanics.” National Research Council Press.

Wood, David M., (1990). “Soil Behaviour and Critical State Soil Mechanics.” Cambridge University Press. London, UK.

Wroth, C., Houlsby, G., (1985). “Soil Mechanics-Property Characterization and Analysis Procedures.” Proceedings of the 11th International Conference on Soil Mechanics and Foundation Engineering, Vol. 1, pp. 1-55.

Wroth, C., Wood, D., (1978). “The Correlation of Index Properties with Some Basic Engineering Properties of Soils.” Canadian Geotechnical Journal, Vol. 15, No. 2, pp. 137-145.

Youssef, M., El Ramli, A., El Demery, M., (1965). “Relationships between Shear Strength, Consolidation, Liquid Limit, and Plastic Limit for Remoulded Clays.” Proceedings of the 6th International Conference on Soil Mechanics and Foundation Engineering, Montreal, Vol. 1, pp. 126-129.

CHAPTER 3: MATERIALS AND PROCEDURES FOR REMOTE MEASUREMENT OF SOIL PROPERTIES

3.1. Chapter Overview

A description of the instrumentation and procedures employed to acquire and process remotely sensed radio detection and ranging (radar) data is contained in this chapter. Specifically, utilization of radar data to measure the soil volumetric water content and the *in situ* density are presented. The two field project sites where radar imagery was acquired, the University of Arkansas Cato Springs Research Center (CSRC) and the WESTAR Jeffery Energy Center (WJEC), are described in Section 3.2. The K_u-Band and C-Band second generation Gamma portable radar interferometer (GPRI-2) instruments are described in Section 3.3. The methods and procedures that were employed to collect radar imagery are presented and discussed in Section 3.4. The techniques and computer software that were utilized to analyze the previously collected radar data and to obtain estimates of soil volumetric water content and *in situ* density, including: 1) preprocessing (Section 3.5.1), 2) image registration (Section 3.5.2), water content inversions (Section 3.5.3 and Section 3.5.4), and 3) *in situ* density inversions (Section 3.5.5.) are presented and described in Section 3.5.

3.2. Project Sites

Radar imagery was collected at the UACSRC and the WJEC. The two project sites are described in detail in this section. Specifically, the physical layout, construction activities, and prominent features are mentioned. The UACSRC project site is described in Section 3.2.1 and the WJEC project site is described in Section 3.2.2.

3.2.1. *University of Arkansas Cato Springs Research Center*

The UACSRC project site was located adjacent to the CSRC building at 1475 Cato Springs Road in Fayetteville, Arkansas. The project site consisted of two clay pads (30m by 15m)

that were compacted in a field to the Southeast of the UACSRC building. The total project area was approximately 3252m^2. The project site was developed as a part of the Mack-Blackwell Transportation Center (MBTC) project number 3031 as documented in Coffman and Garner (2012). The CSRC site layout is presented in Figure 3.1.

The project site had been previously developed and therefore the surface was highly variable. Initial soil conditions at the site generally consisted of approximately 5cm of variably weathered asphalt. At the North end of the project site, the asphalt was overlain by approximately 5cm of vegetated clayey topsoil material. Asphalt that had overburden material was typically intact while exposed sections of asphalt were highly weathered. Underneath the asphalt layer, the project site typically consisted of 15 to 30cm of road base material. Below the subgrade material, the project site consisted of multiple layers of soft, saturated clay to an undetermined depth. The elevation of the site was the highest on the south end of the project site and gradually decreased in elevation to the north until the project site abutted the retention pond that was located next to Cato Springs Road.

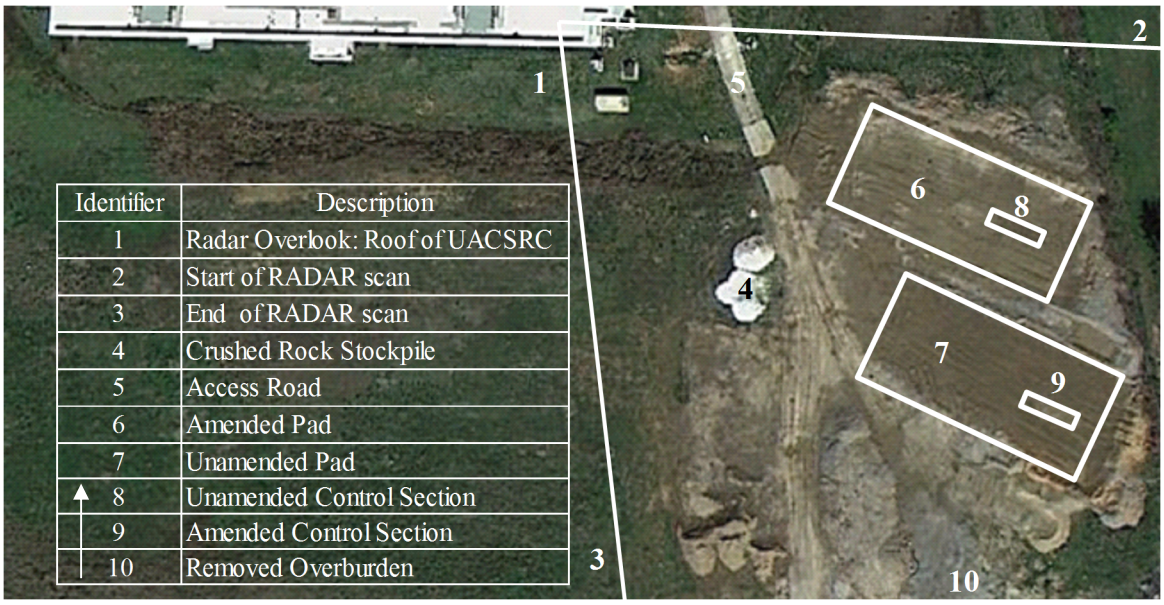

Figure 3.1. Layout of project site including the locations of Sections 1 and 2 and the overlook site on the roof of the UACSRC building (image modified from Google 2012 as cited in Garner and Coffman 2016) [in color].

Construction of the UACSRC project site was performed by University of Arkansas personnel. Project work flow generally followed the following operations: 1) the project site was stripped and grubbed to remove vegetation and topsoil, 2) the overburden material was excavated down to the subgrade, 3) the subsurface was leveled under the two compacted clay pads, 4) a sand drainage blanket was installed, 5) two 20cm thick loose lifts were placed and compacted, and 6) *in situ* instrumentation including time domain reflectometry (TDR) and tensiometers were installed.

Each of the two compacted clay pads were constructed with a 5cm thick sand drainage blanket. The sand material was acquired from a local supplier (Les Rodgers, Inc.) and was placed using a front end loader (CASE Model 50) and spread using a bull-dozer (CASE 530HLT). The clay material for the two pads was acquired from another local vendor (Chev's Trucking, Inc.) from a borrow site that was located to the West of Fayetteville, off of Broyles Road. Prior to transportation of the clay to the UACSRC project site, the clay material was mechanically sifted

to remove any particles greater than 1.3cm in diameter. The pad material was also spread using a bulldozer. One of the two pads (Pad 1) was amended with six percent of a sodium bentonite product (by dry weight). The sodium bentonite product (Enviroplug No. 8) was obtained from WyoBen Inc. (Billings, Montana). Both compacted clay pads were compacted using a padfoot vibratory roller (CASE model SV212). Further description of the UACSRC project site is available in Coffman and Garner (2012) and Garner and Coffman (2014).

3.2.2. *WESTAR Jeffery Energy Center (WJEC)*

Three 750 MW coal fired electrical generation units (total generation capacity of 2.2 GW) are located at the WESTAR Jeffery Energy Center (WJEC). The site was located approximately 11 km North of St. Marys, Kansas. The site that is documented herein was located on a full-scale, proof-of-concept, test section for proposed artificial wetlands. The wetlands were constructed to remove and entomb excess Selenium from the WJEC flue gas desulfurization waste stream. The test section was located on the grounds of the WJEC approximately 2km southwest of the primary power generation facility. The test section was approximately 60m long by 30m wide and was oriented with the long axis running approximately East-West. The test section consisted of 2m of a mechanically prepared sand-clay loam fill material underlain by a 30cm sand drainage blanket. The fill material was prepared by using local topsoil material that was stripped from the site, mixed with fill sand, and stockpiled prior to placement. Both the composition of the fill material and the placement density were intended to provide a material with a minimum hydraulic conductivity of $3.32 \cdot 10^{-5} cm \cdot s^{-1}$ (Coffman 2013b).

To reduce the bulk density of the placed soil, the soil was spread by using an overhead conveyor system and then leveled by using a low-ground pressure bulldozer (Caterpillar Model D6N). The purpose of the test section was to provide validation of 1) the construction materials

and 2) the methods that were proposed to be used for the full-scale wetlands. Spot measurements were collected during placement of the fill material by using a nuclear density gauge. Long term measurements were acquired using *in situ* instrumentation that was installed by University of Arkansas personnel. Remote sensing measurements were acquired concurrently with *in situ* hydraulic testing. The hydraulic conductivity testing included five (5) two-stage borehole tests and an open double ring infiltrometer testing. The layout of the project site is presented in Figure 3.2.

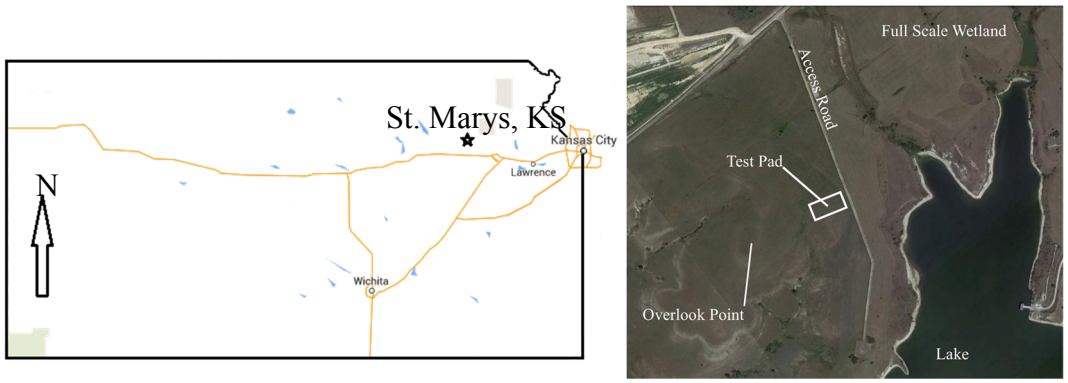

(a) (b)

Figure 3.2. a) Location of the WESTAR JEC site in the state of Kansas (modified from Google 2012), and b) aerial image of the WESTAR JEC project site (image from Google 2014 as cited in Garner and Coffman 2017a).

3.3. Second Generation Gamma Portable Radar Interferometer (GPRI – 2)

Two separate second generation Gamma portable radar interferometer (GPRI-2) systems were utilized. While the two radar instruments were operated at different microwave frequencies and in different polarimetric modes, the instruments shared many commonalities. Both the University of Arkansas (K_u-Band VV) and the University of Missouri (C-Band VV/HH/HV) GPRI-2 instruments that were utilized consisted of multiple real aperture antennas which were attached to an adjustable tower structure (Figure 3.3). The instruments were operated in the scanning mode by pivoting the antenna assembly about the vertical axis. This rotation allowed the instrument to collect radar imagery about the observation point. Images of the two GPRI-2

instruments are presented in Figure 3.3, and each instrument is further described in Section 3.3.1 and Section 3.3.2.

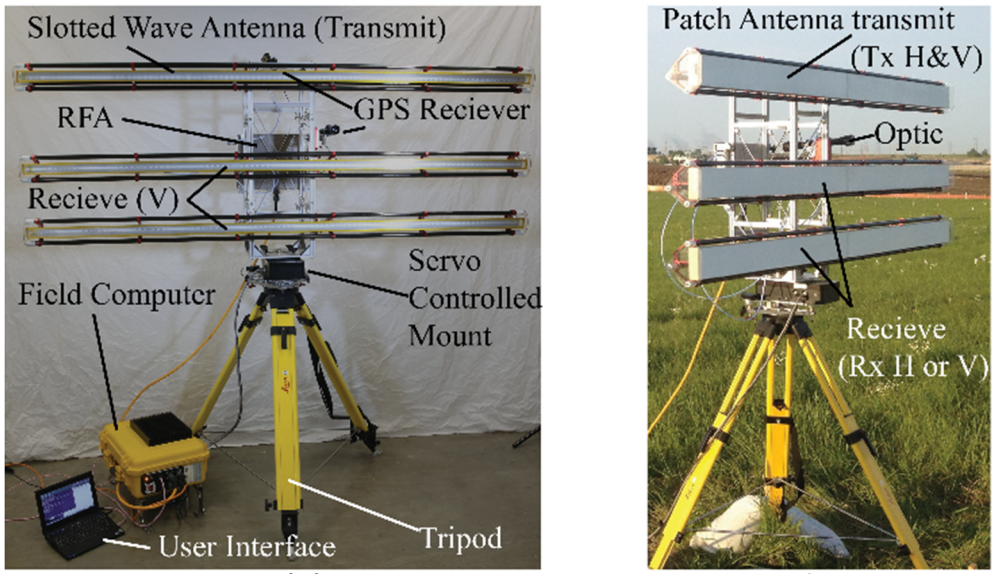

Figure 3.3. a) UA single-polarimetric K_u-Band radar (image from Kuss 2013), and b) modified UMC fully-polarimetric C-Band radar (image from Coffman 2014 as cited in Garner and Coffman 2017a).

3.3.1. *University of Arkansas K_u – Band GPRI-2*

The University of Arkansas (UA) K_u-Band GPRI-2 acquired radar imagery (intensity and phase) by using a wavelength of 1.7cm (17.63 GHz). Three vertically polarized transmission and vertically polarized reception (VV) slotted wave guide antennas were utilized to collect data. In typical operation, the GPRI-2 was configured to transmit through the upper-most antenna (TX) and then simultaneously receive data through the middle and lower antennas, on the RX-1 and RX-2 receive channels.

3.3.2. *University of Missouri C-Band GPRI-2*

The University of Missouri (UMC) C-Band GPRI-2 instrument was configured to acquire polarimetric radar data. The UMC GPRI-2 operated at a wavelength of 5.6cm (5.35 GHz, C-Band). The top patched antenna was configured to transmit in both horizontally and vertically

polarized modes. Depending on the transmit mode (horizontal [H] or vertical [V]) the two bottom antennas were allowed to collect vertically polarized (HV or VV) or horizontally polarized (HH or VH) data.

3.4. Data Acquisition

The techniques employed to acquire radar imagery at both the UACSRC and WJEC project sites are presented in this section. Data collection for both project sites was accomplished using the GPRI-2 instruments and the Gamma Interferometric software suite. The data collection techniques employed at the UACSRC are presented in Section 3.4.1. The data collection techniques employed at the WJEC are presented in Section 3.4.2.

3.4.1. *University of Arkansas Cato Springs Research Center (UACSRC)*

Radar imagery was acquired at the UACSRC from an overlook position in the southeast corner of the roof of the UACSRC building. The UA K_u-Band GPRI-2 was exclusively used to collect radar observations at the UACSRC site. Radar imagery was acquired between January 2012 and July 2012. Additional imagery was collected until November 2012, but due to equipment failure, this data was not able to be utilized. The overlook position was selected because it provided the most topographic relief between the instrument and the project site. To provide a consistent instrument position and orientation between sequential radar observations four concrete masonry unit (CMU) blocks were placed on the roof of UACSRC. Sandbags were placed over each of the CMU blocks to prevent accidental movement of the CMU blocks during the assembly and demobilization of the GPRI-2 instrument. A survey nail was placed into the center of one of the CMU blocks. The other three CMU blocks were employed to provide an anchorage point for the three legs of the GPRI-2 tripod. Prior to each observation, each of the

three tripod legs were affixed to the respective leg-supporting CMU block using a sleeved masonry screw.

Horizontal (North and East) alignment of GPRI-2 was verified using the laser plummet and integral bubble level in the tripod bearing plate of the GPRI-2. Vertical alignment of the GPRI-2 instrument was conducted by 1) recording the leg length (using a tape measure) and orientation of each of the three tripod legs during the first radar observation and 2) reestablishing the leg lengths and locations during subsequent observations. The orientation of the legs were maintained through all subsequent observations. The rotational alignment of the GPRI-2 instrument was accomplished by aligning the cross-hairs of the telescopic optic of the radar instrument (at a known angular deflection from the home position) with a vertical pole approximately 2 km away. An image of the UA GRPI-2 instrument at the CSRC site is presented in Figure 3.4. Similarly, the UACSRC project site, as observed from the overlook position after completion of construction is presented in Figure 3.4. The Gamma Remote Sensing software suite (Gamma Remote Sensing 2012) was utilized to control the instrument via a terminal SSH connection between a laptop computer and the GPRI-2 field computer. Prior to acquisition of radar imagery, equipment status and site conditions were recorded and documented as a text file (proc_commands.txt).

Information recorded included equipment status checks as conducted using Gamma Remote Sensing diagnostic tools (e.g. chupa_status.py, tscc_status.py, and gpsmon, home_run.py) and meteorological and site conditions (e.g. temperature, wind, relative humidity, time, project personnel). Meteorological data was acquired using the publically reported hourly National Oceanic and Atmospheric Administration data (NOAA 2016) for the nearby Drake Airfield (KXNA). An example proc_commands.txt file documenting site conditions, image acquisition,

and pre-processing commands is included as Appendix A.2. Specifically, radar imagery was acquired using the gpri_capture.py executable. The dates and quantity of radar observations at the UACSRC project site are tabulated in Table 3.1 and Table 3.2, respectively. A typical invocation of the gpri_capture.py script included the various inputs and outputs as presented in Table 3.3. The physical configuration and image acquisition profile that were utilized at the UACSRC project site are tabulated in Table 3.4. Included in the instrument settings was the chirp length (250 ms), signal attenuation (32 dB), beginning scan position (5 or -15 degrees) and end scan position (80 degrees). The chirp length of 250 ms was selected due to the limited spatial extent of the project site in the range direction. All of the other instrument parameters remained at the values recommended by Gamma Remote Sensing (2012). The aforementioned image parameters were selected by changing the respective values in the image acquisition profile (.prf) file (included as Appendix A.5.1).

(a) (b)

Figure 3.4. a) UA GPRI-2 radar configuration as employed at the CSRC project site showing instrument orientation, configuration, and anchor points, and b) view of the CSRC project site from the overlook position on the roof of the CSRC building (images by author).

Table 3.1. Radar observations at the UACSRC project site (Coffman and Garner 2012).

Scan No.	Date	Number of Images Acquired	Notes
1	1/10/2012	7	Site Construction
2	1/11/2012	9	Site Construction
3	1/13/2012	9	Site Construction
4	1/14/2012	9	Site Construction
5	1/15/2012	9	Site Construction
6	1/16/2012	9	Site Construction
7	1/18/2012	7	Site Construction
8	1/19/2012	7	
9	1/30/2012	37	Images Taken Over an 8 Hour Period
10	2/6/2012	7	
11	2/13/2012	7	
12	2/20/2012	7	
13	2/28/2012	7	
14	3/5/2012	7	
15	3/12/2012	7	
16	3/22/2012	7	
17	4/16/2012	7	
18	4/26/2012	7	
19	5/16/2012	7	
20	5/16/2012	7	Images Taken After Site Was Mowed
21	5/24/2012	7	
22	6/8/2012	8	One Image Not Capture
23	6/26/2012	7	

Table 3.2. Wide angle (MBTC-3031 wide) radar observations at the MBTC-3031 CSRC project site (Coffman and Garner 2012).

Scan No.	Date	Number of Images Acquired	Notes
1	1/10/2012	7	Site Construction
2	1/11/2012	9	Site Construction
3	1/13/2012	9	Site Construction
4	1/14/2012	9	Site Construction
5	1/15/2012	9	Site Construction
6	1/16/2012	9	Site Construction
7	1/18/2012	7	Site Construction
8	1/19/2012	7	
9	1/30/2012	37	Images Taken Over an 8 Hour Period
10	2/6/2012	7	
11	2/13/2012	7	
12	2/20/2012	7	
13	2/28/2012	7	
14	3/5/2012	7	
15	3/12/2012	7	
16	3/22/2012	7	
17	4/16/2012	7	
18	4/26/2012	7	
19	5/16/2012	7	
20	5/16/2012	7	Images Taken After Site Was Mowed
21	5/24/2012	7	
22	6/8/2012	8	One Image Not Capture
23	6/26/2012	7	

Table 3.3. Example invocation of the gpri_capture.py executable employed at the UACSRC project site including relevant inputs.

Usage:

gpri2_capture.py: [options] -p profile -o output_filename

Help:

-h, --help show this help message and exit
-e INTERFACE, --interface=INTERFACE use specified Ethernet interface [default=eth0]
-m MAC_ADDR, --mac-addr=MAC_ADDR use USRP2 at specified MAC address [default=None]
-f FREQ, --freq=FREQ set frequency to FREQ
-d DECIM, --decim=DECIM set fgpa decimation rate to DECIM [default=16]
-g GAIN, --gain=GAIN set USRP2 gain in dB (default is midpoint)
-K SCALE, --scale=SCALE set rx input scaling of usrp2, scale_iq (default is 1024)
-S SHIFT, --shift=SHIFT 'set rx output shifting of usrp2, shift_iq (default is 0).

--lo-offset=LO_OFFSET set daughterboard LO offset to OFFSET [default=hw default]
--rx-bufsize=RX_BUFSIZE set rx buffer size to RX_BUFSIZE [default=0]
-N NSAMPLES, --nsamples=NSAMPLES number of samples to capture [default=+inf]
-T CAPTURE_DURATION, --capture-duration=CAPTURE_DURATION number of seconds to capture [default=+inf]
-o OUTPUT_FILENAME, --output-filename=OUTPUT_FILENAME output filename for captured samples [default=None]
-s, --output-shorts output interleaved shorts instead of complex floats
-M, --lock-masterclock-to-SMA lock usrp2 100 Mhz master clock to external 10 Mhz reference clock on SMA input
-P, --sync-to-first-1PPS reset the usrp2 samplecounter on the first PPS received on the PPS SMA input
-j RX_START_TIMESTAMP, --rx-start-timestamp=RX_START_TIMESTAMP set start_at time of first RX packet in usrp2 100 Mhz clockpulses (long) [default=-1 start immediately]
-k RX_START_TIME_SECONDS, --rx-start-time-seconds=RX_START_TIME_SECONDS set start_at time of first RX packet in seconds (float) [default=-1.0 start immediately]
-C EXTERNAL_PROGRAM, --external-program=EXTERNAL_PROGRAM give a programname to start this as external program just before streaming starts (string) [default=None do not start an external program]
-v, --verbose verbose output
-p GPRI_PROFILE, --gpri-profile=GPRI_PROFILE GPRI-II acquisition profile [default=None]

Inovacation:

gpri2_capture.py -e eth1 -f 0.0 -M -P -S 1 -k 1.0 -v -p gpri_250us.prf -o RAW/mbtc3031_01102012.raw

Input:

1 gpri_250us.prf	GPRI-2 Profile Parameter File

Output:

1 RAW/mbtc3031_01102012_1.raw	Raw RADAR Image File
2 RAW/mbtc3031_01102012_1.raw_par	RAW RADAR Parameter File

Table 3.4. Instrument configuration and scan settings for the UA GPRI-2 at the UACSRC project site.

Data Acquisition	MBTC-3031		MBTC-3031 Wide		MBTC-3031 Phase 2	
Length Leg 1 (North)	44.10	cm	44.10	cm	44.10	cm
Length Leg 2 (East)	38.80	cm	38.80	cm	38.80	cm
Length Leg 3 (South)	40.20	cm	40.20	cm	40.20	cm
Chirp Length	250.00	ms	250.00	ms	250.00	ms
Radar Center Frequency	1.72	GHz	1.72	GHz	1.72	GHz
Attenuation	32.00	dB	32.00	dB	32.00	dB
Min. Chirp Frequency	100.00	MHz	100.00	MHz	100.00	MHz
Max Chirp Frequency	300.00	MHz	300.00	MHz	300.00	MHz
Number of Chirp Samples	1564.00	DN	1564.00	DN	1564.00	DN
Transmit Power	on	BOOL	on	BOOL	on	BOOL
Antenna Start Angle	5.00	Degrees	-15.00	Degrees	-15.00	Degrees
Antenna End Angle	80.00	Degrees	80.00	Degrees	80.00	Degrees
Motor Gear Ratio	72.00	DN	72.00	DN	72.00	DN
Motor Rotation Rate	5.00	Deg?s^{-1}	5.00	Deg?s^{-1}	5.00	Deg?s^{-1}
Data Capture Time	1.00	ms	1.00	ms	1.00	ms
Sampling Rate	6.25	MS·s^{-1}	6.25	MS·s^{-1}	6.25	MS·s^{-1}
Antenna Elevation	-5.00	Degrees	-5.00	Degrees	-5.00	Degrees

3.4.2. *WESTAR Jeffery Energy Center (WJEC)*

Acquisition of radar images at the WJEC project site was conducted using both the UA and UMC GPRI-2 instruments. As previously described in Section 3.2.2, the UA GPRI-2 tripod was assembled over a construction control point that was located on top of an adjacent topographic feature. The tripod was left erected for the duration of the radar observations to allow for both the UA and UMC GPRI-2 instruments to re-occupy the same point between sequential images. Rotational alignment was accomplished by aligning the radar's telescope optic with the West side of the Number 2 unit exhaust stack.

Depending on which instrument was utilized for a particular observation, the respective servo motor unit, antenna tower, antennas, or radio frequency assembly (RFA) were placed on the tripod. The UA GPRI-2 was configured in the same manner as was employed at the UACSRC project site with: the top antenna connected to "Transmit" (TX V), the middle antenna attached to

"Receive Channel 1" (RX-1 V), and the bottom antenna attached to "Receive Channel 2" (RX-2 V). Typically, seven (7) VV K_u-Band images were acquired rapidly (less than one minute elapsed time between the initiation of the first image capture and termination of the last image capture) to reduce the effects of any temporal variation in the acquired imagery.

Conversely, for the UMC C-Band imagery, two separate passes were required to obtain a set of fully polarimetric images (VV, VH, HH, HV) due to the configuration of the instrument. Due to data storage limitations only three (3) sets of C-Band images were acquired during each observation. Fully-polarimetric data were acquired by the following procedure: 1) the transmission mode "V" was electronically selecting and the RX-1 Channel was connected to the vertically polarized output of one of the patched antennas; and 2) the RX-2 Channel was also connected to the horizontally polarized output of the same patched antenna. The top antenna was always connected to TX for both "H" and "V" transmission modes. Three VV and VH C-Band images were acquired. After completion of the image acquisition the transmission mode was electronically switched (from V to H) and then three subsequent images were acquired (HV and HH). A schematic and image of the instrument connections is presented in Figure 3.5.

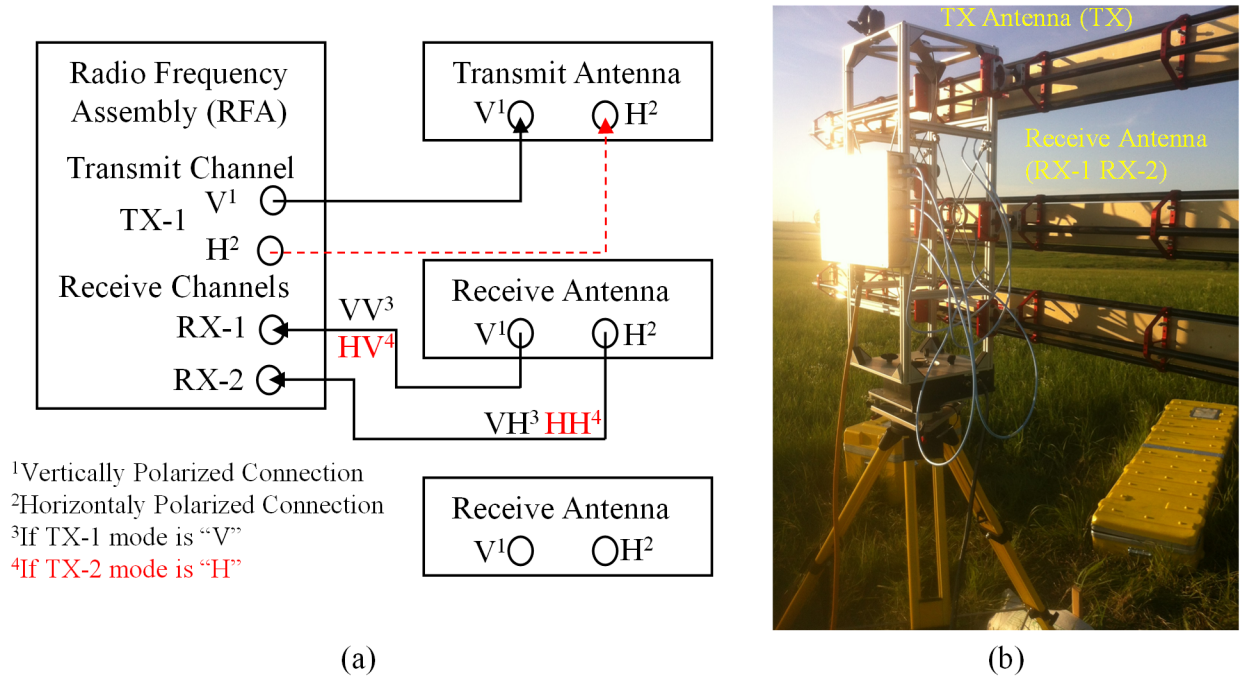

Figure 3.5. a) Schematic of UMC C-Band GPRI-2 connections, and b) image of instrument connections at the WJEC site [image by author, in color].

The number and type of radar images acquired at the WJEC project site is tabulated in Table 3.5. Configuration and instrument settings of the UA and UMC GPRI-2 radar interferometers are presented in Table 3.6. An example of the gpri2_capture.py executable used for C-Band acquisition at the WJEC site is presented in Table 3.7. The instrument acquisition profile (.prf) file is included as Appendix A.4.2. An image of the GPRI-2 instrument at the WJEC site, as well as a view of the project site from the overlook illustrating the site topography, project site is presented in Figure 3.6.

Table 3.5. Radar images captured at the WJEC site between June 10 and June 18, 2013 (Garner and Coffman 2017a).

Date	K_u-Band[a] Images Acquired	C-Band[b] Images Acquired
6/9/2013	7 VV[c]	No Images
6/10/2013	7 VV	No Images
6/11/2013	7 VV	No Images
6/12/2013	7 VV	No Images
6/13/2013	7 VV	4 VV[c], 4 HV[d], 4 HH[e], 4 VH[f]
6/14/2013	7 VV	3 VV, 3 HV, 3 HH, 3 VH
6/15/2013	No Images	3 VV, 3 HV, 3 HH, 3 VH
6/16/2013	No Images	3 VV, 3 HV, 3 HH, 3 VH
6/17/2012	7 VV	3 VV, 3 HV, 3 HH, 3 VH
6/18/2013	7 VV	3 VV, 3 HV, 3 HH, 3 VH

[a]K_u-Band (1.7 cm wavelength, 17.6 GHz), [b]C-Band (5.6 cm wavelength, 5.4 GHz),[c]VV (Vertically Transmitted and Received), [d]HV (Horizontaly Transmitted and Vertically Received), [e]HH (Horizontally Transmitted and Received),[f]VH (Vertically Transmitted and Horizontally Received).

Table 3.6. Example invocation of the gpri_capture.py executable employed at the WJEC project site with relevant inputs.

Data Acquisition	WESTAR Ku-Band		WESTAR C-Band		WESTAR C-Band	
Length Leg 1 (North)	-	cm	-	cm	-	cm
Length Leg 2 (East)	-	cm	-	cm	-	cm
Length Leg 3 (South)	-	cm	-	cm	-	cm
Chirp Length	500.00	ms	1 ms	ms	2.5ms	ms
Radar Center Frequency	1.72	GHz	5.40	GHz	5.40	GHz
Attenuation	32.00	dB	32.00	dB	32.00	dB
Min. Chirp Frequency	100.00	MHz	100.00	MHz	100.00	MHz
Max Chirp Frequency	300.00	MHz	300.00	MHz	300.00	MHz
Number of Chirp Samples	3125.00	DN	3125.00	DN	3125.00	DN
Transmit Power	on	BOOL	on	BOOL	on	BOOL
Transmit Mode	V	BOOL	HV	BOOL	HV	BOOL
Antenna Start Angle	-138.00	Degrees	-138	Degrees	-138	Degrees
Antenna End Angle	5.00	Degrees	5	Degrees	5	Degrees
Motor Gear Ratio	72.00	DN	72.00	DN	72.00	DN
Motor Rotation Rate	10.00	$Deg \cdot s^{-1}$	5.00	$Deg \cdot s^{-1}$	10.00	$Deg \cdot s^{-1}$
Data Capture Time	1.00	ms	1.00	ms	1.00	ms
Sampling Rate	6.25	$MS \cdot s^{-1}$	6.25	$MS \cdot s^{-1}$	6.25	$MS \cdot s^{-1}$
Antenna Elevation	0.00	Degrees	0.00	Degrees	0.00	Degrees

Note: leg length was not recorded but tripod was left standing between observations

Table 3.7. Instrument configuration and scan settings for the UA GPRI-2 and UMC GPRI-2 at the JEC project site.

Usage:

gpri2_capture.py: [options] -p profile -o output_filename

Help:

-h, --help show this help message and exit
-e INTERFACE, --interface=INTERFACE use specified Ethernet interface [default=eth0]
-m MAC_ADDR, --mac-addr=MAC_ADDR use USRP2 at specified MAC address [default=None]
-f FREQ, --freq=FREQ set frequency to FREQ
-d DECIM, --decim=DECIM set fgpa decimation rate to DECIM [default=16]
-g GAIN, --gain=GAIN set USRP2 gain in dB (default is midpoint)
-K SCALE, --scale=SCALE set rx input scaling of usrp2, scale_iq (default is 1024)
-S SHIFT, --shift=SHIFT 'set rx output shifting of usrp2, shift_iq (default is 0).

--lo-offset=LO_OFFSET set daughterboard LO offset to OFFSET [default=hw default]
--rx-bufsize=RX_BUFSIZE set rx buffer size to RX_BUFSIZE [default=0]
-N NSAMPLES, --nsamples=NSAMPLES number of samples to capture [default=+inf]
-T CAPTURE_DURATION, --capture-duration=CAPTURE_DURATION number of seconds to capture [default=+inf]
-o OUTPUT_FILENAME, --output-filename=OUTPUT_FILENAME output filename for captured samples [default=None]
-s, --output-shorts output interleaved shorts instead of complex floats
-M, --lock-masterclock-to-SMA lock usrp2 100 Mhz master clock to external 10 Mhz reference clock on SMA input
-P, --sync-to-first-1PPS reset the usrp2 samplecounter on the first PPS received on the PPS SMA input
-j RX_START_TIMESTAMP, --rx-start-timestamp=RX_START_TIMESTAMP set start_at time of first RX packet in usrp2 100 Mhz clockpulses (long) [default=-1 start immediately]
-k RX_START_TIME_SECONDS, --rx-start-time-seconds=RX_START_TIME_SECONDS set start_at time of first RX packet in seconds (float) [default=-1.0 start immediately]
-C EXTERNAL_PROGRAM, --external-program=EXTERNAL_PROGRAM give a programname to start this as external program just before streaming starts (string) [default=None do not start an external program]
-v, --verbose verbose output
-p GPRI_PROFILE, --gpri-profile=GPRI_PROFILE GPRI-II acquisition profile [default=None]

Inovacation:

gpri2_capture.py -e eth1 -f 0.0 -M -P -S 1 -k 1.0 -v -p gpri_1ms.prf -o RAW/westar_pol_20130613

Input:

1 gpri_250us.prf	GPRI-2 Profile Parameter File

Output:

1 RAW/westar_pol_20130613_005.raw	Raw RADAR Image File
2 RAW/westar_pol_20130613_005.raw_par	RAW RADAR Parameter File

(a) (b)

Figure 3.6. a) UMC GPRI-2 radar configuration as employed at the JEC project site showing instrument orientation, configuration, and anchor points, and b) view of the JEC project site from the overlook position showing relative site topography [images by author, in color].

3.5. Data Processing

Processing of the raw radar data to acquire pixel intensity values, volumetric water content, and soil *in situ* density was accomplished using a combination of 1) commercially available Gamma interferometric software (Gamma 2012) that operated in a Linux environment, and 2) custom MATLAB (Mathworks 2012, 2014) executables that were developed specifically for this application that operated in either the Windows or Linux software environments. Data processing from the raw (as acquired) data to deliverable remote sensing products required numerous of steps. Each of these steps are described in the following sections and are discussed sequentially. These steps included 1) data preprocessing (Section 3.5.1), 2) image registration (Section 3.5.2), 3) soil water content inversion via change detection methods (Section 3.5.3), 4) soil water content inversion via the polarimetric small perturbation method (Section 3.5.4), and 5) extraction of *in situ* density via a combination of water content measurements (Section 3.5.5). A flow chart illustrating an overview of the programmatic processes that are described in this section is presented as Figure 3.7.

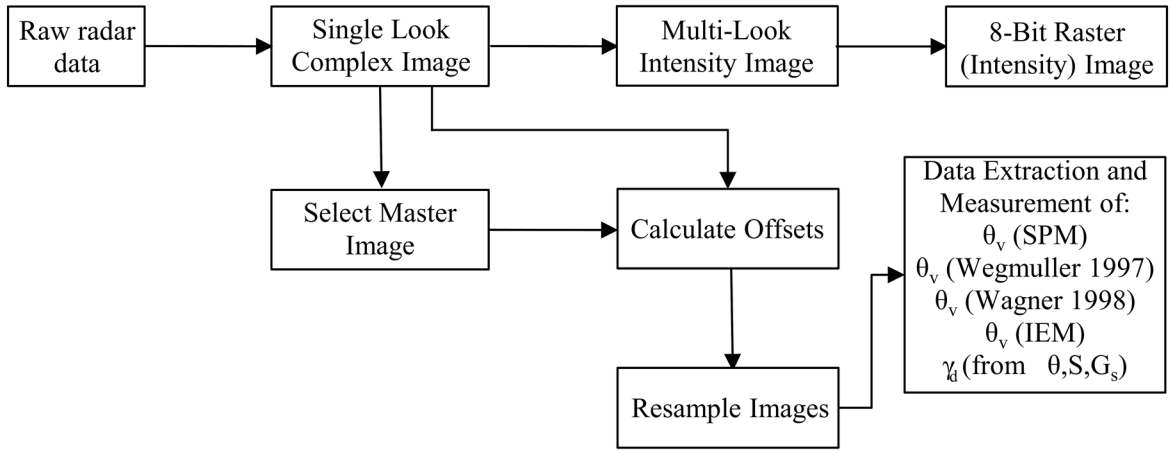

Figure 3.7. Programmatic work flow for extraction of volumetric water content (θ_v) and density (γ_d) from radar imagery (Garner and Coffman 2017a).

3.5.1. *Data Preprocessing*

Data preprocessing, as described herein, encompassed the initial evaluation of the radar data. Preprocessing was conducted in the field, when possible, to ensure both data integrity and proper selection of acquisition parameters (chirp length, attenuation, starting angle, ending angle). Furthermore, the steps described in this data preprocessing work flow were subsequently used for all further analysis of radar imagery. In particular there were three processing steps that were accomplished during radar preprocessing on either the entirety or a subset of the collected imagery. The preprocessing steps included: 1) conversation of the raw binary data files (.raw) into single look complex (SLC) images containing both intensity and phase information (as double precision little endian floating point binary files), 2) conversion of the SLC images into a multi-look intensity (MLI) image containing reflected intensity images (as a 16-bit floating point binary file), 3) transformation of the MLI images from radar coordinates (with bearing lines on the y-axis) into MLI images expressed in range and cross range coordinate, and 4) visualization of the MLI images as eight (8) bit grey scale raster images. All preprocessing steps were completed in the Linux software environment using Gamma Remote Sensing Software executable files

including gpri2_proc.py, multi_look, pol2rec, and raspwr. The required input and output parameters for each of the aforementioned executables, as well as an example invocation in the Linux terminal, is presented as Table 3.8, Table 3.9, Table 3.10, and Table 3.11, respectively.

Table 3.8. Example invocation of the gpri2_proc.py executable with relevant inputs and outputs listed.

Usage:	
gpri2_proc.py: raw_data raw_par slc1 slc2 options	
Help:	
--help show this help message and exit	
--data-type=DATA_TYPE Specify the data type (float32, int16 [default=int16]	
-z ZERO, --zero=ZERO Number of samples to set to 0 at the start of the echo: [default=0]	
-d DEC, --decim=DEC Decimation factor [default=1]	
-R RMAX, --rmax=RMAX Maximum slant range (meters), default is 0.9 of the aliasing slant range	
-a, --ati Turn off azimuth interpolation, required for Along-Track Interferometry [default=False]	
-e, --little_endian Generate little-endian output, default for Gamma Software is big-endian [default=False]	
-h HEADING, --heading=HEADING Heading of radar boresight clockwise from North (deg.)	
Invocation:	
gpri2_proc.py ../RAW/westar_pol_20130613_007.raw ...../RAW/westar_pol_20130613_007.raw_par ... westar_pol_20130613_007Vu.slc westar_pol_20130613_007Vl.slc -d 20 -h 90 -t V	
Input:	
1 RAW/westar_pol_20130613_007.raw	Raw Radar Image File
2 RAW/westar_pol_20130613_007.raw_par	Raw Radar ParameterFile
Output:	
1 westar_pol_20130613_007Vu.slc	Single Look Complex Image (RX-1)
2 westar_pol_20130613_007Vl.slc	Single Look Complex Image (RX-2)
3 westar_pol_20130613_007Vu.slc.par	Single Look Complex Parameter File (RX-1)
4 westar_pol_20130613_007Vl.slc.par	Single Look Complex Parameter File (RX-2)

Table 3.9. Example invocation of the multi_look executable with relevant inputs and outputs listed.

Usage:	
multi_look <SLC> <SLC_par> <MLI> <MLI_par> <rlks> <azlks> [loff] [nlines] [scale] [exp]	
Help:	
SLC (input) single-look complex image	
SLC_par (input) SLC ISP image parameter file	
MLI (output) multi-look intensity image	
MLI_par (output) MLI ISP image parameter file	
rlks number of range looks	
azlks number of azimuth looks	
loff offset to starting line (default: 0)	
nlines number of SLC lines to process (enter - for default: entire file)	
scale scale factor for output MLI (default: 1.0)	
exp exponent for the output MLI (default: 1.0)	
Invocation:	
multi_look ../SLC/westar_pol_20130613_007Vl.slc ../SLC/westar_pol_20130613_007Vl.slc.par ... westar_pol_20130613_007Vl.mli westar_pol_20130613_007Vl.mli.par 1 1 0 - 1 1	
Input:	
1 SLC/westar_pol_20130613_007Vl.slc	Single Look Complex Image File (RX-1)
2 SLC/westar_pol_20130613_007Vl.slc.par	Single Look Complex Parameter File (RX-2)
Output:	
1 westar_pol_20130613_007Vl.mli	Multi Look Intensity Image
2 westar_pol_20130613_007Vl.mli.par	Multi Look Intensity Parameter File

Table 3.10. Example invocation of the pol2rec executable with relevant inputs and outputs listed.

Usage:

pol2rec <data1> <SLC_par1> <data2> <SLC_par2> <pix_size> <type> [mode] [xmin] [nx] [ymin] [ny]

Help:

data1 (input) GPRI data in polar format
SLC_par1 (input) GPRI SLC image parameter file describing the SLC image geometry
data2 (output) GPRI ouput image in rectangular format
SLC_par2 (output) output SLC/MLI image parameter file for the output image
pix_size (output) output pixel size (meters)
type input data type:
0: FLOAT
1: FCOMPLEX
mode interpolation algorithm
0: nearest-neighbor
1: bicubic spline (default)
xmin starting x coordinate (enter - for default: calculated from image)
nx number of x samples in the output image (enter - for default: calculated from iamge
ymin starting y coordinate (enter - for default: calculated from image)
ny number of y samples in the output image (enter - for default: calculated from iamge
NOTE: center line of the scan defines the X axis

Invocation:

pol2rec MLI/westar_pol_20130613_007Vl.mli MLI/westar_pol_20130613_007Vl.mli.par REC/westar_pol_20130613_007Vl.rec_mli REC/westar_pol_20130613_007Vl.rec_mli.par 0.750 0 - - - -

Input:

1	MLI/westar_pol_20130613_007Vl.mli	Multi Look Intensity Image
2	MLI/westar_pol_20130613_007Vl.mli.par	Multi Look Intensity Parameter File

Output:

1	REC/westar_pol_20130613_007Vl.rec_mli	Rectangular Coordinates MLI Image
2	REC/westar_pol_20130613_007Vl.rec_mli.par	Rectangular Coordinates MLI Parameter File

Table 3.11. Example invocation of the raspwr executable with relevant inputs and outputs listed.

Usage:		
raspwr <pwr> <width> [start] [nlines] [pixavr] [pixavaz] [scale] [exp] [LR] [rasf] [data_type]		
Help:		
pwr	(input) intensity image (FLOAT or SHORT INTEGER data type)	
width	samples per row	
start	starting line to display (default=1)	
nlines	number of lines to display (default=0: to end of file)	
pixavr	number of pixels to average in range (default=1)	
pixavaz	number of pixels to average in azimuth (default=1)	
scale	display scale factor (default=1.)	
exp	display exponent (default=.35)	
LR	left/right flipping flag, (default=1: normal, -1: mirror image)	
rasf	(output) raster image (enter - for default = *.ras: SUN raster format, *.bmp: BMP format)	
data_type	input data type (default=0)	
	0: FLOAT	
	1: SHORT INTEGER	
hdrsz	line header size in bytes (default=0, ESA PAF for PRI products=12)	
Invocation:		
raspwr westar_pol_20130613_001Vl.rec_mli 1407		
Input:		
1	westar_pol_20130613_007Vl.rec_mli	Multi Look Intensity Image
Output:		
1	westar_pol_20130613_007Vl.rec_mli.ras	8-bit Raster Grayscale Image

3.5.2. *Image Registration*

Image registration was required for any remote sensing application that required multiple temporally or spatially separated image acquisitions. Image registration was completed by spatially transforming one image into the coordinate system of another image. Radar image registration for data acquired at both the UACSRC and WJEC sites was accomplished using Gamma Remote Sensing interferometric software. With respect to radar image registration this document utilized the methodology that was presented in Gabriel and Goldstein (1988). Furthermore, the programmatic process used to register the images was developed from earlier work documented in Coffman (2009), Conte (2012), and Coffman and Garner (2012).

For this registration scheme, multiple image subsets, or "blocks", were evaluated. A prominent feature (e.g. an identifiable object such as a corner reflector, fence line, structure, etc.) was visually identified in the master image from the preprocessed data. The image block, as an [8 by 8] pixel matrix containing complex data was then multiplied with the complex conjugate of an [8 by 8] pixel matrix from the same pixel coordinates as the block from the master image. The interferometric block was analyzed using a two dimensional Fast Fourier Transform (FFT). The maximum complex absolute value was detected (as a function of the f_x and f_y frequencies). The signal-to-noise ratio (SNR) was calculated by comparing the maximum complex absolute value to the summation of all other values in the block.

The pixel location in the slave block was then adjusted by the surrounding four pixels in the x and y directions. The SNR for each combination was stored as a [9 by 9] matrix (+/- four in each direction plus one aligned center pixel). A [3 by 3] matrix overlay, centered on the maximum calculated SNR, was then subjected to a quadratic interpolation to determine the center of mass of the overlay (and therefore the x and y offsets [x_{off} and y_{off}]). The above procedure was repeated for several training sites across the images that were registered.

The obtained relationship of y_{off} and azimuth direction was used to determine the variation of y_{off} over the image domain. A quadratic interpolation between adjacent pixels in the range direction was applied and the slave image was resampled in the range direction. Subsequently the image was resampled in the azimuth direction using the aforementioned location methodology. To increase accuracy, the relationship the offset calculation was weighted by the SNR to bias the relationship towards training sites that exhibited strong interferometric correlation.

Programmatically, the previously described work flow was accomplished using the following executables in the Gamma Remote Sensing interferometric software suite: 1)

create_offset, 2) init_offset, 3) offset_pwer, 4) offset_fit, 5) init_offset, 6) offset_pwr, 7) offset_fit, and 8) SLC_interp. A visual inspection of the acquired radar data was employed to detect a possible registration target (a strong, small reflector) near the center of the radar image. The master image was typically selected from the imagery acquired on the first day of observation as this would provide a convenient point of origin to describe any changes in the scene as a function of time. Thereby, all of the images would have a positive timeline. A Linux shell script was developed (included in Appendix A) for both the UACSRC and WJEC sites whereby the raw data transferred into a working directory was collated (as symbolic links) and then registration work flow was performed to eventually create a series of registered, resampled SLC and MLI (rSLC and rMLI) images that were in the geometry of the master image.

3.5.3. *Water Content via Change Detection Methodology (Wegmuller 1997, Wagner 1998)*

After the resampled MLI (rMLI) intensity images were generated, the extraction of water content information was completed by using the methodologies proposed by Wegmuller (1997) and Wagner (1998). The Wegmuller (1997) water content inversion was conducted by using a built-in function of the Gamma Remote Sensing software program. Initially, all of the images that were acquired during each observation were stacked (averaged) to increase the signal to noise ratio of the rMLI images. The Gamma Remote Sensing soil_moisture.c executable required the following inputs for each operation: 1) an rMLI intensity image, 2) a reference rMLI image, and 3) a reference soil moisture image (with soil volumetric moisture content values for each pixel in the reference rMLI image).

For the UACSRC project site the Wegmuller (1997) inversion was conducted using two trial intensity images. The first intensity image was captured on January 30th, 2012 when surface temperature had been consistently below 0 C for several days. As reported in Wegmuller (1997),

the volumetric soil moisture content of frozen soil may be assumed to be approximately 0.03. Although there had been significant precipitation during and after construction of the project site (January 10th, 2012 to January 19th, 2012), the assumption of the low (near zero) moisture content was believed to be valid because of the extended period of low temperature and the low penetration of the K_u-Band radar (~1-2cm).

Therefore, a reference soil moisture map was generated in MATLAB containing the assumed dimensionless soil moisture value (0.03) stored as a list of 16-bit little endian floating point. The water map list contained a number of entries; the number of entries was equal to the product of the number of range lines and the number of azimuth lines in the reference image. The rMLI that was acquired on January 30th, 2012, was used as the reference MLI image for the images acquired using the MBTC-3031 acquisition scheme (as previously documented in Table 3.4). A second reference image was utilized for the MBTC-3031 wide and MBTC-3031 Phase 2 acquisitions. The reference image was acquired on July 7th, 2012 after the compaction of the UACSRC project site for Phase 2 of the MBTC-3031. Specifically, this image was acquired approximately two weeks after the UACSRC test sections had been compacted, during a period where there was no recorded precipitation and the maximum daily temperature exceeded 38 C (100 F). It was expected that the elevated temperatures, lack of precipitation, and direct solar irradiation would result in a soil water content that was at or near the residual water content. To verify this assumption, nuclear density gauge tests were performed and loose bulk samples were recovered to determine the average water content of the two compacted clay test sections. Similarly, for the WJEC project site, reference images were collected for the K_u-Band and C-Band images on June 18th, 2013 due to availability of nuclear density gauge test data for that date.

The difference in pixel intensity values, as a function of time, were utilized in the Wagner (1998) water content inversion methods to determine changes in soil saturation. As described in Chapter 2, the Wagner (1998) method utilized the assumption that the changes in the soil reflectivity will be a function of soil moisture. Accordingly it was assumed that the surface reflectivity was greatest when the soil was at or near saturation and that the surface reflectivity was minimal when the soil was at or near the residual water content. Therefore, it was necessary to observe the soil in two of the following three conditions: 1) a saturated state (e.g. imagery acquired immediately after a precipitation event), 2) a residual state (e.g. imagery acquired after prolonged drying) or 3) a state corresponding to known *in situ* water content measurements (e.g. imagery acquired simultaneously with time domain reflectometry and nuclear density gauge testing). For both the UACSRC project site and the WJEC project, imagery was acquired when the soil was highly desiccated and immediately following a precipitation event.

Based on Wagner (1998), the soil saturation was determined by linearly interpolating between the pixel observed radar backscatter coefficient (σ) value, the maximum observed value of pixel σ, and the minimum observed value of pixel σ. The Wagner (1998) inversion was conducted by using the following steps: 1) the rMLIs for each observation date were averaged (r_aMLI), 2) the radar intensity was converted from a linear scale to logarithmic (dB) scale, 3) the maximum and minimum σ values of each pixel during the observation period were measured and recorded, 4) the saturation value was obtained by linearly interpolating between each pixel brightness value (for every pixel in every r_aMLI) and the corresponding maximum and minimum pixel brightness values, and 5) the water content images were transformed from polar to rectangular coordinates.

The initial averaging (Step 1) and the transformation from polar to rectangular coordinates (Step 5) were conducted using the Gamma Remote Sensing software suite. The remaining steps (Step 2 through Step 4) were conducted using a MATLAB executable (soil_moisture.m). The soil_moisture.m program required a list of all r_aMLI images that were to be processed, and outputted a saturation map (in polar coordinates) for each r_aMLI as well as two MLI files containing the initial maximum (.max) and minimum (.min) pixel brightness values. The soil_moisture.m executable processed the Wagner (1998) soil moisture inversion method as two separate steps. Initially, after ingesting the list of the r_aMLIs, each r_aMLI was opened (as a binary file) and each pixel brightness value was compared sequentially to the previous maximum and minimum values that were stored in the .max and .min files, respectively, to populate the .max and .min files with the actual maximum and minimum pixel brightness values.

To reduce effects caused by noise in the image, pixel brightness values of 0 (null) and pixel brightness values of 1 (saturated) values were excluded. Subsequently, all pixel brightness of r_aMLI files were compared to the corresponding (same range and azimuth value) pixel brightness values in the .max and .min files. To extract volumetric water content information, the measured saturation values were multiplied by the porosity of the soil that determined from a previously performed laboratory testing (specific gravity), nuclear density testing (total unit weight, dry unit weight), and phase relationships (Equation 3.1 and Equation 3.2).

$$\eta = \frac{1 - \frac{\gamma_d V_T}{\gamma_w G_s}}{V_T} \qquad \text{Equation 3.1}$$

$$\theta = \frac{S\eta V_T}{V_T} \qquad \text{Equation 3.2}$$

In Equation 3.1 and Equation 3.2, η is the porosity, γ_d is the in situ dry unit weight (obtained from nuclear density gauge), V_T is the total soil volume (assumed to be unity for the

purpose of calculations), γ_w is the unit weight of water, G_s is the specific gravity of soil solids (obtained from laboratory testing), θ is the volumetric water content.

3.5.4. *Moisture Content via Small Perturbation Methods (SPM)*

Direct calculation of the volumetric soil moisture content was conducted by using the Small Perturbation Method (SPM) at the JEC project site. The SPM was selected for use at the WJEC site due to 1) the longer wavelengths of the C-Band instrument (as compared to the K_u-Band) and 2) the project surface had been previously mechanically prepared and was therefore expected to have a low RMS surface roughness value. A flow chart of the process that was employed to compute the volumetric soil moisture content is included as Figure 3.8.

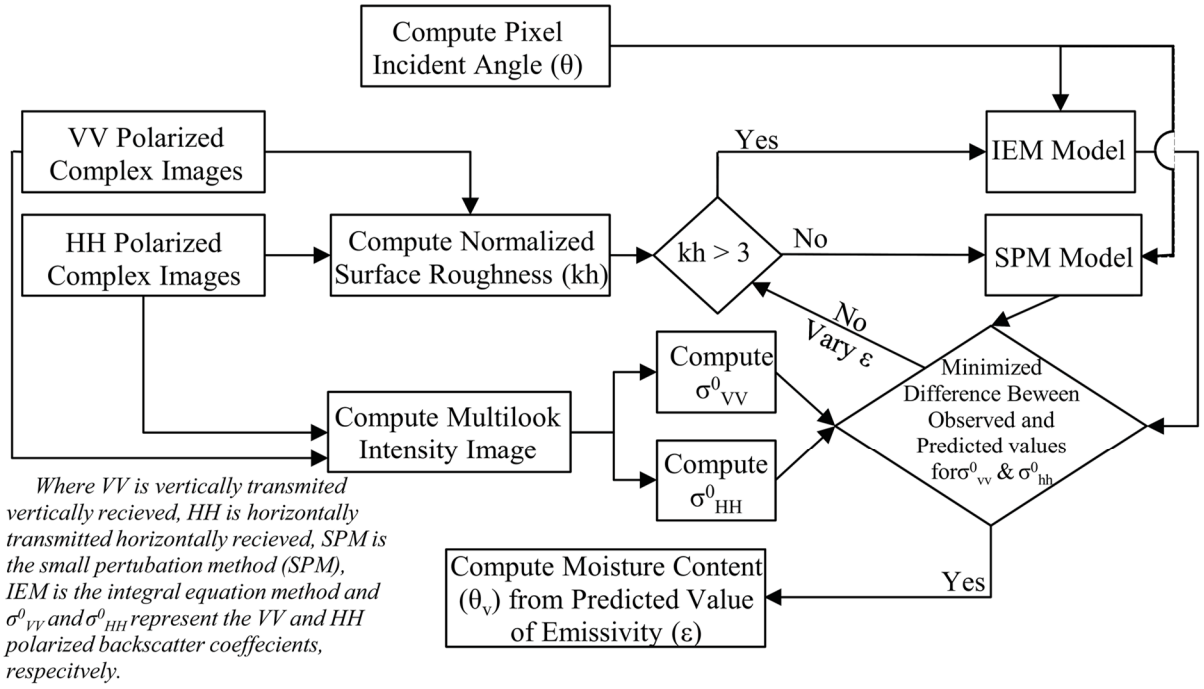

Figure 3.8. Flow chart and workflow for the extraction of volumetric moisture content from polarized radar imagery using the SPM and IEM methods (from Garner and Coffman 2017a).

The SPM moisture inversion was conducted by using a backwards analysis of surface reflectance as a function of the complex values of soil dielectric permittivity, the surface roughness, and incidence angle. Due to limitations in the acquired surface topography and the

Gamma Remote Sensing software, an assumed flat site geometry (with the instrument offset vertically) was utilized to calculate the incidence angle as a function of range. Therefore, for possible combinations of normalized surface roughness (kh), dielectric permittivity (ε), and incidence angle (θ), a reflectance value for HH and VV polarized imagery was computed (spm_initial.m) and stored as two look-up tables (one for HH data and one for VV data, respectively). These computed HH and VV reflectance values were compared to the measured reflectance values, and the corresponding combination of kh and ε values with the lowest error (as determined utilizing Equation 3.3) were selected and stored as roughness and emissivity files (*kh.ini and *e.ini). To reduce error caused by noisy data, pixels that had a backscatter coefficient values that were less than 10^{-4} m^2 were excluded from the analysis.

$$X = \left[\left(\sigma_M^{HH} - \sigma_{kh,\varepsilon}^{HH} \right)^2 + \left(\sigma_M^{VV} - \sigma_{kh,\varepsilon}^{VV} \right)^2 \right] \quad \text{Equation 3.3}$$

In Equation 3.3 X is the sum of squared error, σ_M^{HH} is the measured HH backscatter coefficient, $\sigma_{kh,\varepsilon}^{HH}$ is the predicted HH backscatter coefficient, σ_M^{VV} is the measured VV backscatter coefficient, and $\sigma_{kh,\varepsilon}^{VV}$ is the predicted VV backscatter coefficient.

Due to the homogeneity of the JEC project site, it was anticipated that the kh and ε values would not vary abruptly in both the range and azimuth directions (with the exception of rapid texture changes such as encountering the access road, equipment, and the lake). Therefore, the resulting kh and ε maps were smoothed using a 3 by 3 pixel moving average filter (mli_smooth2.m). The smoothed kh, ε, HH MLI, and VV MLI files were subsequently ingested in another executable (refine_spm.m) and the kh and ε values were reselected based on 1) the initial estimates and 2) using a refined search (e.g. smaller increments of kh and ε). Using the finalized estimate of ε for each pixel, the soil water content was computed by using either a linear or logarithmic soil moisture model as reported by Njoku and Entekahbi (1994). The results were further visualized by using the open source image processing toolbox that was available in the

MATLAB programming suite (e.g. jgge_soil_moisture.m). Examples of the aforementioned MATLAB executables including an example invocation and the relevant inputs and outputs of the spm_initial.m, mli_smooth2.m, and refine_spm.m are included in Appendix A and as Table 3.12, Table 3.13, Table 3.14, respectively.

Table 3.12. Example invocation of the spm_initial.m executable with relevant inputs and outputs listed (note that .amli indicates resampled and averaged intensity files).

Invocation:	
spm_initial('../MLI_HHB/westar20130614hh.amli','../MLI_VVB/westar20130614vv.amli',...	
../mli_temp/westar20130614e91.ini','../mli_temp/westar20130614kh91.ini',...'	
[701 1340 0.75 40 1e-2 1 701 1 1340]);	
Input:	
1 ../MLI_HHB/westar20130614hh.amli	Averaged HH Multi Look Intensity Image
2 ../MLI_VVB/westar20130614vv.amli	Averaged VV Multi Look Intensity Image
Output	
1 ../mli_temp/westar20130614e91.ini	Initial estimate of soil dielectric permissivity
2 ../mli_temp/westar20130614kh91.ini	Initial estimate of soil surface roughness

Table 3.13. Example invocation of the mli_smooth2.m executable with relevant inputs and outputs listed.

Invocation:	
mli_smooth2('../mli_temp/westar20130618e91.ini','../mli_temp/westar20130618e91.smt',701,1340);	
Input:	
1 ../mli_temp/westar20130618e91.ini	Estimate of Soil Dielectric Permissivity Image
Output	
1 ../mli_temp/westar20130618e91.smt	Smoothed Soil Dielectric Permissivity Image

3.5.5. *In Situ Density from Soil Water Content Inversions*

The aforementioned remotely sensed water content information was subsequently combined to determine the soil *in situ* density and phase relationships. This inversion was conducted utilizing the saturation measurements obtained from the Wagner (1998) inversion and the volumetric water content measurements obtained from either the Wegmuller (1997) or SPM water content inversion. The *in situ* density was calculated by using Equation 3.4.

$$\gamma_d = G_s \gamma_w \left(1 - \frac{\theta_v}{S}\right) \qquad \text{Equation 3.4}$$

In Equation 3.14, γ_d is the in situ dry unit, γ_w is the unit weight of water, G_s is the specific gravity of soil solids (obtained from laboratory testing), θ is the volumetric water content, and S is the saturation ratio.

Table 3.14. Example invocation of the refine_spm.m executable with relevant inputs and outputs listed (note .amli files indicate resampled and averaged intensity files).

Invocation:	
refine_spm('../mli_temp/westar20130614kh91.ini','../mli_temp/westar20130614e91.ini',... *../MLI_HHB/westar20130614hh.amli','../MLI_VVB/westar20130614vv.amli',...* *../mli_e/20130614',[701 1340 50 0 15 1 701 1 1340])*	
Input:	
1[a] ../mli_temp/westar20130614kh91.ini	Estimate of Soil Dielectric Permissivity Image
2[a] ../mli_temp/westar20130614e91.ini	Estimate of Soil Dielectric Permissivity Image
3 ../MLI_HHB/westar20130614hh.amli	Averaged HH Multi Look Intensity Image
4 ../MLI_HHB/westar20130614vv.amli	Averaged VV Multi Look Intensity Image
Output	
1 ../mli_e/westar20130614lin_mv.fin	Soil Moisture Image (Linear Model)[b]
1 ../mli_e/westar20130614log_mv.fin	Soil Moisture Image (Logarithmic Model)[b]

[a]If required .smt files were used in place of the initial estimate images

[b]Soil moisture calcualted using a linear or lograthmic fitting to the mixing model proposed in Njoku and Entekahbi(1994)

3.6. Works Cited

Coffman, R., (2009), "Processing of Synthetic Aperture Radar Data as Applied to the Characterization of Localized Deformation Features." Ph.D. Dissertation, University of Missouri, Columbia, August.

Coffman, R., (2013b). "Geotechnical Properties of Vertical Flow Bed Treatment Soil." Coffman Consulting Company, Report No. 2013-BMCD/WESTAR CWTS VFB.

Coffman, R., (2014). "Image of University of Missouri GPRI-2." Personal Electronic Communication to the Author.

Coffman, R., Garner, C., (2012). "Final Report of MBTC-3031 Project." Mack-Blackwell Rural Transportation Center.

Conte, Omar A. R. (2012). "Slope Stability Monitoring Using Remote Sensing Techniques." Master's Thesis. University of Arkansas – Fayetteville. May 2012.

Gabriel, A., Goldstein, R., (1988). "Crossed Orbit Interferometry: Theory and Experimental Results from SIR-B." International Journal of Remote Sensing, Vol. 9, No. 8, pp. 857-872.

Gamma Remote Sensing, (2012). "GAMMA SAR and interferometry software." Version 2006, updated 2012.

Garner, C., Coffman, R., (2014). "Remote Sensing Methods for Monitoring Ground Surface Deformation of Compacted Clay Test Sections." ASCE Geotechnical Special Publication No. 234, Proceedings of the GeoCongress 2014: Geo-Characterization and Modeling for Sustainability, Atlanta, Georgia, February, pp. 963-978.

Garner, C., Coffman, R., (2016). "Volumetric Water Content Measurements as Obtained from Remote Sensing and In-Situ Instrumentation." Journal of Environmental and Engineering Geophysics. Accepted for Publication, Manuscript Number 15-022R.

Garner, C., Coffman, R., (2017a). "Remotely Sensed Soil Volumetric Water Content and Dry Density as Obtained Utilizing Change Detection and Polarimetric Methods." Journal of Environmental and Engineering Geology. (Submitted for Review).

Google, (2012). "Google Earth and Supporting Documentation." The Google Corporation. Imagery Retrieved 2012.

Google, (2014). "Google Earth Imagery." The Google Corporation. Retrieved February 2014.

Haigh, S., Vardanega, P., Bolton, M., (2013). "The Plastic Limit of Clays." Geotechnique, Vol. 63, pp. 435-440.

Kuss, M., (2013). “Image of University of Arkansas GPRI-2.” Personal Electronic Communication with the Author(s) received January 2013.

Mathworks, (2012a). “MATLAB Programing Environment and Documentation.” The MathWorks, Inc. Natick, MA.

Mathworks, (2014b). “The MATLAB R2014B Programming Suite and Supporting Documentation.” The MathWorks, Inc. Natick, Massachusetts.

National Oceanic and Atmospheric Administration (NOAA), (2016). “Weather Observations for Drake Field, Fayetteville, Arkansas.” http://www.srh.noaa.gov/data/obhistory /KFYV.html. Retrieved March 2016.

Njoku, E., Entekahbi, D., (1994). “Passive Microwave Remote Sensing of Soil Moisture.” Journal of Hydrology, Vol. 184, Issue 1-2, pp. 101-129.

Wagner, W., (1998). “Soil Moisture Retrieval from ERS Scatterometer Data.” PhD Dissertation, Vienna University of Technology. November.

Wegmuller, U., (1997). “Soil Moisture Monitoring with ERS SAR Interferometry.” European Space Agency Special Publication ESA SP-414. Proceedings of the 3rd ERS Symposium. pp. 47-51.

CHAPTER 4: MATERIALS AND PROCEDURES FOR TRADITIONAL AND OPTICAL LABORATORY TESTING TECHNIQUES

4.1. Chapter Overview

A description of the materials and procedures utilized to obtain laboratory-based measurements of soil properties are contained within this chapter. Traditional laboratory-based measurements of soil properties including liquid limit (LL), plastic limit (PL), plasticity index (PI), soil particle size distribution (clay fraction, c_f), and clay mineralogy, were performed. Additionally, the methodology and materials employed to prepare soil samples and collect spectral data are contained within this chapter. The techniques used to collect and prepare bulk soil samples are discussed in Section 4.2. Traditional laboratory-based techniques including Atterberg limits (Atterberg 1912), Casagrande 1932, ASTM D4318 2014, BSI 1990), soil particle size distribution (ASTM D422 2014), soil specific gravity (ASTM D854 2014), and clay mineralogy (Skempton 1953) are described in Section 4.3. Additional methods of soil characterization, including qualitative (scanning electron microscopy) and quantitative (X-ray diffraction), were employed for this research project are described and discussed in Section 4.4.

Where possible all tests described in this section were performed in sets of five. A testing matrix for all of the testing that is described in this chapter is presented as Table 4.1. The sample preparation and testing methodologies for the measurement of soil water potential and volumetric water content using a chilled mirror hygrometer is documented in Section 4.5. The preparation of soil samples for diffuse reflectance infrared Fourier transform (DRIFT) or Fourier transform infrared (FTIR) spectroscopy and for the laser analysis of soil tension (LAST) are described in Section 4.6 and Section 4.7, respectively. Specifically, described in Section 4.7.2 is the process by which the pressure plate extractor (PPE) was used to prepare samples for LAST testing and to determine a soil water characteristic curve for use in calibration and validation of the LAST

testing. The acquisition of spectral data using the FTIR and LAST instruments is documented in Section 4.8 and Section 4.9, respectively. The data processing for FTIR testing to obtain soil absorption coefficients and soil scattering coefficients is described in Section 4.10. The data processing for LAST testing is described in Section 4.11. The methods and procedures documented in this chapter are also documented in Garner and Coffman (2017b) as presented in Chapter 7 for DRIFT testing, and Garner et al. (2017) as presented in Chapter 8 for LAST testing.

4.2. Acquisition and Preparation of Bulk Soil Samples

For this project, three separate soil types were selected and tested. The process by which each of the three soil types were purchased or acquired and the processing that was conducted to prepare the raw material for further testing is presented in this section. Two of the soil types ('Donna Fill' and 'kaolinite') were acquired as commercially available products to provide a consistent, repeatable, material for further testing. The third material ('illite'), was also selected due to the fact that 1) it has been well characterized, and 2) it has been extensively described in the geotechnical literature (CMS 2015).

Table 4.1. Traditional testing that was conducted on the soil types used for this project.

Test	Obtained Value	Testing Methodology	Soil	Number of Test Preformed
Liquid Limit	LL	ASTM D4318 (2014)	Donna Fill	5
	LL	ASTM D4318 (2014)	Kaolinite	5
	LL	ASTM D4318 (2014)	Illite	5
	LL	BS-1377 (1990)	Donna Fill	3[a]
	LL	BS-1377 (1990)	Kaolinite	3[a]
	LL	BS-1377 (1990)	Illite	3[a]
Plastic Limt	PL	ASTM D4318 (2014)	Donna Fill	1[b]
	PL	ASTM D4318 (2014)	Kaolinite	5
	PL	ASTM D4318 (2014)	Illite	5
Plastic Index	PI	Wasti (1987)	Donna Fill	3[a]
	PI	Wasti (1987)	Kaolinite	3[a]
	PI	Wasti (1987)	Illite	3[a]
Clay Fraction	CF	ASTM D422 (2014)	Donna Fill	5
	CF	ASTM D422 (2014)	Kaolinite	5
	CF	ASTM D422 (2014)	Illite	5
Specific Gravity	G_s	ASTM D854 (2014	Donna Fill	5
	G_s	ASTM D854 (2014	Kaolinite	5
	G_s	ASTM D854 (2014	Illite	5
Clay Mineralogy		SEM[c]	Donna Fill	3
		SEM[c]	Kaolinite	3
		SEM[c]	Illite	3
		XRD[d]	Donna Fill	3
		XRD[d]	Kaolinite	3
		XRD[d]	Illite	3

[a]3 Test Performed Due to Time Constraints

[b]1 Test Performed Due to Failure to Obtain Valid Results

[c]Scanning Electron Microscopy

The "Donna Fill" material (hereinafter referred to as Donna Fill) was provided to the researchers by the Donna Fill Company of Little Rock, Arkansas. The Donna Fill material is a commercially usable byproduct that is manufactured by the 3M Corporation as a byproduct of the production of ceramic coated roofing granules. The roofing granules are utilized to add color and

UV protection for asphalt roofing shingles. The raw inorganic material that is utilized in the production of the Donna Fill material is locally sourced nepheline synetite (Pulaskkite). The pulaskkite consists of a naturally varying composition containing feldspars, pyrozene, amphibole, nepheline, biotite, magnetite, ilmentite, sodalite, and analcine natrolite (Rogers 2009, 3M 2015). The Donna Fill material that was utilized was obtained from a rejected portion of the processed material. The Donna Fill material has been characterized by the supplier as a synthetic nepheline synetite material. Donna Fill was utilized for this project because it has been previously used in geotechnical and transportation engineering applications as both a fill material (Donna Fill 2015). The material was obtained from the supplier as a single loose bulk sample consisting of approximately 50 kilograms.

The illite material (hereinafter referred to as illite) was obtained from an *in situ* deposit at a mining site in Randolph and Perry Counties, Illinois, in December 2014. The mining site, the Blackhawk Mine, is an open pit coal mine that is owned and operated by the Knighthawk Coal Company. The Blackhawk Mine produced 750,000 tons per year of number 5 (#5) and number 6 (#6) Illinois coal seams (3 percent sulfur, 11,100 BTU, 9 percent ash, 0.01 percent chlorine) with reported reserves of 12 million imperial tons (Knighthawk 2015). The site of the mine consisted of mixed stratigraphy that includes (from top to bottom), a removed organic surface layer, approximately 6m of mixed glacial till, a clay layer of variable thickness, and then interspersed coal and dark grey clay seams to the depth of the excavation. The illite soil that was utilized for this project was sampled from the overburden below the glacial till (approximately 6m below the original ground surface) but above the coal seam (Figure 4.1). Samples were acquired in the field by manual excavation and were transported back to the laboratory in sealed plastic containers.

Figure 4.1. Google Earth (Google 2014) image of approximate location of sample recovery at the Blackhawk Coal Mine (Randolph County, IL).

The kaolinite soil product was acquired from the Theile Kaolin Company of Sandersonville, Georgia. The commercial product, Kaowhite-S, was described as a high brightness, delaminated clay material for use in paper products including "LWC [Light Weight Coated] grades, coated freesheet and in paper for rotogravure or offset printing" (Theile, 2015a). The delaminated product was produced by repeated bleaching, drying, and grinding of the native kaolinite clay material in a rotary mill containing spherical ceramic media. The Kaowhite-S product is described as having a G.E. Brightness value of 88.0 - 90.0 percent, 83 percent clay size particles, and a pH value of 6.5 - 8.0 (Theile 2015b). Soil samples were acquired from a sealed 9.1kg container that was shipped directly from the manufacture.

The soil materials were oven dried, ground, and sieved to remove coarse and sand sized particles, and then stored in a sealed container to prevent moisture contamination. The soils were oven dried in bulk (approximately 1 to 2kg sample sizes) in an electrically controlled oven at a temperature of 105°C +/- 5°C. Due to the large sample size (especially for the illite), oven drying

took an extended period of time (up to 1 week for the illite samples). For both the Donna Fill and kaolinite samples, any aggregated particles were destroyed using either manual finger pressure or with a gentle impact of a rubber mallet. The illite samples, however, required extensive manual preparation to reduce the largest soil aggregates into particles that were small enough to be mechanically ground. The illite samples were reduced to aggregate particles no larger than approximately 2cm in diameter using vigorous blows of a 1.4kg hand maul. All three soil types (Donna Fill, illite and kaolinite) were subsequently by ground using a mechanical grinder (a commercially available meat or sausage grinder).

To prevent cross contamination of the soil types the grinder was disassembled, cleaned, and allowed to air dry prior to the start of grinding for each soil type and after completion of grinding of each soil type. Each sample was ground until 100 percent of the material was passed through the Number 10 sieve (nominal opening size of 2.0 mm). This process was conducted by returning all of the material that was retained on the Number 10 sieve into the grinder hopper and regrinding the sample until all of the material passed through the Number 10 sieve. After completion of grinding, the soil was sieved using a stack of U.S. standard sieves and only the portion of the soil sample that passed the Number 200 sieve (nominal opening size of 0.075 mm) was retained for testing. Prior to use in further testing, the soil was stockpiled in sealed plastic containers.

4.3. Traditional Laboratory Characterization of Processed Soil Samples.

Traditional soil testing in the laboratory including Atterberg limits, grain size distribution, and specific gravity testing. The testing was performed on each sample to determine the engineering index properties, the clay and silt fraction, the clay mineralogy and the specific gravity of the soil solids. The methods used to obtain measurements of the Atterberg limits

(Section 4.3.1), the soil particle size distribution (Section 4.3.2), the soil specific gravity (Section 4.3.3), and the clay mineralogy (Section 4.3.4) are discussed herein.

4.3.1. *Determination of Atterberg Limits*

Atterberg limits were obtained using two different testing techniques, the ASTM D4318 (2014) technique (Casagrande cup and rolling) and the Fall Cone technique that is documented in BSI (1990) and TAMU (2015). ASTM D4318 (2014) testing was conducted using the wet method of preparation. Soil samples for the ASTM D4318 (2014) testing were prepared at least 12 hours in advance of testing and were allowed to sit overnight to lead to a homogenous distribution of water content within the sample. Liquid limit testing was conducted using a standard, calibrated, Casagrande cup liquid limit device. Testing was conducted as per the specifications of ASTM D4318 (2014). Liquid limit testing was conducted using the three point method where blow counts at closure of 15-25, 20-30, and 25-35. As required, and as described in subsequent sentences, the water content of the soil sample was altered by either the addition of water (to decrease blow count) or the removal of water with a cool air blow drier (to increase blow count). Water was added to the sample using a handheld squirt bottle, after adding water the sample was manually mixed to minimize variations of sample water content. Water was removed from the sample by spreading the sample on a smooth glass plate (approximately 30cm by 30cm) and then air drying the sample with a low heat forced hair dryer. After completion of liquid limit testing the gravimetric water content of the various was determined by following the ASTM D2216 (2014) standard. To determine repeatability, five complete sets of liquid limit testing values were obtained for each soil.

Similarly, the plastic limit of each test was obtained by using the rolling method. In accordance with the ASTM D4318 (2014) standard. The rolling process was continued until at

least 10g of sample had been obtained in each of the two separate measuring tins (ASTM D4318 2014). As with the liquid limit, five complete sets of plastic limit tests were conducted for each soil type (or a value of non-plastic was obtained).

Alternatively, the LL and PL for each soil was obtained using a Fall Cone Device (FCD). Testing was conducted in March 2014 by using a fall cone device located at the Texas A&M University (TAMU). Testing was conducted using the procedure documented in TAMU (2015). Bulk samples were prepared (approximately 1kg each) at a water content that approximated the plastic limit values (as previously determined using ASTM D4318 (2014). The samples were then transported to the TAMU laboratory in sealed plastic containers. A 30 degree British standard cone (30g cone plus a 50g weight) was employed by the TAMU FCD. Testing was conducted for each soil by filling the sample container to a flush and level surface with the prepared soil samples. The samples were then loaded into the FCD and the point of the fall cone was placed in contact with the top of the soil surface. The adjustable circular displacement gauge was set to zero. The cone was then released using a mechanical trigger to ensure a consistent release. The trigger mechanism was inspected prior to conducting the test to ensure that no soil particles were present to interfere with the free release and movement of the cone penetrometer. The trigger mechanism was depressed and remained depressed for approximately 1 second to ensure that the fall cone had completed all movement. The resulting penetration was recorded. Following the completion of each test, an approximately 10g sample was removed from the FCD sample cup for gravimetric moisture testing.

To obtain a measurement of plastic limit, the 50g weight on the cone penetrometer was removed and the sample penetration test was repeated by again following the previously described steps. The sample previously used for the liquid limit test was then remixed (no

addition or subtraction of water) and replaced in the sample cup. After removal of the gravimetric water content subsample the remainder of the sample was remixed in a ceramic bowl with additional soil from the bulk soil stockpile. Water was added to the bowl to increase the gravimetric water content. The test process was repeated at the new water content. For each set of fall cone testing the soil was tested at four different water content values (BSI 1990, TAMU 2015). Three sets of fall cone testing were conducted on each soil.

Due to time constraints (all testing was conducted in a 16 hour period) and equipment limitations (no oven was available) a modified moisture content test was performed. The procedures suggested by Beemer (2015) and TAMU (2015) were employed. The 10g of soil from each fall cone test increment (for both the 80 and 30g cone tests) were placed in a pre-measured aluminum weighing boat. The mass of the soil sample and weighing boat were recorded. The sample and the weighing boat were then placed in a commercially available 1300 Watt microwave oven for three minutes. The mass of the soil sample and weighing boat after heating was obtained. The sample and weighing boat were then returned to the microwave oven for one minute. The mass of the soil sample and weighing boat after the second heating was obtained. Additional one minute heating cycles were performed until the change in mass of the soil sample and weighing boat between two sequential heatings was less than 0.01g. The final mass of the soil sample and weighing boat were recorded and the gravimetric water content was calculated using the equation provided in ASTM D2216 (2014).

The LL of each soil sample was obtained by plotting the change in cone penetration as a function of the microwave obtained water content. A linear trendline was fitted to the data using Microsoft Excel (Microsoft 2015). The water content value of the soil at the liquid limit was calculated by finding the x-coordinate of the intercept between the fitted data function and the

calibration function presented in TAMU (2015). This procedure is shown graphically as Figure 4.2. The plasticity index (PI) of the soil was found using Equation 4.1(previously presented as Equation 2.13) as proposed by Wasti (1987). The average of the four PI values (one from each separate water content) obtained from Equation 4.1 was reported as the PI value for a given sample.

$$PI = \Delta \frac{\log_{100}(100)}{\log_{100}\left(\frac{W_1}{W_2}\right)} \qquad \text{(modified from Wasti 1987)} \qquad \text{Equation 4.1}$$

In Equation 4.1, Δ is the vertical separation (relative to water content on the linear plot of w as a function logarithm of the cone penetration depth d, PI is the plasticity index, and $W_{1,2}$ are the weight of the cone (80g and 30g, respectively).

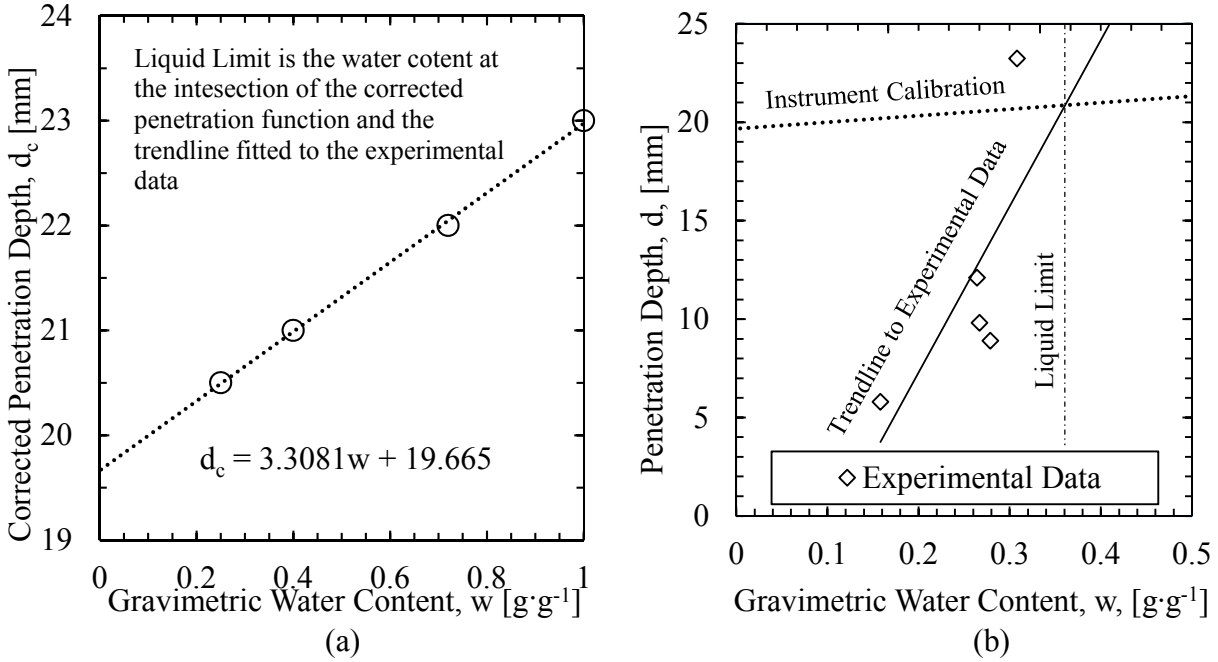

Figure 4.2. a) Corrected penetration depth (dc) for TAMU (TAMU 2015), and b) example of liquid limit determination using the FCD (previously shown as Figure 2.7b).

4.3.2. *Determination of Soil Particle Size Distribution*

The hydrometer method was employed to obtain the particle size distribution for each of the soil types. The hydrometer method was employed instead of the sieve method because all sand sized particles (retained on the number 200 sieve or larger) were previously removed. The

hydrometer testing was performed in accordance with the procedures described in ASTM D422 (2014). Specifically, the hydrometer testing was performed in sets of five with the start of each test offset by 6 minutes. Hydrometer readings were conducted at increments of 5 seconds, 15 seconds, 30 seconds, 1 minute, 2 minutes, 4 minutes, 8 minutes, 15 minutes, 30 minutes, 1 hour, 2 hours, 4 hours, 8 hours, 12 hours, 24 hours, and 48 hours. At least one set of five hydrometer tests were conducted for each soil. An additional of five tests were conducted for kaolinite due to a high variability in the initial test results.

4.3.3. *Determination of Soil Specific Gravity*

The determination of soil specific gravity was obtained using a modification of the procedure as described in ASTM D854 (2014). The deviations from the ASTM D854 (2014) procedure include the omission of the water bath and the reduced amount of time that vacuum was applied to the soil. The vacuum was applied for 30 minutes instead of 2 hours as specified in the ASTM D854 (2014) standard.

4.3.4. *Determination of Clay Mineralogy*

The clay mineralogy for each soil (or analogous value for the Donna Fill) was obtained using the procedures previously described in Section 4.3.1 and Section 4.3.2. The graphical relationship that was proposed by in Skempton (1953) was utilized to evaluate the soil mineralogy. The relationship was determined using previously obtained soil index property data (as obtained using the ASTM D4318 2014 standard and the TAMU FCD testing) in addition to the clay fraction value (as obtained using ASTM D422 (2014) as described in Section 4.3.2).

4.4. Advanced Characterization of Processed Soil Samples

Two different advanced soil characterization techniques were used to evaluate the soil. These two techniques were scanning electron microscopy (SEM) and X-ray diffraction (XRD).

SEM testing was conducted using a Philips XL30 Environmental Scanning Electron Microscope owned and operated by the University of Arkansas Center for Nano-Bio Material Characterization (UACNBMC). At least three sets of images were acquired from 10,000 to 15,000 times magnification from a ground desiccated sample. Samples were prepared to by adhering the soil particles to a pedestal coated with a black carbon tape. The samples were sputter coated with gold (surface coating between 2 and 20nm thick) to: decrease sample charge, improve secondary electron emission, and reduce electron beam penetration depth. All sample preparation was conducted by personnel from the UACNBMC. All images were taken while the sample chamber was under vacuum. Similarly, the XRD testing was conducted with a Phillips PW-1830 X-ray diffractometer. The Phillips PW-1830 X-ray diffractometer sample cradle was configured for use with loose powder samples. Sample preparation, sample spectra collection, and data pre-processing was performed by personnel from the UACNBMC.

4.5. Preparation of Soil Samples and Acquisition of Soil Water Potential Measurement Using a Chilled Mirror Hygrometer.

The methodologies utilized to prepare soil samples, acquire chilled mirror hygrometer (CMH) soil water potential measurements, and process the data are presented in this section. A Decagon WP-4 CMH was used to acquire soil water potential measurements between 0 and -300MPa. Sample plastic tins with a total volume of 5 mL were used for testing all samples (calibration solution, distilled water, and soil samples). As per the manufacturer's specifications (Decagon 2007), instrument calibration was conducted prior to the beginning of daily testing, whenever the WP-4 instrument was turned on, and periodically during testing) using a 2.5mL 0.5 M potassium chloride salt solution (soil water potential of 2.19 +/- 0.1MPa). To verify that no contamination (of soil or calibration solution) was in the sample chamber a 2.5ml sample of de-ionized water (0MPa) was placed in the sample chamber after instrument calibration.

Soil samples were acquired from the bulk soil samples (in a ground, oven dried state). Samples (approximately 30g) of oven dried ground soil were initially mixed to a target gravimetric water content (0, 1, 5, 10, 20, 40, and 80 percent). After the initial testing was complete target gravimetric water contents were adjusted to provide a more complete coverage of the volumetric water content domain. Samples were allowed to equilibrate overnight in sealed metal containers. A 2.5mL volumetric measuring spoon (0.5 teaspoon) was used to acquire a known volume of soil sample and place it in a pre-weighed plastic sample tin.

The plastic sample tins were covered were placed in the designated area of the WP-4 device. Samples were allowed to sit on the device for approximately 30 minutes to allow for temperature equilibrium between the samples and the WP-4 instrument. Soil samples were tested by placing the uncovered sample tin in the WP-4 sample tray and gently closing and latching the sample chamber. WP-4 measurements (soil water potential, sample chamber temperature, sample temperature, temperature differential) were repeated until three soil water potential values were acquired within +/- 0.2MPa and a temperature differential value (temperature of sample chamber minus sample temperature) of less than 0.1℃. The average of the three aforementioned values was reported as the measured soil water potential. After completion of CMH testing the gravimetric water content of the entire sample was determined. The soil sample was oven dried and gravimetric water content was computed by following the ASTM D2216 (2014) standard. The volumetric water content was calculated using Equation 4.2.

$$\theta = \frac{\left(w_{wet} - w_{tin}\right) - \left(w_{dry} - w_{tin}\right)}{\rho_w V_T} \qquad \text{Equation 4.2}$$

In Equation 4.2, θ is the volumetric water content, w_{wet} is the weight of the wet sample and the tin, w_{dry} is the weight of the oven dry sample and the tin, w_{tin} is the empty weight of the sample tin, ρ_w is the density of water, and V_T is the total volume of the soil sample (2.5 mL).

In addition to obtaining a soil water characteristic curve (SWCC), the WP-4 CMH was also used to obtain a measurement of the osmotic potential component of soil water potential by testing saturated samples ($\psi_m = 0$). Soil samples were prepared as a slurry (gravimetric water content of 1.0), and were consolidated in a centrifuge. Two samples of each soil type with equivalent weights (water was added if required) were placed in the centrifuge to ensure that the centrifuge device was balanced. Centrifuge consolidation was performed at 500 revolutions per minute (RPM) for a period of 36 hours. The 36 hours consolidation period consisted of three 12 hour periods. The soil samples were checked at the end of each 12 hour period to ensure that soil surface remained submerged and therefore saturated. After 36 hours, the soil sample was removed from the centrifuge cylinder frame and submerged in a large plastic tub. A 5ml plastic tin was pressed halfway into the bottom of the soil sample. The sample was trimmed using a metal spatula. The sample was pressed down into the tin using the soil spatula. The sample was kept submerged during all preparation to keep the soil saturated. The soil water potential and volumetric water content values were obtained using the technique described in this section.

4.6. Preparation of Soil Samples for Use in DRIFT FTIR Testing

Two hundred grams of spectroscopic grade (greater than 99 percent purity) anhydrous KBr material was obtained from Thermo Fisher Scientific (Waltham, Massachusetts). All of the soil sample types were then prepared using the same procedure that included by mixing the KBr material with various quantities of the dry bulk soil samples. The sample preparation process as described in this section has also been documented in Garner and Coffman (2017b) and is presented here for completeness. Prior to preparing mixed samples, the Donna Fill, illite, kaolinite, and potassium bromide (KBr) materials were removed from the bulk soil stockpile (prepared as described in Chapter 3) and then dried in an electronically controlled oven

maintained at 105 (+/- 5)°C for 12 hours. Soil samples were dried in 30mm steel sample containers. After oven drying, the KBr material and the soil samples were maintained within a desiccator to prevent the hygroscopic absorption of moisture from the atmosphere. After being removed from the desiccator, the dry soil and KBr materials were added together at various mass fractions to obtain mixed samples with 0 percent (15g KBr), 2 percent (0.3g soil and 15g KBr), 4 percent (0.6g soil and 15g KBr), and 6 percent (0.8g soil and 15g KBr) soil samples, as measured by dry weight. Due to the small quantity of samples used (~0.3-0.8g of soil) a specific procedure for the preparation of the mixed samples was employed. A dry stainless steel sample tin (3.0cm diameter) was obtained and if necessary cleaned using an optical grade wipe (ChemWipe) and either methyl or ethyl alcohol to remove any contamination. The sample tin was then allowed to dry under direct light (a halogen light source was employed) until all of the alcohol solvent had evaporated. Additionally, a clean, dry (using the same process as the sample tins), commercially available powder trickler (produced by the Franklin Armory) was loaded with the appropriate soil type and rubber caps fitted to both the soil reservoir and the end of the output tube. The clean dry tin was then placed on an electronic balance with a readability of +/- 0.0001g, and the balance was tared. The loaded powder trickler was placed inside the glass enclosure of the electronic balance off of the weighing platen with the output nozzle of the powder trickler directly above the sample tin.

At least 15g of ground dry KBr was placed in the container directly from the mortar after grinding using a metal spatula with care being taken not to allow any of the KBr material to spill onto the scale. The final weight of the KBr material was recorded. The amount of soil (and the combined mass of the KBr matrix material and the soil) required to achieve the desired mass fraction (e.g. 2, 4, or 6 percent) was calculated. Soil was slowly trickled (after the end cap was

removed) into to the sample container using the powder trickler thumbscrew. Care was taken to minimize the disturbance of the scale during trickling as well as to ensure a consistent rate of dispensing. Additionally, the vertical distance between the output of the powder trickler and the sample container was minimized (approximately 2.5cm) to avoid the accidental dispersion of fine soil particles. The number and dilution of each sample is tabulated in Table 4.2.

Table 4.2. Sample materials reported as the mass fraction of soil and the mass fraction of KBr substrate material (Garner and Coffman 2017b).

Number	Material	Percent KBr[1]	Percent Soil[1]	Number	Material	Percent KBr[1]	Percent Soil[1]
1	KBr	100	0	22	Donna Fill	94	6
2	KBr	100	0	23	Donna Fill	94	6
3	KBr	100	0	24	Donna Fill	94	6
4	Donna Fill	98	2	25	Illite	94	6
5	Donna Fill	98	2	26	Illite	94	6
6	Donna Fill	98	2	27	Illite	94	6
7	Illite	98	2	28	Kaolinite	94	6
8	Illite	98	2	29	Kaolinite	94	6
9	Illite	98	2	30	Kaolinite	94	6
10	Kaolinite	98	2	31	Donna Fill	0	100
11	Kaolinite	98	2	32	Donna Fill	0	100
12	Kaolinite	98	2	33	Donna Fill	0	100
13	Donna Fill	96	4	34	Illite	0	100
14	Donna Fill	96	4	35	Illite	0	100
15	Donna Fill	96	4	36	Illite	0	100
16	Illite	96	4	37	Kaolinite	0	100
17	Illite	96	4	38	Kaolinite	0	100
18	Illite	96	4	39	Kaolinite	0	100
19	Kaolinite	96	4	[1]Denotes the Percent Mass fraction of Each Component by Dry Weight			
20	Kaolinite	96	4				
21	Kaolinite	96	4				

After mixing the soil with the KBr substrate material and prior to testing, each of the mixed samples (KBr with soil) were placed into a desiccator (210mm glass desiccator with a loose anhydrous calcium chlorite desiccant) for at least four hours. Soil samples were also transported in the desiccator to prevent the soil material from imbibing moisture. The mixed samples were also maintained within the desiccator before and after testing; specifically, a given mixed sample was only removed from the desiccator to place a given mixed sample into the $3.14cm^3$ sample holder. The $3.15cm^3$ sample holder was fabricated from a 2.54cm diameter

polyethylene rod. Approximately 4.5g of mixed sample was placed into the 3.14cm^3 sample holder prior to each test. The mixed samples were air pluviated into the sample holder until the sample holder was full. Moreover, a well-rounded heap of material with a height of approximately 0.5cm (above the top of the sample holder), was placed in the sample holder using a dry, non-static, plastic funnel, and the samples were loosely tamped using one blow from a 1.25cm steel dowel and struck off. If required, an additional amount of sample was added to the container, tamped once, and struck off with a clean, straight-edged, steel spatula. The sample surface was struck-off to be flush with the top of the sample container. The flush surface was required to maintain a consistent spacing between the sample surface and the end of the fiber optic probe that was utilized to collect UV-NIR data. The fiber optic probe and the spectra collection process that utilized this probe are discussed in the next section.

4.7. Preparation of Soil Samples for Use in LAST Testing

Preparation of the soil samples for use in the LAST testing procedure was accomplished in multiple steps. Initially, the soil samples were prepared from the raw materials as described in Chapter 4. Soil samples for the LAST testing were subsequently removed from the bulk stockpile and then prepared using a slurry consolidometer (Section 4.7.1) to ensure a consistent soil fabric and then placed in a pressure plate extractor (Section 4.7.2) and were prepared at different values of soil matric potential.

4.7.1. *Preparation of Soil Samples by Slurry Consolidation*

All samples to be utilized or prepared by the pressure plate extractor (PPE) were initially processed using a slurry consolidometer (Figure 4.3). Two slurry consolidometers were utilized over the course of this project due to equipment availability and scheduling concerns. All Donna Fill samples were consolidated in a 6.7cm (inner diameter) slurry consolidometer. The illite and

kaolinite samples were consolidated in 6.7cm (inner diameter) slurry consolidometer. Prior to the preparation of the soil samples the slurry consolidometer was thoroughly disassembled and cleaned. Specific care was taken to ensure that the rubber o-rings in the base platen and the acrylic piston were clean and had been properly lubricated with high-vacuum grease. Considerable difficulty was encountered in ensuring a proper seal between the inside of the acrylic tube and the piston and therefore care was taken to ensure that the piston o-ring channel and ring were free of any soil particles. The apparatus was then partially assembled. The acrylic tube was placed on the bottom plate and then secured in position with the top plate. The three 1.3cm (0.5 inch) hexnuts were finger tightened and then turned one half turn (180 degree rotation) with a crescent wrench.

A piece of filter paper was then placed in the acrylic tube and then pushed into place with broom handle or other implement. The filter paper was subsequently dampened using a squirt bottle containing de-aired, de-ionized (DI-DA) water to 1) ensure that the filter paper was properly seated against the porous stone and 2) to help keep the paper in place during the filling of the slurry consolidometer with soil. All slurry consolidometer samples were prepared at a target water content of fifty percent or at the soil liquid limit plus ten percent (which ever was higher). For the initial illite and kaolinite samples, approximately 800g of oven dry, ground soil was mixed with 400g of DI-DA water. Due to the sample size it was necessary to mix the soil in two 400g batches. For the Donna Fill samples it was necessary to use 400g samples. Four hundred grams of dry soil was placed into a steel bread tin and then 200g of water was weighed out in a graduated glass beaker using an electronic balance (with a readability of +/- 0.01g). Water was added slowly and the soil was continuously mixed using a metal spatula. Soil was mixed using the procedure described in Mahmood (2014). After all the water was added to the soil the

sample was mixed for approximately three minutes using a glass stirring rod, the sample was then allowed to sit for one minute, and then mixed for three additional minutes.

After both batches of soil sample had been mixed then samples were poured into the slurry consolidometer using a plastic funnel with a 1.3cm aperture. For each the Donna Fill and kaolinite samples, it was necessary to continuously agitate the sample by tapping the funnel against the top of the slurry consolidometer and using the glass stirring rod to keep the sample in a liquid state. Once the sample had been placed in the slurry consolidometer, a piece of moistened filter paper (to help keep it in place) was placed on top of the piston porous stone and the piston was fitted into the top of the slurry consolidometer, and then gently pushed into place with the top cap and load frame. Load was then applied to the consolidometer using static loading. Sufficient weight was placed on the load frame in the form of steel weights to achieve an overburden pressure of 138kPa) on the sample.

The sample was then allowed to undergo 1-dimensional consolidation. The deformation of the sample was measured using an electronic dial gauge attached to a standard laboratory stand. The elapsed time for each reading was determined using an electronic stopwatch. The time to complete consolidation was calculated using the methods proposed by Casagrande and Fadum (1940) and Taylor (1948). Each sample was allowed to consolidate for 48 hours past the calculated t_{100} value. Weight was subsequently removed from the consolidometer and the sample was allowed to sit for at least 24 hours (to allow any sample rebound to occur prior to extrusion). Acrylic sample rings were fabricated from tube stock with a diameter of 6.35cm or 6.73cm and a height of 1.5cm. The acrylic sample rings were arranged on a previously saturated ceramic porous plate. The slurry consolidometer was subsequently disassembled and individual samples were extruded from the slurry consolidometer by placing the acrylic tube (after the filter paper had

been removed) on top of the acrylic sample rings and then extruding the soil using the load frame. Once the sample ring had been filled the sample was severed from the soil body using a wire saw. Each ring was filled sequentially until porous plate was filled (Figure 4.4).

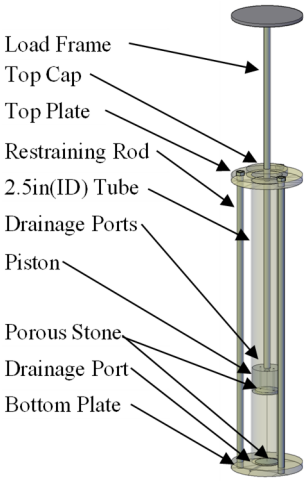

Figure 4.3. Schematic of the slurry consolidometer employed to prepare samples.

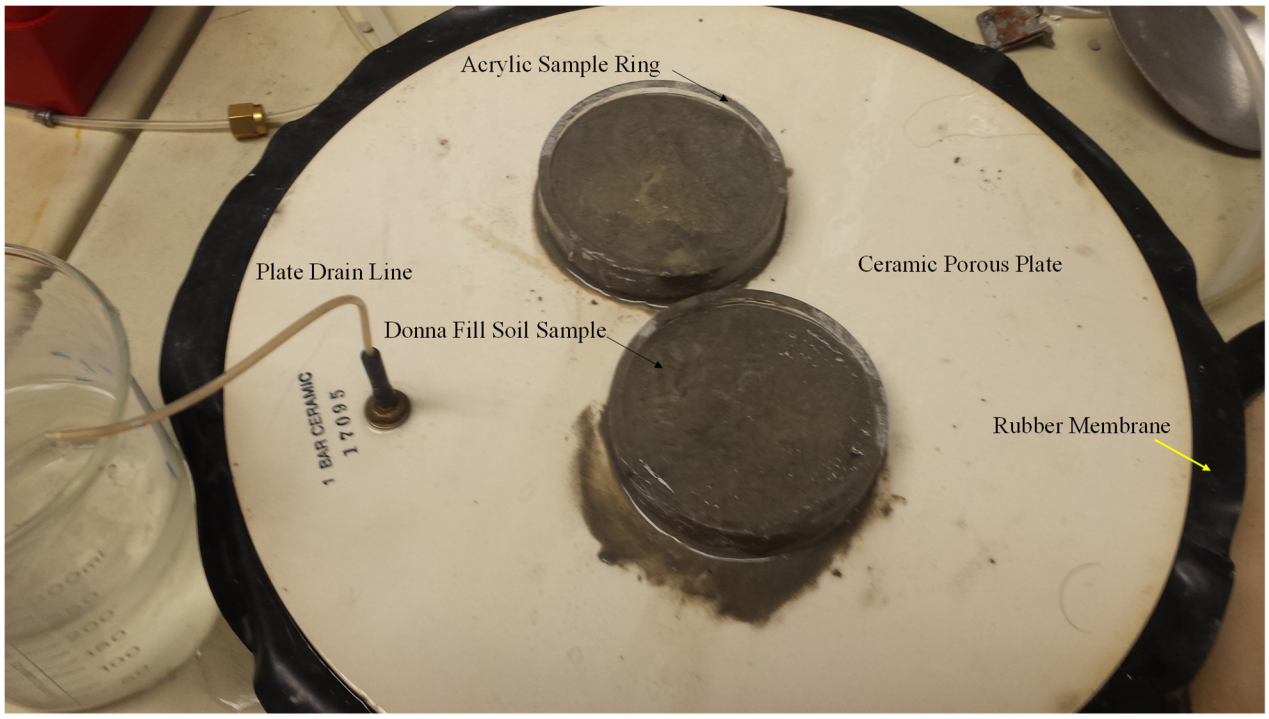

Figure 4.4. Porous plate for pressure plate extractor with two samples placed and extruded into sample rings for testing [image by author, in color].

4.7.2. *Preparation of Soil Samples Using a Pressure Plate Extractor.*

Two separate pressure plate extractor (PPE) apparatus were used during this project to prepare samples for LAST testing. A Soil Moisture, Inc. Model 1500 PPE owned by the University of Arkansas was used to prepare samples with matric potential values between 1 and 500kPa (1 to 5 atmospheres). Similarly, a Soil Moisture, Inc. Model 1600 PPE owned by the University of Missouri was used to prepare samples at matric potential values between 5 and 1500kPa (5 and 15 atmospheres). Pneumatic pressure, monitoring, and control for the Model 1500 PPE was supplied using a laboratory pneumatic panel. Conversely, the pneumatic pressure for the Model 1600 PPE was supplied using an ANSI/CGA-7 gas cylinder containing dry air (at a gauge pressure of 15,000kPa), a CGA-580 adaptor, and a single stage high pressure gas regulator (1724kPa max supply pressure) with a 1.3cm (0.5 inch) MNPT output. An isolation valve, a pressure transducer, and an electronic readout display were used to monitor the applied pressure, and the high pressure regulator was used to control the pneumatic pressure (Figure 4.5).

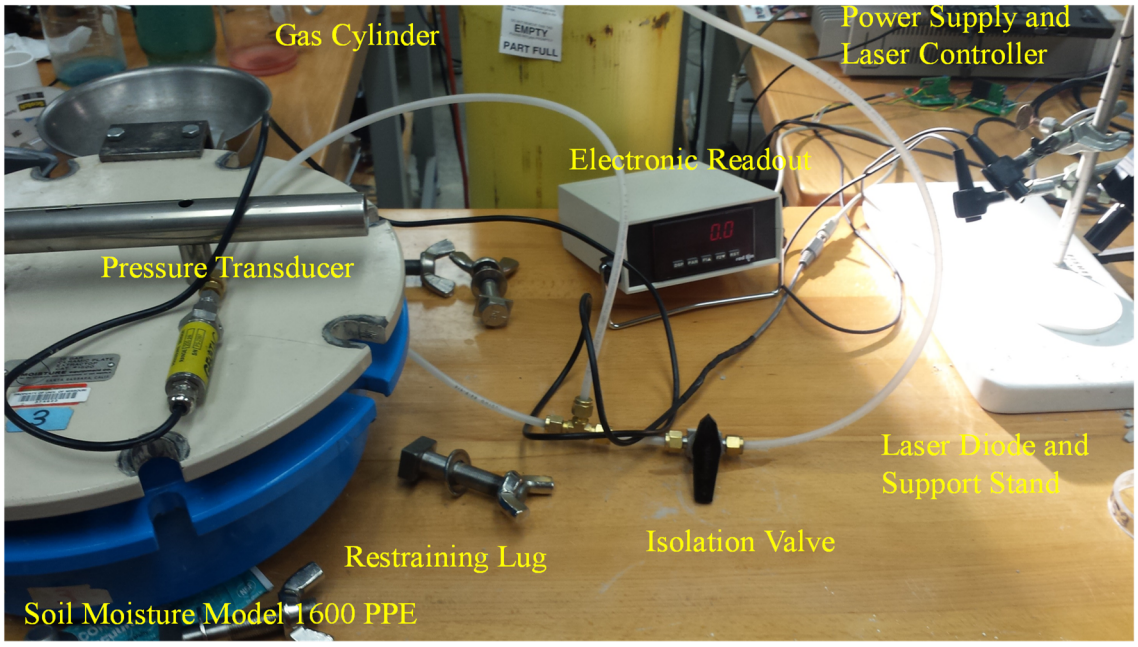

Figure 4.5. Model 1600 pressure plate extractor with pneumatic supply and LAST device [image by author, in color].

The use of the pressure plate extractor (PPE) to prepare samples was accomplished using modifications of the procedures described in Fandry (2012) and ASTM D6836 (2014). Porous plates were initially saturated by submerging the pressure plate in water and allowing it to sit for at least 48 hours. The plate was then removed from the water bath and the surface was wiped dry. A small positive hydraulic pressure was applied to the porous plate by connecting the plate drain line to the laboratory sink faucet and allowing a small amount of water to flow backwards through the system. The proper amount of hydraulic head was gauged by observing the inflation of the rubber membrane on the underside of the porous plate. Plate saturation was verified when water was observed beading on the surface. The samples were then extruded from the slurry consolidometer and placed on the porous plate (as previously described in Section 4.7.1). All porous plates (including the ones used in the Model 1600 PPE) were saturated initially in the Model 1500 PPE due to the larger volume and the presence of multiple pass through ports.

Once the samples had been placed on the porous plate, the porous plate was placed in the PPE device and the drainage line was connected between the plate drain port and the high pressure pass through port in the vessel wall. The PPE device was reassembled with care being taken to ensure that a good, air-tight seal was formed between the lid and the body of the vessel. Particular attention was given to make sure the o-ring between the vessel lid and body was clean, properly lubricated with high-vacuum grease, and that no debris was in the o-ring channel or bearing surfaces. The restraining bolts were tightened using an adjustable crescent wrench in a star pattern to prevent binding of the lid. During tightening of the restraining bolts, care was taken to make sure that each screw remained properly seated in the recess on the vessel body.

For the Model 1500 PPE, pressure was applied slowly by selecting the desired pressure on the pneumatic panel and then opening the fill valve slightly and allow air to slowly fill the vessel.

For the Model 1600 PPE, pressure was applied slowly by leaving the regulator set to the previous pressure increment, or zero pressure if unknown or higher than the desired value, then the isolation valve was opened slightly. In either case, after the pressure had stabilized and no leaks were detected by: 1) audible means (hearing the escaping gas); 2) tactile means by running a wetted finger around areas of concern including the junction between the lid, pass through ports, and the drain line; and 3) closing off the pneumatic air supply and allowing the vessel to sit for several minutes then reapplying the pressure. In the third case a loss of pressure would be detected by hearing the audible flow of gas into the vessel when the pressure was reapplied. For the Model 1600 PPE, after a good air-tight seal had been achieved the desired pressure plate increment was then selected by turning the regulator thumbscrew clockwise (to increase the pressure).

For both the Model 1500 and Model 1600 PPE devices, the drain line to the porous plate(s) was directed into a receiving vessel (either a length of flexible PVC pipe, a flask, or a plastic bottle), and the rate of drainage was observed. For a freshly saturated plate at high pressure the large amount of water expelled from the plate and the space between the ceramic surface and the rubber membrane was directed into a larger vessel until the rate of outflow decreased. Pressure was maintained on the PPE apparatus until the amount of outflow recorded was less than 1 ml in 48 hours as determined by placing the receiving container (with the outflow) on an electronic balance, then discarding the outflow and reweighing the receiving container. After the PPE-prepared sample met the previously described termination criteria, the pressure panels were isolated from the pneumatic supply and a connection or pass through port was loosened to allow for air to escape from the pressure vessel. After verification that all pressure had been dissipated, the restraining lugs were loosened and the samples were removed from the plate.

Care was taken to minimize the amount of disturbance for each sample. The typical removal process consisted of manually applying lateral and torsional load to the acrylic sample container to break the connection between the soil sample and the porous plate. In certain cases (especially with the kaolinite samples) the use of a metal spatula to physically de-bond the sample and the plate was required. After the samples were removed, the mass of each sample was recorded using an electronic balance. The dimensions of the sample were acquired using a pi-tape (for diameter) and a set of Vernier calipers to measure the height of the sample. One measurement of diameter was acquired for each sample. For the Donna Fill samples, due to the fragile nature of the samples and the absence of observable radial shrinkage, the diameter was acquired on the porous plate relative to the acrylic ring using the Vernier calibers. After completion of spectra acquisition (described in Section 4.8), the gravimetric water content of the soil sample was obtained using the procedure described in ASTM D2216 (2014). The volumetric water content was subsequently calculated using the gravimetric water content, the phase relationships, and the total volume of the soil sample as determined from the dimensional measurements of diameter and height.

4.8. Acquisition of Soil Spectra for FTIR Testing

An Ocean Optics USB-2000 ultraviolet visible (UV-Vis) spectrometer (350-1000nm) and a Nicolet 6700 Fourier Transform Infrared (FTIR) spectrometer (1000-2500nm) were utilized to collect the reflectance spectra for the FTIR samples. Additionally mid-infrared spectral data (2500-25000nm) was collected for comparison with existing literature methods of soil classification (e.g. Waruru et al. 2014). The collection of MIR data is described at the end of this section. The process employed to acquire FTIR spectral data as described in this section has also been documented in Garner and Coffman (2017b), and is presented here for completeness The

Nicolet FTIR spectrometer was employed to provide a white light illumination source for both UV-Vis and NIR spectrum collection. A dual purpose sample chamber was fabricated and employed to collect both UV-Vis and NIR reflectance spectrum without causing disturbance to the given sample. The dual-purpose sample chamber was fabricated using commercially available materials (PVC schedule 40 pipe) to minimize cost and fabrication time. Only the sample holder required machining. All other parts were utilized directly as purchased or where modified (by drilling holes for gas and instrument pass-throughs). A schematic of the sample chamber and the associated connections are presented in Figure 4.6.

Each mixed sample, located within the sample holder, was sequentially loaded into the sample chamber and was secured in position by using a metal dowel. The nitrogen (N_2) purge line was connected to the top of the sample chamber and the thermocouple probe was also inserted into the sample chamber. The fiber probe was then placed into the sample chamber; the elevation of the probe was controlled by adjusting a padded mechanical clamp that was attached to the fiber optic probe. Consistent positioning of the probe was verified by using a set of Vernier calipers to measure the position of the fiber optic probe relative to the top of the dual-purpose sample chamber. The aforementioned fiber optic probe was connected to a duplex (transmit-receive) two ended fiber optic cable utilized to: 1) transmit the energy from the white light source into the common sample chamber while also being utilized to 2) obtain the desired spectra. To obtain both UV-Vis and NIR spectra, the receiving end of the fiber optic cable was manually attached to either the Ocean Optics USB-2000 spectrometer or the Nicolet 6700 FTIR spectrometer, as required.

A Spectralon reference material (obtained from ASD-Panalytic of Boulder, Colorado) was utilized as a reflectance reference material. Two steel shims (76mm outside diameter, 62mm inner

diameter, and 3mm thick) were utilized to position the Spectralon reference material so a constant distance between the sample surface and the fiber optic probe was maintained for both the spectralon and. All of the spectra were obtained by averaging 256 sequential independent spectra measurements.

The sample chamber was purged with dry nitrogen gas provided from a 3.5m^3 (125ft^3) ANSI/CGA C-7 gas cylinder (15MPa gauge pressure) through a CGA-580 two stage regulator and 0.635cm (1/4in) rigid plastic tubing. The regulator was set to provide a constant gauge pressure of approximately 100kPa. The rate of the flow of nitrogen into the sample chamber was controlled with a ball valve that was located between the regulator and the sample chamber. The purge gas flow rate was manually adjusted to maintain positive pressure within the sample chamber to displace and prevent moisture contamination of the oven-dry soil samples during testing. Positive pressure was verified by manually obstructing the thermocouple port and tactilely determining an increase in pressure. After verification of positive pressure, the electronic thermocouple controller. Active control of the temperature was not performed during testing. The relative humidity within the room was also monitored using a digital hygrometer (HySkore Digital Hygrometer) located on the laboratory bench.

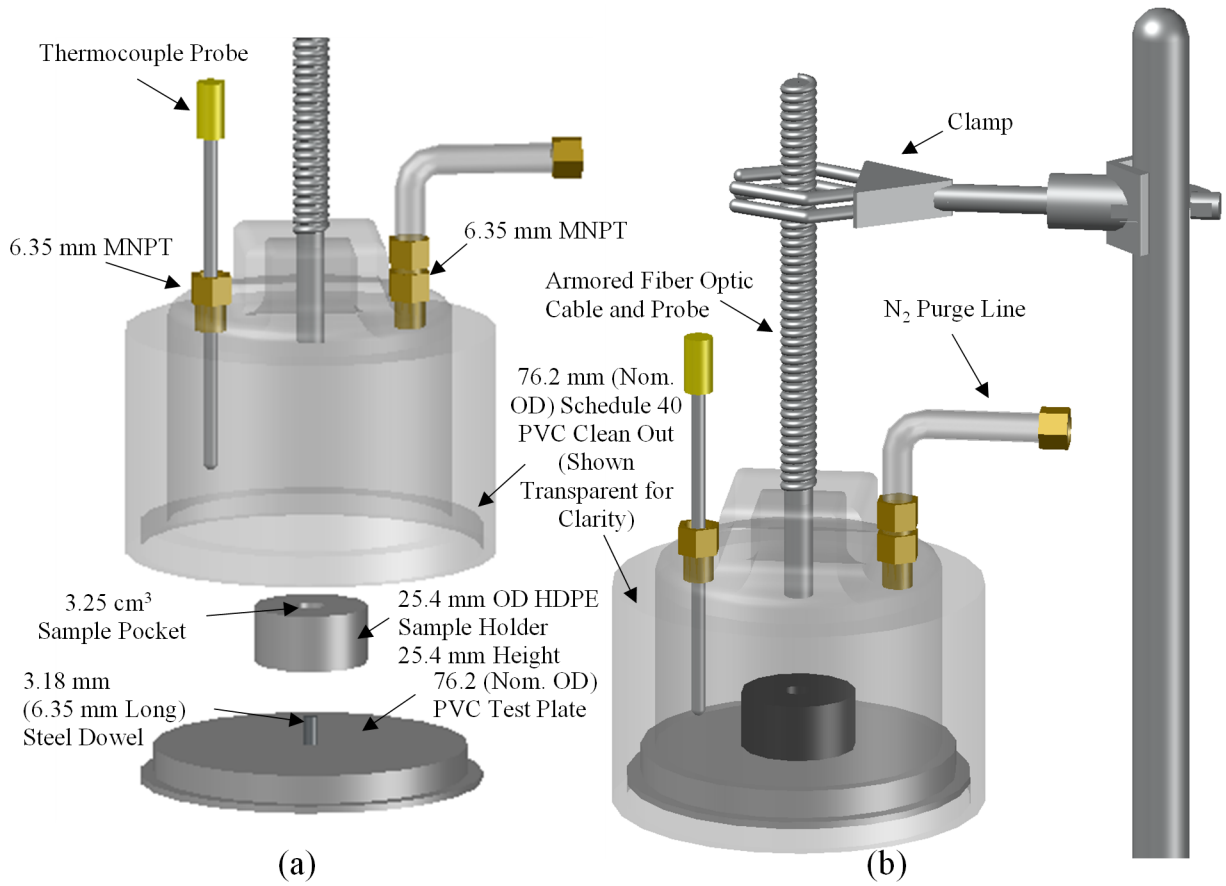

Figure 4.6. Schematic of the University of Arkansas dual purpose sample chamber as a) an isometric view of individual components, and b) an isometric view of the device when assembled for testing (Garner and Coffman 2017b).

A Nicolet 6700 spectrometer with a diffuse reflectance accessory was employed for MIR testing. The instrument was controlled with the OMNIC software suite (Nicolet 2004). A thermo-electrically cooled dueterated triglycine sulfate detector with a potassium chloride window, an MIR source, and a KBr beam splitter were employed. An InfraGold (an electrochemically plated diffuse gold-metallic coating) reference disk was used to acquire a background reflectance. Five gram lots of sample were removed from the glass desiccator and placed into the 0.25cm^3 sample slide. A reference background reflectance spectrum was collected by sliding the sample holder out approximately 2.5cm until the InfraGold reference sample was within the beam path. Background spectra were stored for use in preprocessing of the data prior to the collection of data of each

spectrum. Spectral data were collected at a wavenumber resolution of $1cm^{-1}$. The OMNIC software was used to preprocess the data (to convert the raw intensity values to reflectance valued). A total of 21 MIR-Dry spectra were acquired (five kaolinite, nine illite, and nine Donna Fill).

4.9. Acquisition of Soil Spectra for LAST Testing

Visible-Near Infrared spectral data was obtained using an ASD Panalytic FieldSpec4 Hi-Res Spectroradiometer (Figure 4.7). A laptop computer, using the RS3 software suite (ASD Panalytic 2014), was used to control the instrument, store the acquired spectral data, and perform preprocessing and data export. A fore optic was employed to collimate the reflected light. Reference spectra were collected using a Spectralon (polytetrafluoroethylene [PTFE] polymer) sample. Illumination was provided using a 70W quartz-tungsten-halogen bulb with an integrated reflector. Prior to the extraction of the samples from the pressure plate (to minimize the time the samples were allowed to desiccate or imbibe moisture from the laboratory environment), the FieldSpec4 spectroradiometer was connected to the power supply and instrument controller, and energized. As per the manufacturer's recommendation the FieldSpec4 was allowed to warm up for at least 30 minutes prior to the collection of spectra. The fiber-optic probe was inserted into the ASD pistol grip assembly (PGA) which was mounted on a small camera tripod. The ASD 8 degree instantaneous field of view (IFOV) fore optic was attached to the front of the PGA to provide a more focused field of view for the remotely sensed spectra. During the period of equipment warm up, the LAST device was configured for use (Figure 4.8 and Figure 4.9).

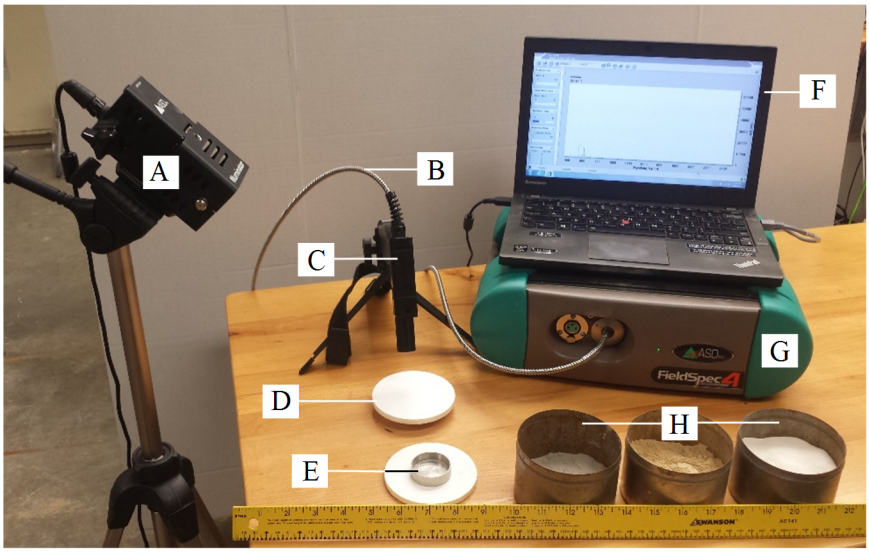

A. Halogen illumination source.
B. Fiber optic cable.
C. Fore optics (eight degree field of view).
D. 7.62 cm diameter Spectralon reference sample.
E. 10 cm^3 Stainless Steel Sample holder.
F. Laptop for data acquisition.
G. FieldSpec4 high resolution spectroradiometer (350-2500 nm)
H. Oven-dried soil samples in 250ml Tin (from left to right: Donna Fill, illite, kaolinite).

Figure 4.7. FieldSpec4 Vis-NIR spectroradiometer and associated accessories (ruler shown for scale). Image by author.

The HL8338MG (50mW at 826nm) and HL8342MG (50 mw at 855nm) laser diodes were mounted in optical tubes (ThorLabs model SR9C, SR9A and LT240P-B) with a 9mm collimating lenses. The focal length of each of the lasers was adjusted until the beam was collimated into a tight spot at a distance of 0.6m. The laser diodes and optical tubes were mounted to a standard laboratory stand using mechanical clamps. The laser diodes were controlled using a ThorLabs constant power controller boards. The constant power controllers were configured for the type A (a ThorLabs EK1101 for the HL8342MG) and type C (a ThorLabs EK1101 and LD1101 for the HL8338MG) laser diodes. Power was supplied to the laser diodes using a 1 amp power supply configured to supply 8 volts direct current (8 VDC). The laser diodes of the LAST device were aligned using the camera feature of a smart phone (since the CCD could visualize NIR

wavelengths). Both laser diodes were aligned so that the beams intersected at the camera aperture. A Spectralon sample was then placed on the laboratory stand base. A 1.5cm sample ring was placed under the Spectralon sample to keep the vertical positioning of the target surface at approximately the same height for both reference and samples spectra collection. After equipment warm up was completed the overhead fluorescent lights were switched off to avoid spectral contamination.

The ASD instrument was configured to measure digital counts (intensity in arbitrary units). Both the laser diodes and the controller rheostat were adjusted until both diodes were lasing (at approximately 0.138-0.142 amps) and the instrument was optimized to prevent saturation of the instrument (by collecting a dark current count and automatically setting the integration time, shortwave IR [SWIR] gain, and SWIR offset). The HL8342MG diode had a higher minimum power (the minimum power at which the laser emitted coherent energy) and therefore the HL8342MG was set to its minimum value. The resistance of the control rheostat was increased until the output of the HL8338MG diode was equivalent to the output from the HL8342MG diode. After the laser diode power had been properly calibrated the halogen light source was energized and the instrument was optimized again. After a reference spectrum was taken with halogen and coherent illumination, a sample was obtained from the PPE as previously described in Section 4.7.2. Samples were placed on a Spectralon sample (with a plastic layer to prevent contamination of the Spectralon sample) to provide proper vertical spacing. Ten spectrum were collected sequentially with a 1 second interval between each spectrum capture. To minimize the effects caused by surface texture, three sets of ten spectra were acquired for each sample with the sample rotated by 90 degrees about the vertical axis. Spectra were stored in a series of .asd binary files with the file nomenclature of sample_XX_YY_00ZZ.asd (where XX was the sample

number, YY is a designator of H/HC for halogen or halogen and coherent illumination, and ZZ is the spectra collection number [01-30]).

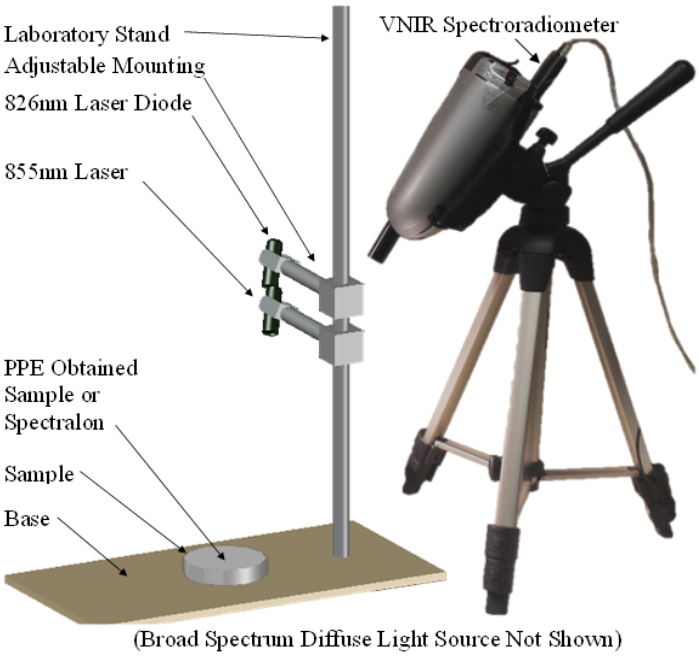

Figure 4.8. Physical arrangement of the LAST proof-of-concept device laser stand and diodes (shown with a HandHeld2 UV-Vis spectroradiometer, image by author).

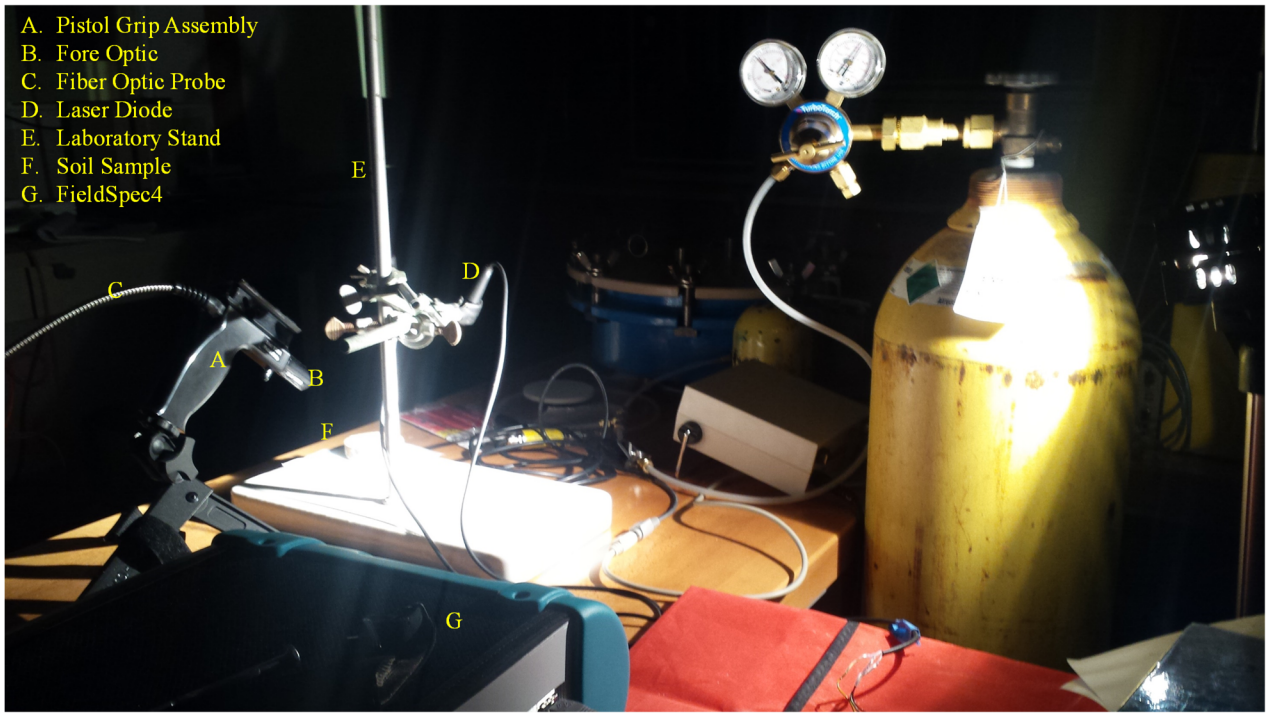

Figure 4.9. Physical arrangement of the LAST proof-of-concept device laser stand (image by author).

4.10. Data Processing for FTIR Testing

Data were collected as a raw digital numbers (350-1000nm) and as a reflection spectra (1000-2500nm). The OceanView software (Ocean Optics 2014) was utilized to collect the UV-Vis spectra and the MATLAB software suite (Mathworks 2014) was utilized to preprocess the raw intensity values into reflectance spectra (by using a reference spectra that was previously obtained from the Spectralon sample). Conversely, the OMNIC software program (Nicolet 2004) was utilized to collect and preprocess the NIR spectra. Specifically, the reflectance spectra were processed within the OMNIC software suite (Nicolet 2004) by referencing a previously collected Spectralon reflectance spectra. The data were then exported as tab or comma delimited ASCII files and subsequently processed utilizing the MATLAB software suite (Mathworks 2014).

Two separate techniques were utilized to obtain measurements of the soil absorption coefficients within the UV-Vis and NIR range. For the pure KBr sample (0 percent soil and 100 percent KBr), the "infinite" depth reflectance (R_∞) was measured and the KM function $\left[(1-R_\infty)^2 \cdot (2R_\infty)^{-1}\right]$ was obtained. Then, the scattering coefficient (s_{KBr}) of KBr was calculated at 1nm resolution, for all wavelengths (350-2500nm) by using Equation 4.3 and Equation 4.4 along with the Hakim et al. (2013) values of absorption for KBr for each of the UV-Vis and NIR wavelengths (350-2500nm). By utilizing the spectra obtained from the two percent soil samples at each 1nm wavelength values for all wavelengths, the previously calculated (s_{KBr})were then utilized to compute the absorption coefficient, of each mixed soil, from the spectra obtained from the two percent soil samples at each 1nm wavelength values (Equation 4.4).

Specifically, the calculation was performed using the two percent samples because it was assumed that the scattering coefficient of the combined mixture was dominated by the scattering behavior of the KBr substrate at low soil mass fractions (e.g. $m_{soil}\, s_{soil} \approx 0$ cm^{-1}). The scattering

coefficients for each soil type (s_{soil}) were then obtained by using the pure (100 percent soil) soil samples (Equation 4.4). A graphical overview of the workflow that was utilized to obtain the various scattering and absorption coefficients is presented as Figure 4.10. The soil absorption coefficient values (k_{soil}) were also directly computed by using the method proposed by Lindberg and Laude (1974) and Patterson et al. (1977) by rearranging Equation 4.4 (into Equation 4.5).

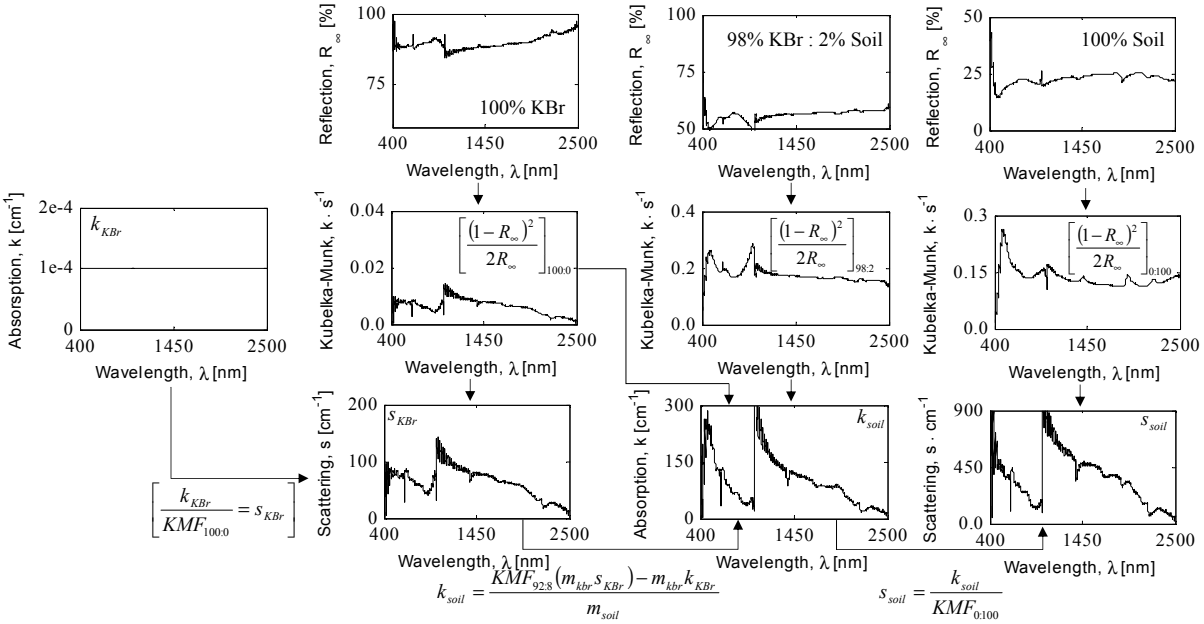

Figure 4.10. Graphical workflow for the computation of soil absorption values using literature absorption coefficient values for KBr (Garner and Coffman 2017b).

$$\frac{m_{KBr}k_{KBr} + m_{soil}k_{soil}}{m_{KBr}s_{KBr} + m_{soil}s_{soil}} = \frac{(1-R_\infty)^2}{2R_\infty}$$ Modified from Barron and Torrent (1986) Equation 4.3

$$\frac{m_{KBr}k_{KBr} + m_{soil}k_{soil}}{m_{KBr}s_{KBr} + m_{soil}s_{soil}} \approx \frac{m_{KBr}k_{KBr} + m_{soil}k_{soil}}{m_{KBr}s_{KBr}}$$ Modified from Barron and Torrent (1986) Equation 4.4

$$\frac{k_{soil}}{s_{KBr}} \approx \frac{1}{m_{soil}} \cdot \frac{k_t - m_{KBr}k_{KBr}}{s_{KBr}}$$ Modified from Patterson et al. (1977) Equation 4.5

Where m_{KBr} is the mass fraction of KBr substrate, m_{soil} is the mass fraction of soil in a mixed sample, k_{KBr} is the absorption coefficient of the KBr substrate, k_{soil} is the absorption of the soil sample, s_{KBr} is the scattering coefficient of the KBr substrate, s_{soil} is the scattering coefficient of the soil sample, R_∞ is the infinite reflection, and k_t is the measured absorption of the mixed sample.

4.11. Data Processing for LAST Testing

Four separate methods of Data processing were employed to extract soil moisture and soil water potential values from the collected spectrum. Two analytical methods were employed using the Kubelka-Munk method (Kubelka and Munk 1931, Kubelka 1947) and the Beer-Lambert method using the soil (k and s) optical properties obtained from the previous section. Two empirical methods using the partial least squares (PLS) and the principle components regression (PCR) on different parts of the spectrum were employed. The analytical methods are described in Section 4.11.1 for Section 4.11.2 for the Kubelka-Munk method and the Beer-Lambert method, respectively.

4.11.1. *Data Processing for the Kubelka-Munk Method*

Spectral data was exported from a binary format (.asd) as tab delimited text files for ingestion into MATLAB for data processing. All data for each series (H and HC) and sample were numerically averaged to increase the signal to noise ratio. The averaging of the reflectance spectrum was performed using a MATLAB executable entitled “asd_reader.m”. The Kubelka-Munk transformation as previously presented in Chapter 2 and as Equation 2.49 was used to convert the measured reflectance spectra into a KM spectrum (using the “kmf.m” MATLAB subroutine). The Kubelka-Munk equations in expanded form (Equation 2.50 and Equation 2.51) were rewritten to account for the three phases of the soil-water-vapor system as presented in Equation 4.9. Two solution methods were employed to improve the results. The first method was a direct algebraic solution of Equation 4.9. The computation of each algebraic solution was conducted using a MATLAB executable (“km_analytical.m”) by comparing each wavelength to each additional wavelength (generating two 2152 by 2152 matrices of water and vapor concentrations with 2.3 million unique values). In the first analysis the previously mentioned 2.3

million unique (the upper triangular matrix and the lower triangular matrix contained duplicate values) values were searched for all water content (since it appeared that the water content value controlled the solution) values greater than zero and less than one. The average value of water content was reported as the solution for the volumetric water content.

Similarly, the average value of water vapor mass was reported. The concentration of water content was then calculated by multiplying the mass fraction of the water vapor by the bulk density of the sample. The computed concentration of water vapor (in units of $g \cdot m^{-3}$) was then divided by the saturation concentration of water vapor under standard temperature and pressure conditions ($0.804 g \cdot L^{-1}$) to obtain the relative humidity. The soil water potential was then calculated using the Kelvin equation. To improve the final result the calculation was subsequently conducted using the known values of soil water content (as previously described in Section 4.7.2) and then solving for the water vapor concentration in the soil.

$$f(R_\infty) = \frac{k}{s} = \frac{(1-R_\infty)^2}{2R_\infty}$$ Barron and Torrent (1986) Equation 4.6

$$\frac{k}{s} = \sum_{i=1}^{n} \frac{k_i m_i}{s_i m_i}$$ Barron and Torrent (1986) Equation 4.7

$$1 = m_t = m_s + m_w + m_v$$ Equation 4.8

$$\frac{k}{s} = \frac{k_s m_s + k_w m_w + k_v (1 - m_w - m_v)}{s_s m_s + s_w m_w + s_v (1 - m_w - m_v)}$$ Equation 4.9

In Equation 4.6 through Equation 4.9, $f(R_\infty)$ is the Kubelka-Munk function, k is the absorption coefficient, s is the scattering coefficient, R_∞ is the infinite depth reflectance, m is the mass fraction of each species, the s subscript represents the soil phase of the system, the w subscript represents the water phase of the system, and the v subscript represents the vapor phase.

4.11.2. *Data Processing for the Beer-Lambert Method*

Similarly, for the Beer-Lambert analytical solution, data was exported as a simulated absorption spectrum (Equation 2.52) using the RSView (ASD Panalytic 2014) software as a tab delimited absorption spectrum. The Beer-Lambert analytical solution required the use of the soil

absorption coefficients as described in Section 4.10 and absorption coefficients for the liquid and vapor phase of water (Kou et al. 1993 and Rothman et al. 2009). The Beer-Lambert equation (previously presented in Chapter 2 and as Equation 4.11) was expanded and is presented in Equation 4.12. The computation was performed using the "bl_analytical.m" MATLAB executable.

$$A_\infty = Log_{10}\left(\frac{1}{R_\infty}\right)$$ (Rossel et al. 2010a) Equation 4.10

$$\frac{I}{I_0} = 10^{-\alpha c l}$$ (Hapke 2012) Equation 4.11

$$Log_{10}\left(\frac{I}{I_0}\right) = 10^{-[k_s m_s + k_w m_w + k_v m_v] l}$$ Equation 4.12

In Equation 4.10 through Equation 4.12, A_∞ is the simulated absorption, R_∞ is the infinite depth reflectance, I is the reflected intensity, I_0 is the incident intensity, α is the molar absorption coefficient, k is the mass absorption coefficient, m is the mass fraction, and l is the empirical path length.

4.11.3. *Data Processing for Empirical Solutions*

Vis-NIR spectral files for each sample were averaged (taking the arithmetic mean of the reflectance intensity at each respective wavelength for all of the spectra that were acquired for a single sample). Two different empirical correlations were generated including, 1) an "active" spectrum correlation that only included data from samples illuminated under both halogen and coherent illumination (with particular emphasis on the spectra region between 800 and 900nm), and 2) a "passive" spectrum correlation which included all of the collected spectrum including from samples under both halogen only, and halogen and coherent illumination. The empirical correlation between the measured sample values (soil water content and the soil water potential) and the observed spectral data (wavelength and intensity) was also determined using the MATLAB software (Mathworks 2014). Both the partial least squares (PLS) regression technique and the principle components (PCR) regression technique were performed using the MATLAB

Statistics and Machine Learning Toolbox. Specifically, the plsregress.m (Mathworks 2010) PLS executable and pca.m PCR executable (Mathworks 2012) were utilized. The PLS regression was conducted using the straightforward implementation of a statistically inspired modification of the PLS method (SIMPLS) as described in (de Jong 1993, Rosipal and Kramer 2006). Approximately 70 percent of the observed data was used to generate the regression. The remaining 30 percent of the observed data was reserved for a validation data set. Spectral reflectance intensities were stored in the X matrix, and measured values of each of the engineering index values were stored as the Y (n by 1) vector (Table 4.3).

Table 4.3. Example X and Y matrix for use in PLS and PCR regression.

	LL	λ_1	λ_2	λ_3	λ_4	…	…	λ_{n-1}	λ_{n-1}	λ_{n-1}	λ_n	
Soil 1	31.5	0.895	0.894	0.893	0.891	0.890	0.888	0.886	0.884	0.882	0.880	< **Spectra1**
	31.5	0.892	0.891	0.890	0.888	0.887	0.885	0.883	0.881	0.879	0.877	< **Spectra2**
	31.5	0.894	0.892	0.891	0.890	0.888	0.886	0.884	0.883	0.880	0.879	< **Spectra3**
Soil 2	46.7	0.730	0.730	0.730	0.730	0.730	0.730	0.730	0.730	0.730	0.730	< **Spectra4**
	46.7	0.722	0.722	0.722	0.722	0.723	0.723	0.723	0.723	0.723	0.723	< **Spectra5**
	46.7	0.724	0.724	0.724	0.724	0.724	0.724	0.724	0.724	0.725	0.725	< **Spectra6**
Soil 3	25.0	0.463	0.463	0.463	0.463	0.463	0.463	0.464	0.464	0.464	0.464	< **Spectra7**
	25.0	0.454	0.454	0.455	0.455	0.455	0.455	0.455	0.455	0.455	0.456	< **Spectra8**
	25.0	0.467	0.467	0.467	0.467	0.467	0.468	0.468	0.468	0.468	0.468	< **Spectra9**
		Y	**X**									

A maximum of 10 PLS or PCR components were considered (Mathworks 2010, 2012). The value of N_c was selected to explain greater than 90 percent of the variation in Y. For the PLS and PCR regressions, two methods of validation were employed. A K-fold (ten folds) cross-validation procedure was employed to measure the estimated mean squared predictive error (EMSPE) value for each model as a function of N_c. Additionally, a subset (approximately 30 percent of the total number of samples acquired) of the original data set was excluded from the regression (calibration) data set. After selecting an appropriate value of N_c, the computed vector containing the PLS regression weighting coefficients (β vector) was subsequently employed to predict values of the index properties (Y_{pred}) from the observed reflectance spectrum of the

validation data set by using Equation 4.13. The PLS and PCR regressions were conducted using the "master_proc.m" MATLAB executable.

$$Y_{pred} = X_{validation} \cdot \beta + F$$ Wold et al. 2001 Equation 4.13

Where $\mathbf{Y}_{pred}$ *is a vector (a rows by one column),* $X_{validation}$ *is the matrix containing the observed reflectance spectrum (a rows by b columns), where a is the number of acquired spectra, b is the number of wavelength values in each spectra, and* $\mathbf{F}$ *is a one by one vector containing the Y-residual values.*

4.12. Works Cited

3M Corporation (2015). "Product Information and Material Safety Data Sheet for Classic Roofing Granules." http://solutions.3m.com/wps/portal/3M/en_US/IMPD/Roofing-Granules/Products/Classic-Roofing-Granules/. Retrieved December 2015.

American Society for Testing and Materials (ASTM) D422, (2014). "Standard Test Method for Particle-Size Analysis of Soils." American Society for Testing and Materials, Vol. 4.08, Soil and Rock (I). West Conshohocken, PA.

American Society for Testing and Materials (ASTM) D854, (2014). "Standard Test Methods for Specific Gravity of Soil Solids by Water Pycnometer." American Society for Testing and Materials, Vol. 4.08, Soil and Rock (I). West Conshohocken, PA.

American Society for Testing and Materials D2216, (2014). "Standard Test Methods for Laboratory Determination of Water (Moisture) Content of Soil and Rock by Mass." Annual Book of ASTM Standards, Designation D2216, Vol. 4.08, ASTM, West Conshohocken, PA.

American Society for Testing and Materials D6836, (2014). "Standard Test Method for Determination of the Soil Water Characteristic Curve for Desorption Using a Hanging Column, Pressure Extractor, Chilled Mirror Hygrometer, and/or Centrifuge." Annual Book of ASTM Standards, Designation D6836, Vol. 4.09, ASTM, West Conshohocken, PA.

ASD Panalytical Inc., (2014). "RS3 and ViewSpecPro Software and Supporting Documentation." The ASD Panalytical Inc. Boulder, Colorado.

Atterberg, A., (1912). "Die Plastizitat der Tone." Internationale Mitteilungen fur Bodenkunde, Vol. 2, pp. 149-188 (in German).

Barron, V., Torrent, J., (1986). "Use of the Kubelka-Munk Theory to Study the Influence of Iron Oxides on Soil Colour." Journal of Soil Science, Vol. 37, pp. 499-510.

Beemer, R., (2015). "Personal Verbal and Electronic Communications to the Author." In person and electronic conversation with the author, College Station, TX. March 16th and 17th, 2015.

British Standard Institute (BSI), (1990) "Methods of Test for Soils for Civil Engineering Purposes." British Standard Institute, London, UK.

Casagrande, A., (1932). "Research on the Atterberg Limits of Soils." Public Roads, Vol. 12, No. 8.

Casagrande, A., Fadum, R., (1940). "Notes on Soil Testing for Engineering Purposes." Harvard Soil Mechanics, Series No. 8, Cambridge, Massachusetts.

Clay Mineral Society (2015), "The Source Clays Project Background." The Clay Mineral Society. http://www.clays.org/SOURCE%20CLAYS/SCBackground.html. Retrieved August 2015.

Decagon Devices (2007). "WP4 Dewpoint PotentiaMeter Operator's Manual and Quick Start Guide." Decagon Devices, Inc. Pullman, Washington.

Fandry, J., (2012). "Pressure Plate Operations Manual." Department of Civil and Environmental Engineering, University of Missouri. Columbia, Missouri.

Garner, C., Coffman, R., (2017b). "Visible and Near-Infrared Diffuse Reflectance Properties of Geotechnical Reference Soils" Applied Clay Science. (Submitted for Review).

Garner, C., Salazar, S., Coffman, R., (2017c). "Volumetric Water Content Measurements as Obtained from Remote Sensing and In-Situ Instrumentation." Soil Science (Submitted for Review).

Google, (2014). "Google Earth Imagery." The Google Corporation. Retrieved February 2014.

Hakim, H., Hashim, A., Abdul-Hafidh, G., Alyaa, H., Mohammed, S., (2013). "Study [of] the Optical Properties of Polyvinylpyrrolidone (PVP) Doped with KBr." European Scientific Journal, Vol. 3, pp. 132-137.

Hapke, B., (2012). "Theory of Reflectance and Remittance Spectroscopy." 2 ed., Cambridge University Press.

de Jong, S. (1993) "SIMPLS: An Alternative Approach to Partial Least Squares Regression." Chemometrics and Intelligent Laboratory Systems." Vol. 18, pp. 251-263.

Knighthawk Coal Company, (2015). "Blackhawk Coal Mine." http://www.knighthawkcoal.com/blackhawk-coal-mine.html. Retrieved November 2015.

Kou, L., Labrie, D., Chylek, P., (1993). "Refractive Indices of Water and Ice in the 0.65- to 2.5-μm Spectral Range." Applied Optics, Vol. 32, No. 19, pp. 3531-3540.

Kubelka, P., (1947). "New Contributions to the Optics of Intensely Light-Scattering Materials, Part I." Journal of the Optical Society of America, Vol. 38, Number 5, pp. 448-457.

Kubelka, P., Munk, F., (1931). "Ein Beitragzur Optik der Farbanstriche." (in German), Z. Technol. Physics., Vol. 12, pp. 593-620.

Lindberg, J., Laude, L., (1974). "Measurement of the Absorption Coefficient of Atmospheric Dust." Applied Optics, Vol. 13, pp. 1923-1927.

Mahmood, N., (2014). “Suggested Mixing Procedure for Kaolinite Samples in a Slurry Consolidometer.” Personal Verbal Communication to the Author. August, 2014, Fayetteville, Arkansas.

Mathworks, (2010). “Plsregress.m.” Partial Least Squares Regression Software. The Mathworks Corporation, Natick, Massachusetts.

Mathworks, (2012b). “Pca.m.” Principle Components Analysis Software. The Mathworks Corporation, Natick, Massachusetts.

Mathworks, (2014a). “The MATLAB R2014A Programming Suite and Supporting Documentation.” The Mathworks Corporation, Natick, Massachusetts.

Nicolet, (2004). “Nicolet FT-IR User’s Guide.” Nicolet 6700 Fourier Transform Infrared Spectrometer User’s Manual and Supporting Documentation. http://mmrc.caltech.edu/FTIR/Nicolet/Nicolet%20Software/Nicolet%202/4700_6700_User.pdf. Retrieved September 2014.

Ocean Optics, (2014). “Ocean Optics USB-2000, OceanView Software, and Supporting Documentation.” The Ocean Optics Corporation.

Patterson, E., Gillete, D., Stockton, B., (1977). “Complex Index of Refraction between 300 and 700nm for Saharan Aerosols." Journal of Geophysical Research, Vol. 82, No. 21, pp. 3153-3160.

Rogers, William, (2009). “Feldspar and Nepheline Syenite.” Mining Engineering, Vol. 61, No. 6, pp. 29.

Rosipal, R., Kramer, N., (2006). "Overview and Recent Advances in Partial Least Squares", in Subspace, Latent Structure and Feature Selection: Statistical and Optimization Perspectives Workshop (SLSFS 2005), Revised Selected Papers (Lecture Notes in Computer Science 3940), C. Saunders et al. (Eds.) pp. 34-51, Springer.

Rossel, R., McBratney, A., Minasny, B., (eds.), (2010a). “Proximal Soil Sensing. Volume 1 of Progress in Soil Science.” Springer Science and Business Media. Springer, New York.

Rothman, L., Gordon, E., Barbe, A., Benner, D., Bernath, P., Birk, M., Boudon, V., Brown, L., Campargue, A., Champion, J., Chance, K., Coudert, L., Dana, V., Devi, V., Fally, S., Flaud, J., Gamache, R., Goldman, A., Jacquemart, D., Kleiner, I., Lacome, N., Lafferty, W., Mandin, J., Massie, S., Mikhailenko, D., Miller, C., Moazzen-Ahmadi, Naumenko, O., Nikitin, A., Orphal, J., Perevalov, W., Perin, A., Predoi-Cross, A., Rinsland, C., Rotger, M., Simeckova, M., Smith, M., Sung, K., Taskun, S., Tennyson, J., Toth, R., Vandaele, A., Auwera, J., (2009). "The HITRAN 2008 molecular spectroscopic database." Journal of Quantitative Spectroscopy and Radiative Transfer. Vol. 110, pp. 533-573.

Skempton, A., (1953). “The Colloidal Activities of Clays.” Proceedings of the 3rd International Conference on Soil Mechanics and Foundation Engineering. Zurich, Switzerland.

Taylor, D., (1948). “Fundamentals of Soil Mechanics.” John Wiley and Sons, Inc., New York.

Texas Agricultural and Mechanical University (TAMU), (2015). “Laboratory Handouts for Determination of Atterberg Limits.” Texas A&M, CVEN-365 Introduction to Geotechnical Engineering. Spring 2015.

Theile, (2015a). “Product Website for Delaminated Coating Clays.” Theile Kaolin Company. http://www.thielekaolin.com/images/thieleimages/Clay_Properties_2015.pdf. Accessed November 2015.

Theile, (2015b). “Product Information for Clay Products.” Theile Kaolin Company. http://www.thielekaolin.com/images/thieleimages/Clay_Properties_2015.pdf. Accessed November 2015.

Waruru, B., Shepherd, K., Ndegwa, G., Kamoni, P., Sila, A., (2014). “Rapid Estimation of Soil Engineering Properties Using Diffuse Reflectance Near Infrared Spectroscopy.” Journal of Biosystems Engineering, Vol. 121, pp. 177-185.

Wasti, Y., (1987). “Liquid and Plastic Limits as Determined from the Fall Cone and the Casagrande Methods.” Geotechnical Testing Journal, GTJODJ, Vol. 10, No. 1, pp. 26-30.

Wold, S., Sjostrom, M., Eriksson, L., (2001). “PLS-Regression: A Basic Tool of Chemometrics.” Chemometrics and Intelligent Laboratory Systems. Vol. 58, Issue 2, pp. 109-130.

CHAPTER 5: VOLUMETRIC WATER CONTENT OBTAINED VIA SINGLE POLARIZATION CHANGE DETECTION METHODOLOGY AT UACSRC

5.1. Chapter Overview

Radar observations were conducted using the University of Arkansas GPRI-2 K_u-Band (1.7cm) radar interferometer on the grounds of the University of Arkansas Cato Springs Research Center (UACSRC) from January 2012 to July 2012. All observations were conducted from an overlook position at the southeast corner of the UACSRC building. GPRI-2 (vertically propagating and vertically received [VV] K_u-Band) images were acquired and processed using the Gamma interferometric software suite (Gamma Remote Sensing 2010). Soil volumetric moisture content measurements were obtained using the Wegmuller (1997) and Wagner (1998) single polarization change detection methods (as previously described in Chapter 2 and Chapter 3). To provide *in situ* verification of obtained measurements of volumetric water content, time domain reflectometry (TDR) *in situ* probes were installed and recorded using a data acquisition unit (Campbell Scientific CR-10x). TDR measurements were calibrated using the methodology proposed by Take et al. (1997).

An introduction including a summary, the limitations of the research project, project description, and project site description is included as Section 5.1 through Section 5.5. A literature review (Section 5.6) of the radar change detection methods (Section 5.6.1) and the time domain reflectometry measurements (Section 5.6.2) is included. The methods and procedures utilized to collect and process the data are presented in Section 5.7. The results obtained from the TDR instrumentation from the calibration study and the field instrumentation are presented in Section 5.8. The radar obtained measurements of soil volumetric water content are documented in Section 5.8.1. The full citation for this document is: *Garner, C., Coffman, R., (2016). "Volumetric Water Content Measurements as Obtained from Remote Sensing and In-Situ Instrumentation."*

Journal of Environmental and Engineering Geophysics, Accepted for Publication, Manuscript Number 15-022R.

5.2. Limitations of the Described Study

Due to several compounding factors there were significant limitations associated with the research described in this chapter. Specifically, the *in situ* instrumentation was intended to acquire data simultaneously with the remotely sensed measurements. Remotely sensed measurements were acquired between January 30, 2012 and July 10, 2012 as part of the separate MBTC-3031 project (Coffman and Garner 2012). The *in situ* instrumentation, including the time domain reflectometry (TDR) probes, was installed in early July 2012. *In situ* data was acquired between July and November 2012. Radar data was acquired concurrently over the same period. However, when the radar data was processed it was discovered that that the GPRI-2 transmit function had been damaged after the July 10, 2012 imagery had been acquired. Therefore, no valid imagery was available for comparison with *in situ* results except for July 7, 2012 and July 10, 2012.

5.3. Volumetric Water Content Measurements as Obtained from Remote Sensing and In Situ Instrumentation

Cyrus D. Garner, MSCE, EIT[1] and Richard A. Coffman, PhD, PE, PLS[2]

[1]Doctoral Candidate, Department of Civil Engineering, University of Arkansas at Fayetteville, USA. (Corresponding Author).
[2]Assitant Professor, Department of Civil Engineering, University of Arkansas at Fayetteville, USA.

5.4. Abstract

A single-polarization (vertical wave propagation transmitted-vertical wave propagation received [VV]) terrestrial imaging radar and time domain reflectometry (TDR) equipment were utilized to monitor the fluctuations of water content within two thin (15.24 centimeters thick) compacted clay test sections (each 30.48m long by 15.34m wide). Radar imagery was obtained on

March 22, June 26, July 7 and July 10 using a second generation Gamma Remote Sensing portable radar interferometer (GPRI-II). *In situ* observations were acquired hourly using TDR probes.

The background, methodology, and comparison of the results of the remote sensing and *in situ* measurements are presented. Specifically, two remote sensing data reduction algorithms were considered, and the water content results obtained from these algorithms were compared with the water content values derived from correlations with the dielectric permittivity values obtained from the *in situ* waveform measurements as obtained from the TDR probes. Key findings include: differences between the values obtained from the data reduction methods, differences between the values obtained from the remote sensing methods and the values obtained from the *in situ* method, and the identification of additional avenues of research. The remotely sensed measurements were, on average, higher than the *in situ* measurements (the average volumetric water content values were 0.2 and 0.5, as obtained via the remotely sensed methods; the average volumetric water content value in the compacted native soil test sections was 22 percent as obtained via the *in situ* method).

Key Words: Water Content; Saturation; Signal Processing; Radar; Remote Sensing; *In situ* Tests

5.5. Introduction

The use of satellite and or aerial based active microwave remote sensing platforms is common in the fields of geoscience and remote sensing. In these fields, significant research has been conducted on the extraction of soil water content values for large geographical areas using active microwave remote sensing devices and technologies (Ulaby, 1974; Dubois, 1995; Wegmuller, 1997; and Wagner, 1998). Although these technologies have provided researchers

with the ability to obtain data for a large spatial extent or a "swath", the data are limited in terms of spatial resolution and temporal resolution (approximately 20 meters [m] and 35 days, respectively). While such limitations are acceptable for broad-scale climatological, geological, or biological research, the limitations of spatial and temporal resolution may prevent the use of these advanced technologies for detailed qualitative and quantitative investigations by geotechnical engineers. To overcome the aforementioned limitations, a single-polarization (vertical wave propagation transmitted-vertical wave propagation received [VV]) portable terrestrial, K_u-Band (1.3cm wavelength) real aperture radar system (the second generation Gamma Remote Sensing portable radar interferometer [GPRI-II]) was utilized to obtain volumetric soil water content measurements and surface deformation measurements with spatial resolution and temporal resolution (approximately one meter, one centimeter, and hourly, or better, respectively) that are sufficient for small-site engineering applications.

The specifications and previous use of the GPRI-II system to detect and quantify ground surface movements induced by slope failures and expansive clay materials are contained in Conte (2012), Coffman and Garner (2012), and Conte and Coffman (2013). Although the K_u-Band GPRI-II radar was optimized to collect high resolution (sub-centimeter) measurements of ground surface displacement (via the use of interferometric techniques), the purpose of the described work was to evaluate the use of the existing GPRI-II system to obtain values for the *in situ* volumetric water content of the soil. Utilizing the data collected from the GPRI-II device, and the data processing techniques developed by Wegmuller (1997) and Wagner (1998), values of volumetric soil water content may be obtained without physically touching the area of interest. The use of the K_u-Band does limit the penetration depth of the incident radiation and therefor the depth for observations. However, the data collection and processing techniques developed for this

project may also be applied for other (lower frequency) terrestrial based radar systems. Specifically, by using remote sensing, values of volumetric soil water content may be obtained without installing probes or collecting soil samples.

Time domain reflectometry (TDR) data were used validate the post-processed volumetric soil water content data that were collected using the GPRI-II. Specifically, pointwise *in situ* TDR measurements were simultaneously collected at the same site that the GPRI-II measurements were collected (at the University of Arkansas Cato Springs Research Center [UACSRC]). TDR was utilized because it: 1) is a technique accepted by the geotechnical and geological engineering community for determining the volumetric water content for soils, 2) enables continuous data collection, 3) does not disturb the soil surface after the initial probe installation, and because 4) the variation in volumetric water content measurements, as obtained from data collected from the GPRI-II and TDR probes, corresponds to changes in the dielectric permittivity of the soil.

5.6. Project Site

Two thin compacted clay test sections (30.48m long, 15.34m wide, and 0.15m thick) were constructed adjacent to the UACSRC building at the UACSRC site. The roof of the building provided an elevated vantage point (incidence angle of approximately 80 degrees) for the GPRI-II. The two sections were constructed from a native sandy clay material. One of the sections was also amended with six percent, by dry weight, sodium bentonite (WyoBen Enviro-Plug No. 8) prior to compaction to increase expansive behavior and hydraulic retention. The construction methodology, soil placement window, and site layout are presented in Garner and Coffman (2014). The sections were compacted at water contents ranging from 18 to 25 percent gravimetric water content for the amended test sections, and from 17 to 24 percent gravimetric water content for the unamended test sections. Each test section was constructed on top of a 0.05m thick freely

draining sand base and a one-meter by seven-meter control section was included in each of the pads. The control sections consisted of a native sandy clay within the bentonite amended pad or a bentonite amended sandy clay within the native sandy clay pad. Vegetation was not allowed to grow on the test sections because the test sections were constructed for engineering observation purposes.

In situ instrumentation (tensiometers, TDR probes, and thermocouples [air and soil]) was installed in each of the sections. Specifically, 14 Campbell Scientific CS-610 (Campbell Scientific 2012) three lead TDR probes (7 probes per pad) were installed into the two thin compacted clay test sections to obtain volumetric water content measurement. The probes were excited and recorded (hourly) using a Campbell Scientific TDR-100 time domain reflectometer device, three Campbell Scientific SDMX-50 multiplexers, and a Campbell Scientific CR-10X datalogger. The placement of the *in situ* instrumentation and surrounding infrastructure including the location of the GPRI-II observation point and the locations of the sensors within the test sections are discussed in Coffman and Garner (2012) and Garner and Coffman (2014).

5.7. Background

The value of dielectric permittivity for dry soil particles, as obtained from microwave frequency excitation, ranges from three to eight. Whereas, the dielectric permittivity value of water is 80 and the dielectric permittivity air is unity (Hanson and Peters 2000, ESA 2014). Fundamentally, similar variations in soil dielectric permittivity, as caused by changes in the volumetric water content of the soil, can be measured from the GPRI-II backscatter or from the TDR waveform (albeit at different frequencies). Because of the high dielectric permittivity value for water, the volume of water within the soil (volumetric water content) is the dominant influence on the overall dielectric permittivity of the porous media. Specifically, water is the

constituent that enables the extraction of soil water content measurements from the radar backscatter data or from the TDR waveform data. The relationship between the complex dielectric permittivity and water content is frequency dependent and has been presented in Topp et al. (1980) and Njoku and Entekahbi (1994) for the frequencies utilized in TDR and radar testing, respectively.

5.7.1. *Active Microwave Remote Sensing*

The interaction of microwave waves with a soil surface, as employed in polarimetric and non-polarimetric imaging radars, is dependent on the dielectric properties of the reflecting surface, the surface texture of the soil surface, the polarization of incident and backscatter radiation, and the local angle of incidence at the soil surface. Specifically, the intensity of the returned electromagnetic energy (EM) is proportional to the volumetric water content of the soil (e.g. the intensity value for each of the pixels increases with increasing water content). Regions of standing water act as a specular ("mirror") reflector and therefore do not return energy to the sensor. While previous researchers have used radar technology to analyze water content of the soil using ground-based systems (e.g. Ulaby 1974, Sarabandi et al. 1994) the systems most commonly implemented in the geoscience fields are orbital-based synthetic aperture radars (e.g. Dubois et al. 1995, Wegmuller 1997, Wagner 1998). For ground- or orbital-based systems, the volumetric water content (θ) is measured by determining the influence of water within the soil (via dielectric permittivity) on the radar backscatter coefficient (σ).

Polarimetric methods are underpinned by electromagnetic scattering theory. The advantage of determining the volumetric water content using polarimetric equipment is that the absolute water content of the soil can be computed from a single pass (as opposed to the repeat pass techniques utilized for non-polarimetric methods, as discussed later). Specifically, the water

content of the soil is obtained by comparing the reflection received from two of the four different polarization (e.g. co-pol including horizontal wave propagation transmitted-horizontal wave propagation received [HH] and vertical wave propagation transmitted-vertical wave propagation received [VV], or cross-pol including horizontal wave propagation transmitted-vertical wave propagation received [HV] and vertical wave propagation transmitted-horizontal wave propagation received [VH]). Commonly employed methods to determine the volumetric soil water content, utilizing polarimetric radar data, include the Small Perturbation Method (SPM) introduced by Rice (1951), the Integral Equations Method (IEM) introduced by Fung et al. (1992), and the Advanced Integral Equations Method (AIEM) introduced by Chen et al. (2003). Although the polarimetric methods are introduced for completeness, the polarimetric methods were not used for this study because a single-polarization (VV) radar was utilized.

The non-polarimetric methods introduced by Wegmuller (1997) and Wagner (1998) are change detection algorithms in which the change in reflectivity of the soil (change in the backscatter coefficient and received power as per Equation 5.1) is correlated to temporal changes in the values of water content and saturation, respectively. The primary advantage of these methods over the polarimetric methods is the assumption that the effects of the physical site parameters on the backscatter intensity do not change between scenes and therefore cancel out. Thereby, the observed changes in backscatter intensity are only attributable to changes in the dielectric permittivity of the soil as shown by Wagner (1998) and presented as Equation 5.2 and Equation 5.3. The assumption of constant parameters for surface roughness, surface autocorrelation length, and local incident angle (for a terrestrial radar reoccupying an observation point) allows for reduced data collection and data processing demands. The principle assumption utilized within the Wagner (1998) method is that the variations in pixel backscatter intensity are

only a function of water content and therefore the maximum and minimum pixel brightness values will correspond to the highest and lowest levels of volumetric water content. For pixel values that are between the aforementioned maxima and minima values, the volumetric water content is obtained by linearly interpolating. Key limitations of the Wagner (1998) method include the assumption of unchanged local ground conditions between observations (neglection of temporal decorrelation) and the requirement that the soil surface be observed at the maximum and minimum saturation levels. Furthermore, a measurement of *in situ* porosity is required to obtain the absolute volumetric water content values using the Wagner (1998) method.

$$\sigma = \frac{P_r 4\pi\lambda^3 R^4}{P_t A_{eff}^2} \qquad \text{(modified from Ulaby et al. 1986)} \qquad \text{Equation 5.1}$$

$$\sigma[dB] = 10 * \log(\sigma)[m^2 m^{-2}] \qquad \text{(modified from Wagner 1998)} \qquad \text{Equation 5.2}$$

$$S(t) = \frac{\sigma(80^o, t) - \sigma_{dry}(80^o, t_{dry})}{\sigma_{wet}(80^o, t_{wet}) - \sigma_{dry}(80^o, t_{dry})} \qquad \text{(modified from Wagner 1998)} \qquad \text{Equation 5.3}$$

In Equations 5.1 through 5.3, σ is the radar cross section (backscatter coefficient) of the target, P_r is the power received, λ is the wavelength, R is the slant range distance between the radar and the target, P_t is the transmitted power, A_{eff} is the effective antenna area, S is the soil saturation, $\sigma(80^o,t)$ is the backscatter coefficient at a given time (t) and at an incident angle of 80 degrees, $\sigma_{dry}(80^o,t_{dry})$ is the backscatter coefficient at a corresponding time (t_{dry}) when the soil is completely dry, and $\sigma_{wet}(80^o,t_{wet})$ is the backscatter coefficient at a corresponding time (t_{wet}) when the soil is completely wet (completely saturated).

Wegmuller (1997) developed an empirical correlation between changes in the backscattered intensity values (logarithmic) and changes in the volumetric water content values (Equation 5.4 and Equation 5.5). Values of volumetric water content of the soil are calculated for pixels in each scene using Equation 5.6 by considering a reference image with values of known water content for corresponding pixels. Wegmuller (1997) further extended the empirical relationship based on satellite observations at test sites in the United States and in Europe (Equation 5.7 and Equation 5.8). The Wegmuller (1997) method allows for the determination of the absolute volumetric water content values within a reference image. The disadvantage of the

Wegmuller (1997) method is that the method requires the collection of *in situ* volumetric soil water content information and temporally registered radar imagery. However, to avoid the need to collect *in situ* measurements, Wegmuller (1997) proposed using observation data that was captured during periods of below freezing conditions.

$$\Delta\theta = 0.042\ \Delta\sigma(80^{o},t)[dB] \quad \text{(after Wegmuller 1997)} \quad \text{Equation 5.4}$$

$$\Delta\sigma(80^{o},t) = \sigma_2(80^{o},t)[dB] - \sigma_1(80^{o},t)[dB] \quad \text{(after Wegmuller 1997)} \quad \text{Equation 5.5}$$

$$\theta = \theta_o + 0.042(\Delta\sigma(80^{o},t)[dB] - \Delta\sigma_0(80^{o},t_0)[dB]) \quad \text{(after Wegmuller 1997)} \quad \text{Equation 5.6}$$

$$i = \frac{\sigma_0(80^{o},t_0) - 8.56\theta_0}{1 - 1.56\theta_0} \quad \text{(after Wegmuller 1997)} \quad \text{Equation 5.7}$$

$$\theta = \frac{\sigma(80^{o},t) - i}{8.56 - 1.56\,i} \quad \text{(after Wegmuller 1997)} \quad \text{Equation 5.8}$$

In Equations 5.4 through 5.8, $\Delta\sigma(80^{o},t)$ is the difference in corrected backscatter coefficient corrected for an incident angle of 80 degrees, $\sigma_2(80^{\circ},t)$ and $\sigma_1(80^{\circ},t)$ are the backscatter coefficients of temporally separated returns, θ is the volumetric water content, θ_0 is the known volumetric water content in the reference image, $\sigma_0(80^{\circ},t_0)$ is the reference backscatter coefficient corresponding to the θ_0 condition, and i is the intercept value of the empirical backscattering [dB]-volumetric soil water content [%] relationship.

5.7.2. *Time Domain Reflectometry*

TDR systems operate by sending individual stepped voltage increases with a fast rise time (<300 ps [Evett 2003]) through the center conductor of a coaxial cable into each probe (typically three wire probes) located within the soil. The variance in travel time is a function of the wave propagation speed in the unshielded portion of the probe, because the physical dimensions and material properties of the cable and probes are known and are unchanged.

Although the dielectric permittivity for soil is a complex number, the real component of the complex number does not contribute to the electric loss term over the range of frequencies employed by TDR systems (Nemmers 1998). Therefore, only the imaginary component is utilized. By combining Equation 5.9 and Equation 5.10 to form Equation 5.11, the dielectric permittivity of the soil may be obtained (Evett 2003).

$$v_p = \frac{v}{c_0} = \frac{1}{(\varepsilon\mu)^{0.5}}$$ (modified from Evett 2003) Equation 5.9

$$v = \frac{2L}{t_t}$$ (Evett 2003) Equation 5.10

$$\varepsilon_a = \left[\frac{c_0 t_t}{2L}\right]^2 = \left[\frac{L_a}{L}\right]^2 = K_a$$ (modified from Evett 2003) Equation 5.11

In Equations 5.9 through 5.11, v_p is the velocity factor setting, v is the velocity of propagation through the shielded cable, c_0 is the speed of light in a vacuum, ε is the dielectric permittivity of the cable shielding, μ is the magnetic permeability of the dielectric material (equal to unity in free space), L is the length of the unshielded probe lead, t_t is the travel time within the unshielded probe lead, and ε_a or K_a is the apparent dielectric permittivity of the soil, and L_a is the apparent length of the unshielded probe lead.

Specifically, the dielectric permittivity is obtained utilizing Equation 5.11 and the Tangent Method (Evett 2003 and Nemmers 1998). An example of a returned TDR waveform containing the implementation of Equation 5.11 and the Tangent Method, and the calculation of the K_a value for that waveform, is presented in Figure 5.1. Multiple relationships have been proposed to utilize the K_a value obtained from the waveform to determine the soil volumetric water content (θ); the most commonly employed relationship is presented as Equation 5.12 (Topp et al. 1980). The Topp et al. (1980) equation is considered to provide acceptable results for most soil types, however it is possible to generate a specific relationship by conducting tests on compacted samples with known volumetric water contents as presented in Take et al. (2007).

$$\theta = AK_a^3 - BK_a^2 + CK_a - D$$ (Topp et al. 1980) Equation 5.12

In Equation 5.12, θ is the volumetric water content, and K_a is the apparent dielectric constant. The constants A, B, C, and D are empirically determined coefficients with values of $4.3\cdot10^{-6}$, $5.5\cdot10^{-4}$, $2.92\cdot10^{-2}$, and $5.3\cdot10^{-2}$, respectively.

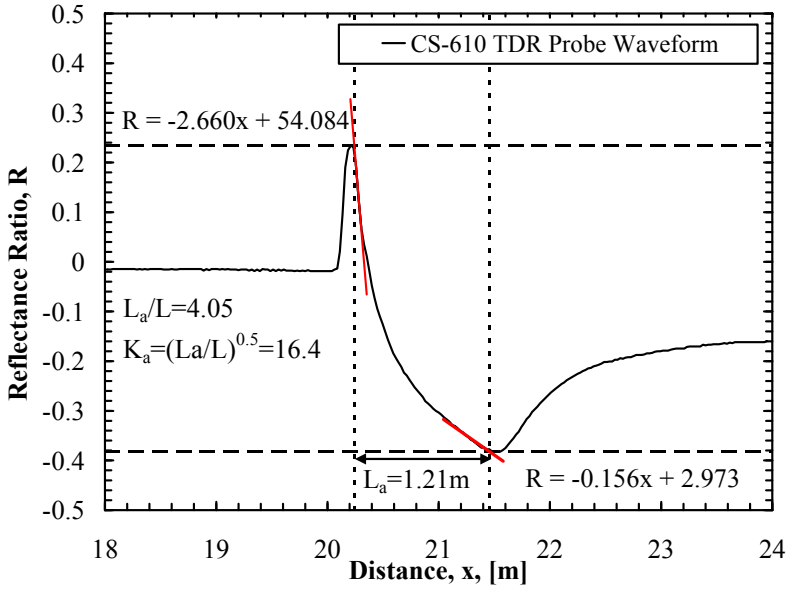

Figure 5.1. Example TDR waveform with the apparent dielectric constant value obtained using tangent method.

5.8. Methods and Procedures

To compare the results obtained from the GPRI-II and the TDR techniques, standardized data acquisition and processing procedures were developed and followed. These procedures included: radar data collection, radar data processing, TDR apparent dielectric permittivity-volumetric water content relationship development, TDR equipment installation, TDR data collection, and TDR data processing. Each of these procedures are discussed in this section.

5.8.1. *Radar Data Collection*

Radar images of the test sections at UACSRC were captured from the roof of UACSRC, using the GPRI-II. To ensure that the observation area and observation geometry were identical for the respective observations, the GPRI-II was repositioned over a survey monument located on the roof of UACSRC for subsequent scans. Scans with a 95-degree field of view were acquired at a rate of 5 degrees per second using a 250 microsecond chirp from the GPRI-II. Specifically, each scan was acquired from -15 degrees to 80 degrees with the basis of rotation being the left side of visible tower approximately 700m to the Southeast of the project site, located at an angle of

rotation of 37 degrees (as observed using a telescopic optical sight affixed to the side of the GPRI-II instrument). Radar imagery was collected during periods of high and low volumetric water content for use in the Wegmuller (1997) and Wagner (1998) methods. Radar imagery collected during late June 2013 and, after allowing several weeks for the soil surface to desiccate with daily high temperatures exceeding 32°C and limited precipitation (less than 2.5E-2m), was used as the Wegmuller (1997) reference imagery. The late June 2013 imagery was also used to obtain "minimum" pixel brightness values for use in Wagner (1998) data processing. During the same period, the volumetric water content of the soil was obtained using manually collected soil samples and the ASTM D2216 (2014) and ASTM D854 (2014) methods. Imagery was also collected during and after a period of significant precipitation (greater than 2.5E-2m) to provide "maximum" pixel brightness values for the Wagner (1998) data processing.

5.8.2. *Radar Data Processing (Wegmuller 1997 and Wagner 1998)*

Radar data were processed in both Linux and Windows software environments. Pre-processing was conducted in Linux using commercially available Gamma Remote Sensing software (Gamma Remote Sensing 2010) to convert the raw radar data into single look complex (SLC, 64-bit complex data comprised or two strings of 32-bit floating point data for the real and imaginary components) and subsequently into multi-look intensity images (MLI, 32-bit floating point data). The MLI files were then exported to Windows for further processing using MATLAB (Mathworks, 2012).

Using MATLAB, the individual MLI files for each day (typically seven scans collected during a period of ten minutes) were temporally averaged to increase the signal to noise ratio. The averaged MLI images were transferred back to Linux and processed, following the Wegmuller (1997) procedure, using a pre-programmed function (soil_moisture.c) within the Gamma Remote

Sensing software. A reference map (of the same size as the MLI images) was also created in MATLAB. The reference map contained the *in situ* water content data that was acquired using the aforementioned sampling techniques and the reference image was also ingested into the soil_moisture.c software. The average MLI images were also processed in MATLAB following the Wagner (1998) procedure. After processing, all of the images were visualized and compared using MATLAB.

Utilizing the Wagner (1998) method, the minimum and maximum backscatter amplitude (intensity) values for each individual pixel (corresponding to the lowest and highest observed volumetric soil water contents) were determined by comparing each of the individual averaged images. These values were utilized to create reference maximum (wet) and minimum (dry) intensity images. For each pixel, a value of soil saturation value was calculated using Equation 5.3 (presented previously), rendering a soil saturation image by referencing the wet and dry images. A volumetric water content image was obtained by multiplying the pixel values in the soil saturation image by the porosity of the soil (0.37, as obtained from the TDR calibration described in the next section). A 3x3 pixel moving average was also applied to the processed data to reduce the variance in the image. All individual dates were then processed sequentially using the same technique. Because the values obtained from the Wagner (1998) method are saturation values, all of the pixel values were multiplied by the porosity of the soil to obtain volumetric water content values.

The use of the GPRI-II platform has significant advantages, in terms of complexity of processing, when using the Wagner (1998) method (the method was originally developed for use with the European Space Agency's [ESA] European Remote Sensing 1 [ERS-1] satellite platform). Specifically, the pre-processing to correct the backscatter coefficient for variations

between multiple satellite passes including: ascending/descending orbits, different incident angles, and amalgamation of data from different antennas, as mentioned in Wagner (1998), is avoided for the GPRI-II system because a constant angle of incidence of 80 degrees and was maintained for all scans. Additionally, information was only compared for images collected using the same antenna (e.g. data obtained from the lower antenna was compared to data obtained from the lower antenna for subsequent observations). Therefore, the only correction applied to the backscatter coefficient data prior to the computation of water content was the transformation of the respective pixel intensity values from a linear scale to a decibel scale (as shown previously in Equation 5.2).

5.8.3. *TDR Apparent Dielectric Permittivity (K_a) - Volumetric Water Content (θ) Relationship*

A relationship between the TDR obtained apparent dielectric permittivity and volumetric water content was created for the soil used within the test sections. Soil samples were compacted following the procedures outlined in American Society of Testing and Materials (ASTM) standard D698 (ASTM D698 2014) with the following deviations from the standard: mold size, compaction energy, and number of lifts. The samples were compacted into a 0.342m long by 0.152m diameter aluminum (6.23E-3m^3 mold volume instead of the 9.43E-4m^3 mold volume) aluminum mold to accommodate the 0.3m long CS-610 probes. Each sample was compacted in nine lifts (3.81E-2m thick) using 25 blows per lift, resulting in a compaction effort of 75 percent of the standard Proctor effort (450kN·m/m^3) to resemble the field compaction effort. Twelve samples (eight calibration samples and four validation samples) were compacted at molding volumetric water contents between 12 and 35 percent (obtained from the phase diagram of each sample). After compaction, a TDR probe was installed into each of the compacted samples and TDR waveforms were collected. The apparent dielectric permittivity was obtained from the TDR

waveform utilizing Equation 5.11 and the Tangent Method (as previously described) as presented in Figure 5.2.

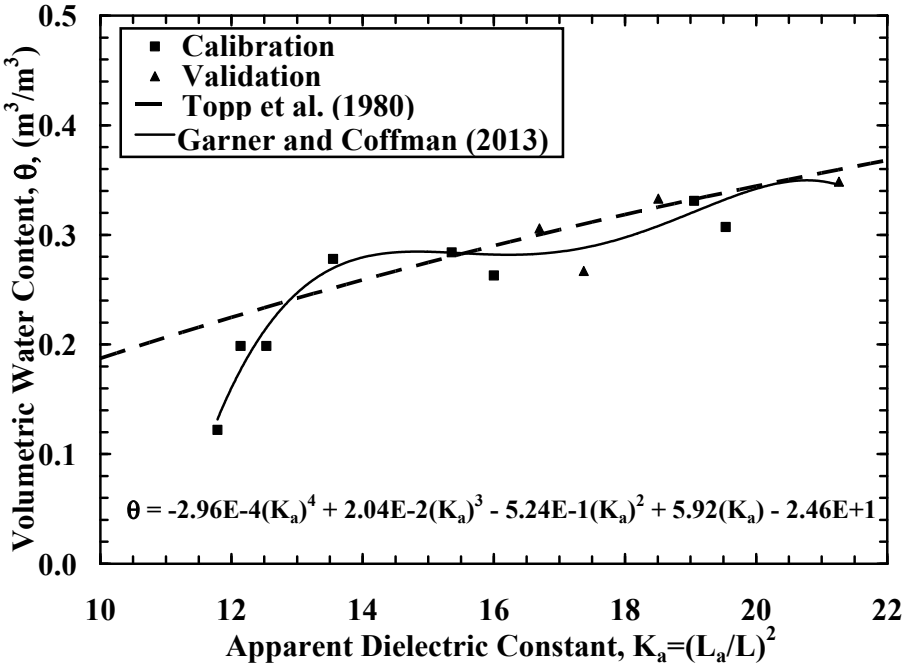

Figure 5.2. Volumetric water content as a function of apparent dielectric constant.

5.8.4. *TDR Installation and Field Data Collection*

The TDR probes were hydraulically pushed horizontally into the side of a manually excavated trench using a custom jig (at mid-depth of each of the sections at each location). After installation, the performance of each TDR probe was verified to ensure that each probe was properly installed and that the probe leads were not in contact with one another. The datalogger was then programmed to remotely capture (hourly) and store the data (waveforms) obtained from each probe. The raw data file was exported from the datalogger at regular intervals (weekly) as a comma delimited ASCII text file, and the data were ingested and processed in MATLAB. The volumetric water content was obtained for each location at each time by utilizing Equation 5.11, the Tangent Method, and the soil specific relationship (as previously described).

5.9. Findings

The results generated by following the aforementioned standardized data acquisition and testing procedures are presented in this section. Specifically, the results of the remote sensing measurements and the results of the *in situ* (TDR) measurements are presented. Comparisons between the remote sensing measurements, as analyzed using the two remote sensing data processing methods (for three different water content conditions ranging between dry and wet) and between the remote sensing measurements and the TDR obtained measurements (for the after rainfall and after drying condition) are presented.

5.9.1. *Volumetric Water Content: Single-Polarimetric Remote Sensing Methods and TDR Methods*

Examples of volumetric water content values, as obtained using the GPRI-II and processed using the Wagner (1998) and Wegmuller (1997) methods, are presented in Figure 5.3, Figure 5.4 , and Figure 5.5. The first set of images (July 7 and July 10) was obtained utilizing the Wagner (1998) method.

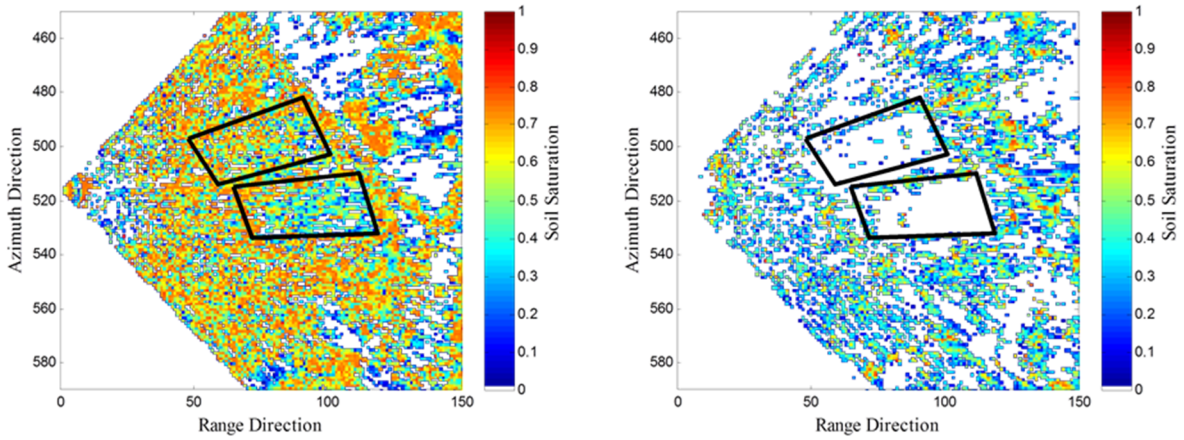

(a) (b)

Figure 5.3. Remotely sensed soil saturation, obtained using the Wagner (1998) method, on (a) July 7, 2012 following a rainfall event, and (b) July 10, 2012 following drying [in color].

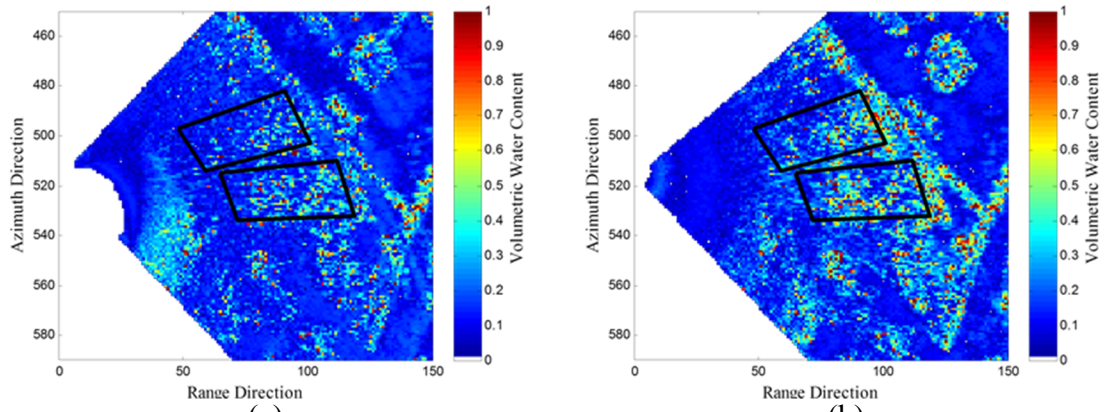

(a) (b)

Figure 5.4. Remotely sensed volumetric water content, obtained using the Wegmuller (1997) method, on (a) July 7, 2012 following a rainfall event, and (b) July 10, 2012 following drying [in color].

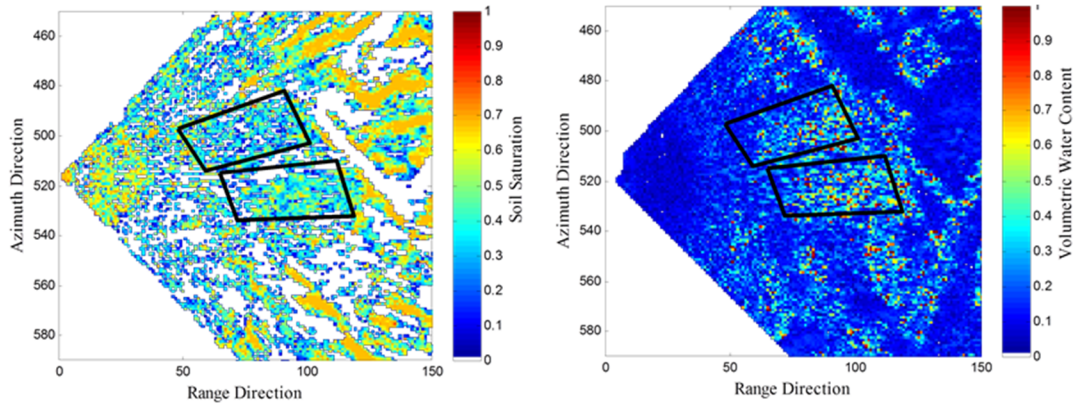

(a) (b)

Figure 5.5. Remotely sensed (a) soil saturation, and (b) volumetric water content, on March 22, 2012, obtained using the Wagner (1998) and Wegmuller (1997) methods, respectively [in color].

The second set of images (also from July 7 and July 10) was obtained using the Wegmuller (1997) method. In both cases the initial image (July 7) was taken during and after a heavy rainfall event (approximately 2.5E-2m of precipitation [NOAA 2012b]) while the subsequent images (July 10) were taken after three days with air temperatures exceeding 32 Celsius (NOAA 2012b). Desiccation of the soil body was expected to occur (and was observed) between the first and second set of radar observations. The third set of images (March 22) was obtained prior to significant rainfall or desiccation and represents partially saturated conditions.

Average values of degree of saturation of 56 percent, 72 percent, 58 percent, and 36 percent, 52 percent, 41 percent were obtained for the amended and unamended sections, respectively on March 22, July 7, and July 10, respectively, using the data reduction method proposed by Wagner (1998). These values corresponded to average values of volumetric water content of 21 percent, 21 percent, 27 percent and 13 percent, 15 percent, 20 percent for the amended and unamended sections, respectively on March 22, July 7, and July 10, respectively. Average volumetric water content values of 31 percent, 15 percent, 27 percent and 37 percent, 19 percent, 28 percent were obtained for the amended and unamended sections, respectively on March 22, July 7, and July 10, respectively, using the method proposed by Wegmuller (1997).

Several factors are responsible for deviations between the values obtained from the two remote sensing data reduction methods. The Wagner (1998) method is a measurement of soil saturation and volumetric water content. Measurements were obtained by multiplying the saturation by a constant porosity value. Although a calibrated constant value of porosity was utilized, porosity values typically vary. Additional measured values of *in situ* porosity, at different locations on the surface, should have been used to calibrate the model to account for spatial variability of porosity. Also, empirical coefficients that match reflectance with volumetric water content are used within the Wegmuller (1997) method. Although the default, empirically derived, coefficients in the Gamma Remote Sensing software program were developed using sites in the United States, it is not certain if the utilized default coefficients were appropriate for the soil type used in this study. Site specific values of radar cross-section and the corresponding measured values of volumetric water at different locations on the surface should have been used to calibrate the model. Additionally, the data were not corrected for contribution from the thermal noise; although the effects of this contribution is not known and may not be able to be characterized. For

the site considered, use of the Wagner (1998) method is recommended due to the empirical constants that are utilized within the Wegmuller (1997) method being calibrated: 1) for satellite based systems operating at lower frequencies (C-Band), 2) at significantly different viewing geometries, and 3) for specific sites in the U.S. and Europe.

As illustrated in Figure 5.6, average volumetric water content values of 22 percent (amended pad) and 23 percent (unamended pad) were obtained on July 10, utilizing the TDR technique. The TDR obtained volumetric water content values are within 10 percentage points of the remotely sensed measurements. Discrepancies between the remotely sensed and *in situ* measurements are attributed to aforementioned factors and the differences in sampling depths (0-1.7E-2m for the GPRI-II and 8-12E-2m for the TDR data). Specifically, these discrepancies are attributed to reduced infiltration depth and high surface evaporation rates. However, by utilizing *in situ* measurements of the surface soil properties (volumetric water content or porosity), the remote sensing measurements may be calibrated to match the *in situ* measurements.

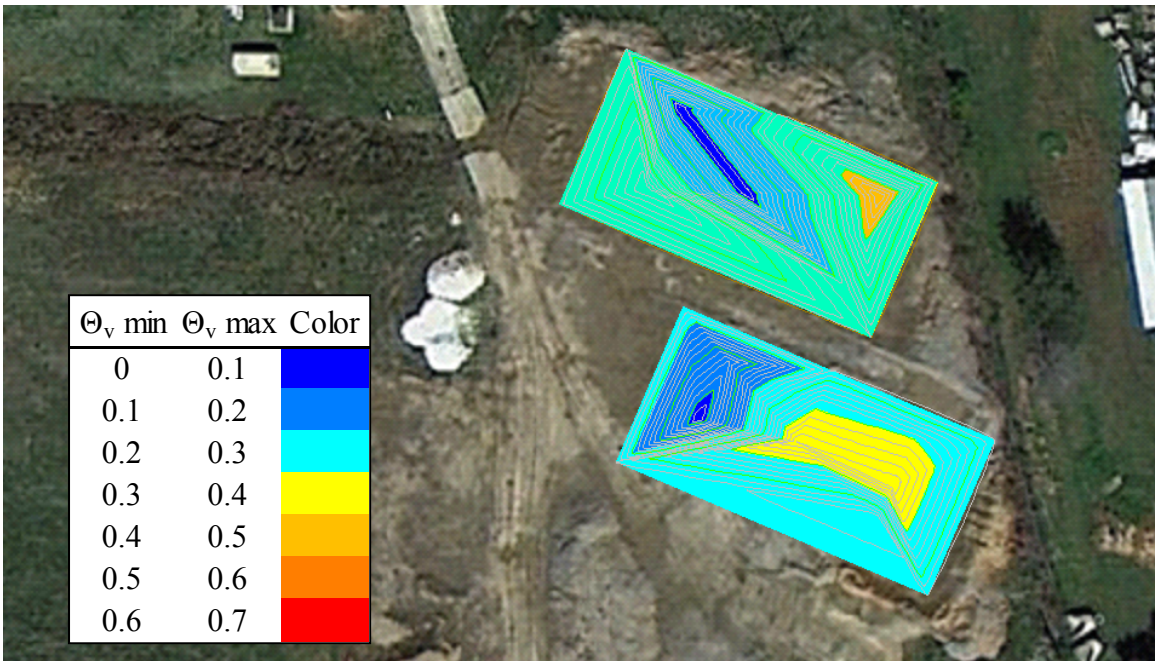

Figure 5.6. *In situ* volumetric water content, obtained from the TDR and using the Garner and Coffman (2016) volumetric water content-apparent dielectric constant function (shown previously in Figure 5.2), on July 10, 2012 [image from Google 2012, in color].

5.10. Conclusion

Remote sensing, when coupled or uncoupled with pointwise *in situ* measurements, offers many potential benefits to both geotechnical researchers and practitioners. The use of ground-based systems (such as the GPRI-II) may eliminate or alleviate many of the disadvantages associated with satellite- or aerial-based technologies. Specifically, the use of ground-based system may allow for the collection of data covering a large spatial extent, with high spatial resolution and high temporal resolution, and with a relatively low marginal cost per observation (as compared to costs associated with satellite imagery, aerial imagery, or additional pointwise TDR measurement equipment that would be required for the same spatial resolution).

A correlation between the volumetric water content values obtained from the *in situ* measurements and the two remote sensing, single-polarization, data reduction methods was observed. Specifically, the average volumetric water contents obtained using the different

methods were within ten percent of each other. However, based on the observed differences between the two remote sensing methods and between the remote sensing and *in situ* methods, additional research is required to: 1) couple the *in situ* measurements, 2) develop model calibrations, and 3) incorporate vegetation and temperature corrections.

5.11. Works Cited

American Society for Testing and Materials (ASTM) D698, (2012). "Standard test methods for laboratory compaction characteristics of soil using standard effort (12400 ft-lbf/ft3 (600 kN-m/m3))." Annual Book of ASTM Standards, 04.08, ASTM, West Conshohocken, PA, USA: 80-90.

American Society for Testing and Materials (ASTM) D854, (2014). "Standard Test Methods for Specific Gravity of Soil Solids by Water Pycnometer." American Society for Testing and Materials, Vol. 4.08, Soil and Rock (I). West Conshohocken, PA.

American Society for Testing and Materials D2216, (2014). "Standard Test Methods for Laboratory Determination of Water (Moisture) Content of Soil and Rock by Mass." Annual Book of ASTM Standards, Designation D2216, Vol. 4.08, ASTM, West Conshohocken, PA.

Campbell Scientific, (2012). "TDR100 manual." http://s.campbellsci.com/documents/us/manuals/tdr100.pdf. Retrieved June 2012.

Chen, K., Wu, T., Tsang, L., Li, Q., Shi, J., Fung, A., (2003). "Emission of rough surfaces calculated by the integral method with comparison to three dimensional moment method simulations." IEEE Transaction on Geoscience and Remote Sensing. Vol. 41, p 90-101.

Coffman, R., Garner, C., (2012). "Final Report of MBTC-3031 Project." Mack-Blackwell Rural Transportation Center.

Conte, O., Coffman, R., (2013). "Characterization of Landslides by Advanced Remote Sensing Techniques, Standard Monitoring Techniques, and Laboratory Testing." Proc. GeoCongress 2013: Stability and Performance of Slopes and Embankments III, San Diego, California, March. Accepted for Publication (in press).

Conte, Omar A. R. (2012). "Slope Stability Monitoring Using Remote Sensing Techniques." Master's Thesis. University of Arkansas – Fayetteville. May 2012.

Dubois, P., van Zyl, J., Engman, E., (1995) "Measuring Soil Moisture with Imaging Radar." IEEE Transactions of Geoscience Remote Sensing, Vol. 33, pp. 916–926.

European Space Agency (ESA), (2014). "Parameters affecting radar backscatter." ESA Earthnet Online. http://earth.esa.int/applications/data_util/SARDOCS/spaceborne/Radar_Courses/Radar_Course_III/parameters_affecting.htm. Retrieved April 11, 2014.

Evett, S., (2003). "Soil Water Measurement by Time Domain Reflectrometry." Encyclopedia of Water Science, Marcel Dekker, Inc. New York p 894-898.

Fung, A., Li, Z., Chen, K., (1992). "Backscattering from a Randomly Rough Dielectric Surface." IEEE Transaction on Geoscience and Remote Sensing, Vol. 30, pp. 356-369.

Gamma Remote Sensing, (2012). "GAMMA SAR and interferometry software." Version 2006, updated 2012.

Garner, C., Coffman, R., (2014). "Remote Sensing Methods for Monitoring Ground Surface Deformation of Compacted Clay Test Sections." ASCE Geotechnical Special Publication No. 234, Proceedings of the GeoCongress 2014: Geo-Characterization and Modeling for Sustainability, Atlanta, Georgia, February, pp. 963-978.

Garner, C., Coffman, R., (2016). "Volumetric Water Content Measurements as Obtained from Remote Sensing and In-Situ Instrumentation." Journal of Environmental and Engineering Geophysics, Accepted for Publication, Manuscript Number 15-022R.

Google, (2012). "Google Earth and Supporting Documentation." The Google Corporation. Imagery Retrieved 2012.

Hanson, B., and Peters D., (2000). "Soil Type Affects Accuracy of Dielectric Moisture Sensors." California Agriculture. pp. 43-47.

Mathworks, (2012a). "MATLAB Programing Environment and Documentation." The MathWorks, Inc. Natick, MA.

National Oceanic and Atmospheric Administration (NOAA), (2012b). "2012 yearly observed high/low temperatures and precipitation for Fayetteville, AR." http://www.srh.noaa.gov/tsa/?n=climateGraphs. Retrieved July, 2012.

Nemmers, C., (1998). "Volumetric Moisture Content Using Time Domain Reflectometry." FHWA publication number: FHWA-RD-97-139.

Njoku, E., Entekahbi, D., (1994). "Passive Microwave Remote Sensing of Soil Moisture." Journal of Hydrology, Vol. 184, Issue 1-2, pp. 101-129.

Rice, S., (1951). "Reflection of Electromagnetic Waves by Slightly Rough Surfaces." Community of Pure Applied Math. Vol. 4, p. 351-378.

Sarabandi, K., Pierce, L., Oh, Y., Dobson, M., Ulaby, F., Freeman, A., (1994). "Cross-Calibration Experiment of JPL AIRSAR and Truck-Mounted Polarimetric Scatterometer." IEEE Transactions on Geoscience and Remote Sensing. Vol. 32, No.5, pp. 975-985.

Take, W., Arnepalli, D., Brachman, R., and Rowe. R., (2007). "Laboratory and Field Calibration of TDR Probes for Water Content Measurement." Ottawa Geo 2007. Ottawa, Canada

Topp, G., Davis, J., Annan, A., (1980). "Electromagnetic Determination of Soil Water Content: Measurements in Coaxial Transmission Lines." Water Resources Research, Vol. 16, Issue 3, pp. 574-582.

Ulaby, F., (1974). “Radar Measurement of Soil Moisture Content.” IEEE Transactions on Antennas Propagation. Vol. AP-22, pp. 257–265.

Ulaby, F., Moore, R., Fung, A., (1986). “Microwave Remote Sensing, Active and Passive. Volume III, from Theory to Application.” Artech House, Massachusetts.

Wagner, W., (1998). “Soil Moisture Retrieval from ERS Scatterometer Data.” PhD Dissertation, Vienna University of Technology. November.

Wegmuller, U., (1997). “Soil Moisture Monitoring with ERS SAR Interferometry.” European Space Agency Special Publication ESA SP-414. Proceedings of the 3rd ERS Symposium. pp. 47-51.

CHAPTER 6: FIELD VOLUMETRIC WATER CONTENT OBTAINED WITH POLARIMETRIC METHODS

6.1. Chapter Overview

Described in this chapter is the methods, procedures, and results for field measurements of soil volumetric water content at the Jeffery Energy Center (JEC) utilizing both change detection methods (as previously described in Chapter 2 and Chapter 6) and a fully polarimetric method. Radar imagery was acquired between June 13th and June 18th, 2013 at a test section at the WESTAR JEC facility in Saint Marys, Kansas. The test section consisted of approximately 2m (6 feet) of fill (a clay and sandy loam) placed over an area of 15m by 30m.

Radar imagery was acquired using both the University of Arkansas GPRI-2 (K_u-Band VV imagery) and the University of Missouri (C-Band VV and HH imagery). Radar observations were captured from a previously established construction control point on a nearby topographic figure. *In situ* measurements of soil volumetric water content were acquired concurrently, after placement of fill, using a nuclear density gauge. This chapter contains a summary and an introduction (Section 6.3 and Section 6.4), a background section on remotely acquired soil moisture measurements (Section 6.5), a description of the methods and procedures utilized to acquire, process, and visualize the data (Section 6.6), a description of the findings of this project (Section 6.7), and a description of conclusions and recommendations generated during this project (Section 6.8). Key findings for this work include that ground-based remotely sensed data were able to obtain soil volumetric water content (and density measurements) in the field. However, site specific features, specifically topographic relief, were an important consideration (and possible limitation) when ground-based radar measurements were employed. The full citation for this document is: *Garner, C., Coffman, R., (2017a). Garner, C., Coffman, R., (2017a). "Remotely Sensed Soil Volumetric Water Content and Dry Density as Obtained Utilizing Change Detection*

and Polarimetric Methods." Journal of Environmental and Engineering Geophysics, Submitted for Review (July 2016), Manuscript Number 16-028.

6.2. Remotely Sensed Soil Volumetric Water Content and Dry Density as Obtained Utilizing Change Detection and Polarimetric Methods

Cyrus D. Garner, SM.ASCE, MSCE, EIT[1] and Richard A. Coffman, M.ASCE, PhD, PE, PLS[2]

[1]Doctoral Candidate, Department of Civil Engineering, University of Arkansas at Fayetteville, USA.

[2]Assistant Professor, Department of Civil Engineering, University of Arkansas at Fayetteville, USA.

6.3. Abstract

Two terrestrial imaging radars consisting of a fully polarimetric C-Band and a single polarization K_u-Band radar were employed to monitor the volumetric moisture content and density of the soil surface at a site in St. Marys, Kansas. Moisture content measurements were acquired over a 9 day period using change detection, polarimetric, and *in situ* (nuclear density gauge) methods. K_u-Band (49) and C-Band (19) images were captured. Remotely sensed volumetric moisture content measurements and dry density measurements were obtained by employing a single polarization change detection technique on the VV polarized imagery, as acquired using the K_u-Band and C-Band instruments. These same measurements were also acquired using the small perturbation method on acquired polarimetric images. The values of moisture content, as obtained using (K_u- and C-Band) change detection, polarimetric, and *in situ* methods were 23 percent, 21 percent, 26 percent, and 21 percent, respectively on June 13, 2013. Following a precipitation event on June 18th, 2013, the average values of volumetric water content as obtained using the (K_u- and C-Band) change detection and polarimetric methods were 38 percent, 37 percent, and 30 percent, respectively.

On June 13, 2013, the average values of the remotely sensed dry unit weight were 1204.3, 1243.8, 1435.1, and 1341.2kg·m^{-3}, as obtained using change detection (K_u- and C-Band) and polarimetric methods, and *in situ* instruments, respectively. On June 18, 2013, the values of the remotely sensed dry unit weights were 887.8, 1469.7, and 1464.9kg·m^{-3}, as obtained using K_u-Band, C-Band, and C-Band obtained measurements, respectively.

Author keywords: Single Polarimetric Radar; Fully Polarimetric Radar

6.4. Introduction

Remote sensing systems, commonly used for measuring *in situ* ground conditions, have been widely employed in the Geosciences (climatological, meteorological, and geological) but have not achieved similar acceptance in the geotechnical engineering community. Advantages of remote sensing systems for geotechnical applications are described in Coffman (2009) and Garner and Coffman (2016, 2017a). The ground-based second generation Gamma portable radio detection and ranging (radar) interferometer, (GPRI-2) couples improved spatial resolution (1m by 7 m posting at 1km) as compared with the currently available satellite technology that is commonly used for geoscience applications, with the ability to occupy and continuously monitor a project site or area of interest. Furthermore, terrestrial radar remote sensing systems offer superior, continuous spatial coverage with improved data acquisition rates when compared with traditionally employed techniques such as laboratory testing, nuclear density gauge testing, and testing conducted using *in situ* instrumentation. Specifically, for geotechnical engineering applications, the use of the ground-based remote sensing offers the potential to overcome existing limitations associated with aerial radar monitoring. The use of the terrestrial imaging radar enables the determination of: volumetric water content, degree of saturation, *in situ* density, and the amount of deformation of the soil, as discussed herein.

The GPRI-2 radar interferometer has been previously employed to remotely detect: ground surface movement associated with slope instability (Coffman and Conte 2012, Conte and Coffman 2012, Conte and Coffman 2013), expansive soils (Coffman and Garner 2012), and volumetric water content (Garner and Coffman 2016, Garner and Coffman 2017a). For the project described herein, a single polarimetric K_u-Band (17.63 GHz) system and a fully polarimetric C-Band (5.35 GHz) GPRI-2 system were utilized to capture radar images over a 9-day period (June 10, 2013 through June 18, 2013).

The two GPRI-2 radars, one owned and operated by the University of Arkansas (UA) and the other owned and operated by the University of Missouri (UM), consist of three 2-meter long: (1) slotted wave guide real aperture antennas (UA K_u-Band) or (2), patch antennas mounted (UM C-Band) to a servo-controlled tower positioned on top of a tripod located over a control point (Figure 6.1). Specifications and prior usage of the UA K_u-Band GPRI-2 are described in Coffman and Conte (2012), Coffman and Garner (2012), and Garner and Coffman (2016). The specifications and usage of the MU C-Band GPRI-2 are described in Deng (2012), Jenkins (2013), Lowry et al. (2013), and Rosenblad et al. (2013).

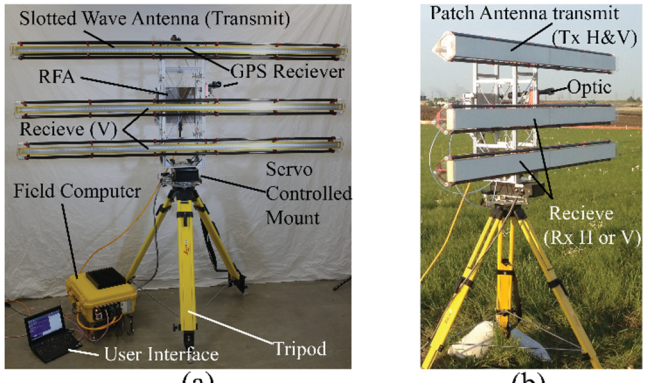

(a) (b)

Figure 6.1. (a) UA single polarimetric K_u-Band radar, and (b) modified UM fully polarimetric C-Band radar (previously presented as Figure 3.3).

The project, on which the radar devices were utilized, consisted of a proof-of-concept artificial wetland being constructed at the WESTAR Jeffery Energy Center (JEC) in St. Marys, Kansas. Specifically, the K_u-Band and C-Band remote sensing systems were deployed to the project site to monitor the volumetric water content, degree of saturation, and density of the soil at the soil surface. As reported in Coffman (2013c), the artificial wetland was being developed with the intended purpose of removing and entombing excess selenium from the flue gas desulfurization waste stream generated at the facility. Prior to the construction of the full-scale project, a 60-meter long by 30-meter wide test section was constructed, for field hydraulic conductivity testing on the treatment soil, to verify if the construction practices that were utilized were acceptable for the full-scale wetland.

6.5. Background

Active microwave remote sensing systems operate by emitting a pulse of electromagnetic (EM) radiation that interacts with a target (aircraft, terrain, ocean surface, etc.) and is then reflected back to a receiving antenna. Historic radar systems are documented in Evans et al. (2005), Richards (2005), Coffman (2009), and Garner and Coffman (2016). Since the 1980s several generations of aerial, orbital, and ground-based imaging radars have been deployed by many nations and many researchers in the fields of geography, geology, and environmental studies (Evans et al. 2005, Coffman 2009, Coffman and Conte 2012). Previous research investigating the registration of radar imagery (Gabriel and Goldstein 1988) and determining the volumetric water content of soils (Fung et al. 1992, Dubois et al. 1995, Wegmuller 1997, Wagner 1998, Chen et al. 2003, Garner and Coffman 2016) are presented and discussed.

6.5.1. *Image Registration*

Image registration is required to extract information from spatially and temporally separated radar imagery. To provide meaningful information, the geometry of each image must be transformed into the geometry of a "master" image. For radar remote sensing, image registration has been typically conducted by selecting (by inspection or by pixel parameters) strong persistent reflectors (e.g. trees, utility poles, permanent infrastructure, and stationary equipment) across multiple images (Gabriel and Goldstein 1988).

As described in the Gabriel and Goldstein (1988) methodology, the same methodology utilized and described herein, each strong reflector was incorporated into an [8 by 8] pixel block containing complex (amplitude and phase) data. The offset between a given image and a selected "master" image was determined in both the range (x) and azimuth (y) directions through an interferometric analysis of the pixel signal to noise ratio (SNR) between the "master" image and subsequent images. Specifically, Gabriel and Goldstein (1988) used a quadratic analysis to determine the location of persistent reflectors within each image block in both the "master" and other images. Range and azimuth offsets were then computed using the difference in pixel location of persistent reflecting elements in the "master" image and in subsequent "follower" images. Finally, the range and azimuth offsets were subsequently computed, for the pixels of the strong reflectors throughout the image, to determine the offset function between each image (in terms of azimuth and range). All of the pixels were relocated within the images based on the function that was generated from the pixels with persistent reflectors.

6.5.2. *Radar Derived Soil Moisture Content*

Extraction of volumetric water content data, utilizing imaging radar systems has been broadly categorized into two categories: change detection methodologies (Wegmuller 1997,

Wagner 1998) and polarimetric methodologies (Rice 1951, Fung et al. 1992, Dubois et al. 1995, Chen et al. 2003). Both the change detection and the polarimetric soil water content methods are used to detect changes in soil moisture by correlating observed changes in radar backscatter intensity with the effect of water on the dielectric properties of the soil. As discussed in Wegmuller (1997) and Wagner (1998), change detection methods utilize time dependent changes in the backscatter coefficient of pixels in an image as an indicator of changes in soil moisture content as a function of time. In contrast, polarimetric methods were developed by employing EM scattering theory to model the backscatter coefficient (σ^0) of the soil as a function of the: incident viewing angle (θ), complex dielectric properties (ε), and normalized surface roughness (ks). As discussed below, the aforementioned change detection and polarimetric methods rely on the observed radar intensity, as affected by the changes in the value of the dielectric constant for the soil body, to determine the water content.

6.5.2.1. Radar Derived Soil Moisture Content (Change Detection)

Change detection methods (Wegmuller 1997, Wagner 1998) were developed using the assumption that variations in the value of the observed radar backscatter coefficient (σ^0), for repeat pass observations, are only a function of changes in the moisture content of the soil. The Wegmuller (1997) method was originally developed for use with the European Space Agency (ESA) European Remote Sensing (ERS-1) satellite. Wegmuller (1997) correlated the backscatter intensity values with the volumetric water content values of the soil using an empirical relationship (θ_v, σ^0) developed for training sites in Europe and the United States. When coupled with a reference image of known volumetric water content, the Wegmuller (1997) method allowed researchers to determine the volumetric water content values for subsequent (temporally separated) images.

Similarly, the Wagner (1998) method used long term observation to characterize variations in backscattered intensity and to correlate those variations with the degree of saturation of the soil. An implicit assumption was made for the Wagner (1998) method; for a long observation period the soil will be observed over the full range of saturation soil values (0.0-1.0).

6.5.2.2. Radar Derived Soil Moisture Content (Polarimetric)

For the polarimetric soil water content inversions, EM scattering theory has been used to predict the backscatter coefficient of each pixel in an image as a function of surface roughness, angle of incidence, and dielectric constant (Fung et al. 1992, Dubois et al. 1995). The Small Perturbation Method (SPM) has been employed (Rice 1951, Dubois et al. 1995) for soil surfaces that have low normalized roughness values, relative to the operating wavelength of the radar system. The Integral Equations Method (IEM), or derivative methods, have been employed for rough soil surfaces, relative to the wavelength of a radar system (Fung et al. 1992, Chen et al. 2003).

In the SPM method and the IEM methods, the observed polarized (horizontal emitted and horizontal received [HH] and vertically emitted and vertically received [VV]) backscatter coefficients, as computed using the radar equation (Richards 2005), were compared with the backscatter coefficients predicted using the Fresnel reflection equations (Fung et al. 1992). Unknown input parameters (surface roughness and dielectric constant) were calculated by minimizing the difference between the predicted (using EM scattering models) and observed values of the backscatter coefficients for the polarized incident radiation (Fung et al. 1992, Dubois et al. 1995, Chen et al. 2003). The polarimetric techniques (SPM and IEM) are mathematically complex, computationally intensive, and may require *in situ* measurements of surface roughness. Specifically, for a dielectric surface, the intensity of backscattered microwave

energy is dependent on the incident angle (θ), the surface dielectric properties (ε), the surface roughness (s), and the wavelength (ESA, 2013). Previous researchers have developed the SPM method (Oh et al. 1992, Dubois et al. 1995) and IEM method (Fung et al. 1992, Chen et al. 2003) to solve the Bragg scattering equations and obtain values of volumetric water content for the soil from the predicted value of the soil dielectric constant of the soil. Dielectric mixing models can be used to relate the observed dielectric constant of the soil to the volumetric water content (Wang and Schmugge 1980, Dobson et al. 1985, Hallikainen et al. 1985, Mironov et al. 2009). Specifically, values of volumetric water content were determined by using empirically determined dielectric constant and volumetric water content relationships. However, in practice, a semi-empirical approach to the SPM method is often implemented (Oh et al. 1992).

6.6. Methods and Procedures

As previously mentioned, extraction of information from radar imagery is a complex and computationally demanding process. The methodologies and procedures utilized by the UA research team to extract volumetric moisture content (θ_v) and dry unit weight (γ_d) from the acquired radar data, at the JEC project site, are presented and described in this section. Real-time data processing was conducted on-site (preprocessing to verify data integrity) and further processing was conducted off-site, at the UA, after demobilization from the project site.

6.6.1. *Construction of Test Section at WESTAR JEC Project Site*

Construction of the test section at the WESTAR JEC project site was conducted using the same construction methods, construction personnel, and construction equipment that was proposed for the full-scale wetland facility. The 60m long by 30m wide test section was constructed on a section of ground that had been previously stripped and grubbed. The removed topsoil material was mixed with sand (40 percent by weight) and stockpiled for use on the full-

scale wetland, as discussed in Coffman (2013c). An aerial image of the project site is presented as Figure 6.2. A portion of this soil was used for the test section; this mixture was intended to increase the hydraulic conductivity of the soil to enable flow of the water through the soil. Thereby, the wetland facility was used to treat the water. The test section was underlain by a 0.6cm thick clean sand blanket to allow for drainage during hydraulic conductivity testing. The test section itself was constructed in three 60cm thick lifts. The fill material was placed using a conveyor system and then spread using a low ground pressure bulldozer to 1) reduce the density of the soil, and 2) to increase the porosity and thereby increase the permeability of the soil. Following placement of each lift, quality control testing was conducted using total station surveying equipment and a nuclear density gauge device (at a depth of 0-15cm).

In situ instrumentation including water soil matric potential sensors and time domain reflectometry sensors were installed into respective lifts (at the lift interfaces) during construction. For the 9-day observation period no significant changes in either vegetation (removed) or soil surface roughness (after mechanical preparation) occurred in the region of interest. Precipitation occurred on site on June 18 and radar imagery was captured immediately afterwards (when the soil surface was saturated). Similarly, the high air temperature and insolation at the site was assumed to result in very low soil moisture contents during the observation period.

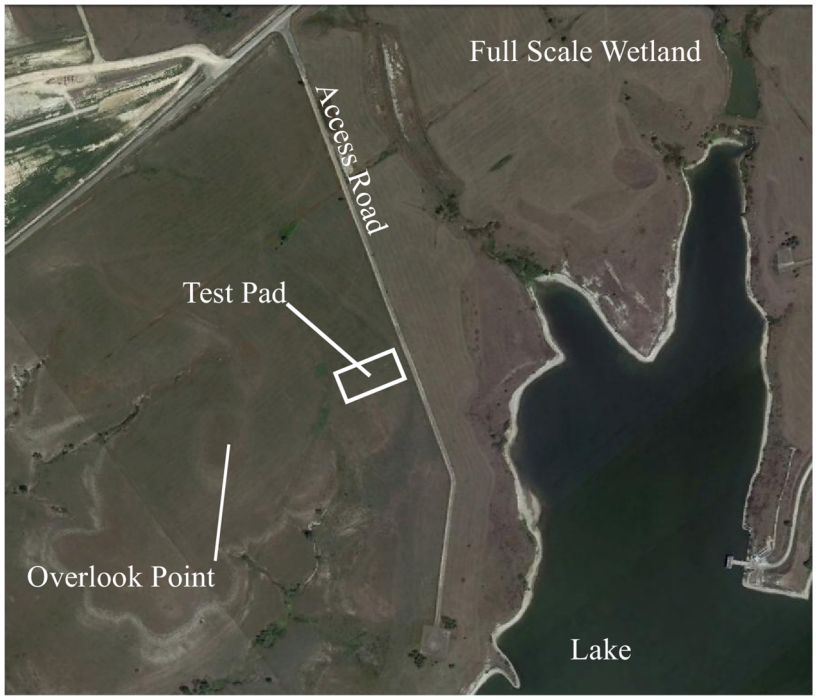

Figure 6.2. Aerial image of WESTAR JEC project site (modified from Google, 2014) previously presented as Figure 3.2.

6.6.2. *Radar Data Acquisition*

Data were acquired over the course of a 9 day period from June 10 to June 18, 2013. Radar observations were conducted from an overlook location that was approximately 300m west of the constructed test section. The GPRI-2 system was horizontally positioned over a previously installed control monument. The tripod legs were pushed into the ground and were not adjusted after the initial scan. Although the antennas and radio frequency assemblies (RFA) of the radar systems were removed during the overnight hours, the tripod remained in position during the entire acquisition period (to maintain sensor position and elevation). K_u-Band and C-Band imagery was captured utilizing the same tripod, servo-controlled mount, support structure, and field computer. Band specific antennas and RFA were installed or removed as required. The physical appearance and layout of the GPRI-2 radars (UA and UM) employed for this project were previously presented as Figure 6.1.

For interferometric K_u-Band observations, vertically polarized EM energy was transmitted utilizing the top slotted wave guide antenna and vertically polarized backscattered EM energy was simultaneously captured using both the middle and bottom antennas. At least two passes of the C-Band system were required for polarimetric observations. During the first pass, VV imagery and VH (vertically transmitted, horizontally received) imagery were simultaneously obtained using the top antenna (transmit) and the middle antenna (receive).

Following collection of the VV and VH data, and during the second pass, the software was changed to enable HH (horizontally transmitted, horizontally received) imagery and HV (horizontally transmitted, vertically received) imagery to be collected using the top antenna (transmit) and the middle antenna (receive). At least one set of seven interferometric K_u-Band images were typically collected in rapid succession (less than one minute between image acquisitions) and three (a smaller quantity due to data storage limitations) polarimetric C-Band (VV, VH, HV, HH) images were collected in rapid succession (less than one minute between image acquisitions) during each day of the observation period. Data observations dates, and the quantity and polarization of the radar imagery that were captured at the JEC site are presented in Table 6.1 (previously presented as Table 3.5).

Table 6.1. Radar images captured at the WJEC site between June 10 and June 18, 2013 (Garner and Coffman 2017a), previously presented as Table 3.5.

Date	K_u-Band[a] Images Acquired	C-Band[b] Images Acquired
6/9/2013	7 VV[c]	No Images
6/10/2013	7 VV	No Images
6/11/2013	7 VV	No Images
6/12/2013	7 VV	No Images
6/13/2013	7 VV	4 VV[c], 4 HV[d], 4 HH[e], 4 VH[f]
6/14/2013	7 VV	3 VV, 3 HV, 3 HH, 3 VH
6/15/2013	No Images	3 VV, 3 HV, 3 HH, 3 VH
6/16/2013	No Images	3 VV, 3 HV, 3 HH, 3 VH
6/17/2012	7 VV	3 VV, 3 HV, 3 HH, 3 VH
6/18/2013	7 VV	3 VV, 3 HV, 3 HH, 3 VH

[a]K_u-Band (1.7 cm wavelength, 17.6 GHz), [b]C-Band (5.6 cm wavelength, 5.4 GHz),[c]VV (Vertically Transmitted and Received), [d]HV (Horizontaly Transmitted and Vertically Received), [e]HH (Horizontally Transmitted and Received),[f]VH (Vertically Transmitted and Horizontally Received).

6.6.3. Processing of Collected Data from the Radar

Processing of collected radar data was conducted in a Linux software environment using commercially available Gamma Remote Sensing Interferometric SAR software (Gamma Remote Sensing 2012) and MATLAB (Mathworks 2012) executable programs developed as part of this research project. The programmatic work flow for the extraction of the volumetric water content values and the dry density values were divided into the following tasks: preprocessing and image registration, volumetric water content (θ_v) determination using the change detection method (Wegmuller 1997), determination of the degree of saturation (S) of the soil using the change detection method (Wagner 1998), and determination of the volumetric water content (θ_v) using the SPM as proposed by Dubois et al. (1995), Fung et al. (1992), and Chen et al. (2003). The values of dry density of the soil were subsequently determined using the results obtained from a phase diagram containing the aforementioned soil moisture measurements (θ_v, S) and the specific gravity of the soil solids (Gs). Processing tasks and the programmatic workflow utilized to obtain values of volumetric moisture content and dry density are presented in Figure 6.3.

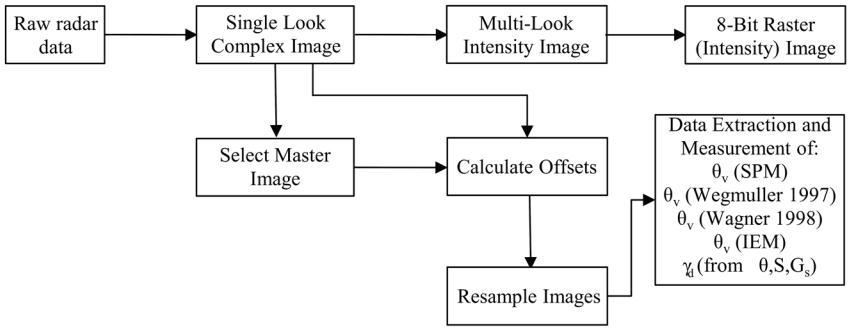

Figure 6.3. Programmatic work flow for extraction of volumetric water content and density from radar imagery (previously presented as Figure 3.7.).

6.6.3.1. Preprocessing of Radar Data and Image Registration

As previously described, on-site preprocessing was performed to ensure data integrity and included conversion of raw radar data files to single look complex images (SLC) that contained amplitude and phase information (32-bit complex data) and multilook intensity images (MLI) that contained amplitude information (16-bit data). Selected imagery was viewed in the field as an 8-bit raster (power) image. Off-site preprocessing was conducted to create SLC images for all of the collected scenes in preparation for image registration.

Resampling of SLC images was conducted utilizing the Gamma Interferometric SAR software suite (Gamma Remote Sensing 2012). A "master" image was selected and each of the subsequent images ("follower" images) were transformed into the geometry of the "master" image. Image registration was conducted by iteratively calculating image offsets (as previously described in Section 6.5.1). Subsequently, the individual SLC files were resampled into the master image geometry using the aforementioned offsets to create registered SLC (or RSLC) files.

6.6.3.2. Volumetric Water Content Inversion

The development and implementation of the change detection methods (Wegmuller 1997, Wagner 1998), using the GPRI-2 ground-based radar interferometer, was previously described in

Garner and Coffman (2016). Like the procedure described in Garner and Coffman (2016), the determination of volumetric water content, using the Wegmuller (1997) method, was conducted using commercial software (Gamma Remote Sensing 2012). Conversely, the Wagner (1998) method was conducted using registered radar imagery that was stacked (averaged) and then ingested into MATLAB as 16-bit "float" binary data. The maximum and minimum pixel brightness (decibel) values were determined over the period of observation. The degree of soil saturation was determined by linearly interpolating between the observed pixel brightness value and the maximum and minimum brightness values.

Processing of polarimetric radar data using the SPM and IEM water content inversion methods was also conducted using the Gamma Remote Sensing software (as described in Section 6.6.3.1 and Section 6.6.3.2). The registered intensity images were then ingested into MATLAB (as 16-bit binary data). The incident angle (θ) of each pixel was calculated using the elevation of the radar observation site (as obtained from traditional surveying techniques) and an assumed flat topography. Because of this assumption, the normalized site roughness was initially estimated utilizing the SPM with a coarse search window. The programmatic work flow for the SPM and IEM polarimetric water content inversions is presented graphically in Figure 3.8. The predicted values of the polarized backscatter coefficient, as a function of surface roughness and dielectric constant, were computed using Equation 6.1, Equation 6.2, and Equation 6.3.

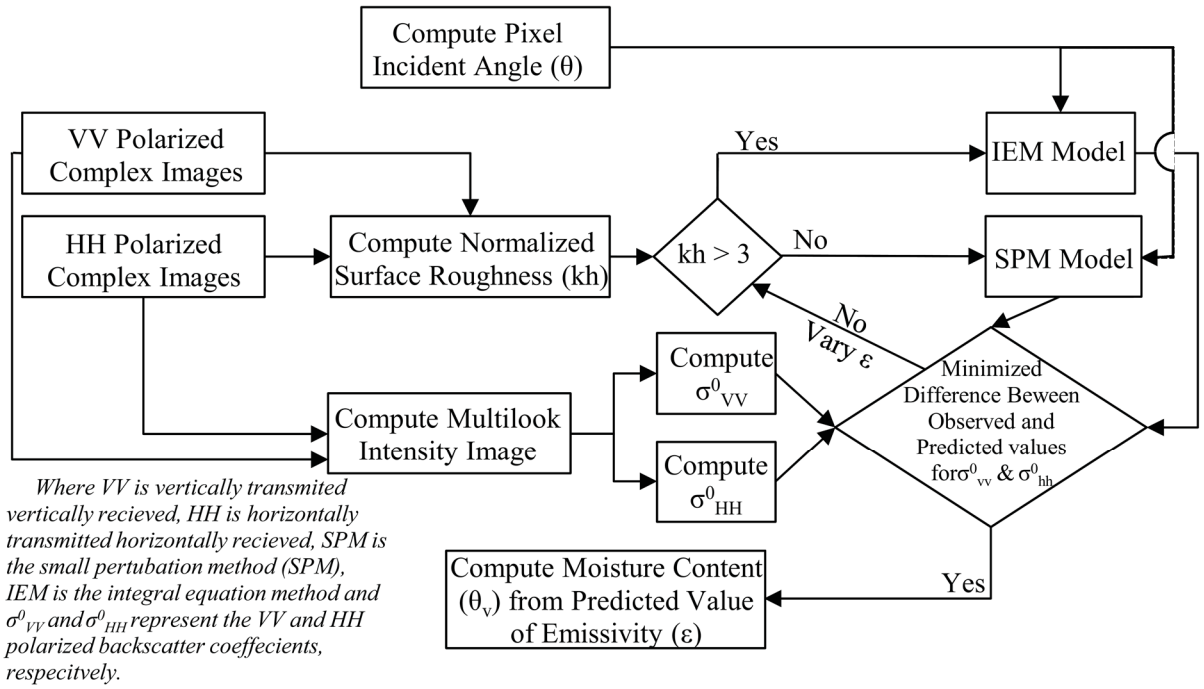

Figure 6.4. Flow chart and workflow for the extraction of volumetric water content from polarized radar imagery using the SPM and IEM methods (previously presented as Figure 3.8.).

$$\sigma_{qq}^{0} = 8k^{4}h^{2}\cos^{4}(\theta)W(2k\sin(\theta))\left|\alpha_{qq}(\theta)\right|^{2} \quad \text{(Dubois et al. 1995)} \quad \text{Equation 6.1}$$

$$\alpha_{HH}^{0} = \frac{\left(1-\varepsilon^{'}\right)}{\left(\cos(\theta)+\sqrt{\varepsilon^{'}-\sin^{2}(\theta)}\right)^{2}} \quad \text{(Dubois et al. 1995)} \quad \text{Equation 6.2}$$

$$\alpha_{HH}^{0} = \frac{\left(\varepsilon^{'}-1\right)\left(\sin^{2}(\theta)-\varepsilon^{'}\left(1+\sin^{2}(\theta)\right)\right)}{\left(\varepsilon^{'}\cos(\theta)+\sqrt{\varepsilon^{'}-\sin^{2}(\theta)}\right)^{2}} \quad \text{(Dubois et al. 1995)} \quad \text{Equation 6.3}$$

Where σ^{0}_{qq} is the polarized (HH or VV) backscatter coefficient, k is the wavelength, h is the surface roughness, W is the surface roughness spectrum, and ε' is the real component of complex term of the dielectric constant.

The initial estimate of soil surface roughness was then filtered using a nearest neighbor method (the average of the five adjacent pixels in range and azimuth direction). The nearest neighbor averaging was selected due to assumption that the surface roughness was consistent over the area of interest (due to mechanical preparation of the project site). Using a refined search grid,

the computed normalized surface roughness values were then utilized to calculate the soil dielectric constant using the SPM method.

Extraction of volumetric water content information has been conducted using empirical relationships between volumetric water content and dielectric constant found in the Geotechnical Engineering Literature (Topp et al. 1980, Njoku and Entekhabi 1994, Garner and Coffman 2016). However, for this research project, the empirical relationships between dielectric constant and moisture content proposed by Njoku and Entekhabi (1994) were employed to account for the frequency dependent nature of the dielectric constant at microwave frequencies. Specifically, the Topp et al. (1980), the Take et al. (2007) and the Garner and Coffman (2016) methodologies were developed using time domain reflectometry (TDR) system which operate in frequency ranges where dielectric constant is dominated by the imaginary component of the electrical loss (ε'') term. Conversely, the Njoku and Entekhabi (1994) volumetric water content and dielectric constant relationships were developed for microwave frequencies where the real component of electrical loss (ε') is the dominant contributor to the dielectric constant value.

6.6.3.3. Extraction of the Dry Unit Weight of Soil using Radar Images

Using the specific gravity value, as obtained from laboratory data (ASTM D854, 2014), along with information obtained from the previously described soil moisture inversions the *in situ* density of the soil surface was calculated through the use of phase relationships. Specifically, radar obtained values of volumetric water content of the soil (Wegmuller 1997 and SPM methodologies) and the degree of saturation of the soil (Wagner 1998) were coupled with laboratory-based measurements of the specific gravity of the soil solids (ASTM D854 2014) to determine the dry unit weight of the soil using phase relationships (Equation 6.4.).

$$\gamma_d = G_s \rho_w \left(1 - \frac{\theta_v}{S}\right)$$ Equation 6.4

Where G_s is the laboratory obtained specific gravity of the soil solids, ρ_w is the density of water, θ_v is the remotely sensed volumetric water content and S is the remotely sensed saturation.

Extraction of the unit weight of the soil from radar imagery was conducted using MATLAB executable software developed as part of this research project. Specifically, three separate remote methodologies for extracting the volumetric moisture content of the soil were implemented. Using C-Band (5.6 GHz) polarimetric imagery, two methods were combined to determine the values of the dry unit weight using the results from 1) SPM and Wagner (1998) methods and 2) Wegmuller (1997) and Wagner (1998) methods. For the VV K_u-Band imagery the dry unit weight values were obtained by combing the results from the Wegmuller (1997) and Wagner (1998) change detection methods.

6.7. Findings

The volumetric water content on the WESTAR JEC site varied considerably over the nine day observation period (June 13, 2013 through June 18, 2013). Daily temperatures on site averaged 24 degrees Celsius (HPRCC, 2013) with daily high temperatures between 27 and 35 degrees Celsius. Rainfall events occurred on June 15, 2013 and June 18, 2013. Density and moisture content data were captured on June 13 and June 14 using the nuclear density gauge, as part of the construction quality assurance on the artificial wetland test section. Eighteen nuclear density gauge were collected on the completed test area. Test locations were selected at random within the aforementioned area. Additionally, the specific gravity of the fill material in (2.52) was obtained from laboratory testing (ASTM D854 2014) conducted on bagged samples of soil from the test section. The results of the *in situ* and laboratory testing are tabulated in Table 6.2.

On June 13, 2013, the average volumetric water content, as obtained via phase relationships from the gravimetric water content data determined using the nuclear density gauge for the fill material, was 0.21. The deviation between the *in situ* soil volumetric moisture content and the volumetric moisture content as obtained using remote sensing was 5, 4, and 2 percentage points higher for the C-Band change detection method (Wagner 1998), the C-Band SPM method, and the K_u-Band change detection method (Wagner 1998). The change detection (Wegmuller 1997, Wagner 1998) and polarimetric water content inversions were performed on the C-Band and K_u-Band imagery captured at the WESTAR JEC project site. The remotely sensed (C-Band) volumetric water content measurements are presented graphically in Figure 6.5 and Figure 6.6 for the change detection method (Wagner 1998) and SPM method, respectively. The average volumetric water content values, as obtained on June 13, 2013, were 21 percent and 26 percent, respectively, with standard deviations of 12 percent and 7 percent. Similarly, after precipitation at the project site on June 18, 2013, the average volumetric water content values for the soil were measured to be 37 percent and 30 percent for the C-Band Wagner (1998) and SPM method, respectively, with standard deviations of 9 and 4 percentage points. Similarly, the remotely sensed volumetric water content values, as obtained from the K_u-Band data utilizing the Wegmuller (1997) and the Wagner (1998) change detection methods on June 13, 2013 (average = 23 percent) and June 18, 2013 (average = 38 percent) are presented graphically as Figure 6.7.

Table 6.2. WESTAR JEC project site results obtained from in situ and laboratory testing.

Quantity	Symbol	Unit	Average	Standard Deviation
Dry Unit Weight[a]	γ_d	$kg \cdot m^{-3}$	1341.52	65.43
Total Unit Weight[a]	γ_t	$kg \cdot m^{-3}$	1550.84	66.51
Weight of Water[a]	w_w	$kg \cdot m^{-3}$	209.32	19.55
Gravimetric Water Content	w	%	15.47	0.01
Specific Gravity[b]	G_s	ρ_w	2.52	0.06
Volumetric Water Content	θ_v	$m^3 \cdot m^{-3}$	0.2	0.02
Porosity	η	$m^3 \cdot m^{-3}$	0.47	0.03
Saturation	S	$m^3 \cdot m^{-3}$	0.45	0.05

[a]Obtained In-Situ with Nuclear Density Guage

[b]Obtained in Laboratory on Recovered Bag Samples as per ASTM D854 (2012)

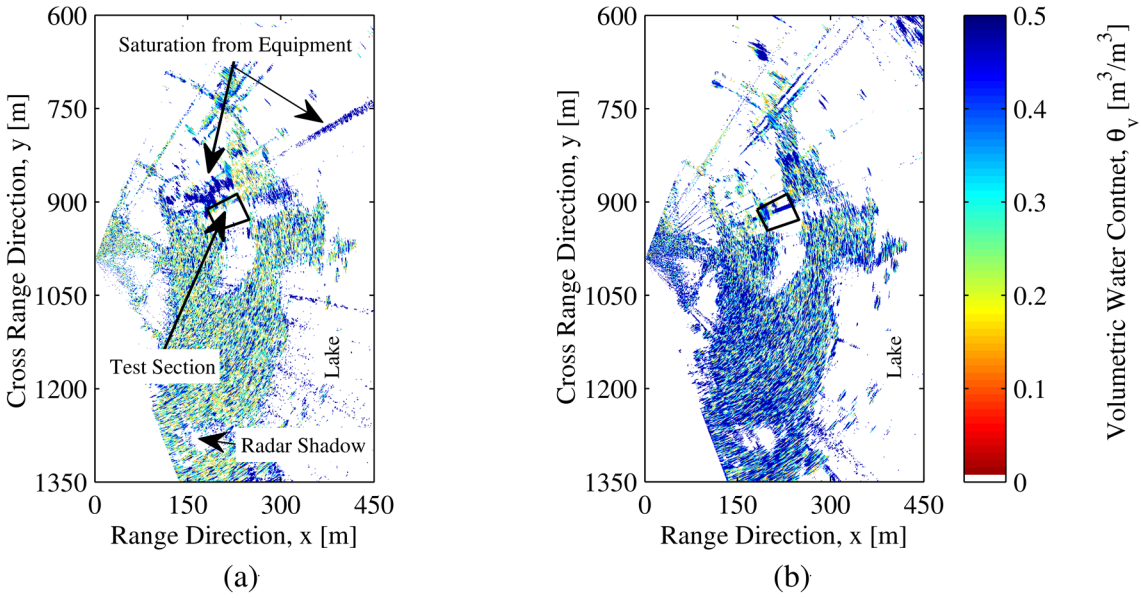

Figure 6.5. Volumetric water content at the WESTAR JEC project site as obtained using the Wagner (1998) change detection method on (a) June 13, 2013 and (b) June 18, 2013 [in color].

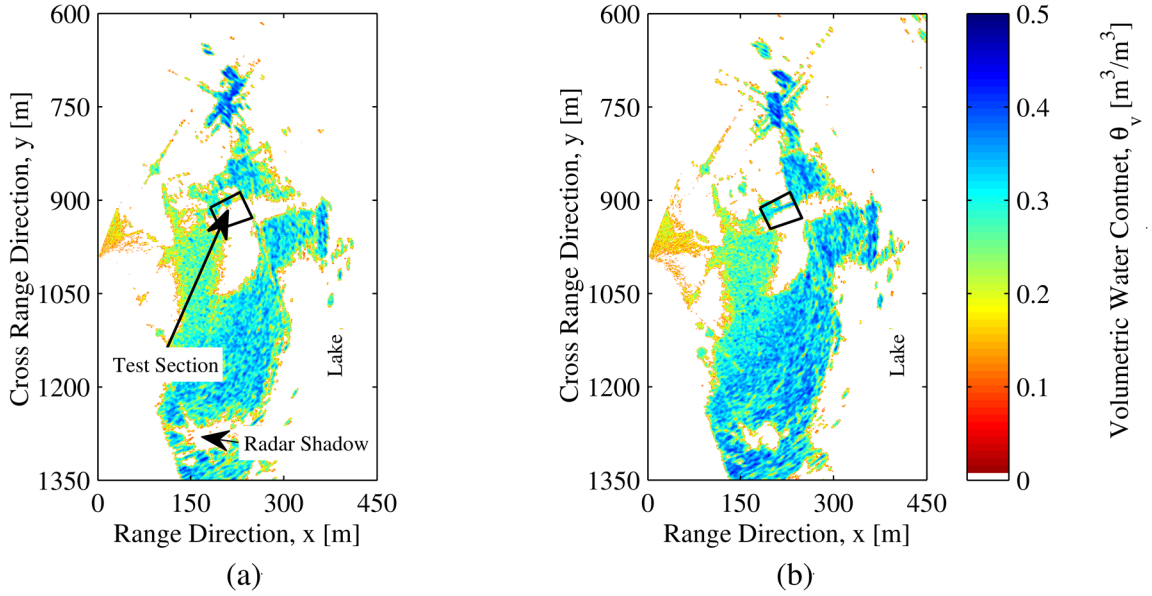

Figure 6.6. Volumetric water content at the WESTAR JEC project site as obtained using the C-Band imagery and the SPM on (a) June 13, 2013 and (b) June 18, 2013 [in color].

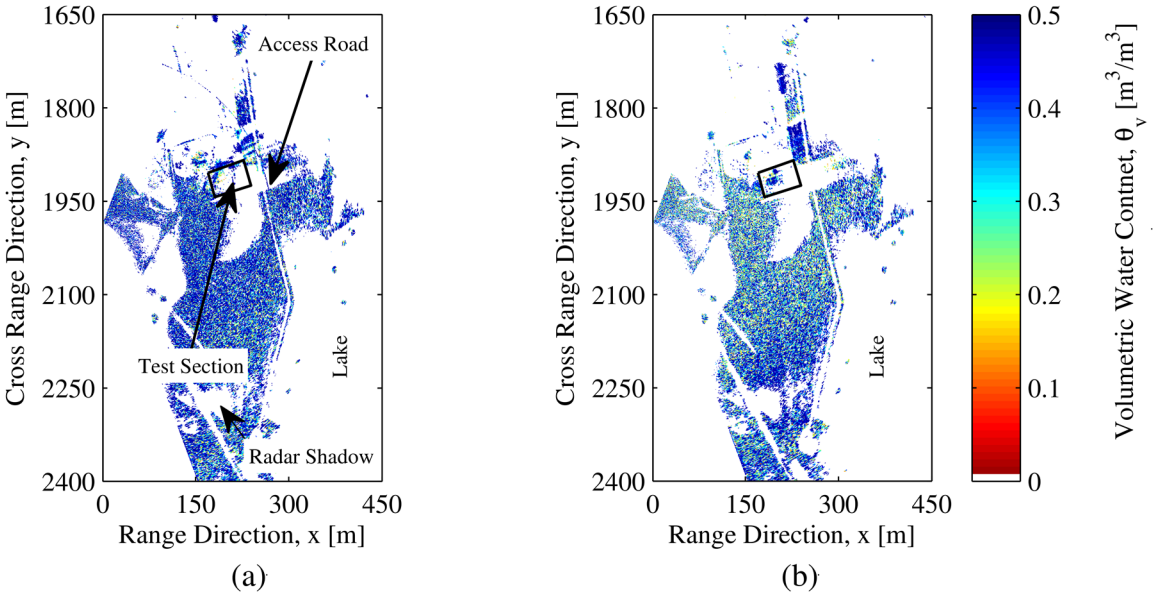

Figure 6.7. Volumetric water content at the WESTAR JEC project site on (a) June 13, 2013 and (b) June 18, 2013 as obtained using K_u-Band imagery and the Wagner (1998) change detection method.

Several challenges were encountered at the project site during the use of the active microwave remote sensing system. The low terrain relief at the JEC site (the overlook point was approximately 300m from the test section with a relative elevation of 30m above the test section) resulted in radar incident angles between 80-85 degrees from nadir. The high incident angle and

the assumption of a flat terrain model is a potential source of error in volumetric water content measurements as obtained from the SPM. Further error was introduced into the determination of pixel specific incident angles because of the lack of a site digital elevation model (DEM) for the site. Additionally, construction equipment (specifically the soil conveyor) interfered with the radar imagery by introducing regions of backscatter intensity saturation (too much microwave energy returned to the instrument) and radar shadowing (by blocking microwave propagation).

Because the site was previously stripped of vegetation and topsoil during construction activities, the assumption of a smooth surface ($kh < 3.0$) was expected to be valid. The average calculated normalized surface roughness values for the area of interest was 0.45 and 0.38 (for the constructed area) and 0.45 and 0.37 (for native prairie areas) on June 13 and June 18, 2013, respectively. The calculated surface roughness values support the validity of the use of the SPM, as opposed to the IEM, to determine volumetric water content at this test site.

When comparing the water content results obtained using the Wegmuller (1997), Wagner (1998), and SPM methodologies it was found that the SPM results were sparse (e.g. the θ_v values for many pixels were null values). It is hypothesized that the sparse nature of SPM results is an artifact of the data processing. Specifically, to increase the signal to noise ratio and reduce computational demand, pixels with backscatter coefficient (σ_{HH} and σ_{VV}) values less than 10^{-2} m^2 were excluded during the calculation of water content.

To overcome the aforementioned limitations, the UA research team has identified several methods to increase the precision and accuracy of the remotely sensed values of volumetric moisture content and *in situ* dry unit weight. Specifically, the use of interferometric methods as described in Gabriel and Goldstein (1988) and Coffman (2009) to develop DEM is suggested due to the inherent availability of the required radar data (registered SLC images). The use of a

simultaneously acquired DEM would allow for a more accurate calculation of the incident viewing angles of the pixels. Another means of improving the accuracy of the remotely sensed volumetric moisture content methods (both change detection and polarimetric) is to incorporate the use of limited training data into the images. Specifically, *in situ* measurements of soil roughness and soil autocorrelation length (l) may enable calibration of the remotely measured soil roughness spectrum (ks, l). Likewise, *in situ* measurements of soil dry unit weight and volumetric moisture content (as obtained using the nuclear density gauge or other *in situ* instrumentation) may enable the calibration of the results as generated using both change detection and polarimetric methods.

Site specific parameters that may affect the aforementioned methods for remote determination of volumetric moisture content are the site topography and the construction activities. The location of the radar instrument should be chosen maximize the local incident angle in the region of interest by either increasing the instrument height (e.g. placing the system on a building) or by taking advantage of site topography. For active construction sites (such as the WESTAR JEC site) the presence of mobile construction equipment may also introduce regions of saturation and radar shadow. Additionally, the movement of equipment (and other strong reflectors) may induce error in the image registration process. Specifically, if the project schedule permits, the ability of the radar system to operate at night may need to be employed to obtain remotely sensed measurements without interference from or to the construction operations.

The remotely sensed values of dry unit weight for the soil are presented in Figure 6.8 and Figure 6.9 (C-Band) and Figure 6.10 (K_u-Band). The average dry unit weight values on June 13, 2013, of 1204.3, 1243.8, 1435.1, and 1341.2kg·m^{-3} (*in situ* value as obtained by traditional nuclear density gauge) were obtained utilizing the K_u-Band, C-Band (SPM and Wagner 1998), the

C-Band (Wegmuller 1997 and Wagner 1998), and the nuclear density gauge, respectively. Specifically, the remotely sensed (C-Band) measurements of dry unit weight values were within 100kg·m^{-3} of the *in situ* measurement (1341.2kg·m^{-3}) as obtained using the nuclear density gauge. Dry unit weight values of 887.8, 1446.9, and 1464.9kg·m^{-3}, on June 18, 2013, were obtained utilizing the K_u-Band, C-Band (SPM and Wagner 1998), and C-Band (Wegmuller 1997 and Wagner 1998).

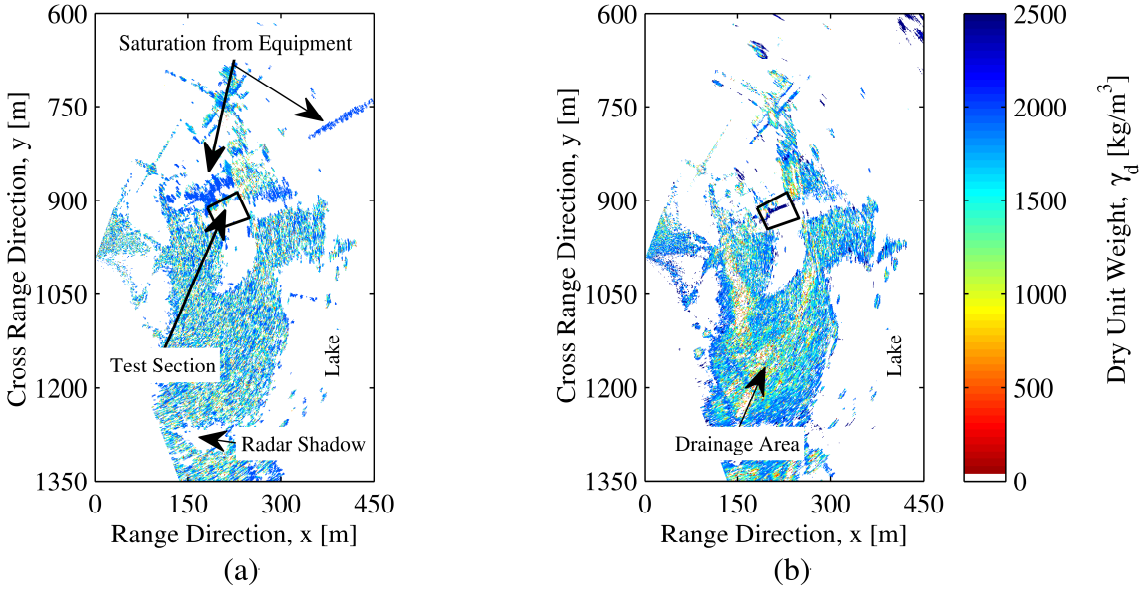

Figure 6.8. Dry unit weight on (a) June 13, 2013 and (b) June 18, 2013, as obtained using C-Band imagery using the Wegmuller (1997) and Wagner (1998) change detection methods.

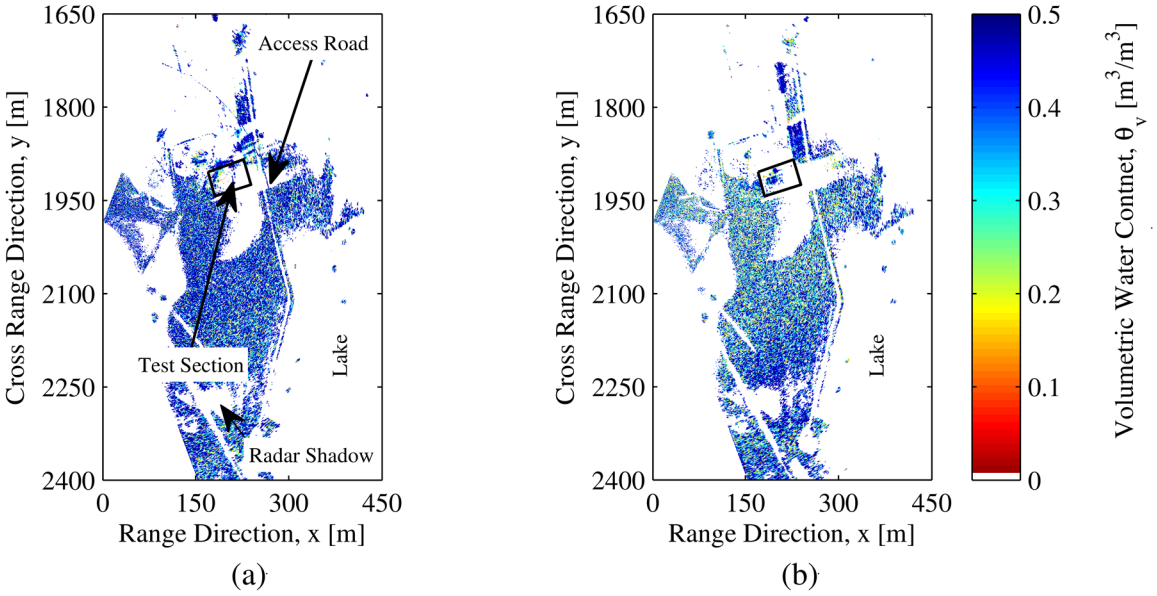

Figure 6.9. Dry unit weight on (a) June 13, 2013 and (b) June 18, 2013, as obtained using a C-Band imagery and the SPM and Wagner (1998) change detection methods.

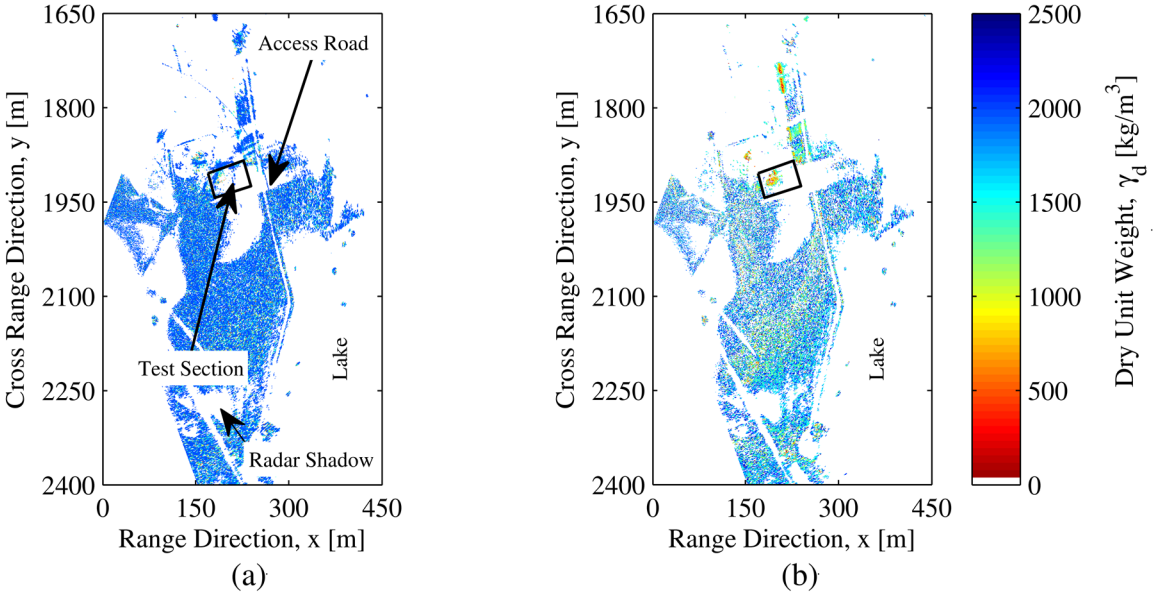

Figure 6.10. Dry unit weight on (a) June 13, 2013 and (b) June 18, 2013, as obtained using a K_u-Band imagery and the Wegmuller (1997) and Wagner (1998) change detection methods.

6.8. Conclusion

The use of remote sensing, specifically the use of ground-based active microwave (radar) systems, offers potential benefits with regards to rapidly monitoring 1) the volumetric content moisture and 2) the unit weight of soil over large spatial areas (up to 4 kilometers away). One of

the employed change detection methods (Wagner 1998) yielded volumetric moisture content values that were in agreement with the *in situ* measurements (21 percent). The separation between the two C-Band remotely sensed methods was within 5 percentage points. The volumetric water content obtained using the polarimetric method also increased following the precipitation event on June 18, 2013. Remotely sensed and *in situ* measurements of the dry density of the soil were within 140kg·m^{-3} for all of the methods computed using the data collected on June 13, 2013. Dry unit weight values, as determined using the K_u-Band data, were numerically lower (between 39 and 577kg·m^{-3}) than all other methods (specifically, for data acquired on June 18, 2013). While the authors found that it was possible to acquire remote measurements of volumetric water content at the JEC Westar test site, it was not an ideal location for ground-based radar remote sensing. Take-away recommendations for future implementation of ground-based radar systems include 1) the use of *in situ* measurements of surface soil roughness and autocorrelation lengths, 2) the use of training data throughout the remotely sensed region, and 3) limiting the use of the device only to locations where the terrain allows for decreased local incident angle values.

6.9. Acknowledgements

The authors would like to thank Burns & McDonnell Engineering Company, Inc. and Westar Energy (Jeffrey Energy Center) for financial and/or in-kind contribution to the project. The authors also thank the University of Missouri for allowing the use of the C-Band GPRI-2.

6.10. Works Cited

American Society for Testing and Materials (ASTM) D854, (2014). “Standard Test Methods for Specific Gravity of Soil Solids by Water Pycnometer.” American Society for Testing and Materials, Vol. 4.08, Soil and Rock (I). West Conshohocken, PA.

Chen, K., Wu, T., Tsang, L., Li, Q., Shi, J., Fung, A., (2003). “Emission of rough surfaces calculated by the integral method with comparison to three dimensional moment method simulations.” IEEE Transaction on Geoscience and Remote Sensing. Vol. 41, p 90-101.

Coffman, R., (2009), “Processing of Synthetic Aperture Radar Data as Applied to the Characterization of Localized Deformation Features.” Ph.D. Dissertation, University of Missouri, Columbia, August.

Coffman, R., (2013b). "Performance of Westar Energy Vertical Flow Bed Test Section." Coffman Consulting Company, LLC Final Report. Client: Burns and McDonnell Engineering, Inc., December.

Coffman, R., Conte, O., (2012). "Slope Stability Monitoring Using Remote Sensing Techniques Final Report for AHTD TRC Project 1102." Client: Arkansas State Highway and Transportation Department, November.

Coffman, R., Garner, C., (2012). “Final Report of MBTC-3031 Project.” Mack-Blackwell Rural Transportation Center.

Conte, O., Coffman, R., (2012). “Slope Stability Monitoring Using Remote Sensing Techniques.” ASCE Geotechnical Special Publication No. 225, Proc. GeoCongress 2012: State of the Art and Practice in Geotechnical Engineering, Oakland, California, March, pp. 3060-3068.

Conte, O., Coffman, R., (2013). “Characterization of Landslides by Advanced Remote Sensing Techniques, Standard Monitoring Techniques, and Laboratory Testing.” Proc. GeoCongress 2013: Stability and Performance of Slopes and Embankments III, San Diego, California, March. Accepted for Publication (in press).

Deng, H. (2012). "Ground Based Interferometric Radar Initial Look at Longview, Blue Springs, Tuttle Creek, and Milford Dams." Master of Science Thesis. University of Missouri-Columbia, July.

Dobson, M., Ulaby, F., Hallikainen, M., El-Rayes, M., (1985). “Microwave Dielectric Behavior of Wet Soil – Part II: Dielectric Mixing Models.” IEEE Transactions on Geoscience and Remote Sensing, Vol. GE-23, No. 1.

Dubois, P., van Zyl, J., Engman, E., (1995) “Measuring Soil Moisture with Imaging Radar.” IEEE Transactions of Geoscience Remote Sensing, Vol. 33, pp. 916–926.

European Space Agency (ESA), (2013). “Rough Surface Scattering Models.” European Space Agency Online Manual. http://earth.eo.esa.int/polsarpro/Manuals/2_Rough_Surface_ Scattering_ Models.pdf. Retrieved December 2013.

Evans, D., Alpers, W., Cazenave, A., Elachi, C., Farr, T., Glackin, D., Holt, D., Jones, L., Liu, W., McCandless, W., Menard, Y., Moore, R., Njoku, E., (2005). “Seasat – A 25-Year Legacy of Success.” Remote Sensing of Environment, Vol. 92, pp. 384-404.

Fung, A., Li, Z., Chen, K., (1992). “Backscattering from a Randomly Rough Dielectric Surface.” IEEE Transaction on Geoscience and Remote Sensing, Vol. 30, pp. 356-369.

Gabriel, A., Goldstein, R., (1988). “Crossed Orbit Interferometry: Theory and Experimental Results from SIR-B.” International Journal of Remote Sensing, Vol. 9, No. 8, pp. 857-872.

Gamma Remote Sensing, (2012). “GAMMA SAR and interferometry software.” Version 2006, updated 2012.

Garner, C., Coffman, R., (2016). “Volumetric Water Content Measurements as Obtained from Remote Sensing and In-Situ Instrumentation.” Journal of Environmental and Engineering Geophysics, Accepted for Publication, Manuscript Number 15-022R.

Garner, C., Coffman, R., (2017a). “Remotely Sensed Soil Volumetric Water Content and Dry Density as Obtained Utilizing Change Detection and Polarimetric Methods.” Journal of Environmental and Engineering Geophysics, Submitted for Review (September 2016).

Google, (2014). “Google Earth Imagery.” The Google Corporation. Retrieved February 2014.

Hallikainen, M., Ulaby, F., Dobson, M., El-Rayes, M., Wu, L., (1985). “Microwave Dielectric Behavior of Wet Soil-Part 1: Empirical Models and Experimental Observations.” IEEE Transactions on Geoscience and Remote Sensing, pp. 25-34.

High Plains Regional Climate Center (HPRCC), (2013). “June 2013 Climate Summary.” http://www.hprcc.unl.edu/publications/files/2013_06_climatesummary.pdf. Retrieved January 2014.

Jenkins, W., (2013). "Evaluation of Ground-Based Interferometric Radar for Civil Engineering Applications." Master of Science Thesis. University of Missouri-Columbia, July.

Lowry, B., Mooney, M., Zhou, W., Grasmick, J., Gomez, F., Held, B., (2013). "High Resolution Displacement Monitoring of a Slow Velocity Landslide Using Ground Based Radar Interferometry." Engineering Geology.

Mathworks, (2012a). “MATLAB Programing Environment and Documentation.” The MathWorks, Inc. Natick, MA.

Mironov, V., Kosolapova, L., Fomin, S., (2009). “Physically and Mineralogically Based Spectroscopic Dielectric Model for Moist Soils.” IEEE Transactions on Geoscience and Remote Sensing, Vol. 47, pp. 2059-2070.

Njoku, E., Entekahbi, D., (1994). “Passive Microwave Remote Sensing of Soil Moisture.” Journal of Hydrology, Vol. 184, Issue 1-2, pp. 101-129.

Oh, Y., Sarabandi, K., Ulaby, F., (1992). “An Empirical Model and an Inversion Technique for Radar Scattering from Bare Soil Surfaces.” IEEE Transactions on Geoscience and Remote Sensing, Vol. 30, No. 2, pp. 370-381.

Rice, S., (1951). “Reflection of Electromagnetic Waves by Slightly Rough Surfaces.” Community of Pure Applied Math. Vol. 4, p. 351-378.

Richards, M., (2005). “Fundamentals of Radar Signal Processing.” Mc-Graw Hill. New York.

Rosenblad, B., Gomez, F., Loehr, J., Held, B., Jenkins, W., (2013). "Ground-Based Interferometric Radar for Monitoring Slopes and Embankments.” Proc. GeoCongress 2013: Stability and Performance of Slopes and Embankments III, San Diego, California, March.

Take, W., Arnepalli, D., Brachman, R., and Rowe. R., (2007). “Laboratory and Field Calibration of TDR Probes for Water Content Measurement.” Ottawa Geo 2007. Ottawa, Canada

Topp, G., Davis, J., Annan, A., (1980). “Electromagnetic Determination of Soil Water Content: Measurements in Coaxial Transmission Lines.” Water Resources Research, Vol. 16, Issue 3, pp. 574-582.

Wagner, W., (1998). “Soil Moisture Retrieval from ERS Scatterometer Data.” PhD Dissertation, Vienna University of Technology. November.

Wang, J., Schmugge, T., (1980). “An Empirical Model for the Complex Dielectric Permittivity of Soils as a Function of Water Content”. IEEE Transactions on Geoscience and Remote Sensing, pp. 288-295.

Wegmuller, U., (1997). “Soil Moisture Monitoring with ERS SAR Interferometry.” European Space Agency Special Publication ESA SP-414. Proceedings of the 3rd ERS Symposium. pp. 47-51.

CHAPTER 7: OPTICAL ABSORPTION AND SCATTERING PROPERTIES OF INVESTIGATED SOILS

7.1. Chapter Overview

Contained in this chapter is a description of the optical characterization of the three soil types investigated. Specifically described is the use of laboratory-based testing (Atterberg limits, particle size analysis), advanced characterization techniques (scanning electron microscope and x-ray diffraction), and the use of a diffuse reflectance infrared Fourier transform (infrared) spectroscopy (DRIFT FTIR). Key findings contained in this manuscript are the spectrum of absorption characteristics for the Donna Fill, illite, and kaolinite soils for ultraviolet to near-infrared wavelengths (350-2500nm). The foreword of this chapter contains the manuscript title as submitted (Section 7.2) and a summary of the manuscript (Section 7.3). Specifically the optical characterization results for the UV-NIR region are contained in Section 7.7.3. Furthermore the chapter has been divided into the following sections: the introduction (Section 7.4), a review of the relevant literature (Section 7.5), the methods and procedures employed (Section 7.6), the results generated using the aforementioned methods and procedures (Section 7.8), and the conclusions drawn (Section 7.9). The full citation for this document is: *Garner, C., Coffman, R., (2017b). "Visible and Near-Infrared Diffuse Reflectance Properties of Geotechnical Reference Soils" Applied Clay Science (Submitted for Review).*

7.2. Visible and Near-Infrared Diffuse Reflectance Properties of Geotechnical Reference Soils

Cyrus D. Garner[a] EIT, MSCE, and Richard A. Coffman[b] PE, PLS, PhD,

[a]Doctoral Candidate, University of Arkansas, 4190 Bell Engineering, Fayetteville, Arkansas. 917-692-1026. cxg021@email.uark.edu (corresponding author).

[b]Associate Professor, University of Arkansas, 4190 Bell Engineering, Fayetteville, Arkansas. 917-692-1026. rick@uark.edu

7.3. Abstract

Soil absorption coefficients are required parameters to determine soil properties when using optical testing techniques. However, these soil absorption coefficients are not well documented within the geotechnical literature. Therefore, three soil types (clay and silt sized artificial nepheline syenite granite silt, clay and silt sized illite clay, and clay and silt sized kaolinite clay) were optically characterized within the visible- and near-infrared portion of the electromagnetic spectrum (350 to 2500nm wavelengths). Three methods for obtaining the soil absorption spectra were evaluated. These methods included: 1) a direct calculation of the absorption coefficient values (as a function of wavelength) by using literature obtained values for absorption of potassium bromide, 2) a direct calculation of the absorption coefficient values by using a subtractive technique of blended samples at different mass fraction values of soil and substrate, and 3) a numerical regression of the absorption coefficient spectra by using blended samples at different mass fraction of soil and substrate. The range of absorption coefficients for the silt sized artificial nephelite syenite granite, the silt sized illite clay, and the silt sized kaolinite clay was found to be between 0.81 and 78.8cm^{-1}, 0.93 to 150.0cm^{-1}, and 0.12 to 4.02cm^{-1}, respectively. The three methods provided divergent results for the absorption spectrum for the artificial nephelite syenite granite. For the illite and kaolinite samples, the maximum percent deviation between the three methods for the calculated absorption coefficients was 26.5 percent and 42.5 percent.

7.4. Introduction

Visible-infrared diffuse reflectance spectroscopy has been previously used to identify and quantify the properties of soil. Specifically, visible (Vis) [300-700nm], near-infrared (NIR) [800-2,500nm], and mid-infrared (MIR) [2,500-25,000nm] spectroscopy has been utilized to

investigate soil properties for agricultural, biological, and engineering applications. Although the majority of the work that has been described within the archival literature has been performed for agricultural or geological applications, the potential for use in geotechnical engineering applications has also been identified (Yitagesu et al. 2009, Waruru et al. 2014).

The use of UV-NIR spectroscopy offers potential benefits for engineering applications over traditional soil evaluation techniques. These benefits include rapid acquisition of results, non-destructive testing, and large spatial coverage (Rossel et al. 2010a). Additionally, the inclusion of the Kubelka-Munk (KM) color theory (Kubelka and Munk 1931, Kubelka 1947) that has been previously employed using UV-NIR techniques to analyze soil properties, may allow for a quantitative analysis of soil properties. However, the absorption and scattering functions that are required to use the KM theory are poorly documented within the archival geotechnical literature. Therefore, three soil types were optically characterized to enable for quantitative analysis of the volumetric water content and the pore water potential of the aforementioned soils. The three methods that were evaluated to obtain and calculate the values of the absorption coefficients of commonly encountered clay and silt sized soil particles are presented. For completeness, the index properties of the soils were also characterized using traditional testing methods including: grain size analysis (ASTM D422 2014), liquid limit (ASTM D4318 2014), plastic limit (ASTM D4318 2014), specific gravity (ASTM D854 2014), scanning electron microscopy, and x-ray diffraction. The employed procedures and the obtained results are provided and discussed herein.

7.5. Literature Review

Spectroradiometry can be utilized to obtain soil properties because the functional hydroxyl groups, tetrahedral groups, silicate/aluminate anions, octahedral metal cations, and interlayer cations that are associated with the lay mineralogy have specific EM reflectance signatures

(Farmer 1974, Busca and Resini 2000, Schroeder 2002, Stuart 2004). The use of traditional transmission spectroscopy has been limited by the requirement of an optically translucent sample. Therefore, the diffuse reflectance infrared Fourier transform (DRIFT) was developed to analyze optically opaque samples. While the majority of DRIFT spectroscopy has been employed to qualitatively detect the presence of chemical species in a sample (e.g. to detect impurities in pharmaceutical products), theoretical methods have also been developed to quantify the chemical species using a reflectance technique. For example, the KM color theory (Kubelka and Munk 1931, Kubelka 1947) was developed to allow for the analysis of the industrial pigment samples (Judd and Wyszeki 1975).

The KM theory enabled quantitative analyses to be conducted by utilizing experimentally obtained coefficients (absorption [k] and scattering [s]) coefficients). The Kubelka-Munk theory was developed using theoretical transfer equations to model the one-dimensional optical flux through a heterogeneous opaque medium (containing both scattering and absorbing types of particles). Specifically, the incident and reflected optical flux was modeled for a thin layer of semi-transparent material underlain by either a perfectly black (absorbing) or perfectly white (reflecting) substrate. According to Barron and Torrent (1986), for most experimental procedures, the sample has been assumed to be sufficiently thick so that no energy could penetrate through the sample into the substrate layer.

Quantitative DRIFT testing has been typically conducted using samples that were diluted with a reference material, and the KM function (Equation 7.1) has been used to relate the absorption and scattering behavior of a sample to the properties of the individual components (Equation 7.2). Due to the uniform behavior of Potassium Bromide (KBr) or Potassium Chloride (KCl), these strongly scattering, weakly absorbing materials (k values of approximately $4x10^{-4}cm^{-}$

[1]) have been previously utilized to assist in the characterization of opaque media. Therefore, for use in the testing soils, or in the testing of other strongly absorbing materials, the use of a sample with a low mass fraction of soil (e.g. a sample consisting mostly of KBr) has been shown to reduce error in the measured optical properties (Smith 2011). Because the sample scattering coefficient may be assumed to be dependent on the non-absorbing material for a sample with a low mass fraction of soil, the scattering of the KBr substrate [s_{KBr}] is equivalent to the scattering of the total sample.

The mass fraction of the sample material has been previously computed by using the sample absorption coefficient and the KM function (Equation 7.1 and Equation 7.2). Moreover, the utilization of the KM theory has allowed for the numerical transformation of a reflectance spectrum into a pseudo-absorption spectrum by using the relationship between reflectance, transmission, and absorption (Equation 7.3 and Equation 7.4). While the majority of previously performed research using DRIFT spectroscopy to measure soil parameters has been conducted on dry, dilute, ground samples, examples of testing being performed on intact soil samples (e.g. not diluted) can also be found in the literature (e.g. Nguyen et al. 1991, Yitagesu et al 2009).

$$f(R_\infty) = \frac{k}{s} = \frac{(1-R_\infty)^2}{2R_\infty}$$ (Barron and Torrent 1986) Equation 7.1

$$\frac{k}{s} = \sum_{i=1}^{n} \frac{k_i m_i}{s_i m_i}$$ (Barron and Torrent 1986) Equation 7.2

$$1 = R + A + T$$ (Workman and Weyer 2007) Equation 7.3

$$A_\infty = Log_{10}\left(\frac{1}{R_\infty}\right)$$ (Workman and Weyer 2007) Equation 7.4

In Equation 7.1 through Equation 7.4, $f(R_\infty)$ is the KM function, k is the absorption coefficient, s is the scattering coefficient, R_∞ is the infinite depth reflectance, m is the mass fraction, the i subscript indicates a given constituent value, R is relative reflection, A is the relative absorption, T is the relative transmission, and A_∞ is the simulated absorption.

7.6. Methods and Materials

The materials (soil and instruments) that were utilized, and the methods and procedures that were employed to acquire and process the measured data are described in this section. The three soil types that were investigated are described within Section 7.6.1. The sample preparation procedures are discussed within Section 7.6.2, and the UV-Vis and NIR spectroscopy instrumentation and the data collection process are discussed within Section 7.6.3. Finally, the data processing techniques and the equations utilized to determine the parameters of interest are detailed within Section 7.6.4.

7.6.1. *Soils Investigated*

Three different soils types were investigated:1) clay and silt sized particles of a manufactured nepheline syenite granite, identified by trade name as Donna Fill, as obtained from Little Rock, Arkansas; 2) clay and silt sized particles of a commercial kaolinite clay product, Kaowhite-S, as obtained from the Theile Kaolin company (Sandersonville, Georgia); and 3) clay and silt sized particles of an illite clay material, as obtained from a mining site operated by the Knighthawk Coal Company (Randolph County, Illinois). The aforementioned soils were selected due to the occurrence of non-expansive clays (kaolinite), expansive clays (illite), and artificial fill material (Donna Fill) within geotechnical engineering applications. Each of the bulk soil samples were oven dried at 105(+/-5)°C, mechanically ground, and sieved through a US standard number 200 sieve (0.075mm nominal opening size) to remove any sand sized or larger particles. The particle size distribution of each of the soil types was determined by using the hydrometer test (ASTM D422 2014). Likewise, the mineralogy for each soil was visually determined by using scanning electron microscopy (SEM), by using the x-ray diffraction (XRD) pattern, and by using traditional index testing (Atterberg Limits according to ASTM D4318 2014).

7.6.2. *Sample Preparation*

Spectroscopic grade (greater than 99 percent purity) anhydrous KBr material was obtained from Thermo Fisher Scientific (Waltham, Massachusetts). All of the soil types were then prepared using the same procedure that included by mixing the KBr material with various quantities of the dry bulk soil samples. Specifically, prior to preparing mixed samples, the Donna Fill, illite, kaolinite, and potassium bromide (KBr) materials were dried in an electronically controlled oven maintained at 105 (+/- 5)°C for 12 hours. After oven drying, the KBr material and the soil samples were maintained within a desiccator. After being removed from the desiccator, the dry soil and KBR materials were added together at various mass fractions to obtain mixed samples with 0 percent (15g KBr), 2 percent (0.3g soil and 15g KBr), 4 percent (0.6g soil and 15g KBr), and 6 percent (0.8g soil and 15g KBr) soil samples, as measured by dry weight. The number and dilution of each sample is tabulated in Table 7.1.

After mixing the soil with the KBr substrate material and prior to testing, each of the mixed samples (KBr with soil) were placed into a desiccator (210mm glass desiccator with a loose anhydrous calcium chlorite desiccant) for at least four hours. The mixed samples were also maintained within the desiccator before and after testing; specifically, a given mixed sample was only removed from the desiccator to place a given mixed sample into the 3.14cm^3 sample holder. Approximately 4.5g of mixed sample was placed into the 3.14cm^3 sample holder prior to each test. The mixed samples were air pluviated into the sample holder until the sample holder was full. Moreover, a well-rounded heap of material with a height of approximately 0.5cm (above the top of the sample holder) was placed in the sample holder using a dry, non-static, plastic funnel and the samples were loosely tamped using one blow from a 1.25cm steel dowel and struck off. If required, an additional amount of sample was added to the container, tamped once, and struck off

with a clean, straight-edged, steel spatula. The sample surface was struck-off to be flush with the top of the sample container. The flush surface was required to maintain a consistent spacing between the sample surface and the end of the fiber optic probe that was utilized to collect UV-NIR data. The fiber optic probe and the spectra collection process that utilized this probe are discussed in the next section.

Table 7.1. Sample materials reported as the mass fraction of soil and the mass fraction of KBr substrate material.

Number	Material	Percent KBr[1]	Percent Soil[1]	Number	Material	Percent KBr[1]	Percent Soil[1]
1	KBr	100	0	22	Donna Fill	94	6
2	KBr	100	0	23	Donna Fill	94	6
3	KBr	100	0	24	Donna Fill	94	6
4	Donna Fill	98	2	25	Illite	94	6
5	Donna Fill	98	2	26	Illite	94	6
6	Donna Fill	98	2	27	Illite	94	6
7	Illite	98	2	28	Kaolinite	94	6
8	Illite	98	2	29	Kaolinite	94	6
9	Illite	98	2	30	Kaolinite	94	6
10	Kaolinite	98	2	31	Donna Fill	0	100
11	Kaolinite	98	2	32	Donna Fill	0	100
12	Kaolinite	98	2	33	Donna Fill	0	100
13	Donna Fill	96	4	34	Illite	0	100
14	Donna Fill	96	4	35	Illite	0	100
15	Donna Fill	96	4	36	Illite	0	100
16	Illite	96	4	37	Kaolinite	0	100
17	Illite	96	4	38	Kaolinite	0	100
18	Illite	96	4	39	Kaolinite	0	100
19	Kaolinite	96	4	[1]Denotes the Percent Mass fraction of Each Component by Dry Weight			
20	Kaolinite	96	4				
21	Kaolinite	96	4				

7.6.3. *Spectra Collection Process*

An Ocean Optics USB-2000 ultraviolet visible (UV-Vis) spectrometer (350-1000nm) and a Nicolet 6700 Fourier Transform Infrared (FTIR) spectrometer (1000-2500nm) were utilized to collect the reflectance spectra for the previously described samples. The Nicolet FTIR spectrometer was employed to provide a white light illumination source for both UV-Vis and NIR spectrum collection. A dual purpose sample chamber was fabricated and employed to collect both

UV-Vis and NIR reflectance spectrum without causing disturbance to the given sample. A schematic of the sample chamber and the associated connections are presented in Figure 7.1.

Each mixed sample, located within the sample holder, was sequentially loaded into the sample chamber and was secured in position by using a metal dowel. The nitrogen (N_2) purge line was connected to the top of the sample chamber and the thermocouple probe was also inserted into the sample chamber. The fiber probe was then placed into the sample chamber; the elevation of the probe was controlled by adjusting a padded mechanical clamp that was attached to the fiber optic probe. Consistent positioning of the probe was verified by using a set of Vernier calipers to measure the position of the fiber optic probe relative to the top of the dual-purpose sample chamber.

The aforementioned fiber optic probe was connected to a duplex (transmit-receive) two ended fiber optic cable was utilized to: 1) transmit the energy from the white light source into the common sample chamber while also being utilized to 2) obtain the desired spectra. To obtain both UV-Vis and NIR spectra, the receiving end of the fiber optic cable was manually attached to either the Ocean Optics USB-2000 spectrometer or the Nicolet 6700 FTIR spectrometer, as required.

A Spectralon reference material (obtained from ASD-Panalytic of Boulder, Colorado) was utilized as a reflectance reference material. Two steel shims (76mm outside diameter, 62mm inner diameter, and 3mm thick) were utilized to position the surface of the Spectralon reference material so that the Spectralon was at the same distance from the fiber optic probe as the surface of the mixed specimens. All of the spectra were obtained by averaging 256 sequential independent spectra measurements.

The sample chamber was purged with dry nitrogen gas provided from a 3.5m^3 (125ft^3) ANSI/CGA C-7 gas cylinder (15MPa gauge pressure) through a CGA-580 two stage regulator and 0.635cm (1/4in) rigid plastic tubing. The regulator was set to provide a constant gauge pressure of approximately 100kPa. The rate of the flow of nitrogen into the sample chamber was controlled with a ball valve that was located between the regulator and the sample chamber. The purge gas flow was manually adjusted to maintain a small constant flow and positive pressure within the sample chamber to displace and prevent moisture contamination of the oven-dry soil samples during testing. Positive pressure was verified by manually obstructing the thermocouple port and tactilely determining an increase in pressure. After verification of positive pressure, the temperature inside of the sample chamber was recorded during testing by using a Sigma electronic thermocouple controller. Active control of the temperature was not performed during testing. The relative humidity within the room was also monitored using a digital hygrometer (HySkore Digital Hygrometer) located on the laboratory bench.

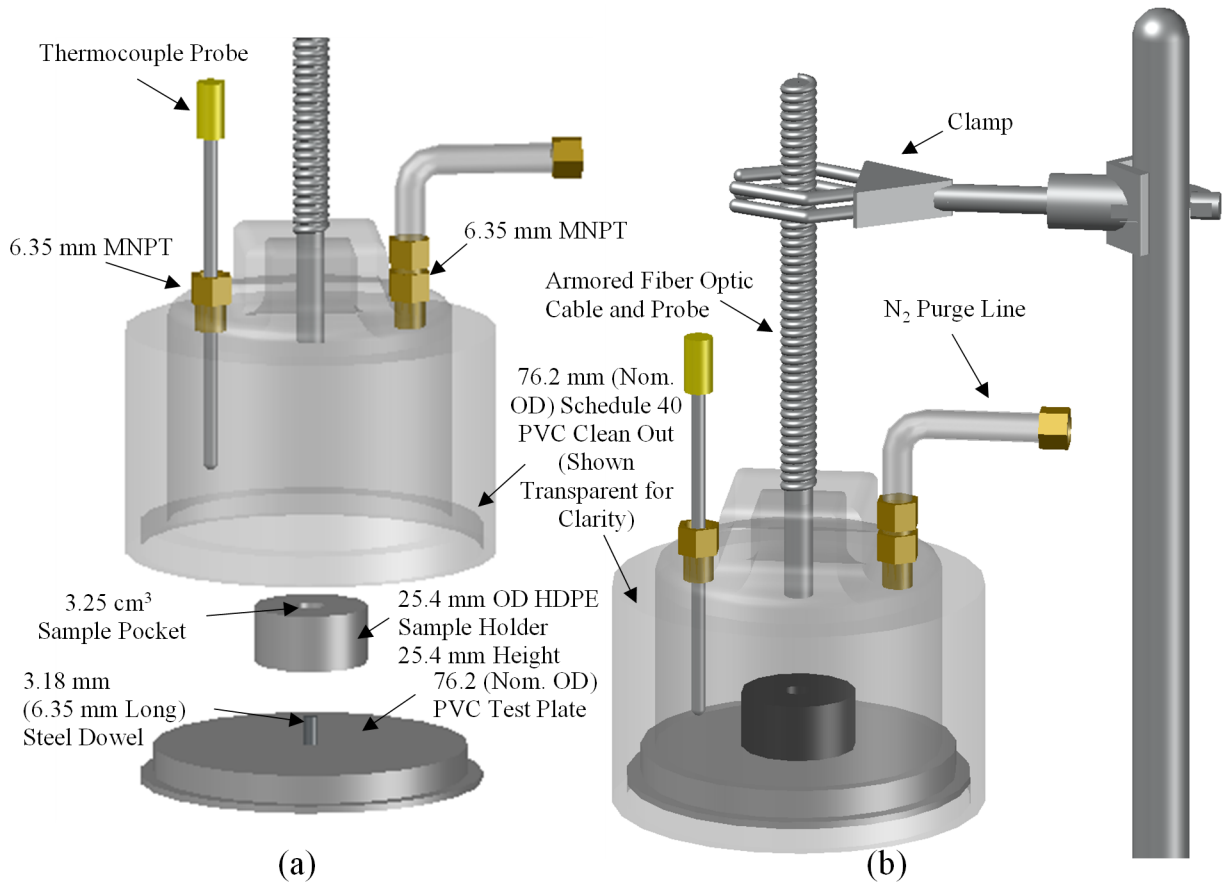

Figure 7.1. Schematic of the University of Arkansas dual purpose sample chamber as a) an isometric view of individual components, and b) an isometric view of the device when assembled for testing.

7.6.4. *Data Analysis – Spectra Collection and Coefficient Determination*

Data were collected as a raw digital numbers (350-1000nm) and as a reflection spectra (1000-2500nm). The OceanView software (Ocean Optics 2015) was utilized to collect the UV-Vis spectra, and the MATLAB software suite (Mathworks 2014) was utilized to preprocess the raw intensity values into reflectance spectra (by using a reference spectra that was previously obtained from the Spectralon sample). Conversely, the OMNIC software program (Nicolet 2004) was utilized to collect and preprocess the NIR spectra. Specifically, the reflectance spectra were processed within the OMNIC software suite (Nicolet 2004) by referencing a previously collected

Spectralon reflectance spectra. The data were then exported as tab or comma delimitated ASCII files and subsequently processed utilizing the MATLAB software suite (Mathworks 2014).

Two separate techniques were utilized to obtain measurements of the soil absorption coefficients within the UV-Vis and NIR range. For the pure KBr sample (0 percent soil and 100 percent KBr), the "infinite" depth reflectance (R_∞) was measured and the KM function $\left[(1-R_\infty)^2 \cdot (2R_\infty)^{-1}\right]$ was obtained. Then, the scattering coefficient (s_{KBr}) of KBr was calculated at 1nm resolution for all wavelengths (350-2500nm) by using Equation 7.5 and Equation 7.6, along with the Hakim et al. (2013) values of absorption for KBr for each of the UV-Vis and NIR wavelengths (350-2500nm). By utilizing the spectra obtained from the two percent soil samples at each 1nm wavelength values for all wavelengths, the previously calculated (s_{KBr})were then utilized to compute the absorption coefficient of each mixed soil from the spectra obtained from the two percent soil samples at each 1nm wavelength values (Equation 7.6).

Specifically, the calculation was performed using the two percent samples because it was assumed that the scattering coefficient of the combined mixture was dominated by the scattering behavior of the KBr substrate at low soil mass fractions (e.g. $m_{soil}\ s_{soil} \approx 0$ cm^{-1}). The scattering coefficients for each soil type (S_{soil}) were then obtained by using the pure (100 percent soil) soil samples (Equation 7.6). The soil absorption coefficient values (k_{soil}) were also directly computed by using the method proposed by Lindberg and Laude (1974) and Patterson et al. (1977) by rearranging Equation 7.6 (into Equation 7.7). A graphical overview of the workflow, that was utilized to obtain the various scattering and absorption coefficients, is presented as Figure 7.2.

$$KMF = \frac{m_{KBr}k_{KBr} + m_{soil}k_{soil}}{m_{KBr}s_{KBr} + m_{soil}s_{soil}} = \frac{(1-R_\infty)^2}{2R_\infty} \qquad \text{After Barron and Torrent (1986)} \qquad \text{Equation 7.5}$$

$$\frac{m_{KBr}k_{KBr}+m_{soil}k_{soil}}{m_{KBr}s_{KBr}+m_{soil}s_{soil}} \approx \frac{m_{KBr}k_{KBr}+m_{soil}k_{soil}}{m_{KBr}s_{KBr}}$$ After Barron and Torrent (1986) Equation 7.6

$$\frac{k_{soil}}{s_{KBr}} \approx \frac{1}{m_{soil}} \cdot \frac{k_t - m_{KBr}k_{KBr}}{s_{KBr}}$$ After Patterson et al. (1977) Equation 7.7

In Equation 7.5 through Equation 7.7, m_{KBr} is the mass fraction of KBr substrate, m_{soil} is the mass fraction of soil in a mixed sample, k_{KBr} is the absorption coefficient of the KBr substrate, k_{soil} is the absorption of the soil sample, s_{KBr} is the scattering coefficient of the KBr substrate, s_{soil} is the scattering coefficient of the soil sample, R_∞ is the infinite reflection, and k_t is the measured absorption of the mixed sample.

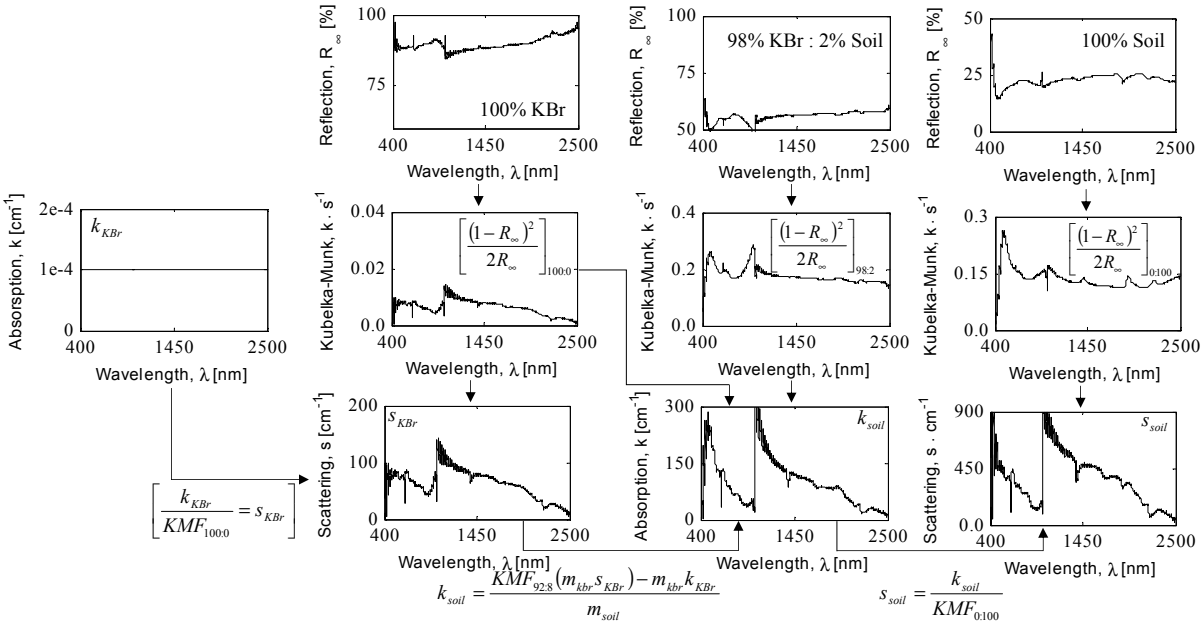

Figure 7.2. Graphical workflow for the computation of soil absorption values using literature absorption coefficient values for KBr and illite soil sample.

7.7. Results and Discussions

The results obtained from the traditional and optical characterization, of the three soil types that were investigated, are presented and discussed in this section. Specifically, the results of the traditional laboratory techniques are presented in Section 7.7.1; the results of the UV-Visible-NIR optical spectroscopy, including the raw reflectance spectra, and KM function are presented in Section 7.7.2; and the absorption spectra are presented in Section 7.7.3.

7.7.1. *Traditional Laboratory Characterization (Hydrometer and XRD)*

The silt fraction of the three soils was 91.14 percent, 53.53 percent, and 52.84 percent for Donna Fill, illite, and kaolinite, respectively. Similarly, the clay fraction was 8.86 percent, 46.47 percent, 47.16 percent, for Donna Fill, illite, and kaolinite soils, respectively. The particle size distributions and XRD results for each soil are presented in Figure 7.3. Utilizing the XRD data (Figure 7.3b), the clay mineralogy for the Donna Fill, illite, and kaolinite material was experimentally determined using XRD.

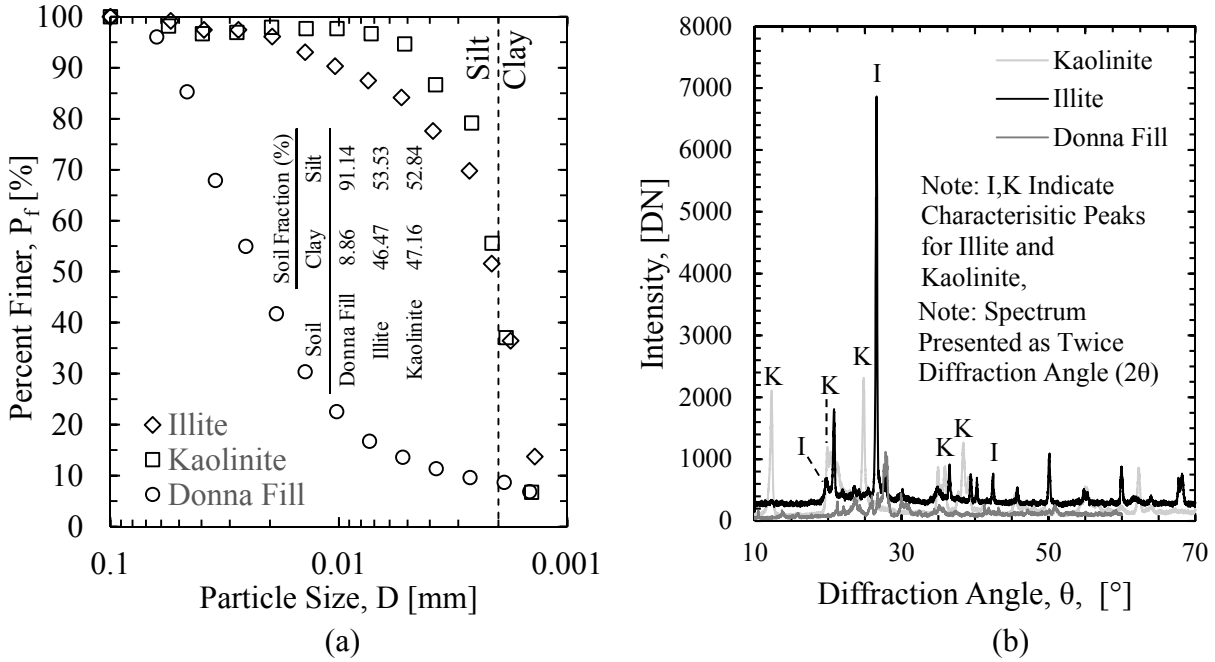

Figure 7.3. a) Soil particle distribution as determined by using ASTM D422 (2014), and b) XRD pattern for each soil type.

Specifically, the acquired XRD spectrum were qualitatively compared to kaolinite and illite peaks within other XRD spectra that have been reported in the literature (Reynolds 1992, Moore and Reynolds 1997) to identify the soil types. The characteristic spectral peaks match those reported in the previously mentioned literature. Moreover, the results from traditional index testing and SEM images, as presented in Figure 7.4, were also utilized to qualitatively

characterize the soil mineralogy. The Donna Fill and kaolinite soils both characterized as low plasticity silts (ML) while the illite soil classified as low plasticity clay (CL).

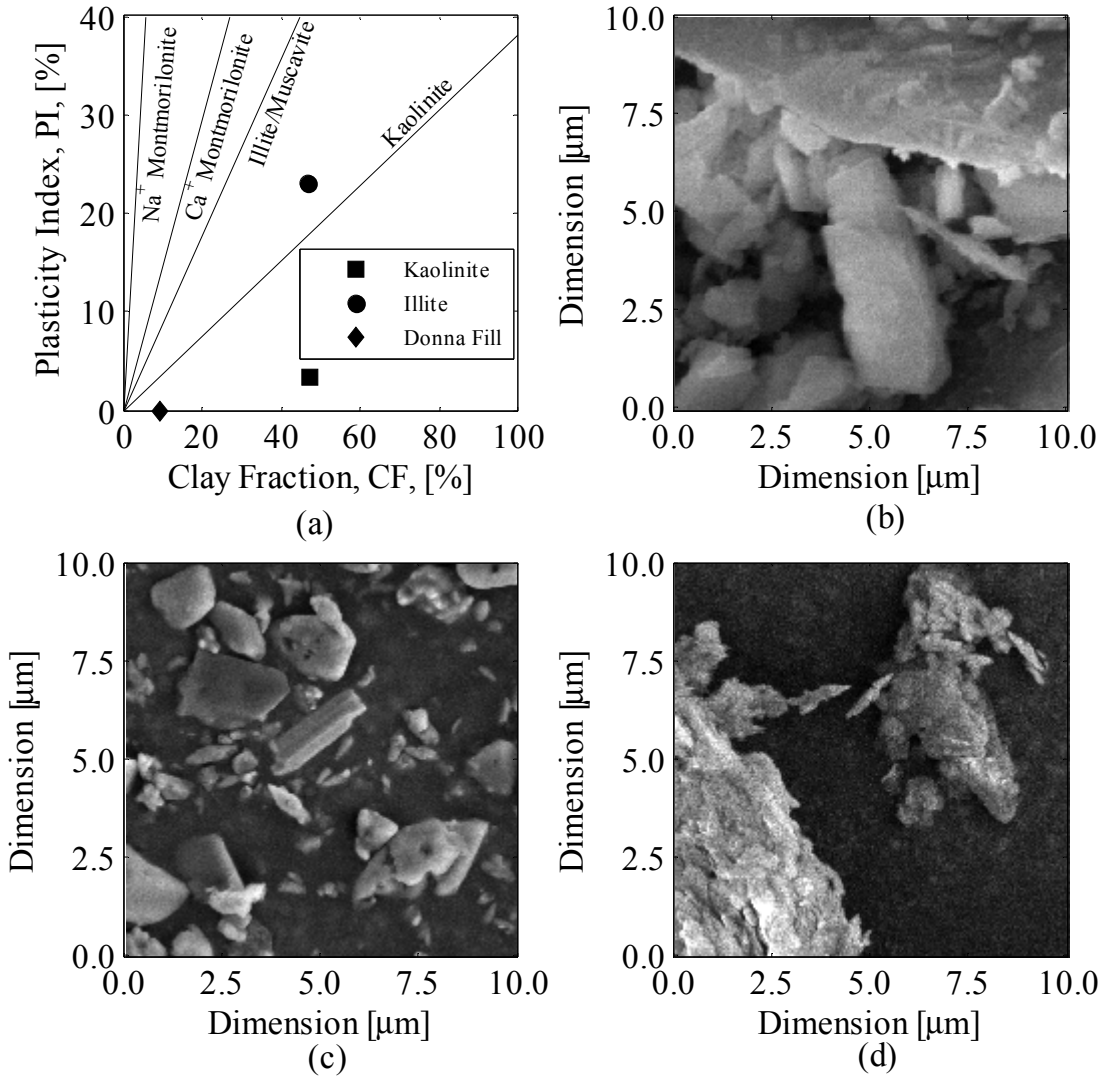

Figure 7.4. Soil mineralogy as obtained using a) traditional index testing (chart based on Terzaghi et al. 1996) and SEM microscopy for b) Donna Fill, c) Illite, and d) Kaolinite.

7.7.2. *Optical Characterization of Investigated Soil (Reflection Spectra and Kubelka-Munk)*

For all three of the types of soil that were investigated, the value of the reflectance ratio for the soil ranged between 0.48 and 0.90. Examples of the recorded reflectance ratio (relative to the reflectance from the Spectralon reference material) for mixed samples (two percent mass fraction) for Donna Fill, illite, and kaolinite are presented as Figure 7.5. As expected, the (100

percent) KBr material was the most efficient reflector over the entire range of UV-NIR wavelengths. The white kaolinite powder was also an efficient reflector. Consistent reflectance spectra between the UV-Vis and NIR spectra were obtained for the KBR/illite and KBR/kaolinite materials. However, for the KBr/Donna Fill mixture there was a discontinuity in the spectra at the sensor transition (UV-Vis to NIR). This transition artifact is expected to be attributable to the reduced sensitivity of the Ocean Optics charge-coupled device (CCD) near the 1000nm (wavelength).

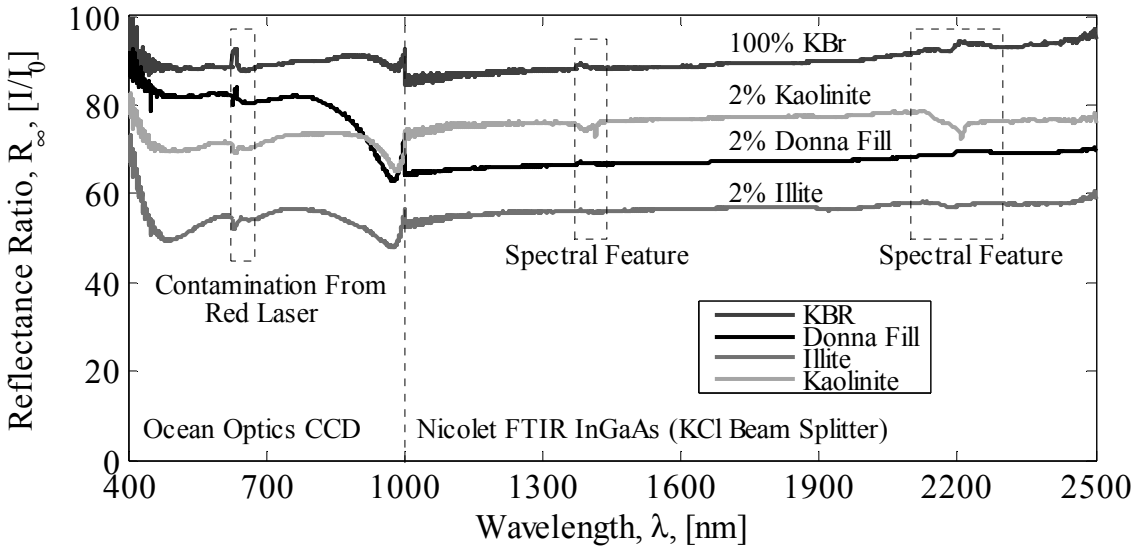

Figure 7.5. Reflectance ratio for KBr substrate material (100 percent KBr) and two percent mass fractions samples of Donna fill illite, and kaolinite (98 percent KBr : 2 percent soil).

Spectral artifacts appeared within the collected spectra for all four materials at approximately 1425 and 2250nm. As described in Rossel et al. 2010b, these spectral artifacts corresponded to the hydroxyl absorption features. Additionally, the white light source for the Nicolet 6700 FTIR instrument utilized a red laser (center frequency of 650nm) that induced anomalous data within the 635 and 675nm range.

7.7.3. *Absorption Spectrum of Investigated Soil Types*

The absorption spectrum were calculated using: 1) the methods proposed by Patterson et al. (1977), and 2) KBr absorption value from Hakim et al. (2013). The spectra for the Donna Fill, illite, and kaolinite soils are presented graphically within Figure 7.6, Figure 7.7, and Figure 7.8, respectively. As observed in Figure 7.6, for each of the mass ratios (2 percent, 4 percent, and 6 percent soil samples), the absorptions spectra that were computed using the various techniques can not be separated by visual inspection of the data. However, the average percent error between the two methods using the Patterson et al. (1977) equation and using the Hakim et al. (2013) absorption value was 41.1, 11.2, 8.9, and 4.8 percent wavelength values within the ranges of 400-600nm (Violet to Green), 800-1000nm (Low NIR, IR-A band), 1000-500nm (High NIR, IR-A Band), and 1500-2500nm (shortwave IR, IR-B band), respectively. From the observed error the agreement between the two methods increases as the wavelengths increased. Spectral features were observed at 1375nm and 2250nm for kaolinite and illite soils. It was expected that a strong absorption feature would be expected at 2250nm due to the high iron content in the Donna Fill material (as reported in White and Keester 1966). However, this spectral feature at 2250nm was not observed in any of the tested samples.

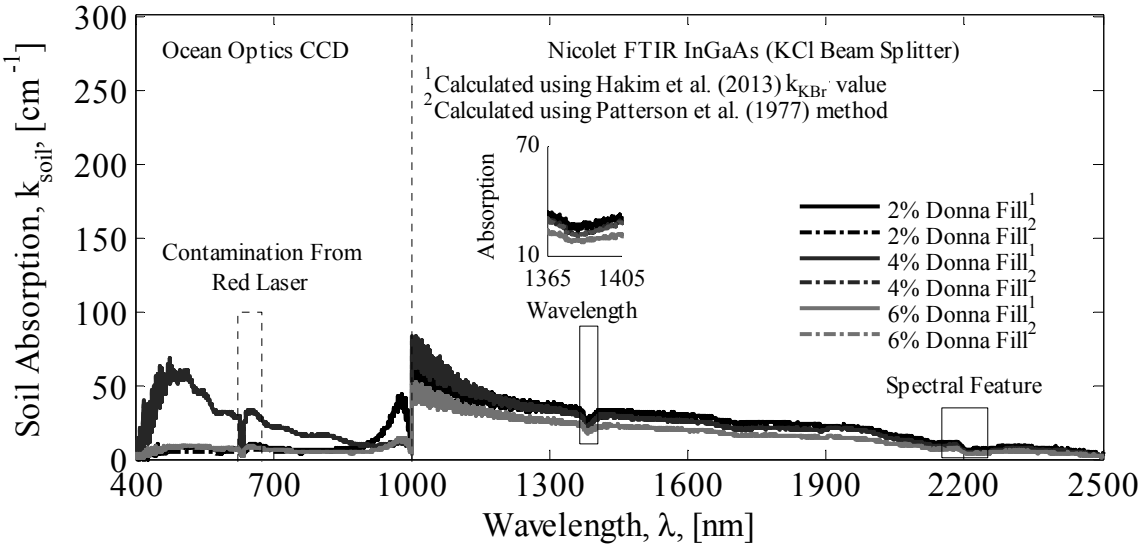

Figure 7.6. Computed absorption coefficient for Donna Fill material as determined using the procedure presented in Paterson et al. (1977), and as determined using the KBr absorption values.

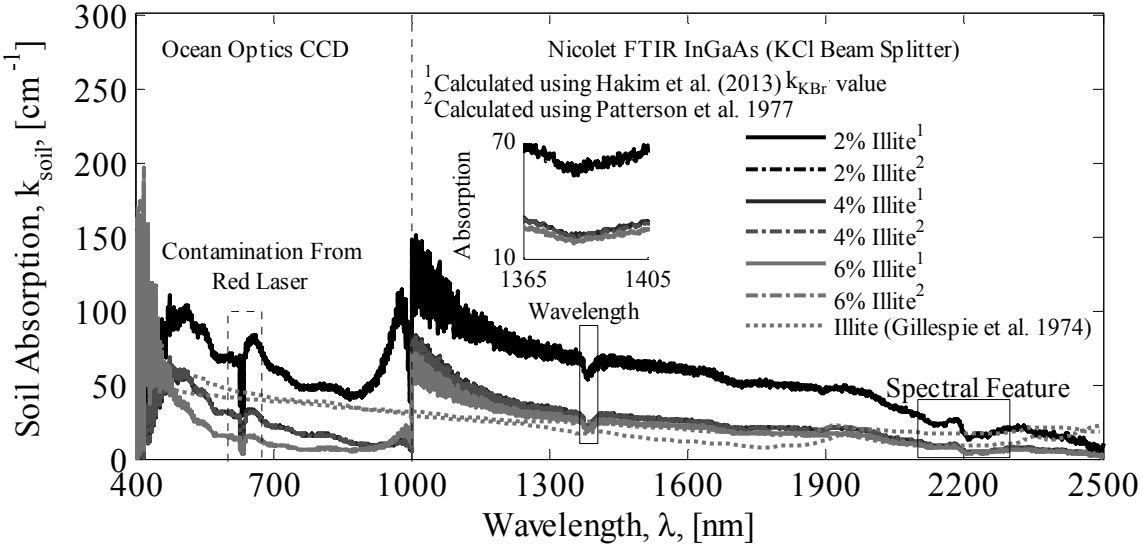

Figure 7.7. Computed absorption coefficient for illite material as determined using the procedure presented in Paterson et al. (1977), and as determined using KBr absorption value.

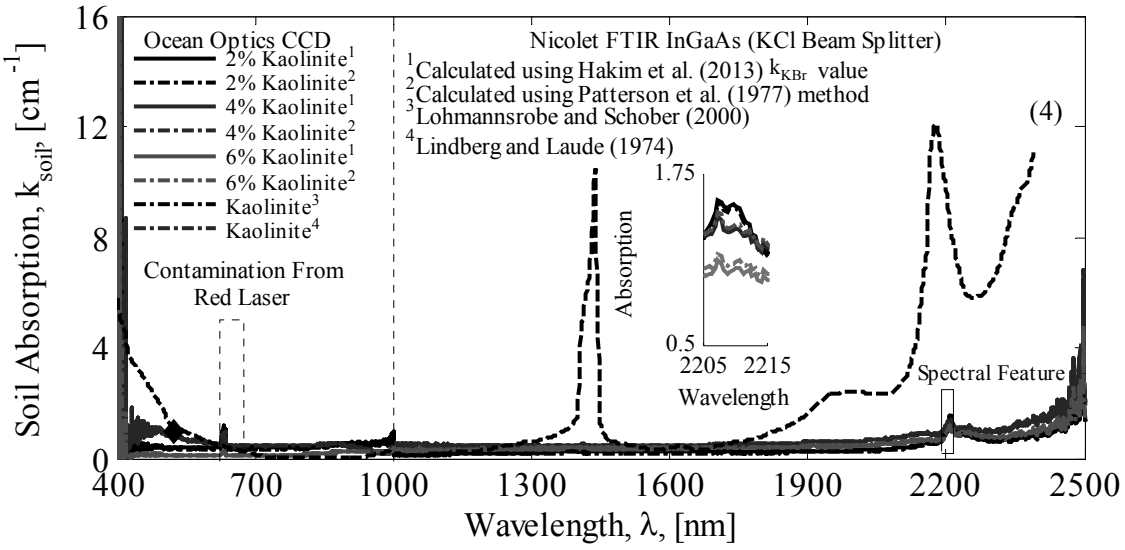

Figure 7.8. Computed absorption coefficient for kaolinite material as determined using the procedure presented in Paterson et al. (1977), and as determined using KBr absorption values (note different vertical scale from Figure 7.6 and Figure 7.7).

A visual agreement between the two methods was observed for the two calculated absorption spectra values (using the Patterson et al. 1977 method and using the Hakim et al. 2013 KBr absorption values with the measured data) for the illite material (as previously shown in Figure 7.8), especially within both the UV-Vis and NIR wavelength ranges. The average percent error between the two calculated absorption spectrum values was 1.6 percent, 0.6 percent, 3.3 percent, and 1.2 percent for wavelength values within the ranges of 400-600nm, 800-1000nm, and 1000-1500nm, and 1500-2500nm, respectively. The measured absorption spectrum values for the two percent spectrum were approximately twice the numeric value reported in Gillespie et al. (1974) for the absorption spectrum for two illite soils except at wavelength values between 2200nm and 2500nm. However, the calculated values for the absorption spectrum obtained from the four percent and six percent samples were numerically closer to the Gillespie et al. (1974) results. Furthermore, the two calculated spectrum (as calculated using the Patterson et al. (1977)

method or using the Hakim et al. (2013) KBr absorption values) are of similar shape, and spectral artifacts at wavelength values of 1375nm and 2250nm are found in both spectra.

The computed kaolinite absorption spectrum are indistinguishable for UV-Vis wavelengths. The average percent error between the two calculated absorption spectra (as obtained using the Patterson et al. 2013 and the Hakim et al. 2013 value of KBr absorption and the measured data) was 10.4 percent, 7.7 percent, 21.7 percent, and 13.7 percent for wavelength ranges of 400-600nm, 800-1000nm, and 1000-1500nm, and 1500-2500nm, respectively. When compared to literature obtained values for the absorption coefficient for kaolinite (as obtained from Lindberg and Laude 1974), the computed absorption values were numerically greater for UV-VIS (350-650nm) and SWIR (greater than 1700nm) wavelengths, and numerically less for NIR wavelengths (650-1350nm). The computed absorption spectrum was approximately $0.60cm^{-1}$ less than the value reported in Lohmannsroben and Schober (2000) at 523nm.

Some of the discrepancy between the Lindberg and Laude (1974) values and the obtained solutions at low wavelength values (less than 400nm) may be an artifact of 1) the low intensity of the illumination source, and of 2) the low sensitivity of the UV-Vis spectrometer at such wavelengths. Furthermore, the large absorption feature at approximately 1425nm that was reported by Lindberg and Laude (1974) was not observed for the soils that were investigated as part of the study. Furthermore, the Lindberg and Laude (1974) values of absorption were larger than the measured values for wavelength values greater than 1600nm. Included in this wavelength range is an absorption peak at 2100nm. A similar peak, albeit 10 percent of the magnitude reported by Lindberg and Laude (1974), and at a wavelength of 2200nm instead of 2100nm, was observed in the recorded data. There was also an increase in the measured and literature absorption spectra at wavelength values between 2200nm and 2500nm; the literature obtained

values were 10 times the measured values. The reduced magnitude of the absorption features within the measured kaolinite spectra (and other soils), as compared to the literature obtained samples, may be an artifact of the use of loose (not pressed) KBr samples.

Due to limitations in the illumination source and the sensitivity of the Ocean Optics USB-2000 CCD sensor, there was increased noise observed in the reflectance spectra, for all three soils, within the Vis-NIR range (below 400nm and again above 900nm). The sensitivity of the CCD sensor was approximately two percent of the peak value at the transition wavelength (1000nm). It is theorized that it may be necessary to average results between 900 and 1100nm to reduce the effects of the transition between the sensors. However, this averaging will mask any spectral features in this area. Conversely, it may be possible to calibrate the results in the transition zone by using the Spectralon reference material (a material of known reflectance spectrum).

7.8. Conclusions

Two separate methods of obtaining the absorption spectra, for three different types of soil that may be encountered in geotechnical practice (non-expansive clay, expansive clay, and an artificial fill material), were presented and evaluated. The obtained results may be used as a general reference of absorption spectrum for the soil types that were investigated. Furthermore, the procedures described herein may be used to obtain specific soil absorption spectrum for additional soil types.

For the instrumentation and methods that were employed, the best results (lowest average percent error) were obtained within the NIR wavelength range ($\lambda > 1100$nm) by using the Nicolet FTIR instrument. The best results (lowest divergence in absorption values between the values that were calculated using the Patterson et al. (1977) method and the absorption values that were calculations by using the Hakim et al. 2014 values for k_{KBr}) was observed for the illite soil at

wavelengths between 800 and 1000nm. The measured absorption spectrum for illite and kaolinite were compared to spectra presented by Gillespie et al. (1974) and Lindberg and Laude (1974), respectively. The measured spectrum were found to be within one order of magnitude of the literature spectra except for the absorption feature that was reported by Lindberg and Laude (1974) to occur between 1400 and 1500nm.

7.9. Works Cited

American Society for Testing and Materials (ASTM) D422, (2014). "Standard Test Method for Particle-Size Analysis of Soils." American Society for Testing and Materials, Vol. 4.08, Soil and Rock (I). West Conshohocken, PA.

American Society for Testing and Materials (ASTM) D854, (2014). "Standard Test Methods for Specific Gravity of Soil Solids by Water Pycnometer." American Society for Testing and Materials, Vol. 4.08, Soil and Rock (I). West Conshohocken, PA.

American Society for Testing and Materials D4318, (2014). "Standard Test Methods for Liquid Limit, Plastic Limit, and Plasticity of Soils." Annual Book of ASTM Standards, Designation D4318, Vol. 4.08, ASTM, West Conshohocken, PA.

Barron, V., Torrent, J., (1986). "Use of the Kubelka-Munk Theory to Study the Influence of Iron Oxides on Soil Colour." Journal of Soil Science, Vol. 37, pp. 499-510.

Busca, G., Resini, C., (2000). "Vibrational Spectroscopy for the Analysis of Geological and Inorganic Materials." Encyclopedia of Analytical Chemistry, Vol. 12, pp. 10984-11020.

Farmer, V., (ed.), (1974). "Infrared Spectra of Minerals." Mineralogical Society. London.

Garner, C., Coffman, R., (2017b). "Visible and Near-Infrared Diffuse Reflectance Properties of Geotechnical Reference Soils" Applied Clay Science (Submitted for Review).

Gillespie, J., Lindberg, J., Smith, M., (1974). "Visible and Near-Infrared Absorption Coefficients of Montmorillonite and Related Clays." American Mineralogist, Vol. 59, pp. 1113-1116.

Hakim, H., Hashim, A., Abdul-Hafidh, G., Alyaa, H., Mohammed, S., (2013). "Study [of] the Optical Properties of Polyvinylpyrrolidone (PVP) Doped with KBr." European Scientific Journal, Vol. 3, pp. 132-137.

Judd, D., Wyszecki, G., (1975). "Color in Business, Science, and Industry." John Wiley and Sons, New York.

Kubelka, P., (1947). "New Contributions to the Optics of Intensely Light-Scattering Materials, Part I." Journal of the Optical Society of America, Vol. 38, Number 5, pp. 448-457.

Kubelka, P., Munk, F., (1931). "Ein Beitragzur Optik der Farbanstriche." (in German), Z. Technol. Physics., Vol. 12, pp. 593-620.

Lindberg, J., Laude, L., (1974). "Measurement of the Absorption Coefficient of Atmospheric Dust." Applied Optics, Vol. 13, pp. 1923-1927.

Lohmannsroben, H., Schober, L., (2000). “Determination of Optical Parameter for Light Penetration in Particulate Materials and Soil with Diffuse Reflectance (DR) Spectroscopy.” Journal of Environmental Monitoring, Vol. 2, pp. 17-22.

Mathworks, (2014a). “The MATLAB R2014A Programming Suite and Supporting Documentation.” The Mathworks Corporation, Natick, Massachusetts.

Moore, D., Reynolds, R., (1997). “X-Ray Diffraction and the Identification and Analysis of Clays Minerals.” Oxford University Press, Oxford, New York.

Nguyen, T., Janik, L., Raupach, M., (1991). “Diffuse Reflectance Infrared Fourier Transform (DRIFT) Spectroscopy in Soil Studies.” Australian Journal of Soil Research Vol. 29, pp. 49-67.

Nicolet, (2004). “Nicolet FT-IR User’s Guide.” Nicolet 6700 Fourier Transform Infrared Spectrometer User’s Manual and Supporting Documentation. http://mmrc.caltech.edu/FTIR/Nicolet/Nicolet%20Software/Nicolet%202/4700_6700_User.pdf. Retrieved September 2014.

Ocean Optics, (2015). “OceanView 1.5 Software and Supporting Documentation.” http://oceanoptics.com/product-catagory/software/. Retrieved May 2015.

Patterson, E., Gillete, D., Stockton, B., (1977). “Complex Index of Refraction between 300 and 700nm for Saharan Aerosols." Journal of Geophysical Research, Vol. 82, No. 21, pp. 3153-3160.

Reynolds, R., (1992). “X-Ray Diffraction Studies of Illite/Smectite from Rocks, <1 μm Randomly Oriented Powders, and <1 μm Oriented Powder Aggregates: The Absence of Laboratory-Induced Artifacts.” Clays and Clay Minerals, Vol. 40, No. 4, pp. 387-396.

Rossel, R., McBratney, A., Minasny, B., (eds.), (2010a). “Proximal Soil Sensing. Volume 1 of Progress in Soil Science.” Springer Science and Business Media. Springer, New York.

Rossel, R., Rizzo, R., Dematte, J., Behrens, T., (2010b). “Spatial Modeling of a Soil Fertility Index Using Visible-Near-Infrared Spectra and Terrain Attributes.” Soil Science of America Journal, Vol. 74, Issue 4, pp. 1293-1300.

Schroeder, P., (2002). “Infrared Spectroscopy in Clay Science.” In Teaching Clay Science, Guggenheim, S., Rule, A., (eds.). Clay Minerals Society Workshop Series. The Clay Mineral Society, Aurora, Colorado Vol. 13, pp. 181-202.

Smith, B., (2011). “Fundamentals of Fourier Transform Infrared Spectroscopy.” 2 ed., CRC Press, Taylor and Francis, Boca Raton, Florida.

Stuart, B., (2004). “Infrared Spectroscopy: Fundamentals and Applications.” John Wiley and Sons. ISBN 0-470-85427-8.

Terzaghi, K., Peck, R., Mesri, G., (1996). “Soil Mechanics in Engineering Practice.” 3 ed., John Wiley and Sons, New York, New York.

Waruru, B., Shepherd, K., Ndegwa, G., Kamoni, P., Sila, A., (2014). “Rapid Estimation of Soil Engineering Properties Using Diffuse Reflectance Near Infrared Spectroscopy.” Journal of Biosystems Engineering, Vol. 121, pp. 177-185.

White, W., Keester, K., (1966). “Optical Absorption Spectra of Iron in the Rock-Forming Silicates.” The American Mineralogist, Vol. 51, pp. 774-791.

Workman, J., Weyer, L., (2007). “Practical Guide to Interpretive Near-Infrared Spectroscopy.” Taylor and Francis Group. Boca Raton, Florida.

Yitagesu, F., van der Meer, F., van der Werff, H., Zigterman, W., (2009). “Quantifying Engineering Parameters of Expansive Soils from Their Reflectance Spectra.” Engineering Geology, Vol. 105, Issue 3-4, pp. 151-160.

CHAPTER 8: INDEX AND HYDRAULIC PROPERTIES OF SOIL USING VISIBLE-THROUGH NEAR-INFRARED SPECTROSCOPY

8.1. Chapter Overview

The methodology and results that were developed in regard to non-destructive, proximal, measurements of 1) soil hydraulic properties (volumetric water content and soil matric potential), and 2) soil index properties (liquid limit, plastic limit, and clay fraction) are described in this chapter. Visible- through near-infrared (Vis-NIR) reflectance spectroscopy was employed to obtain spectral data for 1) oven dry, ground, soil, and for 2) partially saturated soil samples. The suitability of analytical solutions that relate volumetric water content and soil water potential, based on reflectance data, to the observed spectral data, were evaluated using the Kubelka-Munk reflectance theory (Kubelka and Munk 1931, Kubelka 1947). Traditional laboratory testing measurements of: liquid limit (LL), plastic limit (PL), clay fraction (CF), volumetric water content (θ_v), and matric potential (ψ_m) were also utilized to calibrate and validate the obtained empirical relationships between the measured spectral data and the aforementioned engineering properties.

The chapter overview and title (Sections 8.1 and 8.2, respectively), and the abstract and introduction (Sections 8.3 and Section 8.4, respectively) for the included manuscript (Garner et al. 2017) are presented herein. A review of the existing methods for Vis-NIR reflectance spectroscopy, within soil science, is presented in Section 8.5. The methods and materials that were used to: prepare the soil samples, conduct traditional laboratory testing, acquire spectral data, process spectral data, calibrate empirical regressions, and validate the aforementioned regressions, are presented in Section 8.6. The results obtained from this research are presented in Section 8.7. The conclusions, recommendations, and avenues for further research in proximal and remote sensing for partially saturated soil applications are presented in Section 8.8.

The full citation for this document is: *Garner, C., Salazar, S., Coffman, R., (2017). "Index and Hydraulic Properties of Soil Using Visible-Through Near-Infrared Spectroscopy." Soil Science (in Review).*

8.2. Index and Hydraulic Properties of Soil Using Visible-through Near-Infrared Spectroscopy

Cyrus D. Garner, MSCE, EIT[1], Sean E. Salazar, EIT[1], and Richard A. Coffman, PhD, PE, PLS[2]

[1]Doctoral Student, Department of Civil Engineering, University of Arkansas at Fayetteville, USA.
[2]Associate Professor, Department of Civil Engineering, University of Arkansas at Fayetteville, USA.

8.3. Abstract

The use of Vis-NIR spectroscopy was evaluated for obtaining rapid, non-destructive, measurements of volumetric water content (θ_v), soil water potential (ψ_m), liquid limit (LL), plastic limit (PL), and clay fraction (CF) for various types of soils. Three silt and clay sized soils (Donna Fill, illite, and kaolinite) were characterized using traditional testing techniques and Vis-NIR reflectance spectroscopy. Closed-form reflectance algorithms were utilized to predict the θ_v and ψ_m values based on the measured spectra. Two empirical regression techniques, partial least squares (PLS) and principle components regression (PCR), were then utilized to create empirical relationships between the observed reflectance spectra and the engineering properties (θ_v, ψ_m, LL, PL, and CF) by using calibration and validation data sets.

Soil samples were prepared using a slurry consolidometer and then a pressure plate extractor. Vis-NIR spectroscopy was then performed on those samples. Additionally, oven-dried, and ground bulk material that was used to prepare the Vis-NIR samples were also used to prepare samples for index property testing only (LL, PL, and CF). For all three soil types the analytical (closed-form) solutions did not provide usable data (the computed relative humidity values were greater than 100 percent). Soil specific regressions (e.g. calibration and validation data sets

containing only one type of soil data) were developed for the θ_v and ψ_m measurements. Conversely, for the LL, PL, and CF measurements, non-soil specific regressions were developed. The soil specific PLS regressions yielded coefficient of determination (R^2) values of 0.81, 0.75, 0.91, and 0.52 for Donna Fill θ_v, Donna Fill ψ_m, illite θ_v, and illite ψ_m, respectively. For the silt and clay sized kaolinite material, neither PLS or PCR regressions yielded usable θ_v or ψ_m measurements (R^2 value less than 0.10) due to the formation of a surface film prior to the acquisition of spectral data. For the soil index properties, R^2 values greater than 0.90 were obtained for the LL, PL, and CF regressions for all of the soil types.

8.4. Introduction

The hydraulic properties of soils include important variables (θ_v and ψ_m) that are used in engineering, geological, and agricultural applications. In addition, the index properties (LL, PL, PI, CF) of soils are often used to estimate the engineering properties. As described herein, optical reflectance spectroscopy may be employed to estimate both hydraulic properties and soil index properties by utilizing a rapid, non-destructive, technique. Advantages of reflectance spectroscopy over traditional measurements techniques include 1) decreased testing time and 2) non-destructive testing (i.e. samples may be reused for multiple tests).

Previous researchers (Park 1980, Philpot 2010, Rossel et al. 2010a) have demonstrated the use of visible-and near-infrared (Vis-NIR) spectroscopy for quantification of soil volumetric water content and soil index properties (Section 8.5). However, the remote measurement of soil matric potential has not been previously documented. Both analytical (Kubelka-Munk and Beer-Lambert) methods and empirical methods (partial least squares regression) were evaluated to obtain remote measurements of the soil matric potential for various types of soils. The suitability of utilizing Vis-NIR spectroscopy for the measurement of hydraulic and index properties was

investigated and is documented herein. Vis-NIR and middle infrared (MIR) spectra (Vis-NIR-Dry and MIR-Dry) were collected on ground, oven dry, soil. Vis-NIR spectra (Vis-NIR-Wet) were collected on intact, moist, soil. The reflectance, hydraulic, and index properties of the three separate silty soil types were evaluated. The experimental methodology and data processing techniques that were utilized are documented in Section 8.6. The results generated from the analytical and empirical techniques are discussed in Section 8.7.

8.5. Review of Existing Methods

Coupled measurements of matric potential and volumetric water content have historically been used to experimentally establish a relationship between the two variables. The experimentally obtained soil water characteristic data is often used in conjunction with mathematical models (Brooks and Correy 1964, van Genuchten 1980) to develop the soil water characteristic curve (SWCC). The use of mathematical models to develop the SWCC has allowed practitioners to extend experimentally-derived, coupled, soil hydraulic information (θ_v, ψ_m) to predict the entire range of soil volumetric water content values (residual volumetric water content to saturated volumetric water content). Typically, experimentally-derived, coupled, soil-water data is used to numerically fit the mathematical model. Several commercial computer software programs are available (including RETC) to fit a mathematical SWCC model to experimentally-derived data.

Typical methods of obtaining coupled volumetric water content and soil water potential measurements include laboratory-based techniques such as the chilled mirror hygrometer (Neumann and Thurtell 1972, Campbell et al. 1973), the pressure plate extractor (Richards 1941, Richards 1948), the Tempe cell (Reginato and van Bavel 1962), and the transient-release and imbibition method (Wayllace and Lu 2012). These laboratory-based techniques have always

required some degree of sample disturbance due to recovery, transport, and storage of the sample from the field to the laboratory. *In situ* instrumentation has been used to determine the volumetric water content and the soil water potential. These *in situ* techniques have included tensiometers, heat dissipation sensors (Phene et al. 1971, Reece 1996), gypsum block sensors, resistivity sensors, and time domain reflectometry (Nemmers 1998, Evett 2003).

Usually only one component of the SWCC (e.g. either soil water potential or soil water content, but not both) is obtained from the laboratory methods or the *in situ* measurements. A secondary measurement is therefore required to obtain the complete soil water characteristic curve relationship. However, according to ASTM D6836 (2014), the soil water content must be obtained gravimetrically (e.g. ASTM D2216 2014) for many of the aforementioned techniques (chilled mirror hygrometer, pressure plate extractor, and Tempe cell) and then the soil volumetric water content must be computed by using phase relationships. The aforementioned gravimetric water content test (ASTM D2216 2014) is a destructive test and results in an inability to reuse samples for additional testing.

For many years, Atterberg limit values have been used by geotechnical engineers to derive engineering design parameters in the absence of direct measurements (Wroth and Wood 1978, Kulhawy and Mayne 1990). For instance, the liquid limit (LL) and the plastic limit (PL) values have been used to provide an estimate for the: coefficient of consolidation (Skempton 1944), permeability (Carrier and Beckman 1984), normalized void ratio (Morris et al. 2000), and shear strength (Skempton and Northey 1953, Wroth and Wood 1978, Youssef et al. 1965) of soils. However, the use of traditional laboratory testing techniques to determine index properties are destructive and time consuming. Another disadvantage associated with the use of engineering values derived from index properties is that the LL and PL tests, in particular, have been reported

to be poorly repeatable (Casagrande 1958, Wroth and Wood 1978, Shepard and Walsh 2002, Waruru et al. 2014).

The Vis-NIR (wavelengths 400nm to 2500nm) reflectance technique has been employed in agricultural, biological, ecological, and geological research. However, the use of this technique has not yet been largely adopted by design professionals within the transportation, geotechnical, or geo-environmental engineering fields. Remotely-sensed soil properties have included: water content (Park 1980, Philpot 2010), pH (Janik et al. 1995, Chang et al. 2001, Shibusawa et al. 2001, Islam et al. 2003, Kodaira and Shibusawa 2013), clay content (Wroth and Wood 1978, Janik et al. 1995, Ben-Dor and Banin 1995, Chang et al. 2001, Shibusawa et al. 2001, Walvoort and McBratney 2001), sand content (Janik et al. 1995, Chang et al. 2001, Islam et al. 2003), silt content (Wroth and Wood 1978, Janik et al. 1995, Chang et al. 2001, Islam et al. 2003), and index properties (Yitagesu et al. 2009, Waruru et al. 2014). In addition to the use of Vis-NIR spectroscopy data, the MIR (2500nm to 25000nm) spectroscopy technique has also been evaluated by previous researchers (Shepard and Walsh 2002, McCarty et al. 2002). Most of the Vis-NIR and MIR testing previously conducted has been performed on dry, ground, samples. The use of this type of sample (dry, ground) has resulted in testing methods that prevent the samples from being reused for additional testing. Limited research results have been reported which included soils with variable moisture content values (Park 1980, Walvoort and McBratney 2001, Nocita et al. 2013) and variable soil structure (Shibusawa et al. 2001, Goetz et al. 2001, Chabrillat et al. 2002, Goetz et al. 2006, Kodaira and Shibusawa 2013).

The Kubelka-Munk transformation (Kubelka and Munk 1931, Kubelka 1947) and a simulated absorption spectrum (Beer-Lambert) have been employed to solve analytical solutions for soil composition based on reflectance spectroscopy (Richardson et al. 1975, Barron and

Torrent 1986, Torrent and Barron 1993). Richardson et al. (1975) reported the use of the Kubelka-Munk transformation to extract the reflectance components of soil from images of agricultural crops. Likewise, the technique documented in Barron and Torrent (1986) employed the Kubelka-Munk theory to extract an analytical measurement of iron oxides in soil. The use of the Kubelka-Munk technique and the associated testing to develop the absorption and scattering techniques is additionally documented in Garner and Coffman (2017b).

The partial least squares (PLS) and principle component analysis regression (PCR) have been widely employed to extract various soil properties from reflectance spectra (de Jong 1993, Wold et al. 2001, Rosipal and Kramer 2006). Specifically, these multivariate techniques were well suited to correlate spectral data sets with the desired parameters. The PLS technique, in particular, has been previously employed for reflectance spectroscopy studies on soil (Shepherd and Walsh 2002).

8.6. Methods and Materials

8.6.1. *Soil Types Investigated*

Three different soil types were investigated using traditional laboratory, Vis-NIR, and MIR techniques. These soil types included: 1) a commercial kaolinite product ("Kaowhite-S") that was obtained from the Thiele Kaolin Company of Sandersonville, Georgia; 2) an illite that was obtained from the Blackhawk Coal Mine (Randolph County, Illinois); and 3) an artificial nepheline syenite granite that was obtained from the Donna Fill Company (Little Rock, Arkansas). The bulk soil samples were placed in a temperature controlled oven (105°C +/- 5°C) until dry, then mechanically ground. The oven-dried, ground, soil was then sieved to remove any sand-sized particles. Individual test samples were subsequently prepared; the bulk samples were utilized as the source material.

8.6.2. *Laboratory Investigation of Soil Properties*

Traditional laboratory techniques were utilized to 1) characterize the soil and to 2) measure the hydraulic and index properties of the soil. The soil samples were characterized to obtain quantitative and qualitative measurements of: clay fraction (ASTM D422 2014), mineralogy (x-ray diffraction, scanning electron microscopy, Terzaghi et al. 1996), LL (ASTM D4318 2014, BSI 1990), PL (ASTM D4318 2014, BSI 1990), and specific gravity (ASTM D854 2014). For all of the traditional laboratory tests the average values of five individual samples were obtained and utilized. The X-ray diffraction (XRD) and scanning electron microscopy (SEM) techniques were performed at the University of Arkansas Nano-Bio Materials Characterization Center. A chilled mirror hygrometer (Decagon WP-4) was used to develop an initial estimate of the soil water characteristic curve (SWCC) over a large range of soil water potential values. Two additional samples of each soil type were consolidated in a Beckman-Counter J-6 centrifuge (48 hours at 500 RPM) and immediately tested using the WP-4 to determine the value of osmotic potential. The results of characterization techniques (LL, PL, PI, CF, XRD, SEM) were presented and discussed in Garner and Coffman (2017b).

8.6.3. *Sample Preparation for Reflectance Testing*

The intact Vis-NIR-Wet (partially saturated) samples were prepared by using a multi-step method. Approximately 800g of soil was obtained from the respective bulk samples and mixed into a slurry at a target gravimetric water content of 50 percent. The soil slurries were then consolidated using a double drained, 6.4cm diameter, acrylic, static-weight slurry consolidometer under a constant applied stress of 138kPa. For each sample, the applied stress was maintained until 48 hours beyond the end of primary consolidation as obtained for the logarithm of time technique (Taylor 1948). After primary consolidation was complete, sub-samples of the slurry

consolidated sample were extruded into 1.5cm tall, acrylic, sample rings. The soil samples and rings were then placed into one of the two pressure plate extractors (PPE, Soil Moisture Inc. Model 1500 or Model 1600). Following the ASTM D6836 (2014) standard, the PPE samples were then allowed to equilibrate with the applied pneumatic pressure until the volume of the expelled water from the PPE was less than 1ml over a 48 hour period. After the samples reached equilibrium, the samples were subsequently removed from the PPE.

To compute the volumetric soil moisture content, the physical dimensions of the soil samples were obtained using a pi-tape (diameter) and Vernier calipers (sample height). The total volume of the sample was determined assuming that each soil sample was a right circular cylinder. The Vis-NIR data acquisitions were obtained following the volume determination. The gravimetric water content for each soil sample was obtained using the procedure documented in ASTM D2216 (2014).

For Vis-NIR-Dry samples, 500g of the dry, ground, soil was obtained from the prepared soil stockpile, and then oven-dried prior to testing. Similarly, for the MIR samples, approximately 100g of dry, ground, soil was obtained from the soil stockpile, and then oven dried. From the 100g MIR samples, 5g of oven-dried soil was obtained and measured out using a powder trickler and an electronic balance with a +/- 0.0001g readability. The 5g, dry, ground, MIR samples were maintained in a sealed desiccator and only removed immediately prior to testing. Each of the previously prepared 5g samples were placed in the MIR sample holder prior to testing.

8.6.4. *Visible-Near Infrared (Vis-NIR) and Middle Infrared (MIR) Spectroscopic Instruments*

Visible-Near Infrared (Vis-NIR) spectral data were obtained using an ASD PANalytical FieldSpec4 Hi-Res Spectroradiometer (Figure 8.1). A laptop computer, using the RS^3 software suite (ASD 2014), was utilized to control the instrument, store the acquired spectral data, perform

pre-processing, and export the data. An 8˚ fore optic was employed to collimate the reflected light. Prior to collecting the reflected light from each of the soil samples, reference spectra were collected using a Spectralon (polytetrafluoroethylene [PTFE] polymer) calibration sample. Broad spectrum illumination was provided from a 70W quartz-tungsten-halogen bulb with an integrated reflector. Coherent illumination was provided using two 50mW solid state laser diodes (Thor Labs HL8338MG and HL8342MG operating at 826nm and 855nm, respectively). The laser diodes were powered using a 9V direct current laboratory power supply (1260 mW total power draw) and two constant power laser controllers (Thorlabs model EK1102 and LD1100/1). The laser diode power was adjusted using the potentiometer on each controller to observe the reflected laser light without saturating the FieldSpec 4 sensor.

The same device that was utilized by Garner and Coffman (2017b), a Nicolet 6700 spectrometer with a diffuse reflectance accessory, was employed for MIR testing. As reported in Garner and Coffman (2017b), the instrument was controlled with the OMNIC software suite (Nicolet 2004). A thermo-electrically cooled dueterated triglycine sulfate detector with a potassium chloride window, an MIR source, and a KBr beam splitter were employed. Prior to acquiring MIR samples, an InfraGold (an electrochemically plated diffuse gold-metallic coating) reference disk was also used to acquire a background reflectance spectra.

8.6.5. *Collection of Spectral Reflectance Data*

Following the acquisition of the background spectrum, the Vis-NIR samples were placed on the laboratory bench within the field of view of the instrument. For all Vis-NIR samples, at least two repetitions of ten spectra were acquired (twenty total spectra). Between the collection of each set of spectra, the samples were rotated by 90 degrees to mitigate directional effects on the

spectra. A total of 112 Vis-NIR-Wet spectra (48 Donna Fill, 33 illite, and 31 kaolinite) and 21 oven-dry, ground, Vis-NIR-Dry spectra (8 Donna Fill, 8 illite, and 6 kaolinite) were acquired.

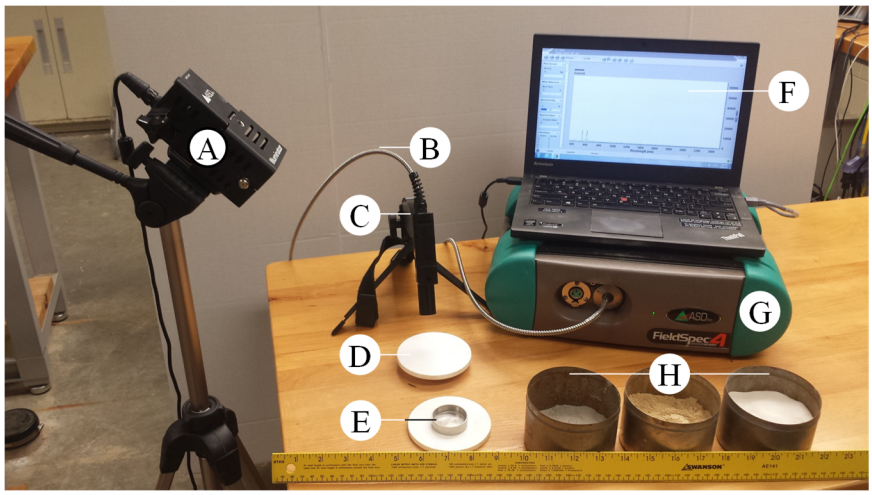

A. Halogen illumination source.
B. Fiber optic cable.
C. Fore optics (eight degree field of view).
D. 7.62 cm diameter Spectralon reference sample.
E. 10 cm^3 stainless steel sample holder.
F. Laptop for data acquisition and instrument control.
G. FieldSpec4 Hi-Res spectroradiometer (350-2500nm)
H. Oven-dried soil samples in 250 ml tin (from left to right: Donna Fill, illite, kaolinite).

Figure 8.1. FieldSpec4 Vis-NIR spectroradiometer and associated accessories (image by author, ruler shown for scale).

MIR spectral data (1cm^{-1} wavenumber resolution) were acquired using the previously described Nicolet 6700 FTIR device. As previously mentioned, the 5g lots of the sub-sample were removed from the glass desiccator and placed into the 0.25cm^3 sample slide. A reference background reflectance spectrum was collected by sliding the sample holder out approximately 2.5cm until the InfraGold reference sample was within the beam path. Prior to the collection of data for each soil spectrum, the background spectra were stored for use in the pre-processing of the data. The OMNIC software was used to preprocess the data (to convert the raw intensity

values to reflectance values). A total of 21 oven-dry, ground, MIR-Dry spectra were acquired (five kaolinite, nine illite, and nine Donna Fill).

8.6.6. *Closed-form Solutions*

An analytical solution to determine the relative humidity of the soil sample was performed by substituting the soil absorption coefficient (k) and soil scattering coefficients (s) that were obtained from the diffuse reflectance infrared Fourier transform (DRIFT) spectroscopy testing (documented in Garner and Coffman 2017b) into the Kubelka-Munk color theory equations (Equation 8.1 and Equation 8.2). Absorption coefficients for water liquid and water vapor were obtained from literature sources (Kou et al. 1993 and Rothman et al. 2009, respectively). The scattering coefficients for liquid water were computed using experimentally derived models of the optical properties for liquid water (Bulcholtz 1995, Cox et al. 2002, Kedenburg et al. 2012). All processing was carried out using the MATLAB processing suite (Mathworks 2014). After acquisition of sample spectral data, the observed reflectance spectra, at each wavelength, were transformed utilizing Equation 8.2. The mass fraction of water vapor was computed using Equation 8.3 (at 826nm and 855nm). Equation 8.3 was derived by substituting Equation 8.2 into Equation 8.1. The relative humidity was computed using the total mass of the sample, the soil bulk density (ρ_b), and the water vapor saturation density (793.17g·m^{-3}).

$$\frac{k}{s}=\frac{m_s k_s + m_w k_w + (1-m_s-m_w)k_v}{m_s s_s + m_w s_w + (1-m_s-m_w)\cdot s_v} \quad \text{(after Hapke 2012)} \quad \text{Equation 8.1}$$

$$KMF = f(R_\infty)=\frac{k}{s}=\frac{(1-R_\infty)^2}{2R_\infty} \quad \text{(Barron and Torrent 1986)} \quad \text{Equation 8.2}$$

$$m_v = 1-\frac{-k_{v1}-\left(\frac{Q_1}{Q_3}\right)k_{v2}}{\left(Q_2-\frac{Q_1Q_4}{Q_3}\right)}-\frac{-k_{v1}}{Q_1}-\frac{-Q_2k_{v1}-\left(\frac{Q_2Q_1}{Q_3}\right)k_{v2}}{\left(Q_1Q_2-\frac{{Q_1}^2Q_4}{Q_3}\right)} \quad \text{Equation 8.3}$$

$$Q_1 = (k_{s1} - k_{v1} - KMF_{\,1}\cdot s_{s1}) \quad \text{Equation 8.4}$$

$$Q_2 = (k_{w1} - k_{v1} - KMF_1 \cdot s_{w1}) \quad \text{Equation 8.5}$$

$$Q_3 = (k_{s2} - k_{v2} - KMF_2 \cdot s_{s2}) \quad \text{Equation 8.6}$$

$$Q_4 = (k_{w2} - k_{v2} - KMF_2 \cdot s_{w2}) \quad \text{Equation 8.7}$$

$$RH = \frac{m_v M_{total}}{\rho_{sat}(\rho_b)^{-1}} 100\% \quad \text{Equation 8.8}$$

In Equation 8.1 through Equation 8.8, k is the absorption coefficient; s is the scattering coefficient (note s_v is assumed to be negligible), m is the mass fraction; $Q_{1,2,3,4}$ are predefined quantities (Equation 8.3 to Equation 8.7); KMF represents the Kubelka-Munk function (Equation 8.2); R_∞ is the infinite depth reflectance; s,w,v subscripts indicate solid, water, and vapor phases; the 1,2 subscripts indicate observations or coefficients at unique wavelengths; RH is the relative humidity (in percent); M_{total} is the total sample mass.

8.6.7. *Data Ingestion, Spectral Averaging, and Statistical Data Analysis*

Vis-NIR spectral files for each sample were averaged (taking the arithmetic mean of the ten reflectance intensity values, at each respective wavelength, for all of the spectra that were acquired for a given sample). The empirical correlations between the measured engineering index values (θ_v, ψ_m, LL, PL, CF) and the observed spectral data (wavelength and intensity) were also determined using the MATLAB software (Mathworks 2014). Specifically, both partial least squares (PLS) regression techniques and the principle components (PCR) regression techniques were performed using the MATLAB Statistics and Machine Learning Toolbox to establish an empirical relationship between the observed spectra and the soil hydraulic properties.

For the volumetric water content and the water potential (θ_v and ψ_m) regressions, the θ_v and ψ_m data obtained from the PPE (and not the WP-4 obtained data, due to the disturbed nature of the samples) were employed to both calibrate and validate the PLS and PCR empirical regressions. The plsregress.m (Mathworks 2010) PLS executable and pca.m PCR executable (Mathworks 2012) were utilized. The PLS regression was conducted using the straightforward implementation of a statistically inspired modification of the PLS method (SIMPLS) as described in de Jong et al. (1993) and Rosipal and Kramer (2006). Approximately 80 percent of the observed data were randomly selected to generate the regression. The remaining 20 percent of the

observed data were randomly reserved as a validation data set. The random nature of the assignment of each spectra to the calibration and validation sets, respectively, resulted in the generation of a unique regression. To ensure a consistent result, multiple regressions were conducted for each empirical relationship that was evaluated.

A k-fold cross validation procedure was employed by dividing the calibration data set into ten equal sets (folds). Each individual set was then sequentially excluded from the calibration set and treated as a validation data set. The cross-validation was repeated until all folds had been tested. The k-fold cross validation was performed using the MATLAB statistics toolbox (Mathworks 2014). Spectral reflectance intensities were stored in the **X** matrix, and measured values of each of the engineering index values were stored as the **Y** (n by 1) vector (Table 8.1). A maximum number of 10 PLS or PCR components (N_c) were considered for the soil specific regressions (Mathworks 2014). Due to the low variance explained by the first 10 terms, a total of 25 terms were considered in the non-soil specific regression for soil matric potential. The value of N_c was selected to explain greater than 90 percent of the variation in **Y**. Additionally, a subset (approximately 30 percent of the total number of samples acquired) of the original data set was excluded from the regression (calibration) data set. The computed vector containing the PLS regression weighting coefficients (β vector) was subsequently employed to predict values of the index properties (Y_{pred}) from the observed reflectance spectrum of the validation data set by using Equation 8.9.

Table 8.1. Example X and Y matrix for use in PLS and PCR regression for liquid limit (LL) where λ_i represents the individual observed reflectance spectra wavelengths.

	LL	λ_1	λ_2	λ_3	λ_4	…	…	λ_{n-1}	λ_{n-1}	λ_{n-1}	λ_n	
Soil 1	31.5	0.895	0.894	0.893	0.891	0.890	0.888	0.886	0.884	0.882	0.880	< **Spectra1**
	31.5	0.892	0.891	0.890	0.888	0.887	0.885	0.883	0.881	0.879	0.877	< **Spectra2**
	31.5	0.894	0.892	0.891	0.890	0.888	0.886	0.884	0.883	0.880	0.879	< **Spectra3**
Soil 2	46.7	0.730	0.730	0.730	0.730	0.730	0.730	0.730	0.730	0.730	0.730	< **Spectra4**
	46.7	0.722	0.722	0.722	0.722	0.723	0.723	0.723	0.723	0.723	0.723	< **Spectra5**
	46.7	0.724	0.724	0.724	0.724	0.724	0.724	0.724	0.724	0.725	0.725	< **Spectra6**
Soil 3	25.0	0.463	0.463	0.463	0.463	0.463	0.463	0.464	0.464	0.464	0.464	< **Spectra7**
	25.0	0.454	0.454	0.455	0.455	0.455	0.455	0.455	0.455	0.455	0.456	< **Spectra8**
	25.0	0.467	0.467	0.467	0.467	0.467	0.468	0.468	0.468	0.468	0.468	< **Spectra9**
		Y	**X**									

$$Y_{pred} = X_{validation} \cdot \beta + F \qquad \text{Wold et al. (2001)} \qquad \text{Equation 8.9}$$

In Equation 8.9, Y_{pred} is a vector (a rows by one column), $X_{validation}$ is the matrix containing the observed reflectance spectrum (a rows by b columns), where a is the number of acquired spectra, b is the number of wavelength values in each spectra, β is the array containing the PLS/PCR regression weighting factors, and F is a one by one vector containing the Y-residual values.

8.7. Results

8.7.1. *Results Obtained from Traditional Laboratory Testing*

Soil water characteristic curve (SWCC) measurements were obtained, for the Vis-NIR-Wet specimens, using the chilled mirror hygrometer (Decagon WP-4), the PPE, and the remotely sensed measurements obtained from the FieldSpec4. For all of the empirical regressions (θ_v, ψ_m, LL, PL, and CF), a numerically higher value of R^2 and lower value of the estimated squared error was found using the PLS regression when compared with the PCR regression. Therefore, the PLS regression was considered to be the regression of choice

As previously described, the PPE samples were used for calibration due to the overlapping range of θ_v and ψ_m data (due to the method of preparation). Additionally, at low absolute values of soil water potential (ψ < 300kPa), the WP-4 data were found to be sensitive to contamination, device calibration, temperature, and osmotic potential. The aforementioned factors resulted in difficulty in obtaining an accurate measurement of saturated volumetric water content (θ_s) within

the WP-4 device. Measured, absolute osmotic potential values of approximately 450kPa, less than 50kPa (below the manufacturer's specified measurement tolerance for the WP4 device), and 100kPa was obtained using the WP-4 on saturated, centrifuge consolidated, samples for the Donna Fill, illite, and kaolinite materials, respectively.

8.7.2. *Results Obtained from Closed-form Solutions*

The analytical solution investigated (Kubelka-Munk) was found to provide 1) an estimate of soil volumetric water content that was numerically lower than the measured value, and 2) a soil water vapor concentration (m_v) that was several orders of magnitude greater than the saturation concentration of water vapor under standard laboratory conditions (RH > 1000 %). The relationship between the calculated soil water concentrations (y-axis) and the measured soil water concentration (x-axis) was found to be non-linear and had a fitted coefficient of determination (R^2) value less than 0.10. Specifically, the reflectance value of the soil samples was found to be non-linear as a function of volumetric water content. In an attempt to improve the accuracy of the closed-form solution, the analysis presented in Section 8.6.6 and Appendix C was solved for all possible combinations of λ_1 and λ_2 to identify particular combinations of wavelength values that provided the most accurate solution (by comparing the predicted values with the experimentally obtained mass fraction of water and vapor). While some candidate wavelengths (including and 830nm through 860nm, and 1480nm through 1580nm) were identified, no set of wavelengths gave R^2 values greater than 0.10 percent.

Backwards analyses were performed using laboratory obtained mass fraction values of water and soil to compare the predicted and measured reflectance spectra. The predicted reflectance spectra were not visually congruent with the observed value. Similar backwards analyses were performed to determine if the experimentally obtained soil absorption and

scattering values were accurate. Based on these analyses, it was hypothesized that several factors degraded the performance of the considered analytical solutions. These factors are described herein.

Typically, the reflectance from the soil, for all Vis-NIR wavelengths, decreased as the amount of water in the soil increased until reaching a minimum value at or around the obtained value of plastic limit (Figure 8.2). Additionally, a switch occurred in the observed reflectance behavior under coherent illumination for soil samples at or above the liquid limit (Figure 8.3).

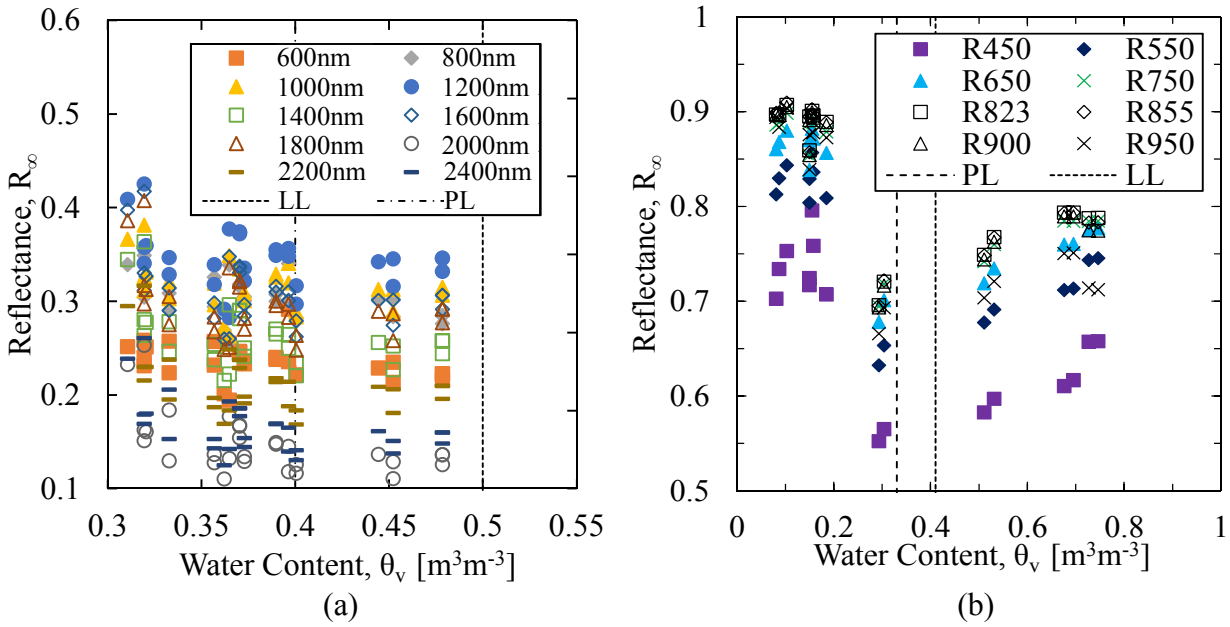

Figure 8.2. Reflectance values, as a function of water content, for selected wavelengths for a) illite and b) kaolinite soil samples [in color].

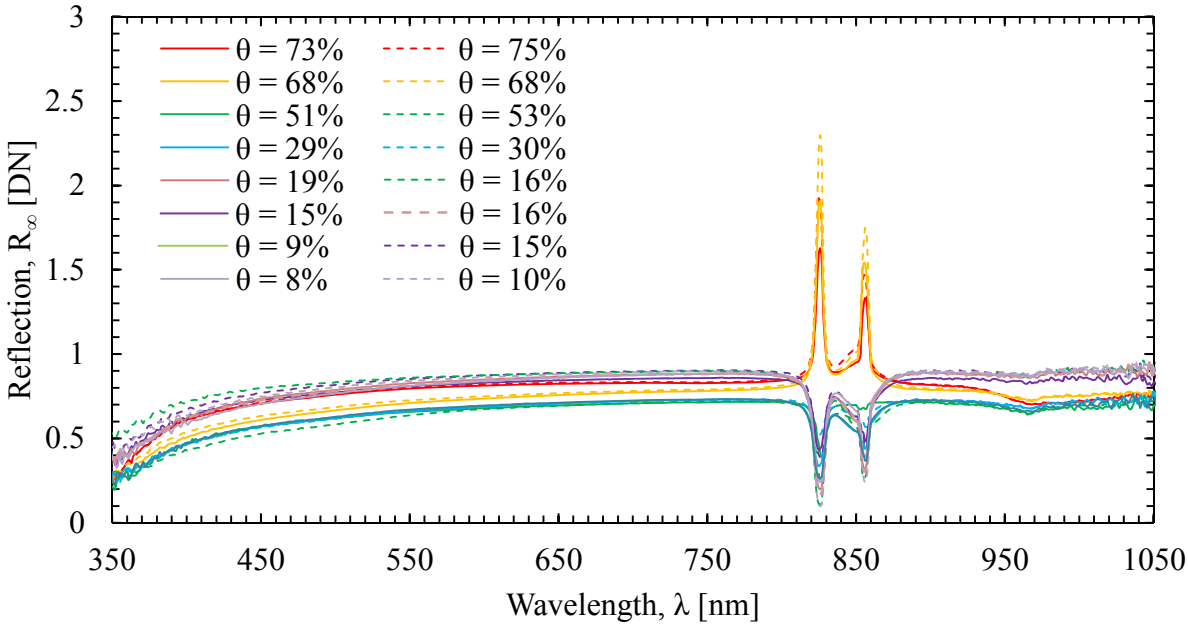

Figure 8.3. Reflectance spectra for ground kaolinite samples prepared (using dry method of preperation) at various water contents [in color].

It was additionally realized that an adsorbed water layer must be explicitly considered when performing the closed-form solutions. A model, such as proposed by Philpot (2010), is suggested. However, since the Philpot (2010) method requires the use of an experimentally obtained, soil specific relationship between the thickness of the adsorbed layer and the volumetric water content, it was not possible to implement this specific method during the previously described closed-form analysis.

8.7.3. *Results Obtained from Hydraulic Property Regression for Visible to Near Infrared Spectroradiometry*

The non-soil specific PLS calibration was found to provide better predictive performance for measurement of θ_v as compared to ψ_m. For the ψ_m regression, the PLS regression had to be extended to a total of 25 terms to obtain a regression that explained greater than 90 percent of the variance in the observed spectra. The bias (as a function of the slope of the linear trendline where 1.0 represents convergence between predicted and measured values), offset, and regression coefficient were found to be 1.05, 0.01 $m^3 \cdot m^{-3}$, and 0.627 for the non-soil specific θ_v values.

Likewise, the non-soil specific ψ_m regression values for bias, offset, and regression coefficient were 0.52, 200.53kPa, and 0.173. These results of the θ_v and ψ_m regressions are presented in Figure 8.4**.**

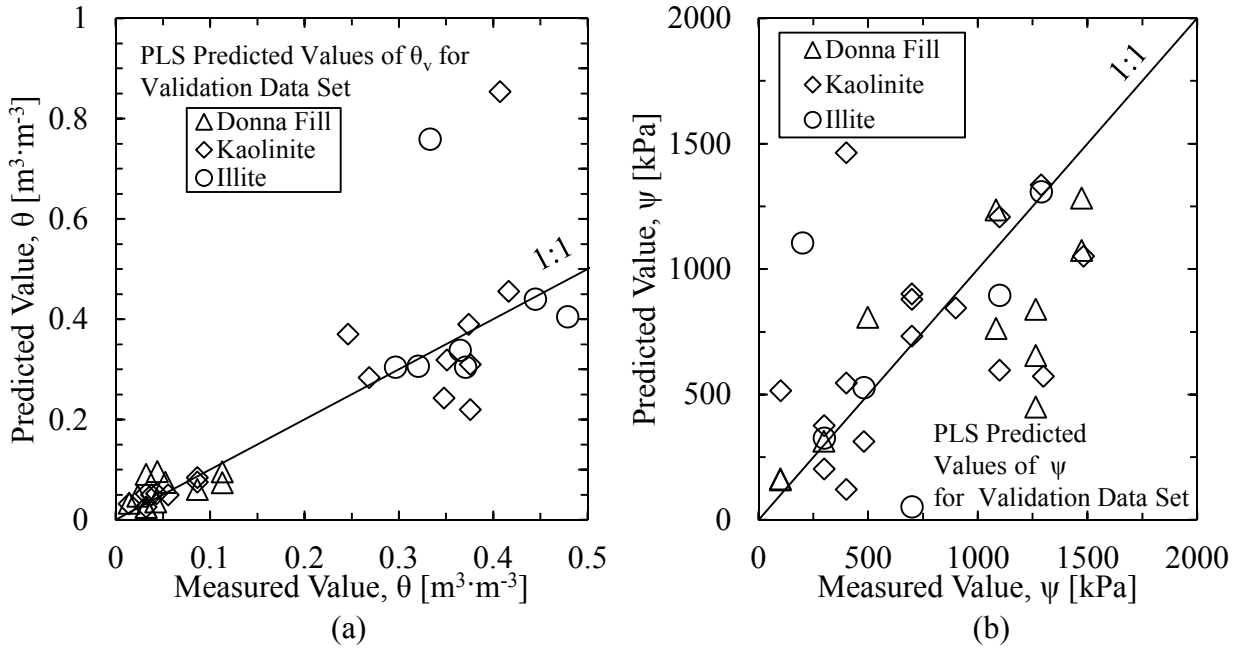

Figure 8.4. Non-soil specific regression between a) volumetric soil water content (θ_v) and b) soil water potential (ψ_m) for Vis-NIR-wet samples (for all soil types considered).

The use of soil specific PLS regressions provided increased performance metrics for both Donna Fill and illite soil types. However, for the kaolinite soil type, no increase in the predictive performance was observed when using a soil specific calibration. One potential causative factor for the poor performance of the kaolinite soil type was that the kaolinite material had a tendency to form a surface film, even for samples with large values of volumetric water content. This surface film reduced the sensitivity of the reflected spectra to changes in the underlying material properties. Additionally, due to the adhesion between the soil sample and the PPE porous plate, it was difficult to remove the kaolinite samples (as compared to Donna Fill and illite samples) from the PPE porous plate without causing excessive sample disturbance. This sample disturbance

adversely affected the accuracy of the measured soil volume, and therefore adversely affected the volumetric water content measurements.

For the Donna Fill soil type, the observed (quantity divided by the maximum value) normalized bias, offset, and regression coefficient values of 0.67, 0.23, and 0.82. Similarly, the observed values for the bias, offset, and regression coefficient were 0.97, 0.09, and 0.75 for the Donna Fill PLS θ_v regression. For the illite soil type, the observed normalized bias, offset, and regression coefficient values were 1.049, 0.052, and 0.906, for the PLS θ_v regression. Similarly, observed normalized bias, offset and regression coefficient values of 1.05, -0.103, and 0.52, respectively (with one outlier excluded because the predicted value was less than 60 percent of the measured value) were obtained for the illite PLS ψ_m regression.

As determined from the fitted trendline for both the Donna Fill and the illite soil types, the average measurements were within approximately 150kPa of the measured value. Conversely, for the kaolinite validation data set, both regressions for both the θ_v and the ψ_m measurements had a calculated R^2 value of less than 0.10, indicating that no usable correlation was found. For each of the three soils, the relationship between normalized predicted values and the normalized predicted values of θ_v and ψ_m are presented graphically as Figure 8.5. Additionally, the percentage of variance, as a function of the number of PLS components, is presented in Figure 8.5. The experimentally obtained (WP-4, PPE, and FieldSpec-4) SWCC for the Donna Fill, illite, and kaolinite soils are presented in Figure 8.6 through Figure 8.8, respectively.

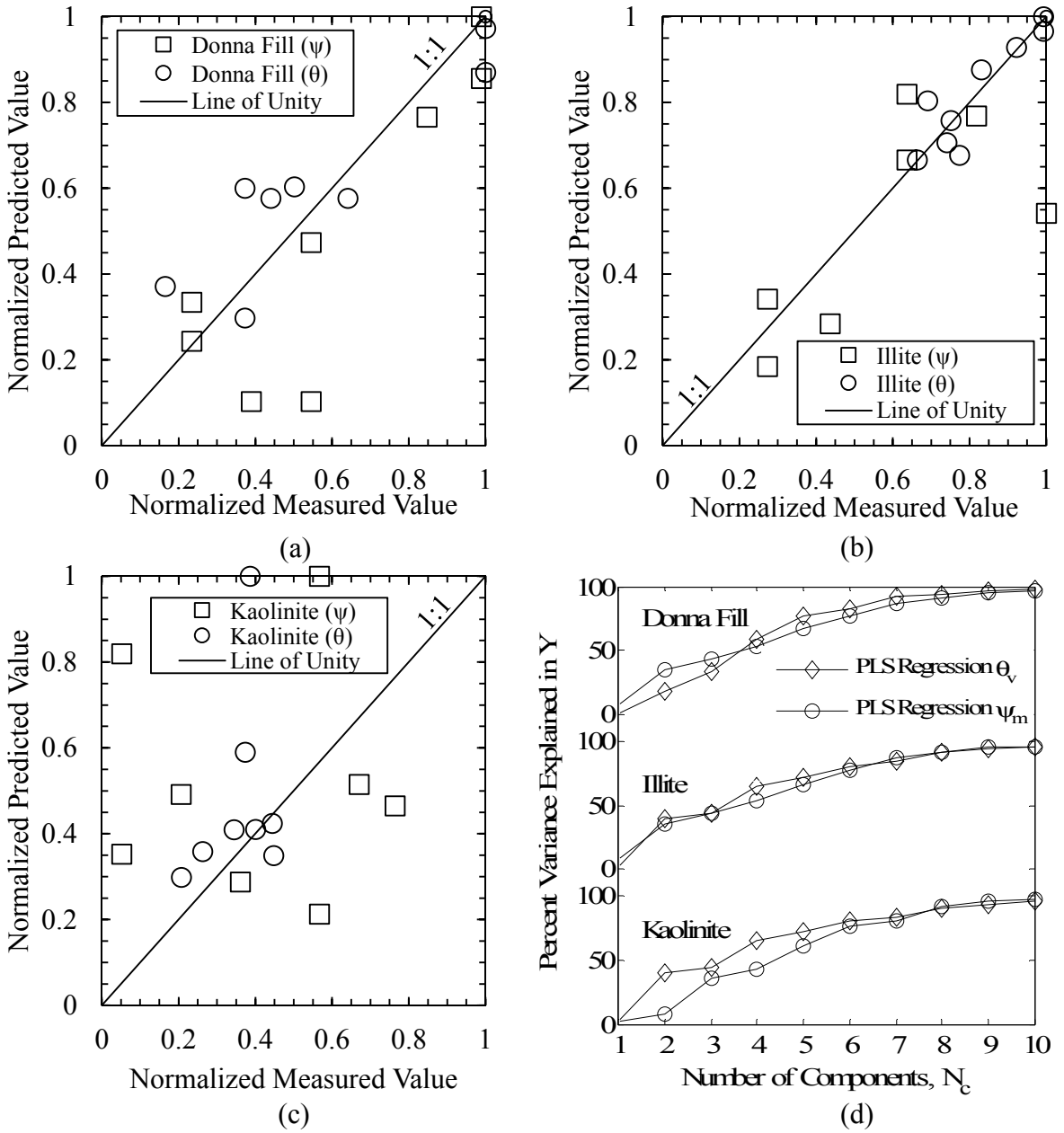

Figure 8.5. Normalized predicted value compared with the normalized measured value for soil specific PLS regression for a) Donna Fill, b) illite, and c) kaolinite; and d) percent variance explained as a function of PLS number of components for soil specific PLS regressions.

As previously described, the best model performance was obtained for the Donna Fill samples (as evaluated by the value of the regression coefficient). When compared to the Donna Fill soil type, decreased predictive accuracy was observed for the illite and the kaolinite soil type samples. The Donna Fill material, being an artificially produced geomaterial, was the most

uniform of the three soil types (as determined from the traditional laboratory classification testing). The homogeneous nature of the material was also observed in the PPE obtained measurements of the SWCC. It was hypothesized that this uniformity contributed with the higher performance of the PLS regression on this material, as compared with the more variable illite and kaolinite materials. For all three materials, the fitted SWCC was obtained using the RETC program (van Genuchten et al. 1991, van Genuchten et al. 1998) for both laboratory-obtained and remotely-sensed values.

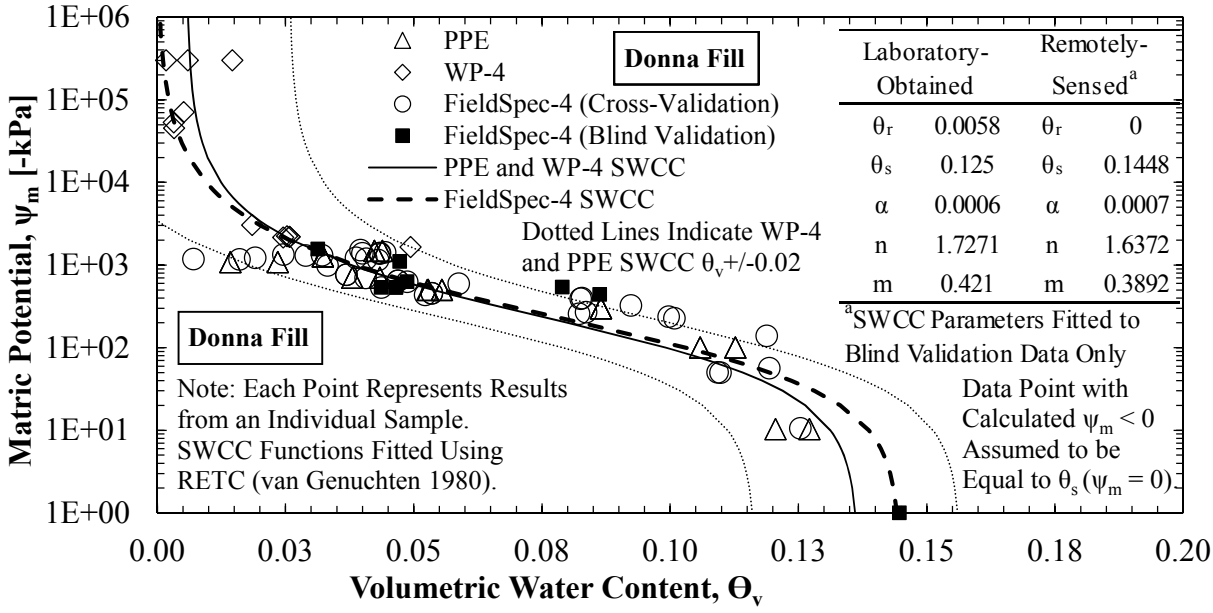

Figure 8.6. WP-4, PPE, and FieldSpec-4 obtained measurements of the soil water characteristic curve, as developed for the Donna Fill Vis-NIR-Wet samples.

The RETC-fitted SWCC functions using the laboratory obtained data (PPE and WP-4) and remotely sensed data (FieldSpec-4 blind validation) for the Donna Fill soil type were comparable for a range of soil water potential (and volumetric water content) values. A θ_v value of 0.1448 and an absolute ψ_m value of -348kPa were obtained for one of the blind validation samples. Therefore, it was assumed that a volumetric water content value of 14.48 percent represented an upper bound for the saturated water content value (e.g. $\psi_m = 0$kPa at $\theta_v > 14.48$ percent). The fitted remotely

sensed SWCC diverged from the laboratory obtained SWCC curve at high values of volumetric water content (maximum percent error of 81 percent). The maximum percent error at low values of matric suction (with respect to volumetric water content) was approximately 5 percent (corresponding to a 0.8 percentage point difference in θ_v values). The maximum calculated percent error occurred at θ_r (ψ_m = 1 GPa). However, at such high values of matric suction the corresponding difference in volumetric water content values was less than 0.5 percent. The percent error between the laboratory obtained-SWCC and remotely sensed-SWCC was less than 10 percent for a range of matric potential values between 0 and 4,000kPa.

For the illite soil, the RETC fitted SWCC curves for the laboratory obtained and remotely sensed data were in agreement (less than 10 percent error between θ_v values) for ψ_m values greater than 400kPa. However, the laboratory- and remotely sensed- SWCC θ_v values were within 2 percentage points for ψ_m values greater than 600kPa. It is hypothesized that the RETC fitted curve would be significantly improved by acquiring and implementing additional data at the wet side of the curve or by establishing an *a priori* value of θ_s.

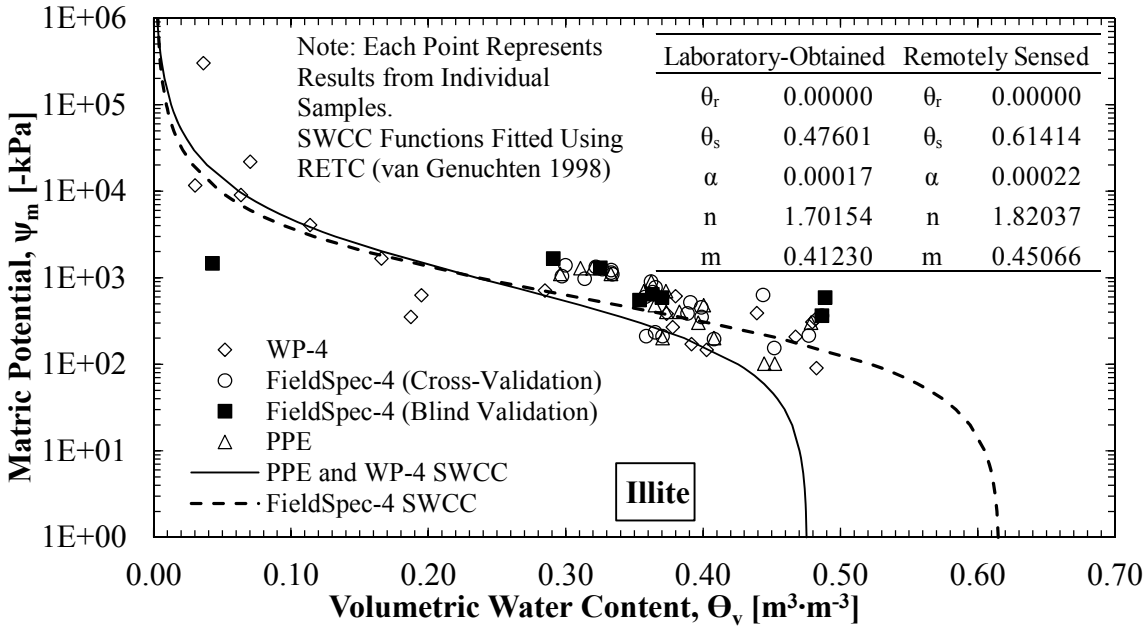

Figure 8.7.WP-4, PPE, and FieldSpec-4 obtained measurements of the soil water characteristic curve, as developed for the Illite Vis-NIR-Wet samples.

The RETC fitted curve for the laboratory-obtained kaolinite SWCC required the assumption of a θ_s value to allow for the program to converge on a solution. Therefore, the average of the two θ_v values (0.54), which were obtained from the centrifuge prepared WP-4 samples, was used as a θ_s value and the SWCC was fitted using this parameter. The remotely sensed and laboratory obtained SWCCs for kaolinite were within approximately 25 percent error (with respect to θ_v values) for ψ_m values less than 4000kPa. The values of θ_v for the two kaolinite SWCCs were within 8 percentage points for all values of ψ_m. However, while the remotely sensed SWCC was at least partially super-imposed on the laboratory obtained SWCC, the cross-validation sample values had lower values of ψ_m than would be predicted by either of the fitted SWCC functions.

For the Donna Fill and illite measurements, the highest absolute weighting ($\Sigma|\beta|$) coefficient values were observed for the wavelengths under laser illumination (indicating that these wavelengths were correlated to the volumetric water content and water potential for the

various soil types). For the θ_v regressions, bands of wavelengths that were important (higher absolute weighting coefficient values) include the following bands: 900nm to 1000nm, 1420nm to 1600nm, and 2250nm to 2500nm (upper limit of instrument range). For ψ_m regressions, higher absolute weighting coefficient values were observed for the Donna Fill and Illite soils between 1100nm and 1400nm.

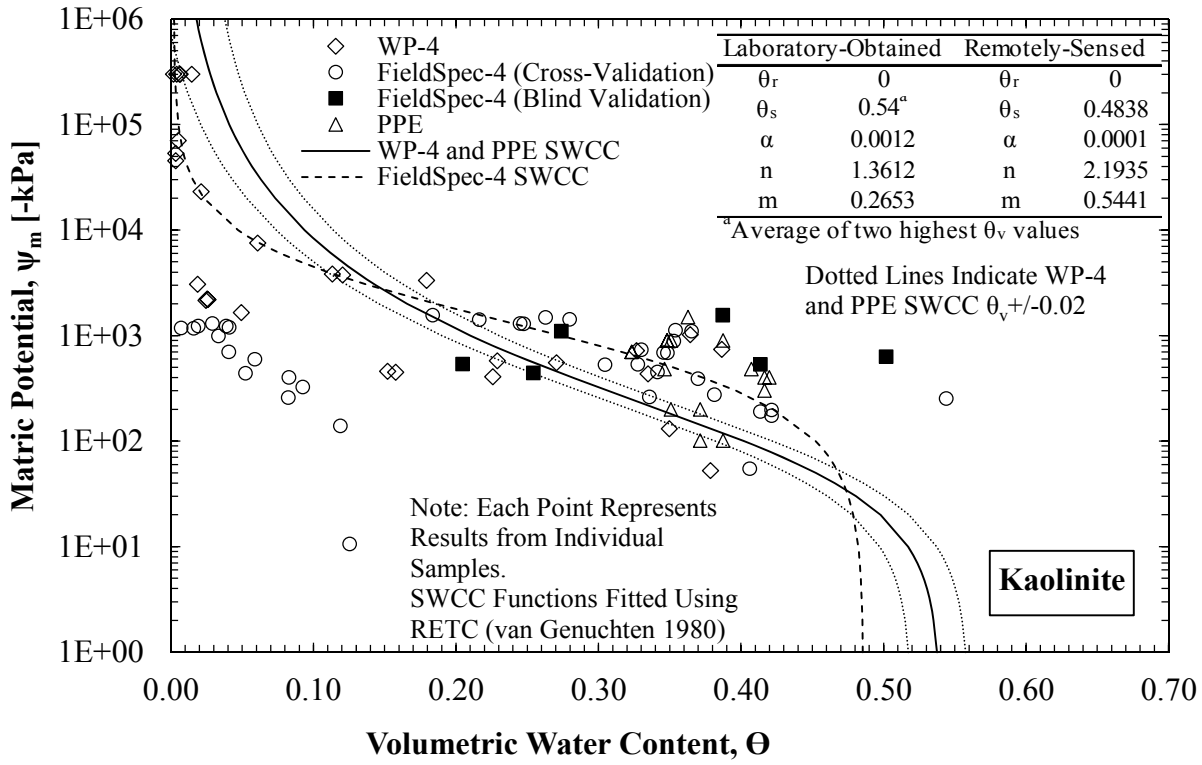

Figure 8.8. WP-4, PPE, and FieldSpec-4 obtained measurements of the soil water characteristic curve, as developed for the Kaolinite Vis-NIR-Wet samples.

8.7.4. *Results Obtained from Index Property Regression for Visible to Near Infrared (400 to 2500 nm Vis-NIR-Wet and Vis-NIR-Dry) Spectroradiometry*

As expected, due to the influence of water within the soil, the observed empirical correlation between the Vis-NIR reflectance spectra and the measured LL, PL, and CF data were not as precise as the empirical correlations obtained for the oven-dry ground samples (Figure 8.9). For the LL and PL data, the PLS model with four components ($N_c = 4$) provided estimated

maximum squared predictive error (EMSPE) values that were near the minimum values encountered. For the CF model, however, the computed value of EMSPE decreased as the value of N_c approached 10. Coefficient of determination (R^2) values of 0.777, 0.909, and 0.589 were calculated for the non-soil specific LL, PL, and CF models, respectively. As previously mentioned, increasing the N_c value to 10 for the CF model increased the R^2 value to 0.875 for the calibration set. The LL PLS model index value had a negative bias value (e.g. the predicted values were less than the observed values) of -0.22 percent for the gravimetric water content and a standard deviation of 2.44 percent for the gravimetric water content measurements. The value of the bias decreased with increasing values of LL. The PL PLS model had a positive bias value of 0.61 and a standard deviation of 0.04 percent water content. Similarly, the CF PLS model had a positive bias value of 0.22 percent and a standard deviation of 5.12 percent for the clay content measurements.

Lower values of EMSPE, at each value of N_c, were observed using the K-fold cross-validation for the PLS models of LL, PL, and CF than for the comparable PCR models. Furthermore, a smaller N_c value was required for the PLS regression method than for the PCR method, to explain greater than 90 percent of the variability in the **Y** vector. While an N_c value of two was sufficient to provide an accurate prediction, as determined using the EMSPE value, and an N_c value of three was sufficient for the CF model, the first four components were used in each of the models for consistency. For all three of the empirical models (LL, PL, and CF), the R^2 values were all 0.999. Values of -0.06 percent gravimetric water content, 0.00 percent water content, and 0.61 percent clay mass content were determined for the LL, PL, and CF models, respectively. The computed standard deviation of the LL, PL, and CF models was 0.32 percent water content, 0.03 percent water content, and 2.86 percent clay mass content, respectively.

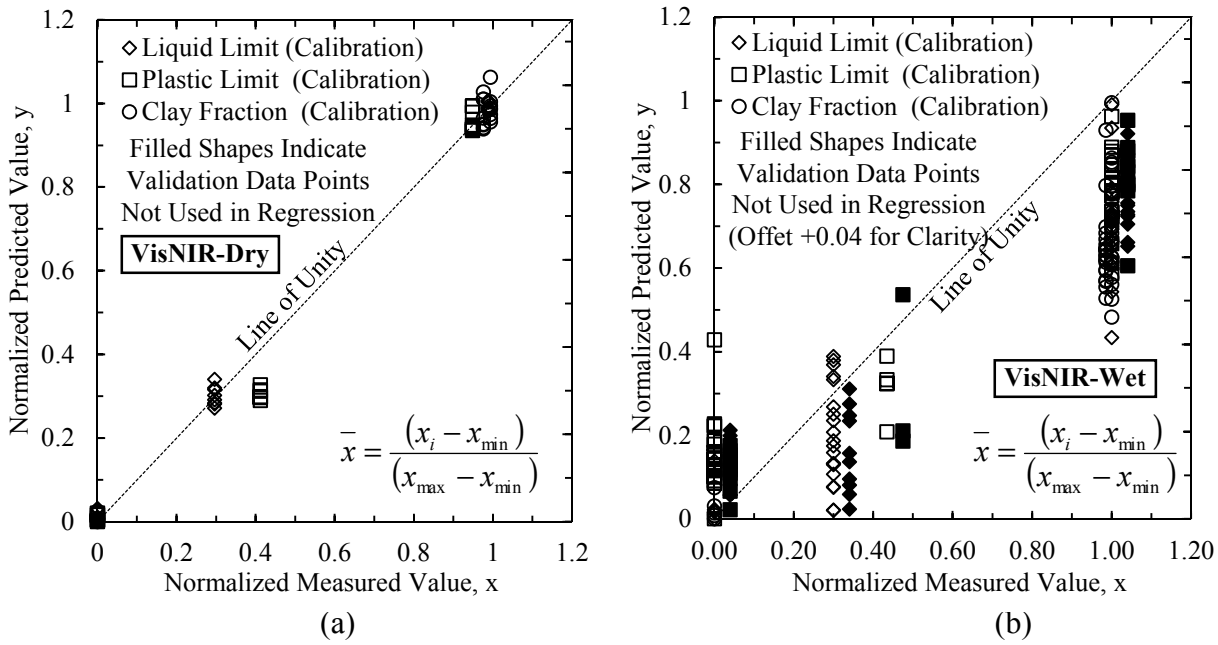

Figure 8.9. a) Normalized predicted values compared to the normalized measured values for the Vis-NIR-Dry spectra and b) normalized predicted values compared to the normalized measured values for the Vis-NIR-Wet spectra.

For the MIR samples, the PLS was found to provide superior predictive performance. The R^2 values for the MIR data were 0.957, 0.931, and 0.876 for the LL, PL, and CF models, respectively. A negative bias of 0.66 percent water content, 0.05 percent water content, and 0.3 percent clay mass fraction were computed for the LL, PL, and CF models, respectively. However, at low values for LL, PL, and CF (specifically for the Donna Fill samples), the models had positive bias. The computed standard deviation of the entire data set (cross-validation and independent validation data) was 1.22 percent water content, 0.32 percent water content, and 2.86 percent clay mass content for the LL, PL, and CF models respectively.

The aforementioned values were indicative of a strong empirical correlation between the MIR spectra and the value of the plastic limit. The CF model, conversely, provided less precise values (+/- 3 percent), but the predicted values were still suitable for soil classification. The performance of the individual PLS models, to predict the soil values, was different from the

performance reported by Waruru et al. (2014). For African soils, as reported by Waruru et al. (2014), the statistical regression provided the best performance, in general, for measurement of LL, and the worst performance for measurement of CF.

For all three testing methods (LL, PL, CF), the empirical correlation between PL and the observed reflectance data provided the lowest value of standard deviation and highest R^2 values. Similarly, the least precise correlation (highest standard deviation) and lowest value of R^2 was computed for empirical correlations between values of CF and the observed reflectance spectra. The Vis-NIR-Dry and MIR-Dry empirical correlations provided similar results for the three soils that were investigated. The values of the computed Vis-NIR-Dry regression coefficients (R^2) were numerically larger than the values calculated for the MIR-Dry empirical regression coefficients (0.999, 0.999, and 0.999 compared to 0.957, 0.931, and 0.876, for LL, PL, and CF, for the different methods, respectively).

The standard deviation values that were obtained for the empirical relationships, using the Vis-NIR-Dry data were lower for all three of the PLS models when compared to the empirical correlation obtained from the MIR-Dry spectra (0.32 percent LL, 0.04 percent PL, and 0.61 percent CF as compared to 1.22 percent gravimetric LL, 0.31 percent PL, and 2.86 percent CF). The standard deviation for the liquid limit methods, as obtained from Vis-NIR-Dry and MIR-Dry spectra, were smaller than or equivalent to the acceptable standard deviation (1.3 percent for ML soils) from traditional laboratory testing techniques, as reported in ASTM D4318 (2014). The predicted standard deviation values from the Vis-NIR-Dry and MIR-Dry PL PLS models were also comparable to the acceptable value of standard deviation of 1.2 percent, as reported in ASTM D4318 (2014). In particular, the coefficient of variability values for the PL relationships, as obtained for the Vis-NIR-Dry, MIR-Dry, and Vis-NIR-Wet techniques (1.0 percent, 0.1 percent,

and 2.5 percent, respectively), were below the variability value reported by Waruru et al. (2014) for the traditional plastic limit testing (9.2 percent). While the variability of the remotely sensed soil index properties (LL, PL, CF) obtained from Vis-NIR-Wet samples were either comparable (PL, CF) or less precise (LL) than traditional laboratory testing techniques, one possible use of this technology is a rapid, field-based, initial characterization technique. By calibrating against traditionally obtained soil data for a specific site, Vis-NIR spectra could then be used to acquire near real-time measurements of soil index properties (e.g. for use at a borrow site to identify soils suitable for use as a structural fill).

The degraded performance of the empirical correlation between the Vis-NIR-Dry and Vis-NIR-Wet samples was hypothesized to be caused by the strong influence of water within specific wavelength ranges. The soil reflectance spectra, within the visible portion of the spectrum, as well between 1800nm and 2100nm, have been reported to be strongly influenced by the water content of the soil (Goetz et al. 2001). These wavelength ranges corresponded to high absolute values of weighting coefficients for the first and fourth PLS components in the LL Vis-NIR-Dry correlation, and the first, third, and fourth components of the CF Vis-NIR-Dry correlation (indicating a strong correlation between data in these wavelength range and the measured values of LL and CF). Conversely, for the LL and CF Vis-NIR-Wet correlation, low absolute values for the weighting coefficients were observed between approximately 1800nm and 2200nm for the first, third, and fourth PLS components in the LL model and for the first, second, third, and fourth PLS components in the CF model. The model performance may be improved by the use of additional soil spectra (particularly from additional types of soil) and a larger calibration and validation data set. Although not investigated as part of this study, other researchers have proposed the use of additional data transformations (e.g. using the first and second derivatives of

the reflectance spectra instead of the raw reflectance spectra) prior to performing the statistical regression analyses.

8.8. Recommendations and Conclusions

Relative to the existing standard of practice for obtaining soil hydraulic properties and soil index properties, Vis-NIR spectroscopy has several potential benefits. Specifically, Vis-NIR spectroscopy is rapid (spectrum acquisition in minutes), repeatable (Wroth and Wood 1978), and has the potential to be non-destructive (e.g. Vis-NIR-Wet). For the Donna Fill and illite materials, the computed SWCC obtained using the PLS technique was found to be coincident (θ_v within 0.02) with the SWCC that was developed from data collected using the PPE apparatus for ψ_m values greater than 1kPa (Donna Fill) and 600kPa (illite). Additional findings of this research indicate that it may be possible to utilize a non-soil specific calibration (if properly calibrated to include all soils that are expected to be evaluated) to make field- or rapid-laboratory estimates of θ_v. The remote measurements of ψ_m however, require the use of a soil specific calibration to provide any usable soil potential measurements.

With further research, it may be possible to extend the range of matric potential values from the Vis-NIR techniques beyond the physical limitations of the calibration equipment (PPE). The amount of variability of the remotely sensed measurements, for the LL values, was similar to the variability reported in ASTM D4318 (2014) for traditional laboratory techniques. However, for measurements of the PL, the results of this investigation indicated a higher precision than the existing standard of practice (ASTM D4318 2014). The use of oven dried, ground soils (Vis-NIR-Dry) led to increased correlation values (R^2) and reduced standard deviation values for all measurements of LL, PL, and CF. Specifically, the lowest variability and bias for the remotely sensed measurements were observed for the Vis-NIR-Dry samples. However, the use of oven-

dried samples does negate the non-destructive, rapid testing benefits of the remotely sensed technology. Although, even by using oven-dried samples, the Vis-NIR spectroscopy technique was less time consuming than the traditional ASTM D4318 (2014) testing methods.

Another potential application for this technology may be as an initial characterization technique to identify soils of greatest interest to engineering professionals. An initial estimate of soil volumetric water content on a project site could be obtained by using the non-soil specific θ_v calibration. For example, in transportation or geo-environmental applications where the index properties (LL, PL, and CF) partially control the selection of suitable borrow material, a remote sensing instrument could be calibrated (site specific) and used to identify locations of suitable materials. Similarly, such an instrument could be utilized in a quality control/quality assurance program to rapidly assess material prior to, and during, placement (similar to the function of the nuclear density gauge for *in situ* density measurements).

The performance of the closed-form solution may be improved by using soil-specific, laboratory-obtained measurements of the adsorbed water layer. At the nanometer scale, due to the intimate interaction between photons, water, vapor, and soil particles, the adsorbed soil layer must be considered as a separate material. An empirical relationship between volumetric water content, the thickness of the adsorbed water layer, and the reflectance spectra was presented in Philpot (2010). Further discussion of methods to estimate the thickness of the adsorbed layer, for use with the Philpot (2010) method, are presented in Tokunaga (2009, 2011) and Baveye (2012). An additional technique to be considered would be to treat the water in the soil as three separate phases as suggested by Ben-Dor et al. (1999), including 1) the chemically bound hydration water in the double diffuse layer, 2) the hygroscopic water adsorbed onto the surface of the soil particles, and 3) the liquid phase water in the soil void space. The previously mentioned Ben-Dor

et al. (1999) method has been used to deconvolute the effects of soil moisture from soil reflectance spectra (Whiting 2009). Furthermore, it may be possible to use models of wavelength dependent optical path length as suggested by Whiting (2009).

8.9. Acknowledgement and Disclosure

Portions of this work were sponsored in part by the United States Department of Transportation Office of the Assistant Secretary for Research and Technology (USDOT/OST-R) under grant number ASRTRS-14-H-UARK: Remote Sensing Based Assessment System for Evaluating Risk to Transportation Infrastructure Following Wildfires. The authors would like to express their gratitude to the USDOT/OST-R. The views, opinions, findings, and conclusions reflected in this manuscript are the responsibility of the authors only and do not represent the official policy or position of the USDOT/OST-R, or any state or other entity. Portions of this manuscript were also based upon work supported by the National Science Foundation Graduate Research Fellowship under Grant No. DGE-1450079, as awarded to S.E. Salazar. The authors also wish to thank the Donna Fill Corporation of Little Rock, Arkansas, the Knight Hawk Coal Company of Percy, Illinois, and the Thiele Kaolin Corporation of Sandersonville, Georgia for providing materials for testing.

8.10. Works Cited

American Society for Testing and Materials (ASTM) D422, (2014). "Standard Test Method for Particle-Size Analysis of Soils." American Society for Testing and Materials, Vol. 4.08, Soil and Rock (I). West Conshohocken, PA.

American Society for Testing and Materials (ASTM) D854, (2014). "Standard Test Methods for Specific Gravity of Soil Solids by Water Pycnometer." American Society for Testing and Materials, Vol. 4.08, Soil and Rock (I). West Conshohocken, PA.

American Society for Testing and Materials D2216, (2014). "Standard Test Methods for Laboratory Determination of Water (Moisture) Content of Soil and Rock by Mass." Annual Book of ASTM Standards, Designation D2216, Vol. 4.08, ASTM, West Conshohocken, PA.

American Society for Testing and Materials D4318, (2014). "Standard Test Methods for Liquid Limit, Plastic Limit, and Plasticity of Soils." Annual Book of ASTM Standards, Designation D4318, Vol. 4.08, ASTM, West Conshohocken, PA.

American Society for Testing and Materials D6836, (2014). "Standard Test Method for Determination of the Soil Water Characteristic Curve for Desorption Using a Hanging Column, Pressure Extractor, Chilled Mirror Hygrometer, and/or Centrifuge." Annual Book of ASTM Standards, Designation D6836, Vol. 4.09, ASTM, West Conshohocken, PA.

ASD Panalytical Inc., (2014). "RS3 and ViewSpecPro Software and Supporting Documentation." The ASD Panalytical Inc. Boulder, Colorado.

Barron, V., Torrent, J., (1986). "Use of the Kubelka-Munk Theory to Study the Influence of Iron Oxides on Soil Colour." Journal of Soil Science, Vol. 37, pp. 499-510.

Baveye, P., (2012). "Comment on Physicochemical Controls on Adsorbed Water Film Thickness in Unsaturated Geological Media." by Tetsu K. Tokunaga, doi:10.1029/2012WR01187.

Ben-Dor, E., Banin, A., (1995). "Near-Infrared Analysis as a Rapid Method to Simultaneously Evaluate Several Soil Properties." Soil Science Society of America Journal, Vol. 59, pp. 364-372.

Ben-Dor, E., Irons, J., Epema, G., (1999). "Soil Reflectance." In Remote Sensing for the Earth Sciences: Manual of Remote Sensing, 3rd ed., Vol. 3, (Rencz, E. ed.). John Wiley and Sons, New York. pp. 3-58.

British Standard Institute (BSI), (1990) "Methods of Test for Soils for Civil Engineering Purposes." British Standard Institute, London, UK.

Brooks, R., Corey, A., (1964). “Hydraulic Properties of Porous Media.” Colorado State University. Fort Collins, Colorado.

Bulcholtz, A., (1995). “Rayleigh Scattering Calculations for the Terrestrial Atmosphere.” Applied Optics, Vol. 34, No. 15, pp. 2765-2773.

Campbell, E., Campbell, G., Barlow, W., (1973). “A Dew Point Hygrometer for Water Potential Measurement.” Agricultural Meteorology, Vol. 12, pp. 113-121.

Carrier, W., Beckman, J., (1984). “Correlations between Index Properties of Remolded Clays.” Geotechnique, Vol. 34, pp. 211-228.

Casagrande, A., (1958). “Notes on the Design of the Liquid Limit Device.” Geotechnique, Vol. 8, No. 2, pp. 84-91.

Chabrillat, S., Goetz, A., Krosley, L., Olsen, H., (2002). “Use of Hyperspectral Images in the Identification and Mapping of Expansive Clay Soils and the Role of Spatial Resolution.” Remote Sensing of Environment, Vol. 82, pp. 431-445.

Chang, C., Laird, D., Mausbach, M., Hurburg, C., (2001). “Near-Infrared Reflectance Spectroscopy-Principle Components Regression Analysis of Soil Properties.” Soil Science Society of America Journal, Vol. 65, pp. 480-490.

Cox, A., DeWeerd, A., Linden, J., (2002). “An Experiment to Measure Mie and Rayleigh Scattering Cross Section.” American Journal of Physics, Vol. 70, No. 6, pp. 620-625.

Evett, S., (2003). “Soil Water Measurement by Time Domain Reflectrometry.” Encyclopedia of Water Science, Marcel Dekker, Inc. New York p 894-898.

Garner, C., Coffman, R., (2016). “Volumetric Water Content Measurements as Obtained from Remote Sensing and In-Situ Instrumentation.” Journal of Environmental and Engineering Geophysics, Accepted for Publication, Manuscript Number 15-022R.

Garner, C., Coffman, R., (2017a). “Remotely Sensed Soil Volumetric Water Content and Dry Density as Obtained Utilizing Change Detection and Polarimetric Methods.” Journal of Environmental and Engineering Geophysics, Submitted for Review (September 2016).

Garner, C., Coffman, R., (2017b). “Visible and Near-Infrared Diffuse Reflectance Properties of Geotechnical Reference Soils” Applied Clay Science (Submitted for Review).

Garner, C., Salazar, S., Coffman, R., (2017c). “Index and Hydraulic Properties of Soil Using Visible-Through Near-Infrared Spectroscopy.” Soil Science (Submitted for Review).

van Genuchten, M., (1980). “A Closed-Form Equation for Predicting the Hydraulic Conductivity of Unsaturated Soils.” Soil Science Society of America Journal, Vol. 44, No. 5, pp. 892-898.

van Genuchten, M., Leij, F., Yates, S., (1991). “The RETC Code for Quantifying the Hydraulic Functions of Unsaturated Soils.” EPA Report 600/2-91/065, U.S. Salinity Laboratory, USDA, ARS, Riverside, California. Version 1.0.

van Genuchten, M., Simunek, J., Leij, F., Sejna, M., (1998). “The RETC Code for Quantifying the Hydraulic Functions of Unsaturated Soils.” Version 6.xx. Software and Supporting Documentation.

Goetz, A., Chabrillat, S., and Lu, Z., (2001). “Field Reflectance Spectrometry for Detection of Swelling Clays at Construction Sites.” Field Analytical Chemistry and Technology. Vol. 5, Issue 3, pp. 143-155.

Goetz, A., Olsen, H., Noe, D., Koehler, J., Humble, J., Fuschino, J., Johnson, E., Johnson, B., (2006). “Spectral Reflectance as a Rapid Technique for Field Determination of Soil Engineering Properties.” Proceedings Geo-volution 2006, pp. 33-61.

Hapke, B., (2012). “Theory of Reflectance and Remittance Spectroscopy.” 2 ed., Cambridge University Press.

Islam, K., Singh, B., McBratney, A., (2003). “Simultaneous Estimation of Various Soil Properties by Ultra-Violet, Visible, and Near-Infrared Reflectance Spectroscopy.” Australian Journal of Soil Research, Vol. 41, pp. 1101-1114.

Janik, L., Skjemstad, J., Raven, M., (1995). “Characterization and Analysis of Soils Using Mid Infrared Partial Least-Squares. I. Correlations with XRF-Determined Major-Element Compositions.” Australian Journal of Soil Research, Vol. 33, pp. 621-636.

de Jong, S. (1993) "SIMPLS: An Alternative Approach to Partial Least Squares Regression." Chemometrics and Intelligent Laboratory Systems." Vol. 18, pp. 251-263.

Kedenburg, S., Vieweg, M., Gissibl, T., Giessen, H., (2012). “Linear Refractive Index and Absorption Measurements in Non-Linear Optical Liquids in the Visible and Near-Infrared Spectral Region.” Optical Materials Express, Vol. 2, pp. 1588-1611.

Kodaira, M., Shibusawa, S., (2013). “Using a Mobile Real-Time Soil Visible Infrared Sensor for High Resolution Soil Properties Mapping.” Geoderma, Vol. 199, pp. 64-79.

Kou, L., Labrie, D., Chylek, P., (1993). “Refractive Indices of Water and Ice in the 0.65- to 2.5-μm Spectral Range.” Applied Optics, Vol. 32, No. 19, pp. 3531-3540.

Kubelka, P., (1947). “New Contributions to the Optics of Intensely Light-Scattering Materials, Part I.” Journal of the Optical Society of America, Vol. 38, Number 5, pp. 448-457.

Kubelka, P., Munk, F., (1931). “Ein Beitragzur Optik der Farbanstriche.” (in German), Z. Technol. Physics., Vol. 12, pp. 593-620.

Kulhawy, F., Mayne P., (1990). “Manual on Estimating Soil Properties for Foundation Design.” Final Report of the Electric Power Research Institute Research Project 1493-6.

Mathworks, (2010). “Plsregress.m.” Partial Least Squares Regression Software. The Mathworks Corporation, Natick, Massachusetts.

Mathworks, (2012b). “Pca.m.” Principle Components Analysis Software. The Mathworks Corporation, Natick, Massachusetts.

Mathworks, (2014a). “The MATLAB R2014A Programming Suite and Supporting Documentation.” The Mathworks Corporation, Natick, Massachusetts.

McCarty, G., Reeves, J., Reeves, V., Follet, R., Kimble, J., (2002). “Mid-Infrared and Near-Infrared Diffuse Reflectance Spectroscopy for Soil Carbon Measurement.” Soil Science Society of America Journal, Vol. 66, pp. 640-646.

Morris, P., Lockington, D., Apelt, C., (2000). “Correlations for Mine Tailings Consolidation Parameters.” International Journal of Surface Mining, Reclamation and Environment, Vol. 14, pp. 171-443.

Nemmers, C., (1998). “Volumetric Moisture Content Using Time Domain Reflectometry.” FHWA publication number: FHWA-RD-97-139.

Neumann, H., and Thurtell, G., (1972). “A Peltier Cooled Thermocouple Dew Point Hygrometer for In Situ Measurement of Water Potentials.” In Brown, R., Haveren, B., (eds.). “Psychometry in Water Relations Research.” Utah Agricultural Experiment Station.

Nicolet, (2004). “Nicolet FT-IR User’s Guide.” Nicolet 6700 Fourier Transform Infrared Spectrometer User’s Manual and Supporting Documentation. http://mmrc.caltech.edu/FTIR/Nicolet/Nicolet%20Software/Nicolet%202/4700_6700_User.pdf. Retrieved September 2014.

Nocita, M., Stevens, A., Noon, C., van Wesemael, B., (2013). “Prediction of Soil Organic Carbon for Different Levels of Soil Moisture Using Vis-NIR Spectroscopy.” Geoderma, Vol. 199, pp. 37-42.

Park, John K., (1980). “A Soil Moisture Reflectance Model in Visible and Near IR Bands.” Symposium on Machine Processing of Remotely Sensed Data and Soil Information Systems and Remote Sensing and Soil Survey. The Laboratory for Applications of Remote Sensing, West Lafayette, Indiana.

Phene, C., Rawlins, S., Hoffman, G., (1971). “Measuring Soil Matric Potential In Situ by Sensing Heat Dissipation within a Porous Body: I. Theory and Sensor Construction.” Soil Science Society of America Journal. Vol. 35, pp. 27-33.

Philpot, W., (2010). “Spectral Reflectance of Wetted Soils.” Proceedings of ASD and IEEE GRS; Art, Science and Applications of Reflectance Spectroscopy Symposium, Vol. II. Boulder, Colorado.

Reece, C., (1996). “Evaluation of a Line Heat Dissipation Sensor for Measuring Soil Matric Potential.” Soil Science Society of America Journal. Vol, 60, pp. 1022-1028.

Reginato, R., van Bavel, C., (1962). “Pressure Cell for Soil Cores.” Proceedings of the Soil Science Society of America, Vol. 26, pp. 1-3.

Richards, L., (1941). “A Pressure Membrane Apparatus for Soil Solution Extraction.” Soil Science, Vol. 51, pp. 377-385.

Richards, L., (1948). “Porous Plate Apparatus for Measuring Moisture Retention and Transmission by Soils.” Soil Science, Vol. 66, pp. 105-110.

Richardson, A., Wiegland, C., Gausman, H., Cuellar, J., Gerbermann, A., (1975). “Plant, Soil, and Shadow Reflectance Components for Row Crops.” Photogrammetric Engineering and Remote Sensing, Vol. 41, pp. 1401-1407.

Rosipal, R., Kramer, N., (2006). "Overview and Recent Advances in Partial Least Squares", in Subspace, Latent Structure and Feature Selection: Statistical and Optimization Perspectives Workshop (SLSFS 2005), Revised Selected Papers (Lecture Notes in Computer Science 3940), C. Saunders et al. (eds.) pp. 34-51, Springer.

Rossel, R., McBratney, A., Minasny, B., (eds.), (2010a). “Proximal Soil Sensing. Volume 1 of Progress in Soil Science.” Springer Science and Business Media. Springer, New York.

Rothman, L., Gordon, E., Barbe, A., Benner, D., Bernath, P., Birk, M., Boudon, V., Brown, L., Campargue, A., Champion, J., Chance, K., Coudert, L., Dana, V., Devi, V., Fally, S., Flaud, J., Gamache, R., Goldman, A., Jacquemart, D., Kleiner, I., Lacome, N., Lafferty, W., Mandin, J., Massie, S., Mikhailenko, D., Miller, C., Moazzen-Ahmadi, Naumenko, O., Nikitin, A., Orphal, J., Perevalov, W., Perin, A., Predoi-Cross, A., Rinsland, C., Rotger, M., Simeckova, M., Smith, M., Sung, K., Taskun, S., Tennyson, J., Toth, R., Vandaele, A., Auwera, J., (2009). "The HITRAN 2008 molecular spectroscopic database." Journal of Quantitative Spectroscopy and Radiative Transfer. Vol. 110, pp. 533-573.

Shepherd, K., Walsh, M., (2002). “Development of Reflectance Spectral Libraries for Characterization of Soil Properties.” Soil Science Society for American Journal, Vol. 66, pp. 988-998.

Shibusawa, S., Imade-Amon, S., Sato, S., Sasao, A., Harako, S., (2001). “Soil Mapping Using the Real-Time Soil Spectrophotometer.” Proceedings of the Third European Conference on Precision Agriculture, Vol. 1, Agro Montpellier, pp. 497-508.

Skempton, A., (1944). “Notes on the Compressibility of Clays.” Quarterly Journal of the Geological Society of London, Vol. 100, C: Parts 1 and 2. Pp. 119-135.

Skempton, A., Northey, R., (1953). “The Sensitivity of Clays.” Geotechnique, Vol. 3, No. 1, pp. 30-53.

Taylor, D., (1948). “Fundamentals of Soil Mechanics.” John Wiley and Sons, Inc., New York.

Terzaghi, K., Peck, R., Mesri, G., (1996). “Soil Mechanics in Engineering Practice.” 3 ed., John Wiley and Sons, New York, New York.

Tokunaga, T., (2009). “Hydraulic Properties of Adsorbed Water Films in Unsaturated Porous Media.” Water Resources Research, Vol. 45, doi: 10.1029/2009WR007734.

Tokunaga, T., (2011). “Physicochemical Controls on Adsorbed Water Film Thickness in Unsaturated Geological Media.” Water Resources Research, Vol. 47. doi:10.1029/2012WR01187.

Torrent, J., Barron, V., (1993). “Laboratory Measurement of Soil Color: Theory and Practice.” In Soil Color. Soil Science Society of America Special Publication No. 31.

Walvoort, D., McBratney, A., (2001). “Diffuse Reflectance Spectrometry as a Proximal Sensing Tool for Precision Agriculture.” Proceedings of the Third European Conference on Precision Agriculture, Agro Montpellier, Vol. 1, pp. 503-507.

Waruru, B., Shepherd, K., Ndegwa, G., Kamoni, P., Sila, A., (2014). “Rapid Estimation of Soil Engineering Properties Using Diffuse Reflectance Near Infrared Spectroscopy.” Journal of Biosystems Engineering, Vol. 121, pp. 177-185.

Wayllace, A., Lu, N., (2012). “A Transient Water Release and Imbibitions Method for Rapidly Measuring Wetting and Drying Soil Water Retention and Hydraulic Conductivity Functions.” Geotechnical Testing Journal, Vol. 35, Issue 1.

Whiting, M., (2009). “Measuring Surface Water in Soil with Light Reflectance.” Remote Sensing and Modeling of Ecosystems for Sustainability VI, Proceedings of the SPIE, Vol 7454, doi: 10.1117/12.826896.

Wold, S., Sjostrom, M., Eriksson, L., (2001). “PLS-Regression: A Basic Tool of Chemometrics.” Chemometrics and Intelligent Laboratory Systems. Vol. 58, Issue 2, pp. 109-130.

Wroth, C., Wood, D., (1978). “The Correlation of Index Properties with Some Basic Engineering Properties of Soils.” Canadian Geotechnical Journal, Vol. 15, No. 2, pp. 137-145.

Yitagesu, F., van der Meer, F., van der Werff, H., Zigterman, W., (2009). “Quantifying Engineering Parameters of Expansive Soils from Their Reflectance Spectra.” Engineering Geology, Vol. 105, Issue 3-4, pp. 151-160.

Youssef, M., El Ramli, A., El Demery, M., (1965). “Relationships between Shear Strength, Consolidation, Liquid Limit, and Plastic Limit for Remoulded Clays.” Proceedings of the 6th International Conference on Soil Mechanics and Foundation Engineering, Montreal, Vol. 1, pp. 126-129.

CHAPTER 9: CONCLUSIONS AND RECOMMENDATIONS

9.1. Chapter Overview

A description of the conclusions drawn from the results of the research that was described in this manuscript, and recommendations to further address avenues of additional research for remote sensing of unsaturated soil properties, are contained in this chapter. Highlights of the contributions, from the scope of work that was described in this document, are provided in Section 9.2. The conclusions drawn from field-scale sensing of the volumetric water content, as described in Chapter 5 and Chapter 6, are presented in Section 9.3.1. The conclusions drawn from the optical characterization of the three soils, as previously described in Chapter 7, are presented in Section 9.3.2. The conclusions drawn from the laboratory-scale research of volumetric water content and soil water matric potential as described in Chapter 8 are documented in Section 9.3.3. The recommendations for future research are presented in Section 9.4. A summary of the items discussed in this chapter is contained in Section 9.5.

9.2. Selected Contributions from this Research Project

The contributions of the research project are described briefly and are highlighted as bullet points in this section. The field portion of this scope of work consisted of applying previously developed active microwave techniques to acquire *in situ* measurements of volumetric water content at two project sites. Innovative aspects of the field-based research campaign included the use of ground-based radar imagery. Previously conducted research had employed either aerial or orbital radar imagery. The change detection methodologies (Wegmuller 1997 and Wagner 1998) had not been previously used for ground-based systems.

Similarly, the laboratory-based portion of the research contributions included the development of an apparatus and methodology for the acquisition of Vis-NIR optical properties of the soils for use in a closed-form solution to determine the volumetric water content and soil

water matric potential from reflectance spectral data. Additionally, the soil absorption and scattering coefficients obtained are expected to be applicable to multi-disciplinary soil science research (e.g. geotechnical, geo-environmental, agricultural, geological, biological, and geochemical). The use of closed-form solutions, based on the Kubelka-Munk color theory, were evaluated and the potential shortcomings and solutions associated with these closed-form methods were identified. The use of Vis-NIR spectroscopy to obtain soil index properties was also investigated. The primary contribution of this research project was the development of a previously unrealized capability to obtain soil water characteristic curve data from Vis-NIR reflectance spectroscopy. For two of the three soil types, the remotely sensed SWCC curve was within 10 percentage points of the laboratory-obtained (WP-4 and PPE) SWCC for soil water matric potential values greater than 100kPa (Donna Fill) and 400kPa (illite). As previously mentioned, these contributions are summarized as the following bullet points.

- Implementation and validation of K_u-Band ground-based change detection methods.
- Implementation and validation of C-Band ground-based fully-polarimetric methods (small perturbation methods).
- Development of characterization methods and optical parameters for the Donna Fill, illite, and kaolinite soil types.
- Evaluation of Vis-NIR reflectance spectroscopy as a rapid, non-destructive means of obtaining soil index properties (liquid limit, plastic limit, plasticity index, and clay fraction).
- Development of a proof-of-concept, remotely sensed method for obtaining a soil water characteristic curve.

9.3. Conclusions of Remote Sensing of Unsaturated Soil Properties

The conclusions of this research into field-scale remote measurements of soil moisture and laboratory-scale measurements of volumetric water content and soil water matric potential are contained in this section. Field-scale active microwave measurements of volumetric water content, as described in Chapter 5 and Chapter 6, are discussed in Section 9.3.1. Laboratory-scale measurements of volumetric water content and soil water potential, as previously presented in Chapters 7 and 8, are described in Section 9.3.2 and Section 9.3.3, respectively.

9.3.1. *Conclusions Regarding Remote Microwave Sensing of Volumetric Water Content*

As compared to traditional measurement techniques that are currently utilized to obtain soil water content, ground-based remote sensing (imaging) offers potential benefits to both geotechnical and multi-disciplinary soil testing fields. Ground-based remote sensing techniques offer increased spatial and temporal resolution, as compared to other remote measurements, and increased spatial coverage as compared to *in situ* or traditional laboratory testing. Additionally, remotely sensed measurements are typically obtained in near real time (minutes or hours depending on the size of the area) provided that the supporting software has been developed.

Three different methods of extracting volumetric water content were evaluated during the scope of work described in this manuscript. Two change detection methods (Wegmuller 1997 and Wagner 1998) and one fully polarimetric method (small perturbation method) were evaluated. In addition, two different instrument wavelengths were considered (K_u-Band and C-Band). All three of the considered methods (the K_u-Band Wagner 1998 method, the C-Band Wagner 1998 method, and the C-Band SPM) at the Westar Jeffery Energy Center (WJEC) project site provided measured volumetric water content values within 0.10 of the observed *in situ* measurement (as obtained using a nuclear density gauge and phase relationships). Although the K_u-Band Wagner

(1998) change detection method provided the volumetric water content measurement that best matched the *in situ* measurements (θ_v within 0.02), it is suggested that the C-Band instrument may be more applicable for a given site due to the increased soil penetration depth and reduced sensitivity to vegetation and other ground clutter at longer wavelengths.

When comparing between the non-polarimetric change detection method and the polarimetric SPM method, both methodologies were found to provide results within 0.10 at various water content conditions (both before and after precipitation events) at the JEC project site. The SPM method was a theoretically rigorous approach; direct measurement of the soil volumetric water content were yielded from this approach. The polarimetric methods were substantially more computationally intensive and required the selection of an appropriate dielectric soil-water mixing model. Therefore, the SPM (and other polarimetric methods) should be conducted with the use of digital terrain model DTM to allow for the calculation of pixel incident angles instead of using the assumed site geometry (as was done during this research project). Based on the findings documented herein, this recommendation is currently being implemented into the commercially available Gamma Remote Sensing software program. The change detection methods did require *in situ* data (specifically porosity) and also required that the ground surface not be disturbed during the time period when observations were collected. For the Wagner (1998) method, an additional requirement was imposed, that the soil be observed in a state of both complete saturation (saturation equal to 100 percent) and complete desaturation (saturation equal to zero percent). Similarly, the Wegmuller (1997) method required that at least one image of known volumetric water content be acquired. Therefore, the use of the change detection methods for short duration observations may not be appropriate because these boundary conditions (knowledge of saturation) may not be observed during the time frame of interest.

9.3.2. *Conclusions Regarding Characterization of Soil Optical Properties*

The soil characterization techniques previously described in Chapter 7 were found to provide soil absorption and scattering coefficients that were in agreement (within one order of magnitude) with published literature values, where available. The sample chamber that was fabricated as part of the characterization methodology was found to be capable of incorporating both ultraviolet-visible (USB-2000) and Vis-NIR (Nicolet 6700) measurements on the same sample. Potential improvements to the sample chamber include the use of a completely contained sample chamber (the current sample chamber is not pressure rated or vented to prevent failure). Additionally, the use of a custom fabricated reference sample would allow for a simplified assembly process. However, the most critical improvement to the sample chamber would be to allow for an illumination source so that the sample chamber could be used with the FieldSpec-4 instrument. The use of the FieldSpec-4 instrument would allow for the removal of the discontinuity in the data between the two spectrometers. It would additionally remove errors caused by interpolation between data acquired at different resolutions (the Nicolet 6700 collected at a wavenumber resolution of $1cm^{-1}$ while the FieldSpec-4 collected data at a 1.5nm resolution).

9.3.3. *Conclusions Regarding Remote Reflectance Measurements of Volumetric Water Content, Soil Water Matric Potential, and Soil Index Properties*

Variable results were obtained from the remote measurement of soil properties. The close form solutions investigated did not provide usable data for either soil volumetric water content or soil water matric potential. Specifically, empirical correlations with a high coefficient of determination (R^2 greater than 0.90) between the observed reflectance spectra and the soil index properties (liquid limit, plastic limit, and clay fraction) were obtained by using the visible to near infrared (Vis-NIR) spectroscopic techniques for all three of the evaluated soil types. For the empirical volumetric water content relationships, R^2 values greater than 0.74 were obtained for

both Donna Fill and illite samples. For the empirical soil water potential relationships R^2 values of 0.75 and 0.52 were obtained for the Donna Fill and illite soil types, respectively. Furthermore, the for the validation samples the calculated soil water matric potential was within approximately 150kPa of the values obtained using traditional laboratory techniques. For kaolinite, however, no useful correlation was developed. It is theorized that the treatment (bleaching) of the kaolinite silt product (Kaowhite-S) was responsible for the material forming a water film on the surface of the various samples. Due to the limited penetration depth of incident radiation in the Vis-NIR spectrum, the measurements that were captured were from the reflection and absorption within this water film and were not representative of the larger sample. This behavior would explain why changes in the observed reflectance spectra were not sensitive to changes in the volumetric water content or the water matric potential.

9.4. Recommendations for Future Research

Recommendations for further research on remote sensing of unsaturated soil properties are described in this section. Recommendations for field-scale microwave sensing of volumetric water content are presented in Section 9.4.1. Specific recommendations for ground-based microwave remote sensing include the use of 1) more favorable site selection, 2) improvements in image registration, 3) incorporation of interferometric or laser scanner obtained measurements of site topography, and 4) selection of a more appropriate wavelength band. Recommendations for the use of laboratory-scale Vis-NIR reflectance spectroscopy are presented in Sections 9.4.2 and 9.4.3. For laboratory-based measurements of soil, recommendations for future research on matric potential and volumetric water content include: 1) utilization of the change in remotely sensed volumetric water content as a boundary condition for numerical modeling (e.g. finite element or finite difference implementation of the Richards 1931 equation) to determine soil matric potential

and 2) utilization of empirical regression techniques to correlate observed reflectance spectra with soil hydraulic properties to determine soil water characteristic parameters (e.g. van Genuchten 1980).

9.4.1. *Recommendations for Future Research on Ground-based Microwave Sensing of Volumetric Water Content*

The following areas of improvement have been identified to improve the performance of ground-based radar systems for the measurement of volumetric water content:

1) site selection (to decrease incidence angle),
2) image registration,
3) incorporation of site specific topographic model or measurement of soil surface roughness, and
4) selection of an appropriate wavelength band.

The primary limitations encountered at both the Cato Springs Research Center and the Westar Jeffery Energy Center project sites were associated with topography. At both project sites, the site topography resulted in a high incident angle. The high incident angle resulted in a degradation in the performance of the volumetric water content measurements by 1) increasing the effect of surface roughness on the backscattered intensity, 2) decreasing the influence of soil dielectric permissivity, and 3) decreasing the value of the backscatter coefficient. Therefore, to increase the measurement accuracy, a site with sufficient topographic relief (look down or look up) should be selected or created. The alternative method to create relief might include the use of artificial means to decrease the incident angle (by placing the radar instrument on a tower or mast). The use of artificial elevation would however only be effective at small ranges or would require an expensive and tall structure. Utilization of such a structure may prohibit reoccupation for repeat measurements. Therefore, the use of a different antenna configuration such as horn

antennas mounted on a mobile base which could be used to acquire close range measurements of volumetric water content as the vehicle moved should be considered. Such a method would require additional image registration processing. This processing would be very difficult and possibly impractical. Finally, if the radar instrument size and weight could be miniaturized sufficiently then it might be possible to use an unmanned aerial vehicle (UAV) to achieve a high incident angle while still maintaining the high spatial resolution (due to the low altitude) and high temporal resolution (due to user selected repeat interval selection).

Image registration is a primary task that is required for the extraction of any information (deformation or soil properties) from temporally or spatially separated radar image series. Strong reflectors near the center of the image are typically used to register sequential radar images. At both the UACSRC and WJEC project sites there were no strong reflectors (metal targets placed in viewing area image before image acquisition) near the image center (the target area). Therefore, the incorporation of radar registration targets could have been used to increase image registration accuracy. In addition, at both the UACSRC and WJEC project sites the instrument was placed on a tripod that was not permanently affixed to the ground. Therefore, despite the best efforts of the researchers, there may have been some movement of the instrument during occupation and re-occupation of the instrument position. The use of a permanent, rigid, instrument mount that could be securely anchored into position and allow for a consistent reoccupation of the same position between temporally separated images would increase the accuracy of the image registration process. Also, due to the variable meteorological conditions between image acquisitions (e.g. wind) there may have been some error introduced into the acquired images. It was noted that during periods of high wind that the rotational rate of the radar antennas was affected (e.g. instrument turned slower into the wind). This non-uniform rotation

rate may have introduced error due to the azimuth bearing of the GPRI-2 instrument being based on a consistent rotation rate. A proposed solution to measure and correct for variable rotation effects includes installing a three-axis accelerometer, as described by Gomez (2014). Alternately, an interferometric fiber-optic gyroscope could be used to obtain high precision measurements of the instrument movement.

The soil surface roughness is a primary component of the microwave backscatter models (small perturbation method [SPM] and the integral equations method [IEM]). In particular, the IEM method is generally a more robust technique (although significantly more computationally demanding) for natural soil surfaces. Measurement accuracy is improved by obtaining *in situ* measurements of the soil RMS height or auto-correlation length (Bryant et al. 2007). Field measurements of surface roughness would improve the estimate of the volumetric water content values. While these methods have been typically acquired for sample measurements (transects) using mechanical pin-meter measurements over small areas and then applying these measurements to the wider project site, it may be possible to use high accuracy LIDAR measurements to obtain pixel specific measurements of surface roughness for a site (Bryant et al. 2007). In addition to measurements of soil surface roughness, LIDAR measurements could be used to create a site specific, high spatial resolution digital terrain map (DTM). Such a DTM model could then be used to compute pixel incident angles and increase the accuracy of the volumetric water content inversions. It might also be possible to use an additional transceiver to create a one stationary bistatic synthetic aperture radar (OS-BSAR) to increase the accuracy of the measurement of volumetric water content (e.g. as proposed by Li et al. 2014). Due to issues such as those encountered during this work, Gamma Remote Sensing is currently working on implementing OS-BSAR into the GPRI-2 platform. Through the use of a scheme like the OS-

BSAR, it is possible to measure both forward- and back-scattering microwave radiation, and use the two separate measurements to obtain accurate measurements of surface roughness and dielectric permissivity.

A final recommendation is that due to several effects (e.g. surface roughness and penetration depth), the instrument operating wavelength should be at C-Band or higher. Specifically, the smaller a wavelength (higher frequency) the lower the penetration depth of energy into the soil. Therefore, for K_u-Band measurements the incident radiation only interacts with soil water in the top centimeter of the soil being observed. Secondly, the smaller wavelength imagery is more sensitive to site vegetation, surface roughness, and other miscellaneous scatters. Conversely, for L-Band measurements, volumetric water content measurements can be measured to tens of centimeters of depth. However, a K_u-Band instrument was selected due to the increased spatial resolution and increased sensitivity to deformation measurements. An additional consideration would be to incorporate active and passive (microwave brightness temperature) measurements. Recent research has indicated that ground-based passive, L-Band, remote sensing measurements have the potential to not only extract volumetric water content values but to also make inferences on other soil hydraulic properties, including the van Genuchten (1980) SWCC parameters (Jonard 2012, Jonard et al. 2015).

9.4.2. *Recommendations for Future Research on Closed-form Solutions to Volumetric Water Content and Soil Water Matric Potential*

While the closed-form solutions that were evaluated during the scope of work described were not successful to obtain measurements of volumetric water content and soil water matric potential, some recommendations for future researchers have been identified. Two specific items have been identified as potential methods to improve the accuracy of the closed-form solutions, including 1) the use of a laboratory-obtained empirical model of adsorbed soil water, and/or 2) to

use multiple phases of soil water (bulk soil water, adsorbed soil water, and chemical hydration water). Laboratory-obtained measurements of the thickness of the adsorbed water film as a function of volumetric water content have been used to predict reflectance spectra for soil samples (Philpot 2010). The methods of obtaining the aforementioned adsorbed layer thickness are discussed in Tokunaga (2009, 2011) and Baveye (2012). The use of multiple soil-water phases to model the different behavior was originally suggested by Ben-Dor et al. (1999), and has been extended to model the effects of volumetric water content on soil reflection spectrum (Whiting 2009). However, this method was not evaluated during this work due to the difficultly of obtaining and separating the optical absorption properties of the individual phases. The efficacy and implementation of analytical and quasi-analytical (using empirically derived closed form) solutions may be to employ salt solutions of known osmotic potential to condition soil samples. This could be further extended by using an inert soil analogue such as ceramic beads to remove the influence of soil particles and only evaluating the changes in the reflectance spectra due to the liquid and vapor phases.

9.4.3. *Recommendations for Future Research on Reflectance Measurements of Volumetric Water Content and Soil Water Matric Potential*

Several areas of potential research regarding the laboratory-based measurements of volumetric water content and soil water matric potential from visible and near-infrared (Vis-NIR) reflectance spectroscopy were identified during the course of this research. Specifically, due to the difficulty in measuring matric potential, it might be possible to increase the measurement accuracy by using temporally separated measurements of soil reflectance. In a laboratory setting, if the conditions (temperature, relative humidity) are known, it could be possible to use a numerical model to obtain measurements of soil water matric potential from measurements of volumetric water content. It is proposed that this method would operate by using the

measurements of volumetric water content, which have a higher confidence than the soil water matric potential values, as boundary conditions in a numerical model. The van Genuchten (1980) SWCC parameters could then be approximated by iteratively varying the parameters' values to match the observed change in water content at the soil surface.

Conversely, another potential approach to obtaining a remotely sensed SWCC would be to employ statistical regressions like partial least squares (PLS), principle components regression (PCR), or other numerical techniques (e.g. artificial neural nets) to relate the observed reflectance spectra to the underlying soil properties (residual water content [θ_r], saturated water content [θ_s], fitting parameters [α,ψ,n]). The aforementioned soil hydraulic properties could then be used to generate an estimate of the SWCC. These parameters, specifically θ_r, α, ψ, n and m, are a function of soil mineralogy and texture (Lu and Likos 2002, Hillel 2012). Since the extraction of soil mineralogy and soil texture measurements from reflectance spectroscopy has been previously demonstrated in the literature (Chabrillat et al. 2002, Goetz et al. 2006), this might provide a more accurate measurement of the SWCC. Once a suitable model had been obtained then it would be possible to use the SWCC to calculate soil water potential for remotely sensed measurements of soil water content.

9.5. Summary

In summation, the use of remote sensing technology for field- and laboratory-scale acquisition of unsaturated soil properties offers benefits when compared to the current state of practice. Specifically, as part of this research project, the use of ground-based radar remote sensing techniques were evaluated and validated for high spatial and temporal resolution measurements of volumetric water content using both change detection and polarimetric methods.

Furthermore, recommendations for further research and application of ground-based microwave remote sensing of volumetric water content have been identified and discussed.

A laboratory-scale method for obtaining remote or proximal measurements of soil hydraulic values (θ_v, ψ_m) has been developed. Both analytical and empirical techniques were evaluated. The empirically obtained and validated SWCC were found to provide θ_v values within 0.02 for a given ψ_m greater than 400kPa. Recommendations have been provided to improve both the closed-form solution and the empirically-calibrated solution.

9.6. Works Cited

Baveye, P., (2012). "Comment on Physicochemical Controls on Adsorbed Water Film Thickness in Unsaturated Geological Media." by Tetsu K. Tokunaga, doi:10.1029/2012WR01187.

Ben-Dor, E., Irons, J., Epema, G., (1999). "Soil Reflectance." In Remote Sensing for the Earth Sciences: Manual of Remote Sensing, 3rd ed., Vol. 3, (Rencz, E. ed.). John Wiley and Sons, New York. pp. 3-58.

Bryant, R., Moran, M., Thoma, D., Collins, C., Skirvin, S., Rahman, M., Slocum, K., Starks, P., Bosch, D., Dugo, M., (2007). "Measuring Surface Roughness Height to Parameterize Radar Backscatter Models for Retrieval of Surface Soil Moisture." IEEE Geoscience and Remote Sensing Letters, Vol. 4, No. 1. pp. 137-141

Chabrillat, S., Goetz, A., Krosley, L., Olsen, H., (2002). "Use of Hyperspectral Images in the Identification and Mapping of Expansive Clay Soils and the Role of Spatial Resolution." Remote Sensing of Environment, Vol. 82, pp. 431-445.

van Genuchten, M., (1980). "A Closed-Form Equation for Predicting the Hydraulic Conductivity of Unsaturated Soils." Soil Science Society of America Journal, Vol. 44, No. 5, pp. 892-898.

Goetz, A., Olsen, H., Noe, D., Koehler, J., Humble, J., Fuschino, J., Johnson, E., Johnson, B., (2006). "Spectral Reflectance as a Rapid Technique for Field Determination of Soil Engineering Properties." Proceedings Geo-volution 2006, pp. 33-61.

Gomez, F., (2013). "Personnel Electronic Communication to the Author." Received July 2013.

Hillel, D., (2012). "Introduction to Environmental Soil Physics." Elsevier Academic Press.

Jonard, F., (2012). "Soil Water Content Estimation Using Ground-Based Active and Passive Microwave Remote Sensing: Ground-Penetration Radar and Radiometer." Doctoral Dissertation. Universite Catholique de Louvain. Faculte d'Ingenierie Biologique, Agronomique et Environmentale Earth and Life Institute – Environmental Sciences. August 2012.

Jonard, F., Weihmuller, L., Schwank, M., Jadoon, M., Vereecken, H., Lambot, S., (2015) "Estimation of the Hydraulic Properties of a Sandy Soil Using Passive and Active Microwave Remote Sensing." IEEE Transactions on Geoscience and Remote Sensing. Vol. 53, Issue 6, pp. 3095-3109.

Li, Z., Huang, Y., Yang, J., Liu, Q., (2014). "Omega-K Imaging Algorithm for One-Stationary Bistatic SAR." IEEE Transactions on Aerospace and Electronic Systems, Vol 50, No. 1. pp. 33-52.

Lu, N., Likos, W., (2002). "Unsaturated Soil Mechanics." John Wiley and Sons, Hoboken, NJ.

Nicolet, (2004). “Nicolet FT-IR User’s Guide.” Nicolet 6700 Fourier Transform Infrared Spectrometer User’s Manual and Supporting Documentation. http://mmrc.caltech.edu/FTIR/Nicolet/Nicolet%20Software/Nicolet%202/4700_6700_User.pdf. Retrieved September 2014.

Philpot, W., (2010). “Spectral Reflectance of Wetted Soils.” Proceedings of ASD and IEEE GRS; Art, Science and Applications of Reflectance Spectroscopy Symposium, Vol. II. Boulder, Colorado.

Richards, L., (1931). “Capillary Conduction of Liquids Through Porous Mediums.” Physics, Vol. 1, Issue 5, pp. 318-333.

Tokunaga, T., (2009). “Hydraulic Properties of Adsorbed Water Films in Unsaturated Porous Media.” Water Resources Research, Vol. 45, doi: 10.1029/2009WR007734.

Tokunaga, T., (2011). “Physicochemical Controls on Adsorbed Water Film Thickness in Unsaturated Geological Media.” Water Resources Research, Vol. 47. doi:10.1029/2012WR01187.

Wagner, W., (1998). “Soil Moisture Retrieval from ERS Scatterometer Data.” PhD Dissertation, Vienna University of Technology. November.

Wegmuller, U., (1997). “Soil Moisture Monitoring with ERS SAR Interferometry.” European Space Agency Special Publication ESA SP-414. Proceedings of the 3rd ERS Symposium. pp. 47-51.

Whiting, M., (2009). “Measuring Surface Water in Soil with Light Reflectance.” Remote Sensing and Modeling of Ecosystems for Sustainability VI, Proceedings of the SPIE, Vol 7454, doi: 10.1117/12.826896.

CHAPTER 10: WORKS CITED

3M Corporation (2015). "Product Information and Material Safety Data Sheet for Classic Roofing Granules." http://solutions.3m.com/wps/portal/3M/en_US/IMPD/Roofing-Granules/Products/Classic-Roofing-Granules/. Retrieved December 2015.

Ahuja, L., Naney, J., Williams, R., (1985). "Estimating Soil Water Characteristics from Simpler Properties or Limited Data." Soil Science Society of America Journal, Vol. 49, No. 5, pp. 1100-1105.

American Society for Testing and Materials (ASTM) D422, (2014). "Standard Test Method for Particle-Size Analysis of Soils." American Society for Testing and Materials, Vol. 4.08, Soil and Rock (I). West Conshohocken, PA.

American Society for Testing and Materials (ASTM) D698, (2012). "Standard test methods for laboratory compaction characteristics of soil using standard effort (12400 ft-lbf/ft3 (600 kN-m/m3))." Annual Book of ASTM Standards, 04.08, ASTM, West Conshohocken, PA, USA: 80-90.

American Society for Testing and Materials (ASTM) D854, (2014). "Standard Test Methods for Specific Gravity of Soil Solids by Water Pycnometer." American Society for Testing and Materials, Vol. 4.08, Soil and Rock (I). West Conshohocken, PA.

American Society for Testing and Materials D2216, (2014). "Standard Test Methods for Laboratory Determination of Water (Moisture) Content of Soil and Rock by Mass." Annual Book of ASTM Standards, Designation D2216, Vol. 4.08, ASTM, West Conshohocken, PA.

American Society for Testing and Materials D4318, (2014). "Standard Test Methods for Liquid Limit, Plastic Limit, and Plasticity of Soils." Annual Book of ASTM Standards, Designation D4318, Vol. 4.08, ASTM, West Conshohocken, PA.

American Society for Testing and Materials D5298, (2014). "Standard Test Method for Measurement of Soil Potential (Suction) Using Filter Paper." Annual Book of ASTM Standards, Designation D5298, Vol. 4.08, ASTM, West Conshohocken, PA.

American Society for Testing and Materials D6836, (2014). "Standard Test Method for Determination of the Soil Water Characteristic Curve for Desorption Using a Hanging Column, Pressure Extractor, Chilled Mirror Hygrometer, and/or Centrifuge." Annual Book of ASTM Standards, Designation D6836, Vol. 4.09, ASTM, West Conshohocken, PA.

Applied Soil Water, (2015). "Applied Soil Water Technologies, LLC. Website." http://www.appliedsoilwater.com/. Accessed October 2015.

Aqil, S., Schmitt, D., (2010). “Dielectric Permittivity of Clay Adsorbed Water: Effect of Salinity.” Proceedings of GeoConvention 2010, Calgary, Canada. No pages listed.

Arcone, S., Grant, S., Boitnott, G., Bostick, B., (2008). “Complex Permittivity and Mineralogy of Grain Size Fractions in a Wet Silt Soil.” Geophysics, Vol. 73, No. 4, DOI:10.1190/1.2890776.

ASD Panalytical Inc., (2014). “RS3 and ViewSpecPro Software and Supporting Documentation.” The ASD Panalytical Inc. Boulder, Colorado.

Aslyng, H. (Chairman), (1963). “Soil Physics Terminology.” International Society of Soil Science Bulletin No. 23, pp. 7-10.

Atterberg, A., (1912). “Die Plastizitat der Tone.” Internationale Mitteilungen fur Bodenkunde, Vol. 2, pp. 149-188 (in German).

Barron, V., Torrent, J., (1986). “Use of the Kubelka-Munk Theory to Study the Influence of Iron Oxides on Soil Colour.” Journal of Soil Science, Vol. 37, pp. 499-510.

Baveye, P., (2012). "Comment on Physicochemical Controls on Adsorbed Water Film Thickness in Unsaturated Geological Media.” by Tetsu K. Tokunaga, doi:10.1029/2012WR01187.

Beemer, R., (2015). “Personal Verbal and Electronic Communications to the Author.” In person and electronic conversation with the author, College Station, TX. March 16th and 17th, 2015.

Ben-Dor, E., Banin, A., (1995). “Near-Infrared Analysis as a Rapid Method to Simultaneously Evaluate Several Soil Properties.” Soil Science Society of America Journal, Vol. 59, pp. 364-372.

Ben-Dor, E., Irons, J., Epema, G., (1999). “Soil Reflectance.” In Remote Sensing for the Earth Sciences: Manual of Remote Sensing, 3rd ed., Vol. 3, (Rencz, E. ed.). John Wiley and Sons, New York. pp. 3-58.

Bevin, K., Kirkby, M., (1979). “A physical based, variable contributing area model of basin hydrology.” Hydrological Science Bulletin, Vol. 24, pp. 43-69.

Bishop, A., (1959). “The Principle of Effective Stress.” Tecnisk Ukeblad, Vol. 39, pp. 859-863.

Blumberg, D., Freilikher, V., (2001). “Soil Water-Content and Surface Roughness Retrieval Using ERS-2 SAR Data.” Journal of Arid Environments, Vol. 49, pp. 449-464.

Blumberg, D., Freilikher, V., Lyalko, I., Vulfson, L., Kotlyar, A., Shevchenko, V., Ryabokenko, A., (2000). “Soil Moisture (Water Content) Assessment by an Airborne Scatterometer; The Chernobyl Disaster Area and the Negev Desert.” Remote Sensing of the Environment. Vol. 71, pp. 309-319.

Bolton, M., Cheng, Y., (2002). "Micro-Geomechanics." Proceedings of a Workshop on "Constitutive and Centrifuge Modelling: A Contrast." Ascona, Switzerland, July.

Bouma, J., van Lanen, J., (1987). "Transfer Functions and Threshold Values: From Soil Characteristics to Land Qualities." In Beek, K., Burrough, P., McCormack, D., "Proceedings of the International Workshop on Quantified Land Evaluation. Washington, DC, International Institute of Aerospace Surveying and Earth Science, Publication No. 6.

British Standard Institute (BSI), (1990) "Methods of Test for Soils for Civil Engineering Purposes." British Standard Institute, London, UK.

Brooks, R., Corey, A., (1964). "Hydraulic Properties of Porous Media." Colorado State University. Fort Collins, Colorado.

Brooks, R., Corey, A., (1966). "Properties of Porous Media Affecting Fluid Flow." Journal of Irrigation Drainage Division of the American Society of Civil Engineers, Vol. 91, pp. 61-87.

Bryant, R., Moran, M., Thoma, D., Collins, C., Skirvin, S., Rahman, M., Slocum, K., Starks, P., Bosch, D., Dugo, M., (2007). "Measuring Surface Roughness Height to Parameterize Radar Backscatter Models for Retrieval of Surface Soil Moisture." IEEE Geoscience and Remote Sensing Letters, Vol. 4, No. 1. pp. 137-141

Buckingham, E., (1907). "Studies on the movement of soil moisture." Soil Bulletin No. 38, United States Department of Agriculture, Washington D.C.

Bulcholtz, A., (1995). "Rayleigh Scattering Calculations for the Terrestrial Atmosphere." Applied Optics, Vol. 34, No. 15, pp. 2765-2773.

Busca, G., Resini, C., (2000). "Vibrational Spectroscopy for the Analysis of Geological and Inorganic Materials." Encyclopedia of Analytical Chemistry, Vol. 12, pp. 10984-11020.

Calafrica, (2015). "Cal Africa: Efficient Irrigation Scheduling Systems Website." http://www.calafrica-sa.co.za/. Accessed October 2015.

Campbell Scientific, (2012). "TDR100 manual." http://s.campbellsci.com/documents/us/manuals/tdr100.pdf. Retrieved June 2012.

Campbell Scientific, (2013). "CS-229 Heat Dissipation Sensors. Use and Calibration." Campbell Scientific Website. Retrieved July 2013.

Campbell, D., (1976). "Plastic Limit Determination Using a Drop Cone Penetrometer." Journal of Soil Science, Vol. 27, No. 3, pp. 295-300.

Campbell, E., Campbell, G., Barlow, W., (1973). “A Dew Point Hygrometer for Water Potential Measurement.” Agricultural Meteorology, Vol. 12, pp. 113-121.

Carrier, W., Beckman, J., (1984). “Correlations between Index Properties of Remolded Clays.” Geotechnique, Vol. 34, pp. 211-228.

Casagrande, A., (1932). “Research on the Atterberg Limits of Soils.” Public Roads, Vol. 12, No. 8.

Casagrande, A., (1948), “Classification and Identification of soils: Transactions of the American Society of Civil Engineers.” Vol. 113, pp. 901-930.

Casagrande, A., (1958). “Notes on the Design of the Liquid Limit Device.” Geotechnique, Vol. 8, No. 2, pp. 84-91.

Casagrande, A., Fadum, R., (1940). “Notes on Soil Testing for Engineering Purposes.” Harvard Soil Mechanics, Series No. 8, Cambridge, Massachusetts.

Chabrillat, S., Goetz, A., Krosley, L., Olsen, H., (2002). “Use of Hyperspectral Images in the Identification and Mapping of Expansive Clay Soils and the Role of Spatial Resolution.” Remote Sensing of Environment, Vol. 82, pp. 431-445.

Chang, C., Laird, D., (2002). “Near-Infrared Reflectance Spectroscopic Analysis of Soil C and N.” Journal of Soil Science, Vol. 17, pp. 110-116.

Chang, C., Laird, D., Mausbach, M., Hurburg, C., (2001). “Near-Infrared Reflectance Spectroscopy-Principle Components Regression Analysis of Soil Properties.” Soil Science Society of America Journal, Vol. 65, pp. 480-490.

Chen, F., (1988). “Foundations on Expansive Soils (Second Edition).” Amsterdam: Elsevier.

Chen, K., Wu, T., Tsang, L., Li, Q., Shi, J., Fung, A., (2003). “Emission of rough surfaces calculated by the integral method with comparison to three dimensional moment method simulations.” IEEE Transaction on Geoscience and Remote Sensing. Vol. 41, p 90-101.

Clay Mineral Society (2015), “The Source Clays Project Background.” The Clay Mineral Society. http://www.clays.org/SOURCE%20CLAYS/SCBackground.html. Retrieved August 2015.

Coffman, R., (2009), “Processing of Synthetic Aperture Radar Data as Applied to the Characterization of Localized Deformation Features.” Ph.D. Dissertation, University of Missouri, Columbia, August.

Coffman, R., (2013b). "Performance of Westar Energy Vertical Flow Bed Test Section." Coffman Consulting Company, LLC Final Report. Client: Burns and McDonnell Engineering, Inc., December.

Coffman, R., (2013a). “CAREER: Incorporation of Statistics and Remote Sensing into Thermal-Hydraulic-Mechanical Modeling of Soils.” A Proposal to the National Science Foundation.

Coffman, R., (2013b). “Geotechnical Properties of Vertical Flow Bed Treatment Soil.” Coffman Consulting Company, Report No. 2013-BMCD/WESTAR CWTS VFB.

Coffman, R., (2014). “Image of University of Missouri GPRI-2.” Personal Electronic Communication to the Author.

Coffman, R., Conte, O., (2012). "Slope Stability Monitoring Using Remote Sensing Techniques Final Report for AHTD TRC Project 1102." Client: Arkansas State Highway and Transportation Department, November.

Coffman, R., Garner, C., (2012). “Final Report of MBTC-3031 Project.” Mack-Blackwell Rural Transportation Center.

Conte, O., Coffman, R., (2012). “Slope Stability Monitoring Using Remote Sensing Techniques.” ASCE Geotechnical Special Publication No. 225, Proc. GeoCongress 2012: State of the Art and Practice in Geotechnical Engineering, Oakland, California, March, pp. 3060-3068.

Conte, O., Coffman, R., (2013). “Characterization of Landslides by Advanced Remote Sensing Techniques, Standard Monitoring Techniques, and Laboratory Testing.” Proc. GeoCongress 2013: Stability and Performance of Slopes and Embankments III, San Diego, California, March. Accepted for Publication (in press).

Conte, Omar A. R. (2012). “Slope Stability Monitoring Using Remote Sensing Techniques.” Master’s Thesis. University of Arkansas – Fayetteville. May 2012.

Controls Group (2015). “Liquid Limit Devices – Casagrande.” http://www.controls-group.com/eng/soil-testing-equipment/liquid-limit-devices-casagrande.php. Retrieved November 2015.

Cox, A., DeWeerd, A., Linden, J., (2002). “An Experiment to Measure Mie and Rayleigh Scattering Cross Section.” American Journal of Physics, Vol. 70, No. 6, pp. 620-625.

Cozzolino, D., Moron, A., (2003). “The Potential of Near-Infrared Reflectance Spectroscopy to Analyze Soil Chemical and Physical Characteristics.” Journal of Agricultural Sciences, Vol. 140, pp. 65-71.

Croney, D., Coleman, J., (1961). “Pore Pressure and Suction in Soils.” Proceedings of the Conference on Pore Pressure and Suction in Soils, London. pp. 31-37.

Dalal, R., Henry, R., (1986). “Simultaneous Determination of Moisture, Organic Carbon, and Total Nitrogen by Near Infrared Reflectance Spectrophotometry.” Soil Science Society of America Journal, Vol. 50, pp. 120-123.

Daniel, K., Tripathi, N., Honda, K., (2003). “Artificial Neural Network Analysis of Laboratory and In Situ Spectra for the Estimation of Macronutrients in Soils of Lop Buri (Thailand).” Australian Journal of Soil Research, Vol. 41, pp. 47-595.

Dash, S., Prusty, G., (2007). “Simulation of Radar Backscattering Coefficients Using IEM Soil Moisture Retrieval.” Proceedings of the Third International Conference on Recent Advances in Space Technologies (RAST ’07). Istanbul, Turkey. pp. 383-388.

Decagon Devices (2007). “WP4 Dewpoint PotentiaMeter Operator’s Manual and Quick Start Guide.” Decagon Devices, Inc. Pullman, Washington.

Deng, H. (2012). "Ground Based Interferometric Radar Initial Look at Longview, Blue Springs, Tuttle Creek, and Milford Dams." Master of Science Thesis. University of Missouri-Columbia, July.

Dobson, G., Brewere, A., Cwilong, B., (1946). “Meteorology of the Lower Stratosphere.” Proceedings of the Royal Society (London), Vol. A185, pp. 144-175.

Dobson, M., Ulaby, F., Hallikainen, M., El-Rayes, M., (1985). “Microwave Dielectric Behavior of Wet Soil – Part II: Dielectric Mixing Models.” IEEE Transactions on Geoscience and Remote Sensing, Vol. GE-23, No. 1.

Dolinar, B., (2009). “Predicting the Normalized Undrained Shear Strength of Saturated Fine-Grained Soils Using Plasticity-Value Correlations.” Applied Clay Science, pp. 428-432.

Dubois, P., van Zyl, J., Engman, E., (1995) “Measuring Soil Moisture with Imaging Radar.” IEEE Transactions of Geoscience Remote Sensing, Vol. 33, pp. 916–926.

European Space Agency (ESA), (2013). “Rough Surface Scattering Models.” European Space Agency Online Manual. http://earth.eo.esa.int/polsarpro/Manuals/2_Rough_Surface_ Scattering_ Models.pdf. Retrieved December 2013.

European Space Agency (ESA), (2014). “Parameters affecting radar backscatter.” ESA Earthnet Online. http://earth.esa.int/applications/data_util/SARDOCS/spaceborne/Radar_Courses/ Radar_Course_III/parameters_affecting.htm. Retrieved April 11, 2014.

Evans, D., Alpers, W., Cazenave, A., Elachi, C., Farr, T., Glackin, D., Holt, D., Jones, L., Liu, W., McCandless, W., Menard, Y., Moore, R., Njoku, E., (2005). “Seasat – A 25-Year Legacy of Success.” Remote Sensing of Environment, Vol. 92, pp. 384-404.

Evett, S., (2003). “Soil Water Measurement by Time Domain Reflectrometry.” Encyclopedia of Water Science, Marcel Dekker, Inc. New York p 894-898.

Fandry, J., (2012). “Pressure Plate Operations Manual.” Department of Civil and Environmental Engineering, University of Missouri. Columbia, Missouri.

Farmer, V., (ed.), (1974). “Infrared Spectra of Minerals.” Mineralogical Society. London.

Filin, S., Abo Akel, N., Kremeike, K., Sester, M., Doytsher, Y., (2007). “Interpretation and Generalization of 3D Landscapes from LIDAR Data.” Cartography and GeoInformation Science, Vol. 34, pp. 231-243.

Fredlund, D., Xing, A., (1994). “Equations of the Soil-Water Characteristic Curve.” Canadian Geotechnical Journal, Vol. 31, pp. 521-532.

Fredlund, D., Rahardjo, H., (1993). “Soil Mechanics for Unsaturated Soils.” Wiley, New York.

Froese, C., Mei, S., (2008). “Mapping and Monitoring Coal Mine Subsidence using LiDAR and InSAR.” GeoEdmonton 2008. Proceedings of the 61st Canadian Geotechnical Conference and Ninth Joint CGS/IAH-CNC Groundwater Conference. September 21-24, Edmonton Canada. pp. 1127-1132.

Fung, A., Li, Z., Chen, K., (1992). “Backscattering from a Randomly Rough Dielectric Surface.” IEEE Transaction on Geoscience and Remote Sensing, Vol. 30, pp. 356-369.

Gabriel, A., Goldstein, R., (1988). “Crossed Orbit Interferometry: Theory and Experimental Results from SIR-B.” International Journal of Remote Sensing, Vol. 9, No. 8, pp. 857-872.

Gabriel, A., Goldstein, R., Zebker, H., (1989). "Mapping Small Elevation Changes over Large Areas: Differential Radar Interferometry." Journal of Geophysical Research, Vol. 92, No. B7, pp. 9183-9191.

Gamma Remote Sensing, (2012). “GAMMA SAR and interferometry software.” Version 2006, updated 2012.

Garner, C., Coffman, R., (2014). “Remote Sensing Methods for Monitoring Ground Surface Deformation of Compacted Clay Test Sections.” ASCE Geotechnical Special Publication No. 234, Proceedings of the GeoCongress 2014: Geo-Characterization and Modeling for Sustainability, Atlanta, Georgia, February, pp. 963-978.

Garner, C., Coffman, R., (2016). “Volumetric Water Content Measurements as Obtained from Remote Sensing and In-Situ Instrumentation.” Journal of Environmental and Engineering Geophysics, Accepted for Publication, Manuscript Number 15-022R.

Garner, C., Coffman, R., (2017a). “Remotely Sensed Soil Volumetric Water Content and Dry Density as Obtained Utilizing Change Detection and Polarimetric Methods.” Journal of Environmental and Engineering Geophysics, Submitted for Review (September 2016).

Garner, C., Coffman, R., (2017b). “Visible and Near-Infrared Diffuse Reflectance Properties of Geotechnical Reference Soils” Clay Mineral Society, In Preparation.

Garner, C., Salazar, S., Coffman, R., (2017c). “Index and Hydraulic Properties of Soil Using Visible-Through Near-Infrared Spectroscopy.” Soil Science (Submitted for Review).

van Genuchten, M., (1980). “A Closed-Form Equation for Predicting the Hydraulic Conductivity of Unsaturated Soils.” Soil Science Society of America Journal, Vol. 44, No. 5, pp. 892-898.

van Genuchten, M., Leij, F., Yates, S., (1991). “The RETC Code for Quantifying the Hydraulic Functions of Unsaturated Soils.” EPA Report 600/2-91/065, U.S. Salinity Laboratory, USDA, ARS, Riverside, California. Version 1.0.

van Genuchten, M., Simunek, J., Leij, F., Sejna, M., (1998). “The RETC Code for Quantifying the Hydraulic Functions of Unsaturated Soils.” Version 6.xx. Software and Supporting Documentation.

GeoNor, (2015). “GeoNor Website.” http://geonor.com/live/. Accessed October 2015.

Gillespie, J., Lindberg, J., Smith, M., (1974). “Visible and Near-Infrared Absorption Coefficients of Montmorillonite and Related Clays.” American Mineralogist, Vol. 59, pp. 1113-1116.

Goetz, A., Chabrillat, S., and Lu, Z., (2001). “Field Reflectance Spectrometry for Detection of Swelling Clays at Construction Sites.” Field Analytical Chemistry and Technology. Vol. 5, Issue 3, pp. 143-155.

Goetz, A., Olsen, H., Noe, D., Koehler, J., Humble, J., Fuschino, J., Johnson, E., Johnson, B., (2006). “Spectral Reflectance as a Rapid Technique for Field Determination of Soil Engineering Properties.” Proceedings Geo-volution 2006, pp. 33-61.

Gomez, F., (2013). “Personnel Electronic Communication to the Author.” Received July 2013.

Google, (2012). “Google Earth and Supporting Documentation.” The Google Corporation. Imagery Retrieved 2012.

Google, (2014). “Google Earth Imagery.” The Google Corporation. Retrieved February 2014.

Grant, W., (1982). "Effect of Differential Spectral Reflectance on DIAL Measurements using Topographic Targets." Applied Optics, Vol. 21, Issue 13, P 2390-2394.

Haigh, S., (2012). “Mechanics of the Casagrande Liquid Limit Test.” Canadian Geotechnical Journal, Vol. 49, No. 9, pp. 1015-1023.

Haigh, S., Vardanega, P., Bolton, M., (2013). “The Plastic Limit of Clays.” Geotechnique, Vol. 63, pp. 435-440.

Haile, A., Rientjes, T., (2005). "Effects of LIDAR DEM Resolution in Flood Modeling: a Model Sensitivity Study for the City of Tegucigalpa, Honduras." ISPRS WG III/3 III/4 V/3 Workshop – Laser scanning. Enschede, the Netherlands. September 2005.

Hakim, H., Hashim, A., Abdul-Hafidh, G., Alyaa, H., Mohammed, S., (2013). "Study [of] the Optical Properties of Polyvinylpyrrolidone (PVP) Doped with KBr." European Scientific Journal, Vol. 3, pp. 132-137.

Hallikainen, M., Ulaby, F., Dobson, M., El-Rayes, M., Wu, L., (1985). "Microwave Dielectric Behavior of Wet Soil-Part 1: Empirical Models and Experimental Observations." IEEE Transactions on Geoscience and Remote Sensing, pp. 25-34.

Hanson, B., and Peters D., (2000). "Soil Type Affects Accuracy of Dielectric Moisture Sensors." California Agriculture. pp. 43-47.

Hapke, B., (2012). "Theory of Reflectance and Remittance Spectroscopy." 2 ed., Cambridge University Press.

High Plains Regional Climate Center (HPRCC), (2013). "June 2013 Climate Summary." http://www.hprcc.unl.edu/publications/files/2013_06_climatesummary.pdf. Retrieved January 2014.

Hillel, D., (2012). "Introduction to Environmental Soil Physics." Elsevier Academic Press.

Holtz, R., and Kovacs, W., (1981). "An Introduction to Geotechnical Engineering: Englewood Cliff." New Jersey, Prentice-Hall.

International Atomic Energy Agency (IAEA), (2005). "Technical Data on Nucleonic Gauges." IAEA Technical Doc No. IAEA-TECDOC-1459. July 2005.

International Commission on Irrigation and Drainage (ICID), (1996). "Multilingual Technical Dictionary on Irrigation and Drainage." 2nd ed. ICID-CIID, New Delhi, India.

Irrometer, (2012). "Irrometer-E Gauge and Probe Documentation." Irrometer website. http://www.irrometer.com/pdf/instruction%20manuals/IRROMETERs/755%20E%20GaugeVACUUM%20hi%20Web4.pdf. Retrieved June, 2012.

Islam, K., Singh, B., McBratney, A., (2003). "Simultaneous Estimation of Various Soil Properties by Ultra-Violet, Visible, and Near-Infrared Reflectance Spectroscopy." Australian Journal of Soil Research, Vol. 41, pp. 1101-1114.

Israelsen, O., West, F., (1922). "Water Holding Capacity of Irrigated Soils." Bulleting No. 183, Utah Agricultural Experiment Station Bulletins, Paper 149.

Jamiolkowski, M., Ladd, C., Germaine, J., Lancellotta, R., (1985). “New Development in Field and Laboratory Testing of Soils.” Proceedings of the 11th International Conference on Soil Mechanics and Foundation Engineering, Vol. 1, pp. 57-153.

Janik, L., Skjemstad, J., (1995). “Characterization and Analysis of Soils using Mid-Infrared Partial Least Squares: II. Correlations with Some Laboratory Data.” Australian Journal of Soil Research, Vol. 33, pp. 637-650.

Janik, L., Skjemstad, J., Raven, M., (1995). “Characterization and Analysis of Soils Using Mid Infrared Partial Least-Squares. I. Correlations with XRF-Determined Major-Element Compositions.” Australian Journal of Soil Research, Vol. 33, pp. 621-636.

Jenkins, W., (2013). "Evaluation of Ground-Based Interferometric Radar for Civil Engineering Applications." Master of Science Thesis. University of Missouri-Columbia, July.

Jonard, F., (2012). “Soil Water Content Estimation Using Ground-Based Active and Passive Microwave Remote Sensing: Ground-Penetration Radar and Radiometer.” Doctoral Dissertation. Universite Catholique de Louvain. Faculte d’Ingenierie Biologique, Agronomique et Environmentale Earth and Life Institute – Environmental Sciences. August 2012.

Jonard, F., Weihmuller, L., Schwank, M., Jadoon, M., Vereecken, H., Lambot, S., (2015) “Estimation of the Hydraulic Properties of a Sandy Soil Using Passive and Active Microwave Remote Sensing.” IEEE Transactions on Geoscience and Remote Sensing. Vol. 53, Issue 6, pp. 3095-3109.

Jones, D., Holtz, W., (1973). “Expansive Soils – the Hidden Disaster.” Civil Engineering-ASCE, Vol. 43, Issue 8, pp. 49-51.

de Jong, S. (1993) "SIMPLS: An Alternative Approach to Partial Least Squares Regression." Chemometrics and Intelligent Laboratory Systems." Vol. 18, pp. 251-263.

Judd, D., Wyszecki, G., (1975). “Color in Business, Science, and Industry.” John Wiley and Sons, New York.

Kansas Geological Society (KGS), (2015). “Kansas Geological Society Website.” http://www.kgs.ku.edu/. Accessed October 2015.

Karrane, J., (2011). “What Are Expansive Soils.” http://www.bensonpc.com/downloads/public/What_Are_Expansive_Soils.pdf. Retrieved January 2014.

Kedenburg, S., Vieweg, M., Gissibl, T., Giessen, H., (2012). “Linear Refractive Index and Absorption Measurements in Non-Linear Optical Liquids in the Visible and Near-Infrared Spectral Region.” Optical Materials Express, Vol. 2, pp. 1588-1611.

Kerr, S., Worthington, P., (1988). “Nuclear Logging Techniques for Hydrocarbon, Mineral, and Geological Applications." IEEE Transaction on Nuclear Science, Vol. 35, pp. 794-799.

Knighthawk Coal Company, (2015). “Blackhawk Coal Mine.” http://www.knighthawkcoal.com/blackhawk-coal-mine.html. Retrieved November 2015.

Kodaira, M., Shibusawa, S., (2013). “Using a Mobile Real-Time Soil Visible Infrared Sensor for High Resolution Soil Properties Mapping.” Geoderma, Vol. 199, pp. 64-79.

Kou, L., Labrie, D., Chylek, P., (1993). “Refractive Indices of Water and Ice in the 0.65- to 2.5-μm Spectral Range.” Applied Optics, Vol. 32, No. 19, pp. 3531-3540.

Kubelka, P., (1947). “New Contributions to the Optics of Intensely Light-Scattering Materials, Part I.” Journal of the Optical Society of America, Vol. 38, Number 5, pp. 448-457.

Kubelka, P., Munk, F., (1931). “Ein Beitragzur Optik der Farbanstriche.” (in German), Z. Technol. Physics., Vol. 12, pp. 593-620.

Kulhawy, F., Mayne P., (1990). “Manual on Estimating Soil Properties for Foundation Design.” Final Report of the Electric Power Research Institute Research Project 1493-6.

Kuss, M., (2013). “Image of University of Arkansas GPRI-2.” Personal Electronic Communication with the Author(s) received January 2013.

Li, Z., Huang, Y., Yang, J., Liu, Q., (2014). “Omega-K Imaging Algorithm for One-Stationary Bistatic SAR.” IEEE Transactions on Aerospace and Electronic Systems, Vol 50, No. 1. pp. 33-52.

Lindberg, J., Laude, L., (1974). “Measurement of the Absorption Coefficient of Atmospheric Dust.” Applied Optics, Vol. 13, pp. 1923-1927.

Liu, X., (2008). “Airborne LIDAR for DEM Generation: Some Critical Issues.” Progress in Physical Geology. Vol. 32, No. 1, pp. 31-49.

Lohmannsroben, H., Schober, L., (2000). “Determination of Optical Parameter for Light Penetration in Particulate Materials and Soil with Diffuse Reflectance (DR) Spectroscopy.” Journal of Environmental Monitoring, Vol. 2, pp. 17-22.

Lowry, B., Mooney, M., Zhou, W., Grasmick, J., Gomez, F., Held, B., (2013). "High Resolution Displacement Monitoring of a Slow Velocity Landslide Using Ground Based Radar Interferometry." Engineering Geology.

Lu, N., Likos, W., (2002). “Unsaturated Soil Mechanics.” John Wiley and Sons, Hoboken, NJ.

Machol, J., Ayers, T., Schwenz, K., Koenig, K., Hardesty, R., Senff, C., Krainak, M., Abshire, J., Bravo, H., Sandberg, S., (2004). "Preliminary Measurements with an Automated Compact Differential Absorption LIDAR for Profiling Water Vapor." Applied Optics 43, pp. 3110-3121.

Mahmood, N., (2014). "Suggested Mixing Procedure for Kaolinite Samples in a Slurry Consolidometer." Personal Verbal Communication to the Author. August, 2014, Fayetteville, Arkansas.

Mastenbrook, H., Dinger, J., (1961). "The Measurement of Water-Vapor Distribution in the Stratosphere." Naval Research Laboratory. Report No. 5551.

Mathworks, (2010). "Plsregress.m." Partial Least Squares Regression Software. The Mathworks Corporation, Natick, Massachusetts.

Mathworks, (2012a). "MATLAB Programing Environment and Documentation." The MathWorks, Inc. Natick, MA.

Mathworks, (2012b). "Pca.m." Principle Components Analysis Software. The Mathworks Corporation, Natick, Massachusetts.

Mathworks, (2014a). "The MATLAB R2014A Programming Suite and Supporting Documentation." The Mathworks Corporation, Natick, Massachusetts.

Mathworks, (2014b). "The MATLAB R2014B Programming Suite and Supporting Documentation." The MathWorks, Inc. Natick, Massachusetts.

McCarty, G., Reeves, J., Reeves, V., Follet, R., Kimble, J., (2002). "Mid-Infrared and Near-Infrared Diffuse Reflectance Spectroscopy for Soil Carbon Measurement." Soil Science Society of America Journal, Vol. 66, pp. 640-646.

Microsoft, (2015). "Microsoft Excel 2014 and Supporting Documentation." The Microsoft Corporation, Redmond, WA.

Mironov, V., Kosolapova, L., Fomin, S., (2009). "Physically and Mineralogically Based Spectroscopic Dielectric Model for Moist Soils." IEEE Transactions on Geoscience and Remote Sensing, Vol. 47, pp. 2059-2070.

Moore, D., Reynolds, R., (1997). "X-Ray Diffraction and the Identification and Analysis of Clays Minerals." Oxford University Press, Oxford, New York.

Morris, J., Porter, D., Neet, M., Noble, P., Schmidt, L., Lapine, L., Jensen, J., (2007). "Integrating LIDAR Elevation Data, Multi-Spectral Imagery and Neural Network Modelling for Marsh Characterization." International Journal of Remote Sensing, Vol. 23, Issue 23, pp. 5221-5234.

Morris, P., Lockington, D., Apelt, C., (2000). “Correlations for Mine Tailings Consolidation Parameters.” International Journal of Surface Mining, Reclamation and Environment, Vol. 14, pp. 171-443.

National Aeronautics and Space Administration (NASA), (2013). "DIAL Concept Description." http://asd-www.larc.nasa.gov/lidar/concept.html. Retrieved October, 2013.

National Oceanic and Atmospheric Administration (NOAA), (2012b). “2012 yearly observed high/low temperatures and precipitation for Fayetteville, AR.” http://www.srh.noaa.gov/tsa/?n=climateGraphs. Retrieved July, 2012.

National Oceanic and Atmospheric Administration (NOAA), (2016). “Weather Observations for Drake Field, Fayetteville, Arkansas.” http://www.srh.noaa.gov/data/obhistory /KFYV.html. Retrieved March 2016.

National Oceanic and Atmospheric Agency (NOAA), (2012a). “Compact Water Differential Absorption LIDAR (CODI).” NOAA CODI project website. http://www.esrl.noaa.gov/csd/groups/ csd3 /instruments /wv_dial/. Retrieved December 2012.

Nemmers, C., (1998). “Volumetric Moisture Content Using Time Domain Reflectometry.” FHWA publication number: FHWA-RD-97-139.

Neumann, H., and Thurtell, G., (1972). “A Peltier Cooled Thermocouple Dew Point Hygrometer for In Situ Measurement of Water Potentials.” In Brown, R., Haveren, B., (eds.). “Psychometry in Water Relations Research.” Utah Agricultural Experiment Station.

Nguyen, T., Janik, L., Raupach, M., (1991). “Diffuse Reflectance Infrared Fourier Transform (DRIFT) Spectroscopy in Soil Studies.” Australian Journal of Soil Research Vol. 29, pp. 49-67.

Nicolet, (2004). “Nicolet FT-IR User’s Guide.” Nicolet 6700 Fourier Transform Infrared Spectrometer User’s Manual and Supporting Documentation. http://mmrc.caltech.edu/FTIR/Nicolet/Nicolet%20Software/Nicolet%202/4700_6700_User.pdf. Retrieved September 2014.

Njoku, E., Entekahbi, D., (1994). “Passive Microwave Remote Sensing of Soil Moisture.” Journal of Hydrology, Vol. 184, Issue 1-2, pp. 101-129.

Nocita, M., Stevens, A., Noon, C., van Wesemael, B., (2013). “Prediction of Soil Organic Carbon for Different Levels of Soil Moisture Using Vis-NIR Spectroscopy.” Geoderma, Vol. 199, pp. 37-42.

Norman, R., Brye, K., Gbur, E., Chen, P., Rupe, J., (2015). “Long-Term Effects of Alternative Residue Management Practices on Soil Water Retention in a Wheat-Soybean, Double-Crop System in Eastern Arkansas.” Open Journal of Soil Science, Vol. 5, pp. 199-209.

Novak, V., Havrila, J., (2006). “Method to Estimate the Critical Soil Water Content of Limited Availability for Plants.” Biologia, Bratislava, Vol. 61, Supplemental 19, pp. S289-293.

Ocean Optics, (2014). “Ocean Optics USB-2000, OceanView Software, and Supporting Documentation.” The Ocean Optics Corporation.

Ocean Optics, (2015). “OceanView 1.5 Software and Supporting Documentation.” http://oceanoptics.com/product-catagory/software/. Retrieved May 2015.

Oh, Y., Sarabandi, K., Ulaby, F., (1992). “An Empirical Model and an Inversion Technique for Radar Scattering from Bare Soil Surfaces.” IEEE Transactions on Geoscience and Remote Sensing, Vol. 30, No. 2, pp. 370-381.

Or, D., Tuller, M., (2002). “Cavitation During Desaturation of Porous Media Under Tension.” Water Resources Research, Vol. 38, No. 5, pp. 1-4.

Padlo, P., Mahoney, J., Aultman-Hall, L., Zinke, S., (2005). “Correlation of Nuclear Density Readings with Cores Cut from Compacted Roadways.” Report No. CT-2242-F-05-5. Report to the Connecticut Department of Transportation. Connecticut Advanced Pavement Laboratory, Connecticut Transportation Institute, School of Engineering, University of Connecticut.

Park, John K., (1980). “A Soil Moisture Reflectance Model in Visible and Near IR Bands.” Symposium on Machine Processing of Remotely Sensed Data and Soil Information Systems and Remote Sensing and Soil Survey. The Laboratory for Applications of Remote Sensing, West Lafayette, Indiana.

Patterson, E., Gillete, D., Stockton, B., (1977). “Complex Index of Refraction between 300 and 700nm for Saharan Aerosols." Journal of Geophysical Research, Vol. 82, No. 21, pp. 3153-3160.

Pelletier, M., Viera, J., Schwartz, R., Evett, S., Lascano, R., McMichael, R., (2011). "Analysis of Coaxial Soil Cell in Reflection and Transmission." Sensors, Vol. 11, No. 3, pp. 2592-2610.

Phene, C., Rawlins, S., Hoffman, G., (1971). “Measuring Soil Matric Potential In Situ by Sensing Heat Dissipation within a Porous Body: I. Theory and Sensor Construction.” Soil Science Society of America Journal. Vol. 35, pp. 27-33.

Philpot, W., (2010). “Spectral Reflectance of Wetted Soils.” Proceedings of ASD and IEEE GRS; Art, Science and Applications of Reflectance Spectroscopy Symposium, Vol. II. Boulder, Colorado.

Rawls, W., Brakensiek, D., (1985). “Prediction of Soil Water Properties for Hydrologic Modeling.” In Jones, E., and Ward, T., (eds.). “Proceedings of the Symposium on Watershed Management in the Eighties.” Denver, Colorado. pp. 293-299.

Reece, C., (1996). “Evaluation of a Line Heat Dissipation Sensor for Measuring Soil Matric Potential.” Soil Science Society of America Journal. Vol, 60, pp. 1022-1028.

Reeves, J., McCarty G., (2001). “Quantitative Analysis of Agricultural Soils Using Near Infrared Reflectance Spectroscopy and Fibre-Optic Probe.” Journal of Near Infrared Spectroscopy, Vol. 7, pp. 179-193.

Reeves, J., McCarty G., Meisinger, J., (1999). “Near Infrared Reflectance Spectroscopy for the Analysis of Agricultural Soils.” Journal of Near Infrared Spectroscopy, Vol. 7, pp. 179-193.

Reginato, R., van Bavel, C., (1962). “Pressure Cell for Soil Cores.” Proceedings of the Soil Science Society of America, Vol. 26, pp. 1-3.

Reynolds, H., (1953). “Ceramics Uses of Arkansas Nepheline Syenite.” Arkansas Academy of Sciences Journal, Vol. 6, pp. 63-65.

Reynolds, R., (1992). “X-Ray Diffraction Studies of Illite/Smectite from Rocks, <1 μm Randomly Oriented Powders, and <1 μm Oriented Powder Aggregates: The Absence of Laboratory-Induced Artifacts.” Clays and Clay Minerals, Vol. 40, No. 4, pp. 387-396.

Rice, S., (1951). “Reflection of Electromagnetic Waves by Slightly Rough Surfaces.” Community of Pure Applied Math. Vol. 4, p. 351-378.

Richards, B., (1965). “Measurement of the Free Energy of Soil Moisture by the Psychrometric Technique using Thermistors.” In Aitchison, G., (ed.) “Moisture Equilibria and Moisture Changes in Soils Beneath Covered Areas.” Butterworth and Co., Sydney, Australia, pp. 39-46.

Richards, L., (1928). The Usefulness of Capillary Potential to Soil Moisture and Plant Investigators.” Journal of Agricultural Research, Vol. 37, 719-742.

Richards, L., (1931). “Capillary Conduction of Liquids Through Porous Mediums.” Physics, Vol. 1, Issue 5, pp. 318-333.

Richards, L., (1941). “A Pressure Membrane Apparatus for Soil Solution Extraction.” Soil Science, Vol. 51, pp. 377-385.

Richards, L., (1948). “Porous Plate Apparatus for Measuring Moisture Retention and Transmission by Soils.” Soil Science, Vol. 66, pp. 105-110.

Richards, L., Gardner, W., (1936). “Tensiometers for Measuring the Capillary Tension of Soil Water.” Journal of American Society of Agronomy, Vol. 28, pp. 352-358.

Richards, L., Waldleigh, C., (1952). “Soil Water and Plant Growth.” In Shaw, B., (ed.) Soil Physical Conditions and Plant Growth. American Society of Agronomy Series Monographs, Vol. 2, pp. 74-251.

Richards, M., (2005). “Fundamentals of Radar Signal Processing.” Mc-Graw Hill. New York.

Richardson, A., Wiegland, C., Gausman, H., Cuellar, J., Gerbermann, A., (1975). “Plant, Soil, and Shadow Reflectance Components for Row Crops.” Photogrammetric Engineering and Remote Sensing, Vol. 41, pp. 1401-1407.

Rogers, William, (2009). “Feldspar and Nepheline Syenite.” Mining Engineering, Vol. 61, No. 6, pp. 29.

Rosenblad, B., Gomez, F., Loehr, J., Held, B., Jenkins, W., (2013). "Ground-Based Interferometric Radar for Monitoring Slopes and Embankments.” Proc. GeoCongress 2013: Stability and Performance of Slopes and Embankments III, San Diego, California, March.

Rosipal, R., Kramer, N., (2006). "Overview and Recent Advances in Partial Least Squares", in Subspace, Latent Structure and Feature Selection: Statistical and Optimization Perspectives Workshop (SLSFS 2005), Revised Selected Papers (Lecture Notes in Computer Science 3940), C. Saunders et al. (eds.) pp. 34-51, Springer.

Rossel, R., McBratney, A., Minasny, B., (eds.), (2010a). “Proximal Soil Sensing. Volume 1 of Progress in Soil Science.” Springer Science and Business Media. Springer, New York.

Rossel, R., Rizzo, R., Dematte, J., Behrens, T., (2010b). “Spatial Modeling of a Soil Fertility Index Using Visible-Near-Infrared Spectra and Terrain Attributes.” Soil Science of America Journal, Vol. 74, Issue 4, pp. 1293-1300.

Rothman, L., Gordon, E., Barbe, A., Benner, D., Bernath, P., Birk, M., Boudon, V., Brown, L., Campargue, A., Champion, J., Chance, K., Coudert, L., Dana, V., Devi, V., Fally, S., Flaud, J., Gamache, R., Goldman, A., Jacquemart, D., Kleiner, I., Lacome, N., Lafferty, W., Mandin, J., Massie, S., Mikhailenko, D., Miller, C., Moazzen-Ahmadi, Naumenko, O., Nikitin, A., Orphal, J., Perevalov, W., Perin, A., Predoi-Cross, A., Rinsland, C., Rotger, M., Simeckova, M., Smith, M., Sung, K., Taskun, S., Tennyson, J., Toth, R., Vandaele, A., Auwera, J., (2009). "The HITRAN 2008 molecular spectroscopic database." Journal of Quantitative Spectroscopy and Radiative Transfer. Vol. 110, pp. 533-573.

Sarabandi, K., Pierce, L., Oh, Y., Dobson, M., Ulaby, F., Freeman, A., (1994). “Cross-Calibration Experiment of JPL AIRSAR and Truck-Mounted Polarimetric Scatterometer.” IEEE Transactions on Geoscience and Remote Sensing. Vol. 32, No.5, pp. 975-985.

Schofield, A., Wroth, C., (1968). “Critical State Soil Mechanics.” McGraw-Hill, London, UK.

Schroeder, P., (2002). “Infrared Spectroscopy in Clay Science.” In Teaching Clay Science, Guggenheim, S., Rule, A., (eds.). Clay Minerals Society Workshop Series. The Clay Mineral Society, Aurora, Colorado Vol. 13, pp. 181-202.

Seed, H., Woodward, R., Lundgren, R., (1964). “Fundamental Aspects of the Atterberg Limits.” Proceedings of the Soil Mechanics and Foundation Division, ASCE, SM6, pp. 75-104.

Shackleford, C., (2004). “Foreword to Unsaturated Soil Mechanics.” Lu, N., Likos, W., 2004.

Shepherd, K., Walsh, M., (2002). “Development of Reflectance Spectral Libraries for Characterization of Soil Properties.” Soil Science Society for American Journal, Vol. 66, pp. 988-998.

Shibusawa, S., Imade-Amon, S., Sato, S., Sasao, A., Harako, S., (2001). “Soil Mapping Using the Real-Time Soil Spectrophotometer.” Proceedings of the Third European Conference on Precision Agriculture, Vol. 1, Agro Montpellier, pp. 497-508.

Sira Ltd., (2004). "Recommendations for Best Practice in the Use of Open-Path Instrumentation." A Review of Best Practice Based on the Project 'Remote Optical Sensing Evaluation' (ROSE) August 2001-2004.

Skempton, A., (1944). “Notes on the Compressibility of Clays.” Quarterly Journal of the Geological Society of London, Vol. 100, C: Parts 1 and 2. Pp. 119-135.

Skempton, A., (1953). “The Colloidal Activities of Clays.” Proceedings of the 3rd International Conference on Soil Mechanics and Foundation Engineering. Zurich, Switzerland.

Skempton, A., Northey, R., (1953). “The Sensitivity of Clays.” Geotechnique, Vol. 3, No. 1, pp. 30-53.

Smith, B., (2011). “Fundamentals of Fourier Transform Infrared Spectroscopy.” 2 ed., CRC Press, Taylor and Francis, Boca Raton, Florida.

Smith, K., Mullins, C., (eds.), (2001). “Soil and Environmental Analysis: Practical Methods.” Marcel Dekker, New York.

Soil Moisture, (2015). “Soil Moisture Inc. Website.” http://www.soilmoisture.com/landing.php. Accessed 2015.

Spagnoli, G., (2012). “Comparison between Casagrande and Drop-Cone Methods to Calculate Liquid Limit for Pure Clay.” Canadian Journal of Soil Science, Vol. 92, No. 6, pp. 859-864.

Stannard, D., (1986). "Theory, Construction and Operation of Simple Tensiometers." Groundwater Monitoring and Remediation, Vol. 6, Issue 3. pp. 70-78.

Stephen, H., Ahmad, S., Piechota, T., (2010). “Relating Surface Backscatter Response from TRMM Precipitation RADAR to Soil Moisture: Results over a Semi-Arid Region.” Hydrology and Earth System Sciences, Vol. 14, Issue, 2, pp. 193-204.

Stewart, J., Hu, J., Kayen, R., Lembo, A., Collins, B., Davis, C., O’Rourke, T., (2009). “Use of Airborne and Terrestrial LIDAR to Detect Ground Displacement Hazards to Water Systems.” Journal of Surveying Engineering, Vol. 135, pp. 113-124.

Stuart, B., (2004). “Infrared Spectroscopy: Fundamentals and Applications.” John Wiley and Sons. ISBN 0-470-85427-8.

Taiz, Z., (2002). “Plant Physiology.” 4 ed. Sinauer Associates.

Take, W., Arnepalli, D., Brachman, R., and Rowe. R., (2007). “Laboratory and Field Calibration of TDR Probes for Water Content Measurement.” Ottawa Geo 2007. Ottawa, Canada

Taylor, D., (1948). “Fundamentals of Soil Mechanics.” John Wiley and Sons, Inc., New York.

Tefera, T., (2013). “Measurement of Plastic Limit of Cohesive Soils.” Report No. 208 for Norwegian Public Roads Administration. Project 603152.

Terzaghi, K., (1926b). “Principle of Final Soil Classification.” Public Roads, Vol. 8, No. 3, pp. 41-53.

Terzaghi, K., (1926a). “Simplified Soil Tests for Subgrades and Their Physical Significance.” Public Roads, No. 8, pp. 153-170.

Terzaghi, K., Peck, R., Mesri, G., (1996). “Soil Mechanics in Engineering Practice.” 3 ed., John Wiley and Sons, New York, New York.

Texas Agricultural and Mechanical University (TAMU), (2015). “Laboratory Handouts for Determination of Atterberg Limits.” Texas A&M, CVEN-365 Introduction to Geotechnical Engineering. Spring 2015.

Theile, (2015a). “Product Website for Delaminated Coating Clays.” Theile Kaolin Company. http://www.thielekaolin.com/images/thieleimages/Clay_Properties_2015.pdf. Accessed November 2015.

Theile, (2015b). “Product Information for Clay Products.” Theile Kaolin Company. http://www.thielekaolin.com/images/thieleimages/Clay_Properties_2015.pdf. Accessed November 2015.

Thunder Scientific, (2015). “Thunder Scientific Corporation Website.” http://www.thunderscientific.com/. Accessed October 2015.

Tokunaga, T., (2009). “Hydraulic Properties of Adsorbed Water Films in Unsaturated Porous Media.” Water Resources Research, Vol. 45, doi: 10.1029/2009WR007734.

Tokunaga, T., (2011). “Physicochemical Controls on Adsorbed Water Film Thickness in Unsaturated Geological Media.” Water Resources Research, Vol. 47. doi:10.1029/2012WR01187.

Topp, G., Davis, J., Annan, A., (1980). “Electromagnetic Determination of Soil Water Content: Measurements in Coaxial Transmission Lines.” Water Resources Research, Vol. 16, Issue 3, pp. 574-582.

Torrent, J., Barron, V., (1993). “Laboratory Measurement of Soil Color: Theory and Practice.” In Soil Color. Soil Science Society of America Special Publication No. 31.

Tyree, M., (2003). “Matric Potential.” Encyclopedia of Water Science. doi: 101.108/E-EWS. pp. 615-617.

Ulaby, F., (1974). “Radar Measurement of Soil Moisture Content.” IEEE Transactions on Antennas Propagation. Vol. AP-22, pp. 257–265.

Ulaby, F., Moore, R., Fung, A., (1986). “Microwave Remote Sensing, Active and Passive. Volume III, from Theory to Application.” Artech House, Massachusetts.

Veihmayer, F., Hendrickson, A., (1949). “Methods of Measuring Field Capacity and Permanent Wilting Percentage of Soils.” Soil Science, Vol. 68, No. 75-94.

Veihmeyer, F., Hendrickson, A., (1927). “+B375+B9” Proceedings of the 1st International Congress on Soil Science, Vol. 3, pp. 498-513.

Wagner, W., (1998). “Soil Moisture Retrieval from ERS Scatterometer Data.” PhD Dissertation, Vienna University of Technology. November.

Walvoort, D., McBratney, A., (2001). “Diffuse Reflectance Spectrometry as a Proximal Sensing Tool for Precision Agriculture.” Proceedings of the Third European Conference on Precision Agriculture, Agro Montpellier, Vol. 1, pp. 503-507.

Wang, J., (1980). “The Dielectric Properties of Soil-Water Mixtures at Microwave Frequencies.” Radio Science, Vol. 15, pp. 977-985.

Wang, J., Schmugge, T., (1980). “An Empirical Model for the Complex Dielectric Permittivity of Soils as a Function of Water Content”. IEEE Transactions on Geoscience and Remote Sensing, pp. 288-295.

Waruru, B., Shepherd, K., Ndegwa, G., Kamoni, P., Sila, A., (2014). “Rapid Estimation of Soil Engineering Properties Using Diffuse Reflectance Near Infrared Spectroscopy.” Journal of Biosystems Engineering, Vol. 121, pp. 177-185.

Wasti, Y., (1987). “Liquid and Plastic Limits as Determined from the Fall Cone and the Casagrande Methods.” Geotechnical Testing Journal, GTJODJ, Vol. 10, No. 1, pp. 26-30.

Watanabe, K., Takeuchi, M., Osada, Y., Ibata, K., (2012). “Micro-Chilled-Mirror Hygrometer for Measuring Water Potential in Relatively Dry and Partially Frozen Soils.” Soil Science Society of America Journal, Vol. 76, pp. 1935-1945.

Wayllace, A., Lu, N., (2012). “A Transient Water Release and Imbibitions Method for Rapidly Measuring Wetting and Drying Soil Water Retention and Hydraulic Conductivity Functions.” Geotechnical Testing Journal, Vol. 35, Issue 1.

Wegmuller, U., (1997). “Soil Moisture Monitoring with ERS SAR Interferometry.” European Space Agency Special Publication ESA SP-414. Proceedings of the 3rd ERS Symposium. pp. 47-51.

White, W., (1949). “Atterberg Plastic Limits of Clay Minerals.” Clay Minerals, Vol. 34, No. 7, No pages listed.

White, W., Keester, K., (1966). “Optical Absorption Spectra of Iron in the Rock-Forming Silicates.” The American Mineralogist, Vol. 51, pp. 774-791.

Whiting, M., (2009). “Measuring Surface Water in Soil with Light Reflectance.” Remote Sensing and Modeling of Ecosystems for Sustainability VI, Proceedings of the SPIE, Vol 7454, doi: 10.1117/12.826896.

Whyte, I., (1982). “Soil Plasticity and Strength: A New Approach Using Extrusion.” Ground Engineering, Vol. 15, No. 1, pp. 16-24.

Wilson, G., Clifton, A., Barbour, S., (1999). “The Emergence of Unsaturated Soil Mechanics.” National Research Council Press.

Wold, S., Sjostrom, M., Eriksson, L., (2001). “PLS-Regression: A Basic Tool of Chemometrics.” Chemometrics and Intelligent Laboratory Systems. Vol. 58, Issue 2, pp. 109-130.

Wood, David M., (1990). “Soil Behaviour and Critical State Soil Mechanics.” Cambridge University Press. London, UK.

Workman, J., Weyer, L., (2007). “Practical Guide to Interpretive Near-Infrared Spectroscopy.” Taylor and Francis Group. Boca Raton, Florida.

Wroth, C., Houlsby, G., (1985). “Soil Mechanics-Property Characterization and Analysis Procedures.” Proceedings of the 11th International Conference on Soil Mechanics and Foundation Engineering, Vol. 1, pp. 1-55.

Wroth, C., Wood, D., (1978). “The Correlation of Index Properties with Some Basic Engineering Properties of Soils.” Canadian Geotechnical Journal, Vol. 15, No. 2, pp. 137-145.

Wu, J., Li, Z., Huang, Y., Liu, Q., Yang, J., (2012). “Processing One-Stationary Bistatic SAR Data Using Inverse Scaled Fourier Transform.” Progress in Electromagnetics Research, Vol. 129, pp. 143-159.

Yitagesu, F., van der Meer, F., van der Werff, H., Zigterman, W., (2009). “Quantifying Engineering Parameters of Expansive Soils from Their Reflectance Spectra.” Engineering Geology, Vol. 105, Issue 3-4, pp. 151-160.

Youssef, M., El Ramli, A., El Demery, M., (1965). “Relationships between Shear Strength, Consolidation, Liquid Limit, and Plastic Limit for Remoulded Clays.” Proceedings of the 6th International Conference on Soil Mechanics and Foundation Engineering, Montreal, Vol. 1, pp. 126-129.

APPENDIX A: SOURCE CODE FOR RADAR IMAGE PROCESSING

A.1. Chapter Overview

Contained in this appendix are the various programmatic code developed to acquire, pre-process, process, and visualize radar data to acquire measurements of soil properties. Radar data acquisition, pre-processing, and registration were conducted using the GAMMA Remote Sensing interferometric software suite in a Linux processing environment (Section A.2). Radar volumetric water content (small perturbation method), soil saturation (Wagner 1998), and soil *in situ* density inversions were conducted using computer code developed using the MATLAB programming suite in both Windows and Linux environments (Section A.3). Radar image acquisition profiles are included in Section A.4. The Wegmuller (1997) soil volumetric water content inversions was conducted using GAMMA software (soil_moisture.c) included in the GAMMA interferometric software suite. Conversion between polar (radar range and azimuth coordinates) and rectangular (x and y directions) coordinates was conducted exclusively using the GAMMA pol2rec.c executable. It should be noted that all calculations were carried out in polar coordinates. Visualization of the radar data was conducted using MATLAB executables (jgge_2_vwc_plot2.m, mli_plot.m, and jgge_2_dens_plot.m). The included software used to acquire and pre-process radar data is tabulated in Table A.1. Similarly, the software utilized to extract soil water content information from radar imagery is tabulated in Table A.2.

Table A. 1. List of included software executables and source code developed to acquire and pre-process radar data.

ID	Executable	Description	Suite
A.2.1	proc_commands	Example script for acquisition and initial verification of radar data	GAMMA[1]
A.2.2	pre_proc.sh	Example script for pre-processing of radar data	GAMMA[1]
A.2.3	image_proc.sh	Example script for registration and generation of interferograms	GAMMA[1]

Note: [1]The Gamma Remote Sensing Software Suite Includes Device Specific Software (GPRI2) and the Interferometric Synthetic Aperature Radar Software Suite

Table A. 2. List of included software executables and source code developed to process radar data to extract measurements of soil water content and soil *in situ* density.

ID	Executable	Description	Suite
A.3.1	jgge_2_vwc_plot2	Visulize volumetric water content plots	MATLAB
A.3.2	mli_plot	Visulize MLI[1] image files as raster images	MATLAB
A.3.3	jgge_2_dens_plot	Visulize soil density plots	MATLAB
A.3.4	c_dens_wag_spm	Compute soil density (c-band)	MATLAB
A.3.5	mli_smooth	Smooth MLI[1] data (nearest neighbor)	MATLAB
A.3.6	soil_wagner	Compute soil saturation (Wagner 1998)	MATLAB
A.3.7	spm_initial	Compute soil permssivity and roughness plots (initial)	MATLAB
A.3.8	spm_refine	Refine soil permissivity and roughness plots	MATLAB
A.3.9	lin_moisture	Compute soil moisture from linear model (Dubois 1995)	MATLAB
A.3.10	log_moisture	Compute soil moisture from logorithmic model (Dubois 1995)	MATLAB
A.3.11	eacf	Compute value of exponential autocorrellation funtion	MATLAB
A.3.12	incident_flat	Estimate pixel incident angle	MATLAB
A.3.13	mli_read	Read MLI[1] image files into memory	MATLAB
A.3.14	mli_write	Write MLI[1] image files to disk	MATLAB

Note: [1]**M**ulti-**L**ook **I**ntensity image (MLI)

A.2. Radar Image Acquisition and On-Site Validation Log (proc_commands.txt)

Included in this section is an example script documenting the typical activities and Gamma Remote Sensing (GRS) software utilized during instrument set-up, data acquisition, and initial verification of acquired data. An individual log of activities was recorded each time the equipment was mobilized to a project site. An example of the information typically documented includes weather and local conditions, instrument status reports (e.g. chupa_status.py, tscc_status.py), orientation information (e.g. leg length and orientation targets), and data

acquisition terminal commands (gpri2_capture.py). Additionally, an initial processing was typically conducted in the field to verify that radar data was captured and that the acquired imagery was suitable for further processing (e.g. looking for saturation and proper selection of the chirp length).

A.2.1. ***Example Script for Acquisition of Radar Data and Observation Log***

The radar image acquisition and on-site validation log ("proc_commands.txt") was generated individually for each set of acquired radar data. An example of the proc_commands.txt file recorded for data acquisition at the WESTAR Jeffrey Energy Center is presented herein.

Invocation: Linux terminal command line shell user interface ("Terminal UI")

Source Code:

```
#WESTAR JEFFREY ELECTRIC CENTER SURVEY
#SUNNY BREEZY
#CDG / RAC / EI
#10 JUNE 2013
#80 F RH 45 E7 29.88 DW 57
#Radar survey from hilltop west of site north of control point
ssh -X gpri2@192.168.1.74
#password: gpri2
cd/data
mkdir WESTAR/20130610
cd 20130610
cp ../../MBTC3031_WIDSE/10192012/proc_commands.txt .
cp ../../gpri2_500us.prf .
gedit proc_commands.txt &
mkdir_RAW
home_run.py
#Scope +5 +0RF_center_freq:          1.720000e+10
```

IMA_atten_dB: 32

CHP_freq_min: 100.0e6

CHP_freq_max: 300.0e6

CHP_num_samp: 3125

TX_power: on

STP_antenna_start: 0.0

STP_antenna_end: 0.0

STP_gear_ratio: 72

STP_rotation_speed: 10.0

ADC_capture_time: 1.0

ADC_sample_rate: 6.25000e+06

antenna_elevation: 20

move_rel.py -133

#Scope aligned with West (left) edge of west stack at top of tower

#Antennas +0

#Check where to start and stop the radar using move_rel/abs command

move_rel.py -143

move_abs.py 5

#Check the profile, the start angle, end angle, antenna elevation

gedit gpri_250us.prf &

RF_center_freq: 1.720000e+10

IMA_atten_dB: 32

CHP_freq_min: 100.0e6

CHP_freq_max: 300.0e6

CHP_num_samp: 3125

TX_power: on

STP_antenna_start: -138

STP_antenna_end: 5

STP_gear_ratio: 72

STP_rotation_speed: 10.0

ADC_capture_time: 1.0

ADC_sample_rate: 6.25000e+06

antenna_elevation: 0

gpsmon

#Time:173650

#Latitude: 3916.3767

#Longitude: 9608.4141

#Altitude: 385.5

#Quality: 2 Sats: 12

#HDOP: 0.9

#Geoid: -27.8

chupa_status.py

#CHUPA Voltages: ['U1 3.27', 'U2 4.80', 'U3 -4.95', 'U4 7.24', 'U5 12.05', 'U6 0.00']

#CHUPA Temperature: ['T1 33.3']

tscc_status.py

#TSCC Voltage: ['U1 23.7']

#TSCC Temperature (C): ['T1 45.4']

home_run.py

#Capture the first image

move_rel.py -143

gpri2_capture.py -e eth1 -f 0.0 -M -P -S 1 -s -k 1.0 -v -p gpri_500us.prf -o
RAW/westar_20130610_001.raw

gpri2_proc.py RAW/westar_20130610_001.raw RAW/westar_20130610_001.raw.par
SLC/westar_20130610_001.slc SLC/westar_20130610.slc.par

#Capture the second image

home_run.py

move_rel.py -143

gpri2_capture.py -e eth1 -f 0.0 -M -P -S 1 -s -k 1.0 -v -p gpri_250us.prf -o
RAW/mbtc3031_wide_11022012_002.raw

#Capture the third image

move_abs.py -20

gpri2_capture.py -e eth1 -f 0.0 -M -P -S 1 -s -k 1.0 -v -p gpri_250us.prf -o
RAW/mbtc3031_wide_11022012_003.raw
#Capture the fourth image
move_abs.py -20
gpri2_capture.py -e eth1 -f 0.0 -M -P -S 1 -s -k 1.0 -v -p gpri_250us.prf -o
RAW/mbtc3031_wide_11022012_004.raw
#Capture the fifth image
move_abs.py -20
gpri2_capture.py -e eth1 -f 0.0 -M -P -S 1 -s -k 1.0 -v -p gpri_250us.prf -o
RAW/mbtc3031_wide_11022012_005.raw
#Capture the sixth image
move_abs.py -20
gpri2_capture.py -e eth1 -f 0.0 -M -P -S 1 -s -k 1.0 -v -p gpri_250us.prf -o
RAW/mbtc3031_wide_11022012_006.raw
#Capture the seventh image
move_abs.py -20
gpri2_capture.py -e eth1 -f 0.0 -M -P -S 1 -s -k 1.0 -v -p gpri_250us.prf -o
RAW/mbtc3031_wide_11022012_007.raw
#Capture the eight image
move_abs.py -20
gpri2_capture.py -e eth1 -f 0.0 -M -P -S 1 -s -k 1.0 -v -p gpri_250us.prf -o
RAW/mbtc3031_wide_11022012_008.raw
home_run.py
sudo shutdown -P now
exit
gpri2_proc.py ../RAW/westar_20130610_002.raw ../RAW/westar_20130610_002.raw_par
westar_20130610_002u.slc westar_20130610_0012.slc -d 20 -h 90
cd ../MLI
multi_look ../SLC/westar_20130610_002l.slc ../SLC/westar_20130610_002l.slc.par
westar_20130610_002l.mli westar_20130610_002l.mli.par 1 1 0 - 1 1
cd ../SLC

ls -l

cd ../

ls -l

cd SLC

gpri2_proc.py

gpri2_proc.py ../RAW/westar_20130610_001.raw ../RAW/westar_20130610_001.raw_par westar_20130610_001u.slc westar_20130610_001l.slc -d 40 -h 90

gpri2_proc.py ../RAW/westar_20130610_002.raw ../RAW/westar_20130610_002.raw_par westar_20130610_002u.slc westar_20130610_002l.slc -d 40 -h 90

cd ../MLI/

multi_look ../SLC/westar_20130610_002l.slc ../SLC/westar_20130610_002l.slc.par westar_20130610_002l.mli westar_20130610_002l.mli.par 1 1 0 - 1 1

ls -l

gedit westar_20130610_002l.mli.par

raspwr westar_20130610_0012.mli 2747

ls -l

raspwr westar_20130610_002l.mli 2747

eog westar_20130610_002l.mli.ras

*eog *.ras*

A.2.2. Example Script for Preprocessing of Multiply Polarized Radar Data.

Included in this section is an example script documenting the typical activities and Gamma Remote Sensing (GRS) software utilized during the pre-processing of radar imagery. Preprocessing activities typically included conversation of the raw radar data files (.raw) into image products (single look complex [SLC] and multilook intensity [MLI]) for visualization, initial inspection, and further processing. Pre-processed data was typically employed to verify proper acquisition parameters (start angle, end angle, antenna angle, chirp length) and to identify potential registration targets in the data. Additionally, conversion from radar coordinates to rectangular coordinates was typically conducted during this step to simplify the visual inspection

and identification of imagery. An example script is presented herein to document an example preprocessing work flow on multiply polarized radar data.

Invocation: Linux terminal command line shell user interface ("Terminal UI")

Source Code:

```
gpri2_proc_multi.py RAW/20150526_233035.raw RAW/20150526_233035.raw_par
        SLC/20150526_233035 -d 20
multi_look SLC/20150526_233035_AAAl.slc SLC/20150526_233035_AAAl.slc.par
        MLI/20150526_233035_AAAl.mli MLI/20150526_233035_AAAl.mli.par 1 1 0 - 1 1
raspwr MLI/20150526_233035_AAAl.mli 638 1 0 1 1 1 0.35 1
        RAS/20150526_233035_AAAl.mli.ras
multi_look SLC/20150526_233035_AAAu.slc SLC/20150526_233035_AAAu.slc.par
        MLI/20150526_233035_AAAu.mli MLI/20150526_233035_AAAu.mli.par 1 1 0 - 1 1
raspwr MLI/20150526_233035_AAAu.mli 638 1 0 1 1 1 0.35 1
        RAS/20150526_233035_AAAu.mli.ras
#make pol2rec files
pol2rec MLI/20150526_233035_AAAl.mli SLC/20150526_233035_AAAl.slc.par
        REC/20150526_233035_AAAl.rec.mli REC/20150526_233035_AAAl.rec.mli.par 0.75 0 1
        - - - -
pol2rec MLI/20150526_233035_AAAu.mli SLC/20150526_233035_AAAu.slc.par
        REC/20150526_233035_AAAu.rec.mli REC/20150526_233035_AAAu.rec.mli.par 0.75 0
        1 - - - -
raspwr REC/20150526_233035_AAAl.rec.mli 705 1 0 1 1 1 0.35 1
        RAS/20150526_233035_AAAl.rec.mli.ras
raspwr REC/20150526_233035_AAAu.rec.mli 705 1 0 1 1 1 0.35 1
        RAS/20150526_233035_AAAu.rec.mli.ras
#proc BAA
gpri2_proc_multi.py RAW/20150526_233035.raw RAW/20150526_233035.raw_par
        SLC/20150526_233035 -d 20 -p BAA
```

multi_look SLC/20150526_233035_BAAl.slc SLC/20150526_233035_BAAl.slc.par
MLI/20150526_233035_BAAl.mli MLI/20150526_233035_BAAl.mli.par 1 1 0 - 1 1
raspwr MLI/20150526_233035_BAAl.mli 638 1 0 1 1 1 0.35 1
RAS/20150526_233035_BAAl.mli.ras
multi_look SLC/20150526_233035_BAAu.slc SLC/20150526_233035_BAAu.slc.par
MLI/20150526_233035_BAAu.mli MLI/20150526_233035_BAAu.mli.par 1 1 0 - 1 1
raspwr MLI/20150526_233035_BAAu.mli 638 1 0 1 1 1 0.35 1
RAS/20150526_233035_BAAu.mli.ras
#make pol2rec files
pol2rec MLI/20150526_233035_BAAl.mli SLC/20150526_233035_BAAl.slc.par
REC/20150526_233035_BAAl.rec.mli REC/20150526_233035_BAAl.rec.mli.par 0.75 0 1
- - - -
pol2rec MLI/20150526_233035_BAAu.mli SLC/20150526_233035_BAAu.slc.par
REC/20150526_233035_BAAu.rec.mli REC/20150526_233035_BAAu.rec.mli.par 0.75 0
1 - - - -
raspwr REC/20150526_233035_BAAl.rec.mli 705 1 0 1 1 1 0.35 1
RAS/20150526_233035_BAAl.rec.mli.ras
raspwr REC/20150526_233035_BAAu.rec.mli 705 1 0 1 1 1 0.35 1
RAS/20150526_233035_BAAu.rec.mli.ras
#proc BBB
gpri2_proc_multi.py RAW/20150526_233035.raw RAW/20150526_233035.raw_par
SLC/20150526_233035 -d 20 -p BBB
multi_look SLC/20150526_233035_BBBl.slc SLC/20150526_233035_BBBl.slc.par
MLI/20150526_233035_BBBl.mli MLI/20150526_233035_BBBl.mli.par 1 1 0 - 1 1
raspwr MLI/20150526_233035_BBBl.mli 638 1 0 1 1 1 0.35 1
RAS/20150526_233035_BBBl.mli.ras
multi_look SLC/20150526_233035_BBBu.slc SLC/20150526_233035_BBBu.slc.par
MLI/20150526_233035_BBBu.mli MLI/20150526_233035_BBBu.mli.par 1 1 0 - 1 1
raspwr MLI/20150526_233035_BBBu.mli 638 1 0 1 1 1 0.35 1
RAS/20150526_233035_BBBu.mli.ras
#make pol2rec files

pol2rec MLI/20150526_233035_BBBl.mli SLC/20150526_233035_BBBl.slc.apar REC/20150526_233035_BBBl.rec.mli REC/20150526_233035_BBBl.rec.mli.par 0.75 0 1 - - - -

pol2rec MLI/20150526_233035_BBBu.mli SLC/20150526_233035_BBBu.slc.par REC/20150526_233035_BBBu.rec.mli REC/20150526_233035_BBBu.rec.mli.par 0.75 0 1 - - - -

raspwr REC/20150526_233035_BBBl.rec.mli 705 1 0 1 1 1 0.35 1 RAS/20150526_233035_BBBl.rec.mli.ras

raspwr REC/20150526_233035_BBBu.rec.mli 705 1 0 1 1 1 0.35 1 RAS/20150526_233035_BBBu.rec.mli.ras

A.2.3. ***Example Shell Script to Create Single Look Complex (SLC), Multilook Imagery (MLI), Resampled (Registered) SLC images (RSLC), Resampled MLI images (RMLI).***

Included in this section is an example script documenting the typical activities and Gamma Remote Sensing (GRS) software utilized to 1) collate raw radar data from multiple acquisitions, 2) preprocess raw radar data (.raw) into single look complex imagery (SLC), 3) register and resample images into a specified master geometry (rSLC), 4) generate multilook intensity images (MLI) for further processing, and (5 if required) to generate interferometric data products. Due to the large number of individual raw radar data files a Linux shell script was written to generate terminal command lines. The shell scripts would be employed to generate text files containing the desired Terminal UI commands and these text files were subsequently stored and executed as additional shell scripts. An example file containing the data processing work flow for radar data is presented herein.

Invocation: Linux terminal command line shell user interface (“Terminal UI”)

Source Code:

#PRE- AND POST- PROCESSING FOR TATS DATA
#4/6/15 CDG SES
global_start=$(date +%s)

```
#CREATE SYMBOLIC LINKS FOR RAW DATA
if [ ! -r RAW]; then mkdir RAW; fi
if [ ! -r SLC]; then mkdir SLC; fi
if [ ! -r MLI]; then mkdir MLI; fi
mkdir RAW
mkdir SLC
mkdir MLI
#observation dates are?
#ls ../201505[0-9][0-9]/RAW/*.raw > temp1
cd RAW
ls ../../20150529/RAW/*raw > temp1
sed 's/^/ln -s /' temp1 > temp2
sh temp2
rm temp1 temp2
ls ../../20150526/RAW/*raw_par > temp1
sed 's/^/ln -s /' temp1 > temp2
sh temp2
#remove 500 ms images will have to process seperatly
rm [0-9][0-9][0-9][0-9][0-9][0-9][0-9][0-9]_163147*
rm [0-9][0-9][0-9][0-9][0-9][0-9][0-9][0-9]_175250*
rm temp1 temp2
cd ../
#preprocess all files in RAW/*.raw
ls RAW/*.raw > temp1
sed 's/.raw/.raw_par/g' temp1 > temp2
sed 's/.raw//g' temp1 > temp10
sed 's/RAW/SLC/g' temp10 > temp11
paste temp1 temp2 temp11 > temp3
sed 's/\t/ /g' temp3 > temp4
sed 's/^/gpri2_proc_multi.py /' temp4 > temp5
sed 's/$/ -d 20 -p AAA/' temp5 > CREATE_SLC.sh
```

```
sh CREATE_SLC.sh
rm temp*
sed 's/AAA/BAA/g' CREATE_SLC.sh > CREATE
_SLC_BAA.sh
sed 's/AAA/BBB/g' CREATE_SLC.sh > CREATE_SLC_BBB.sh
sh CREATE_SLC_BAA.sh
sh CREATE_SLC_BBB.sh
##if [ ! -r SLC_AAAu]; then mkdir SLC_AAAu; fi
#if [ ! -r SLC_AAAl]; then mkdir SLC_AAAl; fi
#if [ ! -r SLC_BAAu]; then mkdir SLC_BAAu; fi
#i#f [ ! -r SLC_BAAl]; then mkdir SLC_BAAl; fi
#if [ ! -r SLC_BBBu]; then mkdir SLC_BBBu; fi
#if [ ! -r SLC_BBBl]; then mkdir SLC_BBBl; fi
#process AAau images first
mkdir SLC_AAAu
cd SLC_AAAu
#this line will grab ALL images - if restricted then have to query individaully
ls ../SLC/[0-9][0-9][0-9][0-9][0-9][0-9][0-9][0-9]_[0-9][0-9][0-9][0-9][0-9][0-9][0-9]_AAAu.slc >
        temp1
sed 's/^/ln -s /' temp1 > temp2
sh temp2
sed 's/.slc/.slc.par/g' temp2 > temp3
sh temp3
rm temp1 temp2 temp3
cd ../
mkdir OFF_AAAu
#create slave slc list
ls SLC_AAAu/*.slc > SLC_SI
ls SLC_AAAu/*.slc.par > SLC_SP
#create master slc list
```

```
sed 's/[0-9][0-9][0-9][0-9][0-9][0-9][0-9][0-9]_[0-9][0-9][0-9][0-9][0-9][0-
    9]/20150526_233910/g' SLC_SI > SLC_MI
sed 's/[0-9][0-9][0-9][0-9][0-9][0-9][0-9][0-9]_[0-9][0-9][0-9][0-9][0-9][0-
    9]/20150526_233910/g' SLC_SP > SLC_MP
#change to offsets
sed 's/.slc/.off/g' SLC_SI > temp1
sed 's/SLC_AAAu/OFF_AAAu/g' temp1 > temp2
rm temp1
mkdir OFF_AAAu
paste SLC_MP SLC_SP temp2 > temp3
sed 's/\t/ /g' temp3 > temp4
sed 's/^/create_offset /' temp4 > temp5
#something wonky
sed 's/$/ 1 - - 0/' temp5 > CREATE_OFFSET.sh
#sed 's/$/ \< ..\/OFFSET_INPUTS.txts
sh CREATE_OFFSET.sh gedit
rm temp1 temp3 temp4
paste SLC_MI SLC_SI SLC_MP SLC_SP temp2 > temp3
sed 's/\t/ /g' temp3 > temp4
#select center of patch for registration
#pt1 roadsign on on ramp at (r) 223 (a) 61
#pt2 unknown sign on i 55 (r) 291 (a) 356
#pt3 direction sign SB I55 near offramp (r) 215 (a) 557
#use unknown sign
#changed SNR from 6.0 to 4.0
sed 's/$/ 1 1 291 356 - - 4.0 1/' temp4 > temp5
sed 's/^/init_offset /' temp5 > INIT_COMM.sh
sh INIT_COMM.sh
sed 's/OFF_AAAu/OFFSET_AAAu/g' temp2 > temp6
sed 's/.off/.offset/g' temp6 > OFFSET
mkdir OFFSET_AAAu
```

```
mkdir SNR_AAAu
mkdir OFFS_AAAU
sed 's/OFFSET_AAAu/SNR_AAAu/g' OFFSET > temp7
sed 's/.offset/.snr/g' temp7 > SNR
sed 's/OFF_AAAu/OFFS_AAAu/g' temp2 > temp8
sed 's/.off/.offs/g' temp8 > OFFS
paste SLC_MI SLC_SI SLC_MP SLC_SP temp2 OFFS SNR > temp9
sed 's/\t/ /g' temp9 > temp10
sed 's/$/ - -/' temp10 > temp11
paste temp11 OFFSET > temp12
sed 's/\t/ /g' temp12 > temp13
sed 's/^/offset_pwr /' temp13 > OFFSET_PWR_COMM.sh
sh OFFSET_PWR_COMM.sh
#create offset_fit commands shell
mkdir COFFS_AAAu
mkdir COFFSET_AAAu
sed 's/OFFS_AAAu/COFFS_AAAu/g' OFFS > temp14
sed 's/.offs/.coffs/g' temp14 > COFFS
sed 's/OFFSET_AAAu/COFFSET_AAAu/g' OFFSET > temp15
sed 's/.offset/.coffset/g' temp15 > COFFSET
paste OFFS SNR temp2 COFFS COFFSET > temp16
sed 's/\t/ /g' temp16 > temp17
sed 's/$/ - - 0/' temp17 > temp18
sed 's/^/offset_fit /' temp18 > OFFSET_FIT_COMM.sh
sh OFFSET_FIT_COMM.sh
mkdir RSLC_AAAu
sed 's/COFFS/RSLC/g' COFFS > temp19
sed 's/.coffs/.rslc/g' temp19 > RSLC
sed 's/.rslc/.rslc.par/g' RSLC > RSLC_P
paste SLC_SI SLC_MP SLC_SP temp2 RSLC RSLC_P > temp20
sed 's/\t/ /g' temp20 > temp21
```

```
sed 's/$/ 0 0/' temp21 > temp22
sed 's/^/SLC_interp /' temp22 > SLC_INTERP_COMM.sh
sh SLC_INTERP_COMM.sh
#create interferograms for AAAu-M & AAAu-S (SLC_intf)
mkdir INTF_AAAu
ls OFF_AAAu/*.off > OFF
sed 's/OFF_AAAu/INTF_AAAu/g' OFF > temp23
sed 's/.off/.intf/g' temp23 > INTF
sed 's/[0-9][0-9][0-9][0-9][0-9][0-9][0-9][0-9]_[0-9][0-9][0-9][0-9][0-9][0-
    9]/20150526_233910/g' RSLC > RSLC_MI
sed 's/[0-9][0-9][0-9][0-9][0-9][0-9][0-9][0-9]_[0-9][0-9][0-9][0-9][0-9][0-
    9]/20150526_233910/g' RSLC_P > RSLC_MP
paste RSLC_MI RSLC RSLC_MP RSLC_P OFF INTF > temp24
sed 's/\t/ /g' temp24 > temp25
sed 's/$/ 1 1 0 - 0 0 1 1/' temp25 > temp26
sed 's/^/SLC_intf /' temp26 > SLC_INTF_AAAU_COMM.sh
sh SLC_INTF_AAAU_COMM.sh
#check interferograms
sed 's/$/ 638 1 0 1 1 1 0.35 1 - 0/' INTF > temp27
sed 's/^/rasmph /' temp27 > RASMPH_COMM.sh
sh RASMPH_COMM.sh
mkdir RMLI_AAAu
sed 's/RSLC_AAAu/RMLI_AAAu/g' RSLC > temp27
sed 's/.rslc/.rmli/g' temp27 > RMLI
sed 's/.rmli/.rmli.par/g' RMLI > RMLI_P
paste RSLC RSLC_P RMLI RMLI_P > temp28
sed 's/\t/ /g' temp28 > temp29
sed 's/$/ 1 1 0 - 1.0 1.0/' temp29 > temp30
sed 's/^/multi_look /' temp30 > MULTI_LOOK_COMM.sh
sh MULTI_LOOK_COMM.sh
mkdir REC_RMLI_AAAu
```

```
sed 's/RMLI_AAAu/REC_RMLI_AAAu/g' RMLI > temp31
sed 's/.rmli/.rec_rmli/g' temp31 > RRMI
sed 's/.rec_rmli/.rec_rmli.par/g' RRMI > RRMI_P
paste RMLI RMLI_P RRMI RRMI_P > temp32
sed 's/\t/ /g' temp32 > temp33
sed 's/$/ 0.749585 0 1 - - - - -/' temp33 > temp34
sed 's/^/pol2rec /' temp34 > POL2REC_COMM.sh
sh POL2REC_COMM.sh
#create and view rasters
sed 's/.rmli/.ras/g' RRMI > RRRI
sed 's/$/ 705 1 0 1 1 1 0.35 1/' RRMI > temp35
paste temp35 RRRI > temp36
sed 's/\t/ /g' temp36 > temp37
sed 's/^/raspwr /' temp37 > RASPWR.sh
sh RASPWR.sh
#one bad image?
mkdir REC_INTF_AAAu
sed 's/INTF_AAAu/REC_INTF_AAAu/g' INTF > temp38
sed 's/.intf/.rec_intf/g' temp38 > RNTF
sed 's/.rslc/.rec.rslc/g' RSLC_P > RRSC_P
paste INTF RSLC_P RNTF RRSC_P > temp39
sed 's/$/ 0.749585 0 1 - - - - -/' temp39 > temp40
sed 's/\t/ /g' temp40 > temp41
sed 's/^/pol2rec /' temp41 > POL2REC2_COMM.sh
sh POL2REC2_COMM.sh
#rasmph for intf
sed 's/$/ 705 1 0 1 1 1 0.35 1/' RNTF > temp42
sed 's/.rec_intf/.rec_intf.ras/g' RNTF > RRTF
paste temp42 RRTF > temp44
sed 's/\t/ /g' temp44 > temp45
sed 's/$/ 1/' temp45 > temp46
```

sed 's/^/rasmph /' temp46 > RASMPH2_COMM.sh

sh RASMPH2_COMM.sh

A.3. Source Code for Extraction of Soil Volumetric Water Content and Soil *In Situ* Density from Radar Data.

Contained in this section is the software developed to ingest pre-processed radar data, extract soil volumetric water content and *in situ* density, and produce visual data products. All custom software utilized in this research project were developed using the MATLAB programming suite. MATLAB executables were developed to be utilized in both the Linux and Microsoft Windows environments. To switch between the two software environments it was necessary to explicitly specify the use of big endian data formats. If not specified the MATLAB fopen, fread, and fwrite commands use the native format of the operating system.

A.3.1. ***Jgge_2_vwc_plot2.m***

A MATLAB executable written to convert MLI images into raster plots for visualization and publication. Programmatic inputs included two mli files, a band designator (C-Band or K_u-Band), and a flag to convert between saturation and volumetric water content computations.

Invocation: jgge_2_vwc_plot('out1.rec','out6.rec',1,1);

Source Code:

```
function jgge_2_vwc_plot(mli1,mli2,band,calc_flag);
%SUBPLOT LEARNING EXERCISE
%mli1 = 'out1.rec';
%mli2 = 'out6.rec';
%band = 1;
%calc_flag = 1;
%band = 1
close all
if band == 1
```

```
   ytic = [1000 1100 1200 1300 1400];
   ytl = [0 100 200 300 400];
   xtic = [230 330 430];
   xtl = [0 100 200];
   ny = 2645
   nx = 1407
   xwin = [230 430];
   ywin = [1000 1400];
   x = [242 306 332 264 242];
   y = [1216 1183 1238 1261 1216];
   ylpos = [-136.812 1303.82 5828.88];
elseif band == 2
   ytic = [2200 2400 2600 2800 3000 3200];
   ytl =  [1650 1800 1950 2100 2250 2400];
   xtic = [1 200 400 600];
   xtl = [0 150 300 450];
   ny = 5291;
   nx = 2813;
   xwin = [1 600];
   ywin = [2200 3200];
      x = [227 303 319 241 227];
   y = [2539 2512 2566 2591 2539];
end
map2 = [    1.0000    1.0000    1.0000
   0.6250         0         0
   0.6875         0         0
   0.7500         0         0
   0.8125         0         0
   0.8750         0         0
   0.9375         0         0
   1.0000         0         0
```

1.0000 0.0625 0
1.0000 0.1250 0
1.0000 0.1875 0
1.0000 0.2500 0
1.0000 0.3125 0
1.0000 0.3750 0
1.0000 0.4375 0
1.0000 0.5000 0
1.0000 0.5625 0
1.0000 0.6250 0
1.0000 0.6875 0
1.0000 0.7500 0
1.0000 0.8125 0
1.0000 0.8750 0
1.0000 0.9375 0
1.0000 1.0000 0
0.9375 1.0000 0.0625
0.8750 1.0000 0.1250
0.8125 1.0000 0.1875
0.7500 1.0000 0.2500
0.6875 1.0000 0.3125
0.6250 1.0000 0.3750
0.5625 1.0000 0.4375
0.5000 1.0000 0.5000
0.4375 1.0000 0.5625
0.3750 1.0000 0.6250
0.3125 1.0000 0.6875
0.2500 1.0000 0.7500
0.1875 1.0000 0.8125
0.1250 1.0000 0.8750
0.0625 1.0000 0.9375

```
    0    1.0000    1.0000
    0    0.9375    1.0000
    0    0.8750    1.0000
    0    0.8125    1.0000
    0    0.7500    1.0000
    0    0.6875    1.0000
    0    0.6250    1.0000
    0    0.5625    1.0000
    0    0.5000    1.0000
    0    0.4375    1.0000
    0    0.3750    1.0000
    0    0.3125    1.0000
    0    0.2500    1.0000
    0    0.1875    1.0000
    0    0.1250    1.0000
    0    0.0625    1.0000
    0         0    1.0000
    0         0    0.9375
    0         0    0.8750
    0         0    0.8125
    0         0    0.7500
    0         0    0.6875
    0         0    0.6250
    0         0    0.5625
    0         0    0.5000];
fid = fopen(mli1,'r','b');
l = fread(fid,'float');
m = mli_read(l,ny,nx);
if calc_flag == 1
   m = 0.47.*m;
elseif calc_flag == 2
```

```
   %m = log_volmoisture(m);
end
m(:,:) = abs(m(:,:));
[a b] = size(m);
for j=1:1:a
   for i = 1:1:b
         md = 0.5;
         m(ny,nx) = 0.5;
         if m(j,i) > 0.5 | m(j,i) < 0.1
            m(j,i) = 0;
         end
    end
end
figure1 = figure('units','inches','pos',[0 0 6.5 4],'colormap',map2);
%axes1 = axes('Parent',figure1,'YDir','reverse',...
%   'Layer','top','FontSize',10,'FontName','Times New Roman');
subplot1 = subplot(1,2,1,'Parent',figure1,'YDir','reverse',...
   'XTick',xtic,...
   'XTickLabel',xtl,...
   'YTick',ytic,...
   'YTickLabel',ytl,...
   'PlotBoxAspectRatio',[599 1000 1],...
   'Layer','top',...
   'FontName','Times New Roman',...
   'FontSize',10,...
   'DataAspectRatio',[1 1 1]);
box(subplot1,'on');
hold(subplot1,'all');
%set(subplot1,'XTick',[1 200 400 600],...
%    'XTickLabel',[1 200 400 600]);
imagesc(m,'Parent',subplot1,'CDataMapping','scaled');
```

```
colorbar('peer',subplot1,'FontName','Times New Roman','FontSize',10);
x1 = xlabel('Range Direction, x [m]');
if band == 1
y1 = ylabel('Cross Range Direction, y [m]',...
   'Position',ylpos);
else
y1 = ylabel('Cross Range Direction, y [m]');
end
set(x1,'FontName','Times New Roman',...
   'FontSize',10);
set(y1,'FontName','Times New Roman',...
   'FontSize',10);
axis('equal');
axis('tight');
xlim(xwin);
ylim(ywin);
p1 = line(x,y);
set(p1,'LineWidth',1,'Color','k');
%annotation('textarrow',[0.505 0.505],[0.51 0.51],'String',...
%   {'Volumetric Water Content,  \theta_v [m^3/m^3]'},'TextRotation',90,...
%   'HeadStyle','none','LineStyle','none','FontSize',10,...
%   'FontName','Times New Roman')
annotation('textarrow',[0.261217948717949 0.261217948717949],[0.032 0.032],'String',...
   {'(a)'},'TextRotation',0,...
   'HeadStyle','none','LineStyle','none','FontSize',12,...
   'FontName','Times New Roman')
sizer = get(subplot1,'Position');
colorbar('off');
set(subplot1,'Position',sizer);
fid = fopen(mli2,'r','b');
l = fread(fid,'float');
```

```
m = mli_read(l,ny,nx);
if calc_flag == 1
   m = 0.47.*m;
elseif calc_flag == 2
   %m = log_volmoisture(m);
end
m(:,:) = abs(m(:,:));
[a b] = size(m);
for j=1:1:a
   for i = 1:1:b
         md = 0.5;
         m(ny,nx) = 0.5;
         if m(j,i) > 0.5 | m(j,i) < 0.1
            m(j,i) = 0;
         end
    end
end
subplot2 = subplot(1,2,2,'Parent',figure1,'YDir','reverse',...
   'XTick',xtic,...
   'XTickLabel',xtl,...
   'YTick',ytic,...
   'YTickLabel',ytl,...
   'PlotBoxAspectRatio',[599 1000 1],...
   'Layer','top',...
   'FontName','Times New Roman',...
   'FontSize',10,...
   'DataAspectRatio',[1 1 1]);
box(subplot2,'on');
hold(subplot2,'all');
imagesc(m,'Parent',subplot2,'CDataMapping','scaled');
p1 = line(x,y);
```

```
set(p1,'LineWidth',1,'Color','k');
colorbar('peer',subplot2,'FontName','Times New Roman','FontSize',10);
x2 = xlabel('Range Direction, x [m]');
y2 = ylabel('Cross Range Direction, y [m]');
set(x2,'FontName','Times New Roman',...
   'FontSize',10);
if band ==1
set(y2,'FontName','Times New Roman',...
   'FontSize',10,...
   'Position',[-205.997 1196.18 5828.88]);
else
set(y2,'FontName','Times New Roman',...
   'FontSize',10);
end
axis('equal');
axis('tight');
xlim(xwin);
ylim(ywin);
annotation('textarrow',[0.97 0.97],...
   [0.85 0.85],'String',...
   {'Volumetric Water Content,  \theta_v [m^3/m^3]'},'TextRotation',90,...
   'HeadStyle','none','LineStyle','none','FontSize',10,...
   'FontName','Times New Roman')
annotation('textarrow',[0.703205128205128 0.703205128205128],...
   [0.032 0.032],'String',...
   {'(b)'},'TextRotation',0,...
   'HeadStyle','none','LineStyle','none','FontSize',12,...
   'FontName','Times New Roman')
if band == 1
annotation(figure1,'textarrow',[0.246915064102564 0.213141025641026],...
   [0.226036741214054 0.215119047619048],'TextEdgeColor','none',...
```

```
    'TextBackgroundColor',[1 1 1],...
    'FontSize',8,...
    'FontName','Times New Roman',...
    'String',{'Radar Shadow'});
% Create textarrow
annotation(figure1,'textarrow',[0.222347756410256 0.201153846153846],...
    [0.803826563213139 0.630952380952381],'TextEdgeColor','none',...
    'TextLineWidth',1,...
    'TextBackgroundColor',[1 1 1],...
    'FontSize',8,...
    'FontName','Times New Roman',...
    'String',{'Saturation from Equipment'},...
    'LineWidth',1);
% Create textarrow
% Create textarrow
annotation(figure1,'textarrow',[0.183854166666666 0.20974358974359],...
    [0.280261676555602 0.47428571428571],'TextEdgeColor','none',...
    'TextLineWidth',1,...
    'TextBackgroundColor',[1 1 1],...
    'FontSize',8,...
    'FontName','Times New Roman',...
    'String',{'Test Section'},...
    'LineWidth',1);
elseif band ==2
% Create textarrow
% Create textarrow
annotation(figure1,'textarrow',[0.2 0.2],...
    [0.18 0.2],'TextEdgeColor','none',...
    'TextLineWidth',1,...
    'TextBackgroundColor',[1 1 1],...
    'FontSize',8,...
```

'FontName','Times New Roman',...

'String',{'Test Section'},...

'LineWidth',1);

% Create textarrow

annotation(figure1,'textarrow',[0.206915064102564 0.224358974358974],...

[0.206036741214054 0282738095238095],'TextEdgeColor','none',...

'TextBackgroundColor',[1 1 1],...

'FontSize',8,...

'FontName','Times New Roman',...

'String',{'Radar Shadow'});

End

A.3.2. ***MLI_plot.m***

A MATLAB executable written to visualize multi-look intensity images as a raster image (8-bit). Programmatic inputs included the multi-look intensity image, the number of rows in the image, the number of columns in the image, and a flag to switch between C-Band and K_u-Band inputs.

Invocation: mli_plot('out1.rec','out6.rec',1,1);

Source Code:

function mli_plot(mli1,ny,nx,band);

%SUBPLOT LEARNING EXCERSICE

%mli1 = 'out1.rec';

%mli2 = 'out6.rec';

%band = 1;

%calc_flag = 1;

%band = 1

%close all

if band == 1

map3 =[1.0000   1.0000   1.0000

0.9841 0.9841 0.9841
0.9683 0.9683 0.9683
0.9524 0.9524 0.9524
0.9365 0.9365 0.9365
0.9206 0.9206 0.9206
0.9048 0.9048 0.9048
0.8889 0.8889 0.8889
0.8730 0.8730 0.8730
0.8571 0.8571 0.8571
0.8413 0.8413 0.8413
0.8254 0.8254 0.8254
0.8095 0.8095 0.8095
0.7937 0.7937 0.7937
0.7778 0.7778 0.7778
0.7619 0.7619 0.7619
0.7460 0.7460 0.7460
0.7302 0.7302 0.7302
0.7143 0.7143 0.7143
0.6984 0.6984 0.6984
0.6825 0.6825 0.6825
0.6667 0.6667 0.6667
0.6508 0.6508 0.6508
0.6349 0.6349 0.6349
0.6190 0.6190 0.6190
0.6032 0.6032 0.6032
0.5873 0.5873 0.5873
0.5714 0.5714 0.5714
0.5556 0.5556 0.5556
0.5397 0.5397 0.5397
0.5238 0.5238 0.5238
0.5079 0.5079 0.5079

0.4921 0.4921 0.4921

0.4762 0.4762 0.4762

0.4603 0.4603 0.4603

0.4444 0.4444 0.4444

0.4286 0.4286 0.4286

0.4127 0.4127 0.4127

0.3968 0.3968 0.3968

0.3810 0.3810 0.3810

0.3651 0.3651 0.3651

0.3492 0.3492 0.3492

0.3333 0.3333 0.3333

0.3175 0.3175 0.3175

0.3016 0.3016 0.3016

0.2857 0.2857 0.2857

0.2698 0.2698 0.2698

0.2540 0.2540 0.2540

0.2381 0.2381 0.2381

0.2222 0.2222 0.2222

0.2063 0.2063 0.2063

0.1905 0.1905 0.1905

0.1746 0.1746 0.1746

0.1587 0.1587 0.1587

0.1429 0.1429 0.1429

0.1270 0.1270 0.1270

0.1111 0.1111 0.1111

0.0952 0.0952 0.0952

0.0794 0.0794 0.0794

0.0635 0.0635 0.0635

0.0476 0.0476 0.0476

0.0317 0.0317 0.0317

0.0159 0.0159 0.0159

```
        0         0         0];
end
fid = fopen(mli1,'r','b');
l = fread(fid,'float');
m = mli_read(l,ny,nx);
m(:,:) = abs(m(:,:));
[a b] = size(m);
for j=1:1:a
   for i = 1:1:b
          md = 0.5;
          m(ny,nx) = 1.0;
          if m(j,i) > 1.0 %| m(j,i) < 0
             m(j,i) = 0;
          end
    end
end
if band == 1
figure1 = figure('units','inches','pos',[0 0 6.5 3.5],'colormap',map3);
else
   figure1 = figure('units','inches','pos',[0 0 6.5 3.5]);
end
%axes1 = axes('Parent',figure1,'YDir','reverse',...
%   'Layer','top','FontSize',10,'FontName','Times New Roman');
imagesc(m,'CDataMapping','scaled');
if band == 2
colormap(gray)
end
colorbar('FontName','Times New Roman','FontSize',10);
x1 = xlabel('Range Direction, x [m]');
y1 = ylabel('Cross Range Direction, y [m]');
cap_str = strcat({'Figure '},num2str(figure1),{'. '},num2str(mli1));
```

```
set(x1,'FontName','Times New Roman',...
   'FontSize',10);
set(y1,'FontName','Times New Roman',...
   'FontSize',10);
axis('equal');
axis('tight');
%xlim(xwin);
%ylim(ywin);
%p1 = line(x,y);
%set(p1,'LineWidth',1,'Color','k');
annotation('textarrow',[0.92 0.92],[0.70 0.70],'String',...
   {'Radar Intensity,  \sigma_0'},'TextRotation',90,...
   'HeadStyle','none','LineStyle','none','FontSize',10,...
   'FontName','Times New Roman')
annotation('textarrow',[0.45 0.45],...
   [0.032 0.032],'String',...
   cap_str,'TextRotation',0,...
   'HeadStyle','none','LineStyle','none','FontSize',12,...
   'FontName','Times New Roman')
End
```

A.3.3. ***jgge_2_dens_plot.m***

A MATLAB executable written to visualize soil *in situ* density by comparing two different methods for obtaining soil volumetric water content and soil saturation. Programmatic inputs included the two multi-look intensity images, a band designator, and a flag to determine calculation (unused in this script).

Invocation: jgge_2_vwc_plot('out1.rec','out6.rec',1,1);

Source Code:

```
function jgge_2_dens_plot(mli1,mli2,band,calc_flag);
```

```
%SUBPLOT LEARNING EXERCISE
%mli1 = 'out1.rec';
%mli2 = 'out6.rec';
%band = 1;
%calc_flag = 1;
%band = 1
close all
if band == 1
   ytic = [800 1000 1200 1400 1600 1800];
   ytl = [600 750 900 1050 1200 1350];
   xtic = [1 200 400 600];
   xtl = [0 150 300 450];
   ny = 2645;
   nx = 1407;
   xwin = [1 600];
   ywin = [800 1800];
   x = [242 306 332 264 242];
   y = [1216 1183 1238 1261 1216];
   ylpos = [-136.812 1303.82 5828.88];
   ztic = [0 500 1000 1500 2000 2500];
   ztl = {'0.0' '0.5' '1.0' '1.5' '2.0' '2.5'};
   calc_flag = 0;
elseif band == 2
  ytic = [2200 2400 2600 2800 3000 3200];
   ytl =  [1650 1800 1950 2100 2250 2400];
   xtic = [1 200 400 600];
   xtl = [0 150 300 450];
   ny = 5291;
   nx = 2813;
   xwin = [1 600];
   ywin = [2200 3200];
```

```
    x = [227 303 319 241 227];
    y = [2539 2512 2566 2591 2539];
    ztic = [0 500 1000 1500 2000 2500];
    ztl = {'0.0' '0.5' '1.0' '1.5' '2.0' '2.5'};
    calc_flag = 0;
end
map2 = [   1.0000    1.0000    1.0000
    0.6250         0         0
    0.6875         0         0
    0.7500         0         0
    0.8125         0         0
    0.8750         0         0
    0.9375         0         0
    1.0000         0         0
    1.0000    0.0625         0
    1.0000    0.1250         0
    1.0000    0.1875         0
    1.0000    0.2500         0
    1.0000    0.3125         0
    1.0000    0.3750         0
    1.0000    0.4375         0
    1.0000    0.5000         0
    1.0000    0.5625         0
    1.0000    0.6250         0
    1.0000    0.6875         0
    1.0000    0.7500         0
    1.0000    0.8125         0
    1.0000    0.8750         0
    1.0000    0.9375         0
    1.0000    1.0000         0
    0.9375    1.0000    0.0625
```

0.8750 1.0000 0.1250

0.8125 1.0000 0.1875

0.7500 1.0000 0.2500

0.6875 1.0000 0.3125

0.6250 1.0000 0.3750

0.5625 1.0000 0.4375

0.5000 1.0000 0.5000

0.4375 1.0000 0.5625

0.3750 1.0000 0.6250

0.3125 1.0000 0.6875

0.2500 1.0000 0.7500

0.1875 1.0000 0.8125

0.1250 1.0000 0.8750

0.0625 1.0000 0.9375

0 1.0000 1.0000

0 0.9375 1.0000

0 0.8750 1.0000

0 0.8125 1.0000

0 0.7500 1.0000

0 0.6875 1.0000

0 0.6250 1.0000

0 0.5625 1.0000

0 0.5000 1.0000

0 0.4375 1.0000

0 0.3750 1.0000

0 0.3125 1.0000

0 0.2500 1.0000

0 0.1875 1.0000

0 0.1250 1.0000

0 0.0625 1.0000

0 0 1.0000

```
        0       0   0.9375
        0       0   0.8750
        0       0   0.8125
        0       0   0.7500
        0       0   0.6875
        0       0   0.6250
        0       0   0.5625
        0       0   0.5000];
fid = fopen(mli1,'r','b');
l = fread(fid,'float');
m = mli_read(l,ny,nx);
if calc_flag == 1
 %   m = 0.47.*m;
elseif calc_flag == 2
   %m = log_volmoisture(m);
end
m(:,:) = abs(m(:,:));
[a b] = size(m);
for j=1:1:a
   for i = 1:1:b
      if calc_flag == 1
         m = 0.0624279606.*m;
         md = 150;
         m(ny,nx) = 150;
         if m(j,i) > 150 | m(j,i) < 0
         m(j,i) = 0;
         end
      else
         md = 2500;
         m(ny,nx) = 2500;
         if m(j,i) > 2500 | m(j,i) < 0
```

```
            m(j,i) = 0;
          end
        end
    end
    j;
end
figure1 = figure('units','inches','pos',[0 0 6.5 3.5],'colormap',map2);
%axes1 = axes('Parent',figure1,'YDir','reverse',...
%   'Layer','top','FontSize',10,'FontName','Times New Roman');
subplot1 = subplot(1,2,1,'Parent',figure1,'YDir','reverse',...
    'XTick',xtic,...
    'XTickLabel',xtl,...
    'YTick',ytic,...
    'YTickLabel',ytl,...
    'PlotBoxAspectRatio',[599 1000 1],...
    'Layer','top',...
    'FontName','Times New Roman',...
    'FontSize',10,...
    'DataAspectRatio',[1 1 1]);
box(subplot1,'on');
hold(subplot1,'all');
%set(subplot1,'XTick',[1 200 400 600],...
%    'XTickLabel',[1 200 400 600]);
imagesc(m,'Parent',subplot1,'CDataMapping','scaled');
colorbar('peer',subplot1,'FontName','Times New Roman','FontSize',10,...
 'YTick',ztic,'YTickLabel',ztl);
sizer = get(subplot1,'Position');
colorbar('off');
set(subplot1,'Position',sizer);
x1 = xlabel('Range Direction, x [m]');
if band == 1
```

```
y1 = ylabel('Cross Range Direction, y [m]',...
   'Position',ylpos);
else
y1 = ylabel('Cross Range Direction, y [m]');
end
set(x1,'FontName','Times New Roman',...
   'FontSize',10);
set(y1,'FontName','Times New Roman',...
   'FontSize',10);
axis('equal');
axis('tight');
xlim(xwin);
ylim(ywin);
p1 = line(x,y);
set(p1,'LineWidth',1,'Color','k');
%annotation('textarrow',[0.513012820512821 0.513012820512821],...
%   [0.542738095238095 0.542738095238095],'String',...
%   {'Dry Unit Weight,  \gamma_d [kg/m^3]'},'TextRotation',90,...
%   'HeadStyle','none','LineStyle','none','FontSize',10,...
%   'FontName','Times New Roman')
annotation('textarrow',[0.261217948717949 0.261217948717949],[0.04 0.04],'String',...
   {'(a)'},'TextRotation',0,...
   'HeadStyle','none','LineStyle','none','FontSize',12,...
   'FontName','Times New Roman')
fid = fopen(mli2,'r','b');
l = fread(fid,'float');
m = mli_read(l,ny,nx);
if calc_flag == 1
  %  m = 0.47.*m;
elseif calc_flag == 2
   %m = log_volmoisture(m);
```

```
end
m(:,:) = abs(m(:,:));
[a b] = size(m);
for j=1:1:a
   for i = 1:1:b
      if calc_flag == 1
         m = 0.0624279606.*m;
         md = 150;
         m(ny,nx) = 150;
         if m(j,i) > 150 | m(j,i) < 0
         m(j,i) = 0;
         end
      else
         md = 2500;
         m(ny,nx) = 2500;
         if m(j,i) > 2500 | m(j,i) < 0
            m(j,i) = 0;
         end
      end
   end
end
subplot2 = subplot(1,2,2,'Parent',figure1,'YDir','reverse',...
   'XTick',xtic,...
   'XTickLabel',xtl,...
   'YTick',ytic,...
   'YTickLabel',ytl,...
   'PlotBoxAspectRatio',[599 1000 1],...
   'Layer','top',...
   'FontName','Times New Roman',...
   'FontSize',10,...
   'DataAspectRatio',[1 1 1]);
```

```
box(subplot2,'on');
hold(subplot2,'all');
imagesc(m,'Parent',subplot2,'CDataMapping','scaled');
p1 = line(x,y);
set(p1,'LineWidth',1,'Color','k');
colorbar('peer',subplot2,'FontName','Times New Roman','FontSize',10);
x2 = xlabel('Range Direction, x [m]');
y2 = ylabel('Cross Range Direction, y [m]');
set(x2,'FontName','Times New Roman',...
   'FontSize',10);
if band ==1
set(y2,'FontName','Times New Roman',...
   'FontSize',10,...
   'Position',[-136.997 1296.18 5828.88]);
else
set(y2,'FontName','Times New Roman',...
   'FontSize',10);
end
axis('equal');
axis('tight');
xlim(xwin);
ylim(ywin);
annotation('textarrow',[0.97 0.97],...
   [0.545714285714285 0.545714285714285],'String',...
   {'Dry Unit Weight,  \gamma_d [kg/m^3]'},'TextRotation',90,...
   'HeadStyle','none','LineStyle','none','FontSize',10,...
   'FontName','Times New Roman')
annotation('textarrow',[0.703205128205128 0.703205128205128],...
   [0.04 0.04],'String',...
   {'(b)'},'TextRotation',0,...
   'HeadStyle','none','LineStyle','none','FontSize',12,...
```

```
    'FontName','Times New Roman')
if band == 1
annotation(figure1,'textarrow',[0.246915064102564 0.213141025641026],...
    [0.226036741214054 0.235119047619048],'TextEdgeColor','none',...
    'TextBackgroundColor',[1 1 1],...
    'FontSize',8,...
    'FontName','Times New Roman',...
    'String',{'Radar Shadow'});
% Create textarrow
annotation(figure1,'textarrow',[0.242347756410256 0.221153846153846],...
    [0.803826563213139 0.630952380952381],'TextEdgeColor','none',...
    'TextLineWidth',1,...
    'TextBackgroundColor',[1 1 1],...
    'FontSize',8,...
    'FontName','Times New Roman',...
    'String',{'Saturation from Equipment'},...
    'LineWidth',1);
% Create textarrow
annotation(figure1,'textarrow',[0.240384615384615 0.3125],...
    [0.788690476190476 0.705357142857143],'TextEdgeColor','none');
% Create textarrow
annotation(figure1,'textarrow',[0.183854166666666 0.233974358974359],...
    [0.360261676555602 0.571428571428571],'TextEdgeColor','none',...
    'TextLineWidth',1,...
    'TextBackgroundColor',[1 1 1],...
    'FontSize',8,...
    'FontName','Times New Roman',...
    'String',{'Test Section'},...
    'LineWidth',1);
annotation(figure1,'textarrow',[0.31 0.31],...
    [0.355838582078198 0.356838582078198],'TextEdgeColor','none',...
```

```
    'TextBackgroundColor',[1 1 1],...
    'TextRotation',90,...
    'FontSize',8,...
    'FontName','Times New Roman',...
    'String',{'Lake'},...
    'HeadStyle','none',...
    'LineStyle','none');
% Create textarrow
annotation(figure1,'textarrow',[0.78 0.78],...
    [0.355838582 0.355838582],'TextEdgeColor','none',...
    'TextBackgroundColor',[1 1 1],...
    'TextRotation',90,...
    'FontSize',8,...
    'FontName','Times New Roman',...
    'String',{'Lake'},...
    'HeadStyle','none',...
    'LineStyle','none');
elseif band ==2
% Create textarrow
annotation(figure1,'textarrow',[0.31 0.31],...
    [0.355838582078198 0.356838582078198],'TextEdgeColor','none',...
    'TextBackgroundColor',[1 1 1],...
    'TextRotation',90,...
    'FontSize',8,...
    'FontName','Times New Roman',...
    'String',{'Lake'},...
    'HeadStyle','none',...
    'LineStyle','none');
% Create textarrow
annotation(figure1,'textarrow',[0.74 0.74],...
    [0.355838582078198 0.356838582078198],'TextEdgeColor','none',...
```

```
    'TextBackgroundColor',[1 1 1],...
    'TextRotation',90,...
    'FontSize',8,...
    'FontName','Times New Roman',...
    'String',{'Lake'},...
    'HeadStyle','none',...
    'LineStyle','none');
% Create textarrow
annotation(figure1,'textarrow',[0.2 0.233974358974359],...
    [0.360261676555602 0.613095238095238],'TextEdgeColor','none',...
    'TextLineWidth',1,...
    'TextBackgroundColor',[1 1 1],...
    'FontSize',8,...
    'FontName','Times New Roman',...
    'String',{'Test Section'},...
    'LineWidth',1);
% Create textarrow
annotation(figure1,'textarrow',[0.298437499999999 0.264423076923077],...
    [0.803826563213139 0.613095238095238],'TextEdgeColor','none',...
    'TextLineWidth',1,...
    'TextBackgroundColor',[1 1 1],...
    'FontSize',8,...
    'FontName','Times New Roman',...
    'String','Access Road',...
    'LineWidth',1);
% Create textarrow
annotation(figure1,'textarrow',[0.246915064102564 0.224358974358974],...
    [0.226036741214054 0.282738095238095],'TextEdgeColor','none',...
    'TextBackgroundColor',[1 1 1],...
    'FontSize',8,...
    'FontName','Times New Roman',...
```

```
    'String',{'Radar Shadow'});
End
```

A.3.4. ***c_dens_wag_spm.m***

A MATLAB executable written to compute soil density by comparing C-Band saturation imagery (obtained via the Wagner 1998 method) and C-Band soil volumetric water content (obtained via the small perturbation method). Programmatic inputs included input mli files, output file path, number of rows in the image (optional), number of columns in the image (optional), and a unit calculation flag to switch between imperial and metric units (optional).

Invocation: [density image(:,:)] = c_dens_wag_spm('westar20130613e91.ini',…

‘out1.mli’,’…

../DENS/20130613.dens’,…

701,…

1340,…

0);

Source Code:

```
function [dens] = c_dens_wag_spm(mli_spm,mli_wag,mli_out,ny,nx,uf)
%mli_spm = 'westar20130613e91.ini',
%mli_wag = 'out1.mli'
%mli_out = '../DENS/20130613.dens'
%ny = 701
%nx =1340
%uf = 0;
if nargin == 6
   if uf == 0
      pw = 1000;
```

```
    disp('METRIC KG/M^3!');
  elseif uf == 1
    pw = 62.4;
    disp('IMPERIAL LBS/FT^3!')
  end
  Gs = 2.51;
  fid = fopen(mli_spm,'r','b');
  l = fread(fid,'float');
  mv = mli_read(l,ny,nx);
  %mv = log_volmoisture(mv);
  fclose('all');
  fid = fopen(mli_wag,'r','b');
  l = fread(fid,'float');
  ms = mli_read(l,ny,nx);
  clear l fid
  fclose('all');
  dens = zeros(ny,nx);
  for j = 1:1:ny
    for i = 1:1:nx
      if mv(j,i) == 0 | ms(j,i) == 0;
        dens(j,i) = 0;
      else
        dens(j,i) = Gs*pw*1*(1-(mv(j,i)/ms(j,i)));
        if dens(j,i) < 0 | dens(j,i) > 2500
          dens(j,i) = 0.0;
        end
      end
    end
  end
  mli_visualize_e(dens,ny,nx,figure,[1 nx],[1 ny]);
else
```

```
   disp('NARGIN ERROR! c_dens_wag_spm!');
end
end
%end
```

A.3.5. ***mli_smooth.m***

A MATLAB executable written to smooth output MLI imagery to using nearest neighbor averaging (relnoise.m). Programmatic inputs included input MLI image, number of image rows, number of image columns.

Invocation: [smoothed_mli] = mli_smooth('out1.mli',701,1340);

Source Code:

```
function [msv] = mli_smooth(mli_e,ny,nx)
fid = fopen(mli_e,'r','b');
l = fread(fid,'float');
m = mli_read(l,ny,nx);
[ms mv] = relnoise(m,5,.1);
%ms = log_volmoisture(ms);
msv = mli_visualize_e(ms,ny,nx,'smooth',[100 700],[1 701]);
end
```

A.3.6. ***soil_wagner.m***

A MATLAB executable written to extract soil saturation imagery from set of registered, temporally separated MLI images using the method proposed by Wagner (1998). The script was executed from the MATLAB GUI (F5) by pressing the F5 key. Requires prior generation of file list (mli_list.txt) containing all files for processing.

Invocation: MATLAB GUI (F5)

Source Code:

```
%% DEFINE PWD AND CREATE FILE LIST FOR PROCESSING
%function soil_wagner(amli_list,ref,a_count, r_count);
fclose('all');
amli_list ='mli_list.txt'
ref = 'westar20130613vv.amli'
a_count = 701;
r_count = 1340;
lv1_path = pwd;
%select ref_img
l_ref_img_name = ref;
fid = fopen(l_ref_img_name,'r','b');
ref_list = fread(fid,'float');
fclose(fid);
%a_count = str2num(a_count);
img = mli_read(ref_list,a_count,r_count);
clear l_pixel_min l_pixel_max
clear ref_list
[a b] = size(img);
for i = 1:a
   for j = 1:b
      l_pixel_min(i,j)=img(i,j);
      l_pixel_max(i,j)=img(i,j);
   end
end
disp('ref_loaded')
fid = fopen(amli_list);
low_l = textscan(fid,'%q');
fclose(fid);
%fid = fopen('avg_mu_list.txt');
```

```
%upp_l = textscan(fid,'%q');
%fclose(fid);
[c d] = size(low_l{1,1});
%[e f] = size(upp_l{1,1});
for k = 1:c
img_id = char(low_l{1,1}(k));
fid = fopen(img_id,'r','b');
mli_list = fread(fid,'float');
fclose(fid);
img = mli_read(mli_list,a_count,r_count);
[a b] = size(img);
for i = 1:a
   for j = 1:b
      if img(i,j) < l_pixel_min(i,j)
          l_pixel_min(i,j) = img(i,j);
      end
      if img(i,j) > l_pixel_max(i,j)
         l_pixel_max(i,j) = img(i,j);
      end
    end
    %disp(strcat('line#_',num2str(i)))
end
end
disp(strcat('image_#',num2str(k)))
%imwrite(l_pixel_min(:,:),'min.mli.ras');
%imwrite(l_pixel_max(:,:),'max.mli.ras');
mli_write('min.mli',l_pixel_min);
mli_write('max.mli',l_pixel_max);
fid = fopen('max.mli','r','b');
l = fread(fid,'float');
maxbv = mli_read(l,a_count,r_count);
```

```
fclose('all');
maxbv = mli_read(l,a_count,r_count);
fid = fopen('min.mli','r','b');
l = fread(fid,'float');
minbv = mli_read(l,a_count,r_count);
fclose('all');
for k = 1:c
img_id = char(low_l{1,1}(k));
fid = fopen(img_id,'r','b');
mli_list = fread(fid,'float');
fclose(fid);
img = mli_read(mli_list,a_count,r_count);
[aa bb] = size(img);
for ii = 1:aa
   for jj = 1:bb
      if img(ii,jj) < 1e-2
         msl(ii,jj) = 0;
      else
         if img(ii,jj) == 0
         imgc = -60;
         else
         imgc = 10*log10(img(ii,jj));
         end
         if minbv(ii,jj) == 0
            minbvc = -60;
         else
         minbvc = 10*log10(minbv(ii,jj));
         end
         if maxbv(ii,jj) == 0
         maxbvc = -60;
         else
```

```
        maxbvc = 10*log10(maxbv(ii,jj));
        end
         num =imgc-minbvc;
        den =maxbvc-minbvc;
        if isnan(den) == 1
        msl(ii,jj) = 0;
        elseif isnan(num) == 1
          msl(ii,jj) = 0;
        else
         msl(ii,jj) = num/den;
        if isnan(msl(ii,jj)) == 1
           msl(ii,jj)=0;
        end
        if msl(ii,jj)>255.1
           disp('WTF BATMAN')
           msl(ii,jj),num,den,maxbv(ii,jj),minbv(ii,jj),msl(ii,jj)
           pause(10)
        end
        end
      end
   end
end
%figure
%mm = msl(a_count,1:(r_count-1));
%m = 3*(mm*(255/(max(max(mm))-min(min(mm)))))&.4;
%image(m);
mli_out = strcat('../WAG/','out',num2str(k),'.mli');
disp(strcat('process_image_#',num2str(k)))
mli_write(mli_out,msl);
[msl msv] = relnoise(msl,3,.1);
mli_out = strcat('avl',num2str(k),'.fmli');
```

```
mli_write(mli_out,msl);
%mli_uint8(mli_out,msl);
clear img mli_list
%image(ms)
%title(img_out)
%pause(1)
%ms = uint8(ms);
%imwrite(ms,img_out)
end
clear l_pixel_max l_pixel_min
```

A.3.7. ***spm_initial.m***

A MATLAB executable written to generate initial estimates of soil surface complex electric permissivity (ε) and soil normalized surface roughness (kh) contained as MLI image files. Programmatic inputs included a horizontally transmitted and horizontally received polarized MLI image, a vertically transmitted and vertically received polarized MLI image, an output file name for estimate of soil permissivity (as mli image), an output file name for estimate of soil normalized roughness (as mli image), and a parameter array. The parameter array contained the number of azimuth lines, number of range line, range pixel dimension, vertical instrument location offset, minimum return intensity for processing (pixels below this tolerance are ignored), and processing window (limits processing to an image subset bound in range and azimuth).

Invocation:
```
spm_initial('../MLI_HHB/westar20130614hh.amli',...
            '../MLI_VVB/westar20130614vv.amli',...
            '../mli_temp/westar20130614e91.ini',...
            '../mli_temp/westar20130614kh91.ini',...
            [701 1340 0.75 40 1e-2 1 701 1 1340]);
```

Source Code:

```
function  spm_initial(mli_hh,mli_vv,mli_e,mli_kh,param);
r0 = 50.2218;
mli_hh
mli_vv
mli_e
mli_kh
a_count = param(1,1)
r_count = param(1,2)
r_size = param(1,3)
zr = param(1,4)
tol = param(1,5)
win = param(1,6:9)
%1.0 HOUSEKEEPING
zp = 0;
k = 2*pi/5.6;
l = 15;
%2.0 INGEST FILES
   fid = fopen(mli_hh,'r','b');
   mli_list = fread(fid,'float');
   img1 = mli_read(mli_list,a_count,r_count);
   fid = fopen(mli_vv,'r','b');
   mli_list = fread(fid,'float');
   img2 = mli_read(mli_list,a_count,r_count);
   fclose('all');
   [a b] = size(img1);
   [c d] = size(img2);
if img1 > img2
   error('image size error')
elseif img2 > img1
```

```
    error('image size error')
end
%3.0 CREATE LOOKUP  TABLE FOR EACH RANGE LINE
imin = win(1,3);
imax = win(1,4);
jmin = win(1,1);
jmax = win(1,2);
for i = imin:1:imax
    fid = fopen(mli_hh,'r','b');
    mli_list = fread(fid,'float');
    img1 = mli_read(mli_list,a_count,r_count);
    fid = fopen(mli_vv,'r','b');
    mli_list = fread(fid,'float');
    img2 = mli_read(mli_list,a_count,r_count);
    fclose('all');
    im1 = img1(:,i);
    im2 = img2(:,i);
    clearvars img1 img2
    ii = 0;
    jj = 0;
    for e = 2:0.01:18
        ii = ii+1;
        jj = 0;
        for kh = 0.1:0.05:3.0
            jj = jj+1;
            incident = incident_flat(i,r0,r_size,zr,zp);
            h = kh/k;
            w = eacf(k,l,incident);
            c1 = 8*(k^4)*h^2*cos(incident)^4*w;
            ahh = abs((1-e)/(cos(incident)+(e-sin(incident)^2)^0.5)^2);
            avv = abs((e-1)*(sin(incident)^2-e*(1+sin(incident)^2)/ ...
```

```
        (e*cos(incident)+(e-sin(incident)^2)^0.5)^2));
    thh = c1*ahh^2;
    tvv = c1*avv^2;
    look_hh(ii+1,1) = e;
    look_hh(1,jj+1) = kh;
    look_hh(ii+1,jj+1) = thh;
    look_vv(ii+1,1) = e;
    look_vv(1,jj+1) = kh;
    look_vv(ii+1,jj+1) = tvv;
  end       %end the kh loop
end         %end the e loop
disp({'lookup table complete for range line: '})
i
for j = jmin:1:jmax
  pq_rat = look_hh./look_vv;
  pq_rat(:,1) = look_hh(:,1);
  pq_rat(1,:) = look_vv(1,:);
  %clear look_hh look_vv
  obs_hh = im1(j,1);
  obs_vv = im2(j,1);
  %4.0 CALCULATE KH INITIAL AND EMISSIVITY INITIAL
  if obs_hh < tol | obs_vv < tol;
    hh_e(j,i) = 0;
    hh_kh(j,i) = 0;
  else
    pq_obs = obs_hh/obs_vv;
    [ly lx] = size(look_hh);
    [~,indx] = min(min(abs(pq_rat(2:ly,2:lx)-pq_obs)));
    [~,indy] = min(abs(pq_rat(2:ly,indx)-pq_obs));
    hh_e(j,i) = pq_rat(indy,1);
    hh_kh(j,i) = pq_rat(1,indx);
```

```
      end
   end
end
mli_out1 = zeros(a_count,r_count);
mli_out1(jmin:jmax,imin:imax)=hh_e(:,:);
mli_out2 = zeros(a_count,r_count);
mli_out2(jmin:jmax,imin:imax)=hh_kh(:,:);
mli_f1 = mli_e;
mli_f2 = mli_kh;
clear a a_count ahh avv awin b c c1 d e h i ii im1 im2
clear imax imin incident indx indy j jj jmax jmin k kh l
clear look_hh look_vv lx ly obs_hh obs_vv pq_rat pq_obs
clear r0 r_count r_size rwin thh tvv w zp zr
mli_write(mli_f1,mli_out1);
mli_write(mli_f2,mli_out2);
```

A.3.8. ***spm_refine.m***

A MATLAB executable written to generate refined estimates of soil surface complex electric permissivity (ε) and soil normalized surface roughness (kh) contained as MLI image files. Programmatic inputs included estimates of soil permissivity (as mli image), estimates of soil normalized roughness (as mli image), output file name for refined SPM estimate of soil permissivity, and a refined estimate of soil normalized roughness, and a parameter array. The parameter array contained the number of azimuth lines, number of range line, range pixel dimension, vertical instrument location offset, minimum return intensity for processing (pixels below this tolerance were ignored), and processing window (limits processing to an image subset bound in range and azimuth).

Invocation: spm_refine('../mli_temp/westar20130614e91.ini',...

'../mli_temp/westar20130614kh91.ini',...

'../mli_out/westar20130614e91.emli,…

'../mli_out/westar20130614kh91.kmli',…

[701 1340 0.75 40 1e-2 1 701 1 1340]);

Source Code:

```
function spm_refine(initial_kh,initial_e,hh,vv,ref_out,param)
azimuth = param(1,1)
range = param(1,2)
zr = param(1,3)
zp = 0;
l = param(1,4)
awin(1,1) = param(1,5)
awin(1,2) = param(1,6)
rwin(1,1) = param(1,7)
rwin(1,2) = param(1,8)
f_e = initial_e;
f_kh = initial_kh;
a_count = azimuth;
amax = param(1,6);
amin = param(1,5);
rmax = param(1,8);
rmin = param(1,7);
tol = param(1,9)
r0 = 50.2218;
k = 2*pi/5.6;
r_size = 0.75;
r_count = range;
fid = fopen(f_e,'r','b');
temp = fread(fid,'float');
```

```
temp_e = mli_read(temp,a_count,r_count);
fid = fopen(f_kh,'r','b');
temp = fread(fid,'float');
temp_kh = mli_read(temp,a_count,r_count);
for i = (rmin+2):1:(rmax-2)
   for j = (amin+2):1:(amax-2)
      ref_kh(j,i) = mean(nonzeros(temp_kh(j-2:j+2,i-2:i+2)));
      if isnan(ref_kh(j,i)) == 1
         ref_kh(j,i) = 0.2;
      end
   end
end
disp({'Refined kh Matrix computed for line ;'})
fin_kh = temp_kh;
fin_kh(amin+1:amax-1,rmin+1:rmax-1) = ref_kh(:,:);
clear temp_kh ref_kh
imin = rwin(1,1);
imax = rwin(1,2);
jmin = awin(1,1);
jmax = awin(1,2);
for i = imin:1:imax
   fid = fopen(hh,'r','b');
   mli_list = fread(fid,'float');
   img1 = mli_read(mli_list,a_count,r_count);
   fid = fopen(vv,'r','b');
   mli_list = fread(fid,'float');
   img2 = mli_read(mli_list,a_count,r_count);
   fclose('all');
   im1 = img1(:,i);
   im2 = img2(:,i);
   clearvars img1 img2
```

```
ii = 0;
jj = 0;
for e = 2:0.05:18
   ii = ii+1;
   jj = 0;
   for kh = 0.1:0.1:3.0
      jj = jj+1;
      incident = incident_flat(i,r0,r_size,zr,zp);
      h = kh/k;
      w = eacf(k,l,incident);
      c1 = 8*(k^4)*h^2*cos(incident)^4*w;
      ahh = abs((1-e)/(cos(incident)+(e-sin(incident)^2)^0.5)^2);
      avv = abs((e-1)*(sin(incident)^2-e*(1+sin(incident)^2)/ ...
         (e*cos(incident)+(e-sin(incident)^2)^0.5)^2));
      thh = c1*ahh^2;
      tvv = c1*avv^2;
      look_hh(ii+1,1) = e;
      look_hh(1,jj+1) = kh;
      look_hh(ii+1,jj+1) = thh;
      look_vv(ii+1,1) = e;
      look_vv(1,jj+1) = kh;
      look_vv(ii+1,jj+1) = tvv;
   end         %end the kh loop
end
disp({'lookup table complete for range line: '})
i
for j = jmin:1:jmax
   pq_rat = look_hh./look_vv;
   pq_rat(:,1) = look_hh(:,1);
   pq_rat(1,:) = look_vv(1,:);
   %clear look_hh look_vv
```

```
      obs_hh = im1(j,1);
      obs_vv = im2(j,1);
      %4.0 CALCULATE KH INITIAL AND EMISSIVITY INITIAL
      if obs_hh < tol | obs_vv < tol;
         hh_e(j,i) = 0;
         hh_kh(j,i) = 0;
      else
         pq_obs = obs_hh/obs_vv;
         [ly lx] = size(look_hh);
         [~,indx] = min(abs(pq_rat(2,:)-fin_kh(j,i)));
         [~,indy] = min(abs(pq_rat(2:ly,indx)-pq_obs));
         hh_e(j,i) = pq_rat(indy,1);
         hh_kh(j,i) = pq_rat(1,indx);
      end
   end
end
mli_out1 = zeros(a_count,r_count);
mli_out1(jmin:jmax,imin:imax)=hh_e(:,:);
mli_f1 = '../mli_e/20130614fin_e.ini';
mli_write(mli_f1,mli_out1);
lin_mv = zeros(a_count,r_count);
mli_out2(jmin:jmax,imin:imax)=lin_volmoisture(hh_e);
mli_f2 = strcat(ref_out,'lin_mv.fin');
mli_write(mli_f2,mli_out2);
mli_out2(jmin:jmax,imin:imax)=log_volmoisture(hh_e);
mli_f2 = strcat(ref_out,'log_mv.fin');
mli_write(mli_f2,mli_out2);
clear mli_out*
clear a ahh avv awin b c c1 d e h i ii im1 im2
clear imax imin incident indx indy j jj jmax jmin k kh l
clear look_hh look_vv lx ly obs_hh obs_vv pq_rat pq_obs
```

```
clear r0 r_size rwin thh tvv w zp zr
```

A.3.9. ***lin_moisture.m***

A MATLAB executable written to calculate soil moisture values (volumetric water content) from previously calculated soil permissivity maps (from spm_initial.m and spm_refine.m) using a linear model for the soil permissivity-water content relationship proposed by Dubois et al. (1995). The programmatic inputs included a finalized estimate of pixel soil emissivity. The program was executed as a subroutine in the spm_initial.m and spm_refine.m scripts.

Invocation: [mv] = lin_moisture(fin_e);

Source Code :

```
function [mv] = lin_volmoisture(fin_e)
mv = 0.0211.*fin_e-0.0359;
[a b] = size(mv);
for i = 1:1:a
   for j = 1:1:b
      if mv(i,j) < 0
         mv(i,j) = 0;
      end
   end
end
```

A.3.10. ***log_moisture.m***

A MATLAB executable written to calculate soil moisture values (volumetric water content) from previously calculated soil permissivity maps (from spm_initial.m and spm_refine.m) using a logarithmic model for the soil permissivity-water content relationship

proposed by Dubois et al. (1995). The programmatic inputs included a finalized estimate of pixel soil emissivity. The program was executed as a subroutine in the spm_initial.m and spm_refine.m scripts.

Invocation: [mv] =log_moisture(fin_e);

Source Code :

```
function [mv] = log_volmoisture(fin_e)
[a b] = size(fin_e);
for i = 1:1:a
   for j = 1:1:b
      mv(i,j) = 0.1691*log(fin_e(i,j))-0.0359;
      if mv(i,j) < 0
         mv(i,j) = 0;
      end
   end
end
```

A.3.11. ***eacf.m***

A MATLAB executable written to compute the value of the auto-correlation function for each pixel in an image using the exponential relationship documented in Dubois et al. (1995). Programmatic inputs includes wavelength (k), soil autocorrelation length (l), and the incident angle (incident).

Invocation: [w] = eacf(5.56,20,10);

Source Code:

```
  %calculate ACF (Exponential)
function [w] = eacf(k,l,incident)
w = (1/271)*(l^2)/((1+4*(k^2)*(sin(incident)^2)*(l^2))^(1.5));
end
```

A.3.12. ***incident_flat.m***

A MATLAB executable written to compute the incident angle for each pixel based on a simple assumption of a flat surface with a known vertical offset to the instrument. Programmatic inputs included the range line (or an individual pixel [r]), the range offset (range distance for initial range line [r0]), the pixel range dimension (dr), the radar elevation (zr), and the pixel elevation (zp).

Invocation: [w] = incident_flat(25,50,0.75);

Source Code:

```
function [theta] = incident_flat(r,r0,dr,zr,zp)
if nargin == 5
   elev = zr-zp;
   rang = r0+r*dr;
   theta = pi/2-asin(elev/rang);
else
   disp('incorrect input arguments')
   disp('[incident angle] = incident_flat(r,dr,zr,zp)')
   disp('<incident angle] = output incident angle for pixel')
   disp('<r> = range pixel coordinates')
   disp('<dr> = range pixel size (0.75 m)')
   disp('<zr> = elevation of radar')
   disp('<zp> = elevation of pixel')
end
end
```

A.3.13. ***mli_read.m***

A MATLAB executable written to read and ingest an MLI image file into memory for further processing. Programmatic inputs included the MLI image file(s) from either the GAMMA

interferometric software or other MATLAB executables (e.g. spm_initial, spm_refine). Additional programmatic inputs included either a MLI file name or a list of MLI file names, the number of azimuth lines in the image file, and the number of range lines in the image.

Invocation: [w] = mli_read(mli_list,701,1340)

Source Code:

```
function [mli_mat] = mli_read(mli_list,a,r)
if nargin < 3
   disp('MLI_READER FUNCTION')
   disp('<mli_matrix_out> = mli_read(<mli_list>.<azimuth lines>,<range lines>')
elseif nargin > 3
   disp('too many input arguments')
else
disp('EXECUTE MLI READER');
[g h] = size(mli_list);
azimuth_line = 1;
line_count = 1;
for i = 1:a
   for j = 1:r
      mli_mat(i,j) = mli_list(line_count,1);
      line_count = line_count+1;
   end
end
clear g h mli_list range_eol_check azimuth_line line_count range_count;
end
end
```

A.3.14. ***mli_write.m***

A MATLAB executable written to write an image matrix from memory as an MLI file for use in further processing. Programmatic inputs included the output file name and the data matrix.

Invocation: [w] = mli_write('out.mli',data_matrix(:,:))

Source Code:

```
function [mli_list] = mli_write(file_name,mli_mat)
%file_name = mli_f1;,%mli_mat = hh_e;
disp('EXECUTE MLI WRITER')
fid = fopen(file_name,'w+','b');
[g h] = size(mli_mat);
s = 0;
smax = g*h;
mli_list = zeros(smax,1);
for i = 1:g
   for j = 1:h
      s = s+1;
      mli_list(s,1) = mli_mat(i,j);
   end
  end
disp('mli_list created');
clear mli_mat
%disp(strcat('Write 64-bit floating point output',' ',file_name));
%fwrite(fid,mli_list,'double');
%fclose(fid);
fid = fopen(file_name,'w+','b');
disp(strcat('Write 32-bit floating point output',' ',file_name));
fwrite(fid,mli_list,'float');
fclose(fid);
%end
```

A.4. Radar Image Acquisition Profiles

The radar images acquisition profiles are documented in this section. The image profile (.prf) files were used to set the parameters used by the GPRI_capture.py command and subsequent pre- and post-processing activities. Parameters of interest that are included in the .prf file include the chirp length, the radar center frequency, the image attenuation, the minimum chirp frequency, the maximum chirp frequency, the number of chirp samples, the transmit mode, the antenna start angle (relative to the home position), the antenna end angle (relative to the home position), the motor gear ratio, the motor rotation rate, the data capture time, the sampling rate, and the antenna elevation look angle. The .prf files used at the University of Arkansas Cato Springs Research Center and the WESTAR Jeffery Energy Center are presented in Section A.4.1 (UASCRC), Section A.4.2 (500 μs WJEC), and Section A.4.3 (1 ms WJEC), respectively.

A.4.1. ***250 μs profile used at UACSRC***

RF_center_freq: 1.720000e+10
IMA_atten_dB: 32
CHP_freq_min: 100.0e6
CHP_freq_max: 300.0e6
CHP_num_samp: 6250
TX_power: on
STP_antenna_start: -138.0
STP_antenna_end: 5.0
STP_gear_ratio: 72
STP_rotation_speed: 10.0
ADC_capture_time: 1.0
ADC_sample_rate: 6.25000e+06
antenna_elevation: 0

A.4.2. ***500 μs profile used at WJEC***

RF_center_freq: 1.720000e+10
IMA_atten_dB: 32
CHP_freq_min: 100.0e6

CHP_freq_max: 300.0e6

CHP_num_samp: 6250

TX_power: on

STP_antenna_start: -138.0

STP_antenna_end: 5.0

STP_gear_ratio: 72

STP_rotation_speed: 10.0

ADC_capture_time: 1.0

ADC_sample_rate: 6.25000e+06

antenna_elevation: 0

A.4.3. ***1000 µs profile used at WJEC***

RF_center_freq: 1.720000e+10

IMA_atten_dB: 32

CHP_freq_min: 100.0e6

CHP_freq_max: 300.0e6

CHP_num_samp: 6250

TX_power: on

STP_antenna_start: -138.0

STP_antenna_end: 5.0

STP_gear_ratio: 72

STP_rotation_speed: 10.0

ADC_capture_time: 1.0

ADC_sample_rate: 6.25000e+06

antenna_elevation: 0

A.4.4. ***2 ms fully polarized profile***

RF_center_freq: 1.720000e+10

IMA_atten_dB: 44

CHP_freq_min: 100.0e6

CHP_freq_max: 300.0e6

CHP_num_samp: 12500

TX_power: on

TX_mode: TX_RX_SEQ

TX_RX_SEQ: AAA

STP_antenna_start: -80.0

STP_antenna_end: 60.0

STP_gear_ratio: 72

STP_rotation_speed: 10

ADC_capture_time: 1.0

ADC_sample_rate: 6.25000e+06

antenna_elevation: 0

A.5. Works Cited

Dubois, P., van Zyl, J., Engman, E., (1995). "Measuring soil moisture with imaging radar." IEEE Trans. Geosci. Remote Sensing, vol. 33, pp. 916–926, July 1995.

Wagner, Wolfgang (1998). "Soil moisture retrieval from ERS scatterometer data." PhD Dissertation, Vienna University of Technology.

Wegmuller, Urs, (1997). "Soil moisture monitoring with ERS SAR interferometery." European Space Agency Special Publication ESA SP-414. Proc. 3rd ERS Symposium. pp. 47-51.

APPENDIX B: SOURCE CODE FOR VISIBLE AND INFRARED SPECTROSCOPY

B.1. Chapter Overview

Contained in this appendix are the various programmatic code developed to acquire, preprocess, process, and visualize visible and near infrared (Vis-NIR) and middle infrared (MIR) diffuse reflectance infrared Fourier transform spectroscopy (DRIFT) obtained data. Data preprocessing was variously conducted in either the Oceanview software suit (Vis OceanOptics 2015), the OMNIC software suite (NIR/MIR data, Nicolet 2004), the RS3 and Viewspec Pro software suites (Vis-NIR data, ASD 2014), Microsoft Excel (Microsoft 2015), and MATLAB (Mathworks 2014). All processing was conducted in a Windows software environment. Several subroutines are not included because they were only used to provide a convenient method of importing established absorption values from either prior testing (killite.m, kdonna.m, kkaolin.m) or from literature sources (kvapor_lit.m and kwater_lit.m). A list of the included software scripts developed to 1) analyze spectral data to obtain measurements of engineering properties and 2) obtain measurements of soil optical properties during the course of this research are presented in Table B.1. and Table B.2, respectively.

Table B. 1. List of included software executables and source code developed to process radar data to extract measurements of soil water content and soil *in situ* density.

ID	Executable	Description
B.2.1	asd_reader	Ingest, average, and output ASD spectral data files by name
B.2.2	beta_calc_h20	Compute backscatter coefficient for H_20 at speciied wavelength
B.2.3	km_analytical	Compute analytical solution (as mass fractions)
B.2.4	km_brute	Compute brute force numerical solution
B.2.5	km_reverse_proc	Compute reverse analytical solution
B.2.6	km_solver	Compute analytical solution (algebraic)
B.2.7	kmf	Compute Kubelka-Munk transform of reflectance spectra
B.2.8	master_proc	Perform PLS[1] and PCR[2] regression for VisNIR[3] and MIR[4] data
B.2.9	master_proc_list	Generate processing list, SWC-SWP[5], and soil type for PLS/PCR[1,2]
B.2.10	master_proc_swcc_mb	Generate PLS/PCR[1,2] for SWC-SWP5 and VisNIR[3] data
B.2.11	ppe_master	Generate master, calibration, and validation lists for PLS/PCR[1,2]
B.2.12	ppe_master_d	Generate Donna Fill specific master, calibration, and validation lists for PLS/PCR[1,2]
B.2.13	ppe_master_i	Generate illite specific master, calibration, and validation lists for PLS/PCR[1,2]
B.2.14	ppe_master_k	Generate kaolinite specific master, calibration, and validation lists for PLS/PCR[1,2]
B.2.15	reformater	resample spectra data to ASD spectral format
B.2.16	spectra_process	Ingest, average, and output ASD spectral data by file handle
B.2.17	spectra_reader	Ingest single ASD spectral data file
B.2.18	x_gen_fspec	Generate X matrix for PLS/PCR1,2 and bulk processing for ASD spectral data
B.2.19	x_gen_mir	Generate X matrix for PLS/PCR[1,2] and bulk processing for MIR spectral data

Notes: [1]**P**artial **L**east **S**quare (PLS) Regression, [2]**P**rinciple **C**omponents **R**egression, [3]**Vis**ible to **N**ear **I**nfra**R**ed (VisNIR), [4]**M**iddle **I**nfra**R**ed (MIR), [5]**S**oil **W**ater **C**ontent - **S**oil **W**ater **P**otential.

Table B. 2. List of included software executables and source code developed to obtain measurements of soil optical properties from Fourier Transform infrared spectroscopy (FTIR).

ID	Executable	Description	Suite
B.3.1	dat_extraction	Ingest graphical data and convert to numerical values	MATLAB
B.3.2	k_absorb	Compute and visulize the kaolinite absorption spectrum	MATLAB
B.3.3	kubelka	Perform Kubelka-Munk transform on reflectance data	MATLAB
B.3.4	KBR_reflect_fig	Generate KBr reflectance spectra for publishing	MATLAB
B.3.5	flow_fig	Generate figure illustrating workflow	MATLAB
B.3.6	u_donna_absorp	Compute and visulize the Donna Fill absorption Spectrum	MATLAB
B.3.7	u_illite_absorp	Compute and visulize the illite absorption Spectrum	MATLAB
B.3.8	u_fig_5_gen	Visulize two percent reflectance spectrum for publication	MATLAB
B.3.9	u_fig_6_gen	Visulize Kubelka Munk function for publication	MATLAB

B.2. Software Developed for Ingestion, Processing and Extraction of Soil Properties for Visible and Near Infrared reflectance spectra on intact samples.

The software contained in this section was written specifically to ingest, process, and extract soil properties from moist intact samples prepared using the pressure plate extractor. Initial preprocessing of the experimentally obtained soil spectra was conducted using the commercially available ASD RS^3 and ViewSpecPro programs (ASD 2014).

B.2.1. ***asd_reader.m***

A MATLAB executable to ingest Vis-NIR file spectrum obtained from the FieldSpec-4 HiRes spectroradiometer, average all spectra containing a search string, and write the resulting averaged spectra to a specified file and file path. Programmatic inputs included the search string (all file names containing the string will be processed), the output string (the output file name), a suppression file (to enable or suppress the file deletion warning), and an output path (the directory for the output file to be stored). The programmatic output included a stacked (averaged) spectrum file. It should be noted that the asd_reader.m executable deleted all .asd (raw data) files (in the working directory) and that care was required to preserve the original data.

Invocation: *[output] = asd_reader(search string, output string, suppression flag, and output path);*

Source Code:

```
%ASD output and stacking script.
function [output] = asd_reader(search_string,out_string,suppress,output_path);
   if suppress == 1
   else
   disp('WARNING THIS SCRIPT WILL DELETE ALL *.ASD FILES FROM THE DIRECTORY')
   disp('THERE IS NO GOING BACK!')
   disp('MAKE SURE THIS IS NOT YOUR ONLY DATA FOLDER (DATA IS BACKED UP!)')
   disp('YOU HAVE BEEN WARNED.')
   disp('IF YOUR ARE NOT SURE THIS IS WHAT YOU WANT CTRL + C TO CANCEL')
   for i = 10:-1:1
   disp(strcat({'T - ',i,' UNTIL FILE DELETE'}));
   pause(1)
   end
   disp('Beginning Delete');
end
delete '*.asd'
clc,fclose('all');
if nargin == 3
   output_path = '\\cveg-file.cveg.uark.edu\CVEG\Research\Coffman Research\Remote Sensing of
        Unsaturated Soils (GARNER)\TRB_Paper\PROCESING_FILES\DONNA_STACKED\';
elseif nargin < 2 | nargin > 4
   disp('NARGIN!');
end
output_path = '\\cveg-file.cveg.uark.edu\CVEG\Research\Coffman Research\Remote Sensing of
        Unsaturated Soils (GARNER)\TRB_Paper\PROCESING_FILES\DONNA_STACKED\';
fid2 = strcat(output_path,out_string,'.txt');
file = ls(strcat('*',search_string,'*'));
[a b] = size(file);
for i = 1:1:a
```

```
   fid_t = file(i,:)
   fid = fopen(fid_t);
   fmt = ['%s %s'];
   data_raw = textscan(fid,fmt,'HeaderLines',1,...
   'Delimiter','\t',...
   'CollectOutput',1);
   data = zeros(size(data_raw{1,1}(:,1)));
   data(:,1) = str2num(str2mat(data_raw{1,1}(:,1)));
   data(:,2) = str2num(str2mat(data_raw{1,1}(:,2)));
   fclose('all');
   if i == 1
     output(:,1:2) = data(:,1:2)./a;
   else
     output(:,1:2) = output(:,1:2) + data(:,1:2)./a;
   end
end
dlmwrite(fid2,output,'delimiter','\t');
```

B.2.2. ***beta_calc_h20.m***

A MATLAB executable subroutine to compute the beta (backscatter coefficient) of liquid water at each wavelength using a mathematical model as proposed by Morel (1974), Zhang and Hu (2009), and Zhang et al. (2009). The programmatic input was the wavelength value and the output was the backscatter coefficient at a specified wavelength.

Invocation: *[beta] = beta_calc_h20(wavelength)*

Source Code:

```
function [beta] = beta_calc_h20(lambda)
t1 = (8*3.14159/3);
t2 =((2*3.14159*1.00027)/(lambda*10^-7))^4;
t3 =(50*10^-9)^6;
```

```
n = 0.75831*lambda^2/(lambda^2-0.01007)+0.08495*lambda^2/(lambda^2-8.91377);
t4 = ((n/1.00027)^2-1)/((n/1.00027)^2+1);
beta = (33.3679*10^21)*t1*t2*t3*t4;
end
```

B.2.3. ***km_analytical.m***

A MATLAB executable written to compute an analytical (Kubelka-Munk) solution for soil mass fraction of water, soil mass fraction of solids, and soil mass fraction of water vapor. Program is executed using the MATLAB graphical user interface (GUI). The input files include soil absorption (e.g.illite_compiled.txt), 100 percent pure dry soil spectra (illite1.txt), water absorption spectrum (kwater_lit and kvapor_lit) were manually input. The km_analytical outputed an estimate of soil mass fraction of solids, soil mass fraction of water, soil mass fraction of vapor, and an output flag indicating physically impossible solutions. The km_analytical script was configurable to use either a direct algebraic solution (km_solver.m) or a brute force numerical solution (km_brute).

Invocation: Program is executed from the MATLAB graphical user interface (GUI)

Source Code:

```
%function [est_mw est_ms est_mv flag] = km_analytical(file_1);
clear,clc
tic;
%Spectrum File
in_file_1 = 'illite_compiled.txt';
spw_c = dlmread(in_file_1,'\t');
%100 Percent Dry Spectrum
in_file_2 = 'illite1.txt';
spd = dlmread(in_file_2,'\t');
%Absorption Water File
```

```
kwater = kwater_lit;
kwater(:,1) = 1000.*kwater(:,1);
spw(:,1) = spw_c(:,1);
spw(:,2) = spw_c(:,2);
kw = reformater(kwater,spw);
%Absorption Vapor File
kvapor = kvapor_lit;
kv = reformater(kvapor,spw);
ks_raw = killite;
ks(:,1) = ks_raw(:,1);
ks(:,2) = (ks_raw(:,2)+...
        ks_raw(:,3)+...
        ks_raw(:,4)+...
        ks_raw(:,5)+...
        ks_raw(:,6))./5;
%kv = reformater(
[a b] = size(spd);
for i = 1:1:a
   sw(i,1) = spd(i,1);
   sw(i,2) = -1.*beta_calc_h20(spd(i,1));
end
[a b] = size(spw_c);
kmfd = kmf(spw);
ss(:,1) = kmfd(:,1);
ss(:,2) = spd(:,2)./kmfd(:,2);
for kk = 1:1:b
   spw(:,1) = spw_c(:,1);
   spw(:,2) = spw_c(:,kk);
 est_mw = zeros(a,a);
 est_ms = zeros(a,a);
 est_mv = zeros(a,a);
```

```
kmfw = kmf(spw);
for j = 1:1:a
   ks1 = ks(j,2);
   kw1 = kw(j,2);
   kv1 = kv(j,2);
   ss1 = ss(j,2);
   sw1 = sw(j,2);
   kmf1 = kmfw(j,2);
   for i = 1:1:a
      if i == j
      est_mw(j,i) = 1;
      est_ms(j,1) = 1;
      est_mv(j,1) = 1;
      flag = 9;
      else
         ks2 = ks(i,2);
         kw2 = kw(i,2);
         kv2 = kv(i,2);
         ss2 = ss(i,2);
         sw2 = sw(i,2);
         kmf2 = kmfw(i,2);
         [est_mw(j,i) est_ms(j,i) est_mv(j,1) flag(j,i)] = km_solver(ks1,...
                                                   ks2,...
                                                   kw1,...
                                                   kw2,...
                                                   kv1,...
                                                   kv2,...
                                                   ss1,...
                                                   ss2,...
                                                   sw1,...
                                                   sw2,...
```

```
                                        kmf1,...
                                        kmf2);
        if flag(j,i) == 2 | flag(j,i) == 3
           %disp('Flagged Result')
        [est_mw(j,i) est_ms(j,i) est_mv(j,1) flag(j,i)] = km_brute(ks1,...
                                        ks2,...
                                        kw1,...
                                        kw2,...
                                        kv1,...
                                        kv2,...
                                        ss1,...
                                        ss2,...
                                        sw1,...
                                        sw2,...
                                        kmf1,...
                                        kmf2);
        end
      end
   end
   disp(strcat({'Percent Complete '},num2str(100*j/2100)));
 end
 [a b] = size(est_mw(:,:));
 count = 0;
 box1 = 0;
 box2 = 0;
 box3 = 0;
box4 = 0;
box5 = 0;
box6 = 0;
box7 = 0;
box8 = 0;
```

```
box9 = 0;
box10 = 0;
box11 = 0;
box12 = 0;
box13 = 0;
 for ii = 1:1:a
   for jj = 1:1:b
      if est_mw(ii,jj) < 0.05
         box1 = box1+1;
      elseif est_mw(ii,jj) > 0.05 & est_mw(ii,jj) <= 0.1
         box2 = box2+1;
      elseif est_mw(ii,jj) > 0.1 & est_mw(ii,jj) <= 0.15
         box3 = box3+1;
      elseif est_mw(ii,jj) > 0.15 & est_mw(ii,jj) <= 0.2
         box4 = box4+1;
      elseif est_mw(ii,jj) > 0.2 & est_mw(ii,jj) <= 0.25
         box5 = box5+1;
      elseif est_mw(ii,jj) > 0.25 & est_mw(ii,jj) <= 0.3
         box6 = box6+1;
      elseif est_mw(ii,jj) > 0.3 & est_mw(ii,jj) <= 0.35
         box7 = box7+1;
      elseif est_mw(ii,jj) > 0.35 & est_mw(ii,jj) <= 0.4
         box8 = box8+1;
      elseif est_mw(ii,jj) > 0.4 & est_mw(ii,jj) <= 0.45
         box9 = box9+1;
      elseif est_mw(ii,jj) > 0.45 & est_mw(ii,jj) <= 0.50
         box10 = box10+1;
      elseif est_mw(ii,jj) > 0.50 & est_mw(ii,jj) <= 0.55
         box11 = box11+1;
      elseif est_mw(ii,jj) > 0.55 & est_mw(ii,jj) <= 0.60
         box12 = box12+1;
```

```
      else
         box13 = box13+1;
      end
   end
end
close('all');
yy = [box1 box2 box3 box4 box5 box6 box7 box8 box9 box10 box11 box12 box13]';
xx = [1:1:13]';
plot(xx,yy)
out_fid = strcat('est_mw_',num2str(kk),'.txt')
dlmwrite(out_fid,est_mv,'\t');
out_fid = strcat('est_ms_',num2str(kk),'.txt')
dlmwrite(out_fid,est_ms,'\t');
out_fid = strcat('est_mv_',num2str(kk),'.txt')
dlmwrite(out_fid,est_mv,'\t');
end
toc
```

B.2.4. ***km_brute.m***

A MATLAB executable written to compute an analytical (Kubelka-Munk) solution for soil mass fraction of water, soil mass fraction of solids, and soil mass fraction of water vapor using a brute force numerical approach. Solutions were obtained by computing possible solutions for values of mass fraction of water (m_w) and mass fraction of vapor (m_v). The mass fraction of soil solids (m_s) was assumed to be a function of the mass fraction of water and vapor (e.g. $m_s = 1 - m_w - m_v$). The solution with the minimum computed error was selected as the most likely solution. Program was executed as a subroutine for the km_analytical. Programmatic inputs and outputs are tabulated in Table B.3.

Table B. 3. Programmatic inputs and outputs for km_brute.m executable.

Variable	Input/Output	Description
ms	Output	Mass fraction of soil solids
mw	Output	Mass fraction of soil water liquid
mv	Output	Mass fraction of soil water vapor
flag	Output	Computation confidence flag
ks1	Input	Soil absorption coffecient value at λ_1
ks2	Input	Soil absorption coffecient value at λ_2
kw1	Input	Water absortion coffecient value at λ_1
kw2	Input	Water absortion coffecient value at λ_2
kv1	Input	Water vapor absortion coffecient value at λ_1
kv2	Input	Water vapor absortion coffecient value at λ_2
ss1	Input	Soil scattering coffecient value at λ_1
ss2	Input	Soil scattering coffecient value at λ_2
sw1	Input	Water scattering coffecient value at λ_1
sw2	Input	Water scattering coffecient value at λ_2
kmf1	Input	Kubelka-Munk function value at λ_1
kmf2	Input	Kubelka-Munk function value at λ_2

Note: $\lambda_{1,2}$ indicates wavelength values and s_v value was assumed to be negligable

Invocation: *[ms mw mv flag] = km_brute(ks1, ks2, ...*

kw1, kw2, ...

kv1, kv2, ...

ss1, ss2, ...

sw1, sw2, ...

kmf1, kmf2);

Source Code:

```
function [est_ms est_mw est_mv flag] = km_brute(ks1,ks2,kw1,kw2,kv1,kv2,...
                                        ss1,ss2,sw1,sw2,...
                                        kmf1,kmf2);
if ks1 < 0, ks1 = 1.0e-9;,flag = 1;, end
```

```
if ks2 < 0, ks2 = 1.0e-9;,flag = 1;, end
if kw1 < 0, kw1 = 1.0e-9;,flag = 1;, end
if kw2 < 0, ks2 = 1.0e-9;,flag = 1;, end
if kv1 < 0, kv1 = 1.0e-9;,flag = 1;, end
if kv2 < 0, kv2 = 1.0e-9;,flag = 1;, end
if ss1 < 0, ss1 = 1.0e-9;,flag = 1;, end
if ss2 < 0, ss2 = 1.0e-9;,flag = 1;, end
if sw1 < 0, sw1 = 1.0e-9;,flag = 1;, end
if sw2 < 0, sw2 = 1.0e-9;,flag = 1;, end
q1 = ks1-kv1-kmf1*ss1;
q2 = kw1-kv1-kmf1*sw1;
q3 = ks2-kv2-kmf2*ss2;
q4 = kw2-kv2-kmf2*sw2;
for jj = 1:1:100
   for ii = 1:1:100
      ms = 0.01*jj;
      mw = 0.01*ii;
      res1 = q1*ms+q2*mw;
      res2 = q3*ms+q4*mw;
      cum_err(jj,ii) = (res1^2 + res2^2)^0.5;
   end
end
seek = min(min(cum_err(:,:)));
for jj = 1:1:100
   row_min = min(cum_err(jj,:));
   if seek == row_min
      [a b] = val2ind(cum_err(jj,:),seek);
      a = min(a);
      est_mw = 0.01*a;
      est_ms = 0.01*jj;
   end
```

```
end
est_mv = 1 - est_mw - est_ms;
```

B.2.5. ***km_reverse_proc.m***

A MATLAB executable written to compute a theoretical Kubelka-Munk function from known values of soil mass fraction of water, vapor, and solids. The program was executed from the MATLAB graphical user interface (GUI) by pressing the F5 key. The soil properties and the file processing list were manually input by the user. The program output is a predicted spectra (KMF) for each solution overlaid on the experimentally obtained spectra.

Invocation: MATLAB GUI (F5)

Source Code:

```
fclose('all');,clear,clc
kkr=3;
%load spectra list
[mast_list path] = master_proc_list;
%load mass fraction list
mass_frac = mass_frac_list;
%load spectra list
x = x_gen_fspec(mast_list(:,1),path)';
x_val = x_gen_fspec(mast_list(:,1),path)';
%load soil properties
in_file_1 = 'illite_compiled.txt';
spw_c = dlmread(in_file_1,'\t');
ks_raw = killite;
ks(:,1) = ks_raw(:,1);
ks(:,2) = (ks_raw(:,2)+...
        ks_raw(:,3)+...
        ks_raw(:,4)+...
```

```
        ks_raw(:,5)+...
        ks_raw(:,6))./5;
%100 Percent Dry Spectrum
in_file_2 = 'illite1.txt';
spd = dlmread(in_file_2,'\t');
spw(:,1) = spw_c(:,1);
spw(:,2) = spw_c(:,kkr);
ks_filt = reformater(ks,spw);
%load water properties
kwater = kwater_lit;
kwater(:,1) = 1000.*kwater(:,1);
kw = reformater(kwater,spw);
kvapor = kvapor_lit;
kv = reformater(kvapor_lit,spw);
%given existing values compute k-m
[a b] = size(spd);
for i = 1:1:a
   sw(i,1) = spd(i,1);
   sw(i,2) = -1.*beta_calc_h20(spd(i,1));
end
[a b] = size(spw_c);
kmfd = kmf(spd);
ss(:,1) = kmfd(:,1);
ss(:,2) = ks_filt(:,2)./kmfd(:,2);
%for i = 1:1:a
%   ks1 = ks_filt(i,2);
%   kw1 = kw(i,2);
%   kv1 = kv(i,2);
%   ss1 = ss(i,1);
%   sw1 = sw(i,1)
%   sv1 = 0;
```

```
%    ms1 = mass_frac(i,1);
%    mw1 = mass_frac(i,2);
%    mv1 = mass_frac(i,3);
%    kmf_theory = (ks1*
% = 2;
Q1 =(ks_filt(:,2).*mass_frac(kkr,1)+...
    kw(:,2).*mass_frac(kkr,2)+...
    kv(:,2).*mass_frac(kkr,3));
Q2 = ss(:,2).*mass_frac(kkr,1)+sw(:,2).*mass_frac(kkr,2);
kmf_theory(:,1) = spw(:,1);
kmf_theory(:,2) = Q1./Q2;
kmf_actual = kmf(spw);
plot(kmf_theory(:,1),kmf_theory(:,2),kmf_actual(:,1),kmf_actual(:,2))
%for kk = 1:1:b
%    spw(:,1) = spw_c(:,1);
%    spw(:,2) = spw_c(:,kk);
% kmfw = kmf(spw);
%for j = 1:1:a
%     ks1 = ks(j,2);
%     kw1 = kw(j,2);
%     kv1 = kv(j,2);
%     ss1 = ss(j,2);
%     sw1 = sw(j,2);
% end
%end
```

B.2.6. ***km_sovler.m***

A MATLAB executable written to compute an algebraic solution for the mass fraction of soil solids, soil water, and soil vapor using the Kubelka-Munk theory. The programmatic inputs

and outputs were identical to those previously described in Table B.3 for the km_brute.m executable. The program was executed as a subroutine to the km_analytical executable.

Invocation: *[ms mw mv flag] = km_solver(ks1,ks2, ...*

kw1,kw2, ...

kv1,kv2, ...

ss1,ss2, ...

sw1,sw2, ...

kmf1,kmf2) ;

Source Code:

```
%km_solver
function [est_ms est_mw est_mv flag] = km_solver(ks1,ks2,kw1,kw2,kv1,kv2,...
                                ss1,ss2,sw1,sw2,...
                                kmf1,kmf2);
if nargin < 12 | nargin > 12
   disp('NARGIN!')
   return
end
if ks1 < 0, ks1 = 1.0e-9;,flag = 1;, end
if ks2 < 0, ks2 = 1.0e-9;,flag = 1;, end
if kw1 < 0, kw1 = 1.0e-9;,flag = 1;, end
if kw2 < 0, ks2 = 1.0e-9;,flag = 1;, end
if kv1 < 0, kv1 = 1.0e-9;,flag = 1;, end
if kv2 < 0, kv2 = 1.0e-9;,flag = 1;, end
if ss1 < 0, ss1 = 1.0e-9;,flag = 1;, end
if ss2 < 0, ss2 = 1.0e-9;,flag = 1;, end
if sw1 < 0, sw1 = 1.0e-9;,flag = 1;, end
if sw2 < 0, sw2 = 1.0e-9;,flag = 1;, end
q1 = ks1-kv1-kmf1*ss1;
```

```
q2 = kw1-kv1-kmf1*sw1;
q3 = ks2-kv2-kmf2*ss2;
q4 = kw2-kv2-kmf2*sw2;
est_mw = (-kv1 + q1/q3*kv2)/(q2-q1*q4/q3);
est_ms = (-kv1/q1)-(q2/q1)*est_mw;
est_mv = 1-est_mw-est_ms;
if est_mv < 0 | est_mw < 0 | est_ms < 0
   %disp('negative results!');
   flag = 2;
elseif est_mv > 1 | est_mw > 1 | est_ms > 1
   disp('mass fracion > 1!');
   flag = 3;
end
```

B.2.7. ***kmf.m***

A MATLAB executable written to compute the Kubelka-Munk function from an experimentally obtained reflectance spectrum. A reflectance spectra was the programmatic input and the output was the Kubelka-Munk function.

Invocation: *[kmf(:,:)] = kmf(spectra(:,1:2))*

Source Code:

```
function [kmf] = kmf(spectra)
[a b] = size(spectra);
kmf = zeros(a,b);
kmf(:,1) = spectra(:,1);
kmf(:,2) = ((1.-spectra(:,2)).^2)./(2.*spectra(:,2));
end
```

B.2.8. ***master_proc.m***

A MATLAB executable written to perform a partial least square (PLS) and principle components regression (PCR) regressions to create an empirical relationship between the observed reflectance spectra and laboratory obtained soil index properties (liquid limit, plastic limit, and clay fraction). The executable was compatible with spectral data obtained from the FieldSpec-4 HiRes spectroradiometer (Vis-NIR) and Nicolet FTIR spectrometer (MIR). The program was executed from the MATLAB GUI. The user was required to manually select the data source, soil index property, and number of regression components by selecting the appropriate dataset, type, and nc variable values, respectively. Additionally, the calibration and validation data sets were manually configured by assigning spectral data files to the arrays cal_list and val_list, respectively. This code was modified from the example code documented in Mathworks (2010, 2012).

Invocation: MATLAB GUI (F5)

Source Code:

```
clear,close('all');
fclose('all');
dataset = 3;
%1 - MIR
%2 - Dry
%3 - Wet
type = 1;
%1 - LL
%2 - PL
%3 - PI
%4 - CF
clc;
```

```
nc = 4
%create y matrix
LL = [31.5 46.7 25]';
PL = [28.1 23.6 25.0]';
PI = [3.4 46.7-23.6 0.0]';
CF = [47.2 46.2 8.9]';
if dataset == 1;
   key = [1 1 1 1 2 2 2 2 2 2 2 2 2 3 3 3 3 3 3 3 3]';
   cal_list = [{'20150608_KN1.CSV'}, ...
{'20150608_KN2.CSV'}, ...
{'20150608_KN3.CSV'}, ...
{'20150608_KN4.CSV'}, ...
{'20150608_IL101.CSV'}, ...
{'20150608_IL102.CSV'}, ...
{'20150608_IL103.CSV'},...
{'20150608_IL104.CSV'}, ...
{'20150608_IL105.CSV'}, ...
{'20150608_il2.CSV'}, ...
{'20150608_il3.CSV'}, ...
{'20150608_il4.CSV'},...
{'20150608_il6.CSV'}, ...
{'20150608_DF102.CSV'}, ...
{'20150608_DF103.CSV'}, ...
{'20150608_DF104.CSV'}, ...
{'20150608_DF106.CSV'}, ...
{'20150608_DF_1.CSV'}, ...
{'20150608_DF_2.CSV'}, ...
{'20150608_DF_3.CSV'},...
{'20150608_DF_6.CSV'}]';
val_list = [{'20150608_KN5.CSV'},...
{'20150608_il5.CSV'},...
```

```
{'20150608_DF_4.CSV'}]';
path = 'MIR';
x = x_gen_mir(cal_list,path);
x_val = x_gen_mir(val_list,path);
elseif dataset == 2
    key = [1 1 1 1 1 2 2 2 2 2 3 3 3 3 3]';
    cal_list = [{'kaolinite1.txt'},...
{'kaolinite3.txt'},...
{'kaolinite5.txt'},...
{'kaolinite7.txt'},...
{'kaolinite8.txt'},...
{'illite1.txt'},...
{'illite3.txt'},...
{'illite5.txt'},...
{'illite7.txt'},...
{'illite8.txt'},...
{'donna1.txt'},...
{'donna3.txt'},...
{'donna5.txt'},...
{'donna7.txt'},...
{'donna8.txt'}]';
val_list = [{'kaolinite2.txt'},...
{'kaolinite4.txt'},...
{'kaolinite6.txt'},...
{'illite2.txt'},...
{'illite4.txt'},...
{'illite6.txt'},...
{'donna2.txt'},...
{'donna4.txt'},...
{'donna6.txt'}]';
path = 'FieldSpec4_Dry';
```

x = x_gen_fspec(cal_list,path);

x_val = x_gen_fspec(val_list,path);

else

key = [1 1 1 1 1 1 1 1 1 1 1 1
1 1 1 1 1 1 1 1 2 2 2
2 2 2 2 2 2 2 2 2 2 2
2 2 2 2 2 2 2 2 3 3 3
3 3];

cal_list = [{'kaolinite_01_h.txt'}

{'kaolinite_02_h.txt'}

{'kaolinite_02_hc.txt'}

{'kaolinite_03_hc.txt'}

{'kaolinite_04_h.txt'}

{'kaolinite_05_hx.txt'}

{'kaolinite_06_h.txt'}

{'kaolinite_06_hc.txt'}

{'kaolinite_08_h.txt'}

{'kaolinite_09_h.txt'}

{'kaolinite_10_h.txt'}

{'kaolinite_10_hc.txt'}

{'kaolinite_11_hc.txt'}

{'kaolinite_12_hc.txt'}

{'kaolinite_13_h.txt'}

{'kaolinite_14_h.txt'}

{'kaolinite_17_h_.txt'}

{'kaolinite_17_hc_.txt'}

{'kaolinite_18_h_.txt'}

{'kaolinite_19_h_.txt'}

{'illite16_hc.txt'}

{'illite_01_c.txt'}

{'illite_01_hc.txt'}

{'illite_02_hc.txt'}

{'illite_03_h.txt'}

{'illite_04_h.txt'}

{'illite_04_hc.txt'}

{'illite_07_h.txt'}

{'illite_07_x.txt'}

{'illite_08_h.txt'}

{'illite_09_h.txt'}

{'illite_09_hc.txt'}

{'illite_11_hc.txt'}

{'illite_12_hc.txt'}

{'illite_13_h.txt'}

{'illite_13_hc.txt'}

{'illite_14_hc.txt'}

{'illite_15_h.txt'}

{'illite_15_hc.txt'}

{'illite_17_h.txt'}

{'illite_18_h.txt'}

{'illite_18_hc.txt'}

{'donna_01_h.txt'}

{'donna_01_hc.txt'}

{'donna_02_h.txt'}

{'donna_02_hc.txt'}

{'donna_03_h.txt'}];

val_list = [{'kaolinite_01_hc.txt'}

{'kaolinite_03_h.txt'}

{'kaolinite_04_hc.txt'}

{'kaolinite_05_hc.txt'}

{'kaolinite_07_hc.txt'}

{'kaolinite_09_hc.txt'}

{'kaolinite_12_h.txt'}

```
{'kaolinite_13_hc.txt'}
{'kaolinite_14_hc.txt'}
{'kaolinite_18_hc_.txt'}
{'kaolinite_19_hc_.txt'}
{'illite_02_h.txt'}
{'illite_03_hc.txt'}
{'illite_05_hc.txt'}
{'illite_07_hc.txt'}
{'illite_08_hc.txt'}
{'illite_09_hx.txt'}
{'illite_11_h.txt'}
{'illite_12_h.txt'}
{'illite_14_h.txt'}
{'illite_16_h.txt'}
{'illite_17_hc.txt'}
{'donna_03_hc.txt'}
{'donna_04_h.txt'}
{'donna_04_hc.txt'}];
path = 'FieldSpec4_Wet';
x = x_gen_fspec(cal_list,path);
x_val = x_gen_fspec(val_list,path);
end
%create y matrix
[a b] = size(key);
for i = 1:1:a
    if type == 1
        y(i,1) = LL(key(i,1));
    elseif type == 2
        y(i,1) = PL(key(i,1));
    elseif type == 3
        y(i,1) = PI(key(i,1))
```

```
   elseif type == 4
      y(i,1) = CF(key(i,1))
   end
end
[n,p] = size(x);
[xloadings,yloadings,xscores,yscores,betapls,plspctvar] = plsregress(x,y,nc);
plot(1:nc,cumsum(100*plspctvar(2,:)),'-bo');
xlabel('Number of PLS Components');
ylabel('Percent Variance Explained in Y');
yfitpls = [ones(n,1) x]*betapls;
%create x matrix
tss = sum((y-mean(y)).^2);
rss_pls = sum(y-yfitpls).^2;
rsquaredpls= 1 - rss_pls/tss;
[xloadings,yloadings,xscores,yscores,betapls,plspctvar] = plsregress(x,y,nc);
yfitpls = [ones(n,1) x]*betapls;
[pcaloadings, pcascores, pcavar] = pca(x, 'Economy', false);
betapcr = regress(y-mean(y), pcascores(:,1:nc));
betapcr = pcaloadings(:,1:nc)*betapcr;
betapcr = [mean(y) - mean(x)*betapcr; betapcr];
yfitpcr = [ones(n,1) x]*betapcr;
figure, plot(y,yfitpls,'bo',y,yfitpcr,'r^');
xlabel('Observed Response');
ylabel('Fitted Response');
legend({'PLSR with 3 Components' 'PCR with 3 Components'}, ...
   'location','NW');
tss = sum((y-mean(y)).^2);
rss_pls = sum(y-yfitpls).^2;
rsquaredpls= 1 - rss_pls/tss
rss_pcr = sum((y-yfitpcr).^2);
rsquaredpcr = 1 - rss_pcr/tss
```

```
figure
plot3(xscores(:,1),xscores(:,2),y-mean(y),'bo');
legend('PLSR');
grid on; view (-30,30);
figure
plot(1:nc,100*cumsum(plspctvar(1,:)),'b-o',1:nc, ...
    100*cumsum(pcavar(1:nc))/sum(pcavar(1:nc)),'r-^');
xlabel('Number of Principle Components');
ylabel('Percent Variance Explained in X');
legend({'PLSR' 'PCR'},'location','SE');
[xloadings5,yloadings5,xscores5,yscores5,betapls5,plspctvar5] = plsregress(x,y,nc);
yfitpls5 = [ones(n,1) x]*betapls5;
betapcr5 = regress(y-mean(y), pcascores(:,1:nc));
betapcr5 = pcaloadings(:,1:nc)*betapcr5;
betapcr5 = [mean(y) - mean(x)*betapcr5; betapcr5];
yfitpcr5 = [ones(n,1) x]*betapcr5;
figure
plot(y,yfitpls5,'bo',y,yfitpcr5,'r^');
xlabel('Observerd Response');
ylabel('Fitted Response');
legend({'PLSR with 5 Components' 'PCR with 5 Components'}, ...
    'location','NW');
figure
[x1,y1,xs,ys,beta,pctvar,plsmsep] = plsregress(x,y,10,'CV',10);
pcrmsep = sum(crossval(@pcrsse,x,y,'KFold',10),1) / n;
plot(0:10,plsmsep(2,:),'b-o',0:10,pcrmsep,'r-^');
xlabel('Number of Components');
ylabel('Estimated Mean Squared Prediction Error');
legend({'PLSR' 'PCR'},'location','NE');
[xloadings,yloadings,xscores,yscores,betapls,plspctvar] = plsregress(x,y,nc);
[a b] = size(betapls);
```

```
y_pred = x_val(:,:)*betapls(2:(a),:)+betapls(1,1);
ybar = mean(y(:,1));
yprb = mean(yfitpls5(:,1));
ystd = std(yfitpls5(:,1));
[ybar yprb ybar-yprb ystd]
figure
[xloadings,yloadings,xscores,yscores,betapls,plspctvar,mse,stats] = plsregress(x,y,nc);
[a b] = size(x);
stats_massage(:,1) = abs(stats.W(:,1)./(max(abs((stats.W(:,1))))));
stats_massage(:,2) = abs(stats.W(:,2)./(max(abs((stats.W(:,2))))));
stats_massage(:,3) = abs(stats.W(:,3)./(max(abs((stats.W(:,3))))));
stats_massage(:,4) = abs(stats.W(:,4)./(max(abs((stats.W(:,4))))));
plot(1:b,stats_massage,'-');
legend({'1st' '2nd' '3rd' '4th'},'location','NW');
```

B.2.9. ***master_proc_list.m***

A MATLAB executable written to generate a user-specified master processing list with spectral files, soil volumetric water content, and soil matric potential for use in PLS and PCR empirical regression. There were no programmatic inputs. The subroutine outputs were a matrix containing file names, soil volumetric water content (m3·m-3), soil matric potential (kPa), and a soil type flag (ie. kaolinite = 1, illite = 2, and Donna Fill = 3). The executable was executed as subroutine of the master_proc_swcc.m executable.

Invocation: *[mast_list path] = master_proc_list;*

Source Code:

```
function [mast_list path] = master_proc_list
%contains list of spectra to process in reverse analysis
%16/9/2015
mast_list = [{'kaolinite_01_h.txt'}  0.3231 700 1
{'kaolinite_02_h.txt'} 0.3479 700 1
```

{'kaolinite_02_hc.txt'} 0.3479 700 1

{'kaolinite_03_hc.txt'} 0.3873 900 1

{'kaolinite_04_h.txt'} 0.3713 900 1

{'kaolinite_05_hx.txt'} 0.3507 900 1

{'kaolinite_06_h.txt'} 0.4163 101 1

{'kaolinite_06_hc.txt'} 0.4163 101 1

{'kaolinite_08_h.txt'} 0.3463 200 1

{'kaolinite_09_h.txt'} 0.4072 200 1

{'kaolinite_10_h.txt'} 0.3626 900 1

{'kaolinite_10_hc.txt'} 0.3626 900 1

{'kaolinite_11_hc.txt'} 0.5439 300 1

{'kaolinite_12_hc.txt'} 0.3740 400 1

{'kaolinite_13_h.txt'} 0.3756 400 1

{'kaolinite_14_h.txt'} 0.3111 480.27 1

{'illite_01_c.txt'}   0.3568 700 2

{'illite_01_hc.txt'}   0.3568 700 2

{'illite_02_hc.txt'}   0.3729 700 2

{'illite_03_h.txt'}   0.3622 900 2

{'illite_04_h.txt'}   0.4522 101 2

{'illite_04_hc.txt'}   0.4522 101 2

{'illite_07_h.txt'}   0.3704 200 2

{'illite_07_x.txt'}   0.3704 200 2

{'illite_08_h.txt'}   0.3965 300 2

{'illite_09_h.txt'}   0.4785 300 2

{'illite_09_hc.txt'}   0.4785 300 2

{'illite_11_hc.txt'}   0.3898 400 2

{'illite_12_hc.txt'}   0.3328 1100 2

{'illite_13_h.txt'}   0.2961 1100 2

{'illite_13_hc.txt'}   0.2961 1100 2

{'illite_14_hc.txt'}   0.3649 480.27 2

{'illite_15_h.txt'}   0.4005 480.27 2

{'illite_15_hc.txt'} 0.4005 480.27 2
{'illite_17_h.txt'} 0.3196 1289.6 2
{'kaolinite_01_hc.txt'} 0.3231 700 1
{'kaolinite_03_h.txt'} 0.3873 900 1
{'kaolinite_04_hc.txt'} 0.3713 900 1
{'kaolinite_05_hc.txt'} 0.3507 900 1
{'kaolinite_07_hc.txt'} 0.4198 101 1
{'kaolinite_09_hc.txt'} 0.4072 200 1
{'kaolinite_12_h.txt'} 0.374 400 1
{'kaolinite_13_hc.txt'} 0.3756 400 1
{'kaolinite_14_hc.txt'} 0.3111 400 1
{'illite_02_h.txt'} 0.3729 700 2
{'illite_03_hc.txt'} 0.3622 900 2
{'illite_05_hc.txt'} 0.4443 101 2
{'illite_07_hc.txt'} 0.3704 200 2
{'illite_08_hc.txt'} 0.3965 300 2
{'illite_09_hx.txt'} 0.4785 300 2
{'illite_11_h.txt'} 0.3898 400 2
{'illite_12_h.txt'} 0.3328 1100 2
{'illite_14_h.txt'} 0.3649 480.27 2
{'illite_16_h.txt'} 0.3106 1289.6 2
{'illite_17_hc.txt'} 0.3196 1289.6 2];
path = 'FieldSpec4_Wet';
end

B.2.10. ***master_proc_swcc_md.m***

A MATLAB executable written to perform a partial least square (PLS) and principle components regression (PCR) regressions to create an empirical relationship between the observed reflectance spectra and laboratory obtained soil water content and soil water potential values. The program was executed from the MATLAB GUI by pressing the F5 key. The user was

required to manually select the number of PLC/PCR regression terms, the number of validation spectra, and the regression data set (i.e. soil volumetric water content or soil matric potential), respectively. The calibration and validation data sets were randomly generated using the ppe_master.m (all soil types), ppe_master_d.m (Donna Fill), ppe_master_i (illite), and ppe_master_k.m (kaolinite) subroutines.

Invocation: MATLAB GUI (F5)

Source Code:

```
%%DEBUG CODE
%clear,
close('all');
fclose('all');
nc = 10
nv = 10
var = 3 %2 == vol water / 3 == matric pot
check_flag = 0; %1 == reset
%%
%path = '../fieldspec
if check_flag == 1
[index master_list cal_list val_list] = ppe_master(nv);
%ppe_master == all soils
%ppe_master_d == donna fill
%ppe_master_k == kaolinite
%ppe_master_i == illite
end
x = x_gen_fspec(cal_list);
x_val = x_gen_fspec(val_list);
%create y matrix
%assign y-vect values as a function of int in key
```

```
y = cell2mat(cal_list(:,var));
[n,p] = size(x);
[xloadings,yloadings,xscores,yscores,betapls,plspctvar] = plsregress(x,y,nc);
figure1 = figure('units','inches','pos',[0 0 2.5 2.5])
axes('FontName','Times New Roman','FontSize',10)
plot(1:nc,cumsum(100*plspctvar(2,:)),'-ko');
out1(:,1) = 1:nc;
out1(:,2) = cumsum(100*plspctvar(2,:));
xlabel('Number of PLS Components','FontName','Times New Roman','FontSize',10);
ylabel('Percent Variance Explained in Y','FontName','Times New Roman','FontSize',10);
yfitpls = [ones(n,1) x]*betapls;
%create x matrix
tss = sum((y-mean(y)).^2);
rss_pls = sum((y-yfitpls).^2);
rsquaredpls= 1 - rss_pls/tss;
[xloadings,yloadings,xscores,yscores,betapls,plspctvar] = plsregress(x,y,nc);
yfitpls = [ones(n,1) x]*betapls;
[pcaloadings, pcascores, pcavar] = pca(x, 'Economy', false);
betapcr = regress(y-mean(y), pcascores(:,1:nc));
betapcr = pcaloadings(:,1:nc)*betapcr;
betapcr = [mean(y) - mean(x)*betapcr; betapcr];
yfitpcr = [ones(n,1) x]*betapcr;
figure2= figure('units','inches','pos',[0 0 2.5 2.5])
axes('FontName','Times New Roman','FontSize',10)
plot(y,yfitpls,'bo',y,yfitpcr,'r^');
xlabel('Observed Response','FontName','Times New Roman','FontSize',10);
ylabel('Fitted Response','FontName','Times New Roman','FontSize',10);
legend({'PLSR with 3 Components' 'PCR with 3 Components'}, ...
   'location','NW','FontName','Times New Roman','FontSize',10);
tss = sum((y-mean(y)).^2);
rss_pls = sum((y-yfitpls).^2);
```

```
rsquaredpls= 1 - rss_pls/tss
rss_pcr = sum((y-yfitpcr).^2);
rsquaredpcr = 1 - rss_pcr/tss
figure3 = figure('units','inches','pos',[0 0 2.5 2.5])
axes('FontName','Times New Roman','FontSize',10)
plot3(xscores(:,1),xscores(:,2),y-mean(y),'bo');
legend('PLSR');
grid on; view (-30,30);
%figure
%plot(1:nc,100*cumsum(plspctvar(1,:)),'b-o',1:nc, ...
%    100*cumsum(pcavar(1:nc))/sum(pcavar(1:nc)),'r-^');
%xlabel('Number of Principle Components');
%ylabel('Percent Variance Explained in X');
%legend({'PLSR' 'PCR'},'location','SE');
[xloadings5,yloadings5,xscores5,yscores5,betapls5,plspctvar5] = plsregress(x,y,nc);
yfitpls5 = [ones(n,1) x]*betapls5;
betapcr5 = regress(y-mean(y), pcascores(:,1:nc));
betapcr5 = pcaloadings(:,1:nc)*betapcr5;
betapcr5 = [mean(y) - mean(x)*betapcr5; betapcr5];
yfitpcr5 = [ones(n,1) x]*betapcr5;
figure4 = figure('units','inches','pos',[0 0 2.5 2.5])
axes('FontName','Times New Roman','FontSize',10)
plot(y,yfitpls5,'bo',y,yfitpcr5,'r^');
xlabel('Observed Response','FontName','Times New Roman','FontSize',10);
ylabel('Fitted Response','FontName','Times New Roman','FontSize',10);
legend({'PLSR with 5 Components' 'PCR with 5 Components'}, ...
   'location','NW','FontName','Times New Roman','FontSize',10);
[x1,y1,xs,ys,beta,pctvar,plsmsep] = plsregress(x,y,nc,'CV',nc);
pcrmsep = sum(crossval(@pcrsse,x,y,'KFold',10),1)/n;
figure5 = figure('units','inches','pos',[0 0 2.5 2.5])
axes('FontName','Times New Roman','FontSize',10)
```

```
plot(0:nc,plsmsep(2,:),'b-o');
xlabel('Number of Components');
ylabel('Estimated Mean Squared Prediction Error');
legend({'PLSR' 'PCR'},'location','NE');
[xloadings,yloadings,xscores,yscores,betapls,plspctvar] = plsregress(x,y,nc);
[a b] = size(betapls);
y_pred = x_val(:,:)*betapls(2:(a),:)+betapls(1,1);
y_pred2 = x(:,:)*betapls(2:(a),:)+betapls(1,1);
ybar = mean(y(:,1));
yprb = mean(yfitpls5(:,1));
ystd = std(yfitpls5(:,1));
[ybar yprb ybar-yprb ystd]
figure
[xloadings,yloadings,xscores,yscores,betapls,plspctvar,mse,stats] = plsregress(x,y,nc);
[a b] = size(x);
stats_massage(:,1) = stats.W(:,1);
stats_massage(:,2) = stats.W(:,2);
stats_massage(:,3) = stats.W(:,3);
stats_massage(:,4) = stats.W(:,4);
stats_massage(:,5) = stats.W(:,5);
stats_massage(:,6) = stats.W(:,6);
stats_massage(:,7) = stats.W(:,7);
stats_massage(:,8) = stats.W(:,8);
stats_massage(:,9) = stats.W(:,9);
stats_massage(:,10) = stats.W(:,10);
total_weight(:,1) = out1(1,2).*stats_massage(:,1)+...
    out1(2,2).*stats_massage(:,2)+...
    out1(3,2).*stats_massage(:,3)+...
    out1(4,2).*stats_massage(:,4)+...
    out1(5,2).*stats_massage(:,5)+...
    out1(6,2).*stats_massage(:,6)+...
```

```
    out1(7,2).*stats_massage(:,7)+...
    out1(8,2).*stats_massage(:,8)+...
    out1(9,2).*stats_massage(:,9)+...
    out1(10,2).*stats_massage(:,10);
figure5 = figure('units','inches','pos',[0 0 6.5 4])
axes('FontName','Times New Roman','FontSize',10)
plot(351:b+350,stats_massage,'-');
legend({'1st Component' '2nd Component' '3rd  Component' '4th
        Component'},'location','NW','FontName','Times New Roman','FontSize',10);
ylabel('Absolute Value of Component Weighting','FontName','Times New Roman','FontSize',10)
xlabel('Wavelength, \lambda, [nm]','FontName','Times New Roman','FontSize',10)
xlim([350 2500]);
close('all');
out2(:,1) = [351:b+350]';
out2(:,2) = total_weight(:,1);
```

B.2.11. ***ppe_master.m***

A MATLAB executable written to randomly generate calibration and validation data sets for use in PLS/PCR regressions. The programmatic input was the number of spectra (and associated θ_v- ψ_m) data to be reserved for blind validation. The program was executed as a subroutine by the master_proc_sw_mb.m executable. The ppe_master.m subroutine generates a non-soil specific master data set (containing all spectral and θ_v - ψ_m data), a non-soil specific calibration list (containing all spectral and θ_v - ψ_m data not reserved for validation), a non-soil specific validation list (containing a user specified number of validation spectra and θ_v - ψ_m data), and an index (for troubleshooting).

Invocation: *[index, master_data,cal_list,val_list] = asd_reader(search string, ...*

output string, ...

suppression flag, ...

output path);

Source Code:

```
function [index,master_data,cal_list,val_list] = ppe_master(number_val)
%disp('Generate Master Matrix');
%%DEBUG CODE SECTION - DISABLE FUNCTION
%clear,clc,fclose('all');,close('all');
%number_val = 30;
%%
master_data = [{'DONNA_03_H1.txt'}        0.055464        498.1293    0   0
{'DONNA_03_H2.txt'}    0.055464    498.1293    0   0
{'DONNA_03_H3.txt'}    0.055464    498.1293    0   0
{'DONNA_04_H1.txt'}    0.052805    498.1293    0   0
{'DONNA_04_H2.txt'}    0.052805    498.1293    0   0
{'DONNA_04_H3.txt'}    0.052805    498.1293    0   0
{'DONNA_05_H1.txt'}    0.038041    697.381    0   0
{'DONNA_05_H2.txt'}    0.038041    697.381    0   0
{'DONNA_05_H3.txt'}    0.038041    697.381    0   0
{'DONNA_06_H1.txt'}    0.043405    697.381    0   0
{'DONNA_06_H2.txt'}    0.043405    697.381    0   0
{'DONNA_06_H3.txt'}    0.043405    697.381    0   0
{'DONNA_10_H1.txt'}    0.032253    1264.905    0   0
{'DONNA_10_H2.txt'}    0.032253    1264.905    0   0
{'DONNA_10_H3.txt'}    0.032253    1264.905    0   0
{'DONNA_11_H1.txt'}    0.10586 100.3129    0   0
{'DONNA_11_H2.txt'}    0.10586     100.3129    0   0
{'DONNA_11_H3.txt'}    0.10586     100.3129    0   0
{'DONNA_12_H1.txt'}    0.112716    100.3129    0   0
{'DONNA_12_H2.txt'}    0.112716    100.3129    0   0
{'DONNA_12_H3.txt'}    0.112716    100.3129    0   0
```

{'DONNA_13_H1.txt'} 0.043872 1473.088 0 0
{'DONNA_13_H2.txt'} 0.043872 1473.088 0 0
{'DONNA_13_H3.txt'} 0.043872 1473.088 0 0
{'DONNA_14_H1.txt'} 0.04231 1473.088 0 0
{'DONNA_14_H2.txt'} 0.04231 1473.088 0 0
{'DONNA_14_H3.txt'} 0.04231 1473.088 0 0
{'DONNA_15_H1.txt'} 0.0865 298.8776 0 0
{'DONNA_15_H2.txt'} 0.0865 298.8776 0 0
{'DONNA_15_H3.txt'} 0.0865 298.8776 0 0
{'DONNA_16_H1.txt'} 0.0865 298.8776 0 0
{'DONNA_16_H2.txt'} 0.0865 298.8776 0 0
{'DONNA_16_H3.txt'} 0.0865 298.8776 0 0
{'DONNA_7_H1.txt'} 0.023514 1083.517 0 0
{'DONNA_7_H2.txt'} 0.023514 1083.517 0 0
{'DONNA_7_H3.txt'} 0.023514 1083.517 0 0
{'DONNA_8_H1.txt'} 0.014244 1083.517 0 0
{'DONNA_8_H2.txt'} 0.014244 1083.517 0 0
{'DONNA_8_H3.txt'} 0.014244 1083.517 0 0
{'DONNA_9_H1.txt'} 0.032253 1264.905 0 0
{'DONNA_9_H2.txt'} 0.032253 1264.905 0 0
{'DONNA_9_H3.txt'} 0.032253 1264.905 0 0
{'donna_01_h.txt'} 0.127115 10.30612 0 0
{'donna_01_hc.txt'} 0.127115 10.30612 0 0
{'donna_02_h.txt'} 0.120524 10.30612 0 0
{'donna_02_hc.txt'} 0.120524 10.30612 0 0
{'donna_03_h.txt'} 0.055464 498.1293 0 0
{'donna_04_hc.txt'} 0.052605 498.1293 0 0
{'illite16_hc.txt'} 0.3196 1289.6 0 0
{'illite_01_c.txt'} 0.3568 700 0 0
{'illite_01_hc.txt'} 0.3568 700 0 0
{'illite_02_h.txt'} 0.3729 700 0 0

{'illite_02_hc.txt'} 0.3729 700 0 0
{'illite_03_h.txt'} 0.3622 900 0 0
{'illite_03_hc.txt'} 0.3622 900 0 0
{'illite_04_h.txt'} 0.4522 101 0 0
{'illite_04_hc.txt'} 0.4522 101 0 0
{'illite_05_hc.txt'} 0.4443 700 0 0
{'illite_07_h.txt'} 0.3704 200 0 0
{'illite_07_hc.txt'} 0.3704 200 0 0
{'illite_07_x.txt'} 0.3704 200 0 0
{'illite_08_h.txt'} 0.3965 300 0 0
{'illite_08_hc.txt'} 0.3965 300 0 0
{'illite_09_h.txt'} 0.4785 300 0 0
{'illite_09_hc.txt'} 0.4785 300 0 0
{'illite_09_hx.txt'} 0.4785 300 0 0
{'illite_11_h.txt'} 0.3898 400 0 0
{'illite_11_hc.txt'} 0.3898 400 0 0
{'illite_12_h.txt'} 0.3328 1100 0 0
{'illite_12_hc.txt'} 0.3328 1100 0 0
{'illite_13_h.txt'} 0.2961 1100 0 0
{'illite_13_hc.txt'} 0.2961 1100 0 0
{'illite_14_h.txt'} 0.3649 480.27 0 0
{'illite_14_hc.txt'} 0.3649 480.27 0 0
{'illite_15_h.txt'} 0.4005 480.27 0 0
{'illite_15_hc.txt'} 0.4005 480.27 0 0
{'illite_16_h.txt'} 0.3106 1289.6 0 0
{'illite_17_h.txt'} 0.3196 1289.6 0 0
{'illite_17_hc.txt'} 0.3196 1289.6 0 0
{'illite_18_h.txt'} 0.3205 1289 0 0
{'illite_18_hc.txt'} 0.3206 1289 0 0
{'kaolinite_01_h.txt'} 0.3231 700 0 0
{'kaolinite_01_hc.txt'} 0.3231 700 0 0

{'kaolinite_02_h.txt'} 0.3479 700   0   0

{'kaolinite_02_hc.txt'} 0.3479700   0   0

{'kaolinite_03_h.txt'} 0.3873 900   0   0

{'kaolinite_03_hc.txt'} 0.3873900   0   0

{'kaolinite_04_h.txt'} 0.3713 900   0   0

{'kaolinite_04_hc.txt'} 0.3713900   0   0

{'kaolinite_05_hc.txt'} 0.35071100   0   0

{'kaolinite_05_hx.txt'} 0.35071100   0   0

{'kaolinite_06_h.txt'} 0.4163 101   0   0

{'kaolinite_06_hc.txt'} 0.4163101   0   0

{'kaolinite_07_hc.txt'} 0.4198101   0   0

{'kaolinite_08_h.txt'} 0.3463 200   0   0

{'kaolinite_09_h.txt'} 0.4072 200   0   0

{'kaolinite_09_hc.txt'} 0.4072200   0   0

{'kaolinite_10_h.txt'} 0.3626 1100   0   0

{'kaolinite_10_hc.txt'} 0.3626   1100   0   0

{'kaolinite_11_hc.txt'} 0.5439   300   0   0

{'kaolinite_12_h.txt'}   0.374 400   0   0

{'kaolinite_12_hc.txt'} 0.374   400   0   0

{'kaolinite_13_h.txt'} 0.3756 400   0   0

{'kaolinite_13_hc.txt'} 0.3756400   0   0

{'kaolinite_14_h.txt'} 0.311   480.27   0   0

{'kaolinite_14_hc.txt'} 0.311   480.27   0   0

{'kaolinite_17_h_.txt'} 0.268431   1482.327   0   0

{'kaolinite_17_hc_.txt'}   0.268431   1482.327   0   0

{'kaolinite_18_h_.txt'} 0.194507   1482.327   0   0

{'kaolinite_18_hc_.txt'}   0.194507   1482.327   0   0

{'kaolinite_19_h_.txt'} 0.246 1300   0   0

{'kaolinite_19_hc_.txt'} 0.2461300   0   0];

[a b] = size(master_data);

master_data(:,4) = {1};

```
for i = 1:1:number_val
    val_num = floor(a*rand)+1;
    index(i,1) = val_num;
    if any(val_num - index(:,:) == 0) == 1
        while any(val_num - index == 0) == 1
            val_num = floor(a*rand) + 1;
            disp('MISS')
            val_num
            index'
        end
        master_data(val_num,5) = {1};
        master_data(val_num,4) = {0};
    else
        disp('HIT');
        master_data(val_num,5) = {1};
        master_data(val_num,4) = {0};
    end
end
count_cal = 1;
count_val = 1;
for i = 1:1:a
    if cell2mat(master_data(i,5)) == 1
        val_list(count_val,1:5) = master_data(i,1:5);
        count_val = count_val + 1;
    else
        cal_list(count_cal,1:5) = master_data(i,1:5);
        count_cal = count_cal + 1;
    end
end
```

B.2.12. ***ppe_master_d.m***

A MATLAB executable written to randomly generate a Donna Fill specific calibration and validation data sets for use in PLS/PCR regressions. The programmatic input was the number of spectra (and associated θ_v - ψ_m) data to be reserved for blind validation. The program was executed as a subroutine by the master_proc_sw_mb.m executable. The ppe_master.m subroutine generates a soil specific master data set (containing all spectral and θ_v - ψ_m data), a soil specific calibration list (containing all spectral and θ_v - ψ_m data not reserved for validation), a soil specific validation list (containing a user specified number of validation spectra and θ_v - ψ_m data), and an index (for troubleshooting).

Invocation: *[index, master data list, calibration list, validation list] = ppe_master_d(…,*

number of validation data sets);

Source Code:

```
function [index,master_data,cal_list,val_list] = ppe_master_d(number_val)
%disp('Generate Master Matrix');
%%DEBUG CODE SECTION - DISABLE FUNCTION
%clear,clc,fclose('all');,close('all');
%number_val = 30;
%%
master_data = [{'DONNA_03_H1.txt'}        0.055464        498.1293    0   0
{'DONNA_03_H2.txt'}    0.055464    498.1293    0   0
{'DONNA_03_H3.txt'}    0.055464    498.1293    0   0
{'DONNA_04_H1.txt'}    0.052805    498.1293    0   0
{'DONNA_04_H2.txt'}    0.052805    498.1293    0   0
{'DONNA_04_H3.txt'}    0.052805    498.1293    0   0
{'DONNA_05_H1.txt'}    0.038041    697.381    0   0
{'DONNA_05_H2.txt'}    0.038041    697.381    0   0
{'DONNA_05_H3.txt'}    0.038041    697.381    0   0
```

{'DONNA_06_H1.txt'} 0.043405 697.381 0 0
{'DONNA_06_H2.txt'} 0.043405 697.381 0 0
{'DONNA_06_H3.txt'} 0.043405 697.381 0 0
{'DONNA_10_H1.txt'} 0.032253 1264.905 0 0
{'DONNA_10_H2.txt'} 0.032253 1264.905 0 0
{'DONNA_10_H3.txt'} 0.032253 1264.905 0 0
{'DONNA_11_H1.txt'} 0.10586 100.3129 0 0
{'DONNA_11_H2.txt'} 0.10586 100.3129 0 0
{'DONNA_11_H3.txt'} 0.10586 100.3129 0 0
{'DONNA_12_H1.txt'} 0.112716 100.3129 0 0
{'DONNA_12_H2.txt'} 0.112716 100.3129 0 0
{'DONNA_12_H3.txt'} 0.112716 100.3129 0 0
{'DONNA_13_H1.txt'} 0.043872 1473.088 0 0
{'DONNA_13_H2.txt'} 0.043872 1473.088 0 0
{'DONNA_13_H3.txt'} 0.043872 1473.088 0 0
{'DONNA_14_H1.txt'} 0.04231 1473.088 0 0
{'DONNA_14_H2.txt'} 0.04231 1473.088 0 0
{'DONNA_14_H3.txt'} 0.04231 1473.088 0 0
{'DONNA_15_H1.txt'} 0.0865 298.8776 0 0
{'DONNA_15_H2.txt'} 0.0865 298.8776 0 0
{'DONNA_15_H3.txt'} 0.0865 298.8776 0 0
{'DONNA_16_H1.txt'} 0.0865 298.8776 0 0
{'DONNA_16_H2.txt'} 0.0865 298.8776 0 0
{'DONNA_16_H3.txt'} 0.0865 298.8776 0 0
{'DONNA_7_H1.txt'} 0.023514 1083.517 0 0
{'DONNA_7_H2.txt'} 0.023514 1083.517 0 0
{'DONNA_7_H3.txt'} 0.023514 1083.517 0 0
{'DONNA_8_H1.txt'} 0.014244 1083.517 0 0
{'DONNA_8_H2.txt'} 0.014244 1083.517 0 0
{'DONNA_8_H3.txt'} 0.014244 1083.517 0 0
{'DONNA_9_H1.txt'} 0.032253 1264.905 0 0

```
{'DONNA_9_H2.txt'}      0.032253    1264.905    0   0
{'DONNA_9_H3.txt'}      0.032253    1264.905    0   0
{'donna_01_h.txt'}      0.127115    10.30612    0   0
{'donna_01_hc.txt'}     0.127115    10.30612    0   0
{'donna_02_h.txt'}      0.120524    10.30612    0   0
{'donna_02_hc.txt'}     0.120524    10.30612    0   0
{'donna_03_h.txt'}      0.055464    498.1293    0   0
{'donna_04_hc.txt'}     0.052605    498.1293    0   0];;
[a b] = size(master_data);
master_data(:,4) = {1};
for i = 1:1:number_val
   val_num = floor(a*rand)+1;
   index(i,1) = val_num;
   if any(val_num - index(:,:) == 0) == 1
      while any(val_num - index == 0) == 1
         val_num = floor(a*rand) + 1;
         disp('MISS')
         val_num
         index'
      end
      master_data(val_num,5) = {1};
      master_data(val_num,4) = {0};
   else
      disp('HIT');
      master_data(val_num,5) = {1};
      master_data(val_num,4) = {0};
   end
end
count_cal = 1;
count_val = 1;
for i = 1:1:a
```

```
   if cell2mat(master_data(i,5)) == 1
      val_list(count_val,1:5) = master_data(i,1:5);
      count_val = count_val + 1;
   else
      cal_list(count_cal,1:5) = master_data(i,1:5);
      count_cal = count_cal + 1;
   end
end
```

B.2.13. ***ppe_msater_i.m***

A MATLAB executable written to randomly generate an illite specific calibration and validation data sets for use in PLS/PCR regressions. The programmatic input was the number of spectra (and associated θ_v - ψ_m) data to be reserved for blind validation. The program was executed as a subroutine by the master_proc_sw_mb.m executable. The ppe_master.m subroutine generates a soil specific master data set (containing all spectral and θ_v - ψ_m data), a soil specific calibration list (containing all spectral and θ_v - ψ_m data not reserved for validation), a soil specific validation list (containing a user specified number of validation spectra and v- ψ_m data), and an index (for troubleshooting).

Invocation: *[index, master data list, calibration list, validation list] = ppe_master_i(…*

number of validation data sets);

Source Code:

```
function [index,master_data,cal_list,val_list] = ppe_master_i(number_val)
%disp('Generate Master Matrix');
%%DEBUG CODE SECTION - DISABLE FUNCTION
%clear,clc,fclose('all');,close('all');
%number_val = 30;
%%
```

master_data = [{'illite16_hc.txt'} 0.3196 1289.6 0 0

{'illite_01_c.txt'} 0.3568 700 0 0

{'illite_01_hc.txt'} 0.3568 700 0 0

{'illite_02_h.txt'} 0.3729 700 0 0

{'illite_02_hc.txt'} 0.3729 700 0 0

{'illite_03_h.txt'} 0.3622 900 0 0

{'illite_03_hc.txt'} 0.3622 900 0 0

{'illite_04_h.txt'} 0.4522 101 0 0

{'illite_04_hc.txt'} 0.4522 101 0 0

{'illite_05_hc.txt'} 0.4443 700 0 0

{'illite_07_h.txt'} 0.3704 200 0 0

{'illite_07_hc.txt'} 0.3704 200 0 0

{'illite_07_x.txt'} 0.3704 200 0 0

{'illite_08_h.txt'} 0.3965 300 0 0

{'illite_08_hc.txt'} 0.3965 300 0 0

{'illite_09_h.txt'} 0.4785 300 0 0

{'illite_09_hc.txt'} 0.4785 300 0 0

{'illite_09_hx.txt'} 0.4785 300 0 0

{'illite_11_h.txt'} 0.3898 400 0 0

{'illite_11_hc.txt'} 0.3898 400 0 0

{'illite_12_h.txt'} 0.3328 1100 0 0

{'illite_12_hc.txt'} 0.3328 1100 0 0

{'illite_13_h.txt'} 0.2961 1100 0 0

{'illite_13_hc.txt'} 0.2961 1100 0 0

{'illite_14_h.txt'} 0.3649 480.27 0 0

{'illite_14_hc.txt'} 0.3649 480.27 0 0

{'illite_15_h.txt'} 0.4005 480.27 0 0

{'illite_15_hc.txt'} 0.4005 480.27 0 0

{'illite_16_h.txt'} 0.3106 1289.6 0 0

{'illite_17_h.txt'} 0.3196 1289.6 0 0

{'illite_17_hc.txt'} 0.3196 1289.6 0 0

```
{'illite_18_h.txt'}     0.3205     1289    0   0];
[a b] = size(master_data);
master_data(:,4) = {1};
for i = 1:1:number_val
    val_num = floor(a*rand)+1;
    index(i,1) = val_num;
    if any(val_num - index(:,:) == 0) == 1
        while any(val_num - index == 0) == 1
            val_num = floor(a*rand) + 1;
            disp('MISS')
            val_num
            index'
        end
        master_data(val_num,5) = {1};
        master_data(val_num,4) = {0};
    else
        disp('HIT');
        master_data(val_num,5) = {1};
        master_data(val_num,4) = {0};
    end
end
count_cal = 1;
count_val = 1;
for i = 1:1:a
    if cell2mat(master_data(i,5)) == 1
        val_list(count_val,1:5) = master_data(i,1:5);
        count_val = count_val + 1;
    else
        cal_list(count_cal,1:5) = master_data(i,1:5);
        count_cal = count_cal + 1;
    end
```

end

B.2.14. ***ppe_master_k.m***

A MATLAB executable written to randomly generate a kaolinite specific calibration and validation data sets for use in PLS/PCR regressions. The programmatic input was the number of spectra (and associated θ_v - ψ_m) data to be reserved for blind validation. The program was executed as a subroutine by the master_proc_sw_mb.m executable. The ppe_master.m subroutine generates a soil specific master data set (containing all spectral and θ_v - ψ_m data), a soil specific calibration list (containing all spectral and θ_v - ψ_m data not reserved for validation), a soil specific validation list (containing a user specified number of validation spectra and θ_v - ψ_m data), and an index (for troubleshooting).

Invocation: *[index, master data list, calibration list, validation list] = ppe_master_k(...*

number of validation data sets);

Source Code:

```
function [index,master_data,cal_list,val_list] = ppe_master_k(number_val)
%disp('Generate Master Matrix');
%%DEBUG CODE SECTION - DISABLE FUNCTION
%clear,clc,fclose('all');,close('all');
%number_val = 30;
%%
master_data = [{'kaolinite_01_h.txt'}  0.3231          700    0   0
{'kaolinite_01_hc.txt'} 0.3231 700    0   0
{'kaolinite_02_h.txt'}  0.3479 700    0   0
{'kaolinite_02_hc.txt'} 0.3479 700    0   0
{'kaolinite_03_h.txt'}  0.3873 900    0   0
{'kaolinite_03_hc.txt'} 0.3873 900    0   0
{'kaolinite_04_h.txt'}  0.3713 900    0   0
```

```
{'kaolinite_04_hc.txt'} 0.3713900    0   0
{'kaolinite_05_hc.txt'} 0.35071100    0   0
{'kaolinite_05_hx.txt'} 0.35071100    0   0
{'kaolinite_06_h.txt'}  0.4163 101    0   0
{'kaolinite_06_hc.txt'} 0.4163101    0   0
{'kaolinite_07_hc.txt'} 0.4198101    0   0
{'kaolinite_08_h.txt'}  0.3463 200    0   0
{'kaolinite_09_h.txt'}  0.4072 200    0   0
{'kaolinite_09_hc.txt'} 0.4072200    0   0
{'kaolinite_10_h.txt'}  0.3626 1100    0   0
{'kaolinite_10_hc.txt'}  0.3626          1100    0   0
{'kaolinite_11_hc.txt'}  0.5439          300    0   0
{'kaolinite_12_h.txt'}   0.374  400    0   0
{'kaolinite_12_hc.txt'} 0.374   400    0   0
{'kaolinite_13_h.txt'}  0.3756 400    0   0
{'kaolinite_13_hc.txt'} 0.3756400    0   0
{'kaolinite_14_h.txt'} 0.311    480.27    0   0
{'kaolinite_14_hc.txt'} 0.311   480.27    0   0
{'kaolinite_17_h_.txt'} 0.268431       1482.327    0   0
{'kaolinite_17_hc_.txt'}    0.268431   1482.327    0   0
{'kaolinite_18_h_.txt'} 0.194507       1482.327    0   0
{'kaolinite_18_hc_.txt'}    0.194507   1482.327    0   0
{'kaolinite_19_h_.txt'} 0.246  1300    0   0
{'kaolinite_19_hc_.txt'} 0.2461300    0   0];
[a b] = size(master_data);
master_data(:,4) = {1};
for i = 1:1:number_val
    val_num = floor(a*rand)+1;
    index(i,1) = val_num;
    if any(val_num - index(:,:) == 0) == 1
        while any(val_num - index == 0) == 1
```

```
        val_num = floor(a*rand) + 1;
        disp('MISS')
        val_num
        index'
      end
      master_data(val_num,5) = {1};
      master_data(val_num,4) = {0};
   else
      disp('HIT');
      master_data(val_num,5) = {1};
      master_data(val_num,4) = {0};
   end
end
count_cal = 1;
count_val = 1;
for i = 1:1:a
   if cell2mat(master_data(i,5)) == 1
      val_list(count_val,1:5) = master_data(i,1:5);
      count_val = count_val + 1;
   else
      cal_list(count_cal,1:5) = master_data(i,1:5);
      count_cal = count_cal + 1;
   end
end
```

B.2.15. ***reformater.m***

A MATLAB written to reformat and, if required, interpolate spectral experimentally (Ocean Optics USB-2000, Nicolet FTIR) and literature (k_water.m and k_vapor.m) obtained spectral data to the format and resolution of the ASD spectral data files. Files were resampled to the same wavelength values as found in a reference ASD spectral file.

Invocation: *[output] = reformater('Lit_Water.txt','ASD_Ref.txt')*

Source Code:

```
%reformater
function [output] = reformater(input,spectra)
%% debug
%input = kwater_lit;
%input(:,1) = 1000.*input(:,1);
%spectra = spectra_ref;
[a b] = size(spectra);
output = zeros(a,b);
output(:,1) = spectra(:,1);
output(:,2) = 0.*spectra(:,2);
%%
[a b] = size(output);
[e f] = size(input);
for i = 1:1:a
   [c d] = val2ind(input(:,1),output(i,1));
   c = min(c);
   if c == 1 | c == e
      output(i,2) = input(c,2);
   elseif output(i,1) < input(c,1)
      output(i,2) = ((input(c,2)-input(c-1,2))/...
                  (input(c,1)-input(c-1,1)))*...
                  (output(i,1)-input(c,1)) + input(c,2);
   elseif output(i,1) > input(c,1)
      output(i,2) = ((input(c,2) - input(c+1,2))/...
                  (input(c,1)-input(c+1,1)))*...
                  (output(i,1)-input(c,1)) + input(c,2);
   elseif output(i,1) == input(c,1)
      output(i,2) = input(c,2);
```

```
    end
    output(i,1:2);
end
```

B.2.16. ***spectra_process.m***

A MATLAB executable to ingest Vis-NIR file spectrum obtained from the FieldSpec-4 HiRes spectroradiometer, average all spectra containing a search string, and write the resulting averaged spectra to a specified file and file path. Programmatic inputs include the search string (all file names containing the string will be processed), the output string (the output file name), a suppression file (to enable or suppress the file deletion waring), and an output path (the directory for the output file to be stored). It should be noted that the asd_reader.m executable will delete all .asd (raw data) files and that care should be taken to preserve the original data.

Invocation: *[output] = spectra_process(date,'*HC.asd.txt');*

Source Code:

```
function [date F_handle] = spectra_process(date,F_handle)
dir
pause(1)
%date = '22MAY';
%F_handle = 'HH';
date_tar = strcat(date,'/',F_handle,'*');
list = dir(date_tar);
[a b] = size(list);
for i = 1:1:a
    data_path = strcat(date,'/',list(i,1).name);
    list2 = dir(strcat(data_path,'/','*.txt'));
    [c d] = size(list2);
    for j = 1:1:c
        fid = strcat(data_path,'/',list2(j,1).name);
```

```
    if j == 1
     data = (spectra_reader(fid))./c;
    else
     data = data +(spectra_reader(fid))./c;
    end
  end
  figure
  plot(data(:,1),data(:,2))
  title(list(i,1).name)
  xlabel('Wavelength(nm)')
  ylabel('Digital Number (DN)')
  pause(1)
  out_dir = strcat(list(i,1).name,'.txt')';
  dlmwrite(out_dir,data)
  clear data
end
```

B.2.17. ***spectra_reader.m***

A MATLAB executable to ingest Vis-NIR file spectrum obtained from the FieldSpec-4 HiRes spectroradiometer, average all spectra containing a search string, and write the resulting averaged spectra to a specified file and file path. Programmatic inputs include the search string (all file names containing the string will be processed), the output string (the output file name), a suppression file (to enable or suppress the file deletion waring), and an output path (the directory for the output file to be stored). It should be noted that the asd_reader.m executable will delete all .asd (raw data) files and that care should be taken to preserve the original data.

Invocation: *[output] = spectra_reader(search string, ...*

output string, ...

suppression flag, ...

output path);

Source Code:

```
%function [data] = spectra_reader(fid)
%program to read tab deliminted ASCII files from fieldspec viewpro
%data = [n by 2] matrix with wavelength and values
%fid = file ID for data;
fid = fopen('Illite00000.asd.txt');
fmt = ['%s %s'];
data_raw = textscan(fid,fmt,'HeaderLines',1,...
   'Delimiter','\t',...
   'CollectOutput',1);
data(:,1) = str2num(str2mat(data_raw{1,1}(:,1)));
data(:,2) = str2num(str2mat(data_raw{1,1}(:,2)));
fclose('all');
%end
```

B.2.18. ***x_gen_fspec.m***

A MATLAB executable to ingest Vis-NIR file spectrum obtained from the FieldSpec-4 HiRes spectroradiometer and generate the X matrix used for PLS/PCR regression and other multiple sample computations. Programmatic inputs include a list of files to be ingested (file_list) and the directory the files are located in (path). Spectral data files are opened and the spectral intensities at each wavelength are stored as sequential columns in the X matrix (and one row per file).

Invocation: *[x(:,:)] = x_gen_fspec(proc_list,'C:/Users/cxg021/Desktop/NIR_WET');*

Source Code:

```
%x_gen_path
function [x] = x_gen_fspec(file_list,path)
```

```
[a b] = size(file_list);
%x = zeros(a,1869);
for i = 1:1:a
   if nargin == 1
   data1 = dlmread(file_list{i,1},'\t');
   elseif nargin == 2
   data1 = dlmread(strcat(path,'/',file_list{i,1}),'\t');
   else
      disp('NARGIN!');
   end
   x(i,:) = data1(:,2)';
end
```

B.2.19. ***x_gen_mir.m***

A MATLAB executable to ingest MIR spectral files obtained from the Nicolet 6700 FTIR spectrometer and generate the X matrix used for PLS/PCR regression and other multiple sample computations. Programmatic inputs include a list of files to be ingested (file_list) and the directory the files are located in (path). Spectral data files are opened and the spectral intensities at each wavelength are stored as sequential columns in the X matrix (and one row per file).

Invocation: *[x(:.:)] = x_gen_mir (proc_list,'C:/Users/cxg021/Desktop/NIR_WET');*

Source Code:

```
%x_gen_path
function [x] = x_gen_mir(file_list,path)
[a b] = size(file_list);
x = zeros(a,1869);
for i = 1:1:a
   data1 = csvread(strcat(path,'/',file_list{i,1}));
   [c d] = size(data1)
```

```
    if c == 1868
        data3 = zeros(1869,2);
        data3(1:1868,1:2) = data1(1:1868,1:2);
        data1 = data3;
    end
    for j = 1:1:c
        data2(j,1) = 1/data1(c+1-j,1)*1e7;
        data2(j,2) = data1(c+1-j,2);
    end
    x(i,:) = data2(:,2)';
end
```

B.3. Source Code and Executables Developed to Extract Optical Properties

The included programs were developed to ingest, process, and extract ultra-violet and visible (OceanOptics USB-2000) and near-infrared to mid-infrared (Nicolet 6700) spectral data. The purpose of this testing and subsequent processing were to extract optical properties of soils including measurements of soil absorption spectrum and soil scattering spectrum.

B.3.1. ***dat_extraction.m***

A MATLAB executable written to enable the acquisition of data from a graphical plot. Specifically, published spectral data were converted into an array of numerical (x,y) values. The data was ingested by loading an image file (.jpg or .gif) into MATLAB (via the immread command). The program was executed from the MATLAB graphical user interface (GUI) by pressing the F5 key.

Invocation: MATLAB GUI (F5)

Source Code:

```
pwd
```

```
close all;, clear
im_mat = imread('Capture2.JPG');
out_fid = 'Figure_Take_Off.dat';
figure1 = figure;
imagesc(im_mat)
axis('equal')
axis('tight')
%define x- and y- axis with extends
disp('Select Origin')
check_flag = 0;
while check_flag == 0
origin = ginput(1);
origin_x = input('Enter x value for origin');
origin_y = input('Enter y value for origin');
check_flag = input('Origin Correct? (1 for yes, 0 for no)');
end
check_flag = 0;
log_flag_y = input('Is Y-axis log scale?')
while check_flag == 0
disp('Select End of Y-Axis')
y_end = ginput(1);
y_endv = input('Value of Y at end of axis?');
if y_end(1,1) ~= origin(1,1)
   flag = input('Is axis vertical?')
   if flag == 1
      y_end(1,1) = origin(1,1);
   end
end
check_flag = input('y-axis correct? (1 for yes, 0 for no)');
end
l_y = ((y_end(1,2)-origin(1,2))^2+(y_end(1,1)-origin(1,1))^2)^.5;
```

```
if log_flag_y == 1
   y_endv = log10(y_endv);
end
y_f = (y_endv-origin_y)/l_y;
check_flag = 0;
log_flag_x = input('Is X-axis log scale?')
while check_flag == 0
disp('Select End of X-Axis')
x_end = ginput(1);
x_endv = input('Value of X at end of axis?');
if x_end(1,2) ~= origin(1,2)
   flag = input('Is axis horizontal?')
   if flag == 1
      x_end(1,2) = origin(1,2);
   end
end
check_flag = input('X-axis correct? (1 for yes, 0 for no)');
end
l_x = ((x_end(1,2)-origin(1,2))^2+(x_end(1,1)-origin(1,1))^2)^.5;
if log_flag_x == 1
   x_endv = log10(x_endv);
end
x_f = (x_endv-origin_x)/l_x;
n_s = input('How Many Series?')
for i = 1:1:n_s
   msg = strcat({'Input Series # '},num2str(i),{' '});
   disp('HIT RETURN TO EXIT');
   [data(:,i+2*1-2) data(:,i+2*1-1)] = ginput;
   if log_flag_y == 1
      out(:,i+2*1-1) = 10.^(y_f.*data(:,i+2*1-1));
   else
```

```
    out(:,i+2*1-1) = y_f.*data(:,i+2*1-1)
  end
  if log_flag_x == 1
    out(:,i+2*1-2) = 10.^(x_f.*data(:,i+2*1-2))
  else
    out(:,i+2*1-2) = x_f.*data(:,i+2*1-2)
  end
end
dlmwrite(out_fid,out(:,:),'delimiter',',');
```

B.3.2. ***kaolinite_absorbtion.m***

A MATLAB executable written to enable computation and visualization of the soil absorption coefficient spectra for illite samples. Programmatic inputs included experimentally obtained values of kaolinite reflectance at a mass fraction of 2 (KN2_REFLECT), 4 (KN4_REFLECT), and (KN6_REFLECT). In addition a pure potassium bromide (KBr) reflectance spectrum was required. The program was executed using the MATLAB GUI by pressing the F5 key.

Invocation: MATLAB GUI (F5)

Source Code:

```
%NEW FIGURE PLOT SCRIPT BECAUSE EXCEL KEEPS CRASHING
%KAOLIN BASED ON EARLIER DONNA SCRIPT
clear
clc
close('all');
%%file list
[KBR] = KBR_REFLECT;
[DF2] = KN2_REFLECT;
[DF4] = KN4_REFLECT;
```

```
[DF6] = KN6_REFLECT;
DF2(:,2) = 100.*DF2(:,2)
figure1 = figure('units','inches','pos',[0 0 6.5 3]);
subplot1 = subplot(1,1,1)
box(subplot1,'on');
hold(subplot1,'all');
plot(KBR(:,1),KBR(:,2),'LineStyle','-','Color',[0 0 0])
plot(DF2(:,1),DF2(:,2),'LineStyle','-','Color',[0.15 0.15 0.15])
%plot(DF4(:,1),DF4(:,2),'LineStyle','-','Color',[0.30 0.30 0.30])
%plot(DF6(:,1),DF6(:,2),'LineStyle','-','Color',[0.45 0.45 0.45])
ylabel('Reflectance Ratio, R_\infty, [I/I_0]','FontName','Times New Roman',...
   'FontSize',12);
xlabel('Wavelength, \lambda, [nm]','FontName','Times New Roman',...
   'FontSize',12);
set(subplot1,'Ylim',[0 100],'Xlim',[400 2500],...
   'FontName','Times New Roman','FontSize',12,...
   'XTick',[400 700 1000 1300 1600 1900 2200 2500],...
   'XTickLabel',[400 700 1000 1300 1600 1900 2200 2500],...
   'YTick',[0 20 40 60 80 100],...
   'YTickLabel',[0 20 40 60 80 100]);
%  legend1 = legend(subplot1,'show');
%  set(legend1,'String',{'Donna Fill' 'Illite' 'Kaolinite'},...
%     'FontName','Times New Roman',...
%     'FontSize',8);
%  set(legend1,'LineStyleOrder',{'d','o','s'})
%  set(legend1,'EdgeColor',[1 1 1],'YColor',[1 1 1],'XColor',[1 1 1],...
%   'Position',[0.328143513497517 0.631983077468714 0.06003716216216216
        0.0793246187363835],...
%   'LineStyleOrder',{'d','s','o'},...
%   'FontSize',8);
kmf_kbr = KUBELKA(KBR);
```

```
kmf_df2 = KUBELKA(DF2);
kmf_df4 = KUBELKA(DF4);
kmf_df6 = KUBELKA(DF6);
%%
k_kbr = 10e-4;
s_kbr = k_kbr./kmf_kbr(:,2);
k_df2(:,1) = kmf_df2(:,1);
k_df4(:,1) = kmf_df4(:,1);
k_df6(:,1) = kmf_df6(:,1);
k_df2(:,2) = (1/.02).*(0.98*kmf_df2(:,2).*s_kbr(:,1));
k_df4(:,2) = (1/.04).*(0.96*kmf_df4(:,2).*s_kbr(:,1));
k_df6(:,2) = (1/.06).*(0.94*kmf_df6(:,2).*s_kbr(:,1));
k_df2_2(:,1) = kmf_df2(:,1);
k_df4_2(:,1) = kmf_df4(:,1);
k_df6_2(:,1) = kmf_df6(:,1);
k_df2_2(:,2) = (1/.02).*s_kbr(:,1).*(kmf_df2(:,2)-kmf_kbr(:,2));
k_df4_2(:,2) = (1/.04).*s_kbr(:,1).*(kmf_df4(:,2)-kmf_kbr(:,2));
k_df6_2(:,2) = (1/.06).*s_kbr(:,1).*(kmf_df6(:,2)-kmf_kbr(:,2));
[ill1 ill2]= illite_gil74;
figure2 = figure('units','inches','pos',[0 0 6.5 3]);
subplot2 = subplot(1,1,1)
box(subplot2,'on');
hold(subplot2,'all');
plot(k_df2(:,1),k_df2(:,2),'LineWidth',2,'LineStyle','-','Color',[0 0 0])
plot(k_df2_2(:,1),k_df2_2(:,2),'LineWidth',2,'LineStyle','-.','Color',[0 0 0]);
%plot(k_df4(:,1),k_df4(:,2),'LineStyle','-','Color',[0.5 0.5 0.5]);
plot(k_df4(:,1),k_df4(:,2),'LineWidth',2,'LineStyle','-','Color',[0.15 0.15 0.15])
plot(k_df4_2(:,1),k_df4_2(:,2),'LineWidth',2,'LineStyle','-.','Color',[0.15 0.15 0.15]);
plot(k_df6(:,1),k_df6(:,2),'LineWidth',2,'LineStyle','-','Color',[0.30 0.30 0.30])
plot(k_df6_2(:,1),k_df6_2(:,2),'LineWidth',2,'LineStyle','-.','Color',[0.30 0.30 0.30]);
%plot(k_df2(:,1),k_df2(:,2),'LineWidth',2,'LineStyle','-','Color',[0 0 0]);
```

```
%plot(k_df2_2(:,1),k_df2_2(:,2),'LineWidth',2,'LineStyle','-.','Color',[0 0 0]);
%plot(k_df4(:,1),k_df4(:,2),'LineStyle','-','Color',[0.5 0.5 0.5]);
%plot(k_df4_2(:,1),k_df4_2(:,2),'LineWidth',2,'LineStyle','-.','Color',[0.15 0.15 0.15]);
%plot(k_df6(:,1),k_df6(:,2),'LineWidth',2,'LineStyle','-','Color',[0.45 0.45 0.45]);
%plot(k_df6_2(:,1),k_df6_2(:,2),'LineWidth',2,'LineStyle','-.','Color',[0.30 0.30 0.30]);
[kn_lit1 kn_lit2] = kn_lit_pat77;
plot(kn_lit1(:,1),kn_lit1(:,2),'LineStyle','none','Marker','d',...
    'MarkerFaceColor',[0 0 0],...
    'MarkerEdgeColor',[0 0 0],...
    'MarkerSize',8);
plot(kn_lit2(:,1),kn_lit2(:,2),'LineWidth',2,'MarkerSize',2,'LineStyle','--','Color',[0. 0. 0.]);
plot([625 625 675 675],[-100 5 5 -100],'LineStyle',':','Color',[0 0 0]);
plot([1000 1000],[-100 1000],'LineStyle',':','Color',[0 0 0]);
ylabel('Absorption, k, [cm ^-^1]','FontName','Times New Roman',...
    'FontSize',12);
xlabel('Wavelength, \lambda, [nm]','FontName','Times New Roman',...
    'FontSize',12);
set(subplot2,'Xlim',[400 2500],'Ylim',[0 15],...
    'FontName','Times New Roman','FontSize',12,...
    'XTick',[400 700 1000 1300 1600 1900 2200 2500],...
    'XTickLabel',[400 700 1000 1300 1600 1900 2200 2500],...
    'YTick',[0 2.5 5.0 7.5 10 12.5 15],...
    'YTickLabel',[0 2.5 5.0 7.5 10 12.5 15]);
%set(subplot1,'Ylim',[0 100],'Xlim',[400 2500],...
%    'FontName','Times New Roman','FontSize',12,...
%    'XTick',[400 700 1000 1300 1600 1900 2200 2500],...
%    'XTickLabel',[400 700 1000 1300 1600 1900 2200 2500],...
%    'YTick',[0 20 40 60 80 100],...
%    'YTickLabel',[0 20 40 60 80 100]);
set(subplot2,'LineStyleOrder',{'-','-.','-','-.','-','-.','d','-.'})
  legend1 = legend(subplot2,'show');
```

```
  set(legend1,'String',{'2 Percent Kaolinite^1' '2 Percent Kaolinite^2' ...
      '4 Percent Kaolinite^1' '4 Percent Kaolinite^2' ...
      '6 Percent Kaolinite^1' '6 Percent Kaolinite^2' ...
      'Kaolinite^3',...
      'Kaolinite^4'},...
      'LineStyleOrder',{'-','-.','-','-.','-','-.','d','-.'},...
     'FontName','Times New Roman',...
     'FontSize',9);
 % set(legend1,'LineStyleOrder',{'-','-','-','-','-','-'})
  set(legend1,'EdgeColor',[1 1 1],'YColor',[1 1 1],'XColor',[1 1 1],...
   'Position',[0.590 0.34 0.1 0.2],...
   'Color','none',...
   'LineStyleOrder',{'-','-.','-','-.','-','-.','d','-.'},...
   'FontSize',9,...
   'PlotBoxAspectRatioMode','manual',...
   'PlotBoxAspectRatio',[1 0.8 1]);
text1 = annotation(figure2,'textbox',...
   'Position',[0.14 0.82 0.1 0.1],...
   'String',{'Ocean Optics CCD'},...
   'Color',[0 0 0],...
   'LineWidth',0,...
   'EdgeColor',[1 1 1],...
   'FontName','Times New Roman',...
   'FontSize',9,...
   'LineStyle','none');
text2 = annotation(figure2,'textbox',...
   'Position',[0.35 0.82 0.1 0.1],...
   'String',{'Nicolet FTIR InGaAs (KCl Beam Splitter)'},...
   'Color',[0 0 0],...
   'LineWidth',0,...
   'EdgeColor',[1 1 1],...
```

```
    'FontName','Times New Roman',...
    'FontSize',9,...
    'LineStyle','none');
text3 = annotation(figure2,'textbox',...
    'Position',[0.14 0.45 0.1 0.1],...
    'String',{'Contamination From'},...
    'Color',[0 0 0],...
    'LineWidth',0,...
    'EdgeColor',[1 1 1],...
    'FontName','Times New Roman',...
    'FontSize',9,...
    'LineStyle','none');
text4 = annotation(figure2,'textbox',...
    'Position',[0.18 0.40 0.1 0.1],...
    'String',{'Red Laser'},...
    'Color',[0 0 0],...
    'LineWidth',0,...
    'EdgeColor',[1 1 1],...
    'FontName','Times New Roman',...
    'FontSize',9,...
    'LineStyle','none');
text5 = annotation(figure2,'textbox',...
    'Position',[0.35 0.78 0.1 0.1],...
    'String',{'^1Calculated from Literature Value of KBr (Hakim et al. 2013)'},...
    'Color',[0 0 0],...
    'LineWidth',0,...
    'EdgeColor',[1 1 1],...
    'FontName','Times New Roman',...
    'FontSize',9,...
    'LineStyle','none');
text5 = annotation(figure2,'textbox',...
```

```
    'Position',[0.35 0.74 0.1 0.1],...
    'String',{'^2Calculated using Patterson et al. 1977'},...
    'Color',[0 0 0],...
    'LineWidth',0,...
    'EdgeColor',[1 1 1],...
    'FontName','Times New Roman',...
    'FontSize',9,...
    'LineStyle','none');
text6 = annotation(figure2,'textbox',...
    'Position',[0.505 0.65 0.1 0.1],...
    'String',{'^4(Lindberg and Laude 1974)'},...
    'Color',[0 0 0],...
    'LineWidth',0,...
    'EdgeColor',[1 1 1],...
    'FontName','Times New Roman',...
    'FontSize',9,...
    'LineStyle','none');
text7 = annotation(figure2,'textbox',...
    'Position',[0.35 0.70 0.1 0.1],...
    'String',{'^3(Schober and Lohmannsrobe 2000)'},...
    'Color',[0 0 0],...
    'LineWidth',0,...
    'EdgeColor',[1 1 1],...
    'FontName','Times New Roman',...
    'FontSize',9,...
    'LineStyle','none');
%text1(boxoff);
%text2(boxoff);
legend('boxoff');
set(subplot2,'Color','none');
plot([2190 2190 2215 2190 2190],[0.25 1.75 1.75 0.25 0.25],'-','Color',[0 0 0])
```

```
handaxes2 = axes('Position',[0.40 0.40 0.05 0.30]);
%set(
hold(handaxes2,'on');
set(handaxes2,'aspectratio',[1 8])
plot(k_df2(:,1),k_df2(:,2),'LineWidth',2,'LineStyle','-','Color',[0 0 0]);
plot(k_df2_2(:,1),k_df2_2(:,2),'LineWidth',2,'LineStyle','-.','Color',[0 0 0]);
plot(k_df4(:,1),k_df4(:,2),'LineWidth',2,'LineStyle','-','Color',[0.15 0.15 0.15]);
plot(k_df4_2(:,1),k_df4_2(:,2),'LineWidth',2,'LineStyle','-.','Color',[0.3 0.3 0.3]);
plot(k_df6(:,1),k_df6(:,2),'LineWidth',2,'LineStyle','-','Color',[0.45 0.45 0.45]);
plot(k_df6_2(:,1),k_df6_2(:,2),'LineWidth',2,'LineStyle','-.','Color',[0.45 0.45 0.45]);
set(handaxes2,'xlim',[2205 2215],...
   'ylim',[0.5 1.75],'YTick',[0.5 1.75],'XTick',[2205 2215],...
   'YTickLabel',[0.5 1.75],'XTickLabel',[2205 2215],'FontSize',9,'FontName','Times New
       Roman');
 ylabel('Absorption','FontSize',9,'FontName','Times New Roman')
 xlabel('Wavelength','FontSize',9,'FontName','Times New Roman')
```

B.3.3. ***KUBELKA.m***

A MATLAB executable written to compute the Kubelka-Munk transform on reflected UV-NIR data. Programmatic inputs included the observed reflectance spectra. Program was executed as a subroutine to other scripts including kaolin_absorption.m

Invocation: *[kmf(:, :)] = KUBELKA(reflect(:,1 :2)] ;*

Source Code:

```
function [KMF] = KUBELKA(REFLECT_DATA)
KMF(:,1) = REFLECT_DATA(:,1);
REFLECT_DATA(:,2) = REFLECT_DATA(:,2)./100;
%KMF(:,2) = ((1.-(REFLECT(:,2))).^2)./(2.*(REFLECT(:,2)));
KMF(:,2) = ((1-REFLECT_DATA(:,2)).^2)./(2.*REFLECT_DATA(:,2));
end
```

B.3.4. ***KBR_reflect_fig.m***

A MATLAB script written to generate a KBr reflectance spectra for publication. The program was executed using the MATLAB GUI by pressing the F5 button. The output figure was exported as an encapsulated post script.

Invocation: MATLAB GUI (F5)

Source Code:

```
clear,clc,close('all');
kbr = KBR_REFLECT;
   figure1 = figure('units','inches','pos',[0 0 2.67 1.08]);
   %subplot1 = subplot(3,3,1)
   figure1 = plot(kbr(:,1),kbr(:,2),'-k');
   set(figure1,'FontName','TimesNewRoman','FontSize',8,...
      'Ylim',[60 100],'Xlim',[400 2500],...
   'FontName','Times New Roman','FontSize',8,...
   'XTick',[400 1450 2500],...
   'XTickLabel',[400 1450 2500],...
   'YTick',[50 75 100],...
   'YTickLabel',[50 75 100]);
   xlabel('Wavelength, \lambda [nm]',...
      'FontName','TimesNewRoman','FontSize',8)
   ylabel('Reflection, R_\infty [%]',...
      'FontName','TimesNewRoman','FontSize',8)
```

B.3.5. ***Flow_fig.m***

A MATLAB script written to generate a figure illustrating the work flow in obtaining soil optical parameters from reflectance data for publication. Programmatic inputs are fixed (i.e. are set in the code) and included Donna Fill and KBr reflectance date. It should be noted that this

script was written to function only with the included data. The program was executed using the MATLAB GUI by pressing the F5 key.

Invocation: MATLAB GUI (F5)

Source Code:

```
%FIGURES FOR RAC
clear,clc,fclose('all'),close('all');
%3 x 2 subplot
figure1 = figure('units','inches','pos',[0 0 6.5 4]);
%figure 1
  %FIGURES FOR RAC
%3 x 3 subplot
    %figure 7
    %KMF FOR KBR (100)
        kbr = KBR_REFLECT;
        kmf = KUBELKA(kbr);
        skbr(:,1) = kmf(:,1);
        skbr(:,2) = (1*10^-4).\kmf(:,2);
        kmf = KUBELKA(IL4_REFLECT)
        kill = kmf(:,1)
        kill(:,2) = skbr(:,2).*kmf(:,2)./0.02;
        kill(:,2) = kill(:,2)./kill(:,2)*1e-4
    subplot8 = subplot(3,3,8)
    plot(kill(:,1),kill(:,2),'-k');
    set(subplot8','FontName','TimesNewRoman','FontSize',8,...
        'Ylim',[0 2e-4],'Xlim',[400 2500],...
    'FontName','Times New Roman','FontSize',8,...
    'XTick',[400 1450 2500],...
    'XTickLabel',[400 1450 2500],...
    'YTick',[0 1e-4 2e-4],...
```

```
'YTickLabel',[{'0'} {'1e-4'} {'2e-4'}]);
xlabel('Wavelength, \lambda [nm]',...
    'FontName','TimesNewRoman','FontSize',8)
ylabel('Absorsption, k [cm^-^1]',...
    'FontName','TimesNewRoman','FontSize',8)
```

B.3.6. ***u_donna_absorb.m***

A MATLAB script written to compute and visualize the absorption spectra for Donna Fill. Programmatic inputs included the 2 percent (DF2_REFLECT), 4 percent (DF4_REFLECT), and 6 percent (DF6_Reflect) mass fraction Donna Fill samples. An additional input was the 100 percent KBr reflectance spectra (KBR_REFLECT). The program was executed using the MATLAB GUI by pressing the F5 key.

Invocation: MATLAB GUI (F5)

Source Code:

```
%NEW FIGURE PLOT SCRIPT BECAUSE EXCEL KEEPS CRASHING
%DONNA FILL
clear
clc
close('all');
%%file list
[KBR] = KBR_REFLECT;
[DF2] = DF2_REFLECT;
[DF4] = DF4_REFLECT;
[DF6] = DF6_REFLECT;
figure1 = figure('units','inches','pos',[0 0 6.5 3]);
subplot1 = subplot(1,1,1)
box(subplot1,'on');
hold(subplot1,'all');
```

```
plot(KBR(:,1),KBR(:,2),'LineWidth',2,'LineStyle','-','Color',[0 0 0])
plot(DF2(:,1),DF2(:,2),'LineWidth',2,'LineStyle','-','Color',[0.15 0.15 0.15])
plot(DF4(:,1),DF4(:,2),'LineWidth',2,'LineStyle','-','Color',[0.30 0.30 0.30])
plot(DF6(:,1),DF6(:,2),'LineWidth',2,'LineStyle','-','Color',[0.45 0.45 0.45])
ylabel('Reflectance Ratio, R_\infty, [I/I_0]','FontName','Times New Roman',...
    'FontSize',12);
xlabel('Wavelength, \lambda, [nm]','FontName','Times New Roman',...
    'FontSize',12);
set(subplot1,'Ylim',[0 100],'Xlim',[400 2500],...
    'FontName','Times New Roman','FontSize',12,...
    'XTick',[400 700 1000 1300 1600 1900 2200 2500],...
    'XTickLabel',[400 700 1000 1300 1600 1900 2200 2500],...
    'YTick',[0 20 40 60 80 100],...
    'YTickLabel',[0 20 40 60 80 100]);
%   legend1 = legend(subplot1,'show');
%   set(legend1,'String',{'Donna Fill' 'Illite' 'Kaolinite'},...
%     'FontName','Times New Roman',...
%     'FontSize',8);
%   set(legend1,'LineStyleOrder',{'d','o','s'})
%   set(legend1,'EdgeColor',[1 1 1],'YColor',[1 1 1],'XColor',[1 1 1],...
%    'Position',[0.328143513497517 0.631983077468714 0.06003716216216216
          0.0793246187363835],...
%    'LineStyleOrder',{'d','s','o'},...
%    'FontSize',8);
kmf_kbr = KUBELKA(KBR);
kmf_df2 = KUBELKA(DF2);
kmf_df4 = KUBELKA(DF4);
kmf_df6 = KUBELKA(DF6);
%%
k_kbr = 10e-4;
s_kbr = k_kbr.\kmf_kbr(:,2);
```

```
k_df2(:,1) = kmf_df2(:,1);
k_df4(:,1) = kmf_df4(:,1);
k_df6(:,1) = kmf_df6(:,1);
k_df2(:,2) = (1/.02).*(0.98*kmf_df2(:,2).*s_kbr(:,1));
k_df4(:,2) = (1/.04).*(0.96*kmf_df4(:,2).*s_kbr(:,1));
k_df6(:,2) = (1/.06).*(0.94*kmf_df6(:,2).*s_kbr(:,1));
k_df2_2(:,1) = kmf_df2(:,1);
k_df4_2(:,1) = kmf_df4(:,1);
k_df6_2(:,1) = kmf_df6(:,1);
k_df2_2(:,2) = (1/.02).*s_kbr(:,1).*(kmf_df2(:,2)-kmf_kbr(:,2));
k_df4_2(:,2) = (1/.04).*s_kbr(:,1).*(kmf_df4(:,2)-kmf_kbr(:,2));
k_df6_2(:,2) = (1/.06).*s_kbr(:,1).*(kmf_df6(:,2)-kmf_kbr(:,2));
[ill1 ill2]= illite_gil74;
figure2 = figure('units','inches','pos',[0 0 6.5 3]);
subplot2 = subplot(1,1,1)
box(subplot2,'on');
hold(subplot2,'all');
%plot(k_df2(:,1),k_df2(:,2),'LineStyle','-','Color',[0 0 0])
%plot(k_df4(:,1),k_df4(:,2),'LineStyle','-','Color',[0.15 0.15 0.15])
%plot(k_df6(:,1),k_df6(:,2),'LineStyle','-','Color',[0.30 0.30 0.30])
plot(k_df2(:,1),k_df2(:,2),'LineWidth',2,'LineStyle','-','Color',[0 0 0]);
plot(k_df2_2(:,1),k_df2_2(:,2),'LineWidth',2,'LineStyle','-.','Color',[0 0 0]);
plot(k_df4(:,1),k_df4(:,2),'LineWidth',2,'LineStyle','-','Color',[0.15 0.15 0.15]);
plot(k_df4_2(:,1),k_df4_2(:,2),'LineWidth',2,'LineStyle','-.','Color',[0.15 0.15 0.15]);
plot(k_df6(:,1),k_df6(:,2),'LineWidth',2,'LineStyle','-','Color',[0.45 0.45 0.45]);
plot(k_df6_2(:,1),k_df6_2(:,2),'LineWidth',2,'LineStyle','-.','Color',[0.45 0.45 0.45]);
%plot(ill1(:,1),ill1(:,2),'LineStyle',':','Color',[0.75 0.75 0.75]);
%plot(ill2(:,1),ill2(:,2),'LineStyle',':','Color',[0.75 0.75 0.75]);
plot([625 625 675 675],[-100 100 100 -100],'LineStyle',':','Color',[0 0 0]);
plot([2150 2150 2250 2250 2150],[1 35 35 1 1],'LineStyle','-','Color',[0 0 0]);
plot([1000 1000],[-100 1000],'LineStyle',':','Color',[0 0 0]);
```

```
ylabel('Soil Absorption, k _s_o_i_l, [cm ^-^1]','FontName','Times New Roman',...
    'FontSize',12);
xlabel('Wavelength, \lambda, [nm]','FontName','Times New Roman',...
    'FontSize',12);
set(subplot2,'Xlim',[400 2500],'Ylim',[0 300],...
    'FontName','Times New Roman','FontSize',12,...
    'XTick',[400 700 1000 1300 1600 1900 2200 2500],...
    'XTickLabel',[400 700 1000 1300 1600 1900 2200 2500],...
    'YTick',[0 50 100 150 200 250 300],...
    'YTickLabel',[0 50 100 150 200 250 300]);
%set(subplot1,'Ylim',[0 100],'Xlim',[400 2500],...
%    'FontName','Times New Roman','FontSize',12,...
%    'XTick',[400 700 1000 1300 1600 1900 2200 2500],...
%    'XTickLabel',[400 700 1000 1300 1600 1900 2200 2500],...
%    'YTick',[0 20 40 60 80 100],...
%    'YTickLabel',[0 20 40 60 80 100]);
  legend1 = legend(subplot2,'show');
  set(legend1,'String',{'2% Donna Fill^1' '2% Donna Fill^2' ...
      '4% Donna Fill^1' '4% Donna Fill^2' ...
      '6% Donna Fill^1' '6% Donna Fill^2' ...
     },...
     'FontName','Times New Roman',...
     'FontSize',9);
 % set(legend1,'LineStyleOrder',{'-','-','-','-','-','-'})
  set(legend1,'EdgeColor',[1 1 1],'YColor',[1 1 1],'XColor',[1 1 1],...
    'Position',[0.705 0.38 0.1 0.2],...
    'Color','none',...
    'LineStyleOrder',{'d','s','o'},...
    'FontSize',9,...
    'PlotBoxAspectRatioMode','manual',...
    'PlotBoxAspectRatio',[1 0.6 1]);
```

```
text1 = annotation(figure2,'textbox',...
    'Position',[0.14 0.8 0.1 0.1],...
    'String',{'Ocean Optics CCD'},...
    'Color',[0 0 0],...
    'LineWidth',0,...
    'EdgeColor',[1 1 1],...
    'FontName','Times New Roman',...
    'FontSize',9,...
    'LineStyle','none');
text2 = annotation(figure2,'textbox',...
    'Position',[0.45 0.8 0.1 0.1],...
    'String',{'Nicolet FTIR InGaAs (KCl Beam Splitter)'},...
    'Color',[0 0 0],...
    'LineWidth',0,...
    'EdgeColor',[1 1 1],...
    'FontName','Times New Roman',...
    'FontSize',9,...
    'LineStyle','none');
text3 = annotation(figure2,'textbox',...
    'Position',[0.14 0.45 0.1 0.1],...
    'String',{'Contamination From'},...
    'Color',[0 0 0],...
    'LineWidth',0,...
    'EdgeColor',[1 1 1],...
    'FontName','Times New Roman',...
    'FontSize',9,...
    'LineStyle','none');
text4 = annotation(figure2,'textbox',...
    'Position',[0.18 0.40 0.1 0.1],...
    'String',{'Red Laser'},...
    'Color',[0 0 0],...
```

```
    'LineWidth',0,...
    'EdgeColor',[1 1 1],...
    'FontName','Times New Roman',...
    'FontSize',9,...
    'LineStyle','none');
text5 = annotation(figure2,'textbox',...
    'Position',[0.35 0.755 0.1 0.1],...
    'String',{'^1Calculated using Hakim et al. (2013) KBr value'},...
    'Color',[0 0 0],...
    'LineWidth',0,...
    'EdgeColor',[1 1 1],...
    'FontName','Times New Roman',...
    'FontSize',9,...
    'LineStyle','none');
text5 = annotation(figure2,'textbox',...
    'Position',[0.35 0.71 0.1 0.1],...
    'String',{'^2Calculated using Patterson et al. (1977) method'},...
    'Color',[0 0 0],...
    'LineWidth',0,...
    'EdgeColor',[1 1 1],...
    'FontName','Times New Roman',...
    'FontSize',9,...
    'LineStyle','none');
text6 = annotation(figure2,'textbox',...
    'Position',[0.72 0.22 0.1 0.1],...
    'String',{'Spectral Feature'},...
    'Color',[0 0 0],...
    'LineWidth',0,...
    'EdgeColor',[1 1 1],...
    'FontName','Times New Roman',...
    'FontSize',9,...
```

```
    'LineStyle','none');
%text1(boxoff);
%text2(boxoff);
legend('boxoff');
set(subplot2,'Color','none');
%set(subplot2,'Color','none');
plot([1365 1365 1405 1405 1365],[10 90 90 10 10],'-','Color',[0 0 0])
handaxes2 = axes('Position',[0.46 0.50 0.06 0.20]);
%set(
hold(handaxes2,'on');
axis('equal')
plot(k_df2(:,1),k_df2(:,2),'LineWidth',2,'LineStyle','-','Color',[0 0 0]);
plot(k_df2_2(:,1),k_df2_2(:,2),'LineWidth',2,'LineStyle','-.','Color',[0 0 0]);
plot(k_df4(:,1),k_df4(:,2),'LineWidth',2,'LineStyle','-','Color',[0.15 0.15 0.15]);
plot(k_df4_2(:,1),k_df4_2(:,2),'LineWidth',2,'LineStyle','-.','Color',[0.3 0.3 0.3]);
plot(k_df6(:,1),k_df6(:,2),'LineWidth',2,'LineStyle','-','Color',[0.45 0.45 0.45]);
plot(k_df6_2(:,1),k_df6_2(:,2),'LineWidth',2,'LineStyle','-.','Color',[0.45 0.45 0.45]);
set(handaxes2,'xlim',[1365 1405],...
    'ylim',[10 70],'YTick',[10 70],'XTick',[1365 1405],'FontSize',9,'FontName','Times New Roman')
 ylabel('Absorption','FontSize',9,'FontName','Times New Roman')
 xlabel('Wavelength','FontSize',9,'FontName','Times New Roman')
```

B.3.7. ***u_illite_absorb.m***

A MATLAB script written to compute and visualize the absorption spectra for Donna Fill. Programmatic inputs included the 2 percent (DF2_REFLECT), 4 percent (DF4_REFLECT), and 6 percent (DF6_Reflect) mass fraction Donna Fill samples. An additional input was the 100 percent KBr reflectance spectra (KBR_REFLECT). The program was executed using the MATLAB GUI by pressing the F5 key.

Invocation: MATLAB GUI (F5)

Source Code:

```
%NEW FIGURE PLOT SCRIPT BECAUSE EXCEL KEEPS CRASHING
%DONNA FILL
clear
clc
close('all');
%%file list
[KBR] = KBR_REFLECT;
[DF2] = IL2_REFLECT;
[DF4] = IL4_REFLECT;
[DF6] = IL6_REFLECT;
figure1 = figure('units','inches','pos',[0 0 6.5 3]);
subplot1 = subplot(1,1,1)
box(subplot1,'on');
hold(subplot1,'all');
plot(KBR(:,1),KBR(:,2),'LineWidth',2,'LineStyle','-','Color',[0 0 0])
plot(DF2(:,1),DF2(:,2),'LineStyle','-','Color',[0.15 0.15 0.15])
plot(DF4(:,1),DF4(:,2),'LineStyle','-','Color',[0.30 0.30 0.30])
plot(DF6(:,1),DF6(:,2),'LineStyle','-','Color',[0.45 0.45 0.45])
ylabel('Reflectance Ratio, R_\infty, [I/I_0]','FontName','Times New Roman',...
   'FontSize',12);
xlabel('Wavelength, \lambda, [nm]','FontName','Times New Roman',...
   'FontSize',12);
set(subplot1,'Ylim',[0 100],'Xlim',[400 2500],...
   'FontName','Times New Roman','FontSize',12,...
   'XTick',[400 700 1000 1300 1600 1900 2200 2500],...
   'XTickLabel',[400 700 1000 1300 1600 1900 2200 2500],...
   'YTick',[0 20 40 60 80 100],...
   'YTickLabel',[0 20 40 60 80 100]);
%   legend1 = legend(subplot1,'show');
```

```
%   set(legend1,'String',{'Donna Fill' 'Illite' 'Kaolinite'},...
%     'FontName','Times New Roman',...
%     'FontSize',8);
%   set(legend1,'LineStyleOrder',{'d','o','s'})
%   set(legend1,'EdgeColor',[1 1 1],'YColor',[1 1 1],'XColor',[1 1 1],...
%    'Position',[0.328143513497517 0.631983077468714 0.06003716216216216
          0.0793246187363835],...
%    'LineStyleOrder',{'d','s','o'},...
%    'FontSize',8);
kmf_kbr = KUBELKA(KBR);
kmf_df2 = KUBELKA(DF2);
kmf_df4 = KUBELKA(DF4);
kmf_df6 = KUBELKA(DF6);
%%
k_kbr = 10e-4;
s_kbr = k_kbr.\kmf_kbr(:,2);
k_df2(:,1) = kmf_df2(:,1);
k_df4(:,1) = kmf_df4(:,1);
k_df6(:,1) = kmf_df6(:,1);
k_df2(:,2) = (1/.02).*(0.98*kmf_df2(:,2).*s_kbr(:,1));
k_df4(:,2) = (1/.04).*(0.96*kmf_df4(:,2).*s_kbr(:,1));
k_df6(:,2) = (1/.06).*(0.94*kmf_df6(:,2).*s_kbr(:,1));
k_df2_2(:,1) = kmf_df2(:,1);
k_df4_2(:,1) = kmf_df4(:,1);
k_df6_2(:,1) = kmf_df6(:,1);
k_df2_2(:,2) = (1/.02).*s_kbr(:,1).*(kmf_df2(:,2)-kmf_kbr(:,2));
k_df4_2(:,2) = (1/.04).*s_kbr(:,1).*(kmf_df4(:,2)-kmf_kbr(:,2));
k_df6_2(:,2) = (1/.06).*s_kbr(:,1).*(kmf_df6(:,2)-kmf_kbr(:,2));
[ill1 ill2]= illite_gil74;
figure2 = figure('units','inches','pos',[0 0 6.5 3]);
subplot2 = subplot(1,1,1)
```

```
box(subplot2,'on');
hold(subplot2,'all');
%plot(k_df2(:,1),k_df2(:,2),'LineStyle','-','Color',[0 0 0])
%plot(k_df4(:,1),k_df4(:,2),'LineStyle','-','Color',[0.15 0.15 0.15])
%plot(k_df6(:,1),k_df6(:,2),'LineStyle','-','Color',[0.30 0.30 0.30])
plot(k_df2(:,1),k_df2(:,2),'LineWidth',2,'LineStyle','-','Color',[0 0 0]);
plot(k_df2_2(:,1),k_df2_2(:,2),'LineWidth',2,'LineStyle','-.','Color',[0 0 0]);
plot(k_df4(:,1),k_df4(:,2),'LineWidth',2,'LineStyle','-','Color',[0.15 0.15 0.15]);
plot(k_df4_2(:,1),k_df4_2(:,2),'LineWidth',2,'LineStyle','-.','Color',[0.3 0.3 0.3]);
plot(k_df6(:,1),k_df6(:,2),'LineWidth',2,'LineStyle','-','Color',[0.45 0.45 0.45]);
plot(k_df6_2(:,1),k_df6_2(:,2),'LineWidth',2,'LineStyle','-.','Color',[0.45 0.45 0.45]);
plot(ill1(:,1),ill1(:,2),'LineWidth',2,'LineStyle',':','Color',[0.45 0.45 0.45]);
plot(ill2(:,1),ill2(:,2),'LineWidth',2,'LineStyle',':','Color',[0.45 0.45 0.45]);
plot([600 600 675 675],[-100 100 100 -100],'LineStyle',':','Color',[0 0 0]);
plot([2100 2100 2300 2300 2100],[1 40 40 1 1],'LineStyle','-','Color',[0 0 0]);
plot([1000 1000],[-100 1000],'LineStyle',':','Color',[0 0 0]);
ylabel('Soil Absorption, k _s_o_i_l, [cm ^-^1]','FontName','Times New Roman',...
   'FontSize',12);
xlabel('Wavelength, \lambda, [nm]','FontName','Times New Roman',...
   'FontSize',12);
set(subplot2,'Xlim',[400 2500],'Ylim',[0 300],...
   'FontName','Times New Roman','FontSize',12,...
   'XTick',[400 700 1000 1300 1600 1900 2200 2500],...
   'XTickLabel',[400 700 1000 1300 1600 1900 2200 2500],...
   'YTick',[0 50 100 150 200 250 300],...
   'YTickLabel',[0 50 100 150 200 250 300]);
%set(subplot1,'Ylim',[0 100],'Xlim',[400 2500],...
%   'FontName','Times New Roman','FontSize',12,...
%   'XTick',[400 700 1000 1300 1600 1900 2200 2500],...
%   'XTickLabel',[400 700 1000 1300 1600 1900 2200 2500],...
%   'YTick',[0 20 40 60 80 100],...
```

```
%    'YTickLabel',[0 20 40 60 80 100]);
   legend1 = legend(subplot2,'show');
   set(legend1,'String',{'2% Illite^1' '2% Illite^2' ...
       '4% Illite^1' '4% Illite^2' ...
       '6% Illite^1' '6% Illite^2' ...
       'Illite (Gillespie et al. 1974)'},...
      'FontName','Times New Roman',...
      'FontSize',9);
  % set(legend1,'LineStyleOrder',{'-','-','-','-','-','-'})
   set(legend1,'EdgeColor',[1 1 1],'YColor',[1 1 1],'XColor',[1 1 1],...
    'Position',[0.705 0.45 0.1 0.2],...
    'Color','none',...
    'LineStyleOrder',{'d','s','o'},...
    'FontSize',9,...
    'PlotBoxAspectRatioMode','manual',...
    'PlotBoxAspectRatio',[1 0.6 1]);
text1 = annotation(figure2,'textbox',...
    'Position',[0.14 0.8 0.1 0.1],...
    'String',{'Ocean Optics CCD'},...
    'Color',[0 0 0],...
    'LineWidth',0,...
    'EdgeColor',[1 1 1],...
    'FontName','Times New Roman',...
    'FontSize',9,...
    'LineStyle','none');
text2 = annotation(figure2,'textbox',...
    'Position',[0.45 0.8 0.1 0.1],...
    'String',{'Nicolet FTIR InGaAs (KCl Beam Splitter)'},...
    'Color',[0 0 0],...
    'LineWidth',0,...
    'EdgeColor',[1 1 1],...
```

```
    'FontName','Times New Roman',...
    'FontSize',9,...
    'LineStyle','none');
text3 = annotation(figure2,'textbox',...
    'Position',[0.14 0.45 0.1 0.1],...
    'String',{'Contamination From'},...
    'Color',[0 0 0],...
    'LineWidth',0,...
    'EdgeColor',[1 1 1],...
    'FontName','Times New Roman',...
    'FontSize',9,...
    'LineStyle','none');
text4 = annotation(figure2,'textbox',...
    'Position',[0.18 0.40 0.1 0.1],...
    'String',{'Red Laser'},...
    'Color',[0 0 0],...
    'LineWidth',0,...
    'EdgeColor',[1 1 1],...
    'FontName','Times New Roman',...
    'FontSize',9,...
    'LineStyle','none');
text5 = annotation(figure2,'textbox',...
    'Position',[0.35 0.755 0.1 0.1],...
    'String',{'^1Calculated using Hakim et al. (2013) KBr value'},...
    'Color',[0 0 0],...
    'LineWidth',0,...
    'EdgeColor',[1 1 1],...
    'FontName','Times New Roman',...
    'FontSize',9,...
    'LineStyle','none');
text5 = annotation(figure2,'textbox',...
```

```
    'Position',[0.35 0.71 0.1 0.1],...
    'String',{'^2Calculated using Patterson et al. 1977'},...
    'Color',[0 0 0],...
    'LineWidth',0,...
    'EdgeColor',[1 1 1],...
    'FontName','Times New Roman',...
    'FontSize',9,...
    'LineStyle','none');
text6 = annotation(figure2,'textbox',...
    'Position',[0.72 0.22 0.1 0.1],...
    'String',{'Spectral Feature'},...
    'Color',[0 0 0],...
    'LineWidth',0,...
    'EdgeColor',[1 1 1],...
    'FontName','Times New Roman',...
    'FontSize',10,...
    'LineStyle','none');
%text1(boxoff);
%text2(boxoff);
legend('boxoff');
%set(subplot2,'Color','none');
plot([1365 1365 1405 1405 1365],[10 90 90 10 10],'-','Color',[0 0 0])
handaxes2 = axes('Position',[0.44 0.50 0.10 0.20]);
%set(
hold(handaxes2,'on');
set(handaxes2,'AspectRatio',[2 2]);
plot(k_df2(:,1),k_df2(:,2),'LineWidth',2,'LineStyle','-','Color',[0 0 0]);
plot(k_df2_2(:,1),k_df2_2(:,2),'LineWidth',2,'LineStyle','-.','Color',[0 0 0]);
plot(k_df4(:,1),k_df4(:,2),'LineWidth',2,'LineStyle','-','Color',[0.15 0.15 0.15]);
plot(k_df4_2(:,1),k_df4_2(:,2),'LineWidth',2,'LineStyle','-.','Color',[0.3 0.3 0.3]);
plot(k_df6(:,1),k_df6(:,2),'LineWidth',2,'LineStyle','-','Color',[0.45 0.45 0.45]);
```

```
plot(k_df6_2(:,1),k_df6_2(:,2),'LineWidth',2,'LineStyle','-.','Color',[0.45 0.45 0.45]);
set(handaxes2,'xlim',[1365 1405],...
    'ylim',[10 70],'YTick',[10 70],'XTick',[1365 1405],'FontSize',9,'FontName','Times New Roman')
 ylabel('Absorption','FontSize',9,'FontName','Times New Roman')
 xlabel('Wavelength','FontSize',9,'FontName','Times New Roman')
```

B.3.8. ***u_fig_5_gen.m***

A MATLAB script written to visualize the two percent mass fraction samples of Donna Fill, illite, and kaolinite. Programmatic inputs included the Donna Fill, illite, and kaolinite reflectance spectrum. The program was executed using the MATLAB GUI by pressing the F5 key.

Invocation: MATLAB GUI (F5)

Source Code:

```
%NEW FIGURE PLOT SCRIPT BECAUSE EXCEL KEEPS CRASHING
%DONNA FILL
clear
clc
close('all');
%%file list
[KBR] = KBR_REFLECT;
[DF2] = DF2_REFLECT;
[IL2] = IL2_REFLECT;
[KN2] = KN2_REFLECT;
KN2(:,2) = 100.*KN2(:,2);
figure1 = figure('units','inches','pos',[0 0 6.5 3]);
subplot1 = subplot(1,1,1)
box(subplot1,'on');
hold(subplot1,'all');
```

```
plot(KBR(:,1),KBR(:,2),'LineWidth',2,'LineStyle','-','Color',[0.25 0.25 0.25])
plot(DF2(:,1),DF2(:,2),'LineWidth',2,'LineStyle','-','Color',[0 0 0])
plot(IL2(:,1),IL2(:,2),'LineWidth',2,'LineStyle','-','Color',[0.45 0.45 0.45])
plot(KN2(:,1),KN2(:,2),'LineWidth',2,'LineStyle','-','Color',[0.65 0.65 0.65])
plot([1370 1370 1440 1440 1370],[50 95 95 50 50],'LineWidth',0.75,'LineStyle',':',...
'Color',[0 0 0])
plot([2100 2100 2300 2300 2100],[50 97 97 50 50],'LineWidth',0.75,'LineStyle',':','Color',...
[0 0 0])
plot([625 625 675 675 625],[45 97 97 45 45],'LineStyle',':','Color',[0 0 0]);
plot([1000 1000],[-10 110],'LineStyle',':','Color',[0 0 0]);
%plot(KBR(:,1),KBR(:,2),'LineStyle','-','Color','r')
%plot(DF2(:,1),DF2(:,2),'LineStyle','-','Color','g')
%plot(IL2(:,1),IL2(:,2),'LineStyle','-','Color','b')
%plot(KN2(:,1),KN2(:,2),'LineStyle','-','Color','c')
ylabel('Reflectance Ratio, R_\infty, [I/I_0]','FontName','Times New Roman',...
    'FontSize',12);
xlabel('Wavelength, \lambda, [nm]','FontName','Times New Roman',...
    'FontSize',12);
set(subplot1,'Ylim',[0 100],'Xlim',[400 2500],...
    'FontName','Times New Roman','FontSize',12,...
    'XTick',[400 700 1000 1300 1600 1900 2200 2500],...
    'XTickLabel',[400 700 1000 1300 1600 1900 2200 2500],...
    'YTick',[0 20 40 60 80 100],...
    'YTickLabel',[0 20 40 60 80 100]);
  legend1 = legend(subplot1,'show');
  set(legend1,'String',{'KBR' ...
      'Donna Fill' ...
      'Illite' ...
      'Kaolinite'},...
     'FontName','Times New Roman',...
     'FontSize',10);
```

```
  % set(legend1,'LineStyleOrder',{'-','-','-','-','-','-'})
   set(legend1,'EdgeColor',[1 1 1],'YColor',[0 0 0],'XColor',[0 0 0],...
    'Position',[0.63 0.25 0.1 0.2],...
    'Color','none',...
    'LineStyleOrder',{'d','s','o'},...
    'FontSize',10,...
    'PlotBoxAspectRatioMode','manual',...
    'PlotBoxAspectRatio',[1 0.4 1]);
text1 = annotation(figure1,'textbox',...
    'Position',[0.13 0.15 0.1 0.1],...
    'String',{'Ocean Optics CCD'},...
    'Color',[0 0 0],...
    'LineWidth',0,...
    'EdgeColor',[1 1 1],...
    'FontName','Times New Roman',...
    'FontSize',10,...
    'LineStyle','none');
text2 = annotation(figure1,'textbox',...
    'Position',[0.35 0.15 0.1 0.1],...
    'String',{'Nicolet FTIR InGaAs (KCl Beam Splitter)'},...
    'Color',[0 0 0],...
    'LineWidth',0,...
    'EdgeColor',[1 1 1],...
    'FontName','Times New Roman',...
    'FontSize',10,...
    'LineStyle','none');
text3 = annotation(figure1,'textbox',...
    'Position',[0.14 0.40 0.1 0.1],...
    'String',{'Contamination From'},...
    'Color',[0 0 0],...
    'LineWidth',0,...
```

```
    'EdgeColor',[1 1 1],...
    'FontName','Times New Roman',...
    'FontSize',10,...
    'LineStyle','none');
text4 = annotation(figure1,'textbox',...
    'Position',[0.18 0.35 0.1 0.1],...
    'String',{'Red Laser'},...
    'Color',[0 0 0],...
    'LineWidth',0,...
    'EdgeColor',[1 1 1],...
    'FontName','Times New Roman',...
    'FontSize',10,...
    'LineStyle','none');
text5 = annotation(figure1,'textbox',...
    'Position',[0.42 0.45 0.1 0.1],...
    'String',{'Spectral Feature'},...
    'Color',[0 0 0],...
    'LineWidth',0,...
    'EdgeColor',[1 1 1],...
    'FontName','Times New Roman',...
    'FontSize',10,...
    'LineStyle','none');
text6 = annotation(figure1,'textbox',...
    'Position',[0.72 0.45 0.1 0.1],...
    'String',{'Spectral Feature'},...
    'Color',[0 0 0],...
    'LineWidth',0,...
    'EdgeColor',[1 1 1],...
    'FontName','Times New Roman',...
    'FontSize',10,...
    'LineStyle','none');
```

```
text7 = annotation(figure1,'textbox',...
    'Position',[0.60 0.82 0.1 0.1],...
    'String',{'100% KBr'},...
    'Color',[0 0 0],...
    'LineWidth',0,...
    'EdgeColor',[1 1 1],...
    'FontName','Times New Roman',...
    'FontSize',10,...
    'LineStyle','none');
text8 = annotation(figure1,'textbox',...
    'Position',[0.60 0.73 0.1 0.1],...
    'String',{'2% Kaolinite'},...
    'Color',[0 0 0],...
    'LineWidth',0,...
    'EdgeColor',[1 1 1],...
    'FontName','Times New Roman',...
    'FontSize',10,...
    'LineStyle','none');
text9 = annotation(figure1,'textbox',...
    'Position',[0.60 0.65 0.1 0.1],...
    'String',{'2% Donna Fill'},...
    'Color',[0 0 0],...
    'LineWidth',0,...
    'EdgeColor',[1 1 1],...
    'FontName','Times New Roman',...
    'FontSize',10,...
    'LineStyle','none');
text10 = annotation(figure1,'textbox',...
    'Position',[0.60 0.56 0.1 0.1],...
    'String',{'2% Illite'},...
    'Color',[0 0 0],...
```

```
    'LineWidth',0,...
    'EdgeColor',[1 1 1],...
    'FontName','Times New Roman',...
    'FontSize',10,...
    'LineStyle','none');
%text1(boxoff);
%text2(boxoff);
%legend('boxoff');
%set(subplot2,'Color','none');
```

B.3.9. ***u_fig_6_gen.m***

A MATLAB script written to visualize the Kubelka-Munk transform of the two percent mass fraction samples of Donna Fill, illite, and kaolinite. Programmatic inputs included the Donna Fill, illite, and kaolinite reflectance spectrum. The program was executed using the MATLAB GUI by pressing the F5 key.

Invocation: MATLAB GUI (F5)

Source Code:

```
%NEW FIGURE PLOT SCRIPT BECAUSE EXCEL KEEPS CRASHING
%DONNA FILL
clear
clc
close('all');
%%file list
[KBR] = KBR_REFLECT;
[DF2] = DF2_REFLECT;
[IL2] = IL2_REFLECT;
[KN2] = KN2_REFLECT;
KN2(:,2) = 100.*KN2(:,2);
[KBR] = KUBELKA(KBR);
```

```
[DF2] = KUBELKA(DF2);
[IL2] = KUBELKA(IL2);
[KN2] = KUBELKA(KN2);
figure1 = figure('units','inches','pos',[0 0 8.5 3]);
subplot1 = subplot(1,1,1)
box(subplot1,'on');
hold(subplot1,'all');
plot(KBR(:,1),KBR(:,2),'LineWidth',2,'LineStyle','-','Color',[0 0 0])
plot(DF2(:,1),DF2(:,2),'LineWidth',2,'LineStyle','-','Color',[0.25 0.25 0.25])
plot(IL2(:,1),IL2(:,2),'LineWidth',2,'LineStyle','-','Color',[0.5 0.50 0.50])
plot(KN2(:,1),KN2(:,2),'LineWidth',2,'LineStyle','-','Color',[0.75 0.75 0.75])
plot([625 625 675 675 625],[0 0.25 0.25 0 0],'LineStyle',':','Color',[0 0 0]);
plot([1000 1000],[-10 110],'LineStyle',':','Color',[0 0 0]);
%plot(KBR(:,1),KBR(:,2),'LineStyle','-','Color','r')
%plot(DF2(:,1),DF2(:,2),'LineStyle','-','Color','g')
%plot(IL2(:,1),IL2(:,2),'LineStyle','-','Color','b')
%plot(KN2(:,1),KN2(:,2),'LineStyle','-','Color','c')
ylabel('Reflectance Ratio, R_\infty, [I/I_0]','FontName','Times New Roman',...
    'FontSize',12);
xlabel('Wavelength, \lambda, [nm]','FontName','Times New Roman',...
    'FontSize',12);
set(subplot1,'Ylim',[0 0.5],'Xlim',[400 2500],...
    'FontName','Times New Roman','FontSize',12,...
    'XTick',[400 700 1000 1300 1600 1900 2200 2500],...
    'XTickLabel',[400 700 1000 1300 1600 1900 2200 2500],...
    'YTick',[0 0.1 0.2 0.3 0.4 0.5],...
    'YTickLabel',[0 0.1 0.2 0.3 0.4 0.5]);
  legend1 = legend(subplot1,'show');
  set(legend1,'String',{'KBR' ...
      'Donna Fill' ...
      'Illite' ...
```

```
    'Kaolinite'},...
    'FontName','Times New Roman',...
    'FontSize',12);
% set(legend1,'LineStyleOrder',{'-','-','-','-','-','-'})
set(legend1,'EdgeColor',[1 1 1],'YColor',[1 1 1],'XColor',[1 1 1],...
    'Position',[0.75 0.45 0.1 0.2],...
    'Color','none',...
    'LineStyleOrder',{'d','s','o'},...
    'FontSize',12,...
    'PlotBoxAspectRatioMode','manual',...
    'PlotBoxAspectRatio',[1 0.6 1]);

text1 = annotation(figure1,'textbox',...
    'Position',[0.13 0.80 0.1 0.1],...
    'String',{'OceanOptics CCD'},...
    'Color',[0 0 0],...
    'LineWidth',0,...
    'EdgeColor',[1 1 1],...
    'FontName','Times New Roman',...
    'FontSize',12,...
    'LineStyle','none');
text2 = annotation(figure1,'textbox',...
    'Position',[0.35 0.80 0.1 0.1],...
    'String',{'Nicolet FTIR InGaAs (KCl Beam Splitter)'},...
    'Color',[0 0 0],...
    'LineWidth',0,...
    'EdgeColor',[1 1 1],...
    'FontName','Times New Roman',...
    'FontSize',12,...
    'LineStyle','none');
text3 = annotation(figure1,'textbox',...
```

```
    'Position',[0.14 0.55 0.1 0.1],...
    'String',{'Contamination From'},...
    'Color',[0 0 0],...
    'LineWidth',0,...
    'EdgeColor',[1 1 1],...
    'FontName','Times New Roman',...
    'FontSize',10,...
    'LineStyle','none');
text4 = annotation(figure1,'textbox',...
    'Position',[0.18 0.50 0.1 0.1],...
    'String',{'Red Laser'},...
    'Color',[0 0 0],...
    'LineWidth',0,...
    'EdgeColor',[1 1 1],...
    'FontName','Times New Roman',...
    'FontSize',10,...
    'LineStyle','none');
%text1(boxoff);
%text2(boxoff);
legend('boxoff');
```

B.4. Works Cited

ASD Panalytical Inc. (2014). "RS3 and ViewSpecPro Software and Supporting Documentation," The ASD Panalytical Inc. Boulder, Colorado.

Mathworks, (2010). "Plsregress.m" Partial Least Squares Regression Software. The Mathworks Corporation, Natick, Massachusetts.

Mathworks, (2012). "Pca.m" Principle Components Analysis Software. The Mathworks Corporation, Natick, Massachusetts.

Mathworks, (2014). "The MATLAB R2014A Programming Suite and Supporting Documentation" The Mathworks Corporation, Natick, Massachusetts.

Microsoft (2015), “Microsoft Excel 2014 and Supporting Documentation.” The Microsoft Corporation, Redmond, Washington.

Morel, A., (1974). “Optical Properties of Pure Water and Pure Seawater.” In Jerlov and Steeman (eds), Optical Aspects of Oceanography. Academic Press, pp. 1-24.

Nicolet, (2004). “Nicolet FTIR User’s Guide.” Nicolet 6700 Fourier Transform Infrared Spectrometer User’s Manual and Supporting Documentation.

Ocean Optics, (2015). “OceanView 1.5 Software and Supporting Documentation.” http://oceanoptics.com/product-catagory/software/. Retrieved May 2015.

Zhang, X., Hu, L., (2009). “Estimating the Scattering of Pure Water from Density Fluctuation of the Refractive Index.” Optical Experiments, Vol. 17, pp. 1671-1678.

Zhang, X., Hu, L, He, M., (2009). “Scattering by Pure Seawater: Effects of Salinity.” Optical Experiments, Vol. 17, pp. 5698-5710.

APPENDIX C: EXAMPLE CALCULATIONS FOR THE CONSIDERED ANALYTICAL SOLUTION

C.1. Chapter Overview

Contained in this appendix is the derivation and example calculations used in the analytical solution of soil properties from visible to near infrared (Vis-NIR) diffuse reflectance spectra. The analytical solution employed both experimentally derived and literature values for soil and hydraulic properties. Symbols used in this appendix are preemptively defined in Table C.1.

The derivation of the algebraic solution for mass fractions of soil, water, and vapor are presented in Section C.2. The computation of theoretical values for scattering of liquid water is presented in Section C.3. The experimental values and example calculations of mass fraction of soil solids, soil water, and soil vapor is presented in Section C.4. The computation of soil potential is presented in Section C.5.

Table C. 1. Definition of symbols.

Symbol	Units[a]	Definition
k	L^{-1}	Absorption Coefficient
s	L^{-1}	Scattering Coefficient
m		Mass Fraction
R_∞		"Infinite" Depth Reflection
KMF		Kubelka-Munk Function
Q_1	L^{-1}	Defined Quantity 1
Q_2	L^{-1}	Defined Quantity 2
Q_3	L^{-1}	Defined Quantity 3
Q_4	L^{-1}	Defined Quantity 4
σ_w	$L^3 \cdot L^{-1}$	Area Extinction Coefficent
a	L	Particle Effect Radius
η		Real Component of Complex Refractive Index
m		(Real) Refractive Ratio at Interface
N	L^{-3}	Number Density (Quantity/L^3)
ρ_b	$M \cdot L^{-3}$	Bulk Soil Density
m_s		Mass Fraction of Soil
m_w		Mass Fraction of Water
m_v		Mass Fraction of Vapor
V_{soil}	L^3	Bulk Soil Volume
M_{total}	M	Total Mass of Soil, Water, Vapor
M_{sat}	M	Mass of Vapor at Saturation (STP)
ρ_{sat}	$M \cdot L^{-3}$	Density of Vapor at Saturation (STP)
RH	%	Relative Humidity
R		Ideal Gas Constant
V		Molecular Volume of Water

[a]L indicates units of length and m indicates units of mass

C.2. Derivation of Analytical Solution

Contained in this section is the algebraic derivation of the analytical solution for mass fraction of soil solids, soil water, and soil vapor using the Kubelka-Munk color theory (Kubelka and Munk 1931, Kubelka 1947). The starting equations are presented in Section C.2.1. The

expanded forms of the starting equations (showing all constitutive terms) are presented in Section C.2.2. Observed spectral data for two separate wavelengths were employed to form a system of equations with three equations and three unknowns (Section C.2.3). Four defined quantities were used in computation and to simplify the algebraic expressions and are presented in Section C.2.4. The algebraic solutions to the mass fraction of soil solids, soil water, and vapor are presented in Section C.2.5. The expanded form of the solution to the mass fraction of soil vapor is presented in Section C.2.6.

C.2.1. ***Starting Equations for Kubelka-Munk Analytical Solution***

The starting equations are presented in Equation C.1, Equation C.2, and Equation C.3. The relationship of the three phase (solid, water, and vapor) is presented in Equation C.4. Experimentally derived optical parameters (k and s) were obtained for all three soil types as previously described in Chapter 3 and Chapter 8. The observed reflectance spectra values were assumed to be infinitely deep (R_∞) due to the sample thickness (1.5cm) being at least 3 orders of magnitude greater than the expected penetration depth of the incident optical energy. Measured absorption, scattering, reflectance, and Kublka-Munk function (KMF) are presented in Figure C.1 and Figure C.2.

$$\frac{k}{s} = \sum \frac{m_i k_i}{m_i s_i} \qquad \text{(Hapke 2012)} \qquad \text{Equation C.1}$$

$$\frac{k}{s} = \frac{(1 - R_\infty)^2}{2R_\infty} = \text{KMF} \qquad \text{(Hapke 2012)} \qquad \text{Equation C.2}$$

$$1 = m_t = m_s + m_w + m_v \qquad \text{Equation C.3}$$

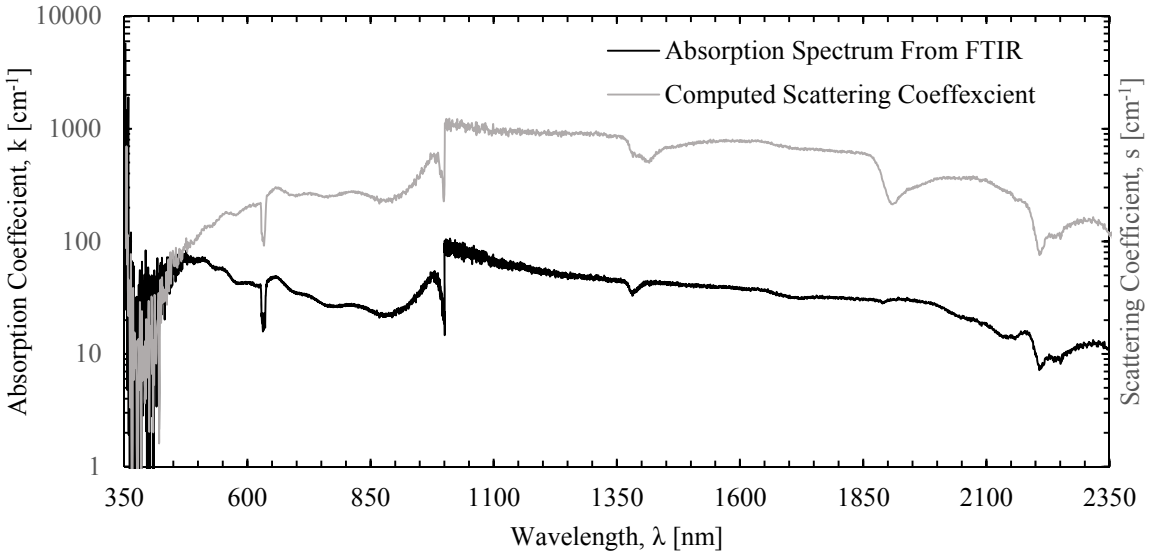

Figure C. 1. Absorption and scattering coefficient spectrum for illite soil used in analytical solution.

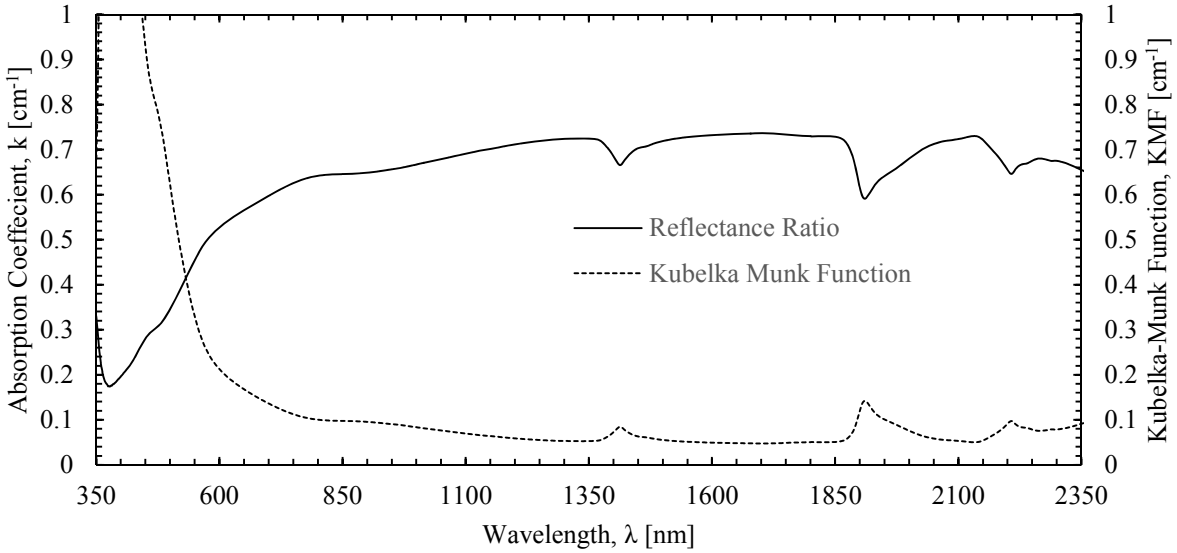

Figure C. 2. Measured reflectance spectrum and computed Kubelka-Munk function for illite soil (100 percent Sample).

*C.2.2. **Expanded Form of Kubelka-Munk Equations***

Contained in this section are the expanded starting equations as applied to the inversion of soil mass fraction values for soil. Presented in Equation C.4 is the expanded form of Equation C.1. Equation C.5 and Equation C.6 were derived using Equation C.3 and Equation C.4.

$$\frac{k}{s} = \frac{m_s k_s + m_w k_w + m_v k_v}{m_s s_s + m_w s_w + m_v s_v} \qquad \text{Equation C.4}$$

$$\frac{k}{s} = \frac{m_s k_s + m_w k_w + (1 - m_s - m_w) k_v}{m_s s_s + m_w s_w + (1 - m_s - m_w) s_v} \qquad \text{Equation C.5}$$

$$\frac{k}{s} = \frac{m_s k_s + m_w k_w + (1 - m_s - m_w) k_v}{m_s s_s + m_w s_w + (1 - m_s - m_w) \cdot 0} \qquad \text{Equation C.6}$$

C.2.3. ***Expanded Form of Kubelka-Munk Equations with Observations***

The value of the Kubelka-Munk function (Equation C.2) was calculated at both of the two wavelengths considered (e.g. 826nm and 855nm). Subsequently, by setting Equation C.1 and C.6 equal Equation C.7 was obtained. Equation C.12, for observations at the first wavelength (e.g. 826nm), was obtained by expanding and simplifying equation C.7 with the intermediate steps presented as Equations C.8 through C.11. Equation C.13 is an identical derivation of Equation C.12 for experimental values at the second wavelength (e.g. 855nm).

$$KMF_1(m_s s_{s1} + m_w s_{w1}) = m_s k_{s1} + m_w k_{w1} + (1 - m_s - m_w) k_{v1} \qquad \text{Equation C.7}$$

$$KMF_1(m_s s_{s1}) + KMF_1(m_w s_{w1}) = m_s k_{s1} + m_w k_{w1} + k_{v1} - m_s k_{v1} - m_w k_{v1} \qquad \text{Equation C.8}$$

$$KMF_1(m_s s_{s1}) + KMF_1(m_w s_{w1}) = k_{v1} + (k_{s1} - k_{v1}) m_s + (k_{w1} - k_{v1}) m_w \qquad \text{Equation C.9}$$

$$-k_{v1} + KMF_1(m_s s_{s1}) + KMF_1(m_w s_{w1}) = (k_{s1} - k_{v1}) m_s + (k_{w1} - k_{v1}) m_w \qquad \text{Equation C.10}$$

$$-k_{v1} = (k_{s1} - k_{v1}) m_s - KMF_1(m_s s_{s1}) + (k_{w1} - k_{v1}) m_w - KMF_1(m_w s_{w1}) \qquad \text{Equation C.11}$$

$$-k_{v1} = (k_{s1} - k_{v1} - KMF_1 \cdot s_{s1}) m_s + (k_{w1} - k_{v1} - KMF_1 \cdot s_{w1}) m_w \qquad \text{Equation C.12}$$

$$-k_{v2} = (k_{s2} - k_{v2} - KMF_2 \cdot s_{s2}) m_s + (k_{w2} - k_{v2} - KMF_2 \cdot s_{w2}) m_w \qquad \text{Equation C.13}$$

C.2.4. ***Defined Quantities***

To simplify the expressions previously presented in Equation C.12 and Equation C.13 as well as to increase computational efficiency by reducing the total number of computations, four quantities (Q_1, Q_2, Q_3, and Q_4) were defined. These aforementioned quantities are presented as Equation C.14 through C.17. Subsequently, Equation C.12 and Equation C.13 were re-written as Equation C.18 and Equation C.19, respectively.

$$Q_1 = \left(k_{s1} - k_{v1} - KMF_1 \cdot s_{s1}\right) \quad \text{Equation C.14}$$

$$Q_2 = \left(k_{w1} - k_{v1} - KMF_1 \cdot s_{w1}\right) \quad \text{Equation C.15}$$

$$Q_3 = \left(k_{s2} - k_{v2} - KMF_2 \cdot s_{s2}\right) \quad \text{Equation C.16}$$

$$Q_4 = \left(k_{w2} - k_{v2} - KMF_2 \cdot s_{w2}\right) \quad \text{Equation C.17}$$

$$-k_{v1} = Q_1 m_s + Q_2 m_w \quad \text{Equation C.18}$$

$$-k_{v2} = Q_3 m_s + Q_4 m_w \quad \text{Equation C.19}$$

C.2.5. ***Algebraic Solution for Quantities of Interest***

To simplify the system of equations represented in Equation C.18 (also presented as Equation C.20) and Equation C.19, Equation C.19 was re-written as Equation C.23 (intermediate steps are presented as Equation C.21 and Equation C.22). Equation C.22 was then subtracted from Equation C.20 (previously presented as Equation C.18) to obtain Equation C.23. Equation C.23 was expanded and simplified to obtain Equation C.26 (intermediate steps are presented as Equation C.24 to Equation C.25). Equation C.26 was then substituted back into Equation C.20 to obtain Equation C.29 (intermediate steps are provided in Equation C.27 and Equation C.28). The algebraic solution (Equation C.32) for mass fraction of water vapor was obtained by combining

Equation C.29, Equation C.30 and Equation C.31. Equation C.31 is presented in expanded form as Equation C.33.

$$-k_{v1} = Q_1 m_s + Q_2 m_w \qquad \text{Equation C.20}$$

$$-\left(\frac{Q_1}{Q_3}\right)k_{v2} = \left(\frac{Q_1}{Q_3}\right)Q_3 m_s + \left(\frac{Q_1}{Q_3}\right)Q_4 m_w \qquad \text{Equation C.21}$$

$$-\left(\frac{Q_1}{Q_3}\right)k_{v2} = Q_1 m_s + \left(\frac{Q_1 Q_4}{Q_3}\right)m_w \qquad \text{Equation C.22}$$

$$-k_{v1} + \left(\frac{Q_1}{Q_3}\right)k_{v2} = Q_1 m_s - Q_1 m_s + Q_2 m_w - \left(\frac{Q_1 Q_4}{Q_3}\right)m_w \qquad \text{Equation C.23}$$

$$-k_{v1} + \left(\frac{Q_1}{Q_3}\right)k_{v2} = Q_2 m_w - \left(\frac{Q_1 Q_4}{Q_3}\right)m_w \qquad \text{Equation C.24}$$

$$-k_{v1} + \left(\frac{Q_1}{Q_3}\right)k_{v2} = \left(Q_2 - \frac{Q_1 Q_4}{Q_3}\right)m_w \qquad \text{Equation C.25}$$

$$\frac{-k_{v1} + \left(\frac{Q_1}{Q_3}\right)k_{v2}}{\left(Q_2 - \frac{Q_1 Q_4}{Q_3}\right)} = m_w \qquad \text{Equation C.26}$$

$$-k_{v1} = Q_1 m_s + Q_2 \frac{-k_{v1} + \left(\frac{Q_1}{Q_3}\right)k_{v2}}{\left(Q_2 - \frac{Q_1 Q_4}{Q_3}\right)} \qquad \text{Equation C.27}$$

$$-k_{v1} - Q_2 \frac{-k_{v1} + \left(\frac{Q_1}{Q_3}\right)k_{v2}}{\left(Q_2 - \frac{Q_1 Q_4}{Q_3}\right)} = Q_1 m_s \qquad \text{Equation C.28}$$

$$m_s = \frac{-k_{v1}}{Q_1} - \frac{Q_2}{Q_1}\frac{-k_{v1} - \left(\frac{Q_1}{Q_3}\right)k_{v2}}{\left(Q_2 - \frac{Q_1 Q_4}{Q_3}\right)}$$ Equation C.29

$$m_s = \frac{-k_{v1}}{Q_1} - \frac{-Q_2 k_{v1} - \left(\frac{Q_2 Q_1}{Q_3}\right)k_{v2}}{\left(Q_1 Q_2 - \frac{{Q_1}^2 Q_4}{Q_3}\right)}$$ Equation C.30

$$m_v = 1 - m_w - m_s$$ Equation C.31

$$m_v = 1 - \frac{-k_{v1} + \left(\frac{Q_1}{Q_3}\right)k_{v2}}{\left(Q_2 - \frac{Q_1 Q_4}{Q_3}\right)} - \frac{-k_{v1}}{Q_1} - \frac{-Q_2 k_{v1} + \left(\frac{Q_2 Q_1}{Q_3}\right)k_{v2}}{\left(Q_1 Q_2 - \frac{{Q_1}^2 Q_4}{Q_3}\right)}$$ Equation C.32

$$m_v = 1 - \frac{-k_{v1} + \left(\frac{(k_{s1} - k_{v1} - KMF_1 \cdot s_{s1})}{(k_{s2} - k_{v2} - KMF_2 \cdot s_{s2})}\right)k_{v2}}{\left((k_{w1} - k_{v1} - KMF_1 \cdot s_{w1}) - \frac{(k_{s1} - k_{v1} - KMF_1 \cdot s_{s1})(k_{w1} - k_{v2} - KMF_2 \cdot s_{w2})}{(k_{s2} - k_{v2} - KMF_2 \cdot s_{s2})}\right)} - \bullet\bullet\bullet$$

$$\frac{-k_{v1}}{(k_{s1} - k_{v1} - KMF_1 \cdot s_{s1})} - \bullet\bullet\bullet$$ Equation C.33

$$\frac{-(k_{w1} - k_{v1} - KMF_1 \cdot s_{w1})k_{v1} - \left(\frac{(k_{w1} - k_{v1} - KMF_1 \cdot s_{w1})(k_{s1} - k_{v1} - KMF_1 \cdot s_{s1})}{(k_{s2} - k_{v2} - KMF_2 \cdot s_{s2})}\right)k_{v2}}{\left((k_{s1} - k_{v1} - KMF_1 \cdot s_{s1})(k_{w1} - k_{v1} - KMF_1 \cdot s_{w1}) - \frac{(k_{s1} - k_{v1} - KMF_1 \cdot s_{s1})^2 (k_{w2} - k_{v2} - KMF_2 \cdot s_{w2})}{(k_{s2} - k_{v2} - KMF_2 \cdot s_{s2})}\right)}$$

C.3. Example Calculation of Liquid Water Scattering (s_w).

The scattering coefficient of water for each individual wavelength was computed using the theoretical and empirical methods proposed by Bulcholtz (1995), Cox et al. (2002), and Kedenburg et al. (2012). All calculations assume standard laboratory conditions (i.e. temperature

and pressure). The volume scattering (extinction) coefficient was computed using the equation proposed by Cox et al. (2002) as presented as Equation C.34 and Equation C.35. The refractive index of water as a function of wavelength (Equation C.368) was computed using the empirical relationship proposed by Kedenburg et al. (2012) and is presented in graphical form as Figure C.1. The absorption coefficient of water was calculated using Equation C.37. An example computation is presented (as it is not documented elsewhere in this manuscript) in Equation C.38 through Equation C.46.

$$\sigma_w = \frac{8\pi}{3}\left(\frac{2\pi\eta_{medium}}{\lambda}\right)^4 a^6\left(\frac{M^2-1}{M^2+2}\right)^2 \qquad \text{(Cox et al. 2002)} \qquad \text{Equation C.34}$$

$$M = \frac{\eta_{partical}}{\eta_{medium}} \qquad \text{(Cox et al. 2002)} \qquad \text{Equation C.35}$$

$$\eta_w^2 - 1 = \frac{0.75831\ \lambda^2}{\lambda^2 - 0.01007} - \frac{0.08495\ \lambda^2}{\lambda^2 - 8.91377} \qquad \text{(Kedenburg et al. 2012)} \qquad \text{Equation C.36}$$

$$s_w = N_w \cdot \sigma_w \qquad \text{(Bulcholtz 1995)} \qquad \text{Equation C.37}$$

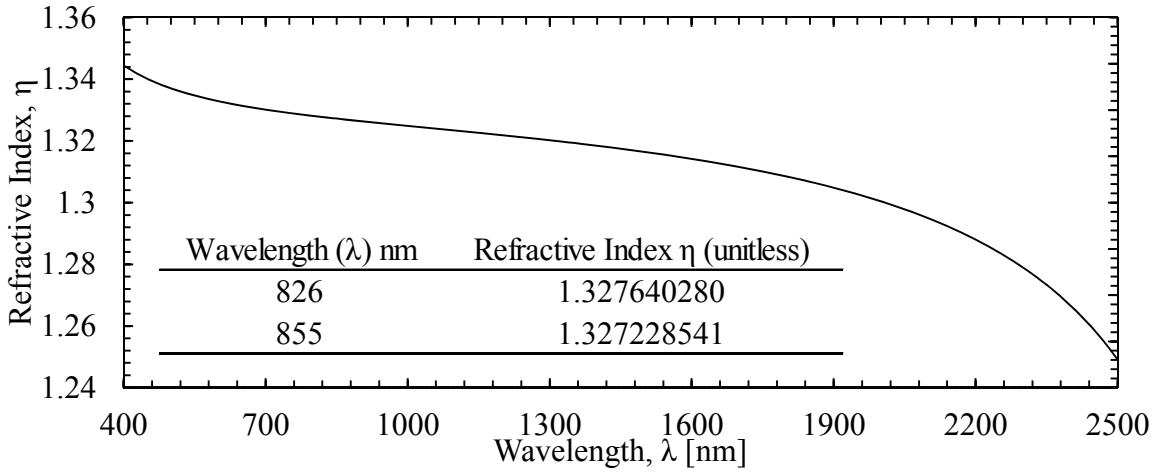

Figure C. 3. Refractive index of water as a function of wavelength using Kedenburg et al. (2012) relationship.

$$\sigma_w = \frac{8\pi}{3}\left(\frac{2\pi(1.0)}{823\cdot 10^{-7}\,cm}\right)^4\left[0.0005\cdot 10^{-6}\,m\cdot\frac{100\,cm}{1m}\right]^6\left(\frac{\left(1.32757/1.0\right)^2-1}{\left(1.32757/1.0\right)^2+2}\right)^2 \quad \text{Equation C.38}$$

$$\sigma_w = \frac{25.13274}{3}\left(\frac{6.283185}{823\cdot 10^{-7}\,cm}\right)^4\left[0.0005\cdot 10^{-4}\,cm\right]^6\left(\frac{0.762444}{3.762444}\right)^2 \quad \text{Equation C.39}$$

$$\sigma_w = 8.37758\left(76067.62\,cm^{-1}\right)^4\left[0.0005\cdot 10^{-4}\,cm\right]^6(0.202646)^2 \quad \text{Equation C.40}$$

$$\sigma_w = 8.37758\left(76067.62\,cm^{-1}\right)^4\left[0.0005\cdot 10^{-4}\,cm\right]^6(0.202646)^2 \quad \text{Equation C.41}$$

$$\sigma_w = 8.37758\times 3.34811\cdot 10^{19}\times 1.56250\,10^{-44}\times 0.041065\,cm^{-4}\cdot cm^6 \quad \text{Equation C.42}$$

$$\sigma_w = 1.80045\cdot 10^{-25}\,cm^2 \quad \text{Equation C.43}$$

$$s_w = N_w\cdot\sigma_w \quad \text{Equation C.44}$$

$$s_w = 33.3679\cdot 10^{21}\,cm^{-3}\times 1.80045\cdot 10^{-25}\,cm^2 \quad \text{Equation C.45}$$

$$s_w = 0.00601\,cm^{-1} \quad \text{Equation C.46}$$

C.4. Example Calculation of Mass Fraction Soil, Mass Fraction Water, Mass Fraction Vapor

An example calculation of mass fraction of soil solids, soil water, and soil vapor from reflected Vis-NIR spectral data using the previously documented analytical technique is contained in this section. All constants, material properties, and experimentally obtained data required to algebraically solve the analytical solution are tabulated as Table C.2. Soil data obtained using traditional laboratory testing methods were obtained using the techniques described in Chapter 3 and Chapter 9. All soil coefficient data was obtained as described in Chapter 4 and Chapter 8. A measured Vis-NIR soil spectra was randomly selected for the example calculation is presented in Figure C.4. Example computation of the Kubelka-Munk function values and the predefined

quantities previously described in Section C.2.4 is presented in Section C.4.1. Example computations for the calculation of soil mass fraction values is presented in Section C.4.2.

Table C. 2. Constants and material properties values for analytical solution**.**

Symbol	Value	Unit	Symbol	Value	Unit
λ_1	826	nm	λ_2	855	nm
k_{s1}	26.5257	cm^{-1}	k_{s2}	24.0231	cm^{-1}
k_{w1}	2.7238	cm^{-1}	k_{w2}	4.32	cm^{-1}
k_{v1}	0.0011	cm^{-1}	k_{v2}	$7.527x10^{-5}$	cm^{-1}
s_{s1}	270.55	cm^{-1}	s_{s1}	247.00	cm^{-1}
s_{w1}	0.00601	cm^{-1}	s_{w2}	0.00523	cm^{-1}
s_{v1}	0	cm^{-1}	s_{v2}	0	cm^{-1}
R_∞	0.353		R_∞	0.26075	

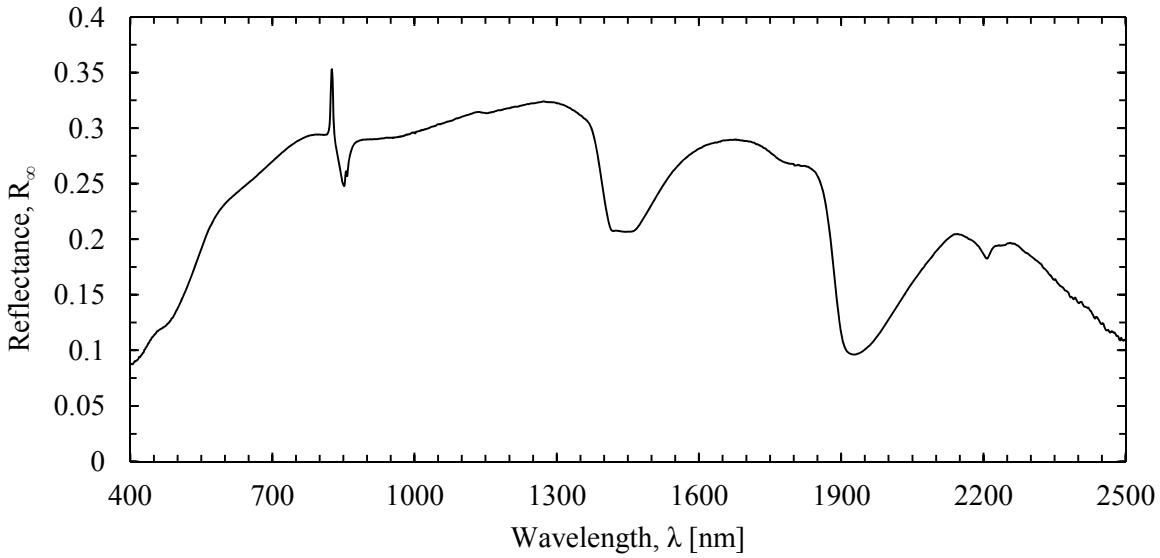

Figure C. 4. Example Vis-NIR spectral data for illite sample.

C.4.1. ***Computation of Kubelka-Munk Function and Predefined Quantities***

Contained in this section is the calculation of the Kubelka-Munk function values for the experimentally observed soil reflectance values and the computation of the predefined quantities previously described in Equation C.14 through Equation C.17. The computation of the Kubelka-Munk function for the two wavelengths considered (λ_1 = 826nm and λ_2 = 855nm) are presented in

Equations C.49 through C.53. Computation of the predefined quantities Q_1, Q_2, Q_3, and Q_4 are presented in Equation C.53 through Equation C.65.

$$\frac{k}{s} = \frac{(1 - R_\infty)^2}{2R_\infty} = \text{KMF} \quad \text{Hapke 2012} \quad \text{Equation C.47}$$

$$\frac{k}{s} = \frac{(1-0.3530)^2}{2 \cdot 0.3530} = KMF_1 \quad \text{Equation C.48}$$

$$KMF_1 = 0.5929 \quad \text{Equation C.49}$$

$$\frac{k}{s} = \frac{(1-0.2608)^2}{2 \cdot 0.2608} = KMF_1 \quad \text{Equation C.50}$$

$$KMF_2 = 1.0479 \quad \text{Equation C.51}$$

$$Q_1 = (k_{s1} - k_{v1} - KMF_1 \cdot s_{s1}) \quad \text{Equation C.52}$$

$$Q_1 = (26.5257 - 0.011 - 0.5929 \cdot 270.55) \cdot cm^{-1} \quad \text{Equation C.53}$$

$$Q_1 = -133.8928 \cdot cm^{-1} \quad \text{Equation C.54}$$

$$Q_2 = (k_{w1} - k_{v1} - KMF_1 \cdot s_{w1}) \quad \text{Equation C.55}$$

$$Q_2 = (2.7238 - 0.0011 - 0.5929 \cdot 0.00601) \cdot cm^{-1} \quad \text{Equation C.56}$$

$$Q_2 = 2.7191 \cdot cm^{-1} \quad \text{Equation C.57}$$

$$Q_3 = (k_{s2} - k_{v2} - KMF_2 \cdot s_{s2}) \quad \text{Equation C.58}$$

$$Q_3 = (24.0231 - 7.527 \cdot 10^{-5} - 1.0479 \cdot 247) \cdot cm^{-1} \quad \text{Equation C.59}$$

$$Q_3 = -234.8133 \cdot cm^{-1} \quad \text{Equation C.60}$$

$$Q_4 = (k_{w2} - k_{v2} - KMF_2 \cdot s_{w2}) \quad \text{Equation C.61}$$

$$Q_4 = \left(4.3144 - 7.527 \cdot 10^{-5} - 1.048 \cdot 0.00523\right) \cdot cm^{-1} \quad \text{Equation C.62}$$

$$Q_4 = 4.3144 \cdot cm^{-1} \quad \text{Equation C.63}$$

C.4.2. ***Example Calculations of Soil Mass Fractions***

Contained in this section are example calculations that were used to obtain measurements of the mass fraction of soil solids, soil water, and soil vapor. The calculations of mass fraction of soil solids was performed using Equation C.64 through Equation C.66. Similarly the mass fraction of water and vapor was calculated using Equation C.67 (previously presented as Equation C.30) through Equation C.73 and Equation C.74 (previously presented as Equation C.32) through Equation C.78, respectively.

$$m_s = \frac{-k_{v1}}{Q_1} - \frac{Q_2}{Q_1} \frac{-k_{v1} + \left(\frac{Q_1}{Q_3}\right) k_{v2}}{\left(Q_2 - \frac{Q_1 Q_4}{Q_3}\right)} \quad \text{Equation C.64}$$

$$m_s = \frac{-0.011\,cm^{-1}}{-133.8928\,cm^{-1}} - \frac{2.7192\,cm^{-1}}{-133.8928\,cm^{-1}} \bullet \bullet \bullet$$

$$\frac{-0.011 cm^{-1} + \left(\frac{-133.8928 cm^{-1}}{2.4915 cm^{-1}}\right) 7.527 \cdot 10^{-5} cm^{-1}}{\left(2.7191 cm^{-1} - \frac{-133.8928 cm^{-1} 4.3144 cm^{-1}}{-234.8133 cm^{-1}}\right)} \quad \text{Equation C.65}$$

$$m_s = -7.4671 \cdot 10^{-5} \quad \text{Equation C.66}$$

$$m_w = \frac{-k_{v1}}{Q_1} - \frac{-Q_2 k_{v1} + \left(\frac{Q_2 Q_1}{Q_3}\right) k_{v2}}{\left(Q_1 Q_2 - \frac{Q_1^{\,2} Q_4}{Q_3}\right)} \quad \text{Equation C.67}$$

$$m_w = \frac{-k_{v1}}{Q_1} - \frac{-Q_2 k_{v1} + \left(\frac{Q_2 Q_1}{Q_3}\right) k_{v2}}{\left(-133.8928 cm^{-1} \cdot 2.7191 cm^{-1} - \frac{\left(-133.8928 cm^{-1}\right)^2 4.3144 cm^{-1}}{-234.8133 cm^{-1}}\right.}$$ Equation C.68

$$m_w = \frac{-k_{v1}}{Q_1} - \frac{-Q_2 k_{v1} + \left(\frac{Q_2 Q_1}{Q_3}\right) k_{v2}}{\left(-34.6782\,\mathrm{cm}^{-2}\right)}$$ Equation C.69

$$m_w = \frac{-k_{v1}}{Q_1} - \bullet\bullet\bullet$$

$$\frac{-2.7191 cm^{-1} \cdot 0.011 cm^{-1} + \frac{2.7191 cm^{-1} \cdot -133.8928 cm^{-1}}{-234.8133 \cdot cm^{-1}} 7.527 \cdot 10^{-5} cm^{-1}}{\left(-34.6782 \mathrm{cm}^{-2}\right)}$$ Equation C.70

$$m_w = \frac{-k_{v1}}{Q_1} - \frac{3.1078 \cdot 10^{-3}\,\mathrm{cm}^{-2}}{\left(-34.6801 \mathrm{cm}^{-2}\right)}$$ Equation C.71

$$m_w = 8.2156 \cdot 10^{-6}\ \mathrm{cm}^{-1} - \frac{3.1078 \cdot 10^{-3}\,\mathrm{cm}^{-2}}{\left(-34.6782 \mathrm{cm}^{-2}\right)}$$ Equation C.72

$$m_w = 9.7827 \cdot 10^{-5}$$ Equation C.73

$$m_v = 1 - \frac{-k_{v1} - \left(\frac{Q_1}{Q_3}\right) k_{v2}}{\left(Q_2 - \frac{Q_1 Q_4}{Q_3}\right)} - \frac{-k_{v1}}{Q_1} - \frac{-Q_2 k_{v1} - \left(\frac{Q_2 Q_1}{Q_3}\right) k_{v2}}{\left(Q_1 Q_2 - \frac{Q_1^2 Q_4}{Q_3}\right)}$$ Equation C.74

$$1 = m_s + m_w + m_v$$ Equation C.75

$$m_v = 1 - m_s - m_w$$ Equation C.76

$$m_v = 1 - \left(-8.139610^{-5}\right) - \left(9.7827 \cdot 10^{-5}\right)$$ Equation C.77

$$m_v = 0.9998$$ Equation C.78

C.5. Example Computation of Soil Potential from Mass Fraction of Vapor

Contained in this section is an example calculation to obtain relative humidity (RH) and soil potential from the previously obtained mass fraction of vapor. The soil bulk density was used to obtain the volume occupied by 1g of soil, water, and vapor (Equation C.79 through C.81). Since in a remote sensing application the bulk density of the sample would not be known apriori the average bulk density of all PPE prepared samples.The mass of vapor was computed using Equation C.82 and C.83. The relative humidity was computed using the density of water vapor at saturation (793.17 $g \cdot m^{-3}$ at STP) and the soil volume (Equation C.84 to C.87). The computation of relative humidity resulted in a physically impossible solution as RH, by definition, cannot exceed 100 percent before condensation occurs. Computations were terminated at this point.

$$\rho_b = 1.7388 \frac{g}{cm^3}$$ Equation C.79

$$V_{soil} = \frac{1g}{1.7388 \frac{g}{cm^3}}$$ Equation C.80

$$V_{soil} = 0.5751 cm^3$$ Equation C.81

$$M_{vapor} = m_v \cdot M_{total}$$ Equation C.82

$$M_{vapor} = 0.9998 \cdot 1.0000 g = 0.9998 g$$ Equation C.83

$$RH = \frac{M_{vapor}}{M_{saturate}} 100\%$$ Equation C.84

$$RH = \frac{0.9998 g}{\rho_{sat} V_{soil}} 100\%$$ Equation C.85

$$RH = \frac{0.9998\,g}{793.17\frac{g}{m^3} * \left(\frac{1}{100}\frac{m}{cm}\right)^3 * 0.5751 cm^3} 100\%$$ Equation C.86

$$RH = 219,181\ \%$$ Equation C.87

C.6. Works Cited

Bulcholtz, Anthony, (1995). “Rayleigh Scattering Calculations for the Terrestrial Atmosphere.” Applied Optics, Vol. 34, No. 15, pp. 2765-2773.

Cox, A., DeWeerd, A., Linden, J., (2002). “An Experiment to Measure Mie and Rayleigh Scattering Cross Section.” American Journal of Physics, Vol. 70, No. 6, pp. 620-625.

Hapke, Bruce, (2012). “Theory of Reflectance and Remittance Spectroscopy.” 2 ed., Cambridge University Press.

Kedenburg, S., Vieweg, M., Gissibl, T., Giessen, H., (2012). “Linear Refractive Index and Absorption Measurements in Non-Linear Optical Liquids in the Visible and Near-Infrared Spectral Region.” Optical Materials Express, Vol. 2, pp. 1588-1611.

Kubelka, P., Munk, F., (1931). “Ein Beitragzur Optik der Farbanstriche.” (in German), Z. Technol. Physics., Vol. 12, pp. 593-620.

Kubelka, Paul, (1947). “New Contributions to the Optics of Intensely Light-Scattering Materials, Part I.” Journal of the Optical Society of America, Vol. 38, Number 5, pp. 448-457.